Piston Ring Lubrication - Influence of Sulphuric Acid Formation From High Sulphur Content Fuel

Falko Alexander Sautermeister

Submitted in accordance with the requirements for the degree of
Doctor of Philosophy

The University of Leeds
School of Mechanical Engineering

August, 2012

The candidate confirms that the work submitted is his own, except where work which has formed part of jointly-authored publications has been included. The contribution of the candidate and the other authors to this work has been explicitly indicated below. The candidate confirms that appropriate credit has been given within the thesis where reference has been made to the work of others.

Publications commenced during the cause of this study:

• Sautermeister, F.A., Priest, M. (2012): *"Physical and Chemical Impact of Sulphuric Acid on Cylinder Lubrication for Large 2-Stroke Marine Diesel Engines"* Tribology Letters, Vol. 47, Issue 2, 261-271, DOI: 10.1007/s11249-012-9979-7, "The final publication is available at <u>www.springerlink.com</u>"

• Sautermeister, F.A., Priest, M., Fox, M.F., Lee, P. M.(2012): *"Impact of Sulphuric Acid on Cylinder Lubrication for Large 2-Stroke Marine Diesel Engines: Contact Angle, Interfacial Tension and Chemical Interaction"*, Tribology International, DOI: 10.1016/j.triboint.2012.06.002

• Sautermeister, F.A., Priest, M., Fox, M.F.(2012): *"Impact of Sulphuric Acid on Cylinder Lubrication: Friction and Surface Modification"*, submitted

• Sautermeister, F.A., Priest, M., Fox, M.F.(2012): *"FTIR Lubricant Analysis – Concentration of Dispersed Sulphuric Acid"*, submitted

Sautermeister: Lead author, Co-authors: Editorial and technical suggestions

The publications can be found in the appendix

Navigare necesse est, vivere non est necesse

Gnaeus Pompeius Magnus, 106 – 48 B.C.

Meinen Eltern

Sybille und Manfred

Ruhet in Frieden

Acknowledgements

Abstract

Large 2-stroke marine Diesel engines burn high sulphur content residual fuel. The sulphur converts to aqueous sulphuric acid, H_2SO_4, and condenses on the cylinder liner surface, where it causes corrosive attack when not neutralised by the high alkaline reserve in the lubricant. Cylinder liner wear and deposit formation are observed to reflect poor lubricant distribution, surface temperature and sulphur fuel content, which all influence acid concentration. Currently neglected by the industry, is the catalysing action of H_2SO_4 on lubricant degradation and the rheology of entrained droplets in the oil film, which was the motivation for this study.

To understand the basic interaction of H_2SO_4 with the lubricant film, the saturated hydrocarbon squalane, $C_{30}H_{62}$, was chosen as a simple model oil in addition to fully formulated lubricants and their corresponding API Group I base oils. Interfacial tension between oil and aqueous solutions of H_2SO_4 was measured. Contact angles of aqueous solutions of H_2SO_4 immersed in $C_{30}H_{62}$ on piston ring chrome coating compared to grey cast iron cylinder liner material were measured. Fully formulated lubricant and API Group I base oil was used pure and emulsified with H_2SO_4 to lubricate a piston ring / cylinder contact on a Plint TE77 Tribometer. The main analytical techniques were the light microscope, SEM/EDX, XPS, FTIR, laser diffraction particle size characterisation, white-light-interferometer and viscometer.

Interfacial tension measurements of aqueous H_2SO_4 against $C_{30}H_{62}$ reveal a close relationship with the dissociation of H_2SO_4, which is also reflected by the formation of bituminous emulsions with API Group I base oil when above 40 %w/w H_2SO_4 and formation of solids when above 80 %w/w H_2SO_4 and high temperatures of around 120 – 165 °C or long storage times. For pure water, the contact angles were found to be large while they were small for concentrated sulphuric acid. Contact angles on chrome coating were bigger than on grey cast iron. Advancing contact angles were larger than static and receding contact angles, which was expected. During the TE77 tests, the degradation temperature of the base oil was lowered when in contact with H_2SO_4 from 250 to 80 °C for oxidation, from 300 to 170 °C for nitration and from 300 to 120 °C for deposit formation. Overall the appearance of the surfaces improved when sulphuric acid was added to both, the API Group I base oil and the fully formulated lubricant.

Table of Contents

List of Tables

List of Figures

Chapter 1
Introduction

A brief introduction to the specialities of the large 2-stroke marine Diesel engine is given in the following, assuming a basic understanding of internal combustion engines. A deeper introduction to ships machinery can be found in Woodyard, 2004.

The reader familiar with large 2-stroke marine Diesel engines might want to begin with section 1.1.4, starting with an introduction to the fluids used and created in the marine Diesel engine and their interaction to form deposits.

This introduction and the following literature review, chapter 2, lay the foundation to understand the aim of the present study, which is to find the impact of aqueous sulphuric acid, a typical condensate, on the cylinder lubricant and on the tribological behaviour of the piston ring – liner contact.

The chapter concludes with a short excurse on surface temperature and finally an overview of the thesis content.

1.1   The Big Diesel Engine

The successful introduction of the Diesel engine as a ship prime mover started only a few years after its invention by Rudolf Diesel in 1893. Between 1903 and 1912 several successful trials on inland and ocean going vessels were commenced. One example of how the new Diesel engine displaced the steam engine is the MV "Selandia", which is regarded as the first ocean going motor vessel. Her maiden voyage took place in 1912 and she sank 30 years later off Japan. During this time her two Burmeister & Wain DM8150X 4-stroke Diesel engines reliably enabled her to maintain a fully loaded service speed of 10.5 knots (Woodyard, 2004).

At the same time the first 2-stroke, engine powered, cargo liner MV "Monte Penedo" entered service. She was powered by the Sulzer 4S47 and was scrapped in 1969 in Rio de Janero (Woodyard, 2004).

These outstanding service times and the low operational costs made the Diesel engine the first choice for investors. Other prime movers like nuclear powered steam turbines, gas turbines or fuel cell powered electro motors can be found mainly in military or super fast ferry applications.

Today's engines are designed to stay in service for about 25 years, the life span of a merchant ship. The decision whether to choose 4-stroke or 2-stroke is guided mainly by two factors: passenger comfort and available space. Whenever possible a 2-stroke engine is the first choice for its more economic fuel consumption, with the drawback of strong low frequency vibrations and its enormous height. An illustration of the outstanding performance of large 2-stroke engines can be found in Figure 1.1. The very first engines achieved thermal efficiencies of 25 – 30 % and today's engines can exceed 50 % whilst also being more and more regulated in terms of nitrogen oxide, NO_x, emissions caused by high, thermodynamically favoured, combustion temperatures.
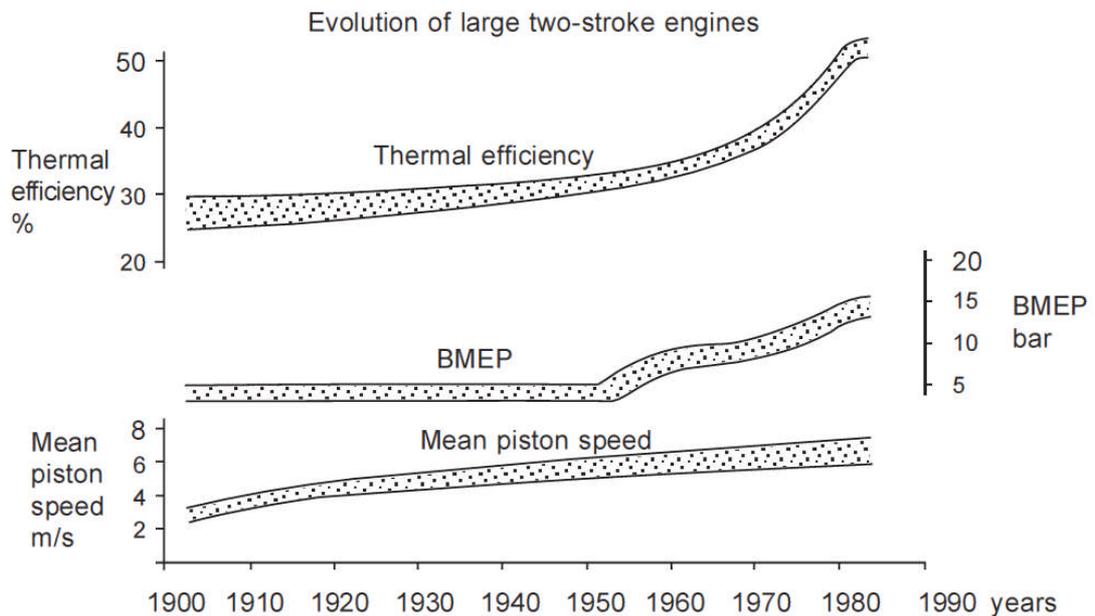
Figure 1.1: Evolution of large 2-stroke engines, (Woodyard, 2004)

100 years after powering the first oceangoing motor vessels, the two pioneering companies "Sulzer", today Wärtsilä, and "B&W", today MAN, with their design centres in Winterthur and Copenhagen are the main drivers for the development of large 2-stroke marine Diesel engines. For completion Mitsubishi as the third developing company must be mentioned. Mitsubishi's strength, however, is not the introduction of new engine technologies but superb know how in the manufacturing of the large components and complete ships, making it a valuable partner for joint development of new engines like the Wärtsilä RTA35 / Mitsubishi UEC35LSE 2-stroke engine. The engines are mainly produced under license in the far east but also some in Europe.

1.1.1 The Working Principle of Large 2-Stroke Diesel Engines

The reader may be most familiar with the working principle of a 4-stroke car engine and is aware of the 2-stroke engine as used in scooters, chain saws and lawn-mowers.

This combined knowledge helps a great deal to understand a large marine 2-stroke Diesel engine, however, there are a few key differences one must be aware of. Figure 1.2 shows the cross section of a Wärtsilä RTA96C.

The auxiliary blower is a electric driven compressor which helps to increase the scavenge air pressure during start up and low load operation of the engine, when the turbochargers are not working.

Back pressure air flaps prevent air flow from the scavenge air receiver back into the turbocharger or 'rotating' of the air through the auxiliary blower. Reasons for higher pressure in the scavenge air receiver than in the turbocharger can be the operating of the auxiliary blower, pumping of the pistons, surging of one turbocharger or a fire in the scavenge air receiver due to unwanted combustion of remaining oil and carbon deposits, which can damage the water separator and charge air cooler.

The oil in the clean oil sump of the crankcase, is unlike other engines, not used to lubricate the piston rings. The crankcase is separated from the piston underside. To ensure the separation of the crankcase from the scavenge air receiver, the piston rod, mounted on the cross head, is sealed by the gas and oil tight gland box.

The piston rings, mounted on the piston head, are lubricated by a forced lubrication, which feeds through the cylinder liner. This lubricant is different from the oil in the crankcase. It has a high alkaline reserve to neutralise sulphuric acid, H_2SO_4, formed during the combustion of heavy fuel oil, HFO, with high sulphur content. Any lubricant scraped off by the piston rings drains off through the waste oil drain.

The engine is started by starting air, blown into the combustion chamber at 30 bar to force the piston down and rotate the engine. There are three fuel injection nozzles situated around the exhaust valve. They spray the heated and pressurized heavy fuel oil tangentially into the combustion chamber. The timing of the injection is controllable either by the fuel pump plunger or in the case of a common rail system by solenoid valves.

In the centre of the cylinder head is the hydraulically driven exhaust valve. The timing of the exhaust valve is controllable, enabling the engine control

system to operate the engine with high efficiency at almost all load conditions and allows reversal of the running direction of the engine.
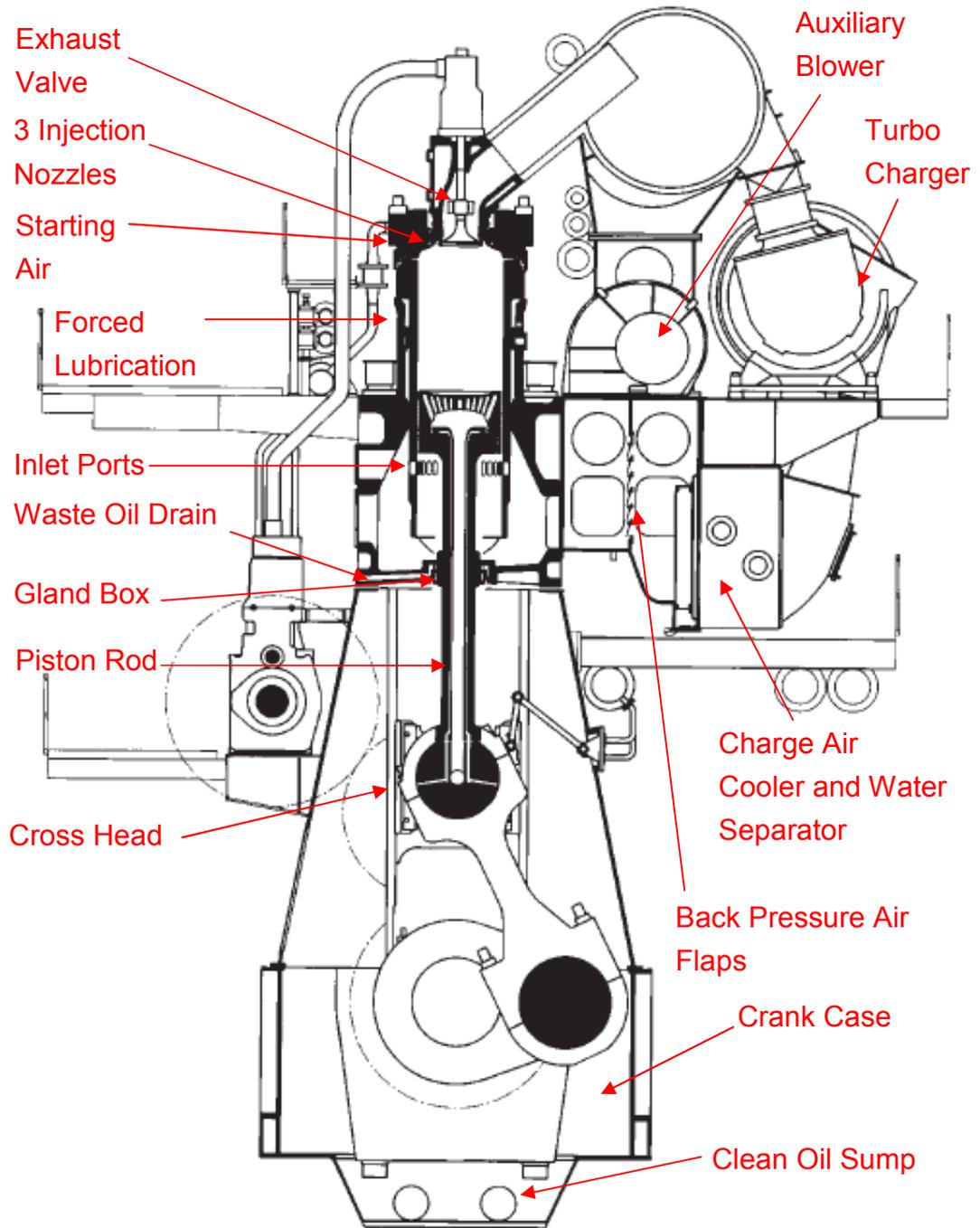
Figure 1.2: Cross-section of a modern large bore 2-stroke low speed Diesel engine, the Wärtsilä RTA96C (Woodyard, 2004)

Figure 1.3 illustrates the flow of fresh air and exhaust gas through the engine. First the fresh suction air is compressed in the turbocharger, spinning at about 7500 – 10000 rpm. Thereby the air pressure increases to about 3.5 bar at 150 °C. The compressed air is directed through the charge air cooler lowering the gas temperature to about 45 °C. In the tropics, huge

amounts of condensed water must be separated and drained from the air flow at this point. Before entering the scavenge air receiver, the compressed and cooled air passes back pressure air flaps, which prevent a back flow into the turbocharger. Fresh air can enter the combustion chamber when a piston approaches bottom dead centre, BDC, thus opening the inlet ports. Remaining hot exhaust gases are forced to leave the cylinder through the already opened exhaust valve. The exhaust gases from all cylinders are blown into one exhaust gas manifold which feeds the expansion side of the turbochargers mechanically fixed to the compression side.
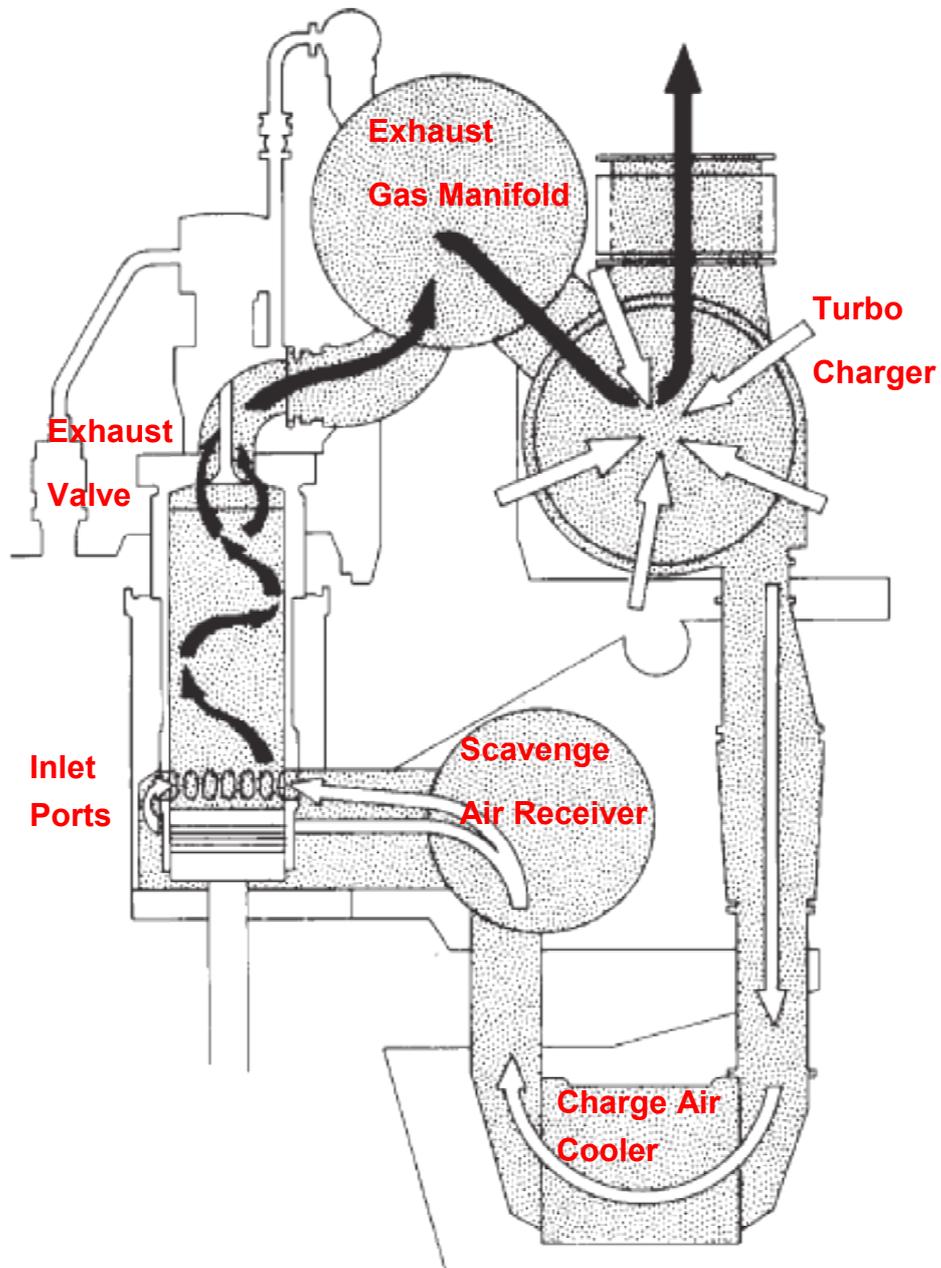
Figure 1.3: B&W uniflow scavenging system (Woodyard, 2004)

The timing of the gas exchange and injection of fuel is shown in Figure 1.4. "*Starting at Top Dead Centre, TDC, combustion is already underway and the exhaust opens at 110 – 120° after TDC to promote a rapid blow-down before the inlet ports open about 20 – 30° later (130 – 150° after TDC). In this way the inertia of the exhaust gases - moving at about the speed of sound - is contrived to encourage the incoming air to flow quickly through the cylinder with a minimum of mixing, because any unexpelled exhaust gas detracts from the weight of air entrained for the next stroke. The exhaust should close before the inlet on the compression stroke to maximize the charge*" (Woodyard, 2004). Due to the fixed position of the inlet ports relative to the piston stroke, the inlet will be closed as many degrees after BDC as it opened before (i.e. again 130 – 150° before TDC) (Woodyard, 2004). Injection commences at about 10° before TDC given by the load dependent control settings, and combustion occurs over 30 – 50°(Woodyard, 2004).
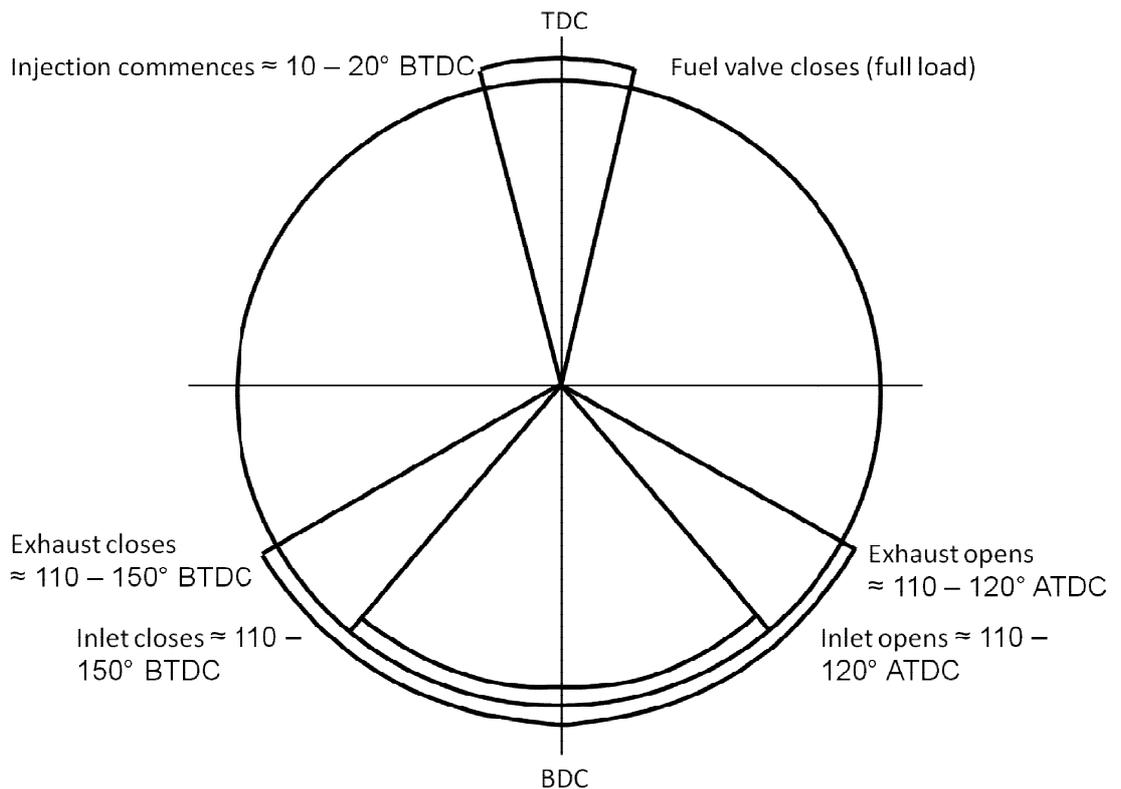
Figure 1.4: Timing of the 2-stroke cycle (Woodyard, 2004)

These events result in a pressure in the combustion chamber as shown schematically in Figure 1.5, referred to as "cylinder pressure".
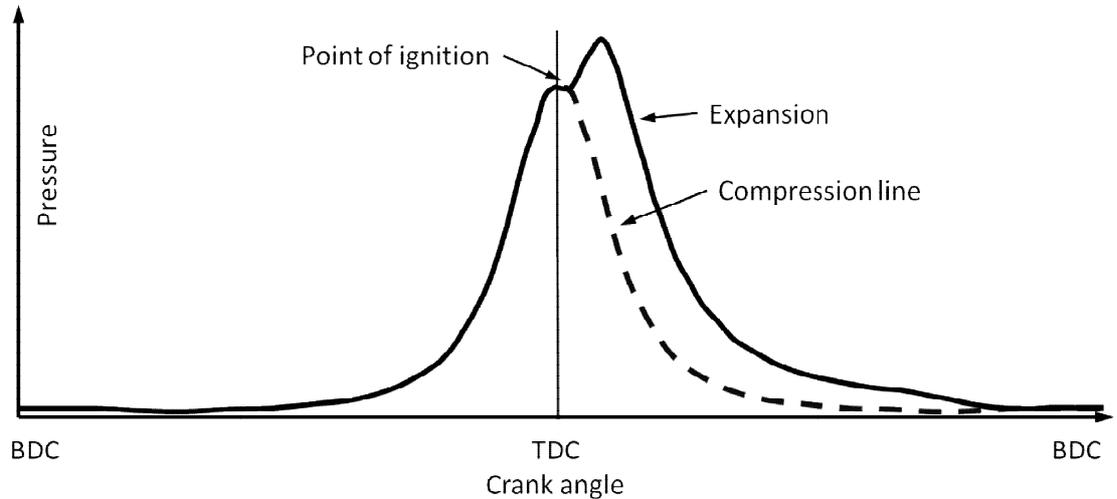
Figure 1.5: Typical indicator diagram of the pressure in the combustion chamber drawn over crank angle (Woodyard, 2004)

The main engine of large ships is fitted directly to the propeller shaft without further transmission. For a fixed pitch propeller the power output of the engine is proportional to the third power of engine speed due to the high resistance of water. For smaller ships, controllable pitch propellers are used in some cases. They can act like a transmission resulting in a dangerous idle load but can also help to dampen shaft vibrations.

1.1.2 Parts Involved in Piston-Running

Figure 1.6 shows a cross section of the engine parts directly involved in piston running, where this study is concentrating upon. It is sketched according to the Wärtsilä RT96 engine type but any modern large bore 2-stroke marine Diesel engine shows in principle the same design features. Since the invention of the single pieced self-expanding piston ring by John Ramsbottom in 1854, a lot of research work was published on the functional behaviour of the piston ring seal in combination with the piston and the cylinder liner. The following is merely a listing and the following literature is recommended for deeper information (Englisch, 1958), (Zima, 2005), (Strachan, 1973), (Ruddy, 1979) and (Economou, 1976). The last three sources being doctoral research studies committed to large bore Diesel engines.

The cylinder liner is made of sand-cast, grey cast iron. There are various kinds of surface machining methods specified, for the case here it is plateau honing, similar to automotive applications. Just above the piston crown bottom dead centre, BDC, scavenge air ports are cut through the liner where fresh charge air enters the combustion chamber before the compression

stroke. Along the length of the cylinder liner, lubricating quills for the various lubrication systems, section 1.1.4, can be found. The cylinder lubricant is force fed through the surrounding cooling water jacked and through the liner wall towards the combustion chamber. Just above the top dead centre, TDC, of the top piston ring a recess is cut for the anti polishing ring.

The anti polishing ring, APR, is made of alloyed steel with a higher thermal elongation coefficient than the grey cast iron cylinder liner material, to create a tight fit during operation. It's inner diameter is slightly smaller than the bore diameter of the cylinder liner. With its sharp bottom edge, it is meant to scrape off any excess deposit from the conical piston crown which would otherwise come into contact with the cylinder liner running surface. An excess of hard deposits on the piston crown can scrape off the oil film and damage the liner surface, by so called 'bore polishing', hence the name of the APR.

The piston crown is usually made of forged steel. It is cooled from the inside by crankcase oil, pumped through the hollow piston rod. Depending upon the number of piston rings, hard chrome plated grooves are turned into the piston crown. Bolted to the bottom of the piston crown is the piston skirt, usually made of cast iron with or without rolled-in soft metal inserts, in the case here made of bronze. The piston skirt has a slightly bigger diameter than the piston crown to cushion lateral movements of the piston in case the gas forces in the piston ring pack cannot centre the piston. This is most common at bottom dead centre, during gas exchange. Piston slap is not a major issue with cross head engines but there is still some back lash from the cross head due to clearances.
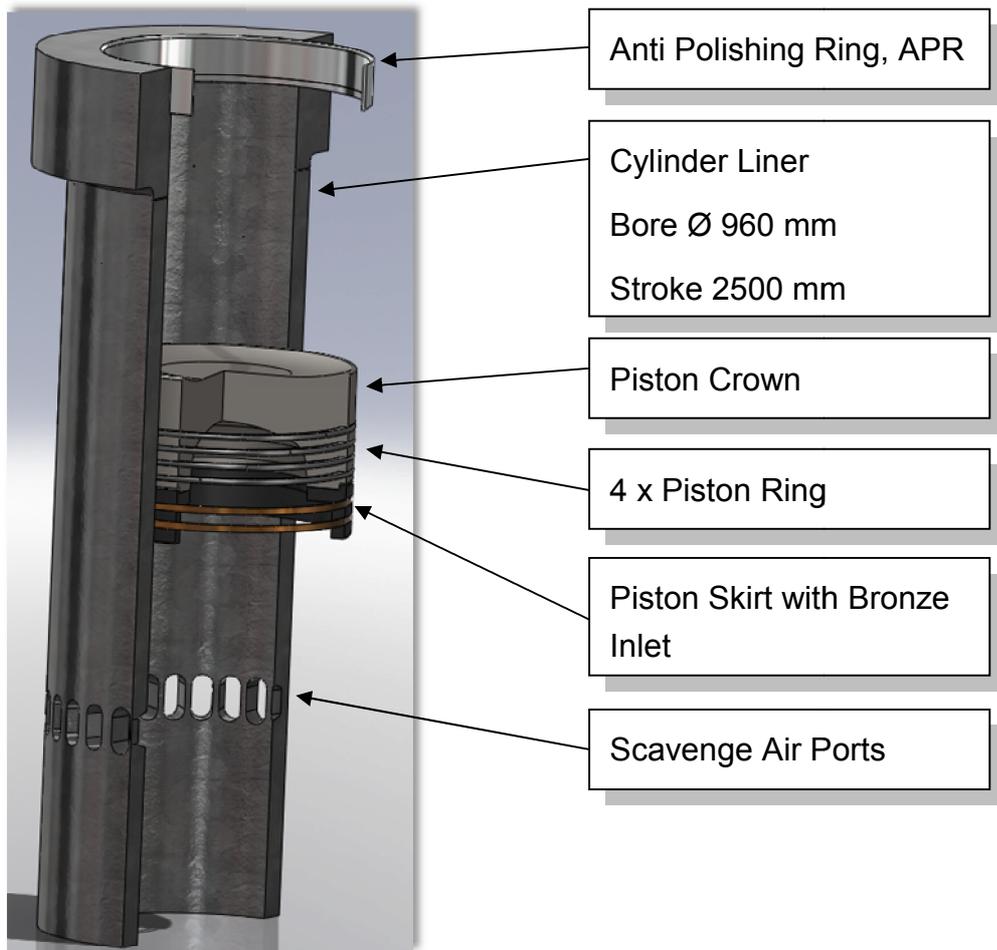
Figure 1.6: Parts directly involved in piston running, sketched after the Wärtsilä RT96 engine type

The piston rings can move freely in the piston ring grooves of the piston crown. They are made of grey cast iron with a great variety of surface configurations. Most modern piston rings are coated to improve wear resistance or improve running-in. In the case here the piston rings are coated with a particle-reinforced, electro plated, chrome coating. Usually the piston rings are pre-profiled with a barrel shape, to improve hydrodynamic lubrication. The piston rings are basically radial compressed springs pressing against the liner surface, creating a tight fit to seal against the hot and highly pressurised combustion gases. Acting as radial springs, the piston rings cannot be completely closed, thus creating a gap where the compressed gas can pass. The piston rings act like a labyrinth seal and the pressure differences between the piston rings create forces in the radial and axial directions, producing a mechanically very dynamic system. Dynamic forces due to inertia are minimal in large 2-stroke marine Diesel engines due to high gas forces and relatively low engine speeds.

1.1.3 The Fuel

A key factor for a commercial competitive marine Diesel engine design is the ability to function on the cheapest available fuel. The current standard fuel for these engines is colloquially called 'Heavy Fuel Oil', HFO, residual fuel with high sulphur content, available in various grades. The high sulphur fuel content traces back to the sulphur crude oil content, ranging from 0.01 - 5.54 %w/w within geologically small areas. Venezuela's sulphur crude oil content for example ranges between 0.09 and 5.54 %w/w (Carrales, et al., 1975). Biological organisms, the source of crude oil, contain sulphur in their cells. Dry tobacco leaves, for example, contain 0.5 – 0.8 %w/w sulphur (Wirtz, et al., 2007) but this is not sufficient to account for the high sulphur crude oil content, which is more readily explained by the dissolution of minerals like anhydrite gypsum following the reaction:

$$CH_4 + CaSO_4 \rightarrow CaCO_3 + H_2S(aq.\,or\,gas) + H_2O \qquad (1.1)$$
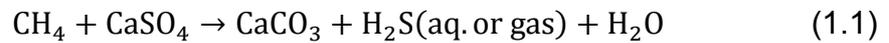
Anhydrite gypsum forms on top of salt domes regularly found locally within the area of oil reservoirs (Saunders, et al., 1996) originating from prehistoric fertile shallow sea water areas under cycles of evaporation and flooding, consequently buried in the earth's crust by tectonic action. The salt is lighter than the surrounding rock and rises, creating cracks, allowing the oil to rise from deeper zones to depths accessible by mining equipment.

The International Maritime Organisation, IMO, reduced maximum sulphur fuel content, Figure 1.7, for ocean going ships (IMO-General) from 4.5 to 3.5 %w/w in 2012 and in Sulphur Emission Controlled Areas (IMO-SECA) from 1.5 to 1 %w/w in 2010. The intention was to reduce SO_x exhaust gas emissions for environmental reasons. Both IMO legislations, however, foresee the use of exhaust gas after-treatment plants to reduce SO_x emissions instead of reduced fuel sulphur content. Apart from the legislation, the available average sulphur fuel content in 2005 was 2.8 %w/w (CIMAC Working Group "Marine Lubricants", 2007). SO_x after-treatment plants are economically only feasible for either large ships or ships primarily operating in SEC areas with a supply of cheap high sulphur fuels. While the demand for low sulphur fuels will rise, the sulphur fuel content for vessels with after-treatment plants might actually rise.

Also shown in Figure 1.7 is the legislation development in Switzerland and in EU-Territorial waters. These figures show the possibility of sulphur reduction during refining and the minimum sulphur fuel content for test bed engines or ships entering strictly legislated territorial waters. Irrespective of the general

trend for fuel sulphur reduction, the engines have to function for both the highest and lowest sulphur fuel content.
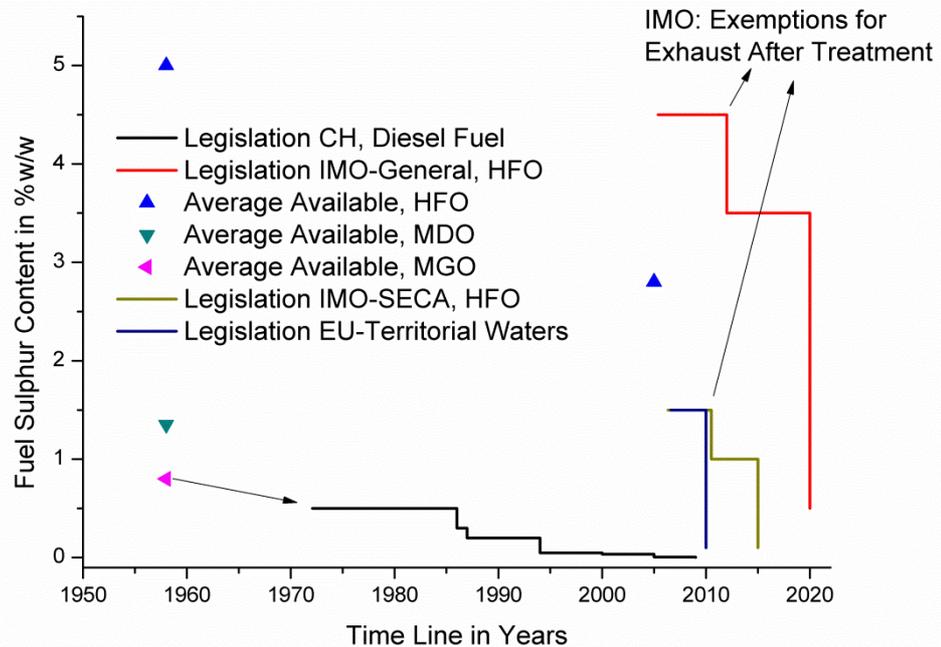
Figure 1.7: Historical development of average available and legislated sulphur fuel content. (Englisch, 1958), (CIMAC Working Group "Marine Lubricants", 2007), (Ministry of Transport and Communications Finnland, 2009), (BAFU & UVEK, 2011)

The high sulphur content is not the only feature of this fuel. High trace metal, water and particle levels require a chemical analysis for each bunkered batch and a extensive onboard fuel treatment plant with settling tanks, water-particle separators and filters. The high viscosity of HFO requires the fuel to be heated throughout the treatment until injection to about 120 – 180 °C.

1.1.4 Piston Ring Lubrication

Large 2-stroke marine Diesel engines feature a forced and once through piston ring lubrication system independent from the crankcase lubricant. The cylinder lubricant has to withstand higher temperatures, dirt and condensate input as well as higher mechanical stress. The functional differences between crankcase and cylinder lubricant explain the separation on the one side but also the degradation of the cylinder lubricant would be unacceptable for the lubrication of the crank web, gears and its use as control oil.

Many researchers and engineers have theoretically predicted minimum oil film thickness between piston rings and cylinder liners by the equation

derived by Prof. Osborne Reynolds in 1885 (Reynolds, 1886). The integration terms for circumferential velocity, as one driver for circumferential lubricant distribution, of the lubricant by circumferential pressure gradient and entraining action (Priest, 2010) is usually neglected to save numerical calculation, arguing negligible influence. The argument is practical, shown by the difficulty of explaining circumferential oil distribution by the movement of the piston rings alone and explains losses of freshly fed lubricant by throwing-off in the turning points. Circumferential oil distribution is assisted by the radial gas flow through the piston ring pack, the squeezing of lubricant between piston ring side flanks and piston ring groove flanks and oil misting due to back pressure when the piston rings pass the scavenge air ports.

Figure 1.8 shows a cylinder liner surface after 6293 operating hours. The cylinder head has been removed and the visible area is from the top dead centre of the top piston ring downwards to about ¾ of the stroke. The position of holes for lubricant entry is indicated by arrows. Towards top dead centre the liner surface shows a inhomogeneous pattern with slim dark lines originating from the lubrication entry. In this area, the circumferential oil distribution is only achieved by the aforementioned mechanisms.

Also visible in Figure 1.8 is a groove connecting the points of lubricant entry. The working principle of this oil distribution groove is shown in Figure 1.9. To both sides of the holes, the groove is declining. The angle is chosen steep enough to bypass one piston ring. The resulting gas flow, caused by the pressure differences between the piston rings, distributes the lubricant mist in the circumferential direction. The main direction of the resulting gas flow however is downwards, hence the inhomogeneous distribution of the lubricant and its additives towards top dead centre, resulting in the pattern shown in Figure 1.8. The dark stripes, originating from the lubricant entry holes, are caused by the high alkaline reserve of the continuously fed fresh cylinder lubricant, which protects the surface from corrosive attack by condensing sulphuric acid, section 1.2 and 1.3, and from abrasive wear by the formation of a calcite boundary layer, chapter 2. In between these stripes of fresh lubricant supply, the lubricant is more depleted from additives and has longer resting times, which increase the lubricant degradation, causing increased corrosive attack and deposit formation, section 1.4.

Figure 1.8: Cylinder liner surface after 6293 running hours (Spahni, et al., 2010). Arrows indicate position of oil quills in the oil distribution groove, Figure 1.9
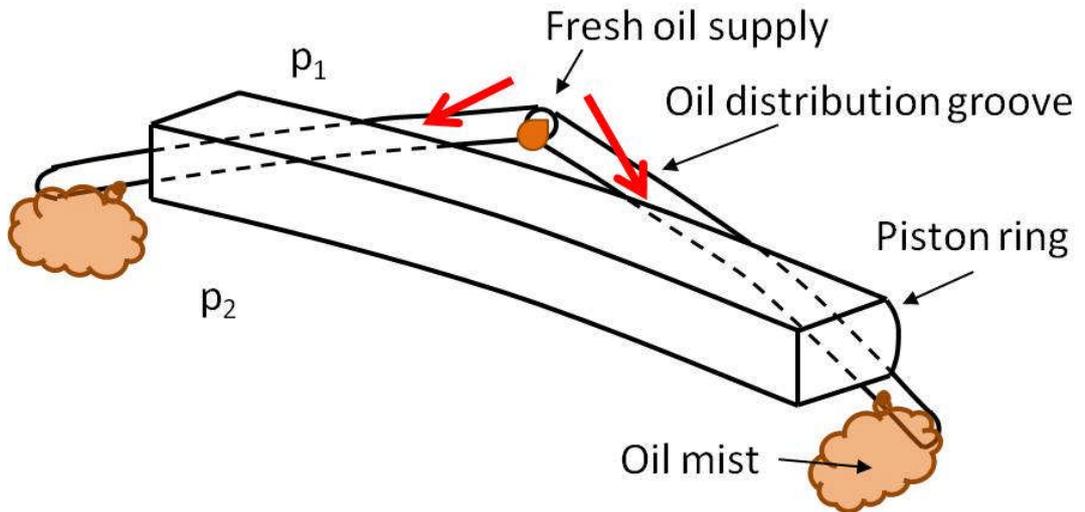
Figure 1.9: Functionality of the oil distribution groove, shown in Figure 1.8, when gas pressure $p_1 > p_2$

This is not only a visual effect but influences local wear and can be measured, especially close to the top dead centre of the piston rings. Scuffing usually starts in midstroke, in-line with the stripes from fresh

lubricant supply. In the clearances between piston rings and piston ring grooves, the lubricant has even longer resting times and lubricant degradation causes the build up of thick and hard deposits, hindering the free movement of the piston rings.

The connecting of lubricant supply holes by a piston ring bypassing groove is one way to assist the circumferential oil distribution. Another method was patented by MAN (Fogh, 1997) and features an overlapping gas tight piston ring gap and angular slots across the piston ring running surface all around the top piston ring. Although the design is claimed to reduce thermal differences around the ring, the flow of lubricant mist is unavoidable.

Other than gas jets, which influence the dynamics of the piston ring pack, the lubricant can also be injected at high pressures through nozzles with radial orifices spraying the lubricant tangentially onto the cylinder liner wall or directly into the piston ring pack. Injection timing is crucial for this system to avoid spraying onto the hot piston crown or into the hot expanding gases. The nozzles require deep grooves in the liner where fresh lubricant can accumulate, creating the same problem of conventional drip-feed lubrication systems with reduced circumferential additive distribution. The same can occur from nozzles with big dead volumes, leading to dripping after the injection has finished.

One of the main challenges for the large 2-stroke marine Diesel engine is inhomogeneous lubricant-additive distribution.

1.2   Acid Concentration on the Piston Running Parts

During combustion the fuel sulphur, section 1.1.3, converts completely to form 100 % sulphur dioxide, SO_2. Further oxidation yields 0.3 – 7 % sulphur trioxide, SO_3, which rapidly reacts with water to form sulphuric acid, H_2SO_4, at various concentrations (CIMAC Working Group "Marine Lubricants", 2007). Catalysis by vanadium pentoxide, V_2O_5, at 450 – 600 °C increases the yield of SO_3 (State of New South Wales through the Department of Education and Training and Charles Sturt University). V_2O_5 arises in marine Diesel engines from the combustion of HFO with restricted maximum vanadium levels of 600 mg/kg (Schlager, et al., 2006), (CIMAC Working Group "Heavy Fuel", 2003). These reactions are specified below.

$$2SO_2(g) + O_2(g) \xrightarrow{V_2O_5\ 450-600°C} 2\,SO_3(g) + heat \qquad (1.2)$$

$$SO_3(g) + H_2O(l) \rightarrow H_2SO_4(aq) + heat \qquad (1.3)$$
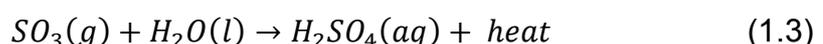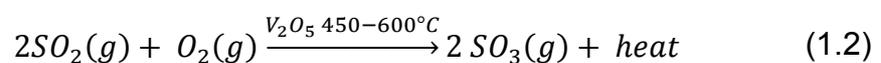
The resulting H_2SO_4 condenses on the cylinder wall and the higher the dew point, the more readily condensation occurs. The dew point equation, (1.4), of SO_3 with H_2O according Verhoff (Huijbregts, et al., 2004) results in a large increase in dew point for small amounts of SO_3. The equation uses the partial pressures p (atm) in the gas phase. The resulting condensate is H_2SO_4.

$$T_d = \frac{1000}{[2.276 - 0.0294 * ln(p_{H_2O}) - 0.0858 * ln(p_{SO_3}) + 0.0062 * ln\,(p_{H_2O} * p_{SO_3})]} \quad (1.4)$$

Also experimental studies have shown the massive increase in dew point for small amounts of SO_3 in the gas phase (Land, 1977).

Applying typical values for an engine to equation (1.4), dew point temperatures, T_d (°C) , are found to be substantially below the gas temperature in the combustion chamber; therefore no condensation occurs in the gas volume. The dew point temperatures, however, are well above cylinder wall temperatures; therefore condensation will take place at the wall. High concentrations of condensing H_2SO_4 can be predicted from the vapour-liquid phase diagram (Land, 1977) for low concentrations of H_2SO_4 in the gas phase.
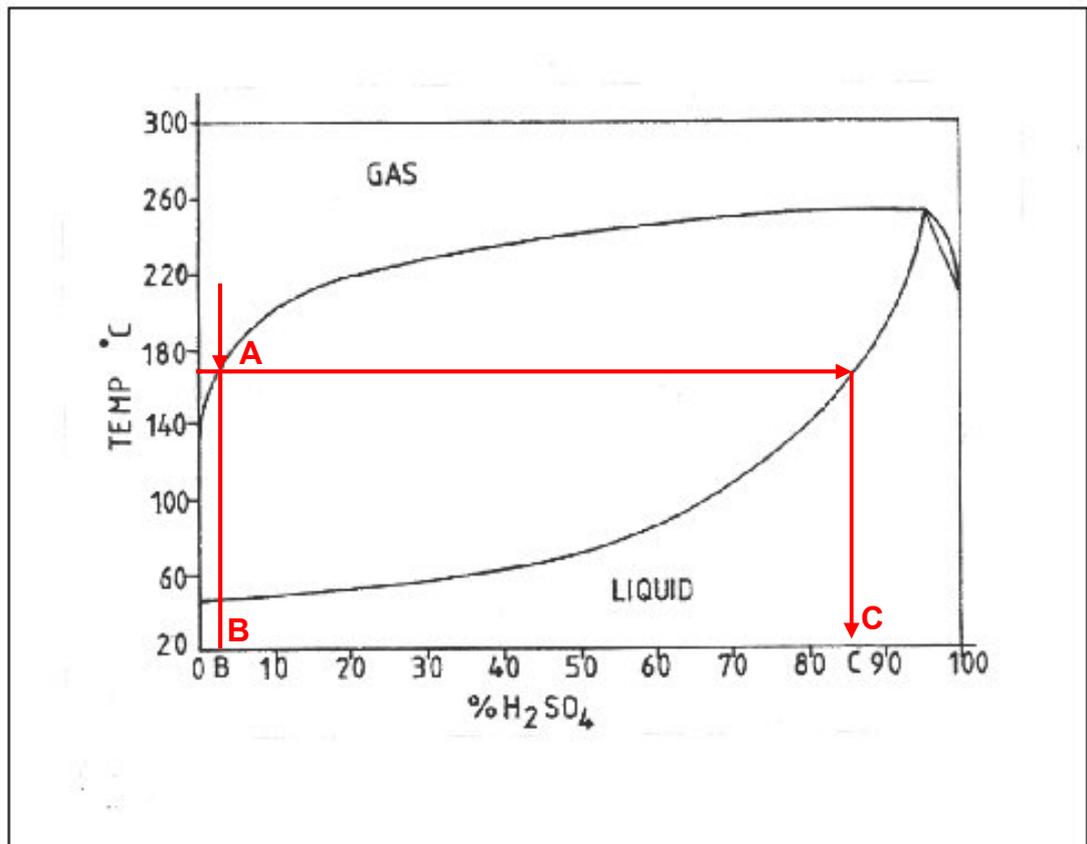
Figure 1.10: The phase diagram for vapour of H_2SO_4 and water for a combined partial pressures of ~0.1 bar (Land, 1977)

Figure 1.10 shows the phase diagram with the example of vapour of the concentration 'B' condensing on a wall with temperature 'A', resulting in a liquid of concentration 'C'. Evaporation follows the same path but the concentration of the remaining acid on the wall gradually increases as evaporation proceeds.

The dew point temperature, T_d(°C) of SO_2 with H_2O, derived from the dew point equation (1.5) according Kiang (Huijbregts, et al., 2004), for all ratios of partial pressure, p (mmHg), is lower than for pure water, meaning pure water condenses before sulphurous acid, H_2SO_3, can be formed as a condensate.

$$T_d = \frac{1000}{[3.9526 - 0.1863 * ln(p_{H_2O}) + 0.000867 * ln(p_{SO_2}) - 0.00091 * ln(p_{H_2O} * p_{SO_2})]} \quad (1.5)$$

Because of the possible condensation of pure water as well as higher concentrations of sulphuric acid with many influencing factors, this study covered the range of concentrations from 0 – 98 %w/w H_2SO_4. Based on exhaust gas composition (CIMAC Working Group "Exhaust Emission Control", 2008), realistic condensate concentrations, however, range from ~5 – 80 %w/w, and is confirmed in literature (Graham, et al., 1960).

Depending upon concentration and temperature, H_2SO_4 dissociates in water to form HSO_4^-, H_3O^+, SO_4^{2-} and pure H_2SO_4 molecules in two steps, (Young, et al., 1959).

$$H_2SO_4 + H_2O \rightleftarrows HSO_4^- + H_3O^+ \quad (1.6)$$

$$HSO_4^- + H_2O \rightleftarrows SO_4^{2-} + H_3O^+ \quad (1.7)$$
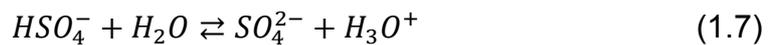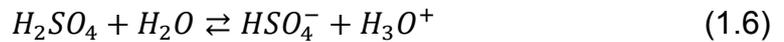
The ionic composition at various concentrations can be found in chapter 4, revealing good correlation with interfacial tension measurements.

Condensation and evaporation are not only influenced by concentration and temperature but also pressure. High pressures and low temperatures enhance condensation while low pressures and high temperatures favour evaporation. The temperatures of the cylinder liner wall must not only be compared with the pressures in the combustion chamber but also with the pressures between the piston rings and pressures in the oil film. The inter-ring pressure during expansion can become higher than the cylinder pressure (Englisch, 1958) for low wall temperatures, thus enhancing condensation. The hydrodynamic oil film pressure on the trailing side of the piston ring can fall below ambient (Dowson, et al., 1979) at high oil film temperatures, thus enhancing evaporation and therefore increasing the remaining acid concentration.

One of the main challenges for the large 2-stroke marine Diesel engine is uncontrolled condensate formation in the lubricant film.

1.3   Corrosive Attack

The engine components can experience corrosive wear due to condensation of H_2SO_4. Corrosion, however, only takes place when condensate droplets adhere to the wall against the shear of the surrounding liquid with viscosity, η, and velocity, U. Adherence of a droplet to a wall under shear is quantified by the capillary number , $Ca=\eta *U/\sigma$. Exceeding a critical value of Ca causes the droplets to deform until they split or completely detach from the wall. Above the critical capillary number, droplets with contact angles between 60 and 90° will split leaving smaller droplets on the wall, while droplets of 120° are likely to detach from the wall completely (Schleizer, et al., 1999). The velocity, U, experienced by the droplet is given by the variation in piston speed and droplet size. Contact angles and interfacial tension, σ, were measured and are presented in chapters 4 and 5.

The cylinder liner material is a non-homogeneous and coarse sand-cast grey cast iron, chapter 6. Depending upon acid concentration the corrosion can be very selective (Demmerle, et al., 2001). In chapter 5, examples of selective corrosion are shown. Concentrated H_2SO_4 dissolves the hard iron phosphides leading to increased abrasive wear by foreign particles. Worse is the corrosion of the pearlitic matrix by dilute H_2SO_4 resulting in protruding hard phases likely to break and fall out, causing deep gouges with protruding edges on the piston ring and liner, which can lead to further damage. The wear rates observed at Top Dead Centre for the latest large bore engines are around 0.01 mm/1000h after 6000h (Spahni, et al., 2010).

The coating materials used for the piston rings are more diverse but this study concentrates on the aluminium oxide filled galvanic chrome coating "CKS" from FM-Goetze (Cantow, 2004), as predominantly used in Wärtsilä 2-stroke engines. In the plating process, hot dilute H_2SO_4 is used to etch porosities to give improved oil retention of the surface (Burstein, et al., 1994). It therefore seems strange to find chrome-plated parts in an environment attacked by H_2SO_4. In this study corrosive attack on the chrome coating was observed down to concentrations of 10 %w/w H_2SO_4, chapter 5. However, service experience with chrome plated piston rings and piston ring grooves in marine Diesel engines is good, although wear rates are high compared to other heavy duty engines burning low sulphur fuels. The top

ring wear rates for the latest large bore engines are approximately 0.02 mm/1000h after 6000h (Spahni, et al., 2010).

The neutralisation of the H_2SO_4 formed by combustion, is taken care of by an alkaline reserve in the lubricant with Total Base Number, TBN, levels of 40 – 70 mg KOH/g. The alkaline reserve is usually added into the lubricant by dispersing calcium carbonate, $CaCO_3$, particles as reversed micelles. An excess of surfactant disperses solid particles and acid droplets and "form(s) a surfactant monolayer on the oil-acid interface" (Plucinski, et al., 1994).

More about neutralisation times and efficiency under various conditions can be found in chapter 2 and 3.

Under sliding and pressure, the dispersed $CaCO_3$ can also be deposited on the surfaces to form a calcite boundary layer (Giasson, et al., 1994). The effect on friction and acid neutralisation of such a film can be found in chapter 7. In an engine such a highly protective boundary layer can lead to uneven wear, so called 'clover leafing' in the case of the lubricant not being homogeneously distributed.

One of the main challenges for the large 2-stroke marine Diesel engine is inhomogeneous H_2SO_4 neutralisation leading to non-homogeneous wear.

1.4 Deposit Formation

Other than corrosion, marine Diesel engine cylinder systems also suffer from deposit formation arising from deposition of unused additives and lubricant degradation by fuel impingement (ClassNK, 2008), (Buhaug, 2003).

Two stroke marine Diesel engines are typically lubricated with API Group I base mineral oils (CIMAC Working Group "Marine Lubricants", 2007), the least refined lubricants containing < 90 %w/w saturated hydrocarbons (alkanes) with the remainder formed from unsaturated hydrocarbons such as alkenes and alkynes. The chain length of these oils lies between C15 and C50 (The Petroleum HPV Testing Group, 2003) and for this study a C30 alkane was chosen as a model oil being typical of this range.

Oxidation in marine lubricants is seen as a plain thermal effect. Test methods introduce heating of the oil for extended time to temperatures well above 300 °C and evaluation of deposit formation and viscosity increase (Garner, et al., 2004),(Lancon, et al., 2010), (Friesen, et al., 2001). This is surprising, as for comparative engine tests with low sulphur fuel, a

significantly smaller deposit formation in the piston ring pack was observed (Lancon, et al., 2010), (Miyazaki, et al., 1993).

In this study, critical acid concentration and temperatures for oil degradation together with the nature of reaction products are shown in chapters 3 and 4. The formation of deposit due to plain thermal effect and catalysed by H_2SO_4 in a piston ring - cylinder liner friction contact was observed and presented in chapter 7.

One of the main challenges for the large 2-stroke marine Diesel engine is lubricant degradation catalyzed by H_2SO_4, leading to build up of deposits.

1.5   Surface Temperatures

In the three sections, 1.2 - 1.4, before, the important influence of temperature was shown. The temperature of the cylinder liner surface wall originates from:

- Convection by the gas flow
- Conduction from the cylinder wall and piston rings
- Hydrodynamic friction loss
- Friction loss by asperity contact
- Radiation from the hot gas volume

While the first four points are quite obvious and also apply in automotive applications, the gas radiation is usually neglected due to the small gas volume. For engines with bore diameters of 1 m, however, gas radiation starts to play a role.

The selectivity of gas radiation, the selectivity of oil absorption experienced during the work with FTIR spectrometer and the coarse structure of cylinder liner material inspired some extra work on thermal properties of the grey cast iron on a microscopic scale. The results can be found in chapter 8.

For the bulk of the study, however, it is sufficient to know the surface temperatures range from 80 – 300 °C

1.6   Overview on Thesis Content

In the above, an introduction to the specialities of the large 2-stroke marine Diesel engine was given, followed by the consequences of burning high sulphur containing residual fuel, leading to the condensation of H_2SO_4. Present in a wide range of concentrations, the H_2SO_4 can act corrosively and catalyse lubricant degradation. Special additives counteracting the bad influence of H_2SO_4, can lead to new problems due to deposit build up if not

used up. The distribution of the additive with the lubricant is not trivial and oil film chemistry is not homogeneous on the piston running parts. Temperature has a major impact on the physical and chemical properties of the lubricant film. Thermal sources are diverse and in addition to classical views on internal combustion engines, thermal radiation is considered to play a role for big bore engines, which is interesting for its selectivity of radiation, transmittance and absorbance.

From the aim to find the impact of condensed sulphuric acid on the lubricant and the tribological consequences for the piston ring – liner contact, the objectives of the study are as follows:

1. Condensing sulphuric acid is dispersed in the oil film as droplets and the physical properties of the lubricant film may change. The extent of these changes should be clarified as well as the behaviour of the droplets after reaching the metallic walls exposed to shear by the piston ring sliding.
2. In industry there is a trend to move to higher refined base oils. The chemical interaction of aqueous sulphuric acid with existing lubricant base oil should be clarified in comparison to a highly refined and well defined hydrocarbon oil.
3. The additives for fully formulated fresh lubricants are designed to neutralise condensed acid and disperse dirt particles. They have been present for a long time and are standard in the marine industry. The circumferential and longitudinal inhomogeneous appearance of cylinder liner surfaces, however, suggests a loss in performance for varying conditions. The sudden failure of cylinder units was regularly observed to start in line with the fresh oil supply. The performance of the fully formulated lubricants purely and when mixed with aqueous sulphuric acid in terms of friction should be demonstrated.
4. In comparison to the last objective, the impact of dispersed sulphuric acid on friction and surface chemistry should be found to build a reference base for future lubricant additive formulation. The lubricant additives are an unknown and therefore emphasis should be laid on the lubricant base oil.

In the following chapter 2 a literature review for the present work is given, which puts the thesis in relation to the work of others and underlines the novelty and relevance of the present study. However, it also shows a lack in depth, which is the nature of a broad engineering study in comparison to a in-depth study of a small aspect, as found usually in natural sciences.

Most of the applied analytical techniques are presented in chapter 3. Mainly standard techniques, but also two simple custom built trials, were used and their outcome is shown.

The interaction of aqueous H_2SO_4 with lubricant and engineering materials is shown by interfacial tension and contact angle measurements in chapters 4 and 5, addressing objective 1 and 2.

After learning a lot about the chemical and physical properties of the involved materials under isolated conditions, the materials were then brought all together in a friction test, presented in chapters 6 and 7. Impact on oil film and surface chemistry is revealed as well as surface topography and friction coefficient, addressing objective 3 and 4.

As for any human activity there were side learnings and paths which are not directly related to encompass a goal but were still interesting enough to be mentioned and increase the general understanding of the subject and the involved techniques. The side findings on the thermal properties of the involved materials are presented in chapter 8.

The key learning points of this study and suggestions for future work are presented in chapter 9, which finalises this thesis and might even be used as a starting or referring point for impatient readers struggling to follow the flow of argument.

In the appendix, fluid properties are listed and the publications commenced during this study can be found.

Chapter 2
Literature Review

This chapter is meant to position the present study in relation to previous work by others. Primary the form of an "outcome oriented" literature review (Randolph, 2009) was chosen as "outcome" is the sole purpose of engineering, by applying available methods and theories to practical applications.

The literature review is structured in the order of the following chapters and is mainly written for the engineer with an interest in lubrication.

2.1 Chemical Interaction Between H_2SO_4 and Hydrocarbon Oil

The results from interfacial tension measurements incorporating a ring tensiometer, brought Vellinger to speculate about the formation of fatty acids by an oxidation of unsaturated hydrocarbons with concentrated sulphuric acid, H_2SO_4, during the treatment of oil in refineries (Vellinger, et al., 1933). He observed the formation of stable emulsions when the acid was neutralised with NaOH and claimed the cause to be the formation of surfactants by combining the fatty acids with Na^+-ions. Veillinger also found a direct correlation between removal of these surfactants in an active coal filter to reduced colour intensity and increased interfacial tension (Vellinger, et al., 1933).

The exothermic reaction of unsaturated hydrocarbons with SO_3 and H_2SO_4, yields hydrocarbon sulphonates and water (Taylor, 2002). Lubricant sampled from the engine, has been found to be degraded by water droplets (Micali, et al., 2010) and solid carbon (Garner, et al., 2004). The rather inert alkanes can also undergo various reactions with H_2SO_4. When the methyl group, -CH_3, moves into the molecular chain during isomerisation, a process used in refineries, a hydrocarbon with the same molecular weight but different properties is formed. Induction times for the reaction to take place of several hours were observed for low temperatures but the time decreased for temperatures between 60 and 70 °C. The induction time was explained by the increasing amount of carbocations, which are an oxidation product of hydrocarbons, RH, by H_2SO_4. The induction time was eliminated by adding

RH's which oxidise easily in H_2SO_4 or by adding strong oxidizing agents like chromium trioxide, CrO_3. The surrounding atmosphere has no influence on the reaction products but the reaction products differ depending upon acid concentration and process temperature (Rudakov, et al., 1988). Possible isomerisation products depend on the carbon chain length and the well known $C_{30}H_{62}$ used in this study has more than 4 billion possible isomers, which makes an analysis or prediction unfeasible.

In addition to isomerisation, alkane oxidation can also take place. Metal ions can act as catalysts of hydrocarbon oxidation; for example Cr^{VI} shows a higher oxidation potential than Pt^{II-IV}, which is more oxidising than pure H_2SO_4. With increasing H_2SO_4 concentration the oxidation rate increases and is highest for pure H_2SO_4 (Rudakov, et al., 1976). In air, alkanes such as the squalane used in this work are rather inert to oxidation. After 3 hours at 150 °C a measurable mass loss due to evaporation of light products occurs and a considerable increase in heavy products is observed after 48 hours at 180 °C (Diaby, et al., 2009).

Instead of an isomerisation reaction or oxidation, where C-H bonds are broken, sulphonation can also take place where a tertiary H-atom is replaced by a $-SO_3H$ group to form a sulphonic acid, which associates in aqueous solution to form micelles (Kosswig, 2000).

$$C_nH_{n+2} + HOSO_2OH \rightarrow C_nH_{n+1}SO_3H + H_2O \qquad (2.1)$$
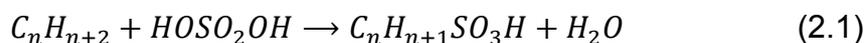
In industrial processes, concentrated and even fuming H_2SO_4 are used in order to obtain a high yield of products. The increased formation of water slows the process down or even stops it completely and it must be removed.

During the above described processes, hydrocarbon radicals are formed which means one carbon atom has an unpaired electron. The radical can be formed by splitting a C-H bond by overcoming the bond energy chemically as described above or at high temperature. Other than the acid, oxygen and nitrogen dioxide NO_2 can also create radicals. In the engine NO_2 is created by the oxidation of nitrogen in the air during combustion at high temperatures or from trace nitrogenated contaminants in the fuel or lubricant (Kramer, et al., 1999). When the hydrocarbon radical $R^{\cdot}$ reacts with the NO_2 radical, a nitrated hydrocarbon is formed, following the reaction (Bachman, et al., 1952):

$$R \cdot + \cdot NO_2 \rightarrow RNO_2 \qquad (2.2)$$

This process is called nitration, a common lubricant degradation process in internal combustion engines. Hydrocarbon nitration can subsequently yield

amine and amide when the N-O bonds are replaced by N-H or NHCO-R bonds. Nitration at elevated temperatures in ambient air was observed and is presented in chapter 7.

In the engine, oxidation products of high molecular weight can act as a binder, causing other material to stick to the surfaces and form hard deposits (Friesen, et al., 2001).

Throughout this study, H_2SO_4 was found to degrade the used oils depending upon acid concentration, temperature and purity of the oil. The consequences for the oil properties can be found in all of the following chapters.

2.2 Neutralisation of H_2SO_4 by Fully Formulated Lubricant

The neutralisation of the H_2SO_4 formed by combustion, as mentioned in the previous chapter, is taken care of by an alkaline reserve in the lubricants with Total Base Number, TBN, levels of 40 – 70 mg KOH/g. The alkaline reserve is usually added into the lubricant by dispersing group-II metal (Ca or Mg) carbonate particles and 5 – 15 % hydroxylic base (Wu, et al., 2000) as reversed micelles.

Neutralisation follows the reaction (Adams, et al., 2007):

$$H_2SO_4 + CaCO_{3(s)} + H_2O \rightarrow CaSO_4 \cdot 2H_2O_{(s)} + CO_{2(g)} \uparrow \qquad (2.3)$$
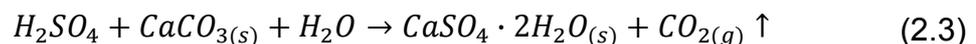
In practice, higher TBN or a increased feed rate reduce the wear of piston rings and cylinder liners (van Helden, et al., 1989) up to a point where problems with deposit build up from unused additive or bore polishing occur. The latter is especially a concern of the designers from MAN B&W who point to the refreshing of the surfaces by 'controlled' corrosion. They therefore give a feed rate adjustment recommendation depending upon fuel sulphur content, TBN of the lubricant in use and the minimum oil requirement for piston ring lubrication (Jakobsen, 2010).
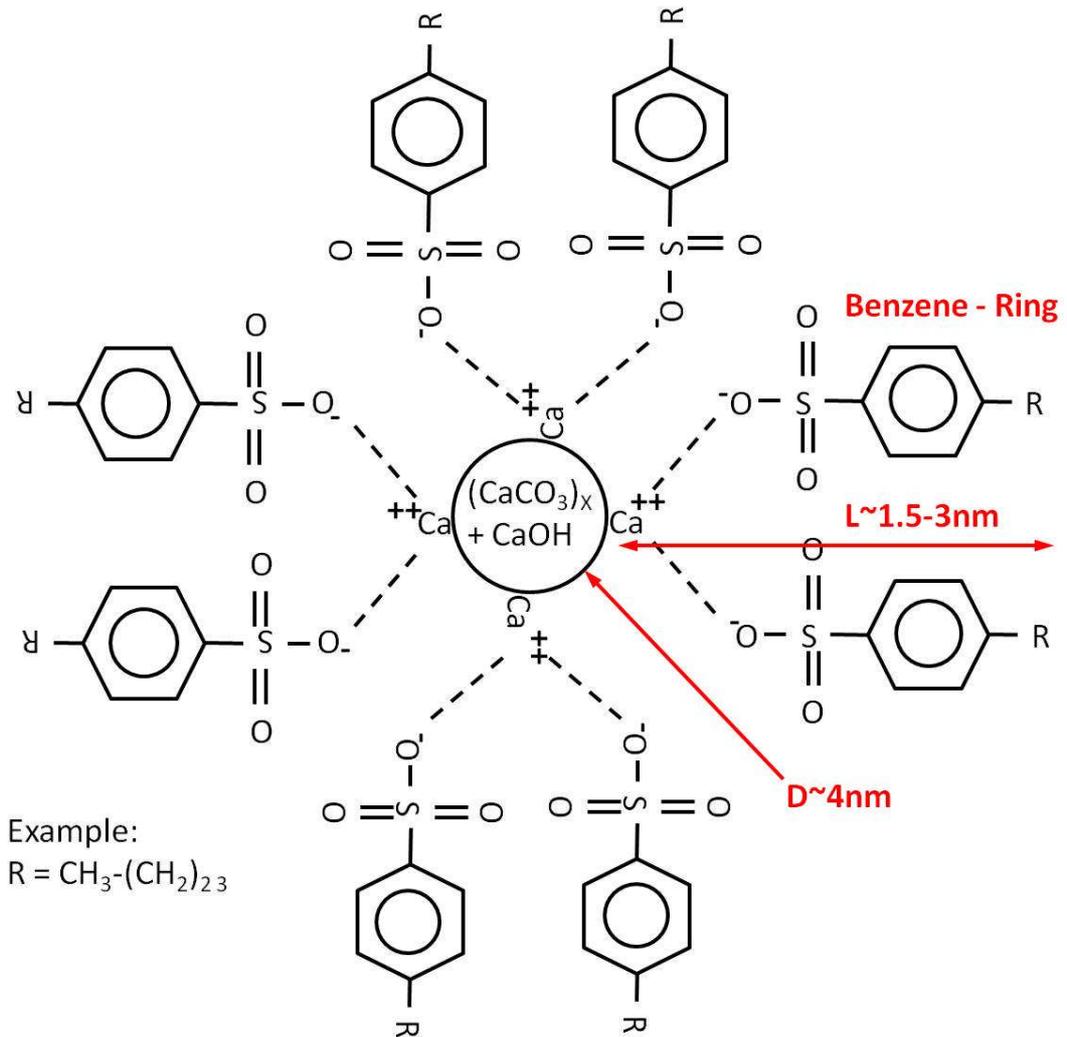
Figure 2.1: Schematic of a overbased calcium sulphonate reverse micelle containing CaCO$_3$ particles and CaOH in aqueous solution (Kubo, et al., 2006), (Giasson, et al., 1993), (Wu, et al., 2000) and (Topolovec-Miklozic, et al., 2008)

The reversed micelles are stabilised by surfactants, shown in Figure 2.1. The surfactant stabilising the core is a metal salt of a surfactant acid (Fu, et al., 2006) namely sulphonates, phenates, carboxylates or salycilates (Hone, et al., 2000).

In addition to the core stabilising surfactants there is also a surplus of surfactants or detergents in the lubricant to disperse acid droplets and solid soot or wear particles (Wu, et al., 2000). The rate at which the surfactants reach the interfaces is mainly governed by convection (Walstra, 1993). The reaction product CaSO$_4$ was also found to stabilise emulsions with a volume fraction of 0.5 H$_2$SO$_4$ in nitrobenzene (Sheppard, 1919).

Several models exist to describe the neutralising path of acid droplets. Some propose the transfer of parts of the micelle core into the acid droplet, where neutralisation then takes place (Hone, et al., 2000). Others describe it the other way around (Wu, et al., 2000). A third party proposes a mixed model, which depends upon the binding strength of the surfactants to the micelle core (Fu, et al., 2006). The neutralisation rate was found to be dependent upon droplet size and temperature. At 110 – 140 °C a 65 %w/w H_2SO_4 droplet of ~160 μm diameter was found to last 23 s in a TBN70 lubricant, whereas it would last 2 h at room temperature (Fu, et al., 2006). For micro emulsions with droplets sizes of ~0.35 nm the reaction was found to be complete after 1 s at 30 °C but also slowed down for lower temperatures (Hone, et al., 2000). A higher TBN concentration increases the reaction rate. This explains faster reaction during the first 70 % of acid neutralisation and for oils with longer hydrocarbon chains, which cannot separate the reverse micelles as well as hydrocarbons with short chains (Hone, et al., 2000). At low temperatures the type of dispersant was also found to influence the speed of reaction. In a TBN75 lubricant without additional detergent, a 63 %w/w H_2SO_4 droplet with a diameter of 90 μm was found to be stable for more than 120 minutes at room temperature. The time decreased to 8 – 72 minutes depending upon the added surfactant type. The optimum detergent concentration was found to be 2 %w/w (Wu, et al., 2000). The dispersing additives can transport the produced hydrated calcium sulphate crystals away from the interface into the lubricant. The crystals would otherwise block the interface for new base containing micelles (Wu, et al., 2000). A counteracting factor to neutralisation is the effect of 'Ostwald ripening', which is the attraction of small droplets by bigger droplets to increase their volume. A 4.4 times prolonged lifetime of a series of droplets was observed due to this effect (Fu, et al., 2007). In a TBN70 lubricant at room temperature a shrinking rate of $1.9*10^{-16}$ m^3/s is given for water droplets, while a 65 %w/w H_2SO_4 droplet shrinks at a shorter rate of $2.6*10^{-15}$ m^3/s (Fu, et al., 2007).

For a residual oil film thickness of 0.01 μm in top dead centre, consisting of a TBN70 lubricant, van Helden calculated the depletion time of the alkaline reserve to be 0.08 – 0.4 s when using fuel with a sulphur content of 5 – 2 %w/w (van Helden, et al., 1989).

The detergents described above do not only act as surfactants but can also act as anti-oxidants. Adding of phenates to sulphonates containing lubricant significantly reduced hard deposit build up on piston crowns, attributed to the anti-oxidant properties of the phenates (Friesen, et al., 2001).

Microscopic investigations at room temperature are interesting to find the mechanisms of acid neutralisation in the oil film. The main influencing factors in an engine oil film of given temperature, however, seem to be droplet size, a function of shear rate and interfacial tension, TBN concentration, depending upon the alkaline reserve of the fresh oil and distribution on the cylinder wall, and acid concentration, which is dependent on temperature, pressure and fuel sulphur content.

A comparison of reaction rates of commercial lubricants used in this study can be found in the following chapter 3.

2.3   Rheology of Emulsions

2.3.1 The Creation of W/O Emulsions

In order to create an emulsion, coarse droplets have to be split into finer droplets by a shearing continuous phase. The shear has to overcome the Laplace pressure in the droplet, which can be written for spherical droplets with radius r and an interfacial tension, σ, as (Walstra, 1993):

$$p_L = \frac{2\sigma}{r}$$
(2.4)

The minimum energy needed to do so is the created net surface free energy, which is the product of the created interfacial surface area and the interfacial tension. In practice the required energy input is by far greater, however, the droplet breakup is more easily achieved for lower interfacial tension. Therefore surfactants are used to lower the interfacial tension and to prevent coalescence of the droplets (Walstra, 1993).

For Newtonian fluids in a laminar shear flow, the critical Weber number of $We \approx 1$ has to be overcome. The Weber number calculates to (Walstra, 1993):

$$We = \frac{\eta_c \cdot G \cdot r}{\sigma}$$
(2.5)

Where η_c is the viscosity of the continuous phase and G the velocity gradient across the droplet radius, r.

No droplet breakup occurs for viscosity ratios of dispersed phase to continuous phase greater than 4 (Walstra, 1993) or 3.8 (Jansen, et al., 2001). This, however, was observed only for single droplets and droplet breakup for viscosity ratios of up to ten were reported in real emulsions (Walstra, 1993). Jansen explains this deviation by an increase of viscosity of the bulk phase due to emulsification and recommends the use of the

resulting viscosity of the emulsion (2.6) instead of the viscosity of the continuous phase. Lucassen found that the interfacial viscoelasticity can raise the effective droplet viscosity to levels where droplet breakup becomes unfavourable and the influence of interfacial tension on droplet breakup is reduced by this effect (Lucassen-Reynders, et al., 1992).

2.3.2 The Viscosity of W/O Emulsions

The viscosity, η_{em}, of dilute emulsions of Newtonian fluids containing spherical droplets can be predicted by the extended Einstein equation according to Taylor (Taylor, 1932):

$$\eta_{em} = \eta_c \cdot \left[1 + 2.5\phi \left(\frac{\eta_d + \frac{2}{5}\eta_c}{\eta_d + \eta_c} \right) \right] \tag{2.6}$$

The volume fraction Φ is the ratio of the dispersed phase, with viscosity η_d, in the continuous phase, with viscosity η_c. Taylor assumed that deformable droplets would break up until they stay spherical.

The validity of Taylor's assumption of spherical drops can be checked by the deformation equation shown by Nawab (Nawab, et al., 1958):

$$\frac{L - B}{L + B} = \frac{G \cdot a \cdot \eta_c}{2\sigma} \left(\frac{1 + \frac{19}{16}\frac{\eta_d}{\eta_c}}{1 + \frac{\eta_d}{\eta_c}} \right) \tag{2.7}$$

In a shear field with the velocity gradient, G, the spherical droplets, with diameter, a, and interfacial tension, σ, deform into ellipsoids with the major axis, L, 45° to the direction of motion. Taylor's equation is still valid for small ratios of major to minor axis, B.

By simulations of flows with small Peclet and Reynolds numbers, both are usually large in technical applications, Danov found the relationship $\eta_c < \eta_{em} < \eta_{em+surfactant}$ for a dilute emulsion and a strong dependence on the volume fraction (Danov, 2001). Nawab explains the influence of the surfactants by the suppression of internal circulation of liquid in the droplet by the emulsifiers which creates higher viscosities than predicted by Taylor (Nawab, et al., 1958). The dependence on the volume fraction is also found experimentally with increasing viscosity for increasing water content below the emulsion inversion point, were the dispersed phase becomes the continuous phase (Alwadani, 2009).

From the relations above, it can be seen that the continuous phase governs the viscosity of a dilute emulsion. By simulations on a molecular level, squalane was found to exhibit shear thinning behaviour above shear rates of ~11*10^{10} s^{-1} (Jabbarzadeh, et al., 2002). For low shear rates and a pressure

rise from ambient to 1.25 GPa, the viscosity of squalane at 65 °C increases almost linearly by ~5 Pa*s (Bair, 2006). Below a volume fraction of 0.2, emulsions were found to be Newtonian in a shear rate range from 0.1 – 50 s^{-1} (Jansen, et al., 2001).

2.3.3 Rheology of Emulsions: Droplet Displacement

In the previous chapter it was pointed out, that corrosion by condensed water droplets can only take place when the droplet can attach to the wall. Very little experimental work on droplet displacement by shear flow was found in literature, which can be explained by the tremendous effort in purity and material selection to be taken to gain reproducible results (Mahe, et al., 1988). Mahe concentrated on the displacement of alkane droplets from glass by a laminar shear flow of water. The adhesion force, F_A, of a droplet towards a wall is given by (Mahe, et al., 1988):

$$F_A = a_P \cdot \sigma \cdot (cos\theta_R - cos\theta_A) \tag{2.8}$$

with the width of the wetted contact area, a_P, the interfacial tension, σ, and $\theta_{R/A}$ the receding and advancing contact angle on the substrate. The critical shear rate, γ_{crit}, across the droplet for its displacement is approximately (Mahe, et al., 1988):

$$\gamma_{crit} \sim \frac{\sigma \cdot a_P \cdot (cos\theta_R - cos\theta_A)}{\eta \cdot a^2} \tag{2.9}$$

with η, the viscosity of the continuous phase and a, the diameter of a equivalent spherical droplet. Mahe finds a linear relationship when plotting his results as $\gamma_{crit} \ast a^2$ over a_P and finds the slope C to be (Mahe, et al., 1988):

$$C = \frac{\eta \cdot \gamma_{crit} \cdot a^2}{\sigma \cdot a_P} \tag{2.10}$$

Below a surface roughness of Ra < 0.1 µm no contact angle hysteresis is found for pure systems and the displacement of droplets from the wall is not influenced by the surface topography. For 0.1 < Ra < 1 µm the contact angle hysteresis plays a major role and higher shear rates are needed to displace a droplet. Above a surface roughens of 1 µm the critical shear rate drops again due to enclosed remaining continuous phase in the roughness valleys which effectively reduces the wetted contact area (Mahe, et al., 1988). For oil soluble surfactants, Mahe found an increase in the contact angle hysteresis and therefore an increase in the critical shear rate (Mahe, et al., 1988) while Thompson found an increase in contact angle for oil droplets on polymer for water soluble surfactants, which enhances droplet displacement

(Thompson, 1994). It must be concluded that droplet adhesion to the wall is strongly dependent on the type of surfactant used.

More literature was found on numerical simulations of droplet displacement. The theoretical studies usually result in a dimensionless critical capillary number Ca_{crit} for droplet displacement to take place. The capillary number is the relationship between viscous and interfacial forces. When the viscous forces are much greater than the interfacial tension forces, the droplet first deforms, creeps along the wall and finally detaches partly or fully from the wall, depending upon the contact angle (Kang, et al., 2005). The capillary number is defined as (Ding, et al., 2010):

$$Ca = \frac{\eta \cdot \gamma \cdot R}{\sigma}$$
(2.11)

where γ is the applied shear rate and R the characteristic droplet diameter defined as:

$$R = \left(\frac{1.5 \cdot V}{\pi}\right)^{\frac{1}{3}}$$
(2.12)

with V being the volume of the droplet. The results are then presented for various Reynolds numbers, Re, defined as:

$$Re = \frac{\rho \cdot \gamma \cdot R^2}{\eta}$$
(2.13)

where ρ is the density of the continuous phase. For a droplet with a contact angle hysteresis of the advancing contact angle $\theta_A = 90°$ and receding contact angle $\theta_R = 40°$, Ding finds a critical capillary number for the onset of drop motion of 0.12 - 0.05 for $Re = 0 - 110$ and $Ca_{crit} = 0.3$ for droplet entrainment (Ding, et al., 2010). The critical capillary number decreases with increasing contact angle (Kang, et al., 2005). For higher interfacial tension, droplets detach more complete than for lower interfacial tension. Viscous droplets are more easily detached than less viscous drops (Ding, et al., 2010), which is a time effect on the droplet shape, equalising over time (Schleizer, et al., 1999). For higher capillary numbers the time to influence the droplet is reduced (Kang, et al., 2005).

In summary, the rheology of emulsions is mainly influenced by the volume fraction which defines the viscosity increase, shear thinning behaviour and droplet break up. The latter being explained by an viscosity increase for increasing volume fractions. The viscosity ratio influences droplet breakup, emulsion viscosity and droplet deformation. The interfacial tension influences droplet size, effective droplet viscosity and the droplet adhesion

force on a wall. The contact angle, which is governed by the materials, surface roughness and surfactants, influences the adhesion forces of a droplet on a wall.

The dispersion of bituminous droplets in the engine is unlikely when the viscosity ratio of droplet to continuous phase exceeds 3.8 but a more viscous droplet is more easily displaced by the shearing action of the moving piston rings.

2.4   Interfacial Tension

The interfacial tension between pure and inert immiscible liquids can be estimated as the difference between their surface tensions (Reynolds, 1921). This however holds only true for a limited combination of liquids and is only valid at room temperature, which was shown in a literature review by Demond where he compares various models against measured values for the water-hydrocarbon interface. He recommends the use of models by Donhue and Fu when miscibility and thermodynamic data of the liquids is known but also concludes measurements to be still the most accurate way to determine interfacial tension (Demond, et al., 1993).

The interfacial tension between oil and an aqueous phase is a highly sensitive test for impurities in either phase and the Du Nouÿ ring method is a standard tool for its measurement (ASTM, 2011). Using the Du Nouÿ ring method, Vellinger reported an increase of interfacial tension for better refined oils. In all cases he found a reduction of interfacial tension with increasing acidity (potassium biphthalate, pH = 2.6 - 7.1) or alkalinity (NaOH, pH = 7.1 – 11.6) of the aqueous phase with a peak for pure water (Vellinger, et al., 1933). Same dependency of interfacial tension on pH by H_2SO_4 and NaOH was found by (Feng, et al., 2010). The pH scale however is attributed to miniscule amounts of ions and a pH of 2 is achieved by a < 0.5 %w/w solution of H_2SO_4 in water. The influence of base oil composition and degree of refining on interfacial tension towards pure water was measured by Furman and Pillon and the values are given in Table 2.1. The purest oils show the highest values. The interfacial tension of concentrated H_2SO_4 against n-pentane ranges from 0.007 - 0.01 N/m and 0.01 - 0.02 N/m for n-nonane at 22 °C, measured by the Du Nouÿ ring method (am Ende, et al., 1995).

Table 2.1: Interfacial tension in N/m of various base oils against pure water (Furman, et al., 1984), (Pillon, 2003)

Base oil type	σ in N/m	Base oil type	σ in N/m
Naphtenic, no aromats	0.0543	Isoparafin, < 7 % aromats	0.038
Naphtenic, < 8 % aromats	0.0343	Isoparafin, < 2 % aromats	0.0291
Ployalphaolephin, syntetic	0.0633	Mineral white oil, aromats/polars > 0.5 %w/w	0.0391
X. Hydrocracked base stock (slack wax isomeris.) aromats/polars > 0.5 %w/w	0.0456	150N (N-methylpyrrolidone extracted) aromats/polars 14 %w/w, S 0.06 %, N 36 ppm	0.0334
as X. but treated in acidic resin to remove surface active contaminants	0.0481	150N (Phenol extracted) aromats/polars 17.2 %w/w, S 0.09 %, N 8 ppm	0.0431

The pendant drop method allowed Chaverot to observe the time dependency of interfacial tension between commercial bitumen and acidic water (pH 2) with a very high resolution. He found a rapid drop in interfacial tension during the first 600 s to reach stable values after about 6000 s between 0.0294 - 0.0352 N/m at 90 °C and 0.0166 - 0.0227 N/m at 140 °C. The time dependency was attributed to the migration of surface active asphaltenes with a size of 0.95 ±0.5 nm by Brownian motion, which are present in the natural bitumen. Only 0.015 % of the asphaltenes, which make up 10 % of the bitumen, were claimed to be surface active (Chaverot, et al., 2008). With the same method Wang observed the time dependency of interfacial tension to be a function of surfactant concentration with stable values after 1000 s for $6.2*10^{-8}$ M and after 50 s for $1.2*10^{-6}$ M surfactant concentration (Wang, et al., 2003).

Vacha numerically simulated the arrangement of hydronium cations, H_3O^+, on the water alkane interface. A layer of H_3O^+ forms directly towards the hydrocarbon molecules while OH^- anions form a layer just below, followed by the bulk water phase, which is a neutral mixture of both (Vacha, et al., 2008). For the oil – saltwater interface, dos Santos found a correlation between interfacial tension and the position of the salt-ion in the Hofmeister-series. Kosmotropic anions, which favour water molecule interaction, get repelled from the oil water interface, while chaotropic anions, disrupting water molecule interaction, get absorbed on the interface, thus influencing the interfacial tension (dos Santos, et al., 2012). Feng studied the influence on interfacial tension between oil and aqueous ionic solutions of NaCl and $CaCl_2$. Increasing the NaCl concentration had no influence on interfacial tension, while an increase in $CaCl_2$ resulted in a decrease and at the same time an increase of NaOH resulted in a decrease in interfacial tension (Feng, et al., 2010). This means Na^+ and Cl^- have no effect while the concentration of OH^- does have an influence on interfacial tension. A change in the OH^- concentration in the case of an alkaline solution should have a influence on the H_3O^+ layer on the oil water interface. In an acidic solution the H_3O^+ concentration increases. For a hydrocarbone - H_2SO_4 interface this would mean the kosmotropic SO_4^{2-} and HSO_4^- are initially repelled from the interface giving opportunity for H_3O^+ to assemble on the interface. The interfacial tension between oil and water was also reduced by applying either a positive or negative electrical field (Shchipunov, et al., 1991). The surface tension of water was reduced by applying a negative electric field while the surface tension of the hydrocarbon hexane was completely unaffected (Sato, et al., 1998). From the above, one can conclude that influencing the H_3O^+ ions on the interface results in an reduction of interfacial tension.

Ende concludes that the hydride, H^-, transport across the interface is important for the degradation, isomerisation and alkylation of the 'anti-knock fuel' 2,2,4-Trimethylpentane by concentrated H_2SO_4. He found this by adding surfactants which would block the interface and observed a change in reaction. He also found sulphate esters, which are intermediate reaction products during alkylation, having a significant influence on interfacial tension (am Ende, et al., 1995).

Over the full range of acid concentrations, from neutral to very strong, one can expect to find two processes influencing the interfacial tension: changes in the H_3O^+ layer on the interface and chemical reaction between acid and oil

creating polar surface active substances. This is reflected by the findings presented in chapter 4.

The above mentioned surfactants created by chemical reactions are basically hydrocarbon chains with a modified end, the so called functional head group. The functional head group has an attraction towards the aqueous phase while the hydrocarbon chain remains in the oil phase when oil and water are in contact. Depending upon their concentration and the thermodynamic state of the system, the surfactants arrange on the interface to find a energetic most favourable position, thus influencing the interfacial tension (Shaw, 2003). By freezing and investigating in an transmission electron microscope Won was able to visualise surfactants arranged to micelles of various forms (Won, et al., 2002).

2.5 Contact Angle

Literature on contact angle measurements of corrosive droplets on metal surfaces submerged in oil was not found. Measurements were either done on pre-corroded surfaces (Schmitt, et al., 1998) or in air (Wang, et al., 2007) or did not involve corrosion at all (Baker, et al., 1961).

Schmitt found corroded steel surfaces not to be wetted by floating oil droplets in a heated water bath due to the build up of carbonate scale (Schmitt, et al., 1998). For water droplets on steel surfaces submerged in oil, Baker reports a correlation between increasing interfacial tension and increasing contact angles. For pure oil he reports a contact angle of 90° and contact angles between 110 - 170° for oils containing transition metal soaps (Baker, et al., 1961). In air Wang reports on the much faster spreading of 5 %w/w H_2SO_4 micro droplets compared to pure water. Both water and acid solution have an initial contact angle of 70° but after ~20 s water reaches ~62° while the acid droplet has already spread to reach ~17°. Wang also reports on the highly reduced corrosion rate with small droplets which he attributes to the covering of only homogeneous surface areas in contrary to larger drops, which cover areas across grain boundaries to form anodes and cathodes (Wang, et al., 2007).

The equilibrium contact angle on a perfect inert surface is described by Young's equation where the interfacial tension between the phases controls the contact angle (Wang, et al., 2004). Above it was shown how the influencing of the H_3O^+ ion changes the interfacial tension between water and oil. The contact to a corroding metallic surface should also influence the

ion distribution on the interface and, therefore, the interfacial tension between oil and water might not be the same as the measured one.

A hysteresis between advancing and receding contact angle due to surface roughness was reported for water on PTFE (Morra, et al., 1989) and on stainless steel (Wang, et al., 2004). An increase in surface roughness causes an increase in advancing and a decrease in receding contact angle. The hysteresis becomes zero for a perfect flat surface, the so called Young's contact angle, which is only dependent on the material properties. By measuring real surfaces of known varying roughness the Young's contact angle can be estimated. For water on stainless steel with a surface roughness Ra of 0.03 - 0.95 µm the advancing contact angle varied from 58 – 82° and the receding contact angle from 46 – 11° which resulted in a Young's contact angle of ~54° (Wang, et al., 2004). Below a surface roughness of 0.1 µm no influence on the contact angle can be expected (Mahe, et al., 1988). For the measurements presented in chapter 5 it was decided to bring the surfaces close to application roughness in worn condition and measure the hysteresis, as the variation in acid concentration was seen to be more important.

A temperature dependency (25 – 170 °C) of contact angles for water droplets on polished aluminium surfaces (Ra = 0.115 µm) was found by Bernadin. The samples were placed in a chamber, pressurised by nitrogen (1 – 8 bar) and heated. Between 25 and 120 °C the contact angle were almost constant at 90° with a decline of -0.1°/K and showed a linear decrease to 65° up to 170 °C. The surfaces were contaminated by organic components from the polishing process, explaining the high contact angles (Bernadin, et al., 1997).

The post processing of images taken to measure contact angles is not trivial. The classical method of drawing a tangent by hand and measuring the angle is not very accurate and dependent on the operator. Stadler pointed out that drops on real surfaces are neither spherical nor axissymetric, the images can be blurred and the camera misaligned to the sample surface. The evaluation software developed by Stadler, showed superior performance under various conditions compared to commercial software and the hand technique (Stadler, et al., 2006). This free available software was used to evaluate the measurements presented in chapter 5.

2.6 Friction Measurements

Friction and wear testing machines are widely used. Unfortunately the studies concentrate mainly on certain aspects of wear mechanisms or on oil additives without giving a reference with non-formulated oil, or the studies are plain qualitative. Very few studies included H_2SO_4 while the deposition of calcium carbonate on the parts under friction from lubricants with an high alkaline reserve is quite well understood.

Montgomery studied the running-in of grey cast iron against steel in white mineral oil at 82 °C at an average speed of 0.04 m/s with an initial surface load of 0.17 GPa, which reduced to 0.015 GPa at the end of the test due to wear. He found the friction coefficient to decrease from an initial 0.21 to a final 0.12. On top of the wear track he found a hard ~25 μm thick glazing layer consisting of Fe_3O_4 and carbon, which he assumed to be graphitic (Montgomery, 1969).

For dry running of piston ring against cylinder liner grey cast iron a friction coefficient of μ = 0.275 with a pin on rotating disc at 3 m/s and loads between 0.001 - 0.0031 GPa was found (Sjogren, et al., 2004)

2.6.1 Friction Measurements With H_2SO_4 in Oil

In the late 1980's Macdonald and Stott published a total of six papers on the wear mechanism of grey cast iron in emulsions of aqueous H_2SO_4 in base oil. They used a reciprocating pin on disc machine with pins manufactured from piston ring grey cast iron and plates manufactured from cylinder liner grey cast iron as used in large 2-stroke marine Diesel engines. Unfortunately their rig was not equipped with a force transducer and no information on friction was gained. The average reciprocating speed was kept at 0.09 m/s and the maximum initial Hertzian contact pressure at ~0.7 GPa. A 17 %w/w H_2SO_4 was mixed into the oil by 10 %v/v and tested at temperatures of 20, 40 and 60 °C. At 60 °C they report a degradation of the oil and dark material deposited on the wear scar, which made them decide to work at a temperature of 20 °C. At a concentration of 55 %w/w and 60 °C they report on a even more rapid degradation of the oil. In general they find a higher wear rate at higher temperatures and the formation of iron sulphate hydrate, $FeSO_4 \cdot 4H_2O$, on the wear scar (Macdonald, et al., 1987). For concentrations of 31.5 – 55 %w/w H_2SO_4 they found lower wear rates than for pure water in oil. The highest wear rates were found with 17 %w/w H_2SO_4 dispersed in quantities of 5 – 10 %v/v in oil (Stott, et al., 1988). The overall conclusion for

their series of trials was corrosion induced abrasive wear to be the wear mechanism in the given environment (Stott, et al., 1990).

By sliding a pure aluminium pin on pure iron in various concentrations of H_2SO_4 at a nominal contact pressure of 0.025 GPa and a mean sliding speed of 0.05 m/s at room temperature for 60 minutes, Mischler found the friction coefficient and plate roughness given in Table 2.2. The higher the acid concentration, the lower the friction coefficient but no correlation to surface roughness nor acid viscosity was found. The non-conclusive surface analysis by Auger electron spectroscopy revealed oxygen content on the iron plate and, for concentrated H_2SO_4, sulphur on the transition between oxygen layer and iron bulk material. No wear on the aluminium pin was found (Mischler, et al., 1993) probably by a inert aluminium oxide layer.

Table 2.2 Friction coefficient μ of Al-pin on Fe-plate at various concentrations of H_2SO_4 and the resulting plate roughness Ra (Mischler, et al., 1993)

%w/w	0	18	45	56	66	82	96
μ	0.21	0.175	0.175	0.18	0.125	0.125	0.105
Ra[μm]	0.06	0.13	0.44	0.25	0.06	0.03	0.04

A TE77 reciprocating pin on plate test was lubricated with fully formulated lubricants mixed with concentrated H_2SO_4. The pin was loaded to a resulting surface pressure of 0.025 GPa at 250 °C for 5.5 hours. The lubricant had an alkaline reserve of 50 mgKOH/g and was premixed with 3.5 %w/w concentrated H_2SO_4, resulting in a theoretical reduction to 10.3 mgKOH/g. The coefficient of friction, COF, was found to be a constant 0.08 but the wear increased for the acid premixed oil and the contact potential, CP, measurement showed almost perfect separation for the fully formulated oil and metallic contact for the premixed oil (Davis, et al., 1993).

The friction results for marine lubricant base oil with aqueous concentrations of H_2SO_4 investigated in this study can be found in chapter 7.

2.6.2 Friction Measurements With $CaCO_3$ in Oil

Since ZDTP (Zinc Dialkylphosphorodithiloate) as a wear modifier has to be replaced in automotive applications (Kubo, et al., 2006), research has concentrated on finding replacements for it. One of the possible candidates is over-based calcium sulphonates, which have been used for a long time in marine Diesel engines, mainly to neutralise H_2SO_4 (Vipper, et al., 1998). Common for all studies is the formation of boundary films on the surfaces.

The thickness of these films range from 10 nm (Topolovec-Miklozic, et al., 2008) to 2 µm (Vipper, et al., 1998) but was for most studies in the range 100 ±50 nm depending upon the lubrication conditions. The boundary layers were reported to be CaO and $CaCO_3$ (Caixiang, et al., 2008) or calcite, which is the crystalline compact form of $CaCO_3$, with adsorbed $CaCO_3$ on top (Giasson, et al., 1994), (Topolovec-Miklozic, et al., 2008). Under friction, a film thickness of 80 nm was reached after only 5 minutes (Topolovec-Miklozic, et al., 2008). The formation of a boundary film only occurred under friction or when submerged at 150 °C but not at room temperature and the compacting of the $CaCO_3$ was shown to be independent of pure pressure (Giasson, et al., 1993). It is proposed that the calcium sulphonate surfactants have to be stripped mechanically or decomposed at high local temperatures from the $CaCO_3$ core to make deposition on the surfaces possible (Zhang, et al., 2009). The displacement of the surfactants from the core is favoured when water penetrates the micelle (Giasson, et al., 1993) but water also delays the calcite formation (Giasson, et al., 1994) and distilled water dissolves the formed boundary layer (Topolovec-Miklozic, et al., 2008). For adsorbed films, which are 15 times thinner than the boundary film formed under friction, calcium sulphonate chains were found to stand perpendicular to the metallic surface and also the core particles were found in a preferential orientation (Giasson, et al., 1994), which clearly points in the direction of surface energies to be a factor in the deposition process.

The concentrations of $CaCO_3$ in the tested lubricants gave a range of equivalent alkaline reserve of TBN 2.2 - 550 mgKOH/g, (Caixiang, et al., 2008), (Giasson, et al., 1993). Caixiang dedicated his research on a four-ball tester to a variation of $CaCO_3$ content of TBN 2.2 - 11.2 and found the friction coefficient to be lower, $\mu = 0.087 – 0.113$, than with pure oil, $\mu = 0.12$. The minimum value is achieved for TBN7. Unfortunately Caixiang did not report the speed and temperature of his tests.

The influence of speed on the friction coefficient was shown by Topolovec-Miklozic in the range of 0.004 – 2 m/s at 100 °C and 0.95 GPa initial Hertzian contact pressure. For low speeds she found the friction coefficient to vary the most within $\mu = 0.06$ and 0.12 for different additives, while the thickness of the built up boundary film played no role. The biggest influence of the boundary film thickness was found at 0.1 m/s where a increased coefficient of friction was measured for all additives. The values range between $\mu = 0.08$ and 0.1 after 2 hours compared to the initial $\mu = 0.05$. At the highest speed of 2 m/s all additives show the same friction of $\mu = 0.04$.

The differences are concluded to originate from the different topography pattern formed by the additives influencing hydrodynamics (Topolovec-Miklozic, et al., 2008). Differences in frictional behaviour, film formation and temperature response was also observed by Vipper and was attributed to differences in the micellar structure (Vipper, et al., 1998), which is given by the property of the detergent.

The friction results for marine lubricants with TBN70 investigated in this study can be found in chapter 7.

2.7   Gas Radiation in the Diesel Engine

Heat flux by thermal radiation originating from the flame, glowing soot particles, hot combustion gases and also the compressed air contribute to a significant amount to the total heat flux in the engine. Tian (Tian, et al., 2006) claims in his article abstract to have experimentally found a total contribution of ~20 % heat flux by gas radiation and a corresponding increase in radiation by increasing load and decreasing speed. With combustion simulations, Chen found a 50:50 contribution of conduction and radiation mainly by soot to heat flux by the hot combustion gases (Chen, et al., 2000). Finol theoretically found a combined contribution of gas radiation and convection of 25 % to total heat flux in a turbocharged 2.0L Ford Diesel engine (Finol, et al., 2009). Common to the theoretical work mentioned above is the treatment of the radiation as black body emission and the receiving wall as a grey absorber. In a motored and fired petrol engine, which has lower soot content, Agnew measured IR intensities and identified the main contributors to the chromatographic radiation as water vapour and carbon dioxide. The measurements were commenced at 10 bar gas pressure and approximately 530 °C gas temperature. The addition of 10 % steam or CO_2 to the intake air increased the IR intensity by 9.5 and 4.5 times compared to compressed ambient air (Agnew, et al., 1955). The trend in modern Diesel engines is clearly to reduce soot content, which is achieved by higher injection pressures, turbo charging, etc. The layout of large 2-stroke marine Diesel engines follows this trend and onboard exhaust gas measurements are conducted. Values found for a MAN12K90MC operating on residual fuel at 57 % load are presented in Table 2.3 (Murphy, et al., 2009). Missing in the results is the water content which accounts for about 6 %v/v (CIMAC Working Group "Exhaust Emission Control", 2008).

Table 2.3: Measured exhaust gas composition of a MAN12K90MC engine, operating on residual fuel at 57 % load in g/kWh (Murphy, et al., 2009).

CO_2	NO_2	SO_2	Particles	CO	H-C's
638	20.1	11.9	2.62	0.29	0.15

As can be seen from Table 2.3, particulates in marine Diesel engines are still a significant contributor to exhaust emissions and will act as black radiators in the combustion chamber.

When the radiation from soot particles does not overshadow the chromatographic radiation from H_2O, the spectral peak ratio can be used to establish the gas temperature by high speed IR imaging as shown by Rhee in a Cummins903 Diesel engine. Rhee found a clearly chromatographic emissivity from the hot combustion gases with main contributors being H_2O and CO_2 (Rhee, 1995). A similar technique was used to measure exhaust gas compositions of jet engines with gas temperatures of about 340 °C (Flores-Jardines, et al., 2005).

So far radiation in the combustion chamber was shown to follow the laws for black body's but to a large extend for chromatographic gases. The absorption by the walls of the combustion chamber to calculate heat flux is seen as plain grey and homogeneous. Sazhin, however, introduced a model for the evaporation of injected fuel droplets, which considers black body gas radiation and the wavelength dependent absorption of the Diesel droplets. The simulation shows contrary to pure convective heat transfer a homogeneous temperature increase over the whole droplet radius by 10 % when considering radiation. The wavelength dependent index of absorption of Diesel fuel, used in the simulation, is established experimentally to show a maximum absorption peak at 3.3 μm (Sazhin, et al., 2004). The model from Sazhin was further used to find that the droplet interior temperature exceeded the dew point temperature on the surface due to the radiative internal heating of the droplet (Abramzon, et al., 2006) and a 30 % reduced ignition delay when considering radiative heat transfer (Goldfarb, et al., 2007).

The model of Sazhin is clearly right to use black body radiation for droplet evaporation as the bulk of the fuel droplets is injected into a propagating flame. Also the use of grey body walls to calculate the radiative heat flux towards the walls of the combustion chamber is a fair assumption. However, no literature was found on the degradation of a chromatographic oil film by

chromatographic gas radiation or the absorbance of the grey cast iron micro-structure or the cylinder surface texture. Measurements even close to the surface cannot pick up the fluctuation of temperatures experienced by the oil film as calculations by Guohua show. At a depth of 1 mm below the surface, a temperature wave of 11 °C is already equalised with the bulk temperature of the material (Guohua, et al., 1991). Some light is shed on this subject in chapter 8, which is not conclusive but might give inspiration for future research.

2.8   Influence of Temperature on Roughness

Grey cast iron is an inhomogeneous assembly of various materials having different chemical compositions arranged in grains. For low cooling rates during casting, the grain sizes can become very large. A comparison of a centrifugal grey cast iron for automotive cylinder liners and a sand cast grey cast iron for large marine cylinder liners can be found in chapter 6. Eutectic iron carbide grains can reach sizes of up to 1 mm in sand cast marine engine liners.

Kagawa reported on the anisotropic thermal expansion coefficient of cementite in carefully cast and heat treated samples incorporating unidiretional growth of the crystals, by measuring thermal elongation against an aluminium reference and found lower thermal expansion coefficients for higher carbon content (Kagawa, et al., 1987). With extreme experimental effort, Hartmann measured thermal expansion on single cementite crystals by X-ray diffraction, confirming the work of Kagawa but exceeding it in preciseness and conclusion (Hartmann, et al., 1995). Hartmann reported iron carbide to have a orthorhombic crystal structure. A orthorhombic body is a prism with unequal side lengths, $a \neq b \neq c$, or "spacing dimensions" between the corners or atoms in case of a crystal. The spacing dimensions reported by Hartmann are a = 0.45246 nm, b = 0.50884 nm and c = 0.67423 nm. Materials lose their ferromagnetism above the so call Curie-temperature, T_c. For iron carbide, ferromagnetism exists only in the c-direction and is lost above T_c = 230 °C for pure Fe$_3$C but was found to be lowered by impurities, to 210 °C by 0.7 % Mn for example. Below 100 °C the thermal expansion coefficient, α, was anisotropic and constant with α_a and α_b being much smaller than for pure iron. Between 100 and 200 °C thermal expansion became smaller and even negative in the b-direction. A sharp increase of thermal expansion around T_c was observed in all directions with α_c exceeding that of pure iron. A hysteresis in thermal elongation for heating

and cooling was observed. The differences in thermal elongation, induce stresses in the cast iron, which are positive in the Fe and negative in the Fe_3C lamellas of the pearlite phase. At room temperature these stresses range between 120 and 240 MPa and become zero at around 250 °C. The cementite in the pearlite is preferentially oriented with its b - direction perpendicular to the direction of heat flow during solidification. The above values were taken from the article by Hartmann (Hartmann, et al., 1995) and were found to be in good agreement with other literature.

At ~170 °C the difference in thermal elongation between pure iron and the b - direction of Fe_3C reaches a maximum of $\Delta\alpha_{Fe3Cb - Fe} = 20*10^{-6}$ 1/K (Hartmann, et al., 1995). For a crystal of 1 mm the difference in elongation would become 3 µm compared to room temperature. This is larger than the achieved surface roughness during honing of the cylinder liners at room temperature. The hard phases in the real cylinder liner material, however, are embedded in a pearlite matrix and the orientation to the surface might have any direction due to the non-laboratory conditions during solidification. In chapter 8 the thermal influence on surface roughness is measured.

Operating a friction contact just below the Curie-temperature might be dangerous as an increase of temperature due to hard contact above the Curie-temperature could quite suddenly cause an Fe_3C crystal, oriented in a or b - direction perpendicular to the surface, to stick out of the surface and worsen the situation in the friction contact. This thought was not followed up in the current study but is suggested for future research as no literature was found on "the friction of grey cast iron at the Curie temperature of Fe_3C".

2.9   Thermal Conductivity

Local temperatures in friction contacts can become significantly higher than the average temperatures of the bulk material (Jaeger, 1942), (Ashby, et al., 1991), (Kennedy, et al., 2006), (He, et al., 2008). The introduced heat in the small area of contact is dissipated into the bulk material and the surrounding oil film by conduction. Knowledge of the thermal physical properties, such as thermal conductivity, is crucial to estimate temperature rise in the surface due to friction.

Thermal conductivity of bulk material is measured on rods of known geometry. A heat source and a heat sink are mounted to each end of the rod and the equilibrium temperature in known distances along the rod is

measured. From the known heat flux, geometry and temperature differences, the thermal conductivity can be calculated (Moore, et al., 1977), (Rukadikar, et al., 1986).

Some pure materials like graphite show strongly anisotropic behaviour, depending upon the orientation of the crystal structure (Slack, 1962) to the direction of heat flow, and material composites like grey cast iron vary with microstructure, which is influenced by alloying elements and the cooling procedure during casting and following heat treatment (Rukadikar, et al., 1986). From conductivity measurements on various grey cast irons, however, little is learned about the conductivity properties of the single phases. The combination of experimental conductivity measurements on grey cast iron followed by numerical simulations using the conductivity values of the single phases can, however, verify values for the single phases (Helsing, et al., 1991), (Chen, et al., 2011). In Table 2.4 values for materials found in piston ring and liner surfaces are given. The values for the single phases in grey cast iron were found by measurement on the pure materials and confirmed by using their values in numerical simulations to find good agreement with real grey cast irons. Some of the phases show great variation in conductivity and depend also on alloying elements. Therefore there is an uncertainty in addressing thermal conductivity to the single phases of an unknown grey cast iron. A method to directly measure thermal conductivity of microscopic phases is given by scanning thermal microscopy, SThM.

Pollock gives a review on SThM (Pollock, et al., 2001). In SThM, the conventional topography probe of a scanning force microscope, SFM, is replaced by a miniature resistive thermal probe, which can be used as heater and thermometer at the same time. The probe also gives information on the topography of the sample but on a lower resolution than conventional probes. In active mode, the temperature of the heated tip is kept constant and the electric power required is recorded. In sample areas of high conductivity more heating power is required. The result is a map of the thermal properties on the sample surface and below. An accuracy of ±15 % can be achieved following a calibration/correlation procedure in air and on known materials. Also information on the probe geometry is required, which varies from probe to probe and is quite difficult to obtain.

Table 2.4: Thermal conductivity of single phases

Material	Thermal conductivity in W/mK	Temperature range in °C	Literature source
Pure Chrome	~93 linear decrease to 76	30-130 130 - 480	(Moore, et al., 1977)
Fe$_3$C Pure Ferrite Alloyed Ferrite	7-8 78.5 (71-80) 30, (65-60)	0-100 27 (0-100) 27 (25-300)	(Rukadikar, et al., 1986), (Chen, et al., 2011), (Helsing, et al., 1991)
Pearlite$_{\parallel}$ Pearlite$_{\perp}$ Pearlite$_{effective}$ Graphite Flake$_{\parallel}$ Graphite Flake$_{\perp}$	58 35 45~50 500 10	25-300 25-300 25-300 25-300 25-300	(Chen, et al., 2011)

An attempt was made to use SThM on the piston ring and cylinder liner. The results are presented in chapter 8.

2.10 Conclusions of the Literature Review

Sulphuric acid is known to have various chemical degrading effects on hydrocarbon oils, which are able to worsen or at least change lubricant properties. Most of these experiences originate from refinery plants where concentrated sulphuric acid is used to achieve high product yields of pure substances. Little, however, is known about the effects such degradation has on friction, viscosity, corrosion or neutralisation efficiency by fully formulated lubricants. The nature of the degradation products is also not very well described, neither is the influence of acid concentration and temperature on degradation known.

The rheology of dilute emulsions is quite well understood but the given theories require knowledge about interfacial tension, contact angle and phase viscosities. Interfacial tension between sulphuric acid and hydrocarbon oils was measured by several researchers but only for very small acid concentrations and room temperature, which are both readily exceeded by the condensate in the engine. For higher concentrations, the formation of hydrocarbon sulphonates and oxidation products can be

expected. Both kinds are known to further lower interfacial tension and if present in larger quantities alter viscosity. Contact angles are influenced by the surface properties but also by interfacial tension.

All the above missing links are relatively easy measured or analysed with standard techniques that have to be adapted for the use with corrosive sulphuric acid. The main difference, however, to previous research must be the separation between ideal hydrocarbon, lubricant base oil and fully formulated lubricant to gain basic understanding but also to reflect the difference between fresh fed lubricant and additive depleted lubricant. Another aspect is the trend in industry to use higher refined base oils as engine lubricants and this study highlights some possible consequences for lubricant formulation.

One major influencing factor on all the above parameters is the temperature. The bulk cylinder liner temperatures close to the lubricated surfaces are quite well known from measurements but the real dynamic lubricant temperature is beyond any conventional measurement. A large marine Diesel engine has some material and dimension features which are different from small bore engines. Namely gas radiation must have a bigger influence but very little is known about absorption of this radiation by the cylinder liner wall, the oil film and formed deposits. The infra red spectroscopy, extensively used in this study, operates in the same wavelength range and can help to increase the knowledge about this absorption properties. The coarse microstructure of the cylinder liner is inspiring to not only treat the material as homogeneous grey cast iron but to find material properties of the single grains, which might influence the Tribological behaviour more than for a material with fine microstructure.

The following six chapters report on the experimental work, which focused upon chemical interaction, interfacial tension, contact angle and friction measurements and thermal properties of marine engine material. The experiments had to be done under ambient atmosphere, which limited the minimum acid concentration or maximum temperature to avoid evaporation of the aqueous phase. The pressure in liquids, however, has less influence on chemical reactions than the temperature. The reduced temperature can be covered by allowing more time for chemical reactions to take place.

The following Figure 2.2 illustrates the earlier described physical processes and gives a preview on how these were investigated in this study.

Condensed acid
→ Droplet size

Alkaline reserve / additives in lubricant
→ Rate of reaction

Degraded oil / deposit formation
→ Interfacial tension
→ FTIR, EDX, XPS
→ Friction test
→ Viscosity
→ Critical Temp. / concentr.

Acid droplets resting on the wall under shear
→ Contact angle
→ Viscosity

Lubricant additives forming boundary layer
→ Friction test

Corrosive attack on metallic parts
→ Microscopy

Water condensation in interring crevices
→ Droplet size

$H_2O + SO_3$

Air

Moving piston ring

$H_2O + SO_3$ gas from combustion

Oil film

$T_{wall} < T_{gas}$ Variable along stroke

p_{gas} variable

Saturated humid air

Figure 2.2: The relation between the physical processes taking place in the engine and the techniques used to characterise this.

Chapter 3
Analytical Methods and Results

In this chapter analytical methods which were used repeatedly are described and some illustrative results are given. Some of the presented techniques were only used once and could not fill a whole chapter due to their limited extent. Other techniques, which were only used once but relate closely to another investigation, are not presented here and can be found in the corresponding chapter.

First the analytical methods are described in section 3.1. Mainly standard techniques such as 'light microscopy', 'SEM/EDX', 'FTIR-spectroscopy', 'particle size characterisation' and 'viscosity measurements' are shown but also two custom built techniques for analysing the neutralisation efficiency of fully formulated lubricants, 3.1.7, and finding critical acid concentration and temperature for oil degradation, 3.1.9, are presented. These last two techniques might be most interesting for a reader fairly familiar with the mentioned standard techniques.

The results are shown in sections 3.2 - 3.8, followed by a concluding section 3.9, where the main findings of each subsection are summarised.

Some of the analytical results have been presented in the articles listed on page i of this thesis.

3.1   Analytical Methods

3.1.1 Light Microscopy

To examine emulsions a Zeiss Axiovert135TV transmission microscope was used. Transmission means, the light is transmitted through a transparent sample before it enters the magnification optics. It is typically used for liquid samples. The samples are prepared by putting a drop of liquid on a microscope slide and covering it with a cover slip to spread it thinly between the two glass slides. For extremely viscous samples, two microscope slides were used and pressed, causing a distortion of the contained droplets but explained a non-Newtonian behaviour of the liquid.

Visual examination of the solids was achieved with a reflected light microscope, PolyvarMET. Reflected means the light is shone through the

optics onto an opaque sample surface where it gets reflected and re-enters the magnification optic.

Also a Leica DM6000M microscope was used which is capable of both transmission and reflection settings.

The pictures were captured by built in CCD cameras. A greater depth of field was achieved by stacking of several pictures with incremental focal lengths using image analysis software (Hadley, 2006).

Length measurements were possible by comparing captured pictures with a known standard. Once calibrated, measurements could be output automatically by the processing software when the correct magnification setting was known. Magnifications between 50 and 500 times could be achieved easily and for very smooth surfaces even 1000 times was feasible.

Some results of light microscopy can be found in section 3.2. but also in other parts of the thesis.

3.1.2 SEM/EDX

A scanning electron microscope, SEM (Philips XL30 with tungsten source operating at 20 kV, working distance of 10 mm) was used for high resolution images of solid reaction products. The sample is raster-scanned by a high energy beam of electrons. The electron beam causes orbital electrons to be ejected from the sample near surface area. Those secondary electrons are detected, amplified and used to create high resolution pictures of the surface topography (Berger, et al., 2001).

The SEM included the possibility for energy-dispersive X-ray spectroscopy, EDX (Oxford Instruments INCA System with X-sight SiLi detector), which gives the analysis capability for elemental identification in the near-surface layer. A beam of electrons is shone on the sample surface. Electrons from the inner orbital shell of the sample atoms are ejected. Electrons from outer orbital shells at higher energy levels fill up the gap, emitting the difference in energy as X-rays. The X-ray dose and energy is characteristic for each element and can be used to analyse the elemental composition of the sample (Berger, et al., 2001).

The technique operates in vacuum, therefore the sample has to be free of liquids. Operation of the instrument was left to trained staff.

Some results of SEM/EDX can be found in section 3.3.

3.1.3 FTIR-Spectroscopy

Fourier transform infrared spectroscopy, FTIR (PerkinElmer Spotlight 400) was used to analyse for chemical bonds of the samples. The instrument has a light source which operates in the infra red region, typically a electric heated glowing solid which gives a Planck distribution of emitted energy. The emitted light is shone on a beam splitter which divides the beam. One half is sent to a fixed mirror, while the other half is sent to a moving mirror. The two beams are combined and shone on the detector, which measures the energy of the received light. Depending on the position of the moving mirror, to the fixed mirror, the light waves are combined constructively or destructively. The sinusoidal wave is measured over time by the detector. Any obstructive sample in the path of the combined beam reduces the intensity of the sinusoidal wave at the absorbed frequency. The characteristic interference pattern allows the simultaneous measurement of the whole frequency bandwidth. A mathematical operation called Fourier transformation converts the intensity over the time spectrum into the final intensity over the frequency spectrum (Sherman Hsu, 1997).

The energy of light excites chemical bonds and gets transformed into movement or vibration of the bonds. This excitation is characteristic to explicit bonds. Possible characteristic movements are symmetric or asymmetric bending, scissoring, stretching and twisting and their combinations. There are also chemical bonds which are not excited at all in the infra red region, nitrogen (N_2) is one example. Carbon dioxide (CO_2) or water (H_2O) get excited. When molecules get excited to vibrate at a certain light wave frequency, the energy of the light wave gets reduced and the material appears opaque at this wavelength band. Vibration of molecules can be measured by an increase of temperature, an effect we see in nature by increased atmospheric temperature when CO_2 levels rise. In the instrument CO_2 and H_2O-vapour reduces light transmission efficiency and the instrument has to be calibrated before the measurements by a so-called background scan. The background scan is the reference for the maximum transmitted energy from light source to sensor.

There are also infra red transparent solids, calcium fluoride (CaF_2) is one example. Such transparent solids can be used as optical windows in the instrument and liquid sample holders. Care must be taken to chose the right material to avoid chemical reaction between sample and optical window. Sodium chloride (NaCl) for example would dissolve in water. It was decided

to do background scans with the empty sample holders in place, as the transparency is not perfect over the whole wavelength range.

From the above it is apparent that we can place a liquid sample between two optical windows within the path length of the light before the energy detector. Any reduction in transmitted energy in correlation with transmitted wavelength will allow a correlation to a chemical bond. This technique is used and called FTIR-spectroscopy in transmittance mode. For repeatability and comparability reasons the thickness of the liquid sample has to be kept constant by spacers between the optical windows. Thick spacers increase absorption, resulting in pronounced and broad peaks. Thin spacers give more distinct peaks at reduced intensity. The selection of the spacer is a compromise and has to be chosen in accordance with the concentration of the analysed species in the bulk liquid sample.

The handling of the liquid cells is very tedious, most optical cells are mechanically weak or not compatible with the samples and a lot of solvent is needed to clean the cells.

Acidic or aqueous liquid samples were placed in a CaF_2 transmission cell, which was found to be resistant to concentrated sulphuric acid. For discoloured oil, potassium bromide (KBr) cells with a 0.05 mm path length were used. The aqueous droplets observed in the oil phase were small and stable and no chemical reaction with the KBr was observed.

A more elegant arrangement is the attenuated total reflectance (ATR) accessory (PerkinElmer Spectrum100 FTIR-ATR) which fits into the pathway between beam splitter and detector of a conventional transmittance arrangement. The light beam is diverted into a crystal of high refractive index where it is reflected on the surface. The light penetrates 0.5 – 5 µm (PerkinElmer, Inc., 2005) into samples with lower refractive index than the crystal. The penetration depth is much smaller than achievable by the spacers in transmission mode. The evanescent light gets reflected by the sample back into the crystal and is guided by the optics into the detector. In wavelength areas of high absorption, the amount of total reflection gets reduced or 'attenuated'. This information is used to create the spectra. Non-transmitting sample surfaces as well as liquids can be analysed. Further information on FTIR-ATR can be found in (Shuttlefield, et al., 2008) and (Shuttlefield, et al., 2008)

The practical benefits of the ATR are easier cleaning and sample preparation procedure. The sample quantity is greatly reduced to about 0.5

µl compared to 1 ml with the transmission cells. The samples can also be very viscous and the trapping of air within the sample is less likely. The ATR zinc selenide (ZnSe) optic surface is covered by a diamond window which is mechanically strong and chemically inert. The optic is embedded into stainless steel (PerkinElmer, Inc., 2005). To prevent the stainless steel from corrosion by sulphuric acid, the plate was covered by Kapton[©DuPont] polyimide tape with an oil-resistant silicon-based adhesive. The optic was freed by cutting a hole in the film. The tape was replaced when signs of deterioration appeared, which only occurred for the highest acid concentration. No influence of the polyimide on the measurements were found. The results were obtained at 22 °C ambient and used without further processing or correction.

Bituminous samples were found to be emulsions of a light liquid in a very dark surrounding matter. The sample was first analysed in its emulsified state. Secondly the surrounding sulphuric acid was neutralised in water and washed with isopropanol and heptanes to remove water and excess oil. A third quantity was washed with water and dissolved in hexane, which liberated encapsulated sulphuric acid. Hexane was extracted from the top and dried off at 40 °C. The remaining matter was microscopic homogeneous.
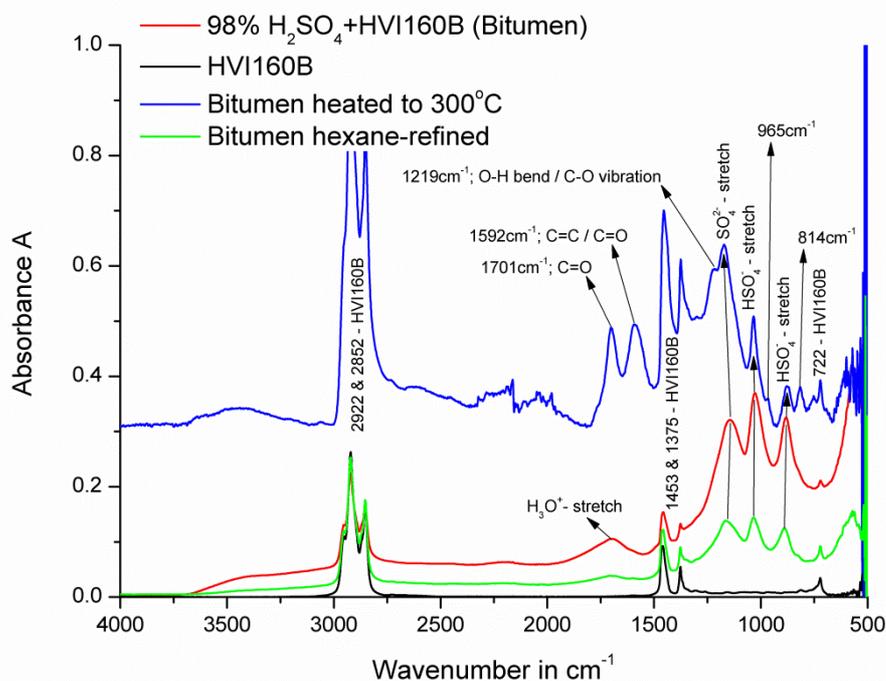
Figure 3.1: Bitumen formed between HVI160B and 98%w/w H_2SO_4 at various treatment stages.

In an first attempt to separate the bitumen from enclosed residual liquid sulphuric acid, the bitumen was heated to 300 °C on a hot plate instead of the above hexane treatment. The difference in FTIR response or better chemical composition, can be seen in Figure 3.1. The heat treatment caused strong oxidation of the hydrocarbons in the bitumen. This finding should be kept in mind when analysing deposits formed during friction tests; the oxidation can be a secondary reaction although probably triggered by the sulphuric acid.

Non homogeneous samples or samples with a inverse curvature that cannot be placed on the ATR, were analysed by an FTIR-microscope (PerkinElmer Spotlight 400). The FTIR-microscope uses a PerkinElmer Spectrum100 as the light source but has its own, liquid nitrogen cooled, detector. The FTIR-microscope can be used in reflectance or transmittance mode. Calibration and background scan was achieved using a gold mirror, which is a perfect reflector in the infra red region. The sample was placed on a moveable stage. A integrated optical microscope with CCD camera was used to focus on distinct areas were spectra had to be taken. The microscope can also scan defined areas to produce a map of material distribution. It was mainly used to investigate the chemical composition of wear tracks and results are shown in chapter 7.

Some design faults were found with the FTIR-microscope. The detector is very sensitive to mechanical shock, which makes the filling with liquid nitrogen delicate. The transmission mode can hardly be used for liquids. It would be ideal to visually locate a droplet within a bulk liquid and do an IR scan on the droplet. However there are no IR-transparent microscope slides or more important cover slips available on the market. With standard thick IR cells it is impossible to visually focus on the liquid. Trials were made using reflecting microscope slides without cover slips but the movement by convection within the sample droplet was too strong for the chemical analysis.

Some results of FTIR spectroscopy can be found in section 3.4. but also in other parts of the thesis.

3.1.4 LC-MS

The liquid chromatography – mass spectroscopy (LC-MS) technique was chosen for the analysis of the viscous reaction products. As the chain length of these products was assumed to be high, the LC-MS technique was preferred to the alternative gas chromatography – mass spectroscopy

technique because this tends to degrade long hydrocarbon chains during evaporation of the liquid (Agilent Technologies, 2001). The instrument used was an Agilent 1200 binary HPLC with a UV/Vis detector coupled to a Bruker HCT ultra ion trap mass spectrometer using an electrospray ionisation source (Warriner, et al., 2011).

The principle of conjoining the two techniques is that the LC system will separate the injected mixture into an orderly procession of compounds which are detected by the UV/Vis system; the MS system will then positively identify the individual compounds.

Unfortunately, the LC expertise of the Chemistry Department at the University of Leeds was unable to separate the components of the viscous reaction products as these products contaminated the LC separation column. A long program of solvent system optimisation would be needed to separate these components, which is not feasible due to time constraints.

3.1.5 Laser Diffraction Particle Size Characterisation

Samples were prepared to find the influence of sulphuric acid concentration on the viscosity of acid in oil emulsions, section 3.7. The volume of the dispersed phase was kept constant but the mass concentration of the acid was changed. The aqueous solutions of sulphuric acid were dispersed in squalane and in API Group I base oil by keeping the mixture in closed glass sample bottles for 30 minutes in an ultrasonic bath.

The size of the droplets produced in the ultrasonic bath were measured in an Malvern "Mastersizer 2000" which uses laser diffraction by the droplets as a measurement principle. A He-Ne laser beam with a wavelength of $\lambda = 0.63$ µm is shone through a liquid flow containing the sample with droplets of various sizes. The laser beam is deflected by the curvature of the droplet. Deflection is depending on droplet size and refractive index of the droplets and the surrounding carrier phase. An array of sensors behind the liquid sample measures the deflection of the laser. The extent of deflection can be used to calculate the droplet size and the number of hits is counted by the device. For known refractive indices, the technique is capable of measuring droplet sizes in the range of 0.1 to 2000 µm with an error of less than 1 % due to the large amount of droplets measured (Rawle, 2012). About 1 – 2 ml of the emulsified sample was diluted in about 50 ml of mineral oil and pumped through the measurement cell. The refractive index of aqueous H_2SO_4 at the corresponding concentration and incident wavelength of $\lambda = 0.63$ µm (Palmer, et al., 1975) was used for the internal calculation of the

droplet diameter. For higher acid concentrations, the colour of the droplets changed due to chemical interaction with the oil, therefore their refractive index becomes unknown and the accuracy of the measurement suffers.

There are various statistical methods to calculate the mean diameter of the droplets in a sample. For the example of acid droplets contained in oil, the shape of the particles is spherical. Droplet breakup is influenced by interfacial tension. The Surface Area Moment Mean (Sauter mean diameter) D[3,2], which rates the surface area higher than the volume seems to be the most appropriate method in this case. However, the Volume Area Moment Mean (De Brouckere Mean Diameter), D[4,3], which rates the volume higher than the surface area, gives information on the extent of droplet break-up. A large deviation between D[3,2] and D[4,3] with the latter being bigger, would mean most of the dispersed volume is contained in a few large droplets (Rawle, 2012).

Some results of Laser Diffraction Particle Size Analysis can be found in section 3.5 together with findings on the stability of the produced emulsions.

3.1.6 Dynamic Light Scattering Particle Size Characterisation

Dynamic Light Scattering, DLS, was applied to characterise dispersed additive particles in fully formulated lubricants such as calcium carbonate in micelles. The "Malvern Zetasizer nano ZS" measures the speed of Brownian motion and relates it to the size of particles using the Stokes-Einstein equation:

$$d(H) = \frac{kT}{3\pi\eta D}$$
(3.1)

where $d(H)$ is the hydrodynamic diameter, k the Boltzmann constant, T the absolute temperature, η the dynamic viscosity and D the translational diffusion coefficient.

Brownian motion is the random movement of small particles excited by the movement of surrounding molecules. The smaller the particle the more extensive and rapid is the movement of the particle. DLS measures the fluctuation rate of scattered light intensity. Internally the software calculates also the volume and number distribution of the particles, which can be used to interpret the results from the intensity results to find the size of the major species of particles in case there is more than one peak. The intensity of scattered light from particles is proportional to d^6 which can lead to a misinterpretation in favour of a few large particles.

The technique is capable of measuring particle sizes in the range of 0.6 nm to 8.9 µm with an error of 5 %.

The technique has three major drawbacks for measuring calcium carbonate particles in micelles, dispersed in oil. First, the resulting hydrodynamic diameter $d(H)$ of the particle is the equivalent diameter of a sphere with the same diffusion coefficient D and gives no information of the real shape of the particle. Second, low conductivity media, like oil, will produce an extended double layer around the particle, reducing the speed of the particle, which increases the resulting particle size. Third, the dispersant forming the micelle around the particle will also lower the diffusion speed, increasing the apparent size of the particle. The resulting diameters for this study are therefore too big with the biggest influence on the smallest particles because the thickness of the surrounding "shell" will stay constant, independent of the particle size. However, the main interest was the relative difference in particle size between the different lubricants.

The above description of DLS was obtained from a technical note of the device manufacturer (Malvern Instruments Ltd., 2001).

The results of DLS can be found in section 3.6.

3.1.7 Neutralisation Rate of Fully Formulated Lubricants

Some information on sulphuric acid neutralisation time in fully formulated marine Diesel lubricants was found in the literature (Garner, et al., 2004). The source, however, was not specific enough and it was found advisable to gain personal experience with the neutralisation efficiency and also with varying test conditions.

The most common additive to achieve a high alkaline reserve in marine Diesel engine lubricants is calcium carbonate, $CaCO_3$ or limestone. Calcium carbonate reacts with H_2SO_4 to form calcium sulphate, $CaSO_4$, water and carbon dioxide, CO_2.

$$H_2SO_4 + CaCO_3 \rightarrow CaSO_4 + H_2O + CO_2 \qquad (3.2)$$
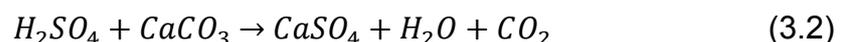
The CO_2 leaves the mixture in its gaseous form. At low to moderate temperatures, the water is captured in the crystalline structure of the calcium sulphate to form calcium sulphate dihydrate, $CaSO_4 \cdot H_2O$. At elevated temperatures, the water also leaves the mixture in its gaseous form.

The release of gas can be used as a measure of reaction speed. The previously mentioned study (Garner, et al., 2004) used the rise of pressure over time in a sealed compartment operating at 200 °C. The rise in pressure

changes the dew point temperature of water and might depress the reaction by influencing the CO_2 release. Also the reaction changes the dew point as the acid dissociates in the produced water. Therefore it was decided to use the change in gas volume at ambient pressure over time to study the neutralisation efficiency. The temperature was kept at 80 °C to be below the boiling point of water, first to avoid evaporation from the reaction product and second to be able to inject low concentrations of aqueous sulphuric acid.

The uncertainty on the nature of the neutralising additive used in a particular lubricant is a drawback. When calcium oxide, CaO, is used to generate the alkaline reserve no gaseous CO_2 is released, equation (3.3). Therefore it is disputable to directly compare two different lubricants.

$$H_2SO_4 + CaO \rightarrow CaSO_4 + H_2O \qquad \qquad (3.3)$$
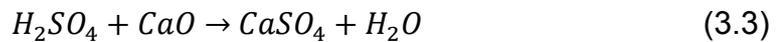
The measurement arrangement is presented in Figure 3.2. A temperature controlled hot plate with integrated magnetic stirrer (A), keeps the water bath (B) in motion and at a constant temperature of 80 °C, measured by a temperature sensor (D). Placed in the water bath at constant immersion depth is a sealed bottle (C) containing the fully formulated lubricant and a second magnetic stirrer. The lubricant is stirred for 30 minutes to allow temperature equalisation before sulphuric acid is injected through a syringe (E). The sealed bottle is connected by a tube (F) to a syringe (G) which has a floating but gas tight plunger. At the start of the test, the plunger was kept floating a few millimetres to keep a constant pressure through the known mass m, 98.59 g, of the plunger with a diameter d of 34.18 mm. The resulting backpressure $P_{plunger}$ of ~1053 Pa increases the response time during the most interesting starting phase. The volume readings from the scale of the syringe are captured by a camera, which is set to a maximum speed of 1 frame per second. The capturing time is recorded within the picture file, which allows a accurate reading of the measurement.

Three different tests were performed with the fully formulated oil. First concentrated acid was injected, second a reacted mixture of API Group I base oil with concentrated acid and third an acid concentration of only 70 %w/w was injected. For the third test, the amount of acid was kept constant, but the total volume was increased. A test with 50 %w/w acid concentration resulted in almost no reaction.
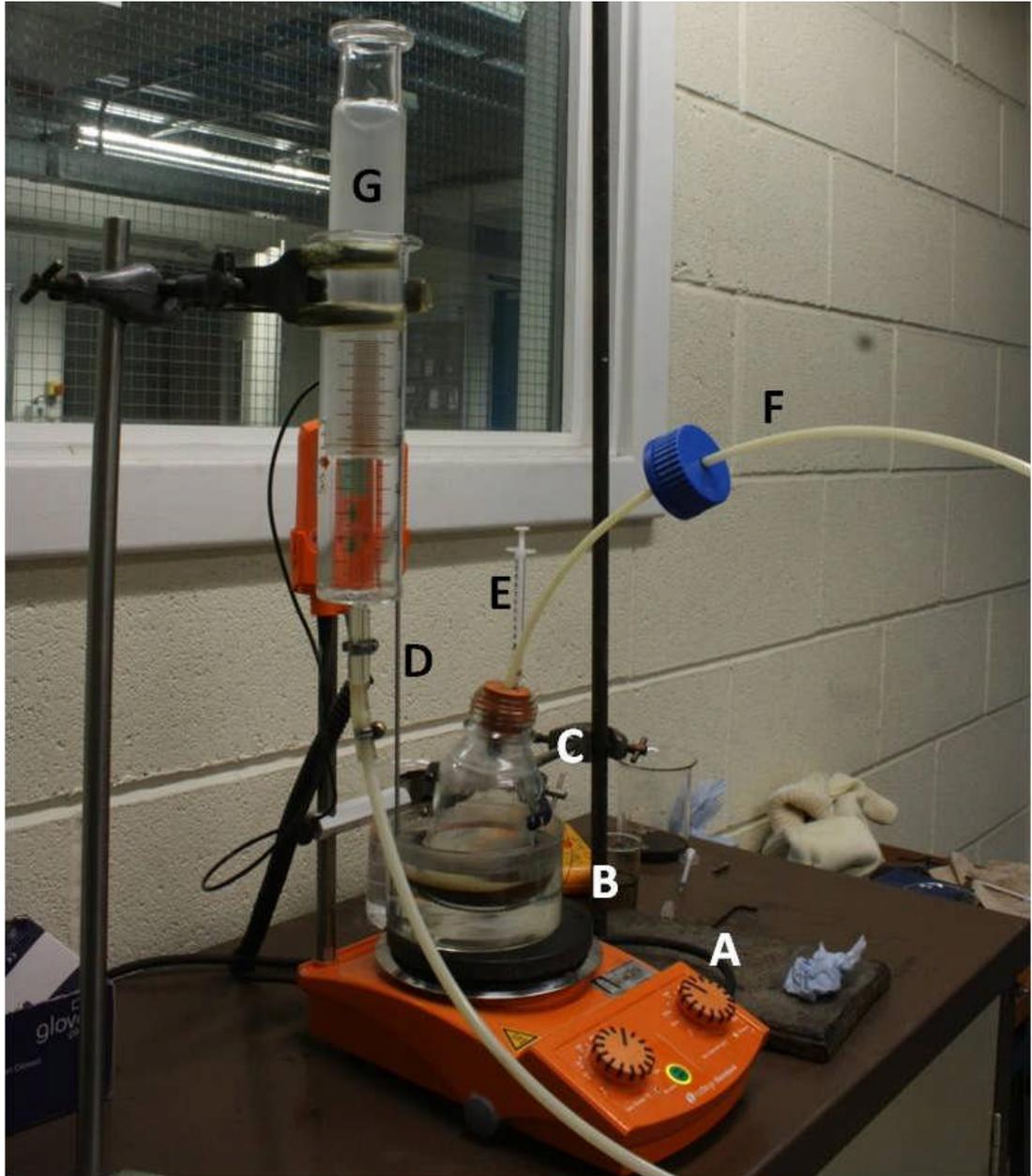
Figure 3.2: Neutralisation efficiency, volumetric measurement arrangement

The amount of acid was balanced to the alkaline reserve of the lubricant with known mass according to equations (3.2) and the following equations (3.4) and (3.5).

The alkaline reserve is given by the total base number, TBN, which represents a theoretical amount of potassium hydroxide per mass oil, mg KOH/g oil. The neutralisation of H_2SO_4 with KOH follows the equation:

$$2KOH + H_2SO_4 = 2H_2O + K_2SO_4 \qquad (3.4)$$
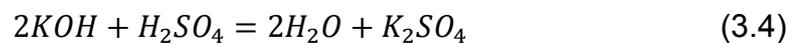
Neutralisation of 1 mol H_2SO_4 (98.0791 g/mol) requires 2 mol of KOH (56.1056 g/mol).

$$TBN70 \cong 70\,\frac{\mathrm{mg}KOH}{\mathrm{g}_{oil}} \cong 0.001248\,\frac{\mathrm{mol}KOH}{\mathrm{g}_{oil}}$$

$$\xLongrightarrow{neutralises} 6.2438 \cdot 10^{-4}\,\frac{\mathrm{mol}H_2SO_4}{\mathrm{g}_{oil}}$$

$$\xLongrightarrow{neutralises} 0.0612\,\frac{\mathrm{g}H_2SO_4}{\mathrm{g}_{oil}}$$

(3.5)

Theoretically, 1 g of oil mixed with 0.0612 g of H_2SO_4 should release $6.24 \cdot 10^{-4}$ mol of CO_2 following the reaction equation (3.2).

With the ideal gas law, the expected gas volume V can be calculated.

$$V = \frac{n \cdot R \cdot T}{P}$$

$$P = P_{plunger} + P_{ambient}$$

$$P = \frac{m \cdot g}{\pi \cdot \frac{d2}{4}} + 1050\mathrm{hPa}$$

(3.6)

For the chosen test condition of 18.2 g of lubricant and a gas temperature T of 20 °C, this results in a maximum expected gas volume of about 300 ml. Losses can only be explained by dissolution of CO_2 in the oil. Leaks were not present with a dry plunger and were additionally excluded by a liquid barrier of iso-propanol. Slight friction on the syringe plunger was present but overcome by regularly rotating the plunger. The gas temperature was ensured to be stable at 20 °C by using a 1 metre long hose and a glass syringe with a big mass – increase in temperature would increase the measurements. Each measurement condition was repeated 3 times, the average is presented. The results showed a very good repeatability.

The results for neutralisation efficiency can be found in section 3.6.

3.1.8 Viscosity Measurements

Viscosities were measured using a Malvern "Kinexus" Rheometer with cone on plate arrangement. Cone geometries were 1/50 and 4/40 mm height to diameter. Temperatures were set at 20, 40, 90, 120 and 150 °C in turn. A shear rate ramp time of 2 minutes between 0.1 and 1000 s^{-1} was chosen.

In the case of emulsions, measurements under equilibrium were not possible as the time until consecutive results are stable within very narrow limits was too long and phase separation would occur.

Some results of the viscosity measurements can be found in section 3.7 but also in other parts of the thesis. Viscosities of the used liquids are given in appendix A.

3.1.9 Bitumen Formation, Critical Temperature and Concentration

The API Group I base oil HVI160B was brought into contact with various concentrations of aqueous sulphuric acid. One batch of samples was stored for two weeks and the lowest acid concentration noted where bitumen formation occurred. A second batch was heated on a hot plate at a ramp time of 2 minutes from 20 to 100 °C. The temperature when the first discolouration on the interface occurred was recorded.

A similar heating and storage cycle was used for $C_{30}H_{62}$ during interfacial tension measurements, chapter 4. The samples were heated up to 90 °C and the point of discolouration noted.

$C_{30}H_{62}$ mixtures with acid concentrations of 0 %, 0.5 %, 10 %, 25 %, 40 %, 65 %, 80 % and 90 %w/w were stored for several days between 80 and 110 °C, 15 °C below their boiling point. The mixtures were freshly prepared and out of contact with any metal that could act as a catalyst. Concentrations which showed discolouration or solid formation were noted.

The results of this study are presented in section 3.8.

3.2   Results: Light Microscope

3.2.1 Light Microscopy on Liquid Reactants

Samples which were used in the interfacial tension measurements, chapter 4, were investigated under a transmission light microscope. They consist of a oil phase and a more dense aqueous acid phase.

In all samples, droplets were found in the acid phase. When the acid phase changed colour due to exposure to heat or long storage time, more droplets of 5 to 70 µm diameter were found. No droplets were found in pure water in contact with squalane.

When the oil phase stayed clear, no droplets were found in the oil phase. When the oil phase did change colour due to exposure to heat or long storage time, tiny droplets of 1 to 8 µm diameter were found in the oil phase.

The droplet sizes are given for guidance only, as the technique is not feasible for a statistical evaluation of a large quantity of droplets.

It was also observed that dark particles, the structure of which was too small to be revealed, would stay on the outside of the droplets in the oil phase and were more likely to be found on the inside of the droplet in the acid phase. This difference is quite apparent in Figure 3.3 and Figure 3.4.

Figure 3.3: Transmission microscopic image of the oil phase ($C_{30}H_{62}$) on top of 80 %w/w H_2SO_4 exposed to 165 °C
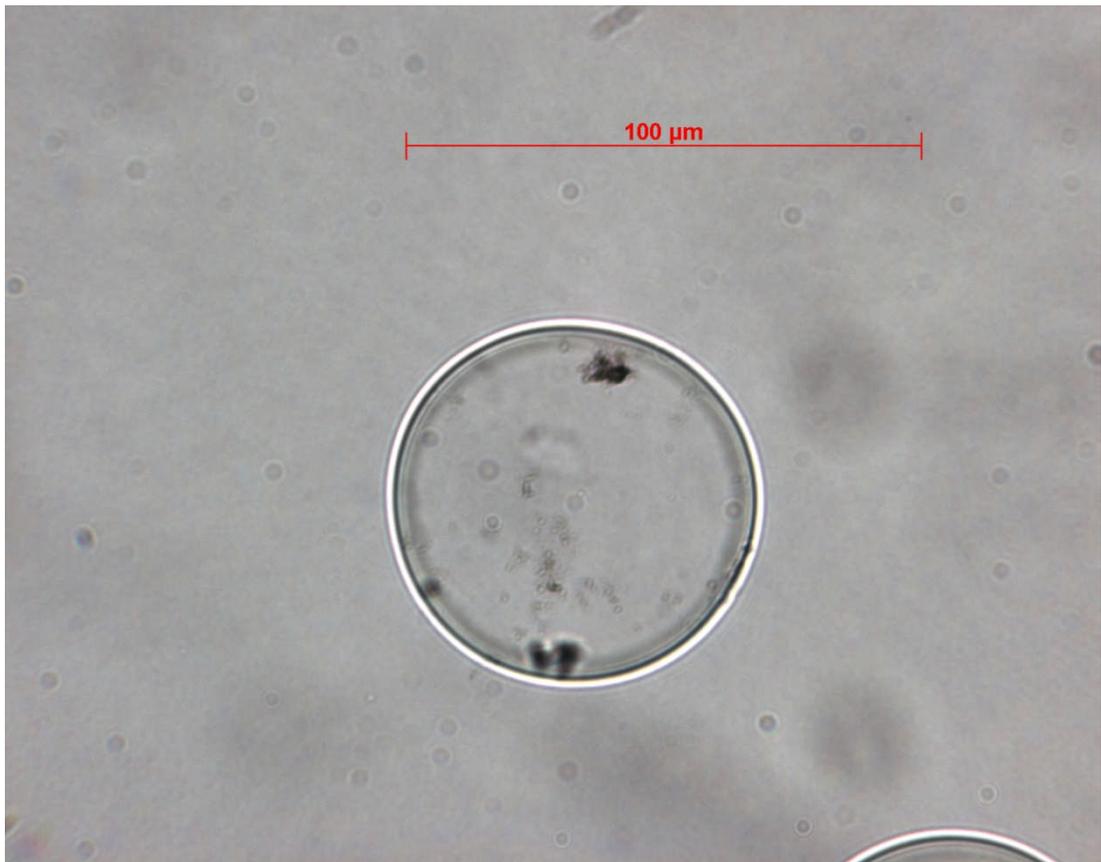
Figure 3.4: Transmission microscopic image of the acid phase (80 %w/w H_2SO_4) below $C_{30}H_{62}$ exposed to 165 °C

Figure 3.3 and Figure 3.4 show an example of $C_{30}H_{62}$ on top of 80 %w/w H_2SO_4 exposed to a temperature of 165 °C over 15 minutes; both phases changed colour. The samples were stored for several weeks at room temperature before the phases were extracted for microscopic examination.

The difference in droplet size, with smaller droplets in the oil phase and larger droplets in the acid phase, suggests the formation of surfactants with hydrophilic head groups and oleophilic tails yielding micelles or inverse micelles. The density of head groups per surface area should be the same for all droplets. However, in the acid bulk phase the oleophilic tails require space within the micelle droplet on the concave side of the interface, therefore enlarging the volume of the oil droplets. In the oil phase, the tails point outwards from the inverse micelle droplets convex side and thereby allow the acid droplets to be smaller in volume.

3.2.2 Light Microscopy on Liquid Reaction Products

On the interface between oil (squalane or API Group I base oil) and aqueous sulphuric acid, bituminous matter was formed. The bituminous reaction products appear to be quite complex emulsions.

The bitumen formed with 80 %w/w H_2SO_4, Figure 3.5, shows a dark bulk phase containing a light phase which contains irregular shaped solids; presumably former cell walls. The microscopic investigation was done after viscosity measurements, section 3.7, which explains the ruptured appearance.

The bituminous phase formed with 98 %w/w H_2SO_4, Figure 3.6, contains three different coloured phases which form droplets within each other.

The bitumen formed with 98 %w/w H_2SO_4 did not settle on a distinct interface. It had to be separated from the oil by pouring the sample in water and then separation was instantaneous. The remaining oil settled on top of clear water and the bitumen settled in the bottom of the beaker. The water and oil were poured away and the residual bitumen heated to evaporate any remaining water. The bitumen formed after separating the bituminous phase formed with 98 %w/w H_2SO_4 in water, Figure 3.7, showed droplets of an emulsion contained in a very dark and viscous phase. Figure 3.7 shows the bitumen after being squeezed hard between two microscope slides. Some drops burst and connected to form fingers and other drops remained contained in the black substance. Some of the light phase got squeezed out on the borders of the bitumen droplet.
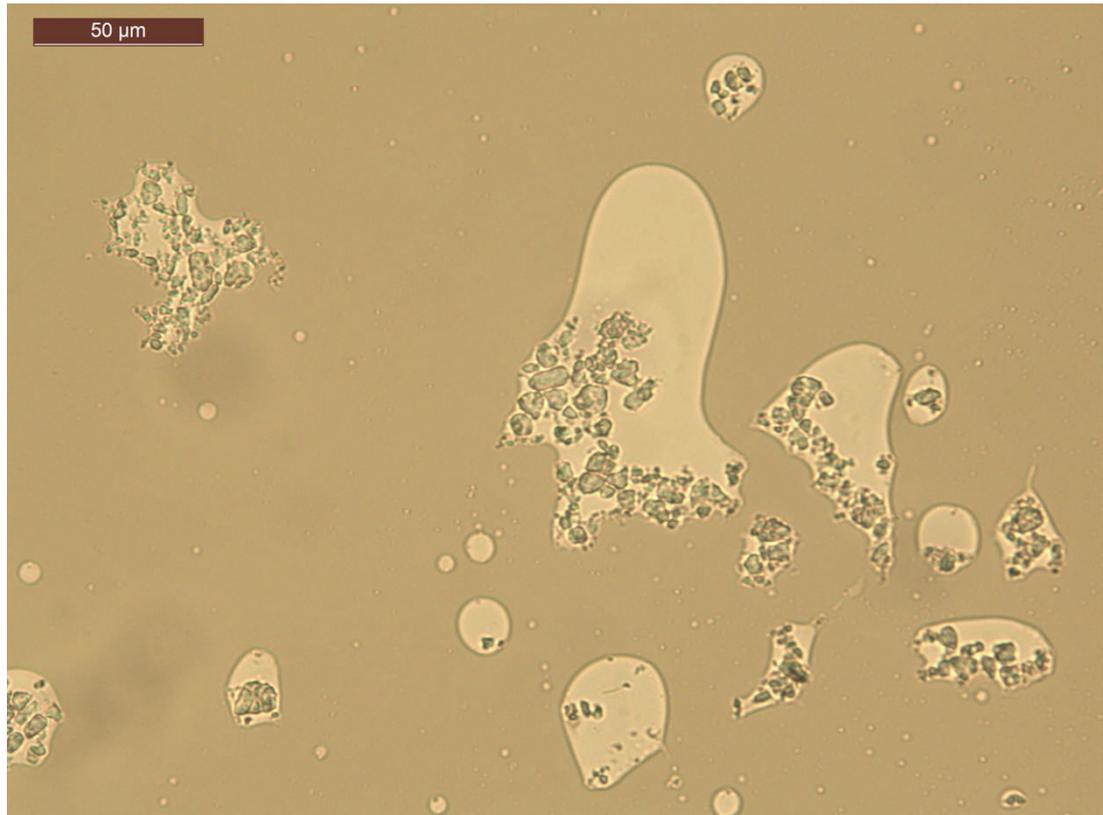
Figure 3.5: Microscopic view on bituminous matter formed between 80 %w/w H$_2$SO$_4$ and HVI160B, after viscosity measurements. 200x
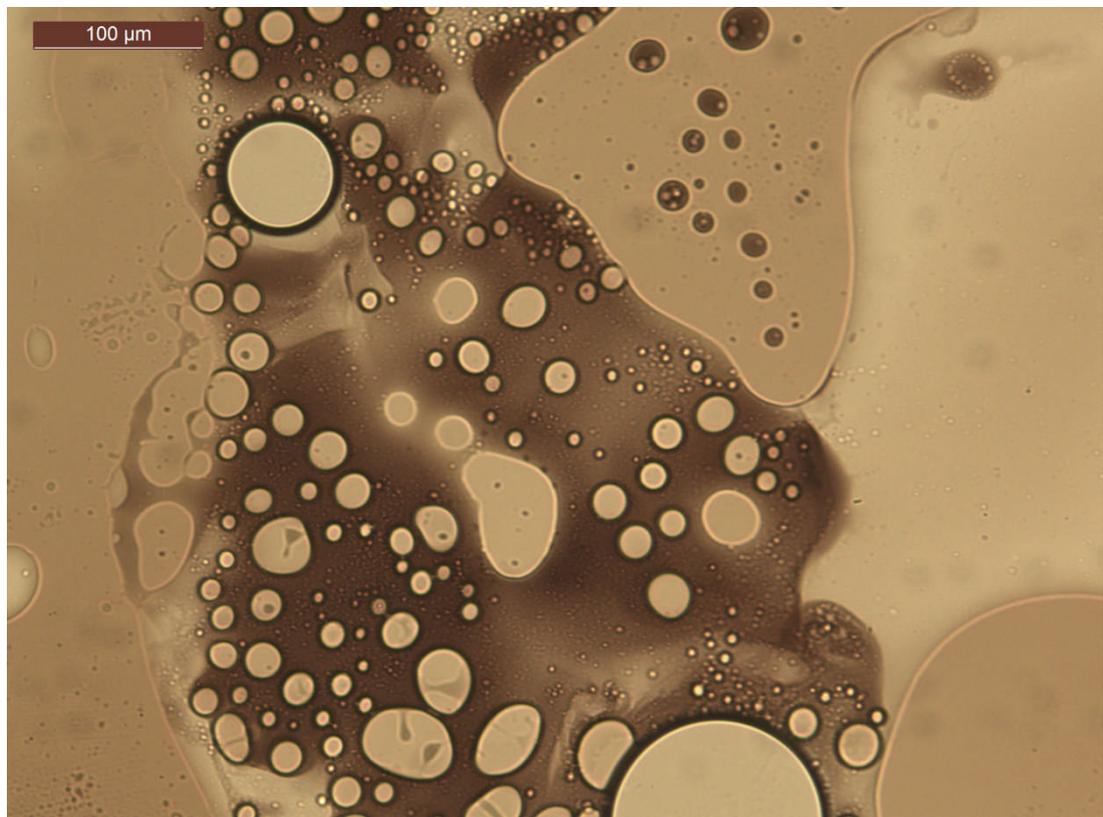
Figure 3.6: Microscopic view on bituminous matter formed between 98 %w/w H$_2$SO$_4$ and HVI160B before separating from oil phase. 100x
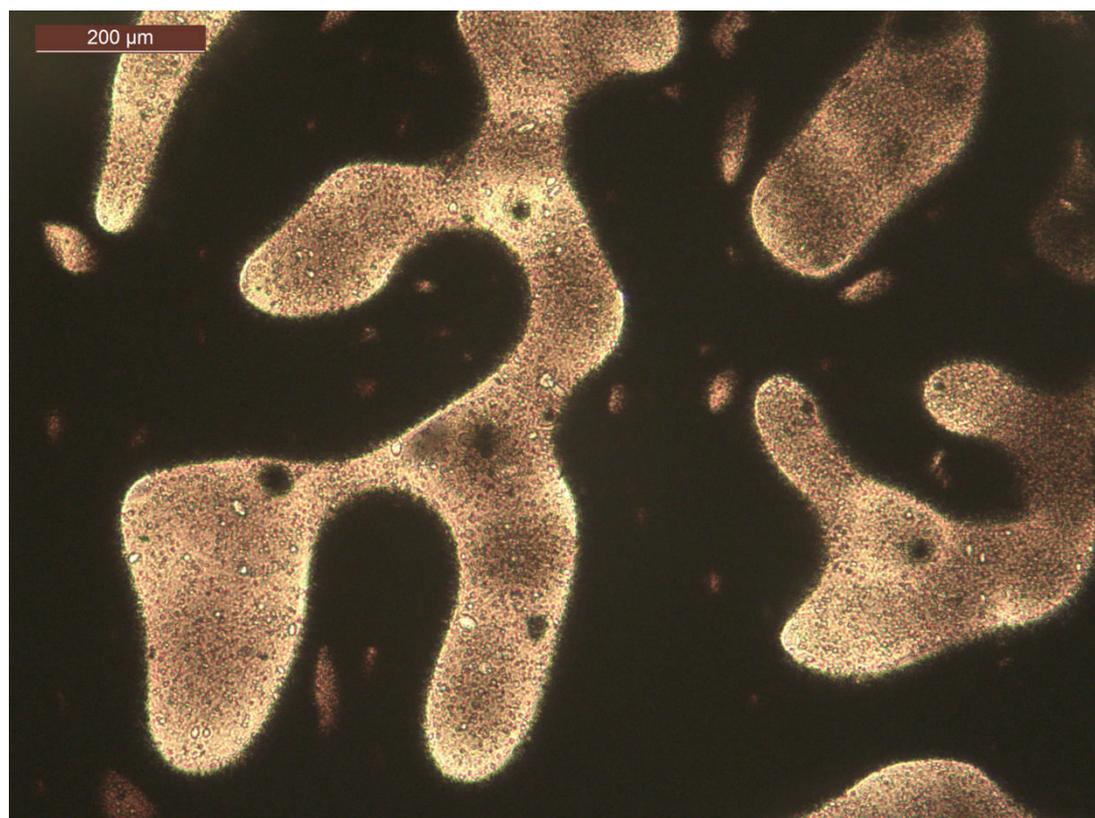
Figure 3.7: Microscopic view on bituminous matter formed between 98 %w/w H$_2$SO$_4$ and HVI160B after separating from oil phase in water. Squeezed between microscope slides. 50x

3.2.3 Light Microscopy on Solid Reaction Products

Figure 3.8 shows a microscopic view of a solid reaction product formed between squalane and sulphuric acid at 165 °C. A microscopic investigation on the reactants can be found in section 3.2.1. The high depth of field was achieved by stacking pictures of varying focal plane as described in section 3.1.1. The picture reveals a foam like structure with feature sizes comparable to droplets found in the acid phase. It was observed that some bubbles shrank after rinsing with solvent, suggesting that the cells were filled with liquid (oil or acid) and the reaction leading to solidification took place at droplet interfaces, meaning on the head groups of surfactants to form micelles.

The investigation was taken a step further by placing solid reaction products in an SEM. The results can be found in section 3.3
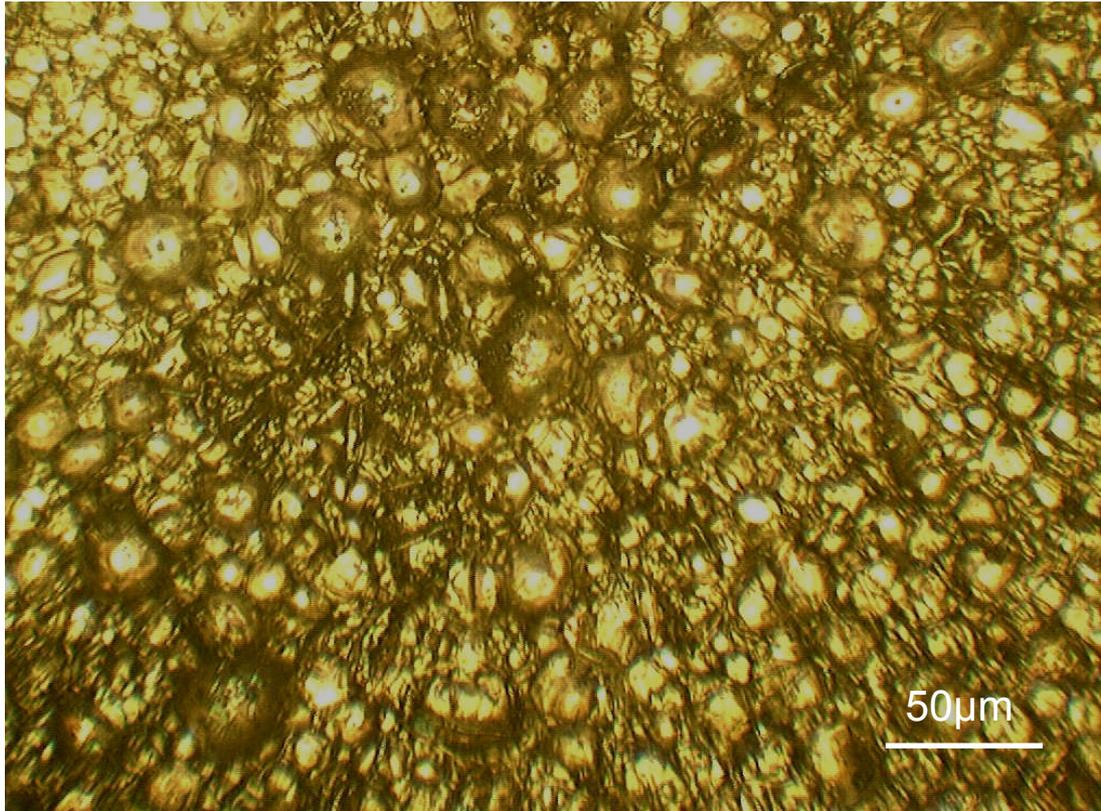
Figure 3.8: 200x magnification of a solid reaction product created between 80%w/w H_2SO_4 and $C_{30}H_{62}$ at 165 °C
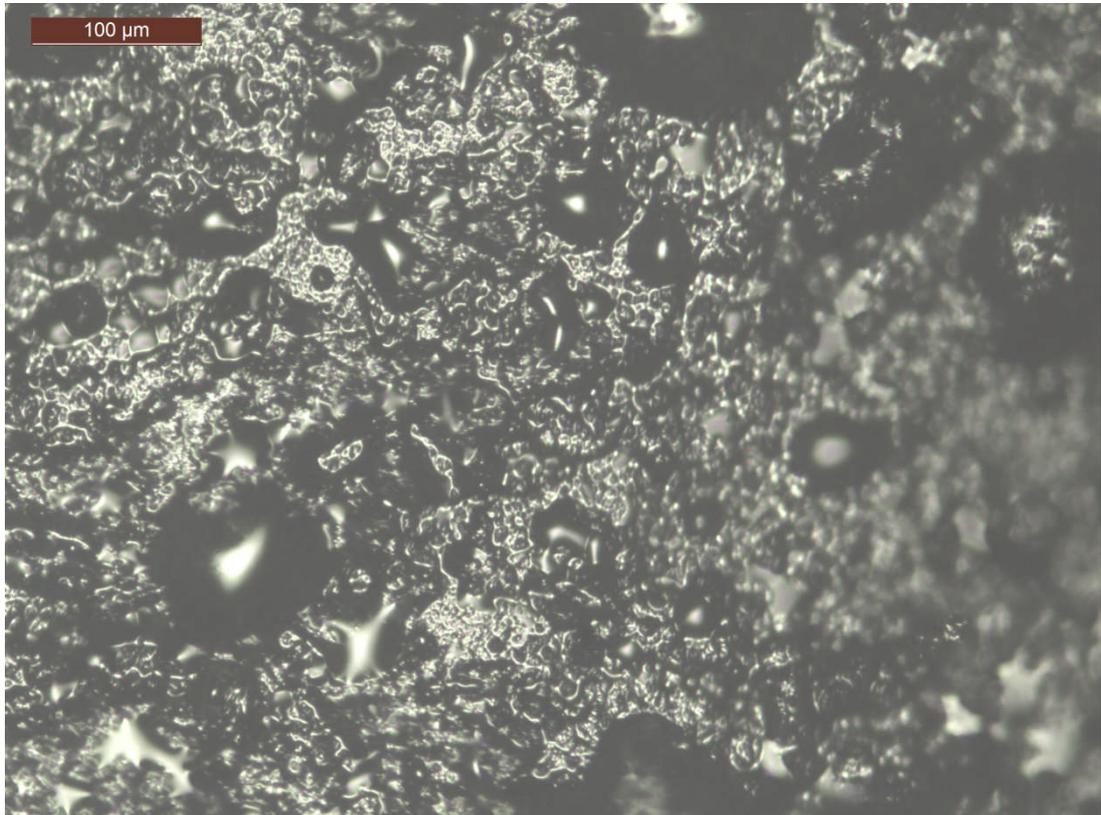
Figure 3.9: Deposit formed during viscosity measurements at 150 °C on bitumen created between 98 %w/w H_2SO_4 and HVI160B. 100x

During viscosity measurements, section 3.7, on bitumen formed between 98 %w/w H_2SO_4 and API Group I base oil HVI160B, the bitumen started to solidify between 120 and 150 °C, Figure 3.35. The deposit, Figure 3.9, shows a porous structure which still contains a liquid phase.

3.3   Results: SEM/EDX

At high temperatures, solids were formed on the interface between squalane and sulphuric acid. The example shown in Figure 3.10 was formed within 3 minutes at 165 °C and an acid concentration of 80 %w/w. The particles were floated on a water surface and could be captured with an SEM aluminium sample holder. During rinsing with heptanes, two edges of the sample rolled up, revealing the bottom side of the flake. Figure 3.11 shows the difference between the top and bottom of the sample. While the top side is smooth, Figure 3.12, the bottom side, Figure 3.13, reveals an open or shrunk, foam like structure with feature diameters between 10 and 50 µm. It seems likely that the bottom surface pointed towards the acid side. Due to the operation under high vacuum the washing of the particle had to be done more extensively compared to the investigation under the light microscope, section 3.2.3. The shrunk appearance of the structure is likely to be an artefact of the method and one has to imagine the structure to be liquid filled.

For a carbon based sample, the image quality of the uncoated sample is very good. This could either mean a conductive form of carbon or the isolating influence of the very thin flake being of minor influence.

EDX elemental analysis revealed 70.31± ~7 % carbon, 26.34 ± ~2.6 % oxygen and 3.3 ± ~0.07 - 0.17 % sulphur. All results are given in atom %. The extent of error correlates with the atom mass and decreases for heavier elements. An aluminium peak was subtracted as this originated from the sample holder as proven by repeating the measurements on a carbon tape covered holder. In this case no aluminium was revealed but the additional carbon was found.
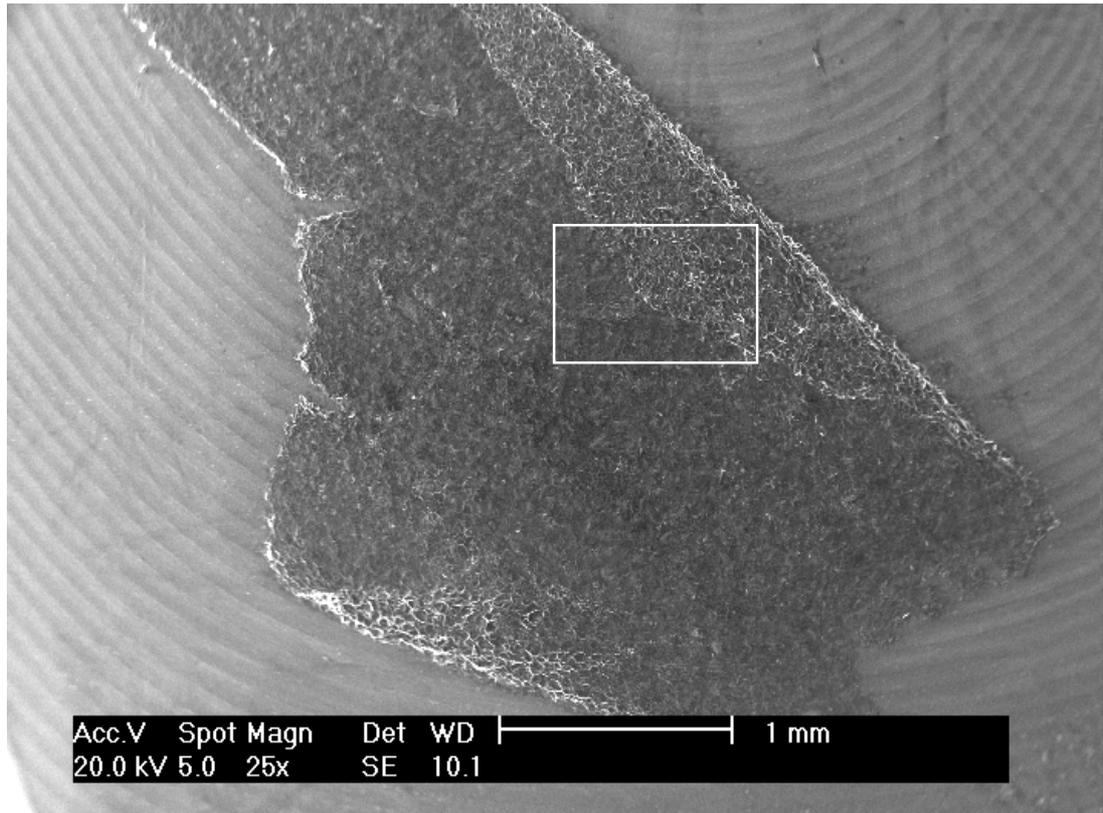
Figure 3.10: SEM picture; overview of solid reaction product created between 80 %w/w H_2SO_4 and $C_{30}H_{62}$ at 165 °C
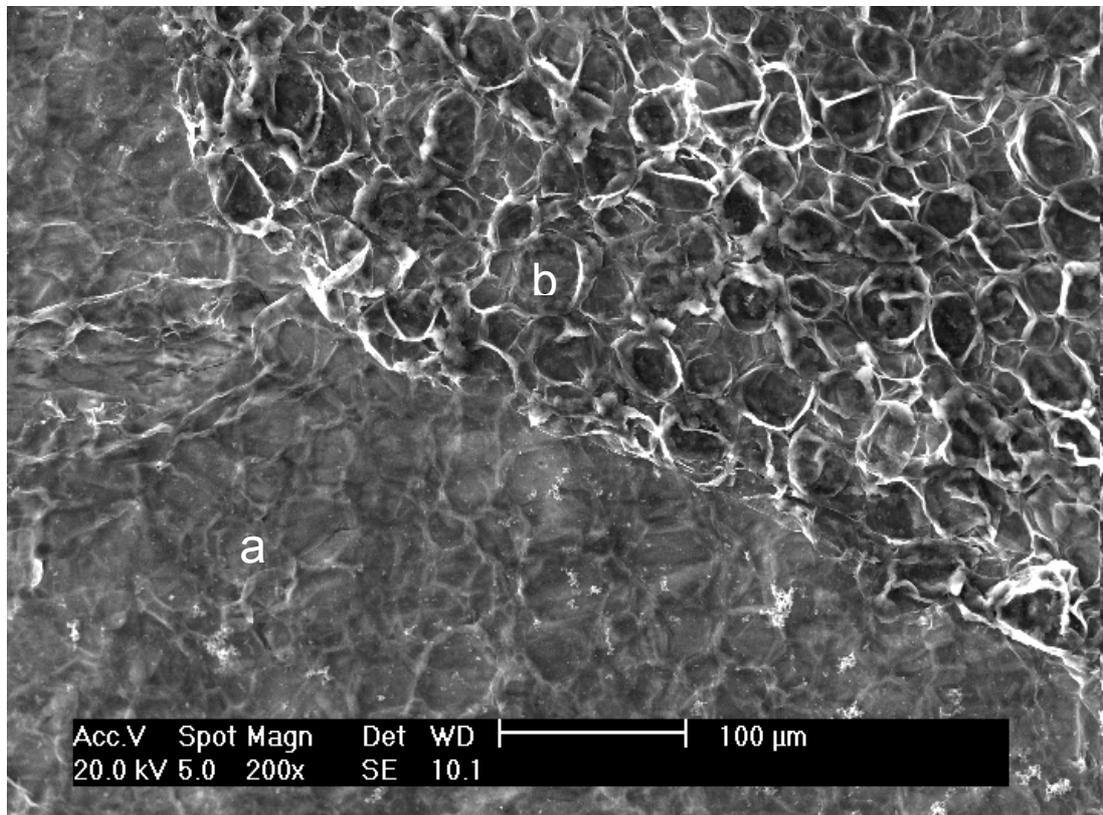
Figure 3.11: Enlargement of Figure 3.10
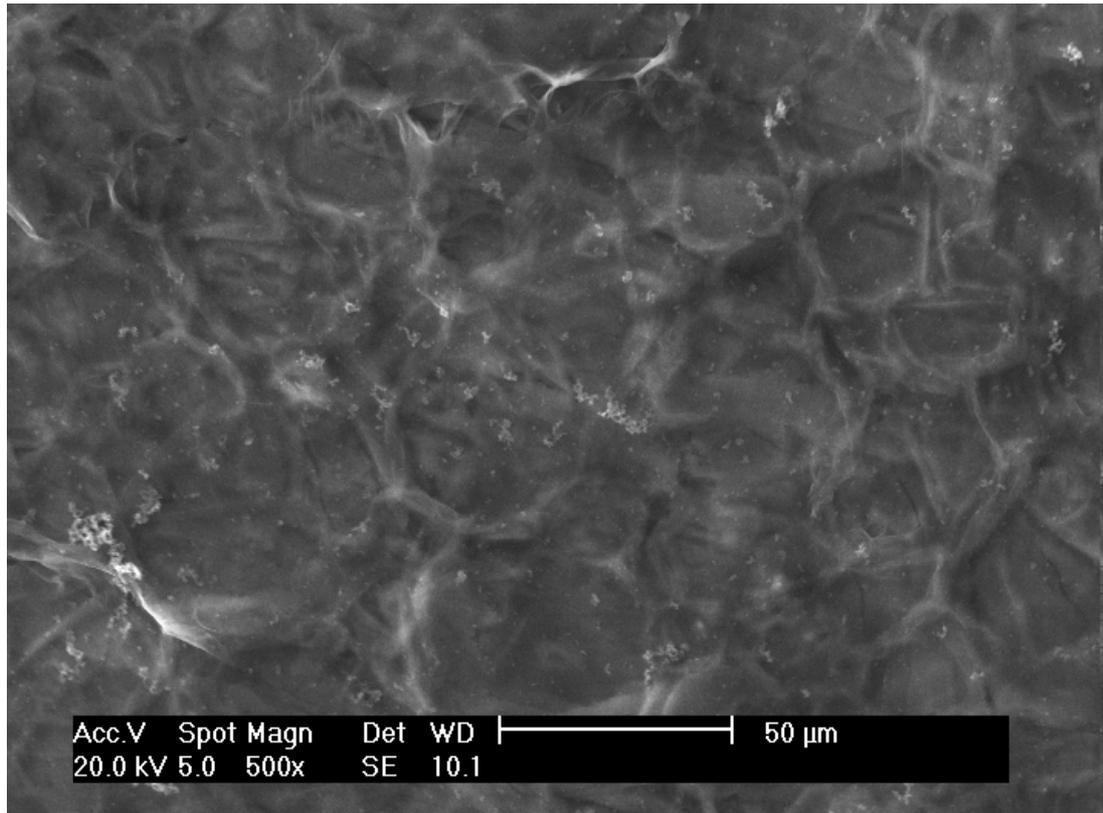
Figure 3.12: Enlargement of Figure 3.11, position a
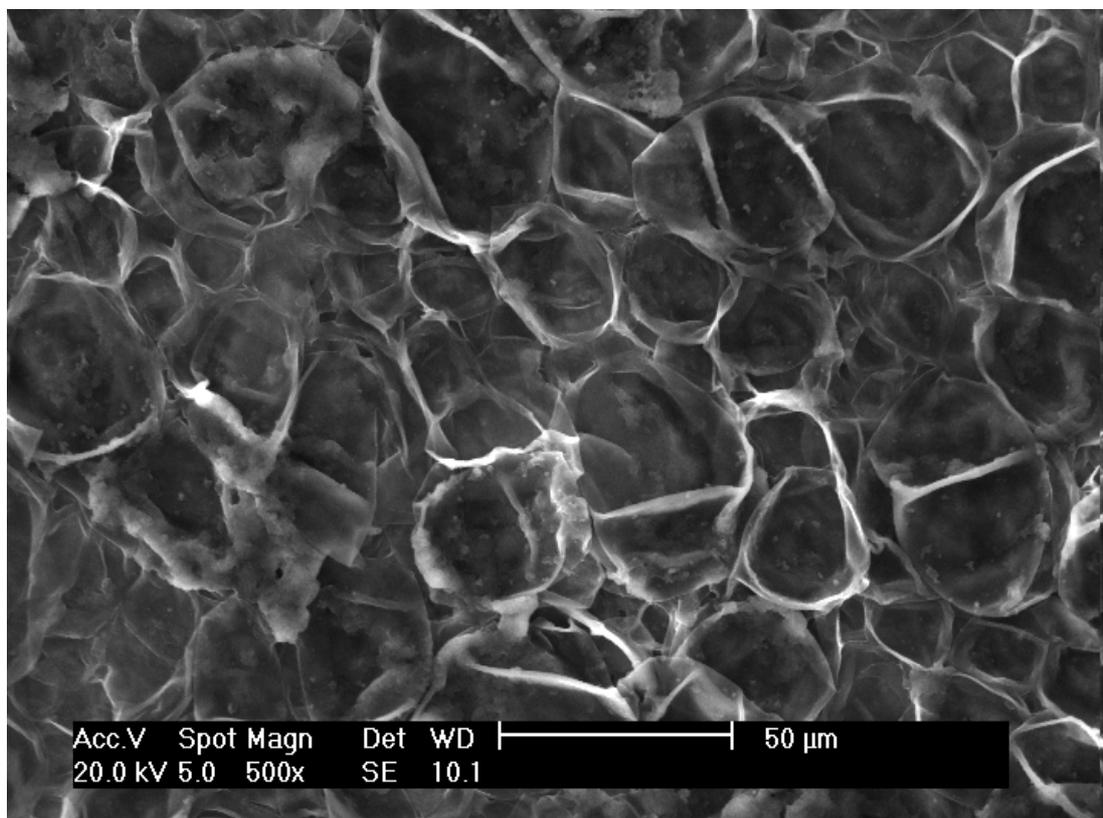
Figure 3.13: Enlargement of Figure 3.11, position b

3.4 Results: FTIR-Spectroscopy

3.4.1 Sulphuric Acid Concentration, Pure and Within Hydrocarbons

The bottom plot of Figure 3.14 shows the FTIR-ATR spectra of water and aqueous H_2SO_4 at thirteen concentrations between 0.5 and 98 %w/w; the dependence of absorbance on concentration is very strong and is also shown in Figure 3.15. The HSO_4^- asymmetric stretch in Figure 3.15 is very similar to measurements presented earlier for dissociation of H_2SO_4 in H_2O (Young, et al., 1959), chapter 4. The conventional method establishes the acid concentration of a sample from its FTIR absorbance peak to peak ratio (Bellamy, 2010), (Sherman Hsu, 1997). The absorbance spectra presented in Figure 3.14 are very similar to spectra of refractive index presented earlier (Palmer, et al., 1975) but at higher resolution in wavelength and acid concentration.

The analyses of the absorption band maxima and their associated absorbance show a complex behaviour in the upper plots of Figure 3.14 and quantified in Table 3.1.

However, Figure 3.16 and Figure 3.17 illustrate the problem when the acid is mixed with a hydrocarbon. Figure 3.16 first compares the FTIR-ATR spectrum of 80 %w/w aqueous sulphuric acid used in the reaction with API Group I base oil HVI160B, and the FTIR-ATR spectrum of pure 80 %w/w H_2SO_4. The two spectra overlay each other although the used H_2SO_4 changed colour. The hydrocarbon content is too small to be detected and the acid peaks are broad and strong and mask any hydrocarbon absorbance peaks. Second, Figure 3.16 compares the 80 %w/w H_2SO_4 with a bituminous reaction product formed at the interface of 80 %w/w H_2SO_4 and API Group I base oil HVI160B. The reaction product was mechanically extracted by a pipette and its FTIR-ATR spectrum obtained without further treatment. Very small indications of hydrocarbons can be seen but more apparent is the significant decrease in absorbance between 500 – 1500 cm^{-1}. This is contrasted by the same absorbance in the region of 3300 – 4000 cm^{-1} and ~1400 cm^{-1} for the three spectra. The concentration of the used H_2SO_4 is stable, therefore it can be stated that no or only minute amounts of water were created during the reaction. However, the absorbance in the reaction product is lowered while the peak position is stable.

When the bituminous reaction product produced at the oil-acid interface was extracted from the interface, contamination was unavoidable with

surrounding H_2SO_4 and oil. To analyse the real H_2SO_4 content of the black bituminous matter the sample was washed with water, to neutralise surrounding H_2SO_4, followed by washing with isopropanol, to remove excess of water, and finally by treatment with heptanes to remove excess of oil and isopropanol. The washing procedure was followed by drying to evaporate all heptanes. In Figure 3.17 the spectrum of a reaction product subjected to the washing process described is compared with the spectrum of the unwashed reaction product. For comparison of the peak positions, the spectrum of 40 %w/w H_2SO_4 is included in Figure 3.17. The massive change in absorbance is apparent but there is also the very distinct presence of hydrocarbons and H_2SO_4 species. The comparison of change in absorbance would lead to a underestimation of H_2SO_4 concentration. The close correlation shown with the peak position of a 40 %w/w solution H_2SO_4 is a more appropriate comparison.

To analyse only the black matter, which encapsulates sulphuric acid, the extracted bitumen was washed with water to neutralise surrounding H_2SO_4 and dissolved in hexane. The more dense sulphuric acid settles and the dissolved bitumen can be extracted and analysed after evaporating the hexane. The results are also shown in Figure 3.17. The analysis reveals a sulphonated hydrocarbon. The sulphur containing species correlate well with an acid concentration of 40 %w/w which is the critical acid concentration for bitumen formation, section 3.8.

From the results of Figure 3.16 and Figure 3.17, attention is drawn to the upper four graphs of Figure 3.14, corresponding to the peak positions as a function of acid concentration, and the values are also given in Table 3.1. This information can be used to estimate the acid concentrations when the acid is contaminated or trapped within a hydrocarbon. The assignment of peak position to species was used as given in literature: (Nakayama, et al., 1999), (Nash, et al., 2001), (Bethell, et al., 1953), (Elzinga, et al., 2001), (Grdadolnik, 2001) and (Faguy, et al., 1996).
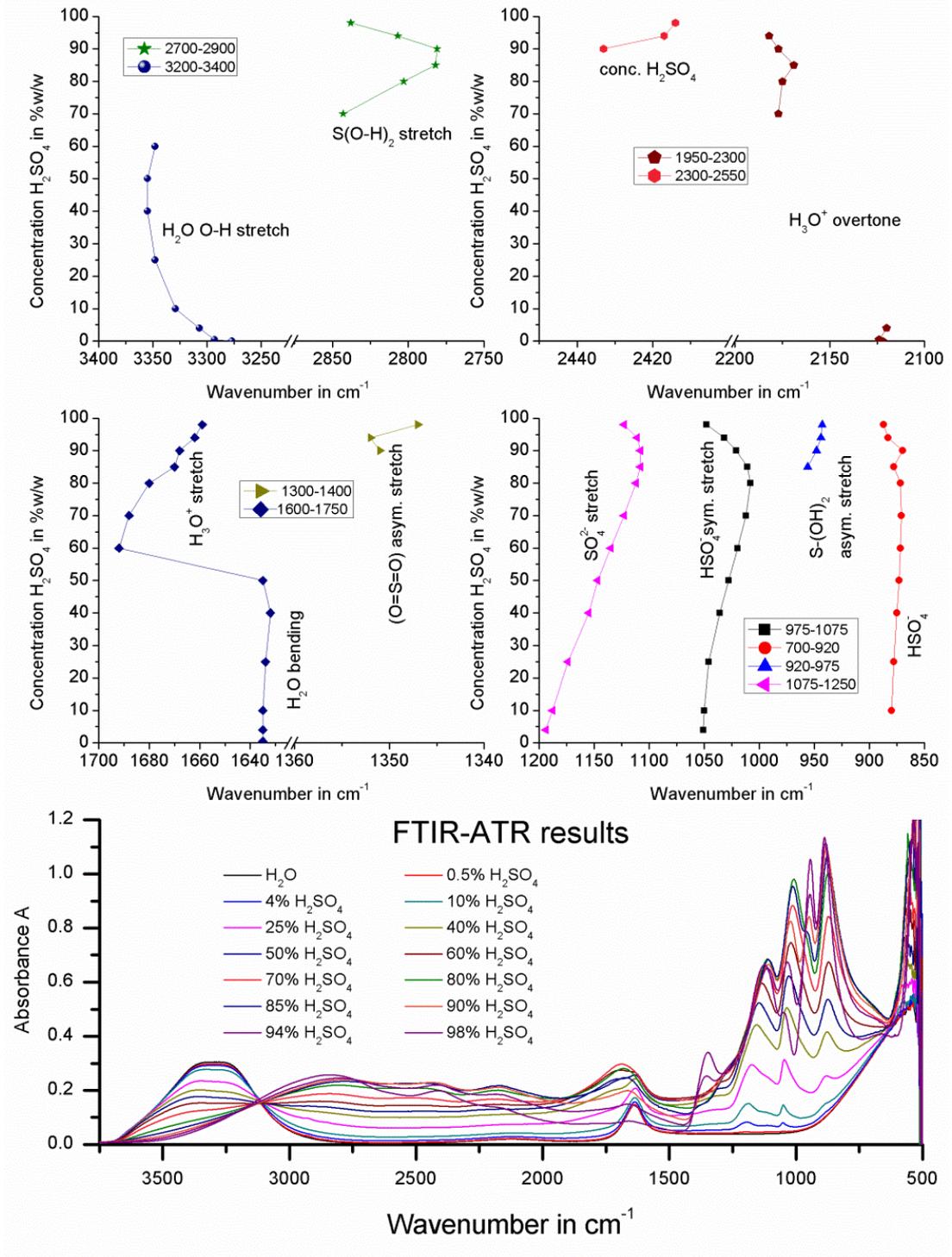
Figure 3.14: FTIR-ATR peak position of aqueous H₂SO₄ of various concentrations.

Table 3.1 FTIR-ATR peak position and absorbance of aqueous H_2SO_4 of various concentrations.

H_2SO_4 conc.	HSO_4^-		S-$(OH)_2$ asymetric stretch		HSO_4^- symetric stretch		SO_4^{2-} stretch		(O=S=O) asymetric strech	
%w/w	cm^{-1}	A	cm^{-1}	A	cm^{-1}	A	cm^{-1}	A	cm^{-1}	A
0										
0.5										
4					1051	0.08	1194	0.08		
10	880	0.15			1050	0.15	1188	0.15		
25	878	0.24			1046	0.31	1174	0.29		
40	875	0.42			1036	0.51	1155	0.44		
50	873	0.54			1028	0.62	1147	0.52		
60	842	0.67			1020	0.75	1135	0.60		
70	871	0.84			1012	0.88	1123	0.66		
80	872	1.00			1008	0.98	1112	0.69		
85	878	1.06	956	0.79	1011	0.95	1108	0.68		
90	870	1.10	948	0.84	1021	0.82	1108	0.67	1351	0.19
94	883	1.12	944	0.92	1032	0.67	1111	0.65	1352	0.25
98	887	1.14	943	1.05	1048	0.49	1123	0.66	1347	0.34

H_2SO_4 conc.	H_2O bending & H_3O^+ stretch		H_3O^+ overtone		H_2SO_4		S$(O-H)_2$ stretch		H_2O O-H stretch	
%w/w	cm^{-1}	A	cm^{-1}	A	cm^{-1}	A	cm^{-1}	A	cm^{-1}	A
0	1635	0.15	2122	0.02					3277	0.30
0.5	1635	0.15	2124	0.02					3293	0.30
4	1635	0.16	2120	0.03					3307	0.29
10	1635	0.17							3329	0.28
25	1634	0.21							3348	0.24
40	1632	0.24							3355	0.20
50	1635	0.26							3355	0.18
60	1692	0.28					2880	0.16	3348	0.15
70	1688	0.30	2177	0.17			2843	0.19		
80	1680	0.28	2175	0.20			2803	0.22		
85	1670	0.25	2169	0.22			2782	0.23		
90	1668	0.20	2177	0.21	2433	0.23	2781	0.24		
94	1662	0.15	2182	0.19	2417	0.22	2807	0.25		
98	1659	0.09			2414	0.20	2838	0.26		
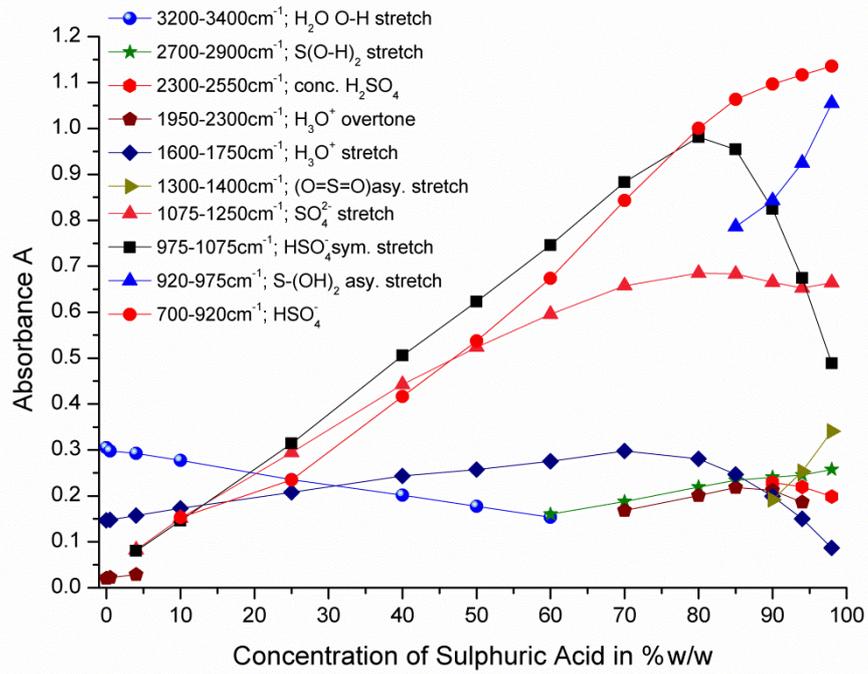
Figure 3.15: FTIR-ATR absorbance in correlation to the concentration of H_2SO_4
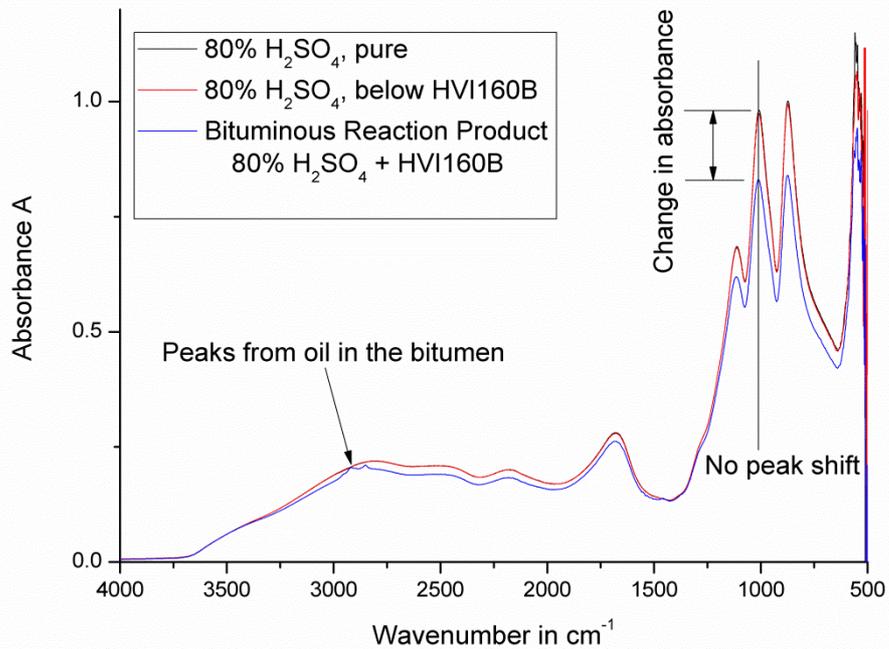
Figure 3.16: FTIR-ATR absorbance spectra of pure 80 %w/w H_2SO_4, remaining acid used in the reaction and the reaction product
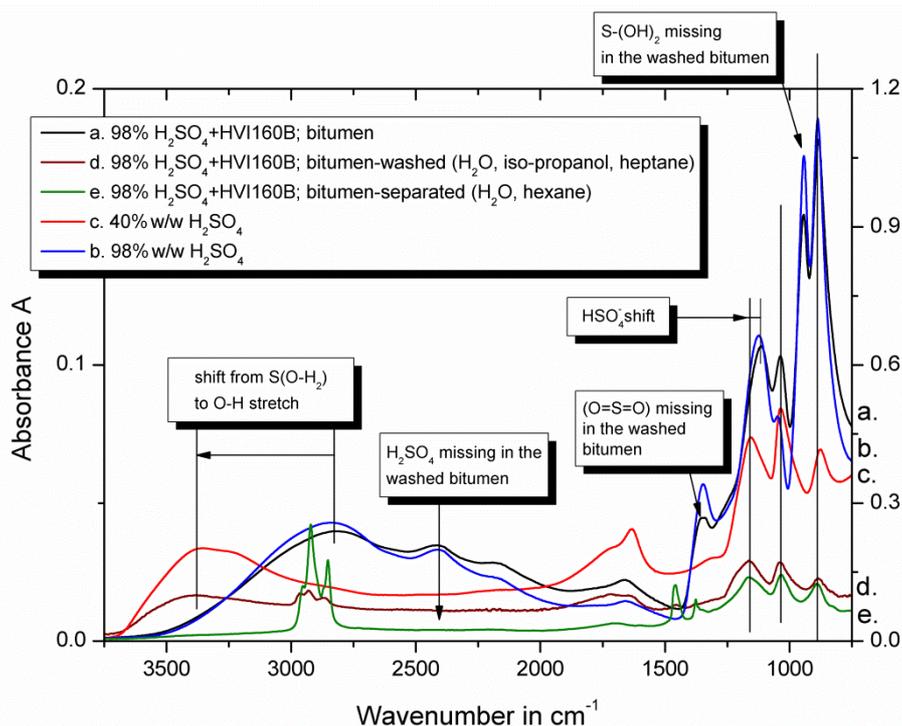
Figure 3.17: FTIR-ATR absorbance spectra of bituminous reaction product (a.), solvent washed bituminous reaction product (d.), solvent separated bituminous reaction product (e.) and pure 40 %w/w and 98 %w/w H₂SO₄ (c. and b.).

3.5 Results: Laser Diffraction Particle Size Characterisation and Stability of Emulsions

The droplet diameter in the prepared emulsions was evaluated before viscosity measurements, section 3.7, took place. Figure 3.18 and Figure 3.19 show the droplet size distributions for $C_{30}H_{62}$ and HVI160B with various acid concentrations. $C_{30}H_{62}$ shows a much wider variety in droplet diameters and interestingly all acid concentrations below 25 %w/w, which corresponds to CMC I, chapter 4, show two main droplet sizes. The droplet size distribution in the case of HVI160B is much narrower and there is a tendency for smaller droplets than $C_{30}H_{62}$. For both oils the results for 80 %w/w acid concentration show a tendency for bigger droplet sizes. This could be a result of a drift in refractive index when the colour of the acid changes due to chemical reactions between acid and hydrocarbon and/or the formation of bigger bituminous droplets.
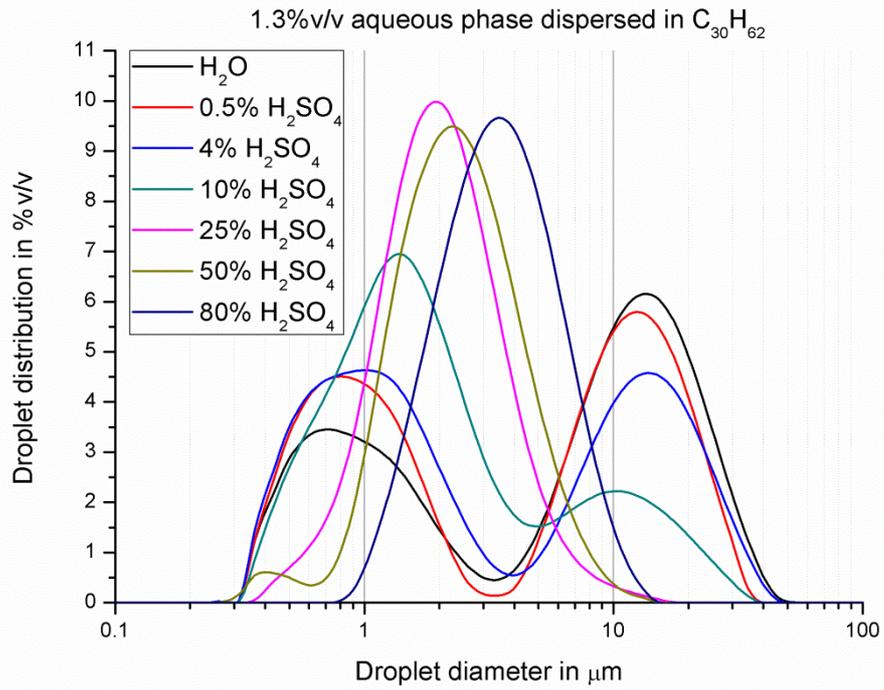
Figure 3.18: Droplet size distribution of 1.3 %v/v aqueous H₂SO₄ dispersed in C₃₀H₆₂
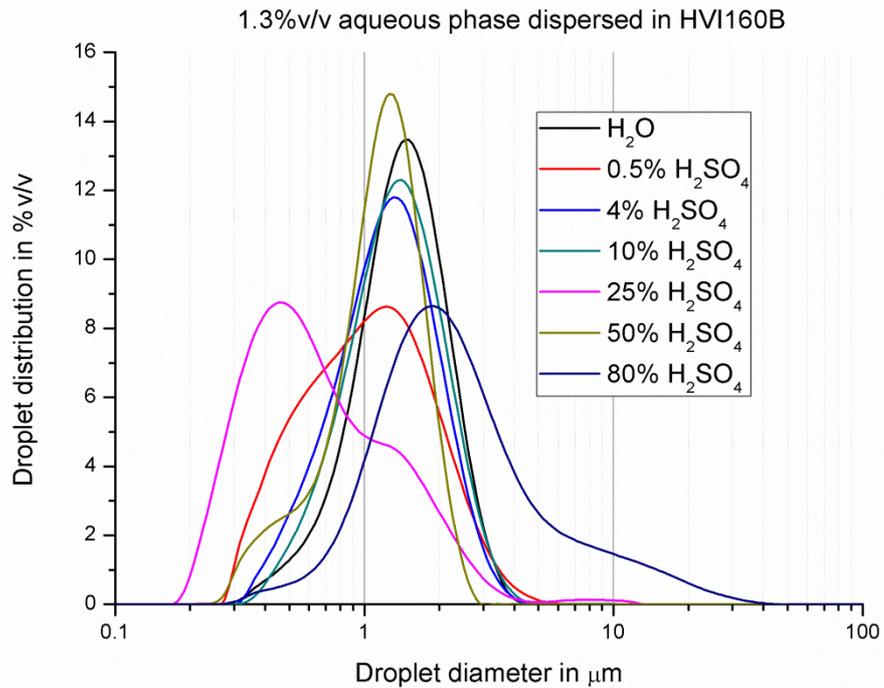
Figure 3.19: Droplet size distribution of 1.3 %v/v aqueous H₂SO₄ dispersed in API Group I base oil HVI160B

Figure 3.20 shows a statistical evaluation of the results in Figure 3.18 and Figure 3.19. The Sauter Mean Diameter, SMD, rates the surface area of the

droplets higher than the Volume Mean Diameter, VMD. For $C_{30}H_{62}$ there is a significant difference between SMD and VMD for acid concentrations below 25 %w/w, showing that a large part of the dispersed phase is present in a few bigger droplets, explaining the double peak in Figure 3.18 with coagulation of droplets starting shortly after dispersing or incomplete droplet breakup during dispersing in the ultra-sonic bath.

For viscosity measurement, however, the active surface area of the droplets is more important, as shown in chapter 2 section 2.3. For both oils the dispersed phases shows a very similar and relatively constant behaviour.
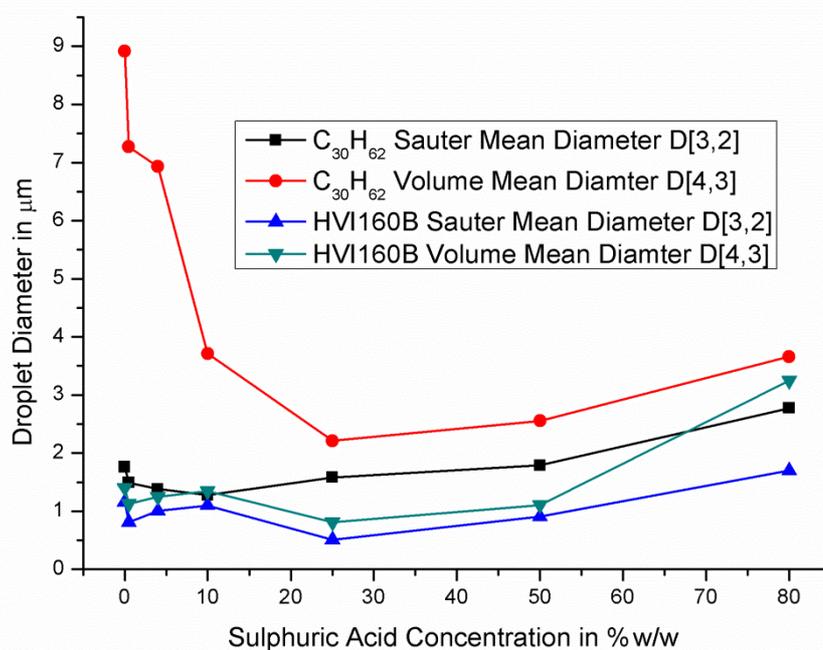
Figure 3.20: Statistic evaluation of the droplet size distribution for dispersed H_2SO_4 in $C_{30}H_{62}$ and HVI160B; volume and surface rated.

Any unused samples were left to settle. The result after 72 hours can be seen in Figure 3.21. In case of $C_{30}H_{62}$ settling was almost complete after 72 hours. Only slight turbidity could be observed but most of the aqueous phase accumulated as big droplets at the bottom of the bottles. Discolouration of the acid phase was only observed for 80 %w/w concentration and settling was complete. In the case of HVI160B, settling was not complete after 72 hours nor 168 hours. The uppermost quarter of the sample showed less turbidity than the lower three quarters and started to clear after 288 hours.

Discolouration was observed for 50 and 80 %w/w acid concentration, which shows the higher reactivity of HVI160B with sulphuric acid.
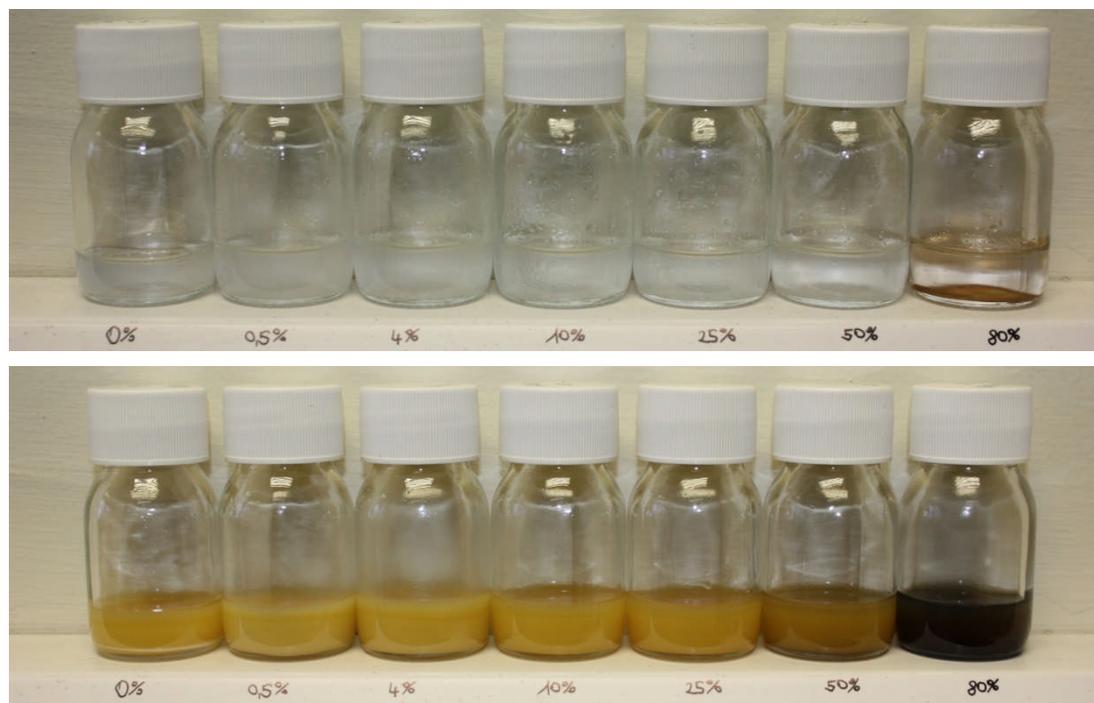
Figure 3.21: 1.3%v/v aqueous H_2SO_4 dispersed in $C_{30}H_{62}$ (upper) and HVI160B (lower) after 72 hours of settling. From left: 0, 0.5, 4, 10, 25, 50 & 80 %w/w

3.6 Results: Neutralisation Rate of Fully Formulated Lubricants

Figure 3.22 shows a typical result obtained from measurements of volumetric gas release over time as described in section 3.1.7. The slope of the starting part of the curve was evaluated and is called initial rate of reaction, v_0. Differences were also found in the time between injection of the acid and gas release, which is called 'delay time'.

Figure 3.23 shows the averaged results for the initial rate of reaction for two different lubricants with an alkaline reserve of TBN 70 mgKOH/g. The error bars, as in all following graphs, indicate extreme measurement values. The difference in formulation makes a comparison between the lubricants difficult as lubricant B may be formulated with non gas releasing CaO and may not have a lower neutralisation efficiency as it appears in the graphs. However, the lubricants can be compared to different test conditions. The first condition was the neutralisation of 98 %w/w H_2SO_4, which was chosen as the 100 % point. The second condition was the neutralisation of a 98 %w/w

H_2SO_4, which was mixed and heated with API Group I, and had a black appearance. Very obvious is the significant reduction in neutralisation efficiency for both lubricants. The third condition was the neutralisation of 70 %w/w H_2SO_4 keeping the acid mass part constant but increasing the total volume. This concentration was chosen as lower concentrations would not show significant gas release. For lubricant A a further significant reduction in reaction rate was observed, whilst lubricant B performs unchanged to the second test condition with dirty H_2SO_4 and shows an even slightly faster initial rate of reaction than lubricant A.

Figure 3.24 shows the initial rate of reaction for lubricants from manufacturer B with a lower alkaline reserve. They are meant to be used when lower sulphur content fuels are used in the engine. It shows, that not the absolute value of the alkaline reserve is the driving force for the rate of reaction but the additive package used to formulate the oil. The lubricant 'By' with a alkaline reserve of TBN 40 mgKOH/g is comparable with lubricant 'A', while lubricant 'Bx' with an alkaline reserve of TBN 55 mgKOH/g is comparable with lubricant 'B'. Lubricant 'Bx' and 'By' were not followed up further.
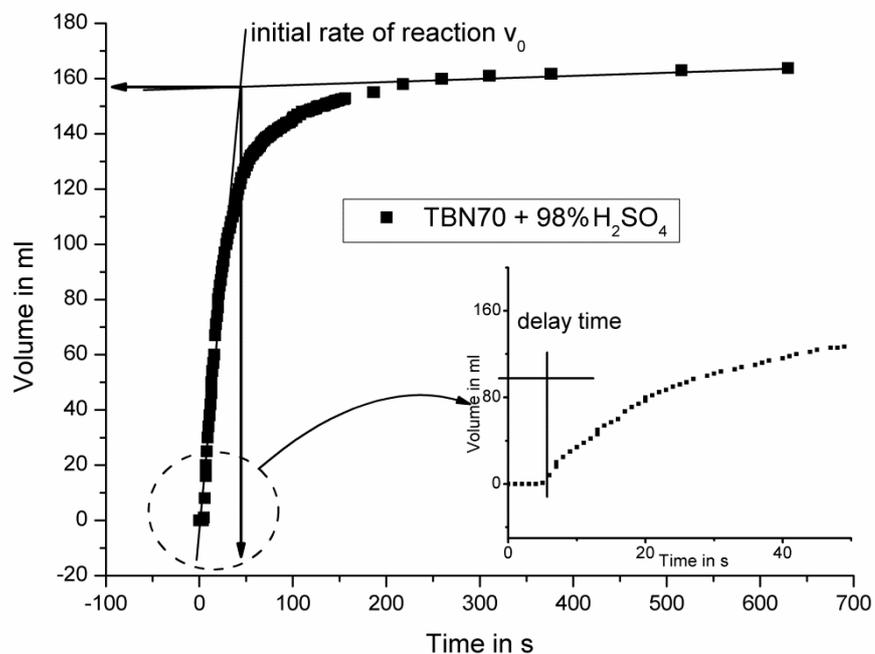
Figure 3.22: Typical result of CO_2 gas release from TBN70 lubricant
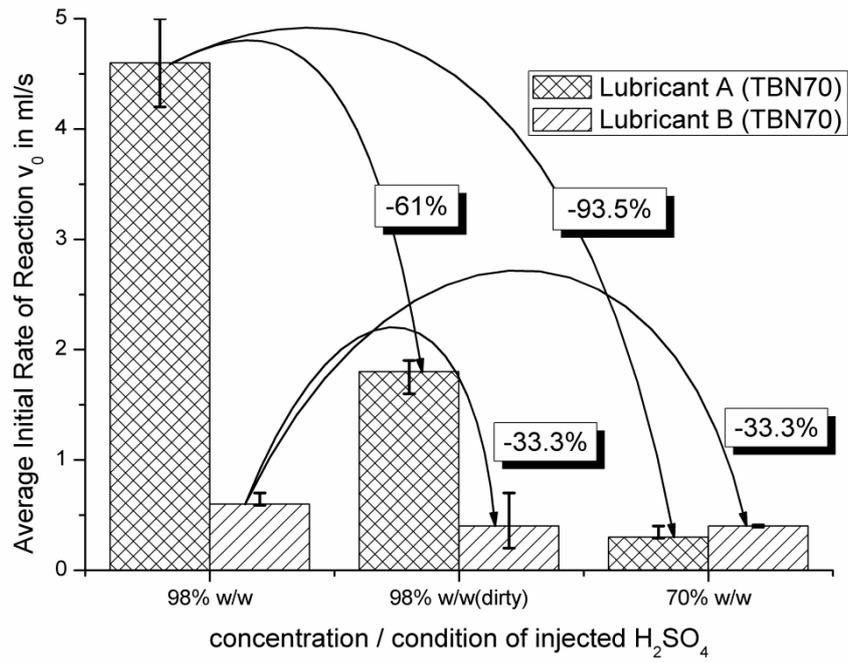
Figure 3.23: Reduction in neutralisation efficiency under varying test conditions
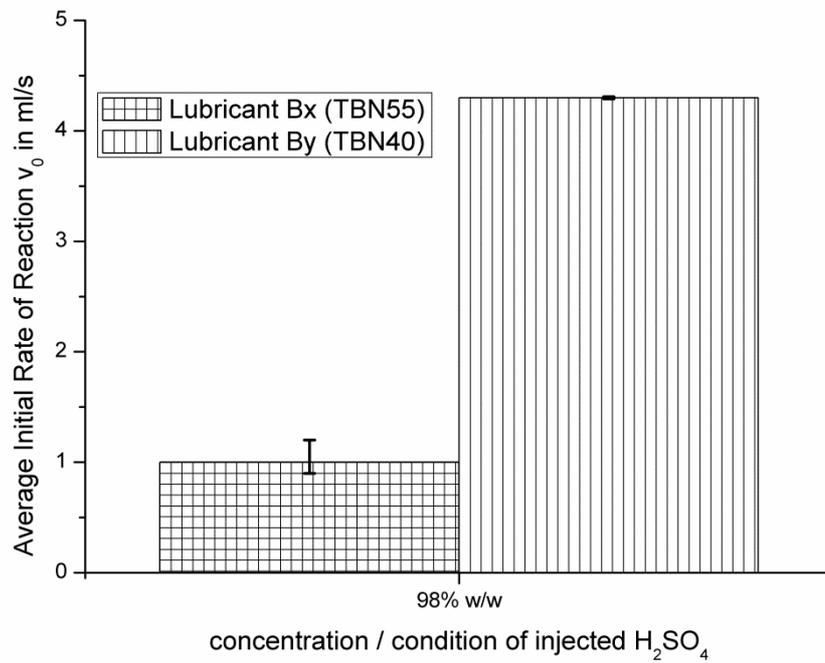
Figure 3.24: Initial rate of reaction for lubricants from manufacturer B with lower alkaline reserve for operation on low sulphur fuel

The reaction between sulphuric acid and calcium carbonate to form the measurable carbon dioxide gas should follow the velocity law of a second order reaction (Atkins, 2001) of the type:

$$A + B \rightarrow P$$

$$\frac{dP}{dt} = k[A][B]$$

$$kt = \frac{1}{[B]_0 - [A]_0} \ln \frac{[A]_0([B]_0 - P)}{([A]_0 - P)[B]_0}$$

(3.7)

A and B are the reactant concentrations, P is the concentration of the product, t the time and k the reaction constant. The index 0 indicates initial conditions. A relatively easy check if the reaction follows a 1st or 2nd order is the plotting of $ln[A]/[A]_0$ or $1/A$ respectively with time. A resulting straight line, the slope of which is the reaction constant k indicates which order the reaction is following. Neither the values found by (Garner, et al., 2004) nor the values in this study show a clear 1st or 2nd order behaviour. This can be explained by the involved micelle migration, which is needed to dock on to dispersed acid droplets and is also dependent on the size of the dispersed additive particles (Wu, et al., 2000).

Another way to find a descriptive law for the reaction velocity is the 'method of initial rates of reaction' (Atkins, 2001):

The initial rates of reaction are measured for various concentrations of one reactant. In this case, the concentration of the sulphuric acid was varied and the CaCO$_3$ content in the oil was kept constant.

For this case, the velocity of the reaction is only dependent on one reactant and it can be written:

$$v = k[A]^a$$

(3.8)

The initial rate of reaction v_0 is therefore dependent on the initial concentration $[A]_0$ of reactant A:

$$v_0 = k[A]_0^a$$

(3.9)

The logarithm of the equation is taken:

$$lgv_0 = lgk + a \cdot lg[A]_0$$

(3.10)

This results in a method to evaluate a. The initial rate of reaction is measured for different initial concentrations. The logarithm of v_0 is plotted against the logarithm of $[A]_0$. The gradient of the straight line gives the exponent a.

The missing reaction constant k can be found by rearranging equation (3.9).

From Figure 3.22 it can be seen that the reaction runs most of the time at v_0 and this, compared to engine speed, for a relatively long time. The initial rate of reaction can be established for any initial concentration of condensing H_2SO_4 at the measured temperature. The temperature was not varied during the measurements and therefore the parameters for the Arrhenius-equation for temperature dependency of the rate of reaction was not established. However, for most reactions the rate of reactions doubles with every 10 °C increase in temperature.

The evaluation of exponent a for lubricant A and B can be found from Figure 3.25 with $a_{Lub\,A}$ = 6.72 ml/s*% and $a_{Lub\,B}$ = 1.21 ml/s*% resulting in the reaction constant $k_{Lub\,A}$ =1.91*10^{-13} ml/s and $k_{Lub\,B}$ = 2.34*10^{-3} ml/s.
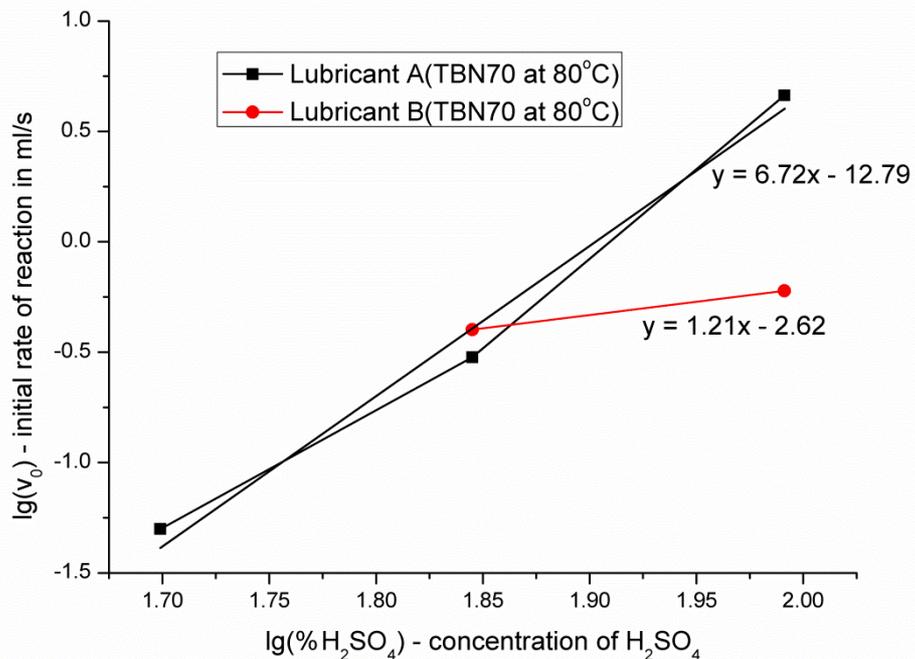
Figure 3.25: Evaluation of exponent a in equation (3.9)

Figure 3.26 shows the calculated, equation (3.9), initial rate of reaction v_0 for all initial concentrations A_0 of H_2SO_4. For lubricant A the CO_2 producing neutralisation of H_2SO_4 becomes 0 at 40 %w/w while lubricant B is capable of neutralising very low concentrations of sulphuric acid and outperforms lubricant B below ~65 %w/w.
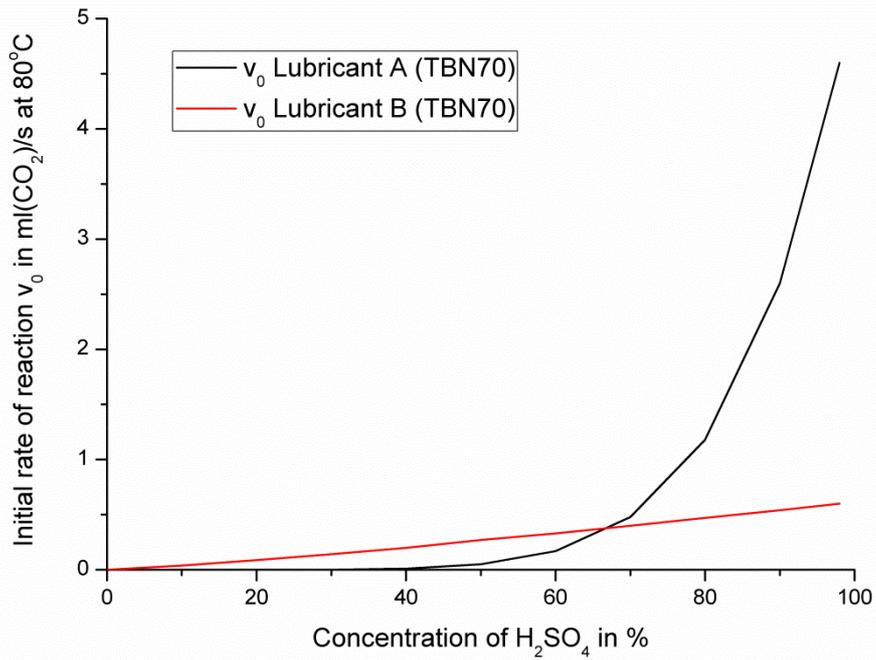
Figure 3.26: H_2SO_4 concentration dependent initial rate of reaction
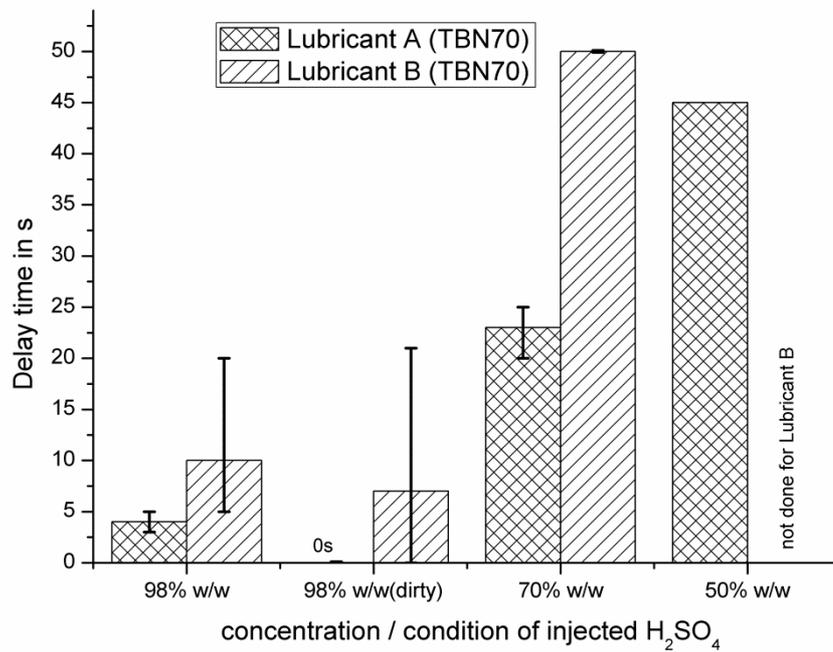
Figure 3.27: Delay time between injection of H_2SO_4 and CO_2 gas release

During the measurements it was found that not only the rate of reaction was dependent on the condition and concentration of the injected H_2SO_4 but, as

illustrated in Figure 3.27, also the delay time between injection and gas release. Both oils struggle most with an increased amount of water, which is surprising, as the volume of injection is much bigger and therefore droplets are more readily available for the dispersed additives. For both oils the acid, which was already in contact with oil, slightly shortened the delay time. This can be explained by the time dependent reduction in interfacial tension as shown in chapter 4 and is roughly 15 s at 80 °C or a smaller initial acid droplet size in the premixed oil. As shown in section 3.5, lower interfacial tension reduces droplet diameters thus increasing the active surface area for the docking of additive containing micelles.
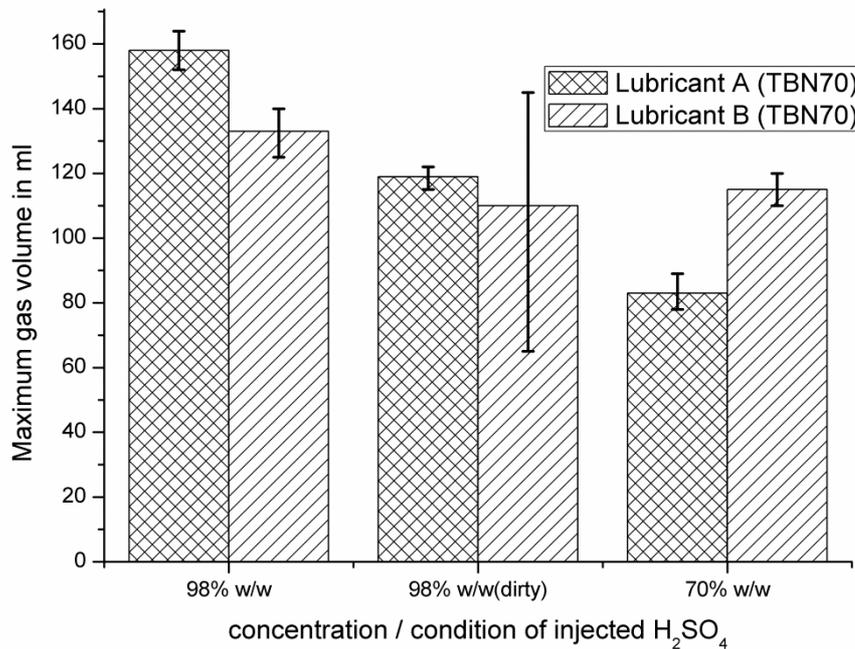
Figure 3.28: Final CO$_2$ gas volume at the end of the test.

The final recorded volume at each test, is shown in Figure 3.28. It can be seen particularly, that the performance of the CO$_2$ producing additive in lubricant A is vulnerable to changes in the acid condition. Lubricant B releases less CO$_2$ than lubricant A at high acid concentration but outperforms it for low concentrations. The influence of dirty acid on lubricant B is less significant.

The expected gas volume was about 300 ml, section 3.1.7, and for lubricant A about 50 % was achieved. For the experimental setup, the values are well in range.

The results from the chemical kinetics study point in the direction of boundary surface phenomena. It was therefore decided to find differences in the diameter of the dispersed additive particles by the dynamic light scattering, DLS, technique, section 3.1.6. The results are shown in Figure 3.29 and Table 3.2.
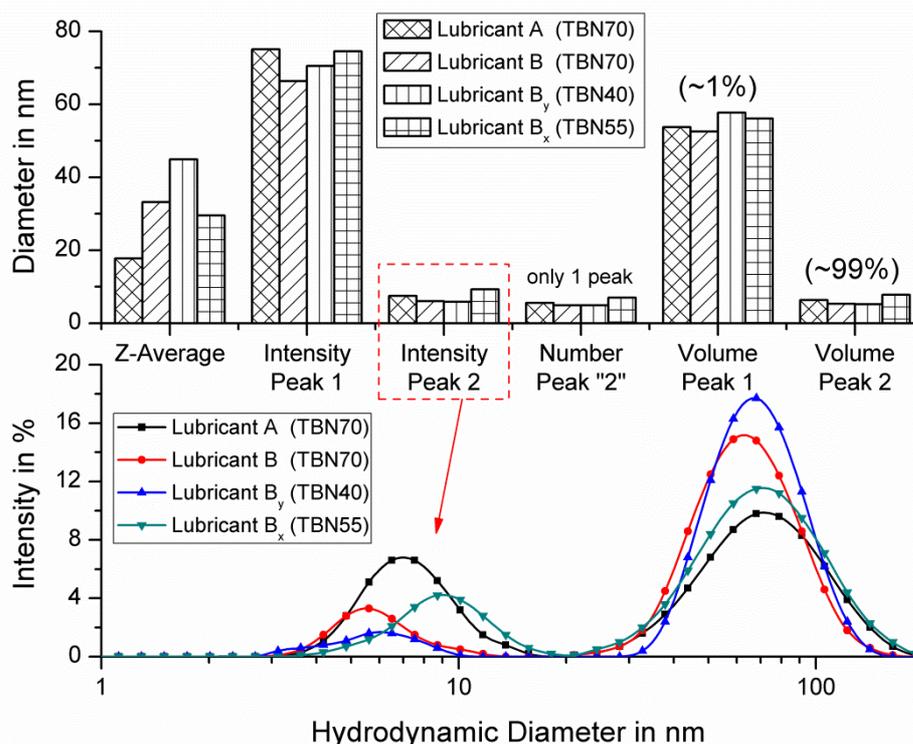
Figure 3.29: Particle size distribution in fully formulated lubricants by dynamic light scattering

The intensity measurements show two significant peaks at around 7 and 75 nm. The statistical evaluation shows that 99 % of the dispersed particle volume is presented by the 7 nm peak, which explains the total suppression of the bigger particles by the evaluation for the total number of particles. The particle size is measured by the intensity of scattered light, therefore the results from the ~7 nm peak are seen as the additive particle size which is influencing the reaction with sulphuric acid. They are in the range of reported particle sizes (Wu, et al., 2000). The "Z-Average" represents a mono-modular average of the bi-modular measurement results and should not be considered but is given for completion.

The particle sizes found are very similar for the different lubricants. No trend for the two fast lubricants 'A' and 'By' and the slower lubricants 'B' and 'Bx' can be found.

Table 3.2: Input data for DLS particle size measurements and the intensity results for the major particle size

Lubricant	Input Data				Result
	Viscosity η in mPa*s	Temp. T in °C	Refractive Index		Intensity $d(H)$ in nm
			CaCO$_3$	Lubricant	
A (TBN70)	533.3	25	1.52	1.4	7.492
B (TBN70)	533.1	25	1.52	1.4	6.065
B$_x$(TBN55)	505.6	25	1.52	1.4	9.283
B$_y$(TBN40)	520.5	25	1.52	1.4	5.872

3.7 Results: Viscosity Measurements

The viscosity with increasing amounts of water dispersed in HVI160B was measured for 1.5 and 7 %w/w water in the lubricant, Figure 3.30. No changes in viscosity was found, as expected for a volume fraction < 0.1. The error bars, as for all following graphs, indicate extreme deviations within the measured shear rate range. Higher temperatures, or lower viscosities respectively, show larger deviations, indicating the difficulty in measuring small forces. 1.5 %w/w is a value found in marine engines under tropical ambient conditions (Micali, et al., 2010) and corresponds to 1.3 %v/v used for the measurements with increasing acid concentration, Figure 3.31 and Figure 3.32, to keep the volume of the dispersed phase constant. Changes in viscosity are minor in the evaluated shear rate range, as expected for a volume fraction < 0.1 and the creation of heavier reaction products did not show an influence either. One possible explanation is that the reaction products stay dispersed as droplets and do not dissolve in the oil to change viscosity as one would expect from lubricant oxidation. The emulsions are Newtonian over a shear rate range from 200 to 700 s^{-1} but below 100 s^{-1} shear thinning was observed. Above 10 %w/w acid concentration, only measurements at 20 °C were performed to prevent corrosive attack of the measurement equipment.
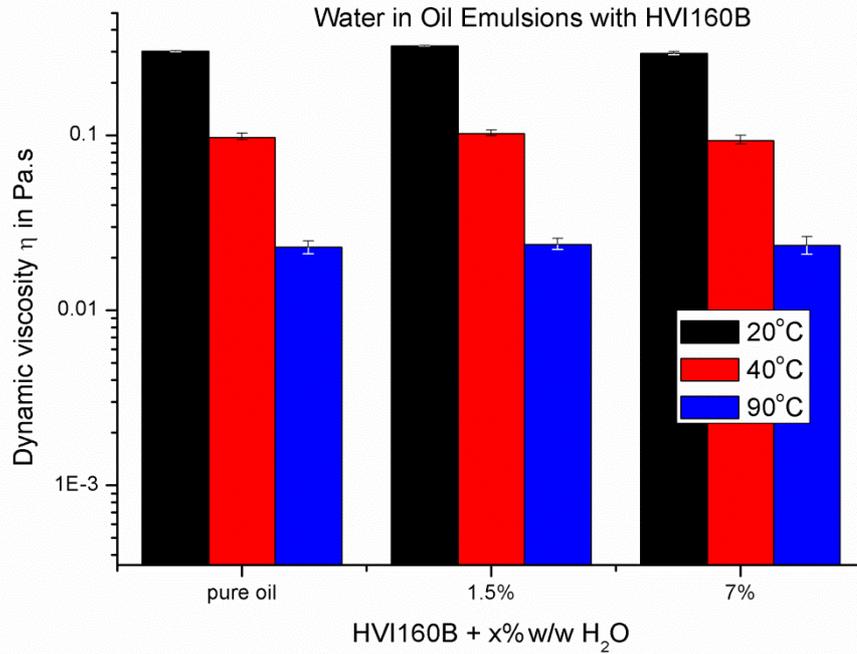
Figure 3.30: Viscosity of pure and emulsified API Group I base oil HVI160B with water as dispersed phase. Applied shear rate was 200 – 700 s^{-1}
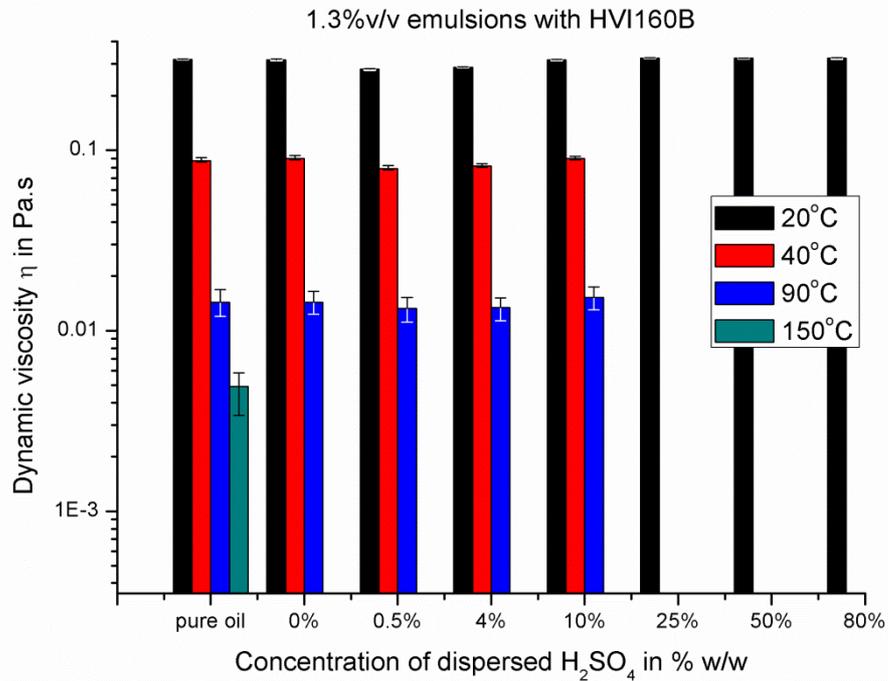
Figure 3.31: Viscosity of pure and emulsified API Group I base oil HVI160B with 1.3 %v/v aqueous H$_2$SO$_4$ as dispersed phase. Applied shear rate was 200 – 700 s^{-1}
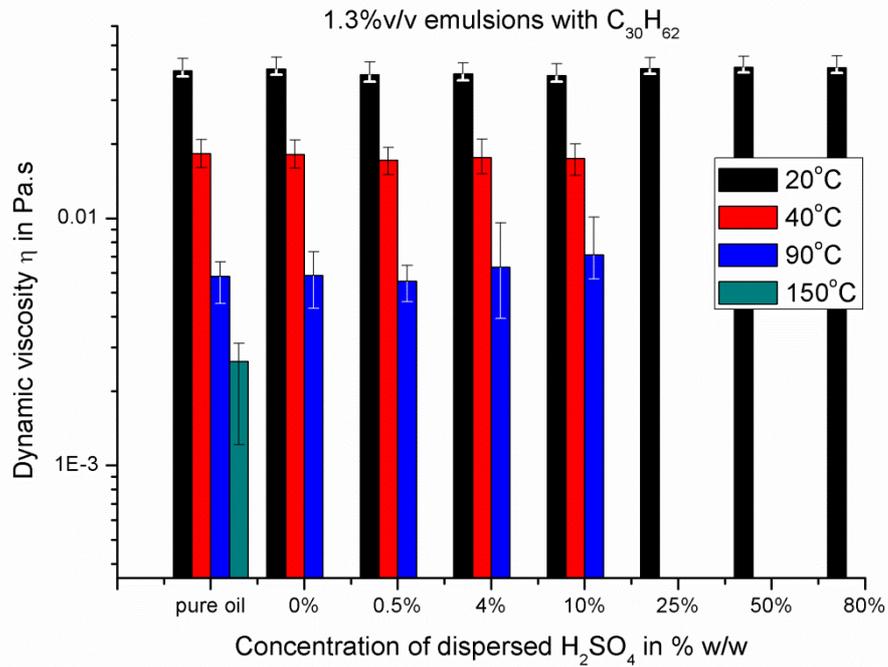
Figure 3.32: Viscosity of pure and emulsified C$_{30}$H$_{62}$ with 1.3 %v/v aqueous H$_2$SO$_4$ as dispersed phase. Applied shear rate was 200 – 700 s^{-1}
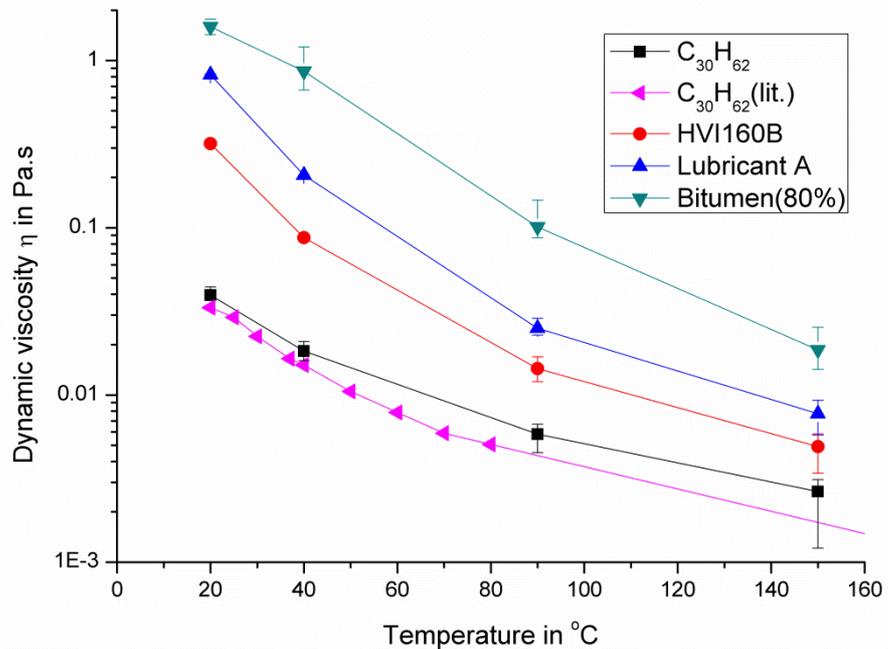
Figure 3.33: Measured viscosity of C$_{30}$H$_{62}$ and values found in the literature (DECHEMA e.V., 2005 - 2008), a fully formulated lubricant A, the corresponding base oil HVI160B and the bitumen formed between HVI160B and 80 %w/w H$_2$SO$_4$

The correct working of the viscometer was verified by measuring $C_{30}H_{62}$ alone. For the given working sequence and cone arrangement, it produced higher results compared with values found in the literature (DECHEMA e.V., 2005 - 2008), especially at low viscosities, Figure 3.33. The measured minima however meet the literature values, which are given with an accuracy of ±3 %. The bitumen formed between HVI160B and 80 %w/w H_2SO_4 exhibits high viscosities and does not form deposits between 20 and 150 °C, Figure 3.33. It shows slight shear thinning behaviour between 200 and 700 s^{-1}, explaining the large error bars which represent minimum and maximum values.
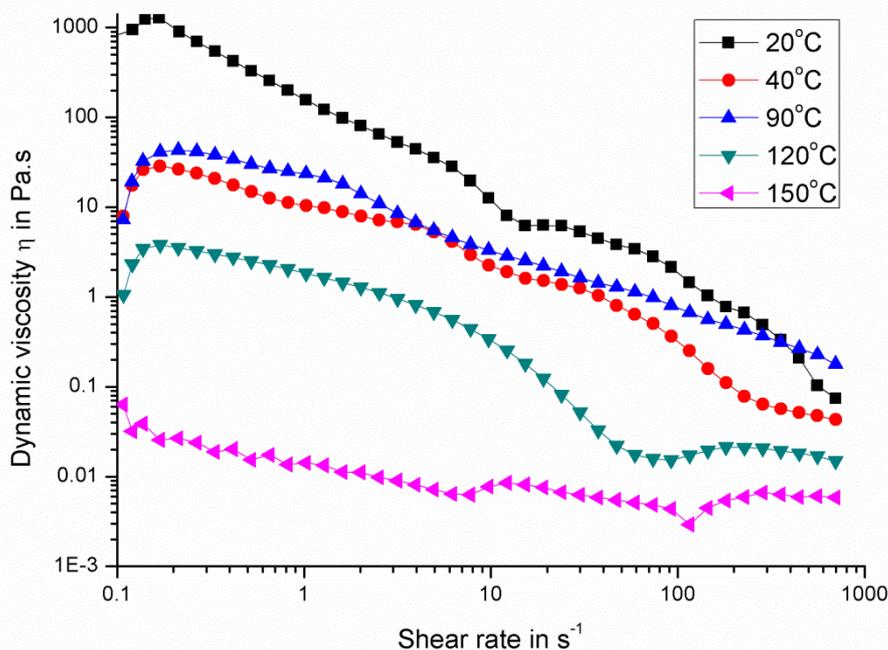
Figure 3.34: Viscosity of bitumen formed between HVI160B and 98 %w/w H_2SO_4. See text for encountered difficulties

The viscosity measurements on the bitumen formed between 98 %w/w H_2SO_4 and HVI160B, Figure 3.36, last bottle, proved to be difficult, Figure 3.34. At low temperatures, the soft bitumen squeezed out of the gap at high shear rates. At increased temperatures, SO_2 gas release was observed. At high temperatures the sample started to solidify and formed a dry, solid deposit on the measurement equipment, Figure 3.35. The deposit was not overly brittle and formed swarfs when scraped off. Despite the gas release, the results at 90 °C seem to be the most realistic. Overall, the bitumen showed a strong shear thinning behaviour, which could be explained by poor

wall adhesion for low temperatures but not for higher temperatures. The shear thinning behaviour can be explained by the revealed physical structure of the bitumen, as discussed in section 3.2.2, Figure 3.7.

Figure 3.35: Solidification of bitumen formed between HVI160B and 98 %w/w H$_2$SO$_4$ during viscosity measurements at 150 °C

3.8 Results: Deposit Formation, Critical Concentration and Temperature

Chemical reaction between H$_2$SO$_4$ and the API Group I base oil HVI160B was observed, yielding bituminous matter that appears to be a complex emulsion, section 3.2.2.

Figure 3.36 shows the samples of HVI160B after their use in the interfacial tension measurements, chapter 4, and a storage time of two weeks. During the measurements the samples were exposed to a maximum temperature of 90 °C after a heating time of 10 minutes. Above 80 % acid concentration both acid and oil phase show a strong discolouration and emitted a strong SO$_2$ odour. Between 60 and 80 % acid concentration only the acid phase shows a discolouration. All samples above 30 % acid concentration, Figure 3.37, form a bituminous substance, which has a high affinity to the glass walls of the sample containers. A comparison with API Group I base oil SN600 & BS150 shows exactly the same behaviour.

Figure 3.36: API Group I base oil HVI160B in contact with various concentrations of aqueous H$_2$SO$_4$, rising from 0 to 98 %w/w. From left: 0, 0.5, 1.5, 4, 10, 20, 30, 40, 50, 60, 70, 80, 90 & 98 %w/w
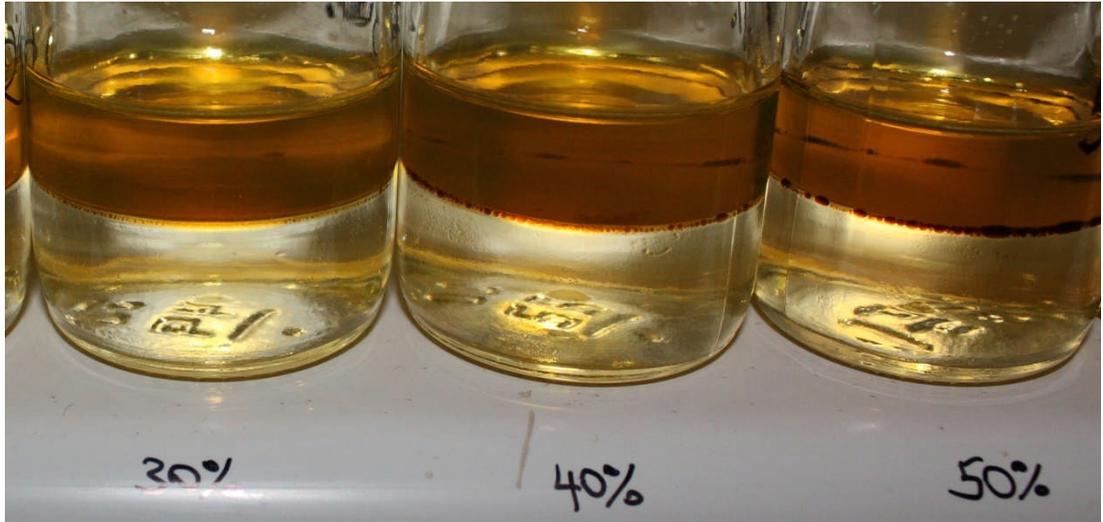
Figure 3.37: Close up of Figure 3.36 on 30, 40 and 50 %w/w H$_2$SO$_4$
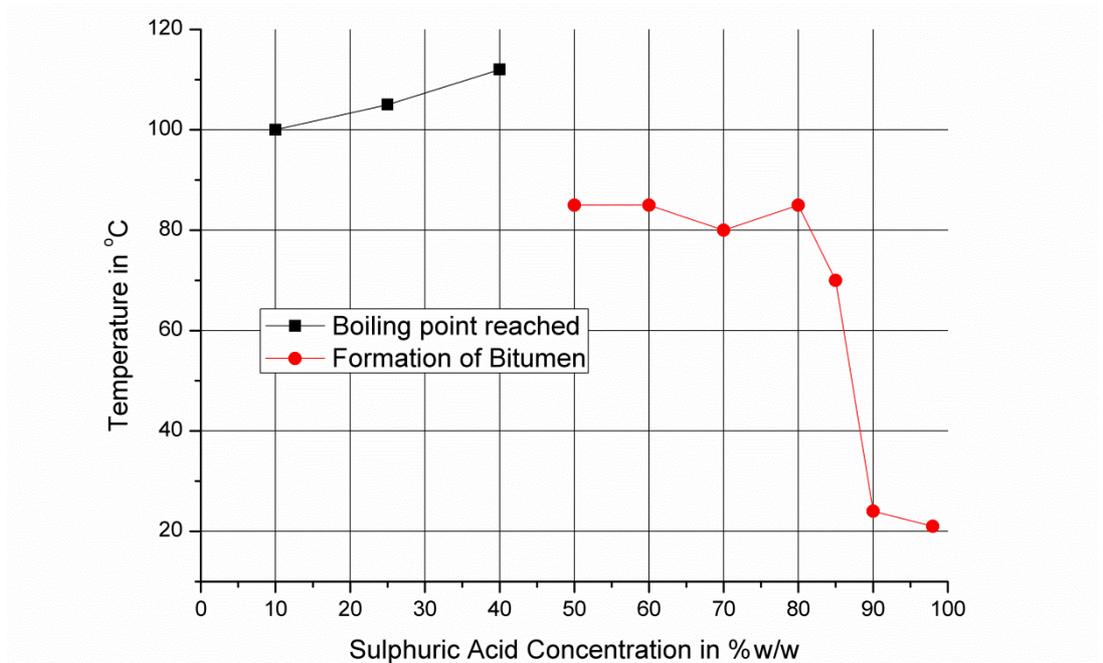
Figure 3.38: Fast heating of API Group I base oil HVI160B in contact with various concentrations of aqueous H$_2$SO$_4$ until bitumen is formed.

The HVI160B base oil was brought into contact with various concentrations of sulphuric acid and heated from room temperature to 100 °C within 2 minutes, Figure 3.38. For concentrations below 50 %, no discolouration was observed up to the limit of the boiling point nor during cooling down. Between 50 and 80 %w/w acid concentration the formation of a bitumen-like substance on the interface was observed at about 85 °C. Between 80 and 90 %w/w acid concentration, this critical temperature significantly dropped to reach room temperature for concentrations of 90 %w/w and above.

The critical H_2SO_4 concentration for the formation of bitumen with API Group I base oil was found to be 40 %w/w after heating to 90 °C and a storage time of two weeks. Between 50 – 80 %w/w, bitumen was formed spontaneously at 85 °C and above 85 %w/w, bitumen was formed spontaneously at room temperature.

The observed concentrations for bitumen formation correlate well with the first and second dissociation steps of H_2SO_4, which will be shown in chapter 4. HSO_4^- ions are likely to be the driving force for bitumen formation.

During interfacial tension measurements, chapter 4, with $C_{30}H_{62}$ only discolouration was observed for the acid phase for highly concentrated sulphuric acid of ~98 %w/w. The discolouration commenced at approximately 70 °C during a fast heating cycle, a value confirmed in the literature (Stecher, et al., 1960).

Mixtures with $C_{30}H_{62}$ and aqueous sulphuric acid with concentrations of 0 %, 0.5 %, 10 %, 25 %, 40 %, 65 %, 80 % and 90 %w/w were stored for several days between 80 and 110 °C, 15 °C below their boiling point. All mixtures below 40 % concentration remained clear, the 40 %w/w mixture did not exhibit discolouration but instead some solid formation and slight clouding and all mixtures above 40 %w/w showed discolouration.

3.9   Conclusions of the Physical and Chemical Analysis

Light microscopy on squalane and sulphuric acid, section 3.2.1, which were exposed to each other show differences in droplet size and arrangement of solid particles in or outside the droplets. Particles pointed towards the oil phase.

Light microscopy on bituminous reaction products, section 3.2.2, formed between API Group I base oil and aqueous sulphuric acid reveals the products to be complex emulsions of, most probably, an acidic phase surrounded by a hydrocarbon shell.

In section 3.2.3 and 3.3 the same solid reaction product was investigated by light microscopy and SEM. A significant difference in structural appearance was revealed, which is likely to be caused by solvent washing and the high vacuum operation in the SEM. It shows how the quite simple light microscopy can complement the more sophisticated SEM technique.

In section 3.2.2 it was shown how the mixing of hydrocarbons with H_2SO_4 causes a chemical interaction yielding bituminous matter in the form of emulsions. In section 3.4.1 an unproportional change in absorbance was observed in the infrared spectra of the acidic components compared to pure H_2SO_4. The concentration-dependent peak positions of H_2SO_4 species, however, remains unaltered when the reaction product was not freed from the surrounding acid contaminant. When the surrounding acid was neutralised, the acid related peaks shifted to values of the enclosed remaining acid. Therefore the peak positions of the H_2SO_4 species can be used to evaluate the concentration of H_2SO_4 in the mixture.

The droplet diameter of freshly dispersed aqueous sulphuric acid in squalane and API Group I base oil was measured. The results are presented in section 3.5. In general the droplets are bigger for $C_{30}H_{62}$ compared to API Group I base oil but no obvious correlation between acid concentration and droplet diameter was found for either oil. The differences in the statistical Sauter- and volume- mean diameters for $C_{30}H_{62}$ reveal a coagulation or incomplete droplet breakup below the first critical micelle concentration, chapter 4, shortly after dispersing. Settling of the aqueous phase is complete after 72 hours for $C_{30}H_{62}$ whilst settling only starts to take place after 288 hours for the API Group I base oil. For engine lubricant formulation, this could mean a need for increased amounts of dispersant when moving to higher refined base oils.

The neutralisation efficiency was found to vary considerably between fully formulated lubricants, as shown in section 3.6. Differences were particularly found for concentrated sulphuric acid, which is unlikely to be found in an marine Diesel engine. For sulphuric acid which was in contact with the base oil previously, both lubricants showed a reduced neutralisation efficiency. Towards dilute sulphuric acid both lubricants showed reduced efficiency. Lubricant A reacts faster and appears to have a more complete reaction, while lubricant B has a more stable reaction with dilute sulphuric acid and reacts more stable under changing conditions. No significant difference was found in the particle size of the dispersed additive particles. Therefore, the size of the particles cannot explain the difference in initial rate of reaction.

Other influencing parameters are the type of dispersant and detergent used and the type of dispersed additive solid. The full explanation for the chemical differences in the fully formulated cylinder oils, however, is out of the scope of this study and the main interest was in the kinetics of fully formulated lubricants and their reaction with environmental changes. Observations with lubricant A and B during friction tests can be found in chapter 7.

The engines are equipped with varying lubrication systems. Some are simply holes where oil drips through, some inject through the holes into the ring pack, others have injection nozzles which distribute the oil very effectively in the circumferential direction. A lubrication system with poor circumferential distribution is probably better matched with a slower and more homogeneously reacting oil to decrease the chance of uneven wear. Lubricant B might be a good choice and the reaction rates will increase for higher temperatures.

In tropical conditions and in cylinder liner areas of low temperature, the concentration of condensing sulphuric acid can be expected to be quite low. Dilute sulphuric acid attacks preferentially the pearlitic matrix in the grey cast iron cylinder liner material, which embosses the austenitic hard phases. The findings in (Micali, et al., 2010) of increased remaining alkaline reserve under tropical conditions can be explained by the reduced efficiency of the lubricant for dilute sulphuric acid. Lubricant B seems to outperform lubricant A under such conditions. However, when top dead centre wear is a big problem, lubricant A might be the right choice.

Most of the freshly injected lubricant is scraped off the cylinder by the piston rings or blown off from the piston rings during gas exchange around BDC, including the additives (Micali, et al., 2010). Long delay times are therefore not favourable. Lubricant A shows a better performance in this respect. Under friction the additives form a protective boundary film, which is capable of neutralising sulphuric acid as shown in chapter 7.

The viscosity measurements in section 3.7 show that the absolute volume and the relative concentration of aqueous sulphuric acid in $C_{30}H_{62}$ and HVI160B have very little influence on viscosity in the shear rate range 200 – 700 s^{-1}. Bituminous matter formed between API Group I base oil and 40 – 80 %w/w H_2SO_4 shows higher viscosities than fully formulated cylinder oil and slight shear thinning behaviour.

The critical acid concentration, section 3.8, to form significant amounts of reaction products with API Group I base oil or the saturated $C_{30}H_{62}$ is 40

%w/w H_2SO_4. This is an important information for engine design and lubricant formulation. When the acid concentration is kept below 40 %, the hydrocarbon will not be attacked nor yield deposit forming bitumen. A personal experience of the author is the reduced amount of black lacquer on the liner surface after a tropical passage with high intake air humidity.

Under thermally dynamic conditions, the critical concentration to form bitumen with API Group I base oil is 50 %w/w at 85 °C for concentrations between 50 – 80 %w/w. Above 85 %w/w, bitumen is formed at room temperature. The concentration range 50 – 80 %w/w corresponds well with the second dissociation step of sulphuric acid, which has its peak at 50 %w/w and is gradually suppressed until 85 %w/w. At 85 %w/w all free water molecules are used up and the first dissociation step gets suppressed while free H_2SO_4 molecules start to appear. Below 50 %w/w the first and second dissociation steps are in a balance and the reaction of HSO_4^- ions with H_2O molecules is favourable (Young, et al., 1959). HSO_4^- ions are likely to be the driving force for bitumen formation.

The reactivity of API Group I base oils is higher than for $C_{30}H_{62}$ due to their higher content of unsaturated and reactive hydrocarbons (CIMAC Working Group "Marine Lubricants", 2007). A change to higher refined base oils will reduce the deposit formation in marine Diesel engines in terms of quantity.

The present chapter is a compendium of regularly used techniques as well as smaller tests used to deepen the knowledge about the interaction between sulphuric acid and hydrocarbon lubricants. The following two chapters 4 and 5 are dedicated to the physical parameters, interfacial tension and contact angle, followed by chapter 6 and 7 which presents the impact of sulphuric acid on a piston ring – cylinder liner friction bench test, which is the closest this study comes to the real application.

Chapter 4
Interfacial Tension Between Hydrocarbon Oil And Aqueous Sulphuric Acid

In this chapter a chemically well defined saturated hydrocarbon is compared with commercial lubricant base oils with a high content of unsaturated hydrocarbons. The aim was to find out whether it makes technical sense to lubricate large marine Diesel engines with more expensive higher refined base stocks, containing less unsaturated hydrocarbons, to achieve a reduced degradation of the lubricant and to find possible side effects.

Interfacial tension measurements were found helpful in finding chemical interactions between hydrocarbons and sulphuric acid as the interfacial tension is very sensitive to small changes in chemical structure on the interface. It is also an important measure for droplet break up and the ability to form emulsions of aqueous phase in the lubricant, which was shown in chapter 3.

Interfacial tension measurements were taken time dependent on fresh interfaces, on fully developed interfaces and temperature dependent. They are presented in the following subsections. The measurements were also presented in the first two articles listed on page i of this thesis.

The chemical analysis of the observed reaction products was shown in chapter 3 and is also shown in the following.

4.1   Materials and Methods: Interfacial Tension Measurements

For the study, the following substances were used: squalane (99 % purity Sigma Aldrich), API Group I base oils HVI160B, BS150 and SN600 (Shell and Chevron) and sulphuric acid (> 95 %w/w Fisher Scientific UK Ltd. analytical reagent grade). Lower concentrations of sulphuric acid were made with deionised water by weighing. Physical properties of the substances can be found in appendix A.

Squalane ($C_{30}H_{62}$) is a saturated, branched alkane with six methyl (CH_3) side groups, Figure 4.1. It was chosen as a model oil as it is very similar to the main components of a typical base oil used for engine lubricants, Figure 4.2.

It is relatively inert to chemical reactions like oxidation processes and a chemical reaction with squalane is therefore likely to be observed also with higher refined base oils.
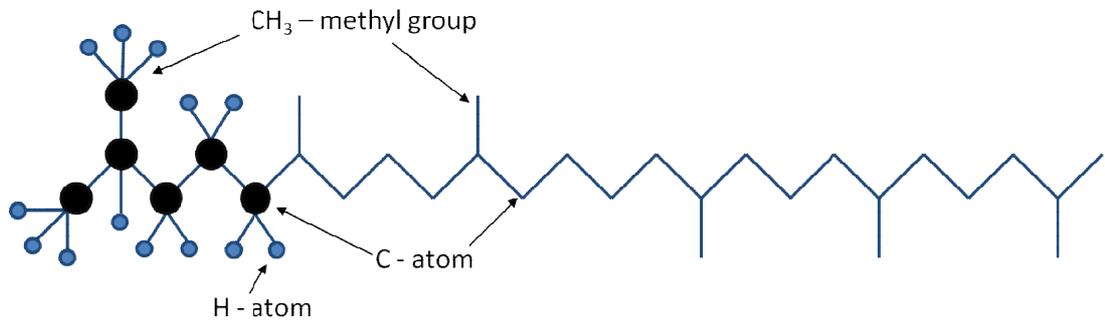
Figure 4.1: Chemical structure of squalane ($C_{30}H_{62}$), for ease of understanding in a mixed, model and skeletal form (Enevoldsen, et al., 2007).
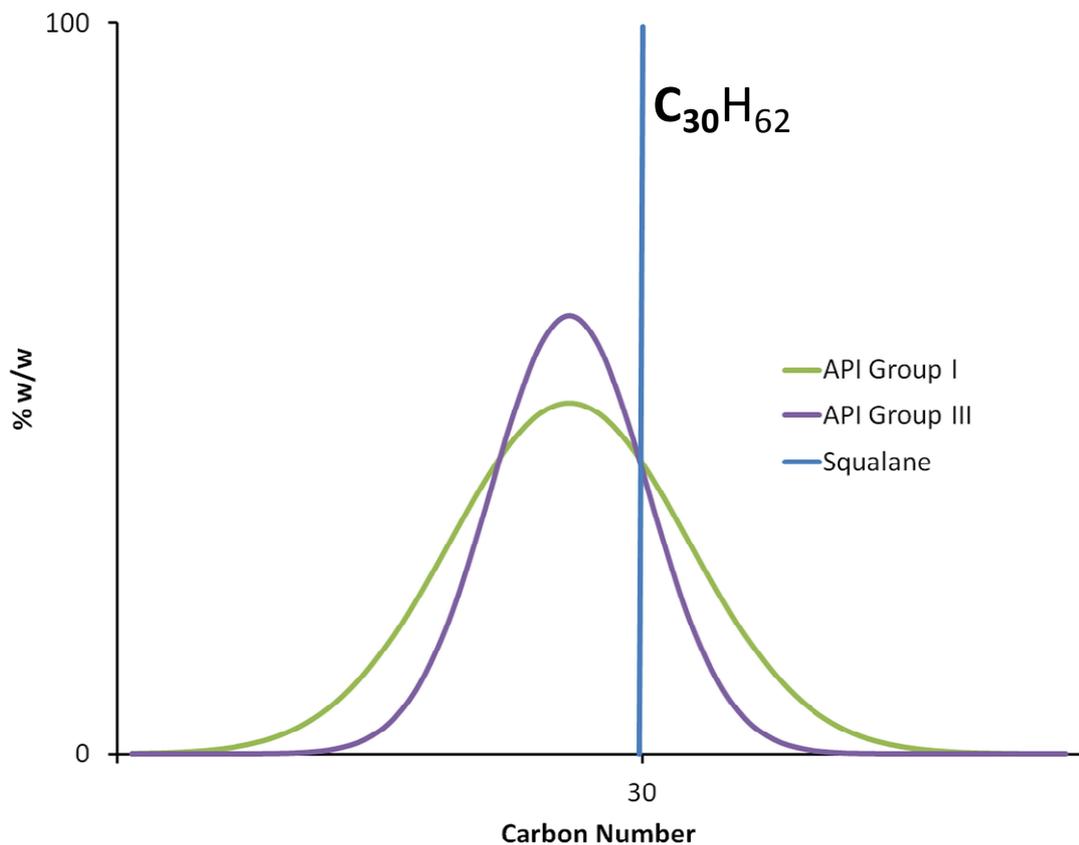
Figure 4.2: Artistic visualization of the carbon chain length distribution in lubricants (Ong, 2008)

API Group I base oils are the least refined lubrication oils and are typically used as 2-stroke marine Diesel engine lubricants. The high content, > 10 %, of unsaturated hydrocarbons (CIMAC Working Group "Marine Lubricants",

2007), makes them chemically more reactive than the aforementioned squalane or higher refined base oils. API Group III base oil, for example, has a narrower molecular weight distribution and contains less unsaturated hydrocarbons. API Group I base oil also comprises hydrocarbons with the same molecular weight as higher refined base oils but possibly in a more readily oxidised chemical state.

Aqueous sulphuric acid, H_2SO_4, is a typical reaction product of the combustion of sulphur containing fuels. In internal combustion engines it can condense on the cylinder liner walls, chapter 1. The concentration of sulphuric acid in the engine is not exactly known and varies with temperature and the partial pressure of SO_3. Therefore a wide range of concentrations was used for this study. In water, sulphuric acid dissociates in two steps into hydrogen sulphate ions (HSO_4^-), sulphate ions (SO_4^{2-}) and hydronium ions (H_3O^+) (CIMAC Working Group "Marine Lubricants", 2007). The extent of dissociation and therefore the concentration of the single ion species in the solution is mainly dependent on the acid concentration and to some extent on the temperature (Young, et al., 1959). Figure 4.3 shows the molecular species present at various concentrations of H_2SO_4. The first dissociation step peaks at around 85 % and the second at around 50 %. Later it is shown how the distribution of species is correlated to interfacial tension. The extent of dissociation correlates also to oil degradation and can be measured by FTIR-spectroscopy to identify the acid concentration in reaction products as shown in chapter 3.

A standard Du-Noüy ring surface tension balance (White Torsion Balance) (Rode, 2010) was modified to incorporate a temperature controlled hot plate under the beaker containing the liquid, Figure 4.4. The correct working of the arrangement was verified by surface tension measurements on distilled water, which has a known surface tension of 0.072 N/m at 20 °C (DECHEMA e.V., 2005 - 2008). The Du-Noüy ring method measures the force needed to pull a defined platinum ring across the interface between two immiscible liquids, Figure 4.5. The force measurement is done by a spring loaded balance. With a circumference of 40 mm, the platinum ring matches the instrument and allowed a direct reading of the interfacial tension in N/m without further conversion.
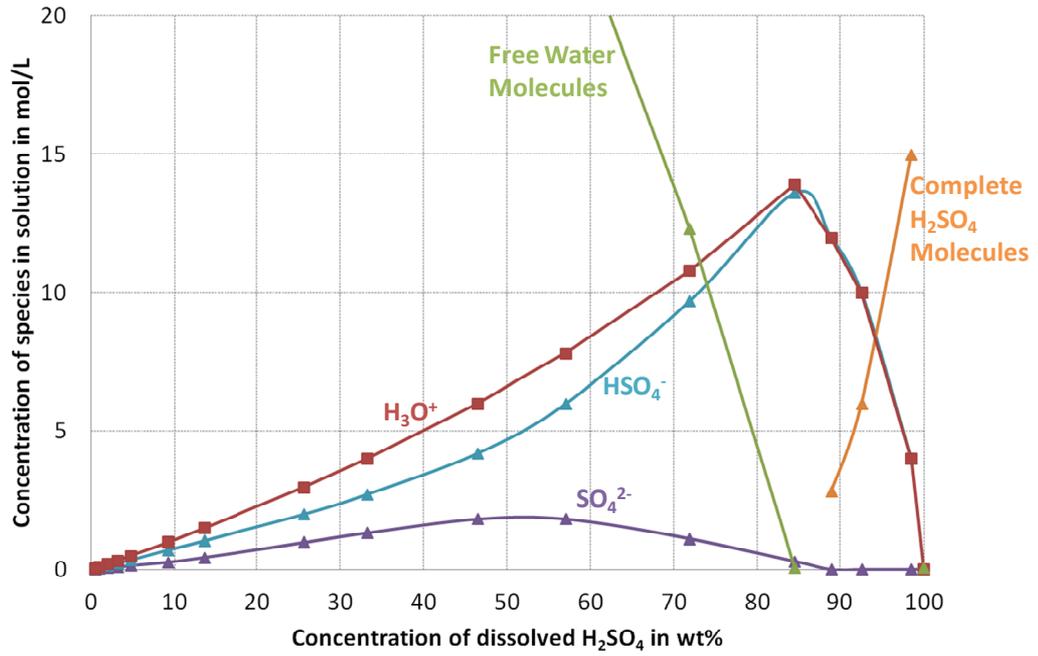
Figure 4.3: Dissociation of sulphuric acid in water according (Young, et al., 1959)
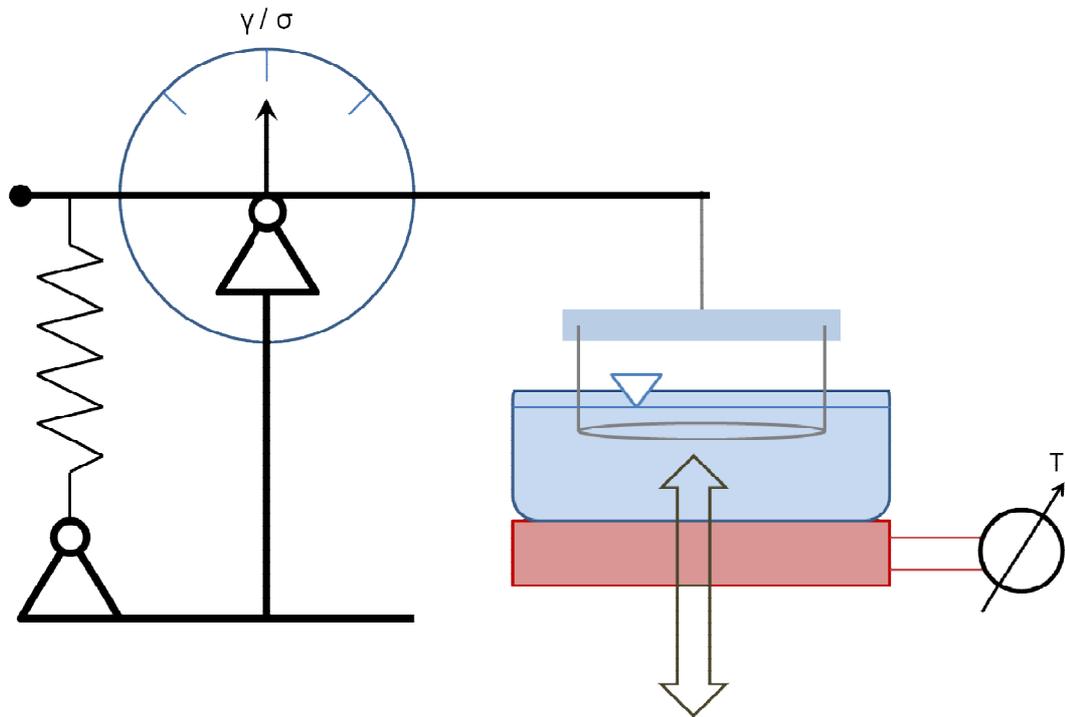
Figure 4.4: Schema of the Du-Noüy ring surface tension balance with temperature controlled hot plate
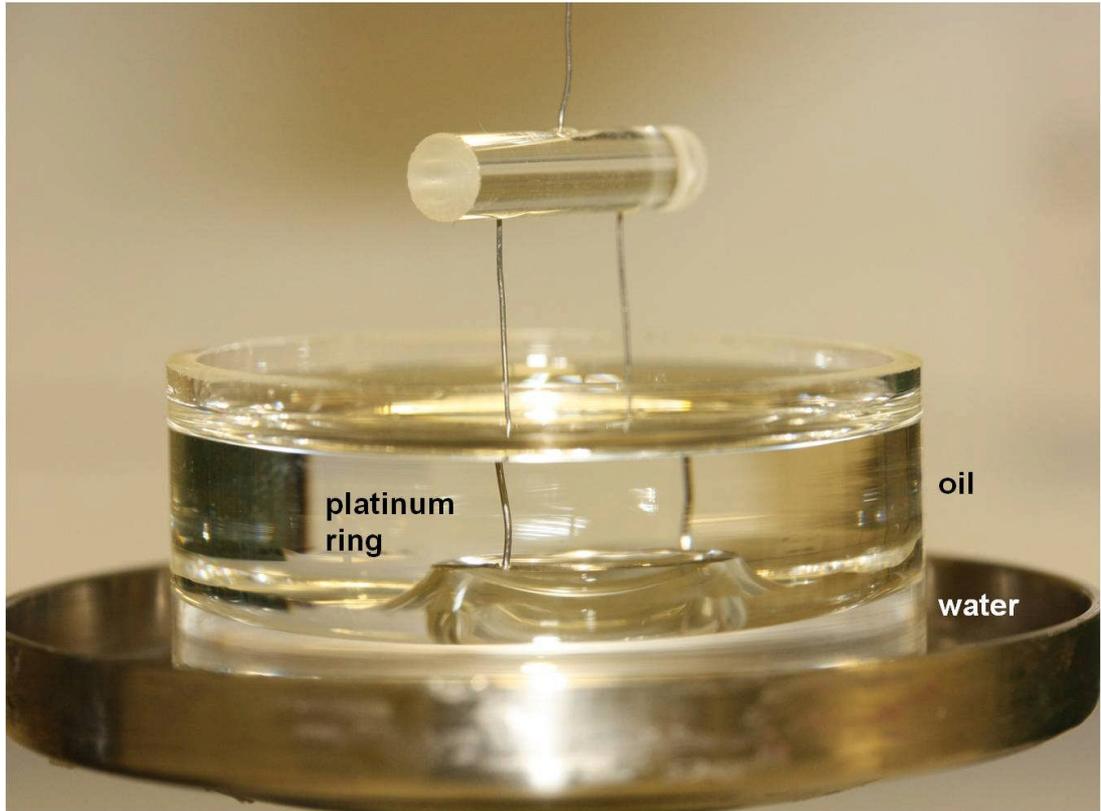
Figure 4.5: Interface between water and squalane during interfacial tension measurement with the Du-Noüy platinum ring
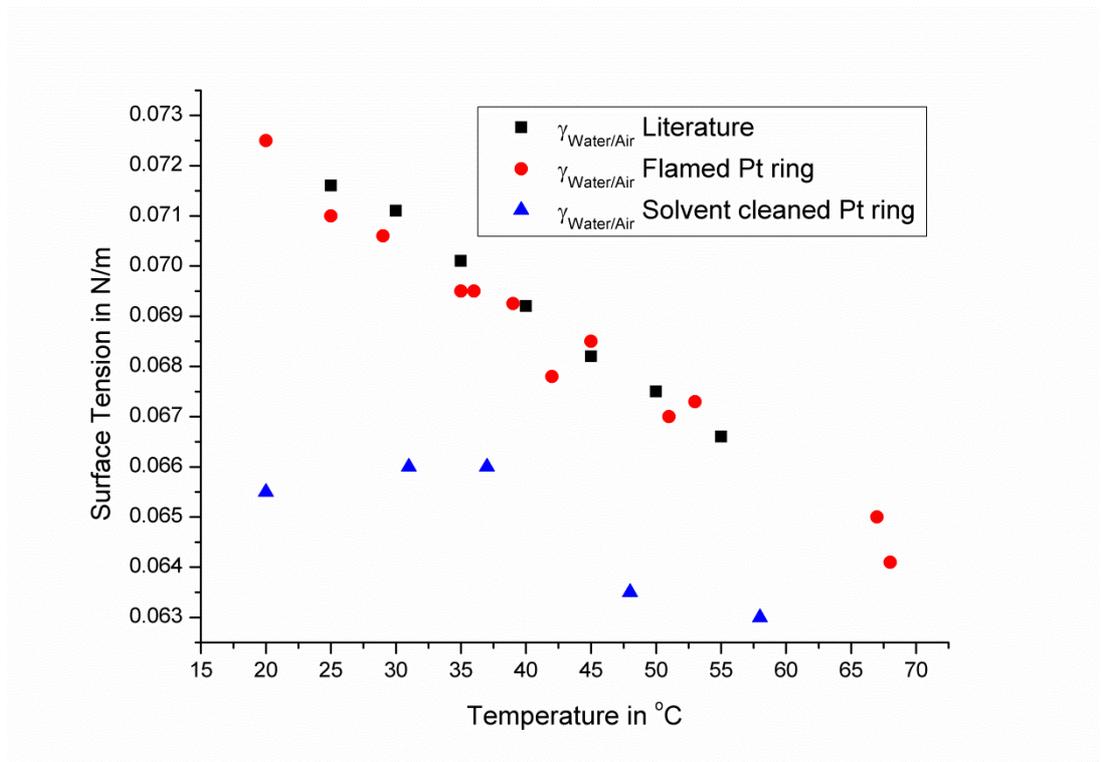
Figure 4.6: Impact of cleaning procedure on the accuracy of interfacial tension measurements with the Du-Noüy ring method on the example of water to air

The inner diameter of the sample beaker was 41 mm which defined the reaction area between oil and sulphuric acid. The platinum ring was cleaned after each measurement, following the order of solubility in deionised water, isopropanol and heptanes. Between each step the ring was dried on laboratory tissue and finally heated until it glowed light red in a blue gas flame. The cleaning procedure was developed after several repeatability issues. In particular flaming of the ring had a major impact but it is important to also remove any excess hydrocarbons with heptanes to avoid carbon deposits on the ring surface. For practical reasons, such as safety and cross contamination, it is important to neutralise the sulphuric acid in water and remove excess water using isopropanol. Figure 4.6 shows the impact of the cleaning procedure on the accuracy of the measurements for the example of the water-air interface at various temperatures.

Measurements were taken under three different conditions. First the oil was added to the top surface of the more dense acid at room temperature and directly measured to see the time dependent development of interfacial tension, section 4.2. Secondly the same samples were heated to 90 °C and than cooled down to measure at room temperature when all reactions between oil and acid were finalised, section 4.3. Thirdly a new batch of samples was prepared by adding oil and acid at room temperature and storing for at least 12 hours. The samples were then cooled in a refrigerator and measured until room temperature was reached. The temperature was then increased in steps of 15 °C and each step was held for 30 minutes to allow for stabilisation before measurements were taken, section 4.4. A K-type thermocouple (NiCr-Ni) was directly placed in the oil phase to avoid corrosion of the sensor. The temperature dependent measurements were only undertaken for squalane as the interfacial tension values for the base oils were too low to expect meaningful results.

During the interfacial tension measurements solid and bituminous reaction products were formed. They were extracted and analysed by FTIR-microscope, FTIR-ATR and SEM/EDX. Results are shown in the following and in chapter 3. The solids were mechanical captured from the interface by a glass rod and carefully released on a water surface were they unfolded and floated. From the water surface, the solids were captured by a glass microscope slide or the aluminium SEM object carrier respectively. On the carriers, the solids were rinsed with isopropanol followed by rinsing with heptanes. Before analysis the solid and carrier were dried at about 50 °C for

30 minutes in an oven. The results are shown in the following and some were presented in, chapter 3.

The bitumen which was captured from the interface was washed with water to neutralise the surrounding acid. The water was poured away and the samples dried off at 50 °C for 1 hour in an oven. The bituminous reaction products were found to be emulsions of light liquid, surrounded by dark matter. The bitumen was dissolved in hexanes and left to allow the more dense water or sulphuric acid phase to settle. Small parts of the hexane-bitumen mixture were taken by a pipette and the hexane allowed to evaporate at 40 °C for 45 minutes in an oven. The remaining bitumen was inspected by a light microscope, found to be homogeneous and was used in the chemical analysis. The results are shown in the following and some were presented in chapter 3.

4.2 Results and Discussion: Time Dependency of Interfacial Tension

For the time variation measurements, following the method described in Section 4.1, the interfacial tension for all concentrations of H_2SO_4 against squalane at 20 °C decreased over time and stabilised after approximately 16 minutes, Figure 4.7. The higher the acid concentration, the sharper the decrease and the lower the resulting values of interfacial tension. This behaviour was not observed for pure water against squalane and the constant value found is in good agreement with Antonov's rule, equation (4.1), (Demond, et al., 1993). Antonov's rule can be used to roughly estimate the interfacial tension between an organic liquid and water, σ_{ow}, from the surface tension of water, γ_w, and the surface tension of the organic liquid, γ_o, when both are immiscible.

$$\sigma_{ow} = |\gamma_w - \gamma_o| \tag{4.1}$$

For extremely clean conditions were already highly pure squalane was further cleaned by shaking with water and aluminium filings, a value of 0.0517 N/m at 19 °C was reported (Mahe, et al., 1988). A lower value of 0.0454 ±0.8 N/m at 25 °C was reported were off the shelf squalane was used (Akiyama, et al., 2007). Mahe observed a contamination of his experiments when using Perspex windows (Mahe, et al., 1988) and the use of polyethylene canisters for the storage of freshly produced deionised water in this study could have a similar effect and reduce interfacial tension.
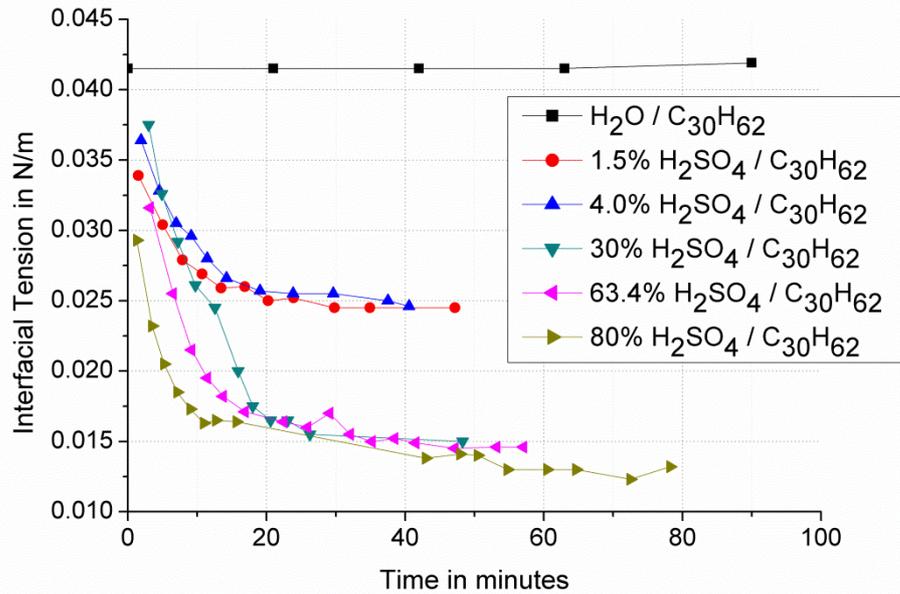
Figure 4.7: Time dependent development of interfacial tension between water (H₂O), aqueous concentrations (%w/w) of H₂SO₄ and C₃₀H₆₂ at 20 °C

The most plausible explanation for the decrease in interfacial tension with time is the reaction of squalane with the acid to form surface active substances or 'surfactants' which form a monolayer, micelles and consequently multiple layers. Surfactants influencing the interfacial tension between water and oil most commonly consist of a hydrophilic head group and a oleophilic hydrocarbon tail. Sulphonated hydrocarbons are a typical group of surfactants used in technical applications. The arrangement of the surfactants on the interface to monolayers, micelles and double layers has an influence on the final interfacial tension. Applying the general rule that chemical reaction rates at least double for every 10 °C increment, the reaction between oil and acid at 200 °C, which is typical value for the engine, would be complete after 0.22 seconds.

Also for API Group I base oils HVI160B, BS150 and SN600 the development of the interfacial tension with sulphuric acid was time dependent, reaching the final value after 8 to 16 minutes, Figure 4.8. This corresponds well to the behaviour observed with squalane as presented above. However, the interfacial tension for the API Group I base oils was also time dependent when in contact with pure water which was not the case with squalane. This indicates the presence of polar substances in the base oils which act as surfactants on the interface.

Due to the adhesive and viscous nature of the base oil, the cleaning process of the platinum ring was more difficult and time consuming than with squalane. After the cleaning process, the platinum ring has to be brought below the interface for the following measurement. The oil tended to form drops on the platinum ring which had to be shook off. Contrary to squalane this was quite tedious and time consuming with the base oils. Therefore it was difficult to obtain meaningful results from the time dependent measurements and only the three conditions in Figure 4.8 with BS150 were successfully obtained. In general however, the other base oils did behave the same.
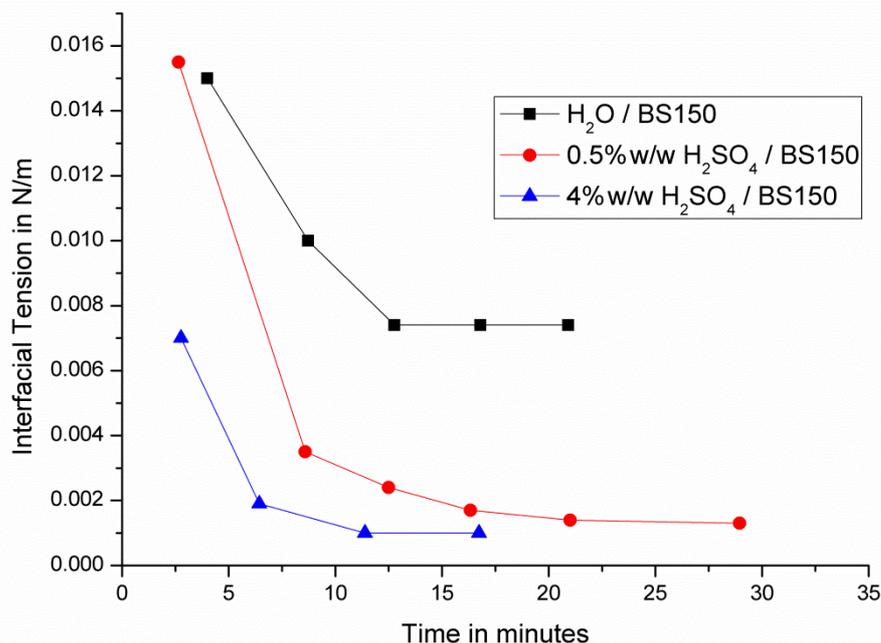
Figure 4.8: Time dependent development of interfacial tension between water (H$_2$O), aqueous concentrations (%w/w) of H$_2$SO$_4$ and API Group I base oil BS150 at 22 °C

4.3 Results and Discussion: Interfacial Tension of Fully Developed Interface

In section 4.2 it was shown that interfacial tension is not stable over time. Therefore the interface was allowed to settle and come to an equilibrium as described in section 4.1.

In Figure 4.9 the interfacial tension of sulphuric acid against squalane (σ H$_2$SO$_4$/C$_{30}$H$_{62}$) is shown. At this temperature and approximately 3 minutes heating time, discolouration was observed for the acid phase for highly concentrated sulphuric acid of ~98 %w/w. The discolouration commenced at

approximately 70 °C, a value confirmed in the literature (Stecher, et al., 1960).

After the interfacial tension measurements, the used samples were stored for a time of about two weeks. All mixtures below 40 %w/w concentration remained clear, the 40 %w/w mixture did not exhibit discolouration but instead some solid formation and slight clouding but all mixtures above 40 %w/w showed discolouration of the acid phase.
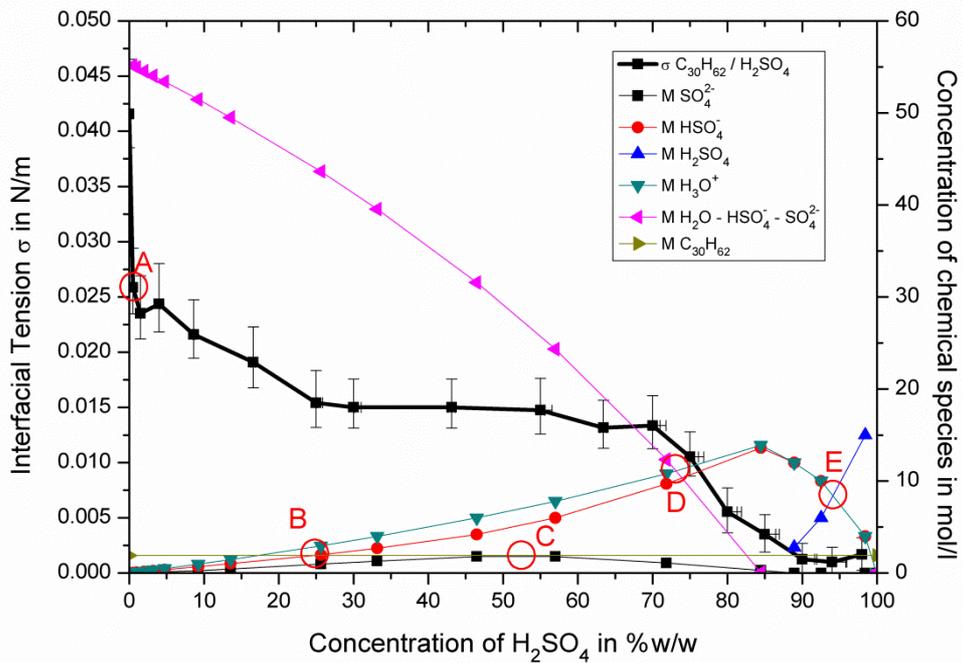
Figure 4.9: Results of interfacial tension measurements between squalane and sulphuric acid (σ C$_{30}$H$_{62}$/H$_2$SO$_4$) at 21 °C in comparison to molecular concentration of species in the acid phase, according to (Young, et al., 1959)

The results for the interfacial tension measurements in Figure 4.9 (σ H$_2$SO$_4$/C$_{30}$H$_{62}$) show a sharp decrease in interfacial tension for a very low concentration (0.5 %w/w) of sulphuric acid. From 0.5 %w/w to 25 %w/w a more shallow drop is observed, followed by a constant level of interfacial tension between 25 and approximately 65 %w/w. A further decrease occurs until 90 %w/w, where the lowest values are reached.

The estimation of measurement errors was undertaken in accordance with DIN1319. The accuracy of the surface tension balance, influence of temperature fluctuations and the accuracy of acid preparation was considered. The repeatability of the measurements showed a standard deviation of ±0.0002 N/m.

The decrease in interfacial tension with increasing concentration is a well established observation in colloid science. For known surfactants the Langmuir-Szyskowski equation (4.2) (Joos, et al., 1990) is used to describe interfacial tension on the oil water interface until the interface is saturated and no more surfactant molecules can be absorbed.

$$\sigma = \sigma_0 - 2RT\Gamma^\infty \ln\left(1 + \frac{C}{a}\right)$$ (4.2)

The initial interfacial tension σ_0 is reduced by a term containing the known factors R, the ideal gas constant, the temperature T and C, the concentration of the surfactant. The saturation adsorption Γ^∞ and the Langmuir-Von Szyskowski constant a require information about the surface area taken by each surface active molecule on the interface and its concentration in each phase. For this study it is assumed that the higher the concentration the more but unknown surface active molecules can be formed, leading to the drop in interfacial tension.

Also shown in Figure 4.9 are the chemical species formed as acid concentration is increased (Young, et al., 1959), a repeat of Figure 4.3. Point A in Figure 4.9 marks the sharp decrease in interfacial tension, which is explained by the large difference in molecular concentration ratio between squalane, at 1.92 mol/l, and sulphuric acid, 18.64 mol/l. It is the maximum range of ph dependent measurements by Feng (Feng, et al., 2010) and Vellinger (Vellinger, et al., 1933) described and explained in chapter 2, page 32-33. Influencing the H_3O^+ concentration on the interface was shown to lower interfacial tension in this range. At point B the HSO_4^- ions reach a concentration of 1.98 mol/l and for every molecule of $C_{30}H_{62}$ at the interface, there is a molecule of HSO_4^- available. At point B, the interface becomes saturated and the interfacial tension remains constant as the concentration of HSO_4^- increases further. In colloid science, this point is called the first critical micelle concentration 'CMC I'. At point C the second dissociation step reaches a maximum and from this point onwards as the concentration of sulphuric acid increases, the second step of dissociation into SO_4^{2-} becomes increasingly suppressed. This effect increases the rate of HSO_4^- ion release and the interfacial tension begins to decrease slowly. At point D the number of ionic acid species becomes greater than the number of free H_2O molecules and a second sharp decrease in interfacial tension is observed. This point is called 'CMC II' and indicates the formation of double layers of surfactants on the interface (Shaw, 2003). At point E the available HSO_4^- ions are in equilibrium with free H_2SO_4 molecules and interfacial tension reaches its minimum. Finally, a slight increase in interfacial tension is

observed when squalane is exposed to the most concentrated sulphuric acid.

For the API Group I base oils HVI160B, BS150 and SN600, the interfacial tension towards aqueous solutions of sulphuric acid on the fully developed interface, Figure 4.10, was substantially lower compared to the measurements done with squalane. At 4 %w/w acid concentration the minimum or critical micelle concentration was reached and no further reduction was observed.
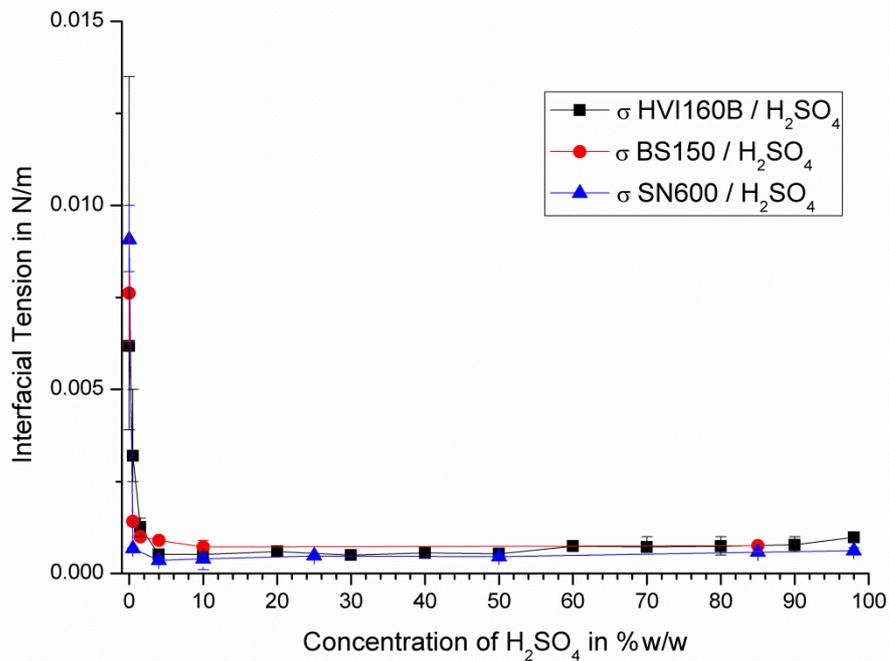
Figure 4.10: Results of interfacial tension measurements between API Group I base oils and aqueous sulphuric acid at 22 °C after heating to 90 °C

4.4 Results and Discussion: Temperature Dependency of Interfacial Tension

Figure 4.11 and Figure 4.12 are the results for the temperature dependent interfacial tension measurements between squalane and aqueous sulphuric acid as described in Section 4.1.

During the temperature dependent interfacial tension measurements, discolouration of the samples containing higher acid concentrations was observed in the acid and the oil phase together with the formation of solids. The moment of discolouration was captured during the interfacial tension measurements for 65 %w/w and 80 %w/w acid concentration, Figure 4.11.
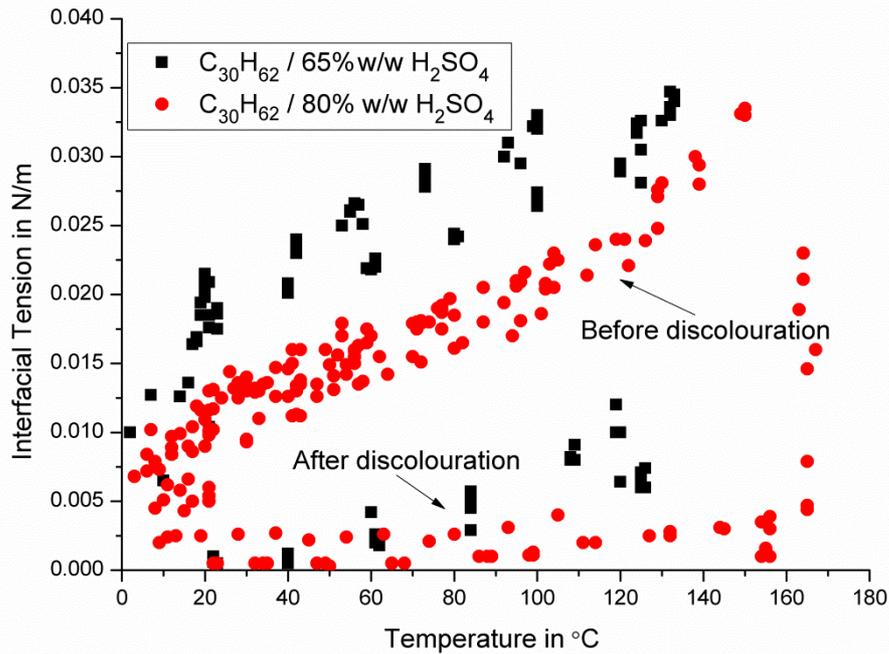
Figure 4.11: Temperature dependent interfacial tension of 65 % and 80 %w/w H_2SO_4 towards $C_{30}H_{62}$

Before discolouration occurred, the interfacial tension was directly correlated to the temperature of the liquids and followed the upper values in Figure 4.11. When a certain high temperature was reached, or a lower temperature was held for several days, the sample started to change colour and the interfacial tension decreased significantly. After the decrease, the correlation between interfacial tension and temperature was changed irreversibly, as shown by the lower values in Figure 4.11.

The upper values, without discolouration, were measured for nine acid concentrations and for each a closest fit function was found, presented in Table 4.1 and illustrated in Figure 4.12. For comparison and orientation the corresponding values at 21 °C from Figure 4.9 are added in the plot as single points. Measurements of the two different treated sample batches show good agreement at most concentrations but are higher for 0.5 %, 65 % & 80 %w/w in the case of the samples that were only stored for extended time at room temperature.
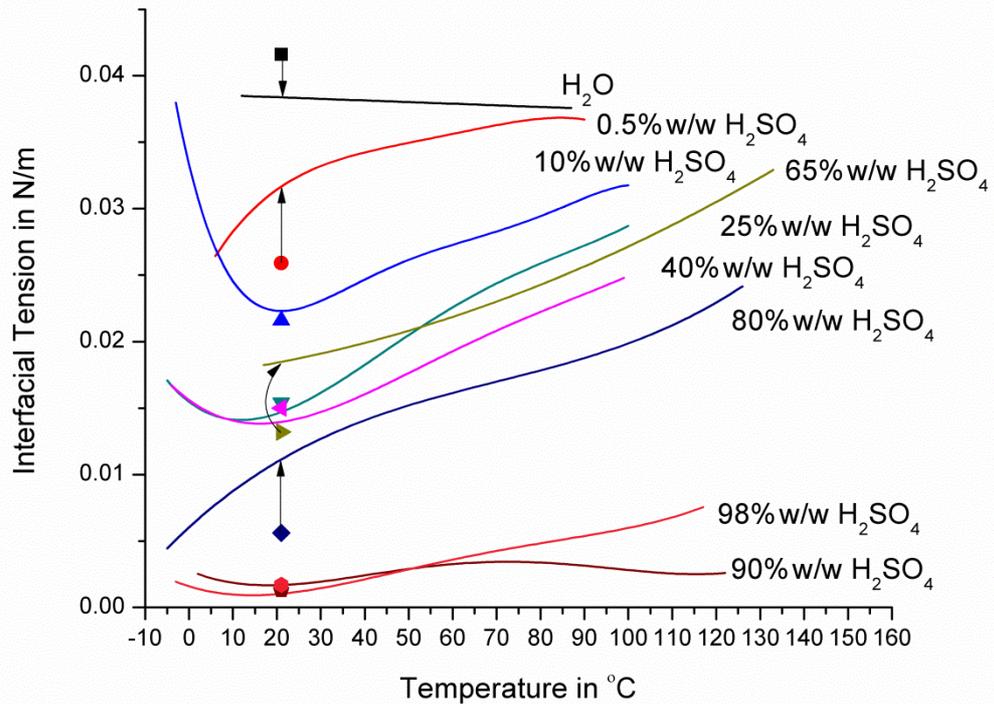
Figure 4.12: Concentration and temperature dependency of the interfacial tension between sulphuric acid, H₂SO₄ , and squalane, C₃₀H₆₂. The values from Figure 4.9 are added for comparison.

The interfacial tension between squalane and deionised water decreases linearly with increasing temperature but at a lower rate than the also linear decreasing surface tension of pure squalane or pure water against air for which the linearity is described by the Eötvös rule, equation (4.3) (Rode, 2010).

$$\gamma = \frac{\gamma_{mol}}{V_m^{\frac{2}{3}}} = \frac{\alpha \cdot [(T_c - 6\text{K}) - T]}{\left(\frac{M}{\rho}\right)^{\frac{2}{3}}} \tag{4.3}$$

Equation (4.3) results directly in the measurable surface tension γ when the critical temperature T_c, the molar mass M and the density ρ of the substance is known. The Eötvös constant α has a value of $2.7*10^{-7}$ J/K*mol$^{2/3}$. γ_{mol} is the molar surface tension and V_m the molar volume. However, the combination with equation (4.1) to find the interfacial tension between squalane and water does not reflect the measurements.

For all solutions containing sulphuric acid, the interfacial tension rises with increased temperature above approximately 20 °C. For 0.5 %w/w and 80 %w/w solutions, the interfacial tension decreases disproportionately at temperatures below 20 °C. All other solutions show a contrary disproportionate increase in interfacial tension at temperatures below 20 °C.

Table 4.1: Best fit equations as shown in Figure 4.12

conc. in %w/w	Interfacial Tension $\sigma(T)$ in N/m	T in °C
0	= -1.2236E-5*T+0.03864	12 – 87
0.5	= -8.43983E-10*T^4 + 1.92715E-07*T^3 - 1.64371E-5*T^2 + 6.87675E-4*T + 0.02285	6 – 90
10	= -2.86798E-11*T^5 + 8.95547E-09*T^4 - 1.06049E-06*T^3 + 5.86861E-5*T^2 - 1.3666E-3*T + 0.03332	-3 – 100
25	= 5.79812E-10*T^4 - 1.5079E-07*T^3 + 1.31115E-5*T^2 - 2.50671E-4*T + 0.01547	-5 – 100
40	= 3.50765E-10*T^4 - 9.849E-08*T^3 + 9.68993E-06*T^2 - 2.41447E-4*T +0.0156	-4 – 99
65	= 5.78778E-07*T^2 + 3.98494E-5*T + 0.01738	17 – 133
80	= 1.46677E-08*T^3 - 3.10118E-06*T^2 + 3.01794E-4*T + 6.03057E-3	-5 – 126
90	= 2.34344E-10*T^4 - 6.43761E-08*T^3 + 5.51694E-06*T^2 - 1.41965E-4*T + 2.78768E-3	2 – 122
98	= 1.94661E-10*T^4 - 5.1293E-08*T^3 + 4.65421E-06*T^2 - 1.0321E-4*T + 1.58747E-3	-3 - 117

The temperature-interfacial tension correlation for all concentrations of sulphuric acid was non-linear, while the single phases show a linear decrease of surface tension with increasing temperature, appendix A. A similar fishhook or J-shape behaviour was observed at the interface between water and liquid paraffin when POE (polyoxyethylene) stearyl ether was dissolved in the water phase (Mitsui, et al., 1971). This behaviour was also concentration dependent. The authors explained the temperature dependency of the interfacial tension in terms of the pulling forces on the polar head groups of the surfactant. The hydrophilic head group and the oleophilic tail find a concentration dependent energetic ideal position at a certain temperature, where the interfacial tension therefore is at a minimum. When the temperature rises or falls, the head group changes its position to the oil or water side and thereby increases the interfacial tension. Another explanation was given by Thompson who relates the minimum of interfacial tension to the phase inversion temperature. When the head group of surfactants is hydrated and large, o/w emulsions are formed and when the head group dehydrates and become small, w/o emulsions are formed. At the

turning point when the head group and the tail is of similar size, the interfacial tension reaches a minimum (Thompson, 1994).

No correlation was found between the temperature dependent extent of dissociation of H_2SO_4 in water (Young, et al., 1959) to the temperature dependency of interfacial tension. This can be explained by a chemical reaction which binds the HSO_4^- ion stronger to the oil phase and excludes it from the dissociation process.

The surface tension of squalane to air was unaffected by the contact with sulphuric acid and was in good agreement with values found in the literature (DECHEMA e.V., 2005 - 2008). Also the API Group I base oils did not change their surface tension with air, which was ~10 % higher than for squalane, when reacted with sulphuric acid. This indicates that any surface active substances formed act only upon interfaces to polar fluids and not with the non-polar air.

4.5   Results and Discussion: Analysis of Reaction Products

This subsection is an extract of the more global analytical work presented in chapter 3.

Figure 4.13 shows an FTIR-ATR spectrum of a solid formed between 80 %w/w H_2SO_4 and $C_{30}H_{62}$ at 165 °C. Peaks from $C_{30}H_{62}$ are still present and in addition carbon-oxygen double bonds were formed. Peaks which are also found in the 80 %w/w H_2SO_4 are shifted to positions of lower acid concentration of about 50 – 55 %w/w, see chapter 3.

An EDX elemental analysis, chapter 3, under high vacuum revealed 70 % carbon, 26 % oxygen and 3 % sulphur in the solid reaction product formed between 80 %w/w H_2SO_4 and $C_{30}H_{62}$. All results are given in Atom %.

Figure 4.14 shows a FTIR-ATR spectrum of hexane-refined bitumen formed between 98 %w/w H_2SO_4 and API Group I base oil HVI160B during a short heating period to 90 °C and a following storage time of 4 weeks at room temperature. Peaks from HVI160B are still present and in addition carbon-oxygen double bonds are present. Peaks which are also found in the 98 %w/w H_2SO_4 are shifted to positions of lower acid concentration of about 35 – 40 %w/w, see chapter 3. Other peaks which are found in 98 %w/w H_2SO_4 are missing.
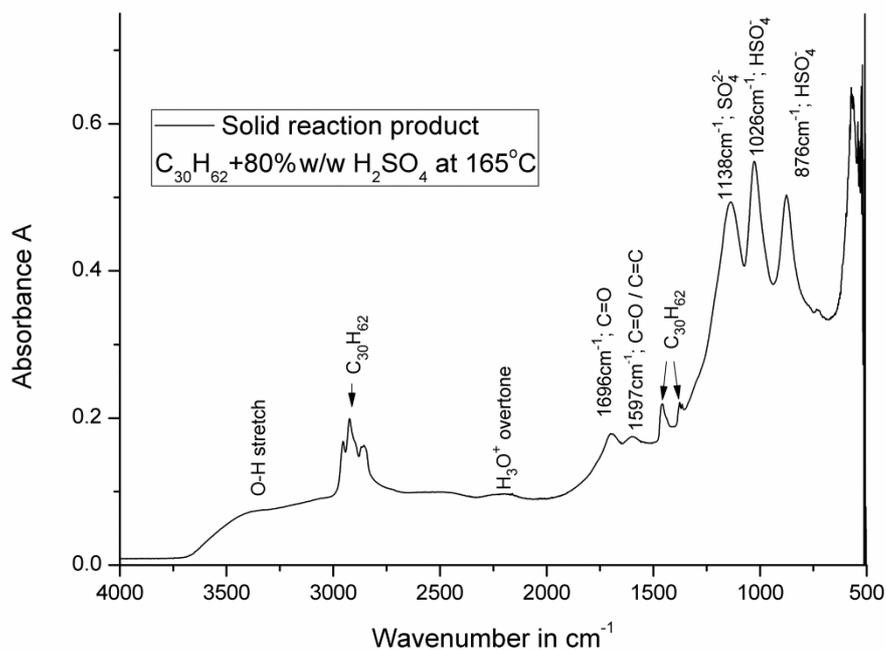
Figure 4.13: FTIR-ATR spectrum of a solid formed between C₃₀H₆₂ and 80 %w/w H₂SO₄ at 165 °C
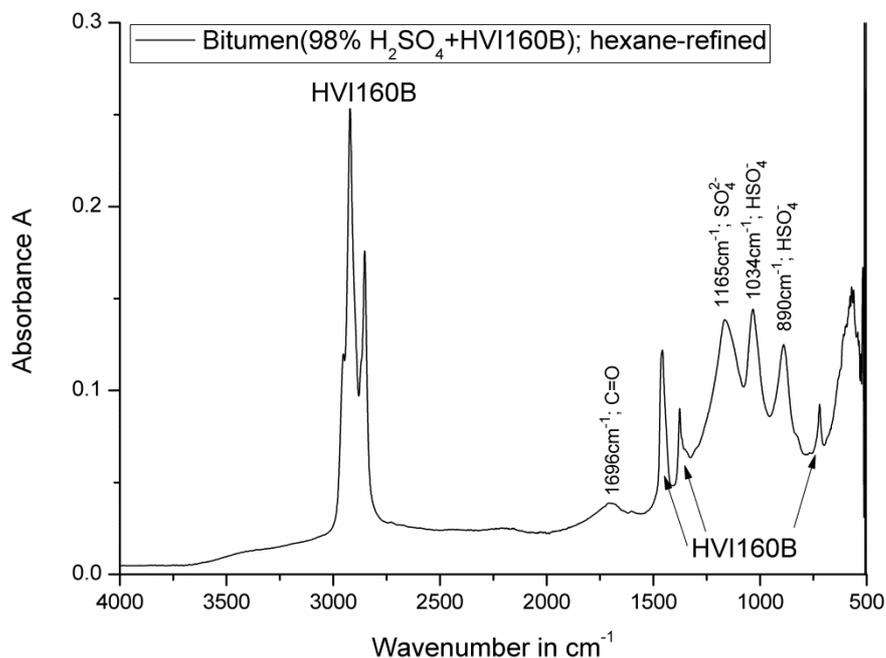
Figure 4.14: FTIR-ATR spectrum of hexane-refined bitumen, formed between 98 %w/w H₂SO₄ and API Group I base oil HVI160B at 90 °C and four weeks storing at room temperature

The results from FTIR-ATR and EDX give strong evidence for the creation of hydrocarbon sulphonates on the interface between sulphuric acid and oil phase. Hydrocarbon sulphonates are a well known group of surfactants used to lower the interfacial tension between water and oil. The shift of peak

positions to values of 50 – 55 %w/w H_2SO_4 correspond well to findings of critical acid concentration to form bitumen, chapter 3. The second dissociation step of sulphuric acid in water peaks at 50 %w/w, Figure 4.3, and the interfacial tension measurements with squalane show a turning point at 40 – 50 %w/w, Figure 4.9.

4.6　Conclusions of the Interfacial Tension Measurements

The interfacial tension between aqueous sulphuric acid and hydrocarbon based lubricants was measured. It was found that the development of interfacial tension is dependent on time with the one exemption of squalane against pure water. A close correlation of interfacial tension to the dissociation of sulphuric acid in water was found. The interfacial tension was also temperature dependent up to a point where discolouration and solid formation set in and the interfacial tension breaks down irreversibly.

Antonov's rule (4.1) can be used to predict interfacial tension of squalane against water at 20 °C but not for higher temperatures. The real decrease is more shallow than predicted, which indicates an effect of increased polarity of warm water against the non-polar squalane, compare with chapter 2, page 33. The interfacial tension between squalane and sulphuric acid is closely related to the dissociation of sulphuric acid. CMC I is reached when the molar concentration of $C_{30}H_{62}$ equals the molar concentration of HSO_4^- ions. A turning point in the interfacial tension curve is reached when the second dissociation step peaks. Close to the second dissociation step, clouding and discolouration can also be observed – an indication of increased chemical activity, yielding excess of hydrocarbon sulphonates. CMC II is reached when the molar concentration of cations (H_3O^+) and anions (HSO_4^- & SO_4^{2-}) equals the declining amount of free water molecules.

Surface active substances are present in the API Group I base oils. This can be seen in the time dependent decrease of interfacial tension towards pure water, Figure 4.8, which was not observed with squalane, Figure 4.7.

API Group I base oil is more reactive towards sulphuric acid than squalane which can be seen in the low acid concentrations, 4 %w/w compared to 25 %w/w, needed to reach CMC I, Figure 4.10 and Figure 4.9, and also the slightly faster reduction in interfacial tension, Figure 4.7 and Figure 4.8. The absolute values of interfacial tension are also much lower for the API Group I base oils, which indicate a large amount of surface active substances on the interface. The higher reactivity was expected due to the higher content of

unsaturated and reactive hydrocarbons in the API Group I base oils (CIMAC Working Group "Marine Lubricants", 2007).

The spectral analysis of bitumen and solids formed at the interface of oil and sulphuric acid indicate the creation of hydrocarbon sulphonates, formed in excess at acid concentrations of 40 %w/w and higher.

The change from API Group I to higher refined base oils is a step in the right direction, reducing degradation of the oil including formation of solid deposits. Solid formation was observed during the measurements with squalane, Figure 4.11, at 165 °C. API Group I base oil in contact with sulphuric acid, shows solid formation at 120 °C. More about deposit formation can be found in chapters 3 and 7. In chapter 3 an analysis of chemical and physical state of solid deposit and bituminous reaction product is given and the viscosity of the bituminous matter is presented, the temperature and acid concentration for its creation is revealed. The impact of oil degradation by the action of sulphuric acid on a piston ring liner lubrication contact is shown in chapter 7.

The interfacial tension between squalane and aqueous sulphuric acid is temperature dependent, Figure 4.12, which indicates the presence of surface active molecules on the interface (Mitsui, et al., 1971). Exceeding a certain high temperature, the colour changes from clear to yellow and the interfacial tension breaks down, Figure 4.11. The colour of the base oils is yellow to brown and the interfacial tension as low as for squalane after the change in colour. It is likely that very similar substances, hydrocarbon sulphonates for example, are responsible for the very low interfacial tension in both cases.

The development of interfacial tension, and therefore chemical interaction, was time dependent. When extrapolating to higher temperatures, the reaction of oil with sulphuric acid cannot be completely avoided by the relatively slow neutralisation process in fully formulated lubricants, chapter 3. In chapter 3 it is shown how the degradation of the base oil negatively influences the initial rate of reaction of fully formulated base oils while improving the delay time for the reaction, most probably due to the low initial interfacial tension and reduced initial droplet size.

The higher interfacial tension between squalane and sulphuric acid compared to API Group I base oils indicates an increased dispersant requirement for higher refined base oils, to keep acid droplets dispersed and make them available for the neutralisation process by calcium carbonate

containing micelles, as used in fully formulated lubricants (Wu, et al., 2000). In chapter 3 the breakup of droplets and the stability of emulsions prepared with squalane and API Group I base oils was described.

In the following chapter 5 the contact angle of aqueous sulphuric acid on piston ring and cylinder liner surfaces is measured. Surprisingly, the interfacial tension has no influence on contact angle but plays a major role in mechanical droplet displacement from the wall by the influence of shear flow.

Chapter 5
Contact Angle Between Engineering Materials Submerged in $C_{30}H_{62}$ And Aqueous Sulphuric Acid

The wettability of engine parts with corrosive sulphuric acid can be characterised by the contact angle. The contact angle of aqueous H_2SO_4 (0 – 98 %w/w) on a grey cast iron cylinder liner material (Wärtsilä, RT84) and a piston ring chrome-ceramic coating (Federal Mogul Goetze, CKS, ø 960 mm) immersed in squalane, $C_{30}H_{62}$, was measured over a temperature range from 20 to 165 °C. The custom built arrangement and the results are presented in this chapter.

The aim was to find differences in contact angle with acid concentration, temperature and between the materials. The contact angle, together with the interfacial tension measured in chapter 4, is an important input parameter for mechanical removal of droplets from a surface by shear forces in a surrounding liquid flow.

Contact angle measurements were taken with advancing, receding and static droplets on freshly polished surfaces. They are presented in the following subsections and have also been published (Sautermeister, et al., 2011).

In the following chapter 7, the build up of calcium carbonate, $CaCO_3$, boundary layers from the fully formulated lubricant and modification of surface chemistry due to the tribological impact is shown. Those surface modifications are not covered in the present chapter and left for future research. However, a case of corrosion on a moving piston ring with corrosive attack in the valleys of machining marks, chapter 7, seems interesting in comparison to the findings presented in this chapter.

5.1   Materials and Methods: Contact Angle Measurements

For the study, the following substances were used: squalane (99 % purity Sigma Aldrich) and sulphuric acid (> 95 %w/w Fisher Scientific UK Ltd., analytical reagent grade). Lower concentrations of sulphuric acid were made with deionised water by weighing. Physical properties of the substances can be found in appendix A. An introduction to squalane, $C_{30}H_{62}$, in comparison to real lubricant base oils is given in chapter 4, an introduction to aqueous

sulphuric acid, H_2SO_4, and its relation to marine Diesel engines is given in chapter 1 and 4.

Surface samples were prepared from a galvanic chrome-coated piston ring (Ø 960 mm, CKS, FM-Goetze) and a grey cast iron cylinder liner segment (RT84, Wärtsilä Switzerland Ltd.). The samples were hand-ground and polished with a 15 µm Buehler Diamond suspension to a roughness of Ra ~0.15 µm and then cleaned in an ultrasonic bath with a Decon90 solution and then deionised water for 10 minutes each. After cleaning, the samples were dried on a hot plate at 150 °C for 5 minutes and oiled with squalane after a short cooling down period to protect the surface. In chapter 6, the materials are presented in detail.

After the contact angle measurements, the surfaces were examined by a light microscope to evaluate the influence of corrosive attack on the surfaces.

The contact angle of a liquid droplet resting on a solid surface is the angle formed between the surface and a tangent on the droplet, where the fluid-vapour, or in this case liquid-liquid interface, meets the solid. It is conventionally measured towards the inside of the droplet Figure 5.1. The contact angle of various acid concentrations on surfaces submerged in squalane was measured by the 'pendant' or 'sessile' drop method (Stadler, et al., 2006), Figure 5.1. To avoid corrosive attack the steel needle of a glass syringe containing the aqueous acid was replaced by a 1 mm glass capillary with one tapered end to create a tight fit in the small hole of the syringe. A custom-built oil bath with parallel glass windows was placed on a temperature controlled hot plate mounted on a 3-axis movable stage and the surface samples were placed in the oil bath. Pictures of the droplets were taken using a Canon 450d camera with 60 mm macro objective lens. A monochromatic light source was used for optimum contrast. The evaluation was undertaken using the ImageJ software plug-in (Stadler, et al., 2006).

The correct operation and accuracy of the whole arrangement was shown by measuring 1 mm diameter steel balls located in various smaller holes in a calibration plate. The bigger the diameter of the hole, the deeper the steel ball would penetrate the hole and the smaller the 'contact angle' becomes. In this way, six different angles between 115 and 150° were measured and the evaluation showed an accuracy between calculated and measured angle of ±5°. A practical problem was the preparation of the calibration plate. A small burr or a dent on the edge of a hole has a big effect on the measured contact angle. Burrs were reduced to a minimum by filling the holes with cold

castable mounting compound (Buehler VariDur10) followed by a polishing of the steel plate. The resin was then removed by acetone in an ultrasonic bath. However, the sharp edges of the holes were still vulnerable to dents created by measuring the height of the balls protruding from the holes by a screw micrometer calliper. Against this background, the deviation between the two measurement techniques was seen as a good result. The steel balls also helped to find a distortion created by a previously mounted CCD camera, which gave the steel balls an oval shape most probably due to the rectangular sensor array, which was not corrected by the image software.
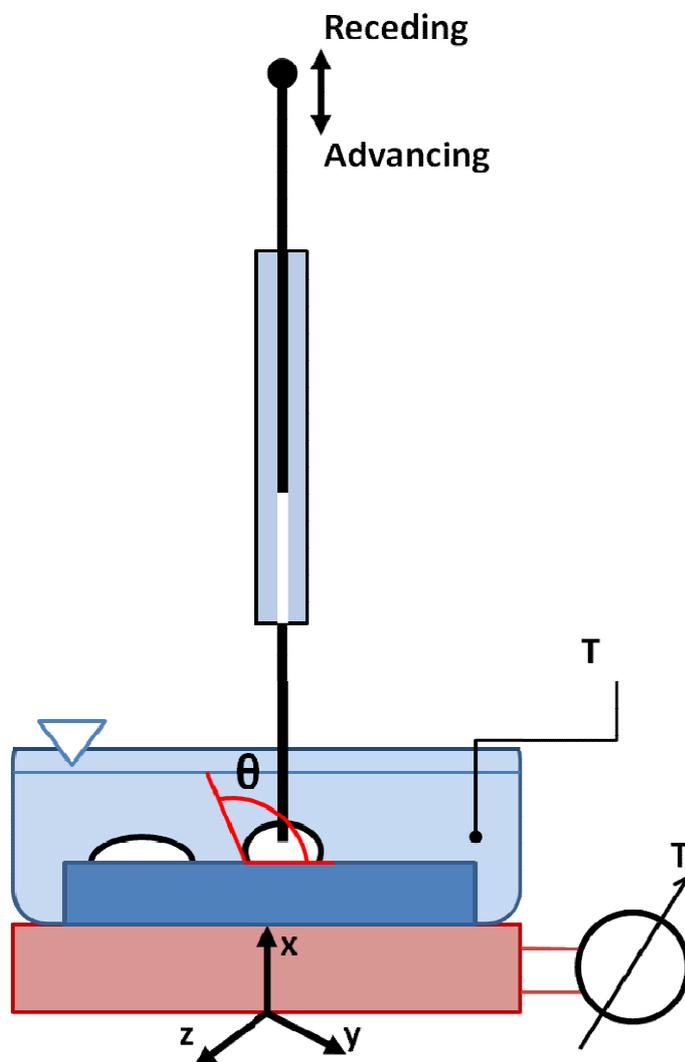
Figure 5.1: Experimental arrangement of the contact angle measurements

First trials in air, with water on a hot plate, showed the big influence of liquid temperature on contact angle. Cold water on a warm surface showed bigger

contact angles than preheated water. Preheating of the water was achieved by bringing the needle in contact with a temperature controlled soldering iron. This problem was overcome by submerging the surface samples and the needle in a temperature controlled oil bath instead of using oiled surfaces. It is also a more realistic arrangement as the influence of gravity on the droplet is reduced by the density of the oil. In the engine, the tiny condensed acid droplets are also surrounded by lubricant oil. The interfacial tension of the droplet skin to the surrounding media was also kept constant in this way.

Also indicated in Figure 5.1 is the creation of advancing, receding and static contact angles. For the measurement of advancing contact angles, the droplet was set on the fresh surface and its volume increased gradually by lowering the plunger, which is fixed to a micrometer screw, into the syringe. The pictures were taken as soon as the border of the droplet moved across the surface. Receding contact angles were created by pulling the plunger out of the syringe which reduces the volume of the droplet. As before, the pictures were taken as soon as the border of the droplet moved across the surface. Advancing angles were taken against fresh surfaces, while receding angles were taken against surfaces which were already in contact with the droplet liquid. They show the difference between wetting and de-wetting a surface. Static angles were created by placing a droplet on the surface. The shape of the droplet changed until equilibrium was reached. Pictures were taken continuously. Unless sudden corrosion set in, no big changes in contact angle over time were observed. Gas produced during corrosion disturbed the measurements in some occasions. The corrosion is obviously changing the surface configuration and the measurements must not be understood as a contact angle towards pure iron or chrome but towards their modified state by the corresponding acid concentration. This is important to keep in mind when comparing advancing, receding and static contact angles. It is, however, realistic for wetting and de-wetting in an engine.

5.2 Results and Discussion: Contact Angle on Piston Ring Chrome Coating and Grey Cast Iron Cylinder Liner Material

Contact angle measurements were made for a piston ring chrome coating (CKS) and for a cylinder liner grey cast iron (RT84). Advancing angle, receding angle and static angle were measured. Advancing and receding angle were not averaged, as is normal practice, because the parts in the

engine do move and to understand transport phenomena it is important to know the difference. Figure 5.2 shows an example of corrosive droplets resting on chrome coating and on grey cast iron submerged in $C_{30}H_{62}$.
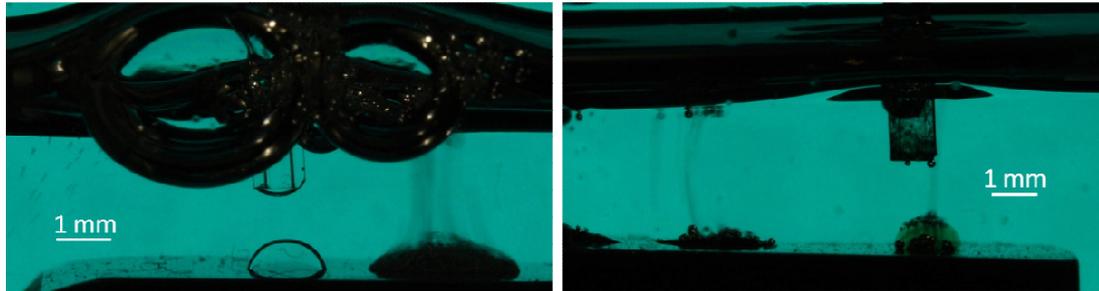
Figure 5.2: Examples for the contact angle measurements under corrosive conditions. Left: 40 %w/w H_2SO_4 on chrome coating. Right: 80 %w/w H_2SO_4 on grey cast iron

In general it can be said, that observed contact angles for the CKS piston ring coating were larger than for the RT84 cylinder liner material as illustrated in Figure 5.3 and Figure 5.4. Receding angles, θ_R, are less than static angles, θ_{St}, which in turn are less than advancing angles, θ_A:

- $\theta_{CKS\,A}$: stays high between 0 and 80 %w/w H_2SO_4, with a sharp drop at 98 %w/w acid concentration

- $\theta_{CKS\,R}$: unstable for 25 % but between 0 and 40 %w/w higher than between 65 and 98 %w/w H_2SO_4 where it is stable

- $\theta_{CKS\,St}$: higher between 0 and 40 %w/w than 65 to 98 %w/w H_2SO_4

- $\theta_{RT84\,A}$: high for 0 %w/w, sharp drop to 0.5 % than rising to 80 %, lower than 0 %w/w for 90 and 98 %w/w H_2SO_4

- $\theta_{RT84\,R}$: sharp drop from 0 to 0.5 % and stable and low towards 98 %w/w

- $\theta_{RT84\,St}$: high for 0 %w/w, stable and low for 0.5 to 98 %w/w

The combined results of the contact angle measurements are given in Table 5.1. The first column gives the concentration of the H_2SO_4 droplet. The last column shows the temperature of the oil bath during the measurement. The table is divided into a section for the chrome coating and the grey cast iron. Each section gives a result for advancing, receding and static contact angle as well as an indication for the observation of corrosion during the measurements.

Table 5.1: Combined results of the contact angle measurements

Contact angle of aqueous H_2SO_4 on engineering material submerged in squalane ($C_{30}H_{62}$) in degrees

CKS (galvanic piston ring chrome coating) — RT84 (grey cast iron cylinder liner)

H_2SO_4 conc. %w/w	T. °C	CKS Advancing angle rec. range	CKS Adv. aver.	CKS Receding angle rec. range	CKS Rec. aver.	CKS Static angle rec. range	CKS Static aver.	CKS corrosion + = yes	RT84 Advancing angle rec. range	RT84 Adv. aver.	RT84 Receding angle rec. range	RT84 Rec. aver.	RT84 Static angle rec. range	RT84 Static aver.	RT84 corrosion + = yes
0	20	100-140	130	50-90	104		88			138	15-35	33	80-120	121	+(slow)
	50		132		72		115			110		20		94	+(slow)
	100		117		47		25			98		29		88	+(slow)
0.5	20		127		88	90-110	106		30-60	56	10-25	14	25-45	29	+
	50		105		66		97			41		22		39	+
	100		115		59		96			47		16		31	+
10	20		128	10-40			116			56		17	20-55	47	+
	50		101		29		69			36				33	+
	100		116		20		59	+		36				21	+
25	20		134		91		119			51	5-20		25-35	32	+
	50		139		101		89			27		15		33	+
	100		103		34		78	+				21			+
40	20		110	35-65	41	80-100	88		30-70	67		15	30-50		+
	50		119		50		95	+		40				39	+
	100		122		57		85	+		33					+
65	20		116	10-25	19		46			102			25-45		+
	50		122		19		67			115		19		43	+
	100		61		18		37	+		49					+
	145		24				19							22	+
80	20		132		12		75		100-120	119				55	+
	50		119		8		50			107					+
	100						27	+						29	+
	165		110							109				25	+
90	20	60-100	127	5-20	8	20-60	43		50-90	68	5-20			29	+
	50		79		10		52			75		3		57	+
	100		44		12		27			71				27	+
	155		91				31			59				17	+
98	20	25-65	27		8	15-50	25		60-90	72		8		41	+
	50		22		13		24			79		2		56	+
	100		68		9		39			80		10		40	+
	165									62				0	+

For some measurements, the corrosion was too vigorous to measure contact angles and this is indicated by blank fields. The results are quite wide ranging and for ease of use, a recommended range is given.

The results are also presented graphically for the chrome coating in Figure 5.3 and for the grey cast iron in Figure 5.4. The error bars reflect the minimum and maximum values measured.
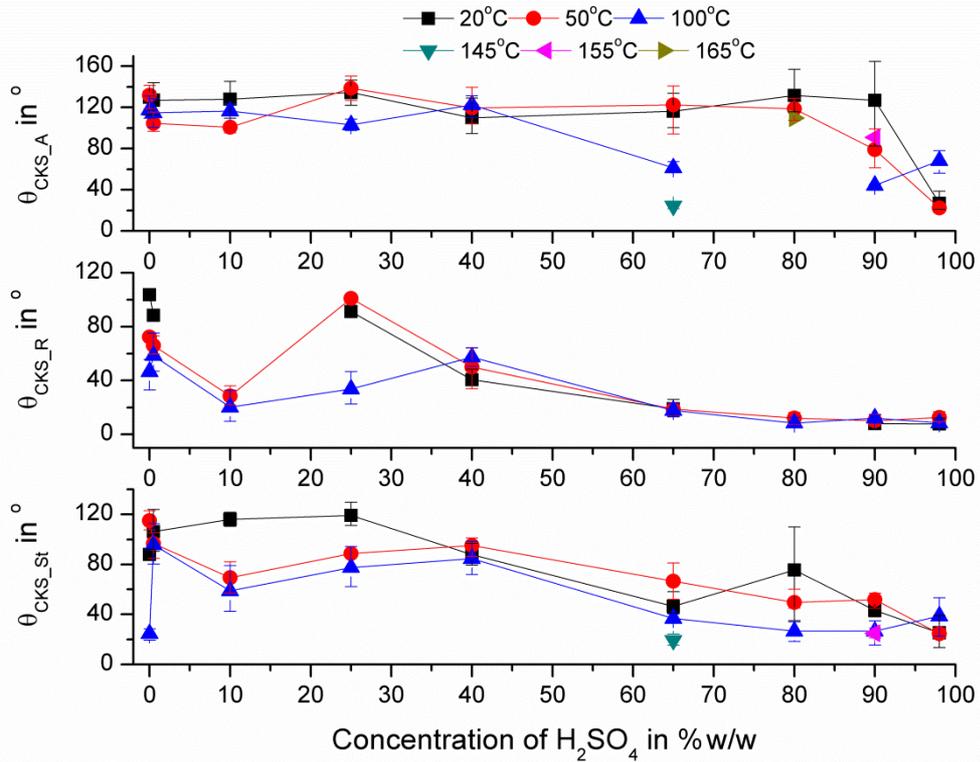
Figure 5.3: Contact angle measurement results for piston ring chrome coating, CKS, over H₂SO₄ concentration and at various temperatures

For low interfacial tension, presented in chapter 4, one would expect a low contact angle due to the weakness of the droplet skin and the influence of gravity. This thought is underlined by Young's equation (5.1) (Wang, et al., 2004). The numerator is of course unknown, but a declining denominator however should decrease the resulting contact angle.

$$cos\theta_{Young} = \frac{\sigma_{solid-liquid} - \sigma_{solid-droplet}}{\sigma_{liquid-droplet}}$$

(5.1)

However, for the chrome surface the contact angles stayed stable at a high level for most of the acid concentrations, Figure 5.3. Also for the grey cast

iron surface, no clear correlation to the interfacial tension measurements was found. Surface phenomena seem to be predominant. The effect of the metallic surface on the hydronium and surfactant balance on the liquid-liquid interface, chapter 2 and 4, influencing interfacial tension is unknown. One could imagine the ions and polar surfactants to be influenced by charges on the metal surface, thus keeping the real liquid-liquid interface stable over a large range of acid concentrations.
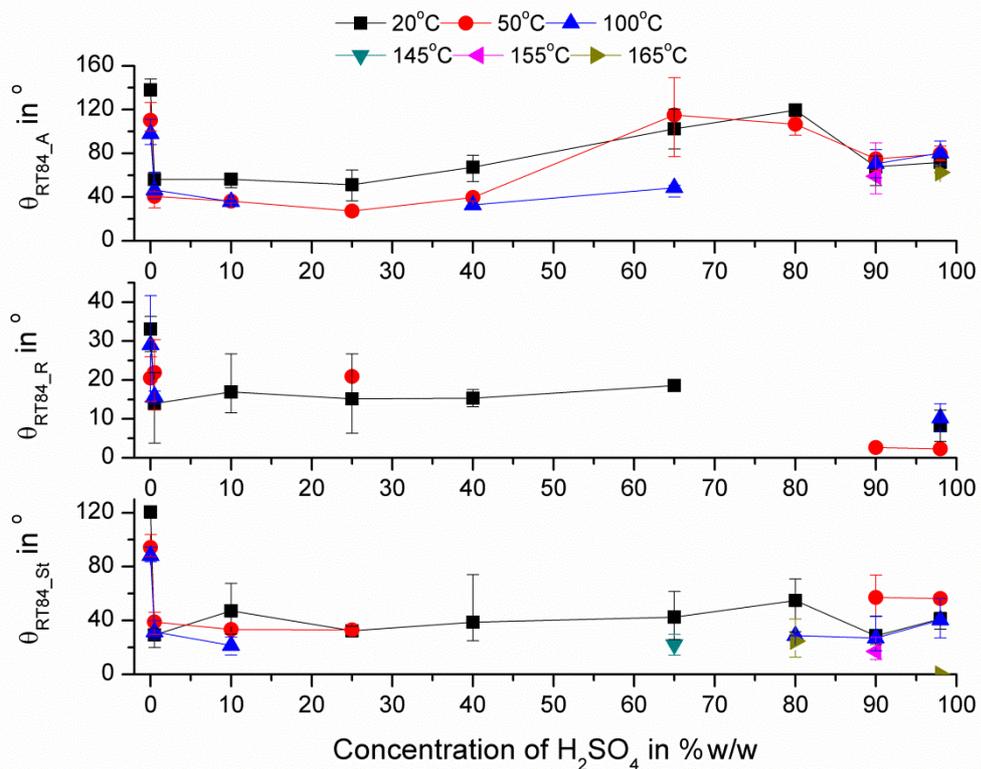
Figure 5.4: Contact angle measurement results for cylinder liner grey cast Iron, RT84, over H_2SO_4 concentration and at various temperatures

With the measured contact angles θ, the critical capillary numbers Ca for mechanical droplet displacement by flow induced shear given by (Schleizer, et al., 1999), and interfacial tension σ_{ow} shown in chapter 4, it is possible to predict where droplets will remain stable on the walls. The velocities acting on the acid droplets are given by the piston speed, oil film thickness and droplet diameter. Assuming planar parallel plates, the velocity profile in the oil film is linear and therefore the absolute shear stress is equal near both walls. Latest measurements (Saito, et al., 2010) and theoretical studies (Cantow, 2004) show good agreement in the range of minimum oil film thickness between piston ring and liner. Minimum film thicknesses at TDC

are between 2 and 5 µm and at higher piston speed reach 10 to 12 µm. Typical water droplet diameters found in engines are reported (Micali, et al., 2010) to be between 5 and 30 µm. The authors measured the droplets by light microscopy, which is not suitable for statistical reasons and after considerable shipping times of the samples from the vessel to the laboratory, which allows coagulation of the droplets. Real droplet diameters are therefore expected to be smaller.

The critical speed for droplet displacement from a wall (Schleizer, et al., 1999) calculates to:

$$U_{crit} = \frac{Ca_{crit} \cdot \sigma_{ow}}{\eta}$$

(5.2)

Table 5.2: Calculation of critical speeds for droplet displacement, after (Schleizer, et al., 1999) for 100 °C and 40 %w/w H_2SO_4 concentration

Interfacial tension in N/m	capillary number (linear interpolated)		Dynamic viscosity in Pa*s
σ_{C30H62} = 0.0248	$Ca_{crit\,CKS}$	$Ca_{crit\,RT84}$	η_{C30H62} ~0.004
$\sigma_{API\,Group\,I}$ ≈ 0.001	for θ_{CKS} ~90° 0.37	for θ_{RT84} ~15° >0.52 ~0.7	$\eta_{API\,Group\,I}$ ~0.018
Result $U_{crit\,C30H62}$	2.29 m/s	4.34 m/s	
Result $U_{crit\,API\,Gr\,I}$	0.02 m/s	0.04 m/s	

The maximum piston speed in the engine is 16 m/s, resulting in an estimated 10 µm oil film. Assuming a moving plate on stationary plate, laminar couette flow for the piston ring – liner contact, the velocity distribution in the oil film is linear. For this case and the values given in Table 5.2, the critical speed for droplet displacement is reached at a distance h from the wall surface of 1.4 µm / 12.5nm from the chrome coated piston ring and at 2.7 µm / 25nm from the grey cast iron cylinder liner wall using values for squalane and API Group I base oil respectively. The 100 times smaller values for API Group I base oil are a result of the ratio of interfacial to viscous forces. It also means higher corrosive attack on the parts is to be expected when moving to higher refined low viscosity base oils, which is a trend seen in the industry. Care must be taken to cover this deficiency of the higher refined base oil by a suitable additive formulation.

The droplets start creeping on the wall, when the shear forces on the droplet become bigger than the adhesion forces between droplet and wall. The critical shear rate, γ_{crit}, for droplet movement was presented by Mahe's approximation (Mahe, et al., 1988).

$$\gamma_{crit} \sim \frac{\sigma \cdot a_P \cdot (cos\theta_R - cos\theta_A)}{\eta \cdot a^2} \tag{5.3}$$

Assuming that a spherical droplet with diameter a forms a spherical cap on the surface with the static contact angle, θ_{st}, before shear is applied, the diameter of the contact area can be calculated by:

$$a_p = 2 \cdot \sqrt{h \cdot (a_c - h)} \tag{5.4}$$

with h, the total height of the spherical cap:

$$h = \frac{a_c}{2} - \frac{a_c}{2} \cdot cos\theta_{st} \tag{5.5}$$

and the resulting diameter of the spherical cap a_c, which has the same volume as the spherical drop with diameter a:

$$a_c = a \cdot \sqrt[3]{\frac{8}{6 \cdot (cos\theta_{st} - 1)^2 \cdot \left(1 - \frac{1 - cos\theta_{st}}{3}\right)}} \tag{5.6}$$

The contact angles θ must be entered in radians. With the total height h of the spherical cap, the minimum oil film thickness between piston ring and liner surface and the piston speed, the critical and the real shear rate can be compared to find the maximum droplet size that can adhere stably to the walls.

Table 5.3: Calculation of maximum droplet diameter and droplet height on the wall for droplet creeping under shear flow, using the approximation after (Mahe, et al., 1988) for 100 °C and 40 %w/w H_2SO_4 concentration from the contact angles, θ

	θ_{CKS_A}	θ_{CKS_R}	θ_{CKS_St}	θ_{RT84_A}	θ_{RT84_R}	θ_{RT84_St}
θ in °	122	57	85	40	15	39
h_{max_C30H62}	3.3 µm			0.51 µm		
a_{max_C30H62}	5.49 µm			1.49 µm		
h_{max_APIGrI}	27 nm			4 nm		
a_{max_APIGrI}	45 nm			13 nm		

This method is quite elegant as it does not require a capillary number from a secondary source but uses measured contact angles. For the same

conditions as above but using the measured contact angles, the results are given in Table 5.3.

Also for the droplet movement on the wall, the droplets are much smaller in API Group I base oil compared to squalane. On the cylinder liner wall, however, the droplets start to creep for smaller shear rates thus wetting a larger area. Corrosive attack on the chrome coating is therefore expected to be more localised creating pit holes while on the grey cast iron the attack is expected to be more homogeneous over an area. This conclusion seems to be confirmed by the results presented in chapter 7 where pit holes were found on the chrome coated piston ring running surface, while the grey cast iron cylinder liner showed a homogeneously worn surface.

Closer to the piston reversal points, the droplet size can become bigger due to reduced piston speeds. The maximum acid droplet size for wall adhesion in API Group I base oil becomes extremely small and for perfectly smooth surfaces corrosion would become unrealistic in midstroke. The droplets cannot become arbitrarily small due to the increase of vapour pressure, p, expressed by the Kelvin equation (Atkins, 2001):

$$p = p^* \cdot e^{\frac{2\sigma V_m}{rRT}} \qquad (5.7)$$

The smaller the droplet radius r, the bigger the increase in vapour pressure. For very small droplets, however, equation (5.7) becomes invalid due to quantum effects between the single molecules.

Droplet sizes produced in the laboratory under high shear conditions range between 0.45 and 1.05 µm, chapter 3, and are smaller than droplets found in the engine. However, surface roughness is in the range of micrometres and droplets are likely to get trapped first in machining marks, a result which seems to be confirmed by findings presented in chapter 7, where corrosion was found on a piston ring surface in the valleys of machining marks.

The above approximation illustrates that small acid droplets can be picked up and transported by the piston ring. In non-wetted, unsheared areas of the piston ring profile, the droplets may become bigger. For piston rings with asymmetric barrel shaped profiles, typically of axial piston ring heights of 20 to 24 mm in marine engines, one would expect to find acidic attack on the upper half of the ring profile.

Gas velocities in the piston ring gap are much higher than the piston speed. However, the gas temperatures are well above the boiling point of sulphuric acid for the top ring and in addition the influenced surface area is very small

compared to the main circumference of the piston ring. Therefore the piston ring gap is not included in this consideration.

5.3 Results and Discussion: Light Microscopy on Used Surfaces

After taking the contact angle measurements, the sample surfaces were examined under the light microscope. The resting times of the acid droplets on the surface are considerably longer than needed for the contact angle measurements. Which means the state of the surfaces shown below is not the state of the surfaces during the contact angle measurements.
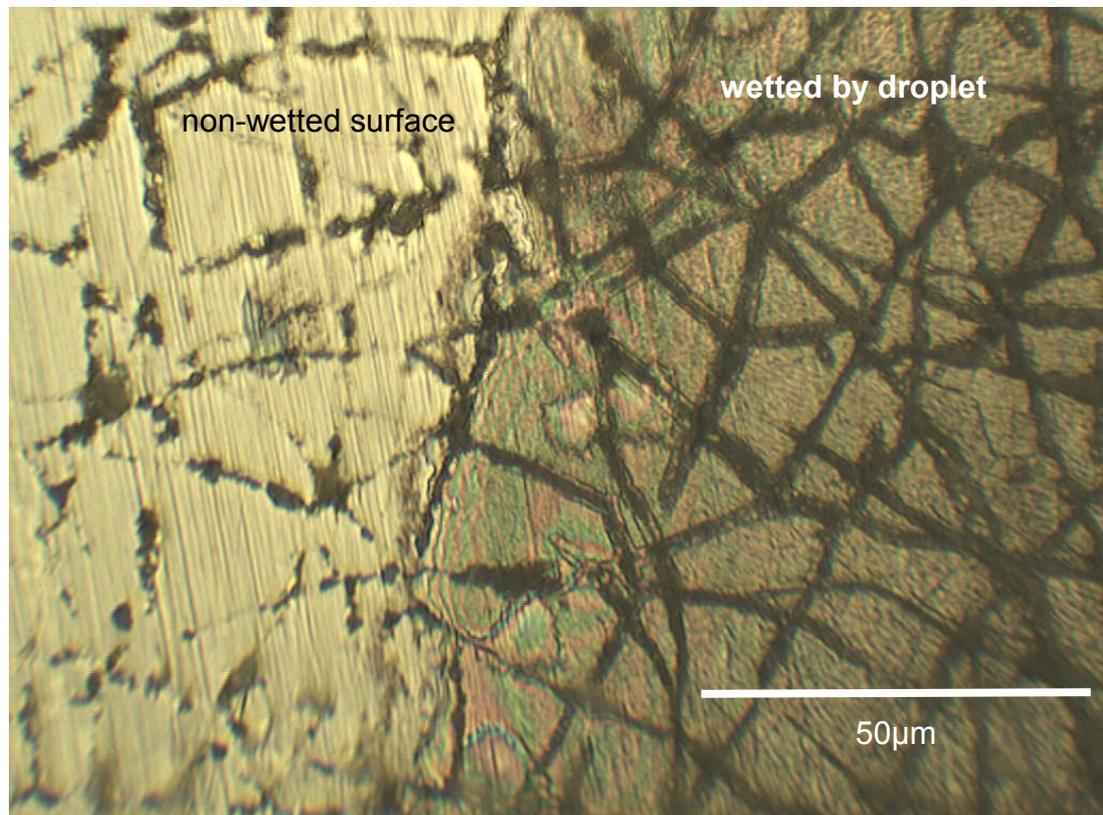
Figure 5.5: 500x enlargement of CKS coating in contact with 25 %w/w H$_2$SO$_4$ at 100 °C

The corrosion products on the chrome coated piston ring samples had a dark green colour and were soluble in water. Therefore, they are believed to be chromium(III)-sulphate pentahydrate Cr$_2$(SO$_4$)$_3$·5H$_2$O following the reaction Cr$_2$O$_3$+3H$_2$SO$_4$→Cr$_2$(SO$_4$)$_3$+3H$_2$O (Burstein, et al., 1994). A separate test was done on a untreated and dry piston ring surface to ensure that corrosion is not enhanced by the pre-treatment or reaction of acid with

the oil. No differences were found and corrosion took place for acid concentrations as low as 10 % at elevated temperatures.

Corrosion on the galvanic chrome coating started from the surface as well as in the crack network. Figure 5.5 shows the former border of a 25 %w/w H_2SO_4 droplet at 100 °C, with un-corroded surface to the left.

Corrosion of the cylinder liner surface with pure water droplets was very mild, without gas release and showed the typical appearance of the Ewan's water drop experiment, Figure 5.6. The centre of the drop depletes of oxygen due to initial oxidation of the iron surface and becomes anodic. The outer volume of the drop near the water – oil interface stays rich in oxygen due to refreshment by the dissolved air in the oil and the outer volume becomes cathodic. These differences in potential cause corrosive attack. The corrosive attack was very localised within the droplet as can be seen from the black holes in the microscopic view in Figure 5.7, a typical example for 'pitting corrosion' within a continuous aqueous phase.

Corrosion initiated by sulphuric acid (0.5 – 98 %) on grey cast iron at low temperatures starts in the pearlitic matrix where it borders the carbides/phosphides. This is nicely illustrated by Figure 5.8 where corrosion is limited to the borders of the hard phases. The hard phases are not attacked at all and most probably have a higher electric potential, which increases corrosive attack on their borders towards the pearlitic matrix. Further away from the hard phases, the pearlitic matrix shows hardly any corrosive attack.

From the form of corrosion on the grey cast iron cylinder liner, conclusions can be drawn on the concentration of sulphuric acid. Protruding hard phase is correlated with attack by dilute sulphuric acid, while corroded hard phase is correlated with concentrated sulphuric acid (Demmerle, et al., 2001). This however is only half of the truth. The very same acid concentration will react differently on the different phases of the grey cast iron in the hot top dead centre, mid-stroke and bottom dead centre. This is illustrated by Figure 5.9 and Figure 5.10.

Both surfaces were exposed to a droplet of 65 %w/w H_2SO_4 but at different temperatures of 20 and 145 °C. At 20 °C again the corrosive attack towards the pearlitic matrix next to the hard phase is quite apparent and also slight attack on the iron phosphide is visible, while the iron carbide is not attacked at all. At 145 °C, the pearlitic matrix is homogeneously attacked or passivated while the hard phase shows considerable attack also on the iron

carbides. The borders of the hard phase seem to be protected from corrosion.
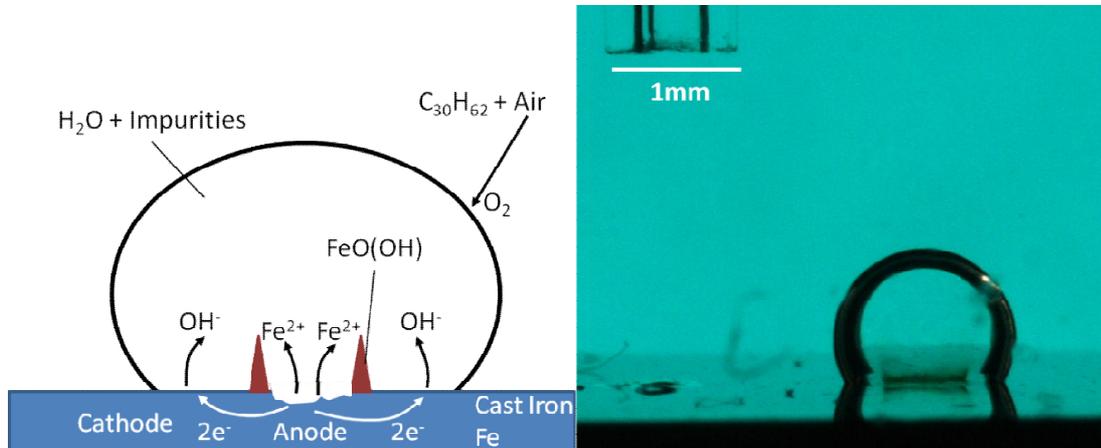
Figure 5.6: Observation of corrosion on grey cast iron with pure water and the correlation to Ewan's water drop experiment (Schreiter, 2010)
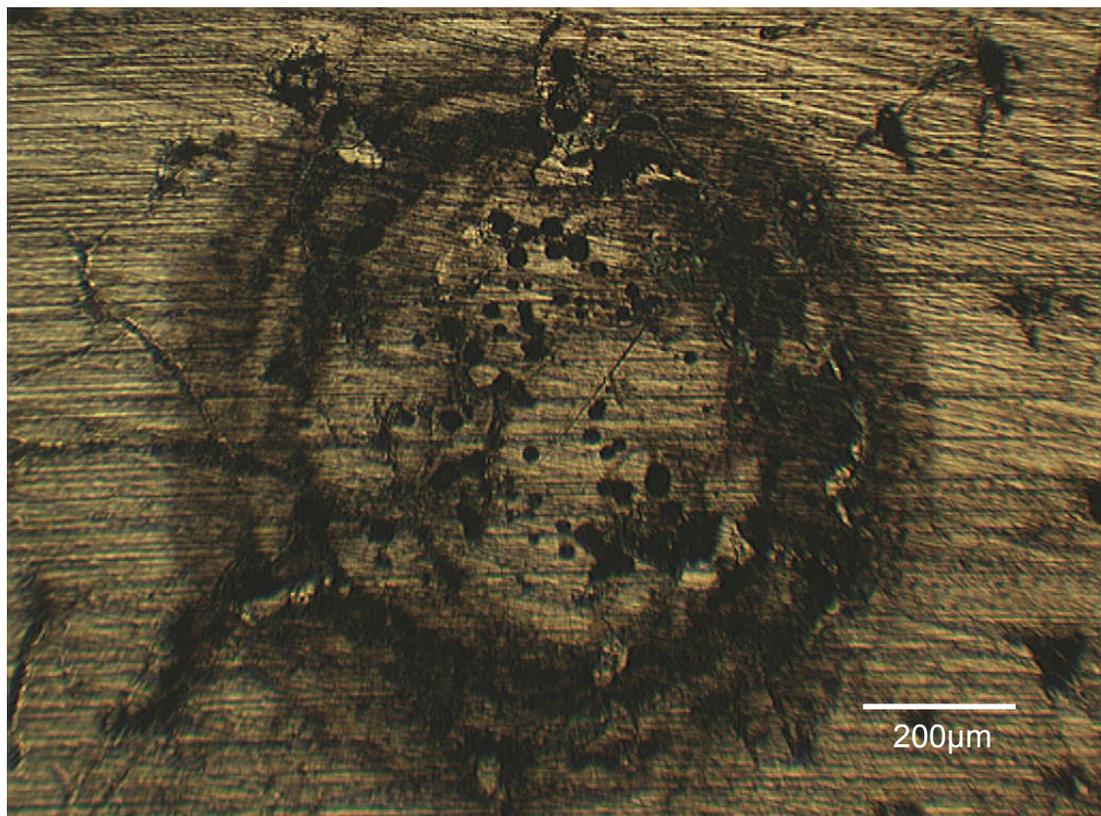
Figure 5.7: Corrosive attack on grey cast iron after contact angle measurements with pure water at 20 °C
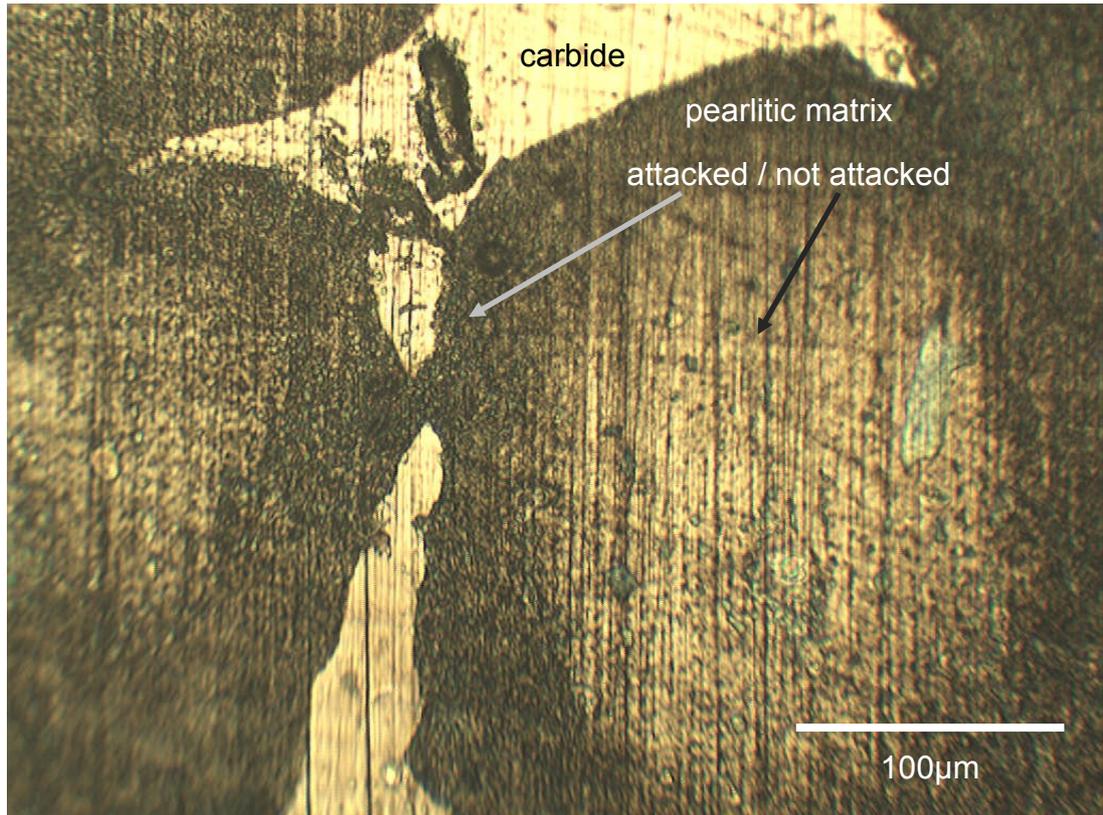
Figure 5.8: Corrosive attack on grey cast iron after contact angle measurements with 25 %w/w H_2SO_4 at 20 °C
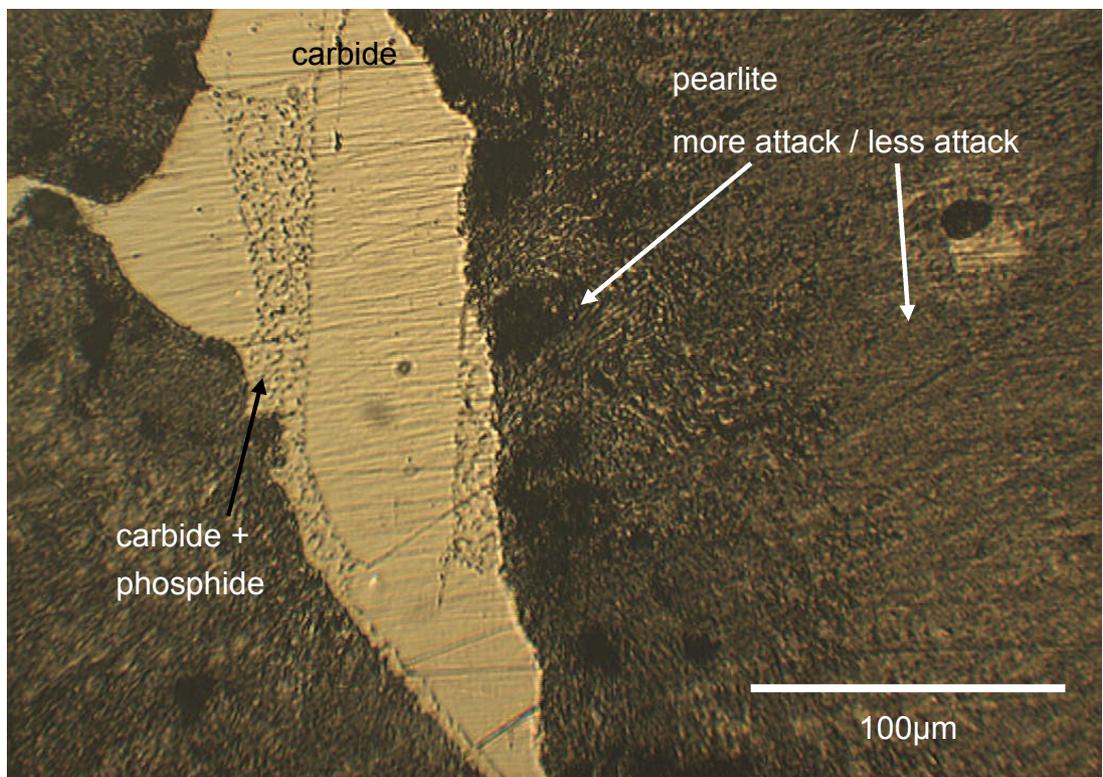
Figure 5.9: Corrosive attack on grey cast iron after contact angle measurements with 65 %w/w H_2SO_4 at 20 °C
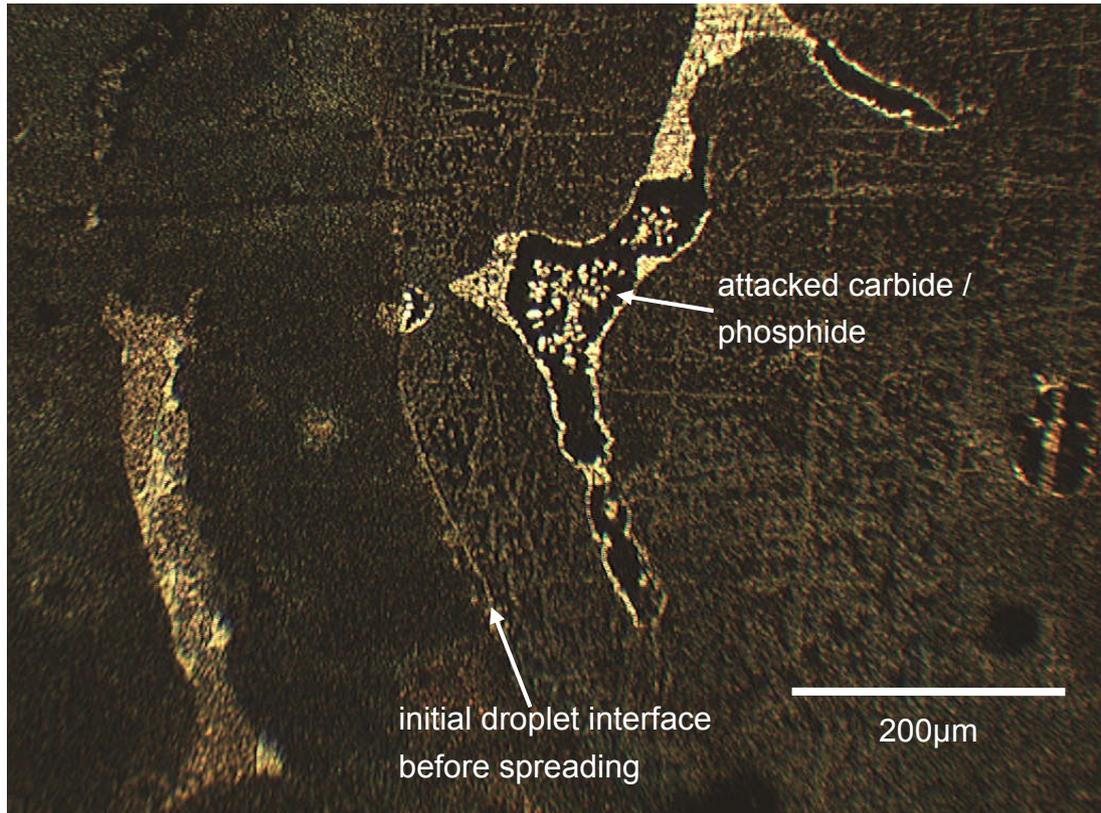
Figure 5.10: Corrosive attack on grey cast iron after contact angle measurements with 65 %w/w H_2SO_4 at 145 °C

5.4   Conclusions of the Contact Angle Measurements

Contact angles between various concentrations of sulphuric acid were measured by a custom built arrangement between 20 and 165 °C on a piston ring chrome coating and grey cast iron cylinder liner material, submerged in squalane.

The contact angles were found to be larger for the chrome coating. Acid concentration showed a major influence on grey cast iron between pure water and the smallest concentrations of sulphuric acid and on chrome for the highest concentration. Temperature only showed a major influence for pure water where contact angles were decreased by increasing temperature. For water, the interfacial tension towards squalane declines with increasing temperature, chapter 4, which should increase contact angles according equation (5.1). This finding indicates a modification of the surface energy by the aqueous phase. The solid surface energy seems to have a higher influence on the contact angle than the interfacial tension between droplet and surrounding liquid phase.

No obvious correlation between the interfacial tension measurements, shown in chapter 4, and the contact angle measurements were found.

However, interfacial tension together with viscosity of the surrounding phase significantly contributes to droplet displacement. The bigger the contact angle, the smaller the interfacial tension and the higher the viscosity of the surrounding phase, the lower the shear velocity needed to displace a droplet from the wall. Therefore higher corrosion rates are to be expected when moving to higher refined low viscosity base oils, which is a trend seen in industry. The critical shear rates to move a droplet on the wall were found to be lower for grey cast iron and a more localised corrosive attack is expected on the piston ring chrome coating compared to the grey cast iron cylinder liner surface. This conclusion seems to be confirmed by findings presented in chapter 7.

The contact angle measurements indicate that droplets adhering to the moving chrome coated piston ring will be more easily displaced and will have to be smaller than droplets on the stationary grey cast iron cylinder liner under the same shearing conditions.

For temperatures at ~95 °C, chrome was found to be not corrosion resistant down to acid concentrations of 10 %w/w. The advancing contact angle of acid to chrome under oiled conditions however was found to be very large, therefore only small droplets will attach to a moving piston ring. The receding angles are quite small so it is likely that an attached droplet will stay on the piston ring. Due to the large contact angles between acid and chrome, the oil will preferentially enter the crack network in favour of the acid. It is important to note, that only a small portion of the piston ring running surface is under the influence of shear by the oil film and corrosion is expected to be higher in non sheared areas.

In comparison to the piston ring chrome coating, the contact angles between acid and grey cast iron are quite small, therefore the droplets will easily attach to the liner and will stay on the liner. They are likely to spread on the surface and de-oil it. Depending upon concentration and temperature, the acid will preferentially attack the pearlitic matrix or the hard phase. In either case, corrosion will start on the edge of the hard phase towards the pearlite. The large size of the hard phase increases this effect due to increased potential difference.

The in-homogeneity of the used cylinder liner material and the large crack-network on the piston ring material did not show any influence on the contact angle measurements. Also the preparation by polishing was fine enough to eliminate spreading of the droplet in the direction of the machining marks.

The following chapter 6 and 7 shows experiments on a friction test bed with a chromium coated piston ring running against a grey cast iron cylinder liner. Corrosion was found to be more prone in the valleys of machining marks on the running surface of a piston ring, creating pit holes.

Also shown in chapter 7 is the development of surface chemistry and topography during the frictional tests. In the present chapter, the contact angles were measured on polished surfaces. The influence of changes in surface chemistry is pointed out, however, a drawback of the contact angle measurements is the use of surfaces without a frictional induced boundary film, a so called 'tribofilm'.

Chapter 6
Influence of Aqueous Sulphuric Acid on Tribological Parameters in a Piston Ring – Cylinder Liner Bench Test: Method Development

The API Group I base oil SN600 was used as a lubricant in a piston ring on cylinder liner bench test. Aqueous sulphuric acid of various concentrations was dispersed in the oil in constant volumetric quantities. The lubricant was fed very close to the piston ring in small quantities, similar to real engine feed rates. The aim was to find the influence of acid concentration and temperature on friction, surface and lubricant chemistry.

Instead of using real marine Diesel engine materials, more readily available automotive parts of similar material configuration were used. This way, the negative influence of the material was excluded and the study concentrated on the lubricant. Differences of the marine Diesel engine to the materials used in the test bench are given. Previous research was done with the same part configuration and test machine, which makes the study comparable to the work of others.

Specialities of the test bench and the parts in contact are given in detail.

Chemical analysis of the lubricant was undertaken using FTIR-ATR.

An indirect in-situ measure for surface chemistry is the measurement of friction force and the very sensitive measurement of contact potential differences by the Lunn-Furey circuit. After the tests, the cylinder liner samples were analysed by FTIR-Microscope and XPS.

The wear on the test specimens and developed surface topography was analysed using a white light interferometer and a light microscope. The tests required changes to conditions during running, which gives only a few wear measurements statistical relevance. However, a trend can be seen.

The complexity of the arrangement, influencing parameters and large variety of analysis techniques required the presentation of the study in two parts. The present part develops the methods used and in the following chapter, the results are presented and conclusions drawn.

After learning much about the lubricant and its interaction with sulphuric acid and in combination with engine surfaces, the following is the closest to the practical application in this study.

6.1 Materials Used in the Bench Test

A piston ring – cylinder liner contact was chosen for the study to force dispersed acid droplets into the contact zone.

The piston rings were segments of a chrome coated automotive piston ring for a 86 mm cylinder liner bore diameter. Only the 25 mm sections next to the ring ends were used as their special shape, which in the engine compensates for circumferential temperature gradients, would fit best to the used cylinder liner. Their radius was found to be 43.34 mm with a profile of 10.56 mm radius, which is offset by 0.1 mm towards the top side of the piston ring from its centre.

 The cylinder liner were segments of a SJ4213 Jaguar/Daimler automotive cylinder liner with a bore diameter of 90 mm. Their radius was found to be 45.47 mm.

The parts were chosen from automotive applications for their ease of acquisition and the readily available holders for the bench test machine. Table 6.1 and Table 6.2 give a direct comparison of marine versus automotive top piston ring and cylinder liner. The values were requested from the companies Federal Mogul Goetze and Wärtsilä. Despite the difference in size also the base material shows some differences, while the surface machining and finishing is very similar. In the following, the used automotive parts are compared to parts from a typical marine application.

Table 6.1: Comparison of marine vs. automotive top piston ring

TOP PISTON RING:	Marine:	Automotive:
Manufacturer	FM Goetze	FM Goetze
Base Material	GOE50A, vermicular cast iron	GOE32, grey cast iron, alloyed, heat-treated
Young's Module	$>150*10^3$ N/mm^2	$130 – 160*10^3$ N/mm^2
Hardness	110 – 113 HRB	109 – 116 HRB
Coating	CKS 37 (chrome + Al$_2$O$_3$ particles)	chrome
Surface Finish	Ra max 0.4 µm (lapped)	Ra = 0.075 µm (measured)
Ring Height	20 mm	1.5 mm
Profile Radius	~950 mm	10.5 mm

Table 6.2: Comparison of marine vs. automotive cylinder liner

CYLINDER LINER	Marine:		Automotive:	
Manufacturer	Various		AE (FM Goetze)	
Material	lamellar grey cast iron		lamellar grey cast iron	
Tensile Strength	≥230 MPa		207 MPa	
Hardness	180 – 230 HBS 10/3000		230 – 300 HBS 10/3000	
Chemical Composition	C	1.3 %	C	3.0 - 3.4 %
	Si	1 %	Si	1.8 – 3 %
	Mn	0.5 %	Mn	0.7 – 1.2 %
	P	0.25 %	P	0.5 – 1 %
	S	≤ 0.06 %	S	≤ 0.12 %
	Cu	1.4 %	Cr	0.35 – 1 %
	V	≤ 0.15 %		
	B	0.02 %		
Surface Finish	Cross-hatch plateau honing ~45 – 60°		Cross-hatch plateau honing 45 – 60°	
	Ra	≤ 1.0 µm	Ra	= 0.46 µm
	Rk	< 0.5 - 1.3 µm	Rk	= 1.4 µm
	Rpk	< 0.3 µm	Rpk	= 0.42 µm
	Rvk	= 1 – 4 µm	Rvk	= 0.7 µm

Figure 6.1 - Figure 6.4 show a direct comparison of grey cast cylinder liner material as used in large 2-stroke marine Diesel engines and in the automotive Jaguar engine, used in this test. Quite apparent is the 10 – 20 times more coarse grain structure of the marine Diesel material compared to the automotive material. In the marine Diesel material, big eutectic carbides in the hard phases and free iron around the graphite lamellas are present which is not the case for the automotive material.
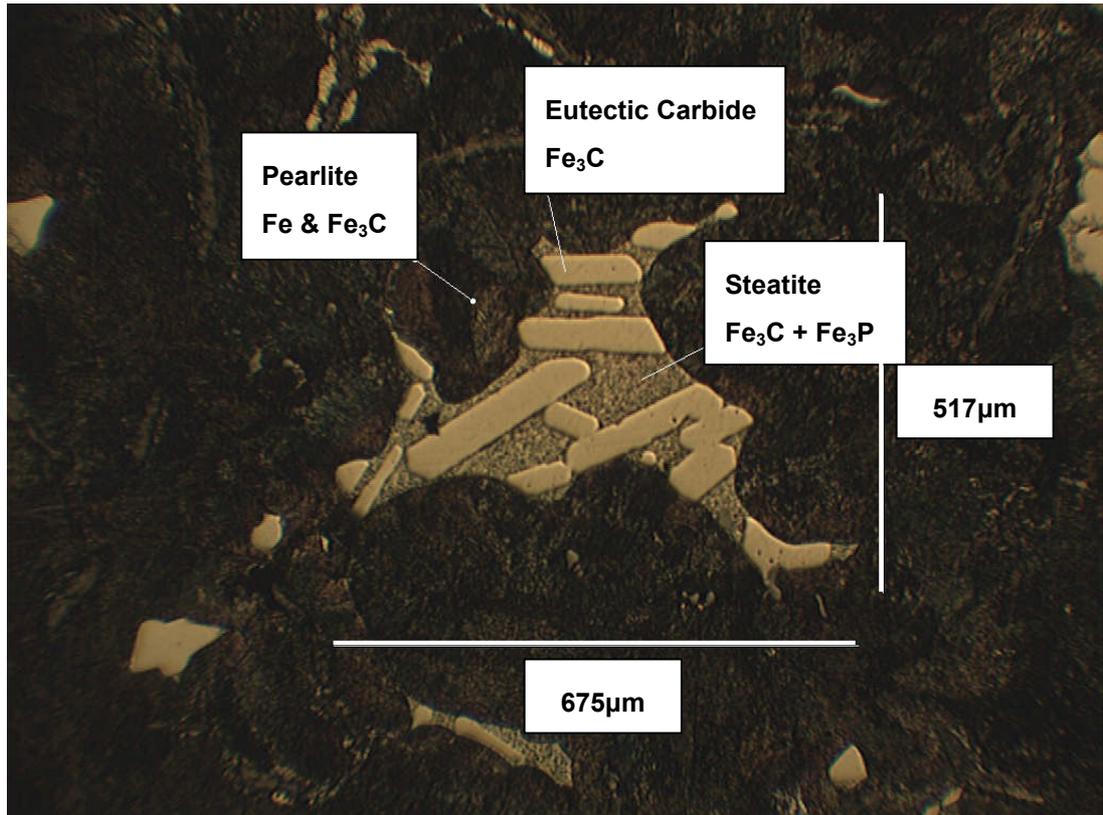
Figure 6.1: Hard phase of a marine cylinder liner grey cast iron
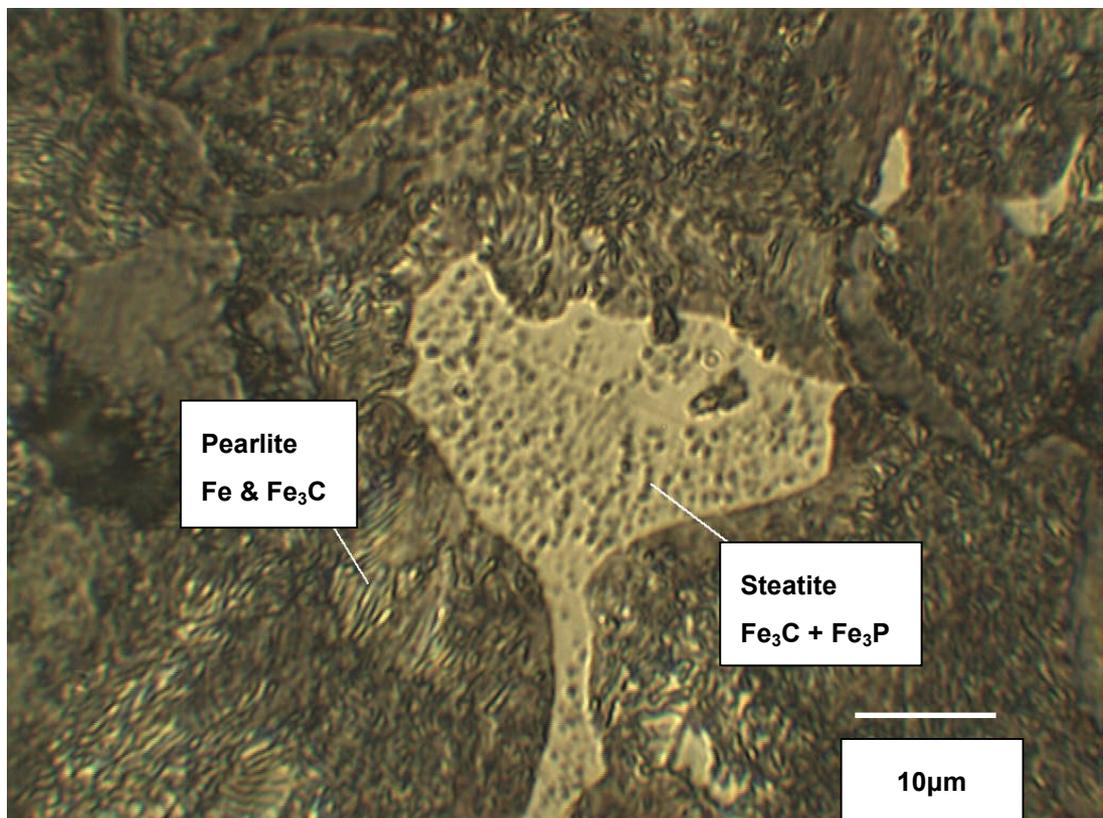
Figure 6.2: Hard phase of a grey cast iron automotive cylinder liner as used in this study
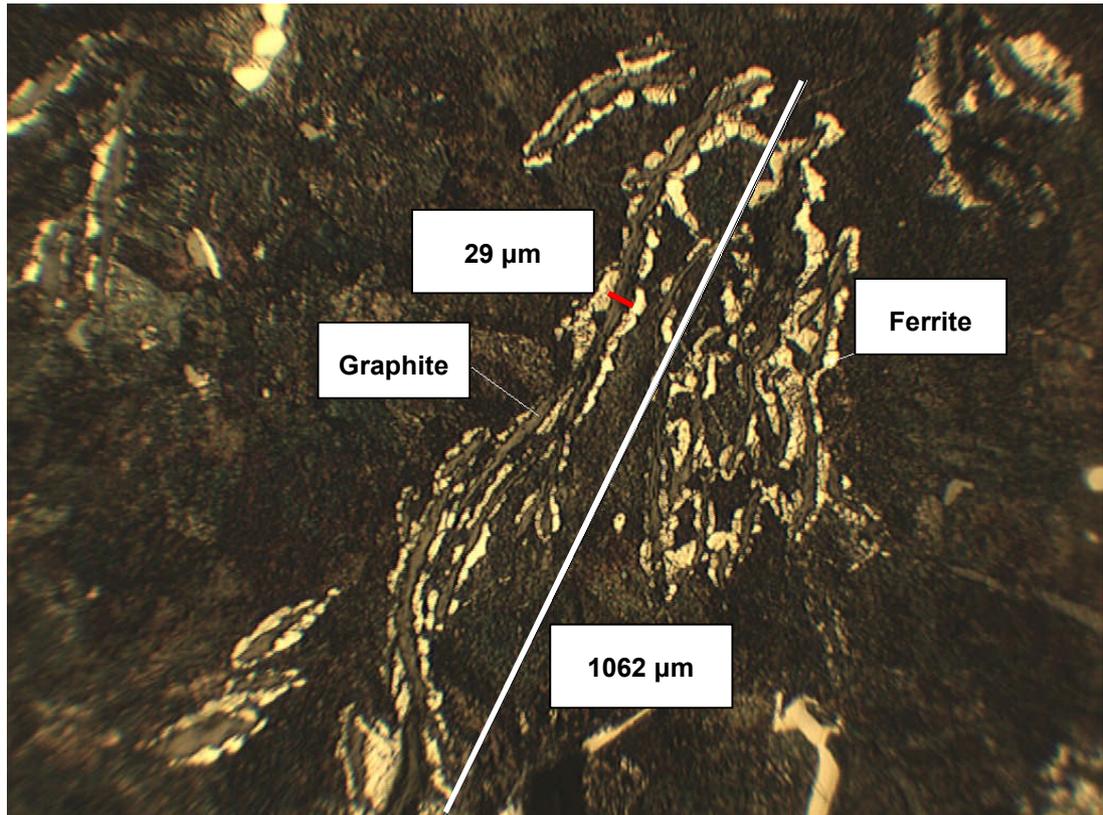
Figure 6.3: Graphite lamella of a grey cast iron marine cylinder liner
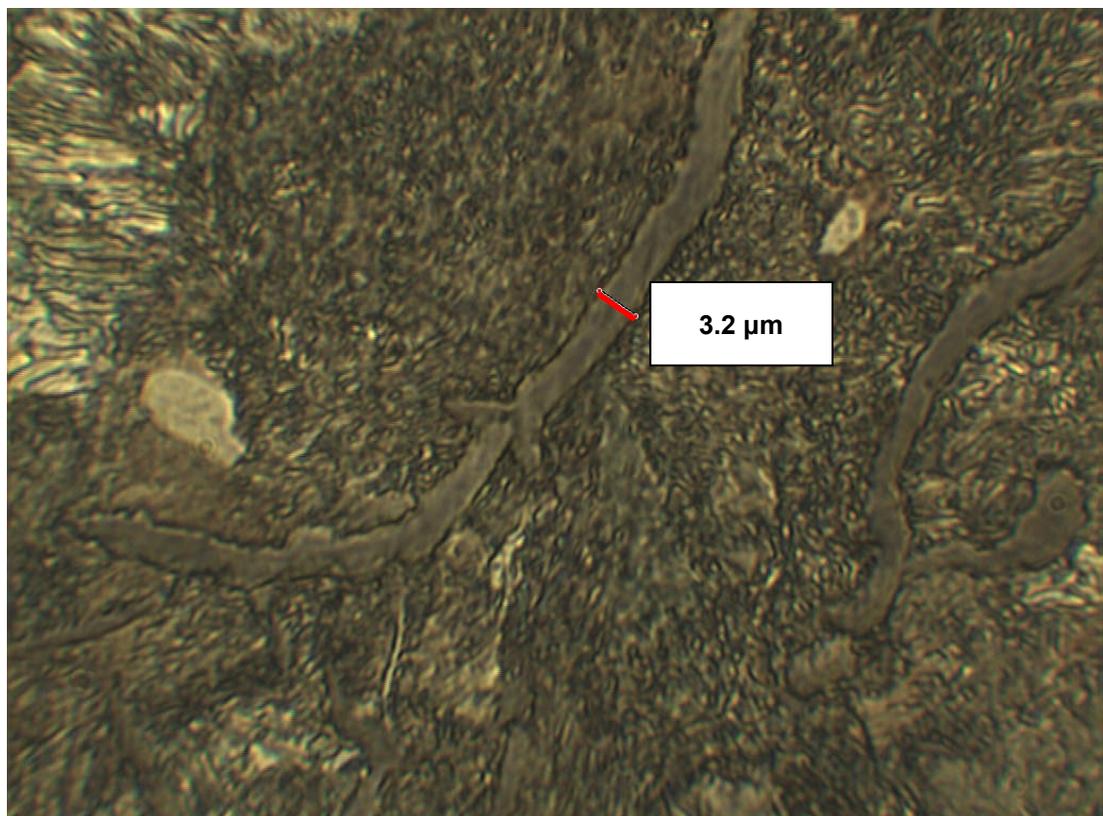
Figure 6.4: Graphite lamella of a grey cast iron automotive cylinder liner as used in this study
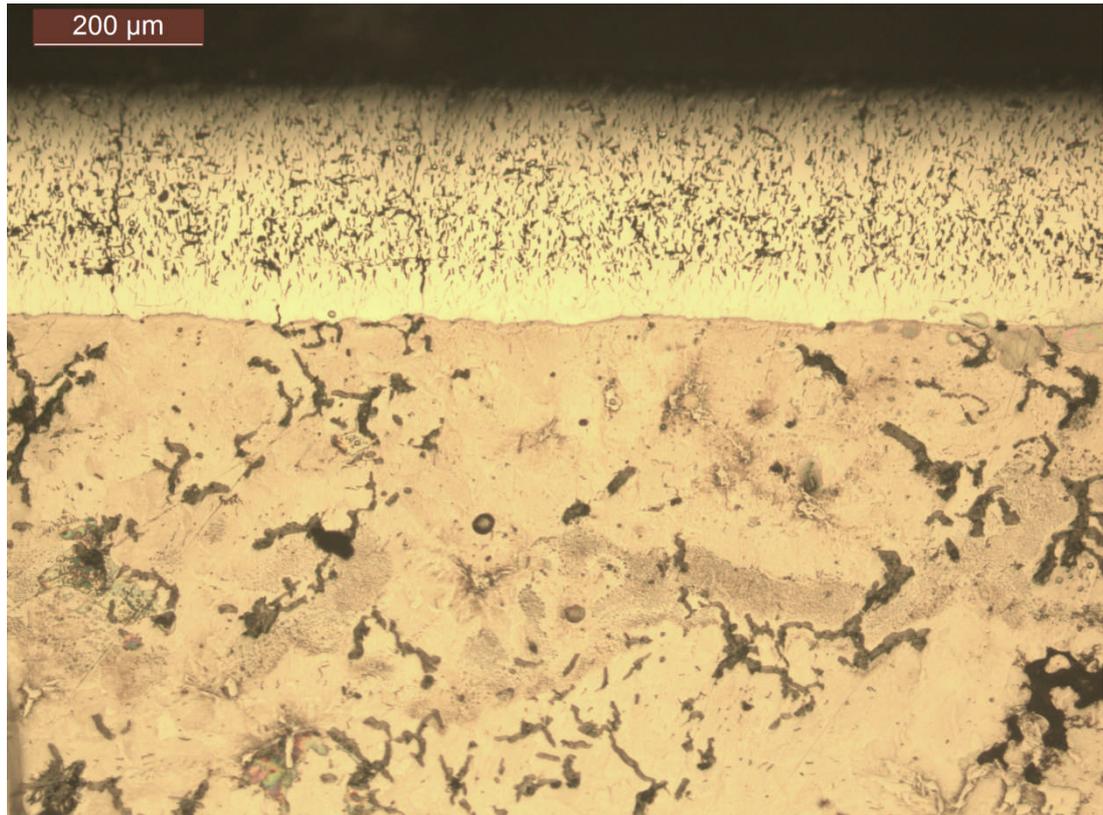
Figure 6.5: Chrome (CKS) coating and base material of a marine piston ring
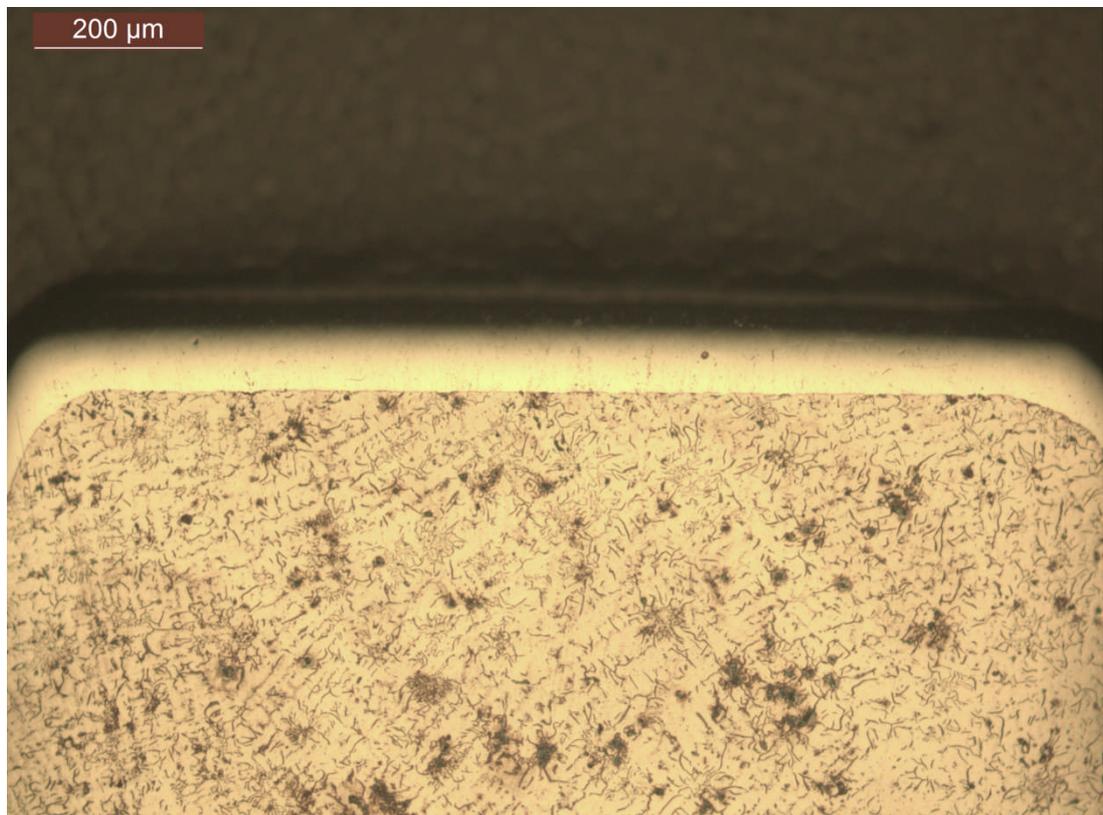
Figure 6.6: Chrome coating and base material of a automotive piston ring as used in this study

Figure 6.5 and Figure 6.6 show a direct comparison of chrome coated grey cast piston ring material as used in large 2-stroke marine Diesel engines and in the automotive gasoline 'Hydra' engine, which was used in this test. Quite apparent is the thicker chromium coating on the marine piston ring of ~0.27 mm compared to the automotive coating of only 0.08 mm thickness. The marine coating is built up of a thin binding layer of pure chromium on the cast iron, followed by a aluminium oxide particle reinforced chromium layer. The particles are embedded in the crack-network of the chromium layer which appears dark in Figure 6.5. The centrifugal cast automotive base material shows also a significant finer structure than the sand cast marine material.

From the illustrated differences, one could argue that the study is not relevant for materials used in marine Diesel engines. On the other hand, all potential tribological anomalies, especially of the cylinder liner material, like free ferrite and big eutectic carbides which can breake and fall out, were removed from the study. This puts greater emphasis on the properties of the lubricant.

For the lubrication of the piston ring – cylinder contact, the following substances were used: API Group I base oil SN600 (Chevron) and sulphuric acid (> 95 %w/w Fisher Scientific UK Ltd. analytical reagent grade). Lower concentrations of sulphuric acid were made with deionised water by weighing. Two fully formulated marine lubricants, A & B (Chevron and Shell), with a alkaline reserve of 70 mgKOH/g were chosen as typical and well known representatives. They are a blend of API Group I base oils and an unknown additive package which performance was tested in chapter 3 and most likely consists of calcium carbonate as acid neutralising agent and dispersants as described in chapter 2. For tests with sulphuric acid, 1.3 %v/v of the acid was dispersed in SN600 in an ultra-sonic bath. The physical properties of the substances are given in Table 6.3 and, in greater detail, in appendix A. For orientation it can be said that the base oil SN600 ranges between viscosity class SAE30 – 40 while lubricant A & B exceed SAE50 (Tomanik, 2008). The acidic and the over based lubricant were always fed from one distinct side of the piston ring, which is typical for the situation in the engine and allowed simultaneous or selective feeding of the lubricant without interruption of the test. The feed rate was adjusted accordingly to keep the flow rate constant throughout the test series.

Table 6.3: Physical properties of the liquids used

Name	Viscosity in Pa*s at 40 and 100 °C		Density in kg/m³
SN600	0.1	0.0103	886 (15 °C)
Lubricant A + B	0.11	0.011	930 (15 °C)
70 %w/w H_2SO_4	0.0015	-	1606 (25 °C)

A justification for the use of API Group I base oil and aqueous sulphuric acid can be found in chapter 3. The fully formulated marine lubricants are defined closer and compared in chapter 3.

6.2   Method: The TE77 Reciprocating Friction Testing Machine

6.2.1 General Setup of the TE77

Figure 6.7 shows an overview of the TE77 Reciprocating Friction Testing Machine (Phoenix Tribology Ltd.). Point 'A' is a spring loaded balance to apply a normal force over cross beam 'G' to the piston ring holder 'H'. The piston ring holder 'H' is also shown in Figure 6.8 where point 'D' shows the roller which allows the piston ring holder to reciprocate below the cross beam. The normal force is transmitted from the roller 'D' through two 3mm pins 'C' to the back of piston ring segment 'A'.
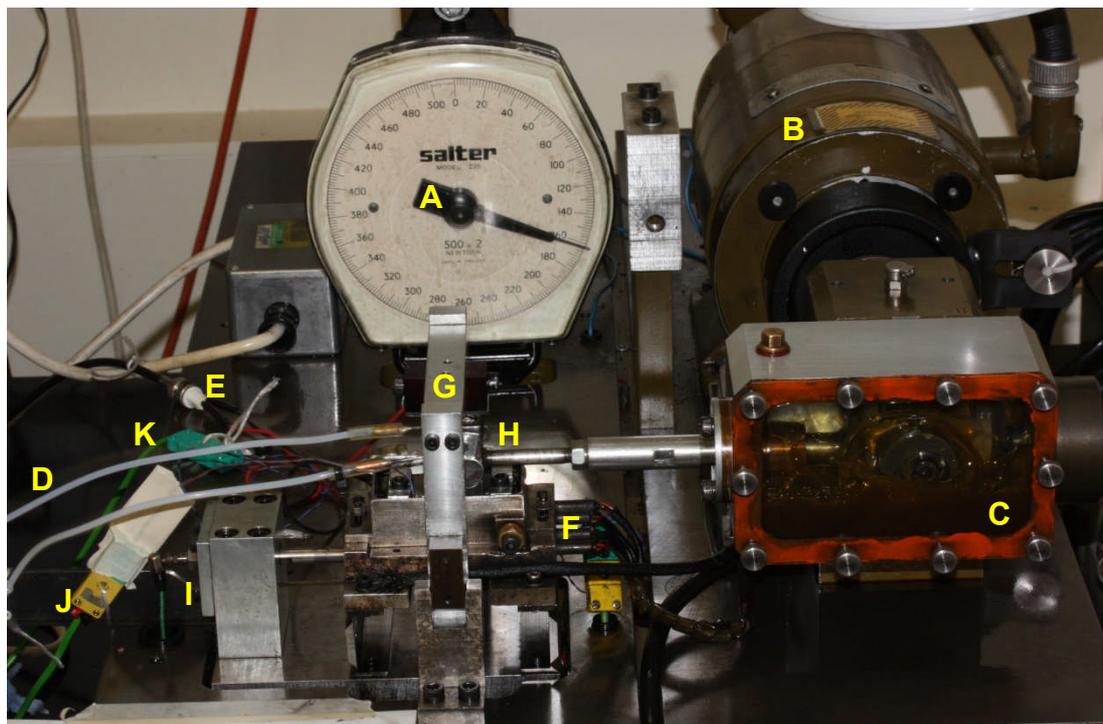
Figure 6.7: Overview of the TE77 friction testing machine

The piston ring segment 'A' slides against the cylinder liner sample, Figure 6.10, which is fitted on the temperature controlled holder 'F', Figure 6.7. The lubricant is supplied to the piston ring - cylinder liner contact from two syringe pumps (Aladdin, World Precision Instruments, Inc.) through flexible PTFE tubes 'D', Figure 6.7, to the front (TDC) or back (BDC) of the piston ring, point 'B', Figure 6.8. Top dead centre, TDC, and bottom dead centre, BDC, corresponds to the orientation of the piston ring side faces in the engine. A block diagram of the arrangement is given in Figure 6.9.
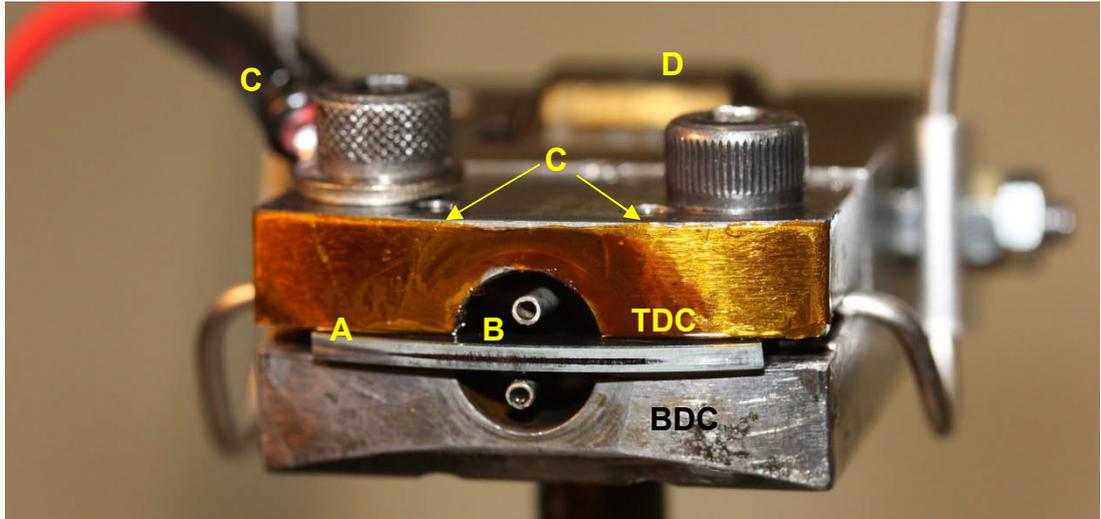
Figure 6.8: Piston ring holder of the TE77
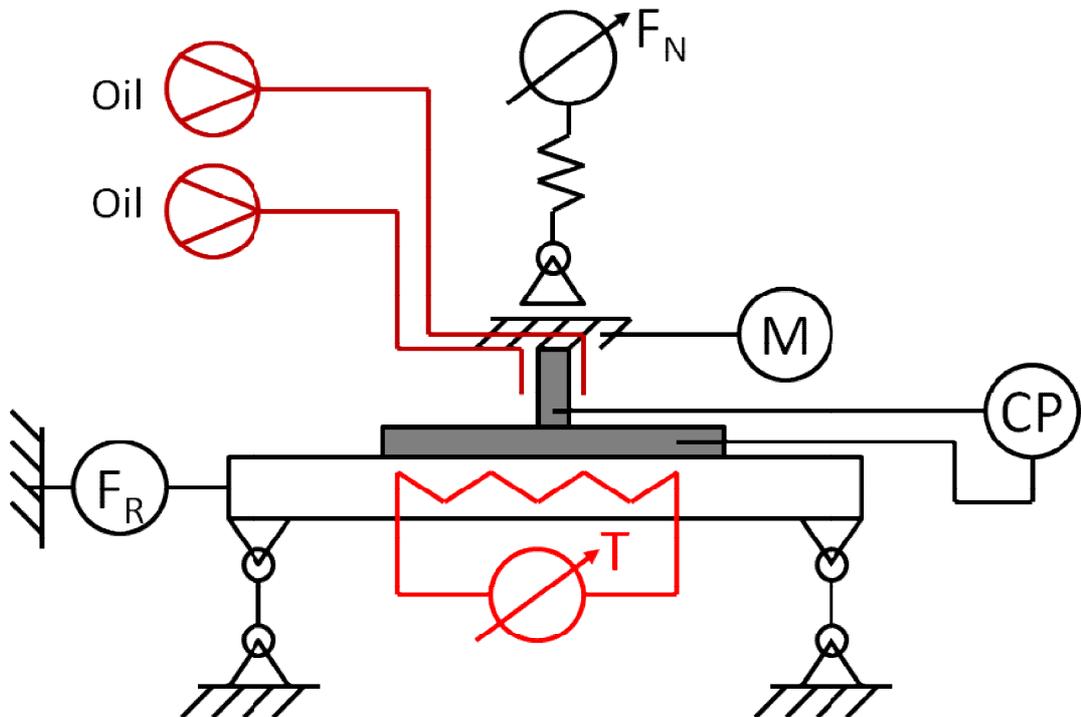
Figure 6.9: Block diagram of the TE77 friction testing machine

Before each test, the piston ring and cylinder liner had to be aligned. To check for proper alignment, the cylinder liner was painted with a black ink pen (Staedtler Lumocolor 317 permanent M) and the piston ring slid over by driving the motor shaft by hand. Proper symmetrical removal of the colour indicated good alignment, Figure 6.10. Residual colour was removed from piston ring and cylinder liner using isopropanol.
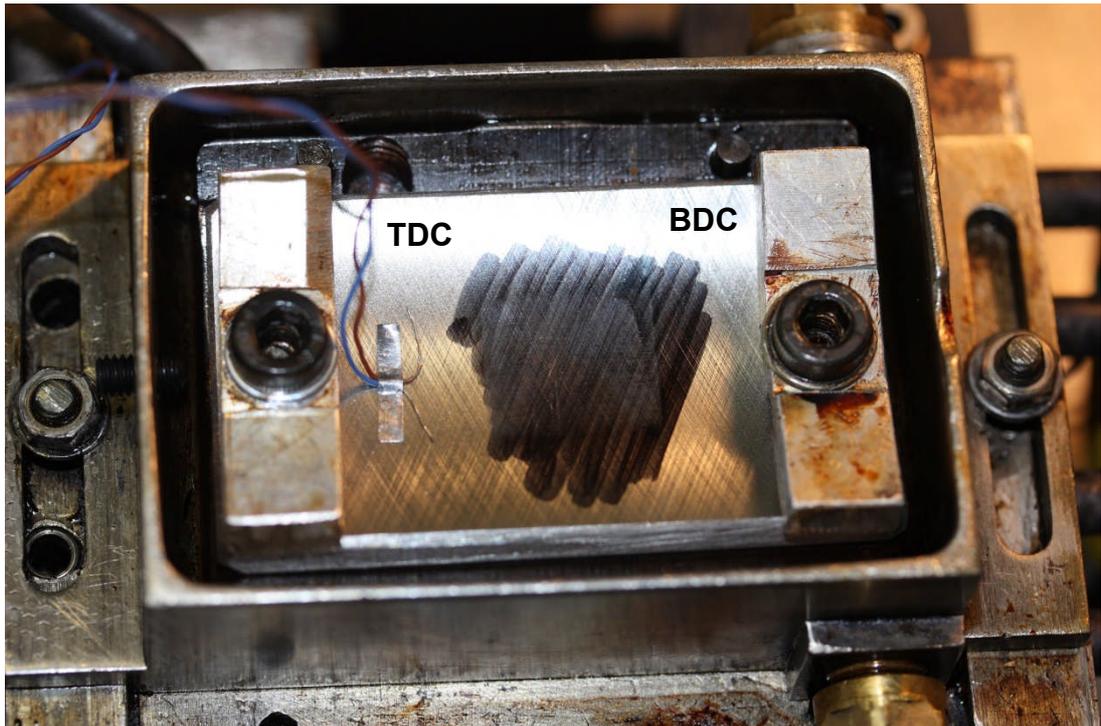
Figure 6.10: Cylinder liner sample with spot welded K-type thermocouple after the alignment check

6.2.2 Temperature Monitoring and Control on the TE77

The temperature of piston ring and cylinder liner sample was measured through K-type thermocouples which were spot welded to the running surface of the cylinder liner, Figure 6.10, and the flank of the piston ring. The cables were secured by spot welded shim metal lashes. The technique was compared to traditionally welded K-type thermocouples, up to 100 °C with a mercury filled thermometer. Correlation was found to be within 1 °C up to 230 °C which was achieved by placing the sensors in a oven. Figure 6.11 shows a correlation between set point temperature on the temperature control unit and the resulting ring and liner temperature on a lubricated and running TE77 with 160 N normal force applied. Figure 6.7, shows the temperature sensor cables for piston ring 'J' and 'K' for the cylinder liner.
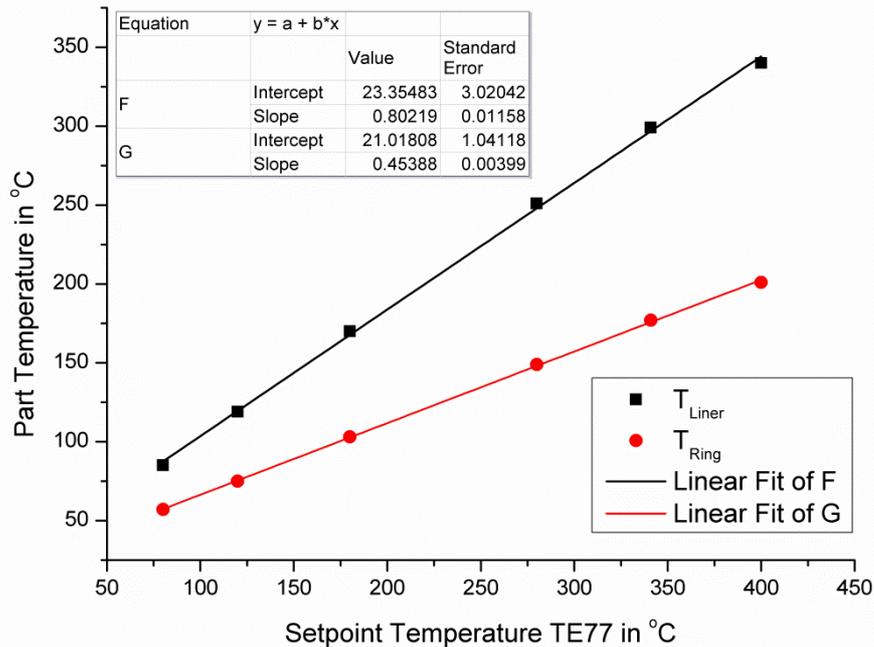
Figure 6.11: Correlation of temperature control set point to piston ring and cylinder liner temperature in the running TE77 friction testing machine

6.2.3 Electrical Resistance of the Contact Zone on the TE77

The resistance of the contact zone between the electrical isolated cylinder liner and piston ring was measured by a Lunn-Furey Contact Potential Circuit, CP, (Braunovic, et al., 2007),(Plint, 2005). The measurement wires can be seen in Figure 6.7 point 'E' and fixed to the piston ring holder, Figure 6.8 point 'C'. The correlation between the measured contact potential and electrical resistance is shown in Figure 6.12. Resistance was applied by a resistor switch box. The lower the metallic contact in the contact zone, the higher the measured contact potential difference. Electric isolators in the contact zone can be an oil film, deposits, boundary surface films or oxide layers.

From the law of electrical resistivity (Tipler, 1998) the area of a wire with given length l, known electrical resistivity ρ and resistance R can be calculated.

$$A = \frac{l \cdot \rho}{R} \qquad (6.1)$$

The electric resistivity ρ is temperature, t_c, dependent and requires a temperature coefficient α for its calculation.

$$\rho = \rho_{20°C}[1 + \alpha(t_C - 20°C)] \qquad (6.2)$$
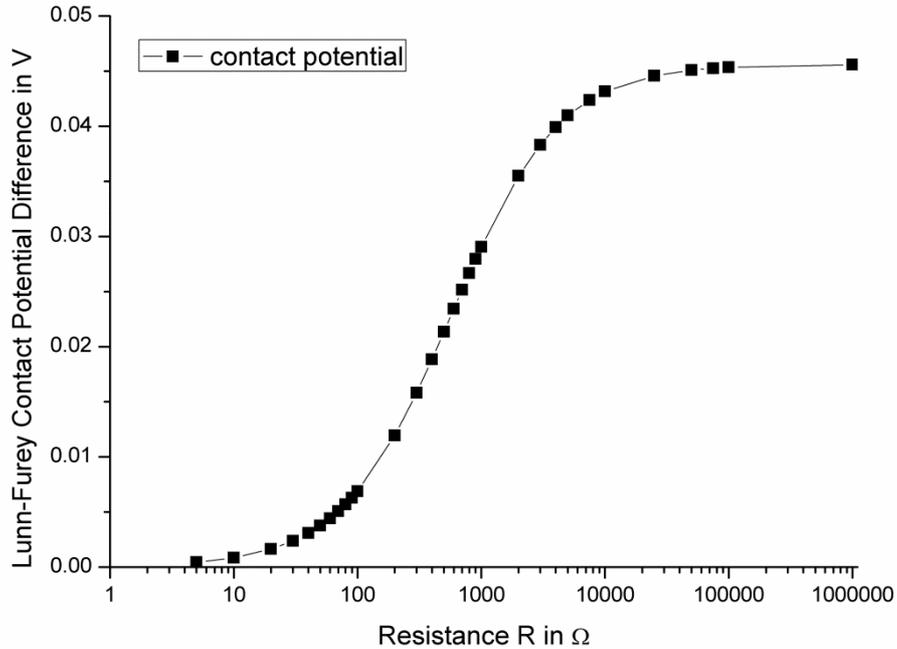
Figure 6.12: Lunn-Furey contact potential difference versus applied electrical resistance

From roughness measurements on worn cylinder liners, the "wire length" is known and can be set to the average peak to valley height Rz which is around 1 μm. Resistivity $\rho_{20°C}$ of iron is $10*10^{-8}$ Ωm with a temperature coefficient α of $5*10^{-3}$ K^{-1} (Tipler, 1998). Assuming the temperature in the surface to be 200 °C, the resistivity becomes $1.9*10^{-7}$ Ωm. The Lunn-Furey contact potential difference might give a typical value of 25 mV which correlates to 700 Ω. Set in equation (6.1) this results in a total conducting contact area of 271 nm^2, an incredible small area compared to the total worn apparent contact area of estimated 9 mm^2 on the piston ring in Figure 6.8. This rough calculation is showing the extreme sensitivity of the Lunn-Furey contact potential circuit to metallic contact. Obviously the load carrying real contact area can be bigger as the metals are usually covered by a oxide layer with high electric resistance. Also scattering effects that occur when electrons flow through very thin wires are not taken into account. However the current, a measure for the electron flow density is very small, therefore scattering effects will be small too.

6.2.4 Monitoring Friction Force and Calibration of the TE77

As indicated in Figure 6.9, the stationary support with the mounted cylinder specimen is rigid in the vertical but flexible in the horizontal direction of movement, supported by a load cell. The load cell is a piezo force transducer, Figure 6.7 point I, which measures the friction force F_R. The calibration of the force transducer was achieved by applying known mass, m, over a pulley and a string to the cylinder liner holder. Figure 6.13 shows the results for either direction and results with increasing mass.
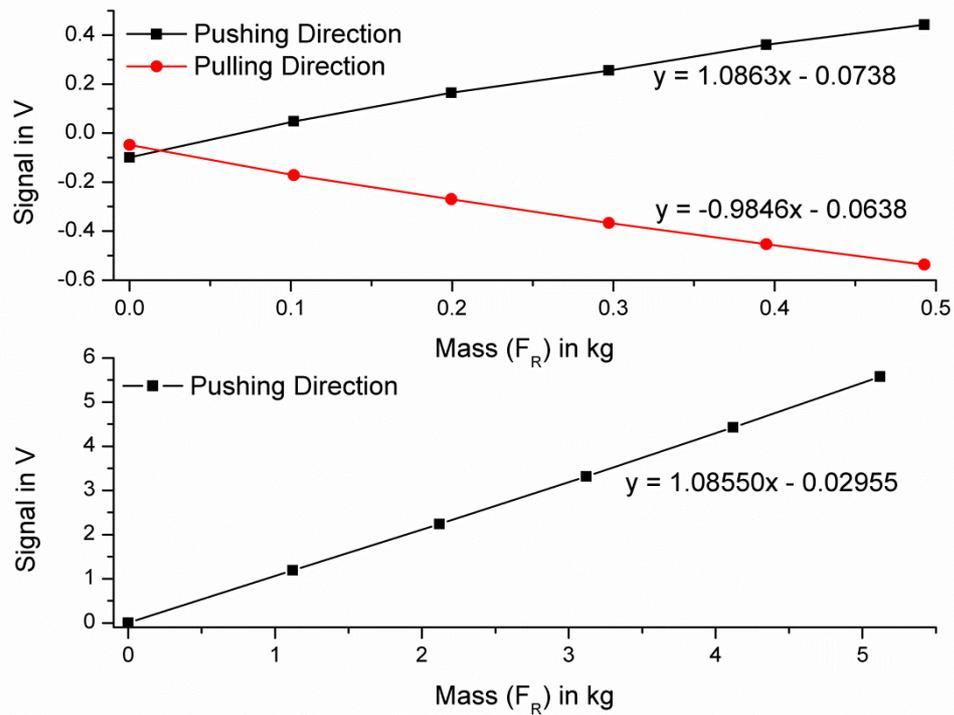
Figure 6.13: Calibration of TE77 force transducer with known mass

Applying Newton's second law of gravity, the electric signal from the force transducer can be transformed into a frictional force:

$$F = m \cdot a \tag{6.3}$$

$$m = \frac{Signal + 0.02955}{1.0855} \tag{6.4}$$

$$a = g = 9.8064 - 0.0259 cos\,(2\alpha) \tag{6.5}$$

The gravity acceleration g in equation (6.5), (Atkins, 2001), is dependent on the latitude which is 53,48° for Leeds, which results in the constant g_{Leeds} = 9.781m/s^2.

The temperature controlled cylinder liner holder is connected to the force transducer by a steel rod. To find the influence of temperature on the force transducer, the calibration was repeated at increased and stabilised temperatures, Figure 6.14. A drift in the force signal but no clear tendency was found, therefore no correction was applied during experiments. The higher the temperature, the higher the deviation from linearity.
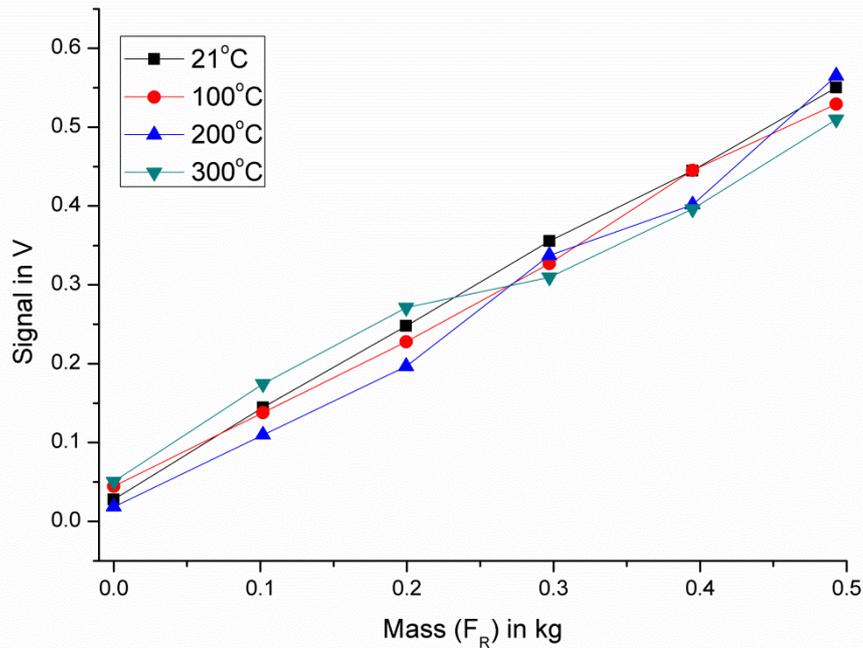
Figure 6.14: Influence of temperature on the stability of signals from the force transducer

During the calibration, the electric motor was found to generate a 50 Hz noise whilst standing still. The noise was used to see the influence of external mechanical noise from the motor or the Scotch-Yoke mechanism on the force measurements. A weight was applied to gain a clear signal from the force transducer. The samples were fitted and the piston ring pressed on the cylinder liner with increasing force. No drift due to change in normal force was found, which means the normal force is applied perpendicular to the cylinder liner. The results can be seen in Figure 6.15. When the piston ring is only resting on the cylinder liner, almost no noise is transmitted. When the contact between piston ring and cylinder liner is mechanically closed, the noise is transmitted. This means, the measurement arrangement is well isolated through the cast iron table but any noise from the motor or in the transmission influences the force signal through the piston ring holder. Back-

lash from the Scotch-Yoke mechanism was found to be a problem in this respect, as shown later in Figure 6.20.
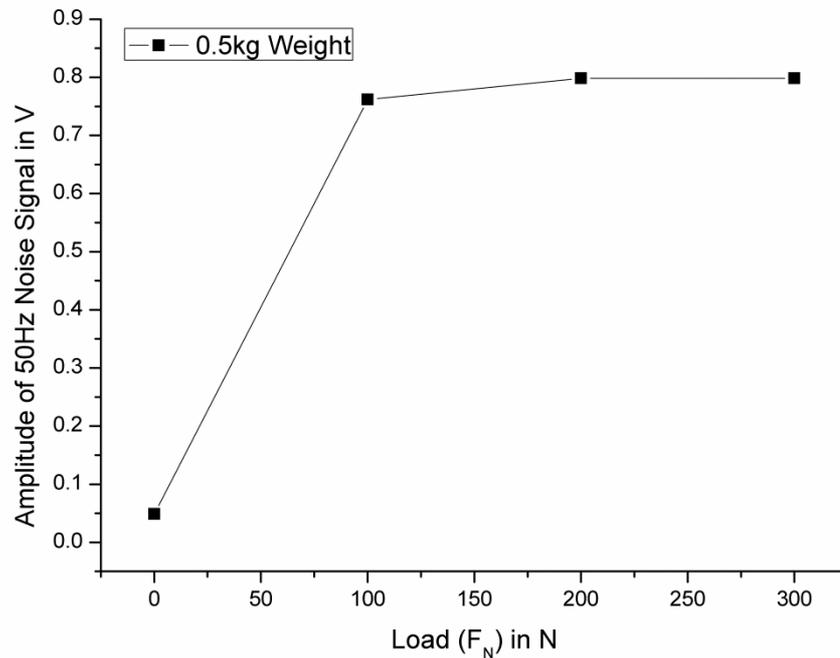
Figure 6.15: Amplitude of 50 Hz noise in correlation to increasing normal force

6.2.5 Kinetics and Signal Evaluation on the TE77

The linear motion of the piston ring is achieved by a Scotch-Yoke mechanism, Figure 6.7, point C, which is driven by an electrical motor, B. The Scotch-Yoke mechanism, Figure 6.16, on the TE77 allows the variation of the total stroke length, x, and was set to 15 mm for this study.

The slider speed or piston ring sliding speed v_x is given by:

$$v_x = r * 2\pi * f * sinCA_{rad} \qquad (6.6)$$

With r being the half stroke or crank web radius, f the frequency and CA the crank angle in radians.

The stroke position x is given by:

$$x = |r * cos(CA_{rad}) - r| \qquad (6.7)$$

Figure 6.17 illustrates the kinetics of the TE77 Scotch-Yoke mechanism with the chosen parameters of f = 14 Hz and r = 7.5 mm.
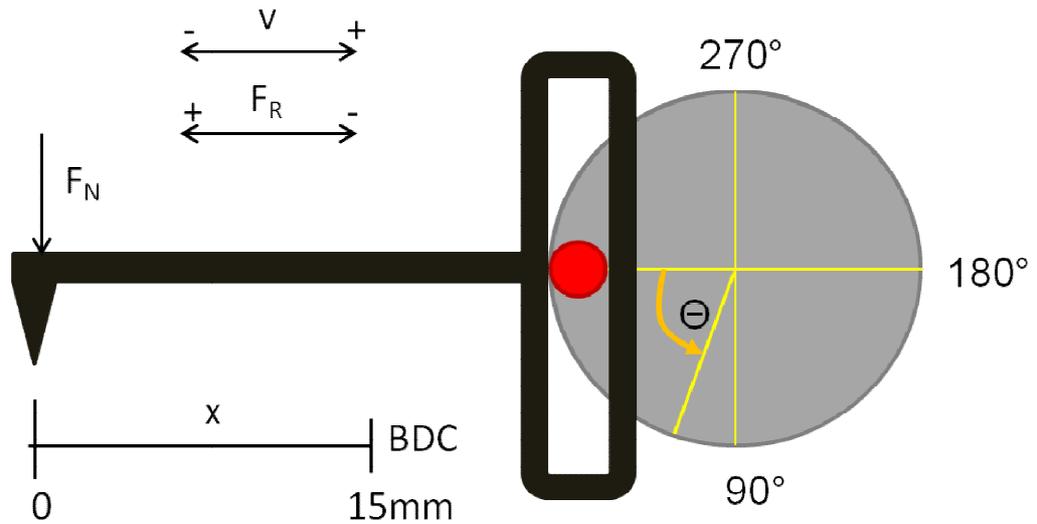
Figure 6.16: Definition of directions in the TE77 friction testing machine
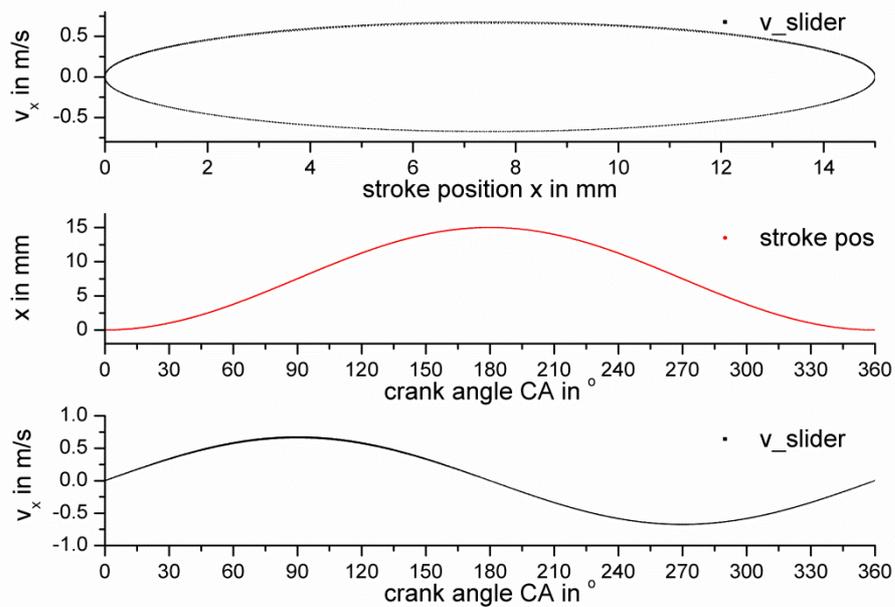
Figure 6.17: Kinetics of the Scotch-Yoke mechanism

Figure 6.18 and Figure 6.19 illustrate how the signals from the force transducer are evaluated to gain information on the friction coefficient and the kinetics of the arrangement. In Figure 6.19 it is quite apparent, that the frequency analysis requires one full period to establish the stroke position. The results were cleaned of the first non-full periods to make a correlation to exact piston ring position.
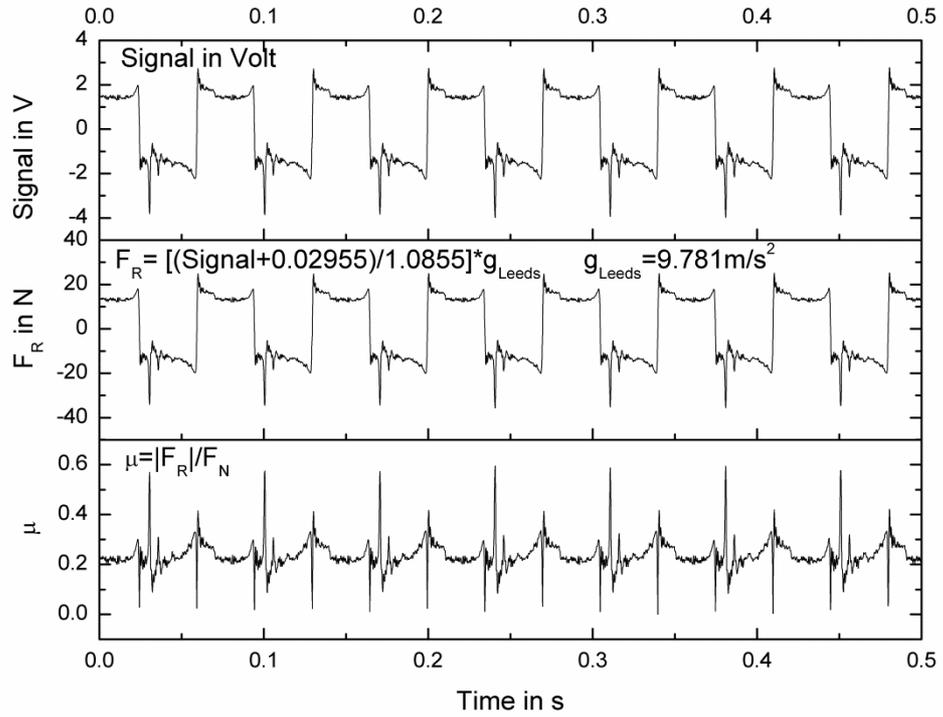
Figure 6.18: Evaluation of force transducer volt signal into a friction coefficient
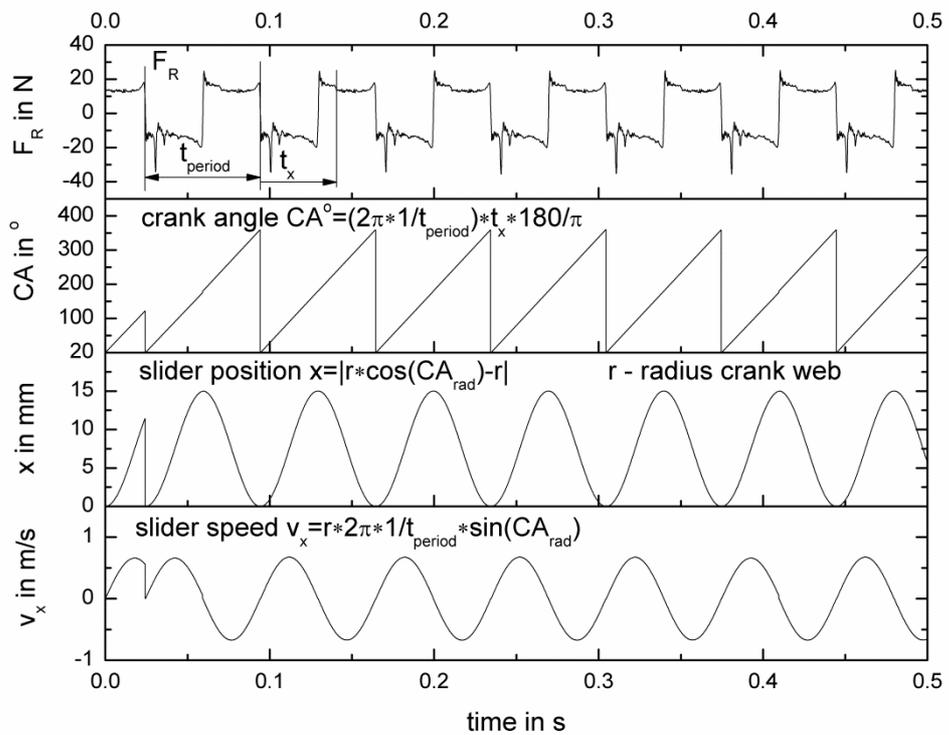
Figure 6.19: Use of the signal from the force transducer to establish the kinetics of the measurement
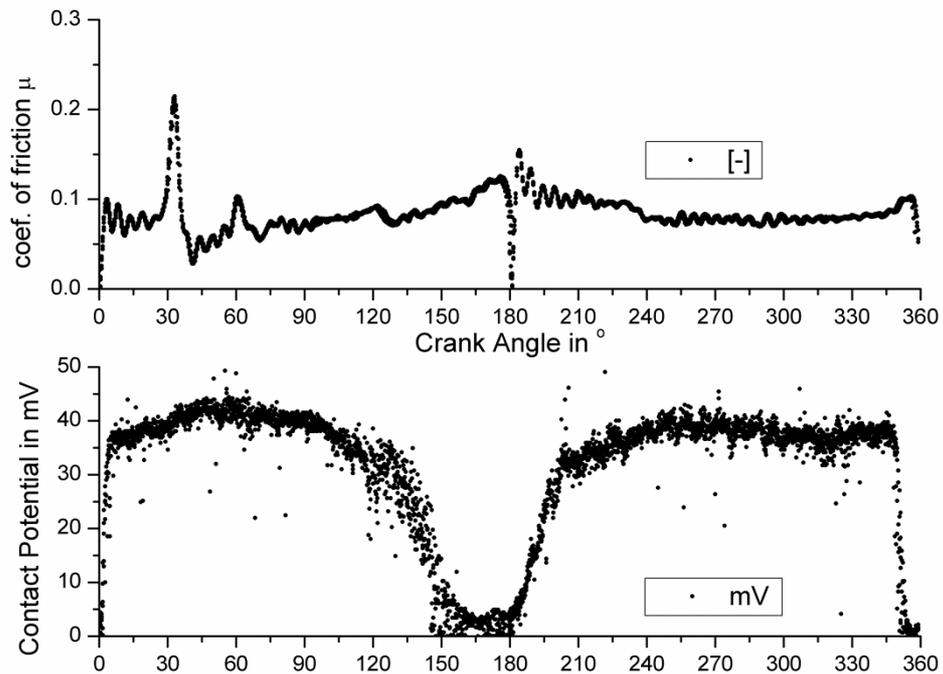
Figure 6.20: Typical result from the evaluated force transducer signal and the Lunn-Furey contact potential difference over the crank angle

Figure 6.20 shows a typical result of the above evaluation. The coefficient of friction and the contact potential difference can be plotted over crank angle. As mentioned before, external mechanical noise can be transmitted through the piston ring holder. The coefficient of friction in Figure 6.20 shows peaks at 30 and 60° *CA* without any apparent reason when considering only the piston ring cylinder liner contact. However, other research (Elson, et al., 1974) investigating a compressor application using the Scotch-Yoke mechanism, reports a backlash at exactly the same crank angle position.

Also quite apparent in the coefficient of friction of Figure 6.20 is the overlaying periodic high frequency noise, which has a strong amplitude after changes in direction at 0 and 180° *CA*. This was identified to be the eigen- or characteristic frequency of the cylinder liner holder – force transducer arrangement. For the experiment shown in Figure 6.21, one end of the Lunn-Furey contact potential circuit was fitted to a metallic hammer which was used to knock on the cylinder liner holder. The declining response was at 1250 Hz which is the eigenfrequency of the arrangement. The experiment also shows the perfect alignment of the two signals by the data acquisition system.
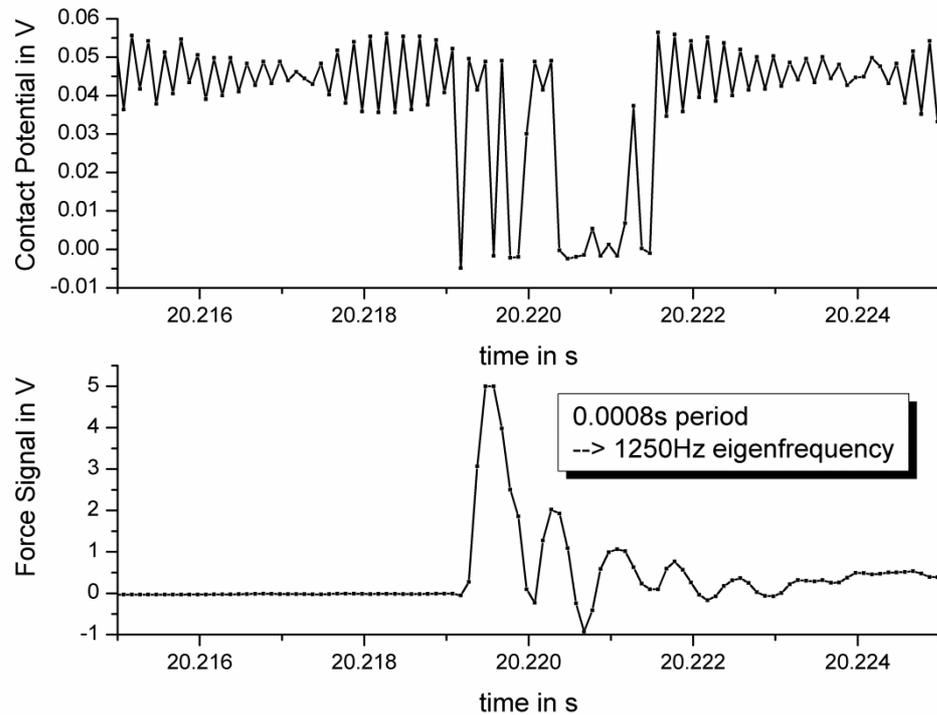
Figure 6.21: Evaluation of the eigenfrequency of the cylinder liner holder – force transducer arrangement

6.2.6 Monitoring of Ambient Conditions on the TE77

Previous researchers found a significant impact of air humidity on friction results and it became good practise to monitor ambient laboratory conditions. During the tests, the relative air humidity was recorded by measuring the air pressure ("Tissot T-Touch", meteo-function) and recording the dry bulb air temperature, T_{dry}, and the wet bulb air temperature, T_{wet}, in °C. The temperature sensors were small K-type thermo couples hanging free in the air and placed in a wet cotton hose respectively.

The relative humidity RH is the ratio of vapour pressure, p_{vap}, to the saturation vapour pressure, p_{vsat}, in percent, (Georg-August Universität Göttingen):

$$RH = \frac{p_{vap}}{p_{vsat}} \cdot 100 \tag{6.8}$$

with the saturation vapour pressure, p_{vsat}, in hPa given by the Magnus equation, with e being the Euler number:

$$p_{vsat} = 6.10780 \cdot e^{\left[\frac{17.08085 \cdot T_{dry}}{234.775 \cdot T_{dry}}\right]} \tag{6.9}$$

and the vapour pressure, p_{vap}, from the approximation:

$$p_{vap} \approx p_{vsat-wet} - 0.66 \cdot \frac{p_{amb}}{1000} \cdot (T_{dry} - T_{wet})$$ (6.10)

where $p_{vsat\text{-}wet}$ was calculated by equation (6.9) with T_{wet}.

6.2.7 Conformity and Hertzian Contact Pressure Between Piston Ring and Liner on the TE77

Before each test, the samples were run-in for 2.5 hours on SN600 with a normal force of 160 N applied and at 80 or 170 °C cylinder liner temperature respectively. The running-in time was found sufficient to stabilise the friction force. The normal force of 160N was chosen to achieve good conformity of the parts and is in the range of previous research. The temperature range was chosen for the dew point of dispersed aqueous phase and is in the range of marine Diesel engine cylinder liner temperatures.

In Figure 6.8 it was already seen that the piston ring is pressed down on to the cylinder liner by two pins in the back of the ring. Figure 6.22 is a model for the piston ring deformation in the piston ring holder. The aim is to find the real radius of the piston ring which is needed to calculate the Herzian contact pressure at the beginning of the test. There will be uncertainty in the calculations as the material properties are only known at 25 °C. However, the deviations are within the range of the given values.

The problem can be reduced to a beam clamped in a stiff wall.

The deformation $w(x)$ at any point x is than given by formula (6.11) (Lackmann, 2001):

$$w(x) = \frac{F l^3}{6 E I_y} \left[2 - 3\frac{x}{l} + \left(\frac{x}{l}\right)^3 \right]$$ (6.11)

With F the applied force, l the length from wall to the application point of the force, E the Young's modulus of the material, I_y the axial moment of area and x the point of interest.

The piston ring cross section, Figure 6.23, can be reduced to a rectangle and a trapezium to find the combined axial moment of area, I_y, which is given by:

$$I_y = \sum \left(I_{yi} + a_{yi}^2 \cdot A_i \right)$$ (6.12)

with I_{yi} the single axial moment of area A_i which has its centre of gravity in a distance a_i from the combined centre of gravity.
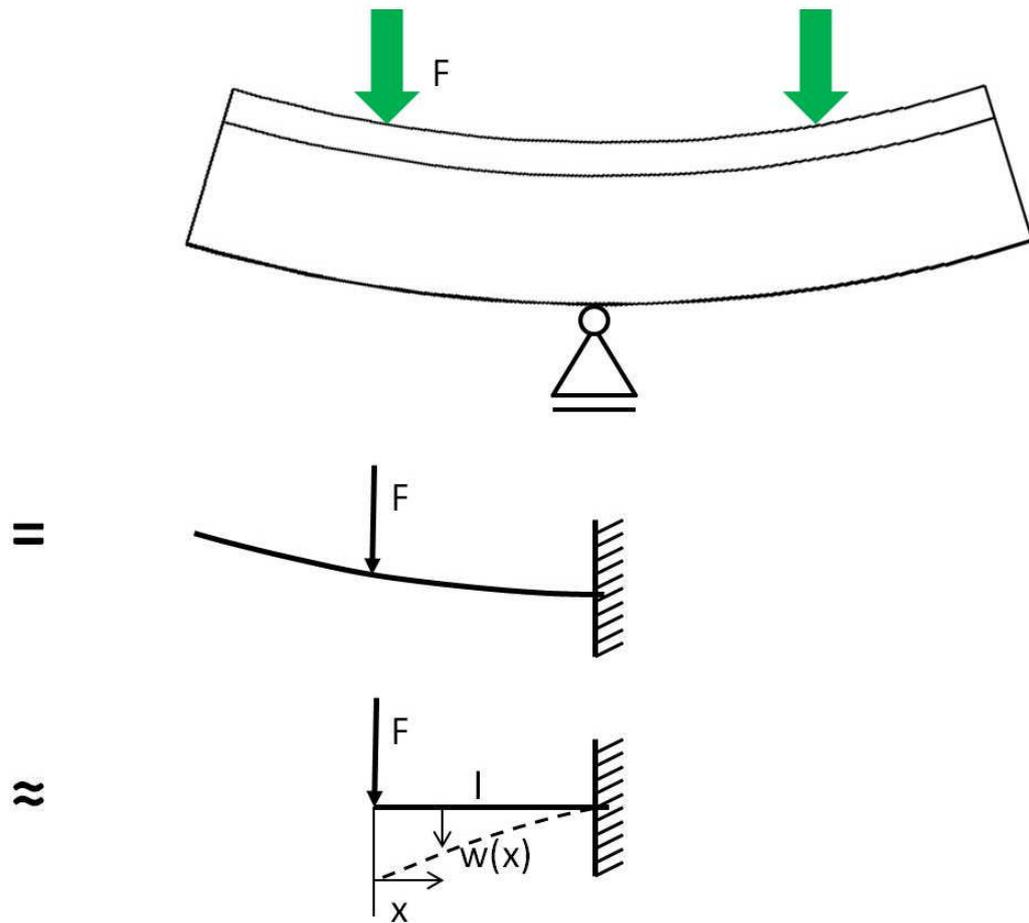
Figure 6.22: Deformation model of the piston ring in the TE77 holder

For the trapezium:

$$I_{y1} = \frac{h_1^3}{36} \frac{b_1^2 + 4b_1 b_2 + b_2^2}{b_1 + b_2} \tag{6.13}$$

For the rectangle:

$$I_{y2} = \frac{b_1 \cdot h_2^3}{12} \tag{6.14}$$

The centre of gravity for the trapezium is:

$$S_{1y} = \frac{h_1}{3} \frac{b_1 + 2b_2}{b_1 + b_2} \tag{6.15}$$

The centre of gravity for the rectangle is at $h_2/2$. Combined with the result from (6.15) the combined centre of gravity can be found and the distances a_1 and a_2 calculated.
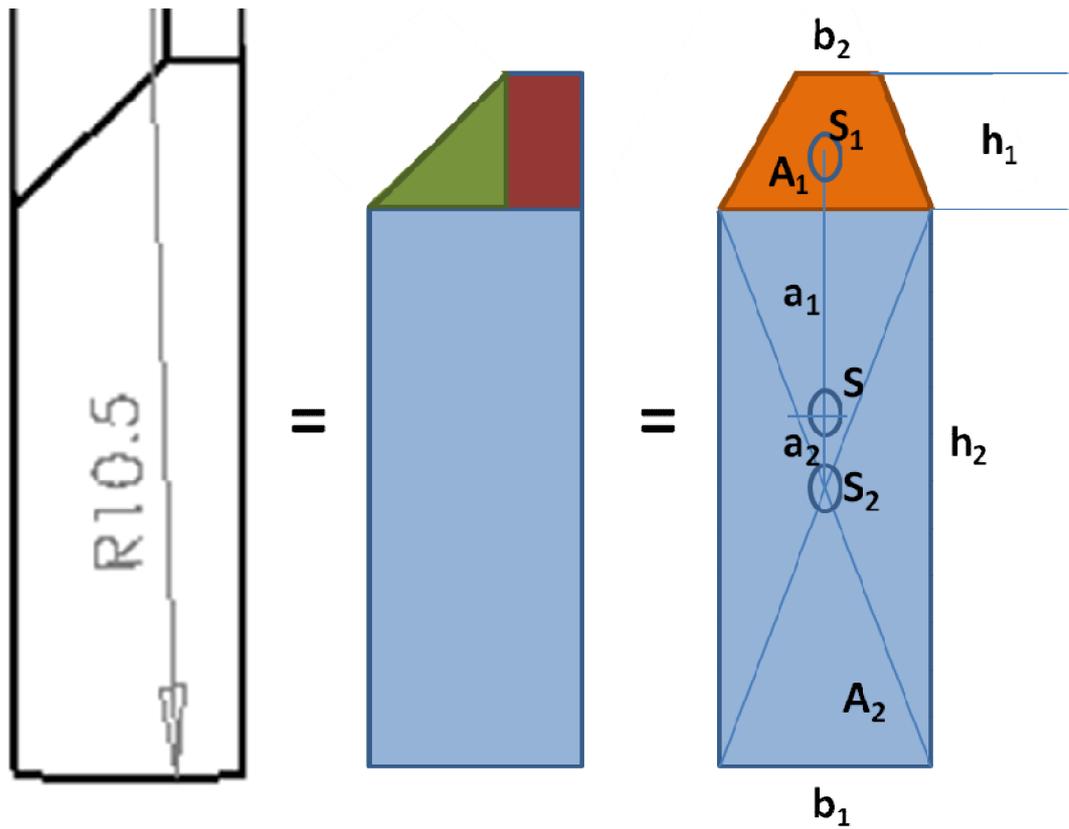
Figure 6.23: Evaluation of the axial moment of area I_y
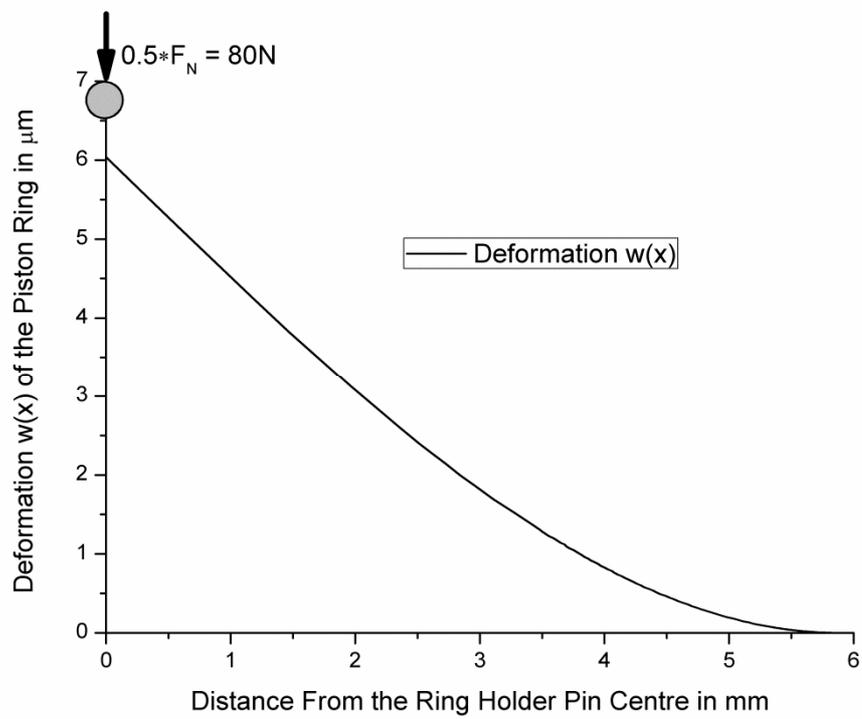
Figure 6.24: Results for deformation $w(x)$ of the piston ring segment in the TE77 piston ring holder

The deformation $w(x)$, equation (6.11), can be subtracted from the circumferential piston ring shape to find the new piston ring shape $y(x)$ and consequently the deformed radius R_{def} in the contact zone:

$$R_{def} = \frac{y^2 + \frac{(2x)^2}{4}}{2y}$$

(6.16)

Results for deformation $w(x)$ are given in Figure 6.24. The analysis for the Hertzian contact pressure was done according (Priest, 2009). Index A indicates values for the piston ring and index B for the cylinder liner respectively. An illustration of the problem is given in Figure 6.25

$$\frac{1}{R_x} = \frac{1}{r_{Ax}} + \frac{1}{r_{Bx}}$$

(6.17)

With r_{Ax} and r_{Bx} the radii of piston ring and cylinder liner in circumferential direction.

$$\frac{1}{R_y} = \frac{1}{r_{Ay}} + \frac{1}{r_{By}}$$

(6.18)

With r_{Ay} and r_{By} the radii of piston ring and cylinder liner in running direction. The cylinder liner is flat in longitudinal direction which makes the term insignificant.
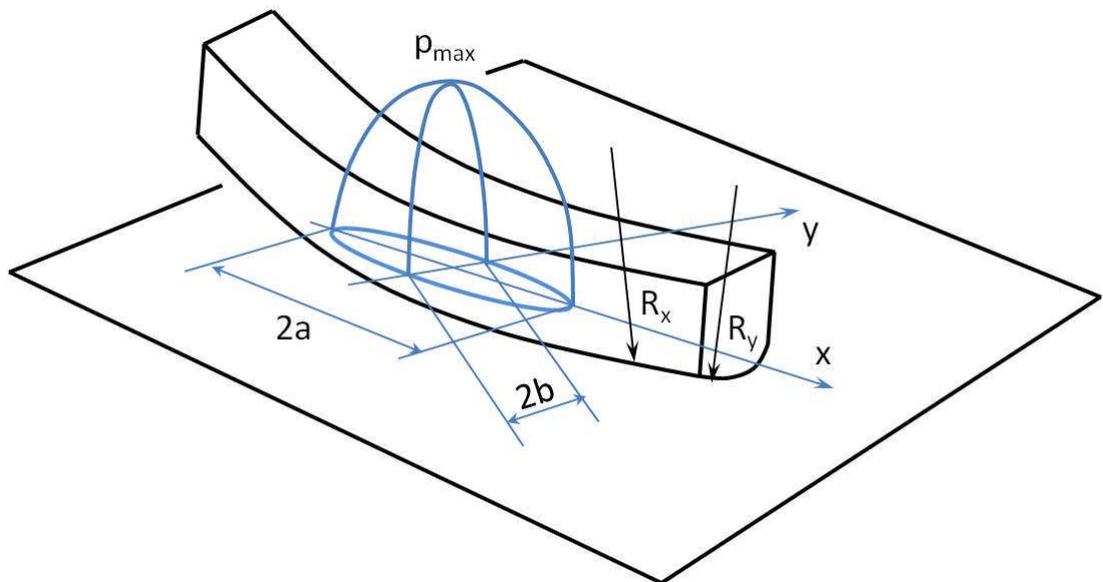
Figure 6.25: Equivalent elastic piston ring on a rigid plane "cylinder liner" and the resulting semi-eliptical Hertzian contact pressure distribution

Combining of (6.17) and (6.18) gives the curvature sum, R:

$$\frac{1}{R} = \frac{1}{R_x} + \frac{1}{R_y}$$

(6.19)

The Hertzian pressure distribution, p, is given by:

$$p = p_{max} \left[1 - \left(\frac{x}{a}\right)^2 - \left(\frac{y}{b}\right)^2 \right]^{\frac{1}{2}}$$

(6.20)

with the maximum pressure, p_{max}:

$$p_{max} = \frac{3W}{2\pi ab}$$

(6.21)

were W is the normal load ($=F_N$),

the semi-minor, a:

$$a = \left(\frac{6\bar{k}^2 \bar{\xi} WR}{\pi E'} \right)^{\frac{1}{3}}$$

(6.22)

the empirical relationship for the ellipticity ratio $k \geq 1$:

$$\bar{k} = 1.0339 \left(\frac{R_x}{R_y} \right)^{0.6360}$$

(6.23)

the semi-minor, b:

$$b = \left(\frac{6\bar{\xi} WR}{\pi \bar{k} E'} \right)^{\frac{1}{3}}$$

(6.24)

the equivalent elastic modulus;

$$E' = \frac{2E_A E_B}{(1 - v_A^2)E_B + (1 - v_B^2)E_A}$$

(6.25)

where E and v are the material properties Young's modulus and Poisson's ratio of the surfaces;

and the approximation of the complete elliptic integrals of the first and second kind:

$$\bar{\psi} = 1.5277 + 0.6023 ln \left(\frac{R_x}{R_y} \right)$$

(6.26)

$$\bar{\xi} = 1.0003 + \frac{0.5968}{\frac{R_x}{R_y}}$$

(6.27)

The deformation at the centre of the contact is given by:

$$\delta = \bar{\psi} \left[\left(\frac{9}{2\bar{\xi}R} \right) \left(\frac{W}{\pi \bar{k} E'} \right)^2 \right]^{\frac{1}{3}}$$

(6.28)

The results for unworn parts are shown in Figure 6.26. The definitions from Figure 6.22 were kept the same, with the centre of the pin being zero. The influence of piston ring deformation was found to have a significant influence

on Hertzian contact pressure due to the increase of the piston ring circumferential radius. The deformation δ, equation (6.28), at the centre of the contact due to Hertzian contact pressure was subtracted from the purely geometric gap, to find the initial metal to metal contact zone of ~5 mm around the centre of the piston ring.
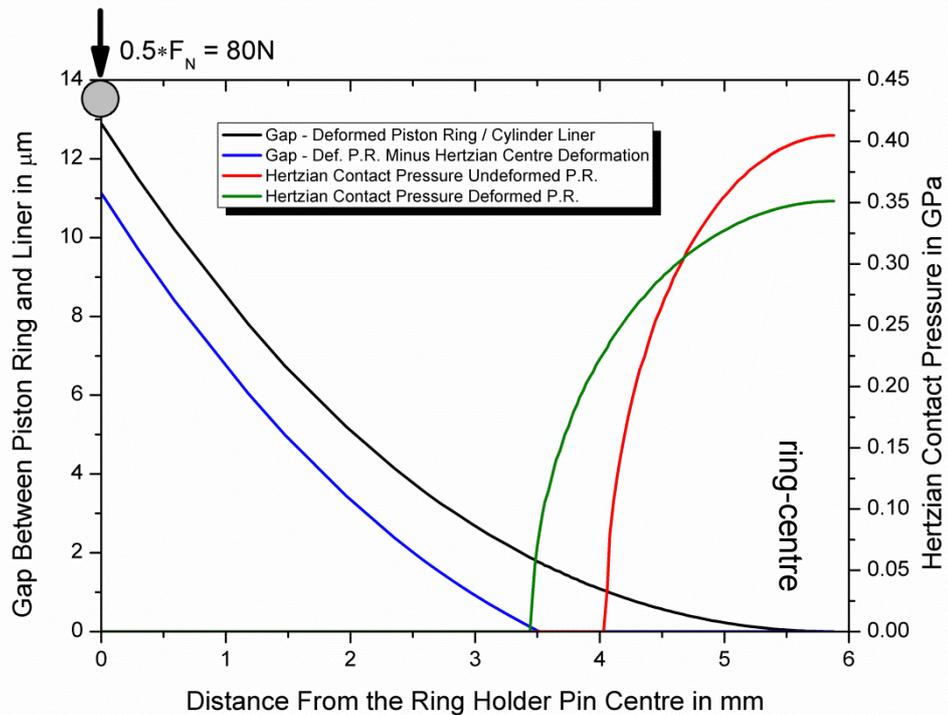
Figure 6.26: Influence of piston ring deformation on the Hertzian contact pressure and conformity of the parts in unworn condition on the TE77 test bed

From Figure 6.26 it is quite apparent, that the model for the piston ring deformation presented in Figure 6.22 does not hold anymore as the Hertzian contact pressure will also deform the piston ring and the Hertzian pressure will have two centres left and right of its geometric centre line. This was also observed during the tests, with hard running marks being situated left and right of the centre of the contact.

Figure 6.27 illustrates a first idea to describe the problem by a double supported cantilever beam, where the Hertzian contact pressure is replaced by a equivalent constant area load. The red arrows, however, illustrate the drawback. The pins where the normal force is applied to the piston ring can move vertically and the centre of the piston ring is connected to the other half of the piston ring.
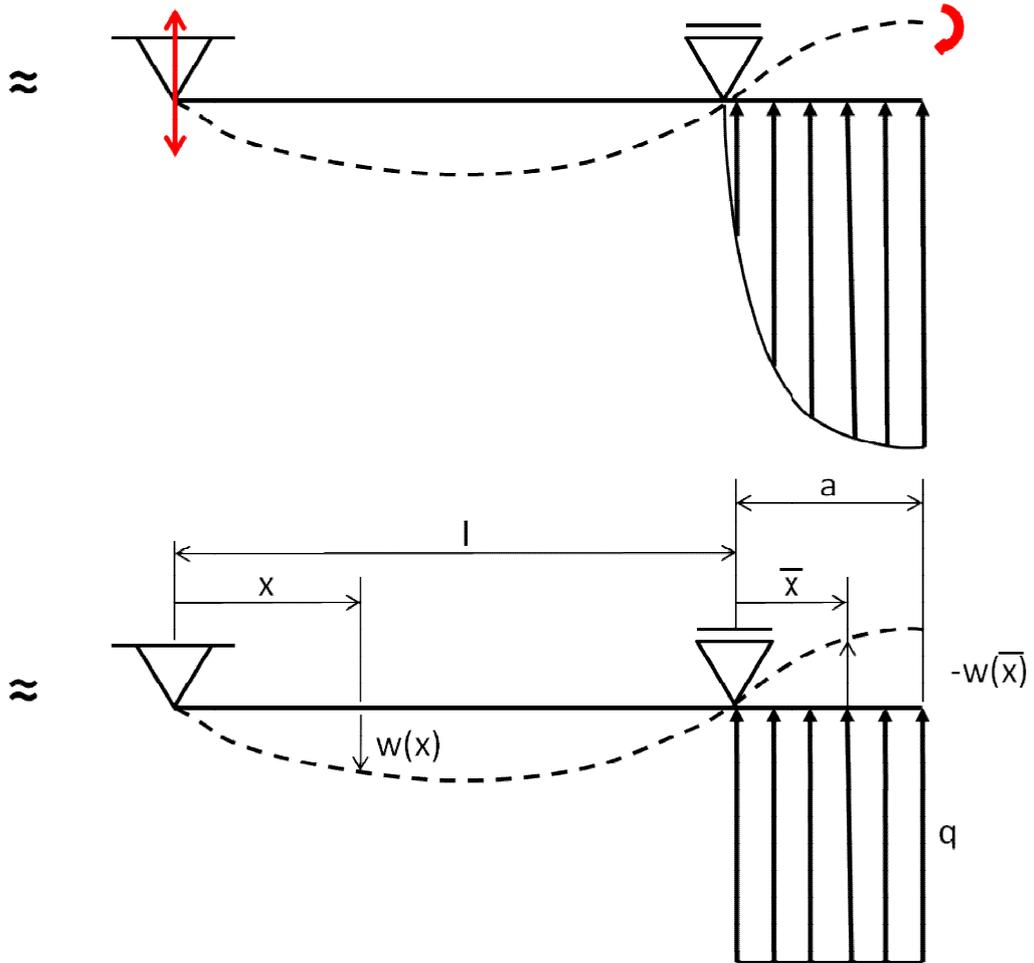
Figure 6.27: First approach to piston ring deformation with Hertzian contact pressure
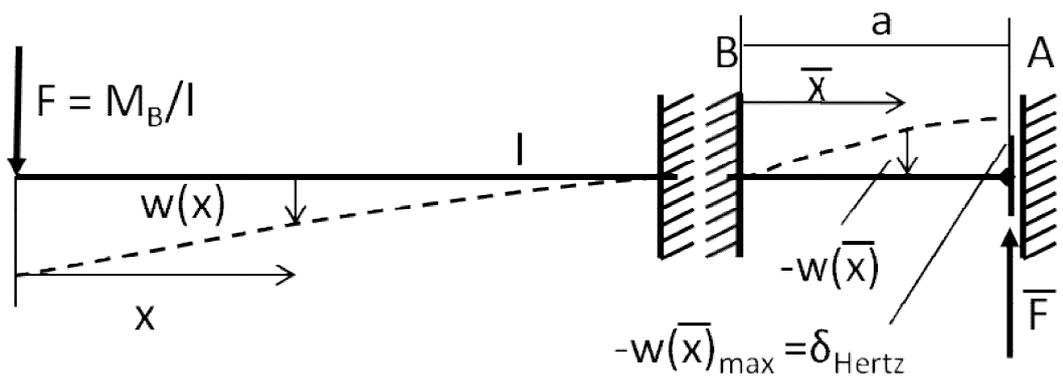
Figure 6.28: Second approach to piston ring deformation with Hertzian contact pressure.

Figure 6.28 illustrates an approach to overcome the drawbacks of the model shown in Figure 6.27. The model is split into the area of Hertzian contact and an area were the resulting moments from the Hertzian area are used as input. From equation (6.28), the maximum Hertzian deformation, δ, at the

centre of the contact is known. With the model for a elastic beam, a equivalent force can be found which would cause the same deformation over the whole piston ring cross section.

$$\bar{F} = \frac{\delta_{Hertz}12EI_y}{a}$$
(6.29)

The length a equals the semi minor a found in equation (6.22). With the equivalent force, $\bar{F}$, the deformation of the piston ring in the Hertzian contact area can be calculated:

$$w(\bar{x}) = \frac{\bar{F}a}{12EI_y}\left[3\left(\frac{\bar{x}}{a}\right)^2 - 2\left(\frac{\bar{x}}{a}\right)^3\right]$$
(6.30)

and also the moment, M_B, in point B which is used as an input to the other half of the model in Figure 6.28:

$$M_B = -\frac{1}{2}\bar{F}a$$
(6.31)

The length l in Figure 6.28 is the distance from the pin to the centre of the piston ring, reduced by the semi minor a, a corresponding force at the pin can be found originating from the moment M_B:

$$F = \frac{M_B}{l}$$
(6.32)

The deformation $w(x)$ can be found by equation (6.11) when using the new values. Figure 6.29 shows the resulting gap between piston ring and cylinder liner due to piston ring deformation by the Hertzian contact pressure of the deformed piston ring shown in Figure 6.26. It can be seen, that the Hertzian contact pressure causes the piston ring to lift from the cylinder liner in the centre of the ring by 0.51 µm. The resulting Hertzian radius, R_x, left and right of the contact point can be calculated from the resulting gap between piston ring and cylinder liner. The deformation is not symmetric and it was decided to use an average of the closest points.

Figure 6.30 shows the resulting Hertzian contact pressure left of the centre of the piston ring. Two maxima of Hertzian contact pressure between piston ring and liner can be found due to the deformation of the piston ring. The final maximum Hertzian contact pressure is reduced by about 20 % from the assumption of a undeformed piston ring to the assumption of a deformed piston with the influence of Hertzian contact pressure on the deformation. The area of total conformity increased by 53 %.
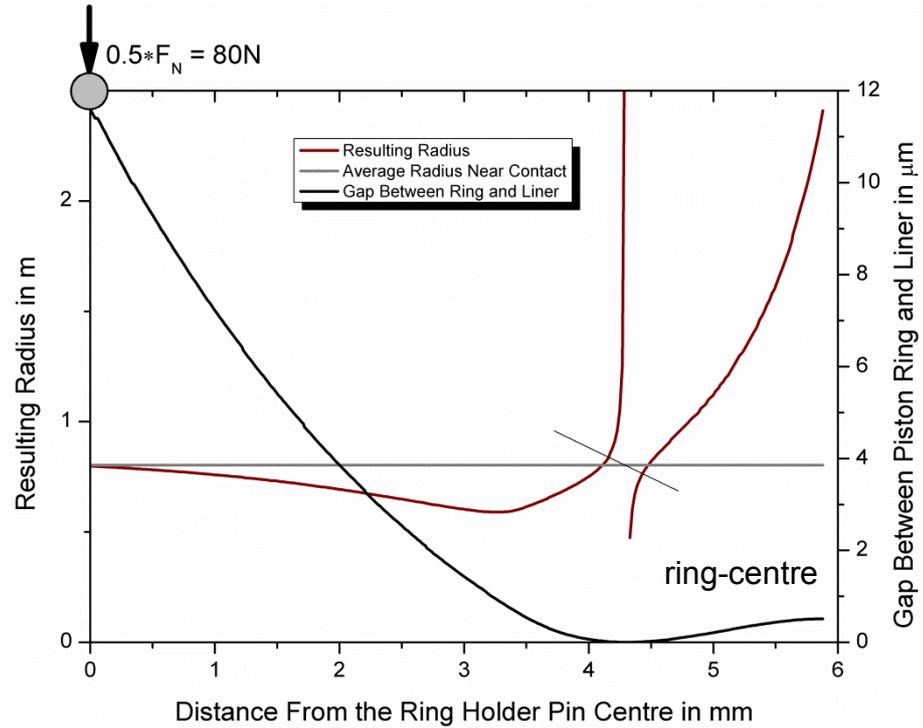
Figure 6.29: Influence of Hertzian contact pressure on piston ring deformation and conformity of the parts in unworn condition on the TE77 test bed according to the model shown in Figure 6.28
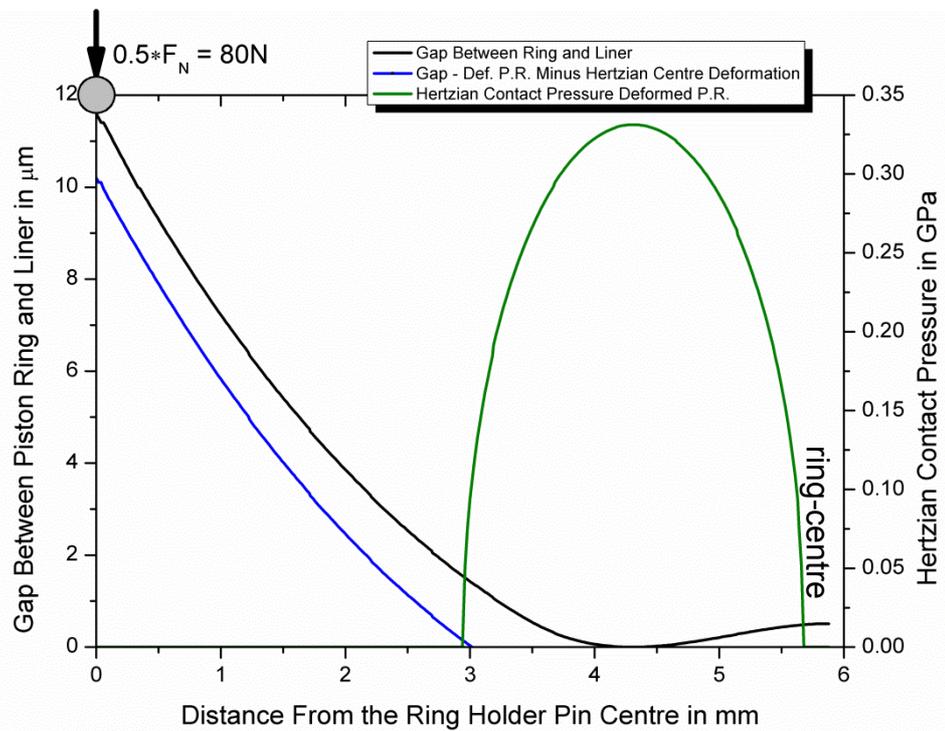
Figure 6.30: Influence of piston ring deformation on the Hertzian contact pressure and conformity of the parts in unworn condition on the TE77 test bed according to the model shown in Figure 6.28.
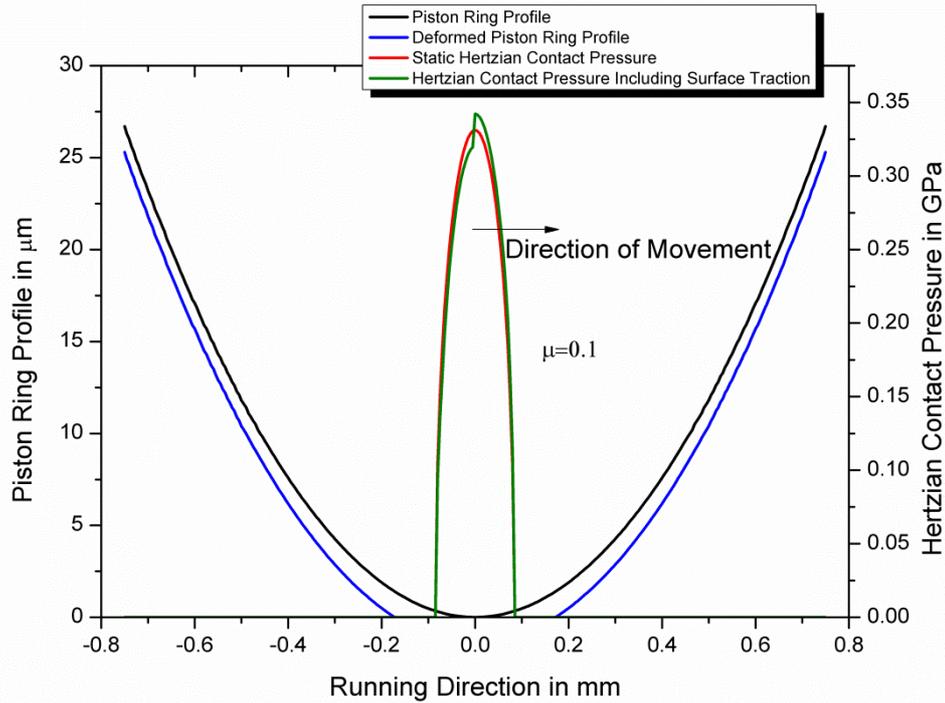
Figure 6.31: Side view of Figure 6.30 at the centre of the contact. Hertzian contact pressure in unworn condition on the TE77 test bed in static and moving condition

So far, the evaluation of the Hertzian contact pressure was purely static without movement of the piston ring. The tangential friction force, however, induces additional stresses into the surface, the so called surface tractions. In a lubricated contact, the fluid experiences extremely high pressures and a analysis considering elastohydrodynamic lubrication would be required. Such an analysis is beyond the scope of this study and an analysis for dry contacts is used instead which will result in higher values. The distribution of the surface tractions, $\tau(x)$, can be calculated (Williams, 1994) by:

$$\tau(x) = \frac{F}{bL\pi\sqrt{1 - \frac{x^2}{b^2}}} \tag{6.33}$$

with

$$\tau_{max} = \mu \cdot p \tag{6.34}$$

The tangential force F will be the measured friction force which results, together with the applied normal force or load F_N in the friction coefficient μ. Semi-major b results from equation (6.24). The length L via the force F is fed into the contact is known as four times semi-major a, equation (6.22). The pressure p at any point in the contact is known from equation (6.20). Anticipating the results from chapter 7, the friction coefficient after running-in

under a load of F_N = 160 N, lubricated with SN600 was measured as $\mu_{80°C}$ = 0.088 and $\mu_{170°C}$ = 0.102. During running-in, mainly the surface roughness peaks get smoothed out and the geometry of the parts stay constant, therefore it is a fair assumption to use the values after running-in. The results of this analysis are shown in Figure 6.31, which is a side view through the piston ring profile at the point of contact. In front of the contact point, indicated by the direction of movement, $\tau(x)$ has to be added to the static Hertzian contact pressure as the material gets compressed, while on the trailing side $\tau(x)$ has to be subtracted because the material is stretched. It is quite apparent that semi-major b which defines the elliptical area of Hertzian contact pressure together with semi-major a is not equal to the deformation of the piston ring – liner contact. This can be explained by the deformation of the liner which forms a radial wedge towards the Hertzian contact zone as the surface cannot form a step.

The yield point σ_y for the cylinder liner material is around 0.2 GPa. From the Tresca maximum shear stress criterion (Priest, 2009):

$$\tau_{max} = \frac{\sigma_y}{2} \tag{6.35}$$

it is apparent, that the material will deform plastic under the Hertzian contact pressure.

The penetration depth of the Hertzian contact pressure is given by 0.47 times semi-major a which is 0.64 mm in above case. The Hertzian contact pressure analysis was done using values assuming a solid chromium piston ring. The piston ring however is only thinly, < 0.1 mm, coated. When using the Young's modulus and Poisson's ratio of grey cast iron also for the piston ring, the maximum Hertzian contact pressure reduces to 0.25 GPa. But even with this assumption, the contact deforms plastic.

The severity of the tests are revealed quite clearly in the microscopic analysis of the piston ring running surface in chapter 7.

Wear causes an increase in the ring profile radius and greater conformity of the parts, which considerably reduces the Hertzian contact pressure. After running in and especially during tests with high wear rates, the geometry becomes an unknown therefore shuttle-tests where necessary were the test conditions are switched in intervals back to the reference test conditions. This way the influence of geometry, hydrodynamics and Hertzian contact pressure on friction can be found and consequently excluded.

6.2.8 Conditions for the TE77 Tests

The test conditions for all tests are given in Table 6.4. The test number is identical with the later used "sample number". The lubricant was fed at a rate of 0.5 ml/h through pipes next to the piston ring profile for which the position is given by the abbreviation "TDC" and "BDC", which can also be found in Figure 6.8, Figure 6.10, Figure 6.16 and Figure 6.35. The feed rate corresponds to a typical engine running-in feed rate of 2 g/kWh, considering the lubricated cylinder area. The study is referenced to lubrication with pure SN600 under the same physical conditions. Tests 3 – 21 started with a running-in procedure of 2.5 hours at the test temperature of either 80 or 170 °C. When the addition of aqueous phase is indicated, it must be read as 1.3 %v/v aqueous phase, a typical value found in the engine (Micali, et al., 2010), with a concentration of the indicated value in %w/w. The normal load F_N and the liner temperatures were varied during some of the tests to find their influence.

Tests 8 and 13 were reference tests with plain base oil at different temperatures but they are statistically backed up by the data captured during running-in for each test.

After testing, the samples were allowed to cool down, were rinsed with isopropanol and heptanes and oiled with SN600 before storing in self closing plastic bags.

Table 6.4: Test conditions for all trials. Running-in was performed for test 3 – 19 & 21 at T_{Liner} with SN600 for 2.5 hours.

Test No.	F_N in N	T_{Liner} in °C	Lub. TDC	Lub. BDC	Ø RH %
1	160	150	-	Lubr. A	-
2	160	150	-	Lubr. A	-
3	160	80 / 30	SN600+H_2O	-	-
4	160	80	SN600+4%H_2SO_4	-	57.8
5	160	80	SN600+10%H_2SO_4	-	54.5
6	160	80	SN600+40%H_2SO_4	-	58.3
7	160	80	SN600+70%H_2SO_4	-	53
8	160	80	SN600	-	56.3
9	160	80	SN600+98%H_2SO_4	-	56.5
10	160	80	SN600+70%H_2SO_4	-	53.4
11	160	170	SN600+70%H_2SO_4	-	47.5
12	160	170	SN600+70%H_2SO_4	-	47.4
13	160	170	SN600	-	45.8
14	160	170	SN600+70%H_2SO_4	-	44.4
15	160	80 – 170	SN600+70%H_2SO_4	-	48.5
16	160	80 – 170	SN600+98%H_2SO_4	-	44.2
17	160	170	SN600+70%H_2SO_4	Lubr. A	43.1
18	160	170	SN600+70%H_2SO_4	Lubr. B	44.4
19	160	170	SN600+70%H_2SO_4	Lubr. B	50.9
21	160	80 – 340	SN600	-	43.5

6.3 Method: Lubricant Chemistry by FTIR-ATR

Excess lubricant gets thrown off in the turning points of the piston ring. The lubricant was sampled with a syringe needle for analysis by Fourier Transformation Infra Red Spectroscopy with Attenuated Total Reflectance accessory, FTIR-ATR, see also chapter 4. The samples were kept separated to distinguish between oil feeding side of the piston ring and trailing side. Especially for the emulsions this was thought to be interesting to see whether droplets could pass the lubrication gap or not. It was found that most of the oil was thrown off at the BDC side of the piston ring.

6.4 Method: Roughness and Wear Evaluation by White Light Interferometer

A white light vertical scanning interferometer (Veeco – WYKO NT3300S) was used to analyse the samples for their roughness and profile.

White light interferometry uses the differences in fringe pattern created between a split and re-merged light beam on a surface topography to measure height distributions on a plane. Therefore one part of the beam is sent directly to the measurement object while the other part travels a longer, known path length. The re-merging of the two beams can be destructive or constructive as the light travels in a waveform. This causes light – shadow fringes on the surface which can be analysed and information gained about the surface topography.

The length of the wear scar was bigger than the field of view of the lens, therefore the measurements had to be stitched, which was done with an overlap of 50 %.

The concave or convex samples were measured in the centre at their lowest or highest point respectively. The lens was then tilted to its maximum and the stage moved so the lens was perpendicular to the surface tangent. For the given curvature of piston ring and cylinder liner, this resulted in a distance of 2.5 mm to the left and to the right of the centre. The wear scar on the liner was not perfectly rectangular and varied in width from test to test. Therefore it was decided to analyse only for the highest loaded 5 mm in the centre of piston ring and liner. The problem is also illustrated in Figure 6.32.

A median filter was applied to remove noise from the measurements and for the analysis of surface roughness, curvature and tilt had to be removed from the raw measurement data. Figure 6.33 shows a typical example for surface roughness results on a worn piston ring in the direction of movement. The left table shows the analysis for the 'Y-Profile' which is taken in the middle of the scanned area indicated by a blue line. In the top right corner the settings for the roughness analysis are shown. The results in the right column represent average results for 731 lines as represented by the 'Y-profile'. Those averaged results were used in this study.
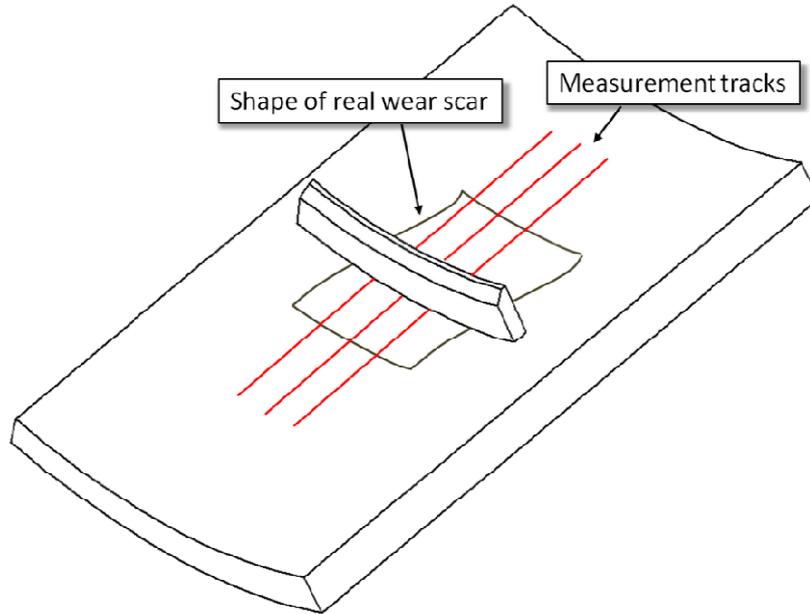
Figure 6.32: Measurement tracks along the cylinder liner wear scar and across the piston ring profile

Figure 6.33: Typical result of surface roughness analysis on the worn part of the piston ring in the direction of movement

Of all the averaged results shown in Figure 6.33, two are used in the following analysis of the results. Ra and Rp are described below and their values measured in the running direction used in the following.

The roughness peak, Rp, is the highest peak distance from the mean line per cut off length. The sum of the Rp values of two surfaces in contact equals the minimum oil film thickness, h_{min}, required to hydrodynamically separate the two surfaces. It is also an important measure to understand the contact potential measurement described in section 6.2.3.

The roughness average, Ra, is the arithmetic average deviation from a surface centreline. Ra is a traditional value and is not adequate to fully describe a surface. However, it is still in use for production drawings and also often found in tribology literature, for example in the specific film thickness λ which is h_{min} over the sum of Ra and sometimes used as the abscissa for the Stribeck diagram. To make the present study comparable to the work of others, an analysis with Ra is also presented in the following.

The evaluation of the profile of the wear scar and the wear volume on the cylinder liner required removal of the tilt from the raw data, as the long piece of liner could not be laid perfectly flat on the stage. Figure 6.34 shows a typical result for a wear scar. The unworn surface, just outside the turning points of the wear scar, was set to zero. It can be seen that the wear scar is slightly longer than the set 15 mm stroke. This can be explained by the width of the piston ring. The cylinder liner samples were always measured in the same direction with zero being the side which meets the top dead centre side, TDC, of the piston ring. This was also the convention and arrangement during the friction measurements, as shown earlier in Figure 6.16.
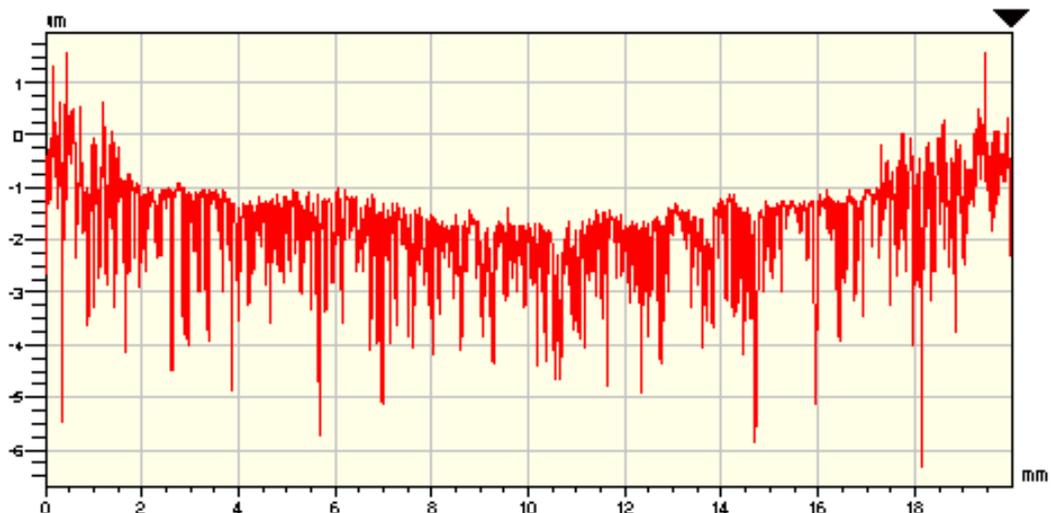
Figure 6.34: Typical measurement profile along the wear scar on a cylinder liner

For the measurement of the piston ring profile, the lens was aligned perpendicular to the vice top surface where the piston ring was clamped during the measurements. This allowed information on the offset of the piston ring profile to be obtained. The profile offset is the deviation of the profile radius centre from the centre of the piston ring, defining the highest point of the profile. For the analysis, no form-removal, like curvature and tilt, was applied to gain information on the profile radius and angular orientation to the piston ring side flanks. Figure 6.35 shows a typical ring profile of a worn piston ring. The piston rings were always oriented in the same way. The side which usually points towards top dead centre, TDC, is indicated by a chamfer on the back of the piston ring. The other side point towards bottom dead centre, BDC. The wear volume on the piston ring was established by subtracting the worn profiles from a new profile multiplied by the before mentioned length of the measured area.
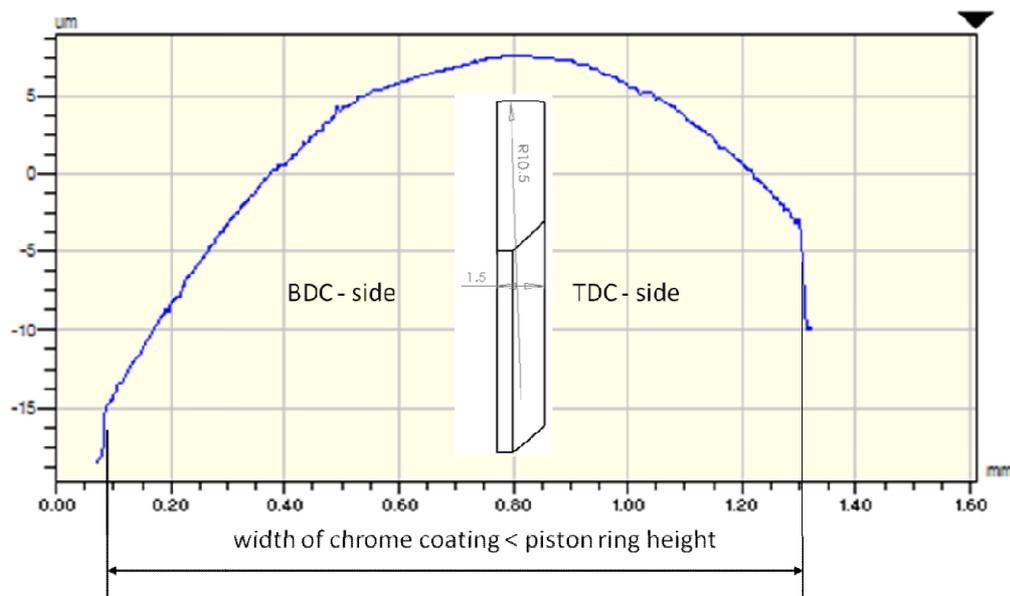
Figure 6.35: Typical measurement profile across a worn piston ring profile

6.5   Method: Surface Chemistry by FTIR-Microscopy

The liner samples with their cross hatched honing structure have a non homogeneous surface. Their inverse curvature does not allow them to be placed on the FTIR-ATR and they were therefore analysed by a FTIR-Microscope (PerkinElmer Spotlight 400). The microscope uses a PerkinElmer Spectrum100 as light source but has its own detector which needs liquid nitrogen as coolant. The microscope was used in reflectance

mode. Calibration and background scan was done using a gold mirror; a perfect reflector in the infra red region.

The sample was placed on a moveable stage. An optical microscope with CCD camera was used to focus on distinct areas where spectra shall be taken. The microscope can also scan defined areas to produce a map of material distribution. Figure 6.36 illustrates the possibilities of the FTIR-microscope. First an area can be examined with the light microscope and a larger area combined by stitching various images. Second, a defined area can be scanned with the IR beam and the resulting absorbance map correlates to the visual image. For every scanned pixel an FTIR spectrum is created. The FTIR spectra of a hole area can be averaged and viewed over the corresponding wavelength.
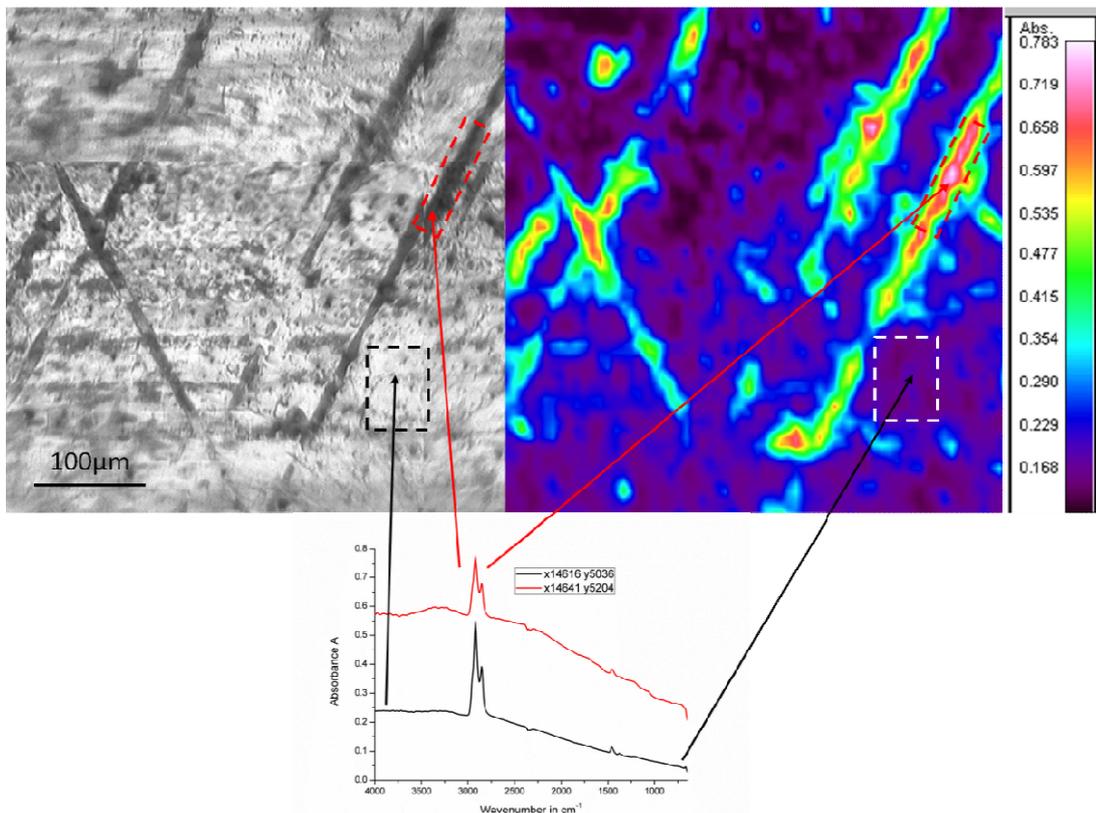
Figure 6.36: Typical result from a FTIR-microscope area scan. Comparison of visual stitched image, absorbance map and averaged spectra

The XPS study, section 6.6, resulted in a whole list of possible compounds on the cylinder liner surfaces. When a IR reference spectra of these compounds is available, it can be compared with the results from FTIR

spectroscopy. Figure 6.37 shows an FTIR spectrum of ferrous sulphate (NIST, 2011) contaminated with oil, one of the compounds found by XPS. This example shows also the restriction of the technique. Some peaks like the vibration of the Fe-O bond which is expected at 565 cm^{-1}, lay just outside the range of the usual Mid-IR spectrometers.
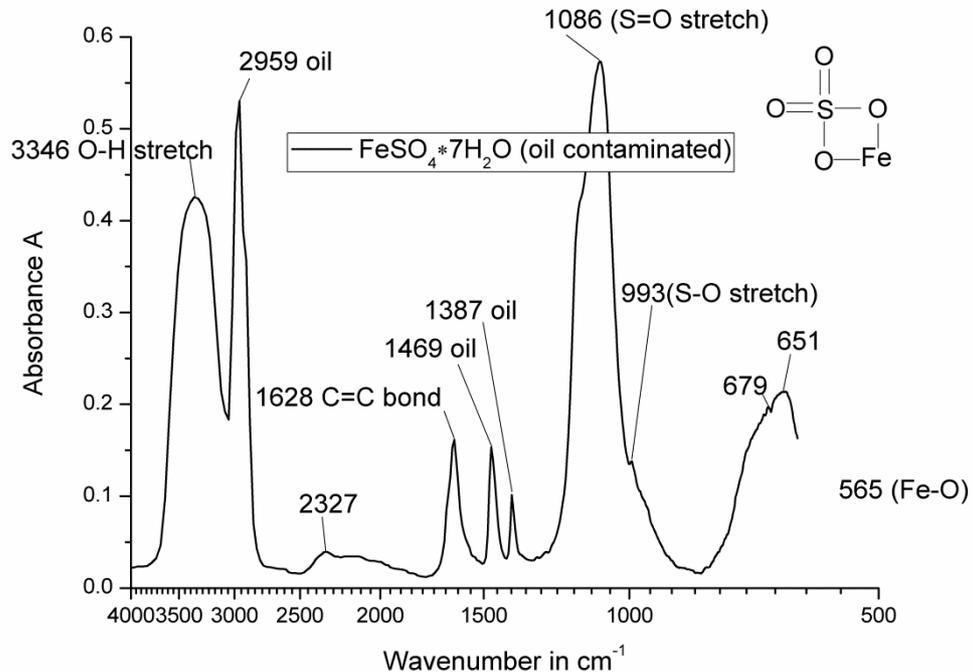
Figure 6.37: FTIR-spectrum of ferrous sulphate, FeSO$_4$·7H$_2$O, in oil (NIST, 2011), a compound suggested by the XPS results

6.6 Method: Surface Chemistry by XPS

X-ray photoelectron spectroscopy, XPS, was used to find chemical compounds in the boundary layer of the cylinder liner wear scar. In ultra high vacuum, the surface of the sample is irradiated with an X-ray beam. This causes electrons to be liberated from the element atoms in the surface by the photoemission effect. The characteristic kinetic energy of electrons causes the electrons to deviate from their path in an applied magnetic field. This deviation is measured by an electron counting array. The characteristic energy gives information about the irradiated substance elements and the electron count corresponds to the quantity of the elements in the surface. Chemical binding of elements cause a electron binding energy shift and therefore a peak shift in the spectrum (Zimmermann, 2010).

Overall, six samples were scanned by XPS. The scanning time was 19 hours which is the major drawback of XPS. The samples were cut out from the cylinder liner near the turning points by hand to avoid high temperature impact or contamination from organic cutting wheel binder or cooling liquid. The samples were cleaned by rinsing with heptanes for five seconds.

The long scanning time and the limited space on the sample holder reduced the amount of samples to six. A new liner sample was treated with the same alignment, storing, cleaning and cutting procedure and used as a reference to exclude misinterpretations due to possible contamination.

The scanning was undertaken over a spot of 500 µm which is sufficient to level out differences in the inhomogenious grey cast iron base substrate and the honing structure, which can be filled with deposit.

A quick survey scan was performed after loading the samples to find major element content. It was decided, to perform a survey scan for each sample and a more dense scan at the major element peak positions Fe2p3/2, Cr2p3/2, O1s, N1s, C1s and S2p3/2. The notation means: element name; electron shell number; sub-shell name; peak notation in case of spin orbital splitting.

The results were evaluated using an online XPS-database (Benoit, et al.). The peaks can appear within a certain band, overlapping with other bands and at one peak position, various compound correlations are possible. Therefore results from the database must be filtered for possibility and compared with other peaks. Ideally $FeSO_4$ would show a corresponding peak at Fe2p3/2, S2p3/2 and O1s. In case the S2p3/2 peak is missing, the compound might be iron oxide. Ideally $FeSO_4$ would also show a elemental ratio of 1Fe : 1S : 4O in atom %. However, the sample can be contaminated by Silicon for example, which would distort the ratio if not filtered out. The oxygen peak is also not very reliable as oxygen bonds are very common and peak shifts can originate from many sources.

6.7 Summary

In the present chapter the Plint TE77 Tribometer with piston ring – cylinder liner contact was analysed and the analytical techniques for lubricant and surface condition FTIR, XPS and white light interferometer presented.

The results of the methods introduced above are presented in the following chapter.

Chapter 7
Influence of Aqueous Sulphuric Acid on Tribological Parameters in a Piston Ring – Cylinder Liner Bench Test: Results

In this chapter, the results from the tests described in the previous chapter 6 are presented and conclusions drawn. The complexity of the arrangement, influencing parameters and large variety of analysis techniques required the presentation of the study in two parts.

7.1 Results and Discussion: Friction and Contact Potential

7.1.1 Result and Discussion: Reference Tests with SN600

Figure 7.1 shows the resulting average coefficient of friction before and after running-in and the corresponding average contact potential after running-in. In the beginning of the running in phase the contact potential, CP, shows 0 mV, indicating high metallic contact. After running-in, there is almost no metallic contact between the parts. Interesting to note is that the decrease in contact potential at higher temperature is due to a dip in midstroke, not in the turning points. During running-in the separation starts in midstroke. This indicates the influence of oil viscosity on part separation and a reduction in surface roughness. The electrical resistance of metals usually increases at increased temperatures, which might also have some influence on the difference. Therefore it must be stated that the contact potential measurement is very close for both temperatures as the surface chemistry is very similar as shown later in section 7.4. The influence of viscosity and surface roughness is also shown by the slightly increased coefficient of friction, $\Delta\mu = 0.014$, at higher temperatures after running-in and low metallic contact. The film thickness is reduced which increases the surface contact resulting in lower roughness values. In the beginning of the running-in, at the same surface roughness and high metallic contact, the influence of temperature dependent material properties can be found by subtracting the earlier described influence of viscosity ($\Delta\mu = 0.014$) from the resulting total difference, to find $\Delta\mu_{Tmat} = 0.069 - 0.014 = 0.055$. The Young's modulus reduces with increased temperature, resulting in a higher piston ring deformation and Hertzian contact area, chapter 6 section 6.2.7, thus bringing more asperities into contact.
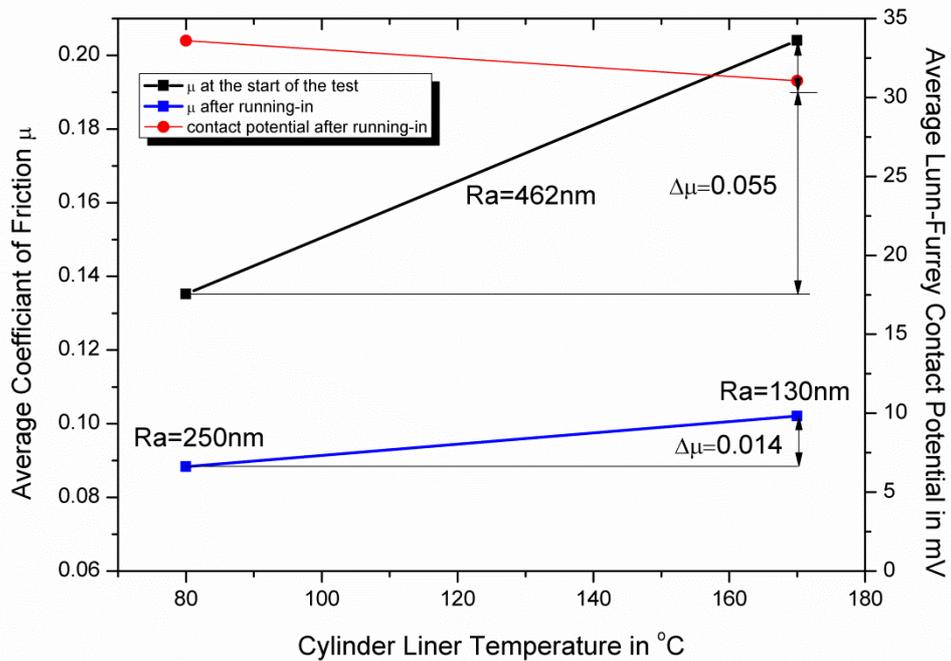
Figure 7.1: Coefficient of friction before and after running-in with SN600 and the corresponding contact potential measurement after running-in.

A malfunctioning temperature control unit caused a drop in temperature on some occasions. A sharp drop in temperature causes an increase in viscosity without changing the surface roughness. Figure 7.2 shows the influence of increasing viscosity on the coefficient of friction. The drop from 80 to 40 °C occurred just on the end of a running-in phase and the starting coefficient ($\mu_{80°C}$ = 0.097) is slightly higher than the value shown in Figure 7.1 ($\mu_{80°C}$ = 0.088). The drop from 170 to 80 °C ends at a lower value (0.072) than the other starting value, which can be explained by the differences in surface topography, which is $\Delta\mu_{Ra}$ = 0.025. If both surfaces were fully run-in, the difference would be $\Delta\mu_{Ra\_theoretic}$ = 0.088 - 0.072 = 0.016. The drop in coefficient of friction with increasing viscosity, indicates the lubrication regime to be elastohydrodynamic towards the mixed lubrication regime, despite the good separation of the parts found by the contact potential measurement. The viscosity was established using an average temperature formed from piston ring and liner temperature. The temperature dependent viscosity was measured using a Malvern "Kinexus" Rheometer with cone on plate arrangement at a shear rate of 1000 s^{-1}, chapter 3. The Lunn-Furey contact potential indicates a slight touching of roughness peaks. The sum of the measured peak heights from the mean, R_p, for piston ring and liner

surface combines to 1.3 µm for 80 °C and 1.1 µm for 170 °C. In the mixed to elastohydrodynamic lubrication regime, this is a reasonable value for oil film thickness (Priest, 2009). The average speed of the test bed is 0.43 m/s, resulting in a shear rate of 3.3 - $3.9*10^5$ s^{-1}.
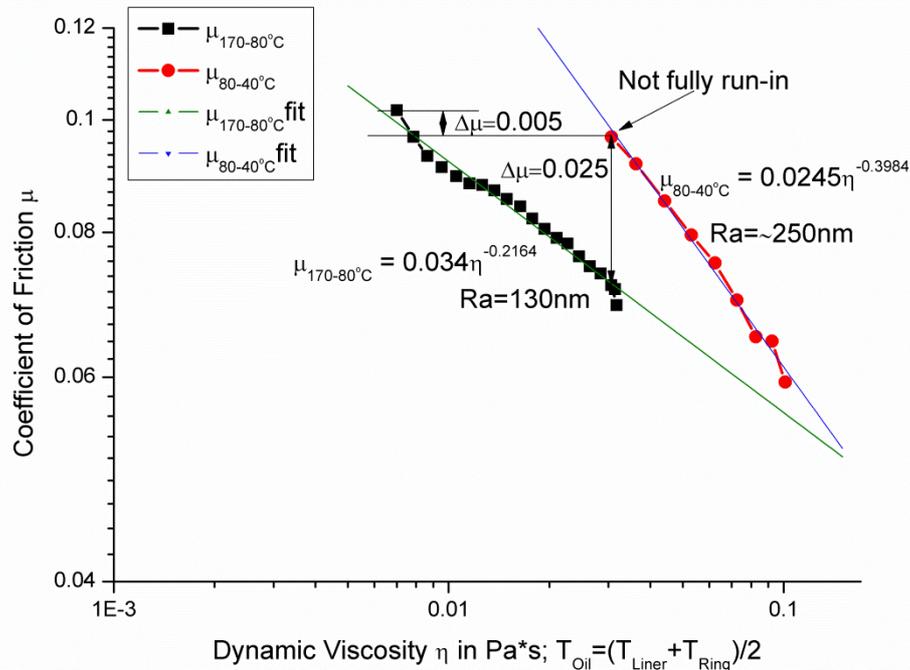
Figure 7.2: Influence of viscosity on the coefficient of friction, measured by dropping the temperature on two run-in surfaces with different surface roughness's, lubricated with SN600.

Squalane was predicted to exhibit shear thinning behaviour when exceeding a shear rate of $\sim11*10^{10}$ s^{-1} (Jabbarzadeh, et al., 2002) while showing a linear increase of viscosity at low shear rate by ~5 Pa*s at 65 °C when pressures increased from ambient to 1.25 GPa (Jansen, et al., 2001). A simulation using the software package Mahle – Summits (V3.2010) & VTL (V3.8) (Tomanik, 2004),(Tomanik, 2008) with SAE40 oil at 80 and 170 °C predicts maximum hydrodynamic pressures of 61 and 33 MPa resulting in maximum viscosity pressure corrections of 123 and 24 %. The viscosity corrections for shear thinning are within ±2 % for resulting maximum shear rates of $7.2*10^6$ and $19.3*10^6$ s^{-1}. The significant influence of hydrodynamic pressure on the viscosity must be noted but was not incorporated as the non - homogeneous lubrication gap, as shown in the previous chapter, cannot be reflected by the two dimensional simulation. An average temperature across the lubrication gap was used to establish the viscosity rather than an average viscosity from each part temperature, as the latter would overrate

the lower temperature because viscosity decreases exponentially with temperature.

The information gained from the drop in temperature can later be used to distinguish between influence of viscosity and surface active substances when fully formulated lubricants are used, which have a higher viscosity than the reference oil. The reduction of friction due to the increased Young's modulus at lower temperatures is not taken into account for this assumption. However, the contact potential indicates very little surface contact, which on the other hand could also result from isolating oxide layers.
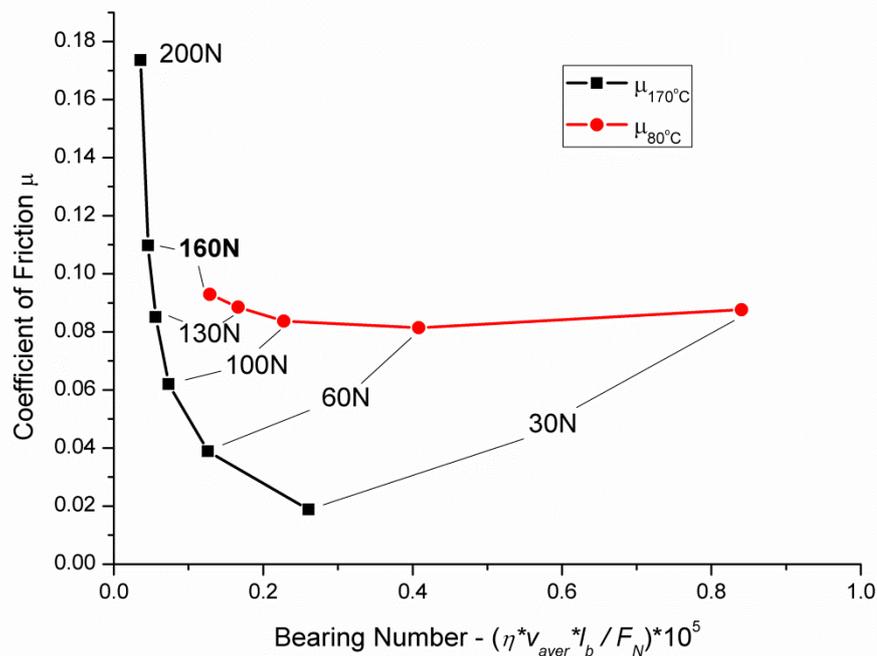
Figure 7.3: Partial Stribeck diagram for piston ring cylinder liner contact lubricated with SN600 at 80 and 170 °C.

Instead of changing the viscosity in a contact, the load can be varied to find the lubrication regime given by the Stribeck diagram. Figure 7.3 shows the coefficient of friction plotted over the bearing number for varying loads. The bearing number combines viscosity η with slider speed v and load F_N applied over the wetted piston ring circumference l_b. Also this diagram shows, that the lubrication regime for the reference test at an applied load of 160 N is elastohydrodynamic towards the mixed lubrication regime. At both temperatures, the coefficient of friction decreases with decreasing load which increases the film thickness and decreases the surface contact area. For 80 °C a minimum is found at 60 N and the coefficient of friction

increases due to hydrodynamic friction for lower loads. The tests were both commenced from 160 N towards lower loads which keeps the surface topography stable, therefore a difference between the curves of $\Delta\mu_{Ra160N}$ = 0.017 can be seen in good agreement with the earlier findings. At 170 °C a point at 200 N was added and recorded after the coefficient of friction was stabilised.

7.1.2 Result and Discussion: Tests with SN600 + H$_2$SO$_4$

For the impact on lubricant chemistry and to find most interesting acid concentrations, a screening test was undertaken over the whole range of concentrations. Figure 7.4 shows the effect of acid concentration on the coefficient of friction, mainly at 80 °C. It is pointless to perform tests with low acid concentrations at increased temperatures and ambient pressure, as the aqueous phase would boil, increase the acid concentration but lose volume. Previous tests have also shown, that an impact on the oil starts at 40 %w/w H$_2$SO$_4$. To be sure, the main tests were performed with 70 %w/w H$_2$SO$_4$. However the screening tests showed a clear impact on the coefficient of friction at 40 %w/w.
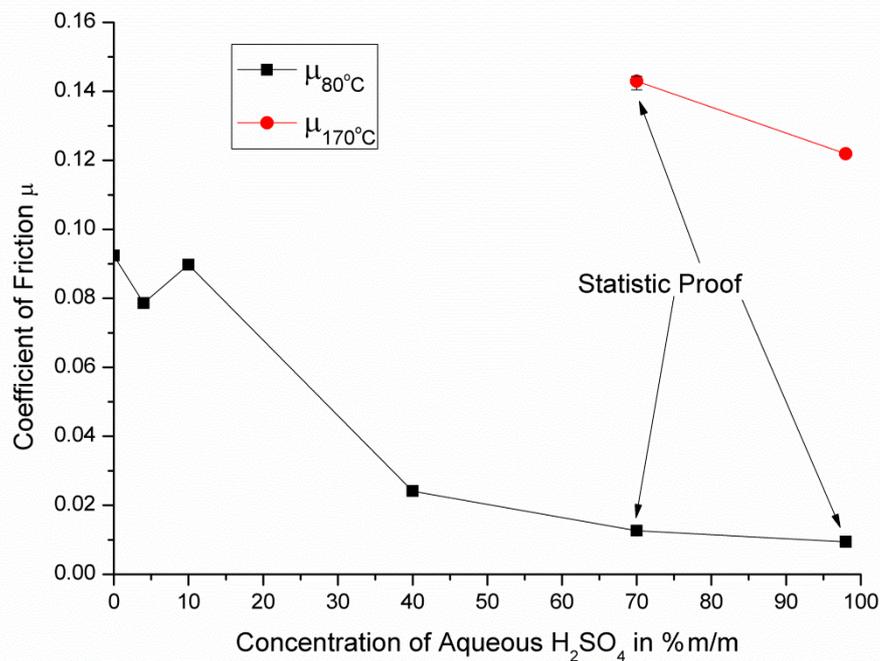
Figure 7.4: Coefficient of friction for various concentrations of aqueous H$_2$SO$_4$ dispersed in SN600 at 80 and 170 °C

As mentioned earlier, the geometry of the contact changes over the test duration due to wear. Furthermore, operating in corrosive media was expected to increase the contact area considerably. Therefore "shuttle tests" were done and the lubricant switched during running. Figure 7.5 shows the outcome of one shuttle test between SN600 and SN600+70%H_2SO_4 at 80 °C. The coefficient of friction drops almost instantly after switching to a acid containing lubricant, so quick in fact that a reduction in friction due to changed contact geometry can almost be excluded. The surface roughness also increases when operating with acid containing oil, which should increase friction and not lower it. When switching to acid containing oil, the contact potential also drops quite sharply but recovers after a short period of time. A possible explanation is the release of ions in the beginning and the formation of a non-conducting boundary layer with superior low friction properties as it is observed when adding friction modifiers like oleic acid to the lubricant (Harnoy, 2005). The impact of wear and modification of the boundary film chemistry is indicated in Figure 7.5.
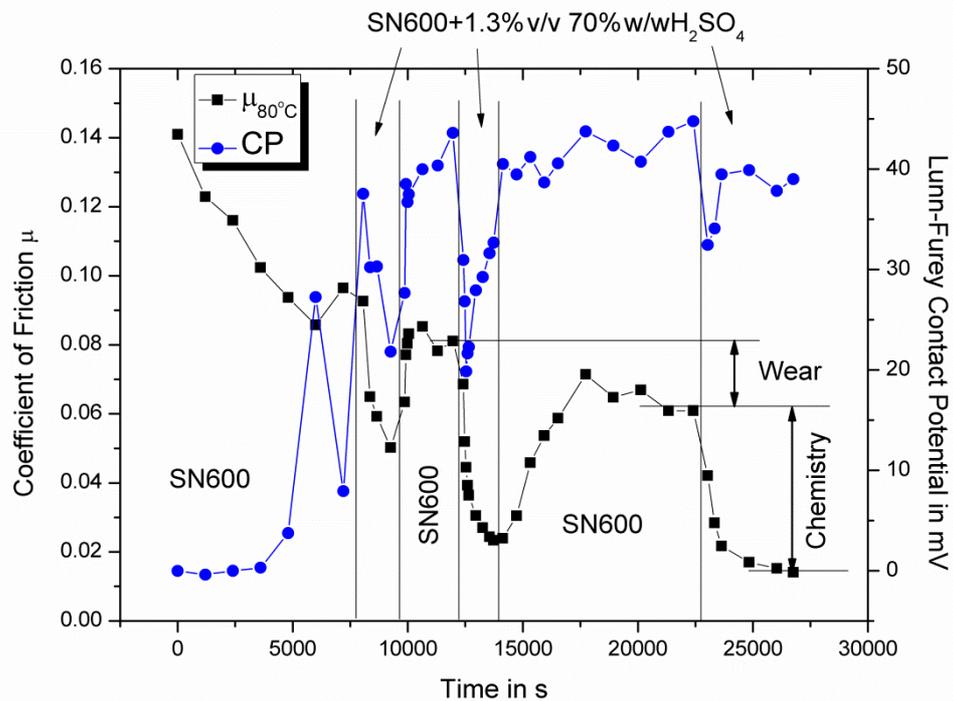
Figure 7.5: Shuttle test between pure SN600 and SN600 + 70 % H_2SO_4 at 80 °C, revealing the influence of wear and chemistry on friction

A shuttle test with the same lubricant was also undertaken at 170 °C and the outcome is shown in Figure 7.6. Instantly after switching to acid containing lubricant, the contact potential drops, possibly by the release of ions and the

friction increases significantly. Visually, the formation of black deposit was observed on the cylinder liner wear scar. After switching back to pure SN600, the friction slowly decreases while the contact potential stays at a high level. The repeated switch to acid containing lubricant again creates a drop in contact potential. This suggests that the deposit has worn flush with the metal roughness peaks.
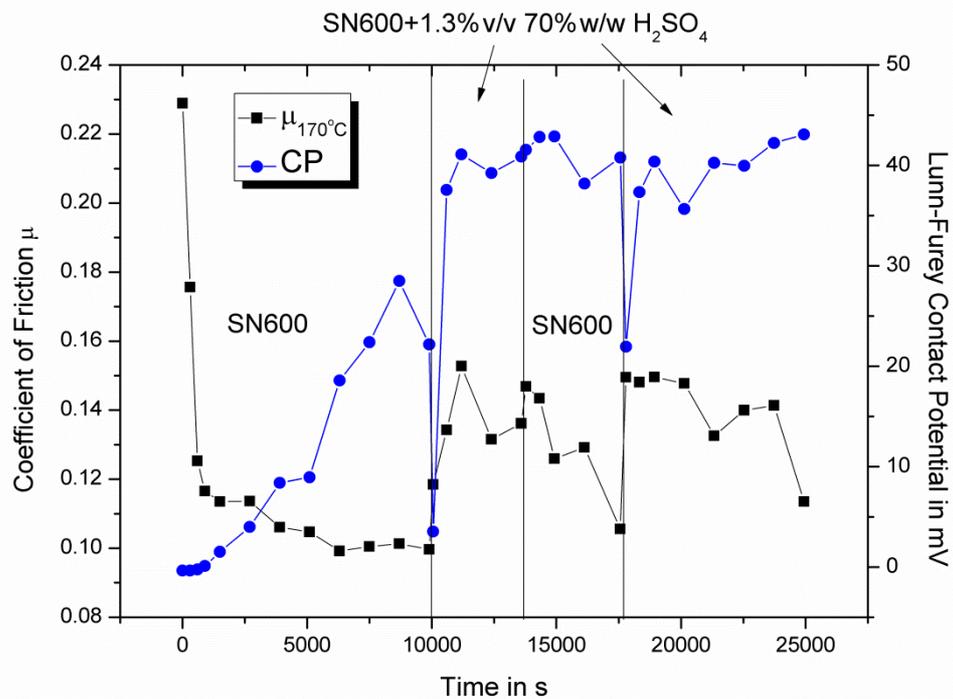
Figure 7.6: Shuttle test between pure SN600 and SN600 + 70 % H$_2$SO$_4$ at 170 $^{\circ}$C showing higher friction due to lubricant degradation

Figure 7.7 compares the temperature dependency of the coefficient of friction when running with pure SN600 and when 70 %w/w H$_2$SO$_4$ is dispersed in the oil. Also the measured cylinder liner surface roughness at the end of similar tests is indicated to exclude smoothening effects. The surfaces exposed to acid show a higher roughness at low temperatures while being smoother at high temperatures. This is counterintuitive to the measured coefficient of friction. When the temperature is increased, the coefficient of friction stays constant until 120 °C where visually the formation of deposit on the cylinder liner wear scar was observed. At about 140 °C, the friction exceeds the values found for pure SN600. The contact potential shows a good electrical separation for all conditions other than running-in. However, when deposit formation sets in, the contact potential is approaching its maximum value.

An attempt was made to understand the nature of the low friction contact by varying the load. Decreasing the load, increases the coefficient of friction, which indicates potentially a still elastohydrodynamic lubrication regime but towards the hydrodynamic side.
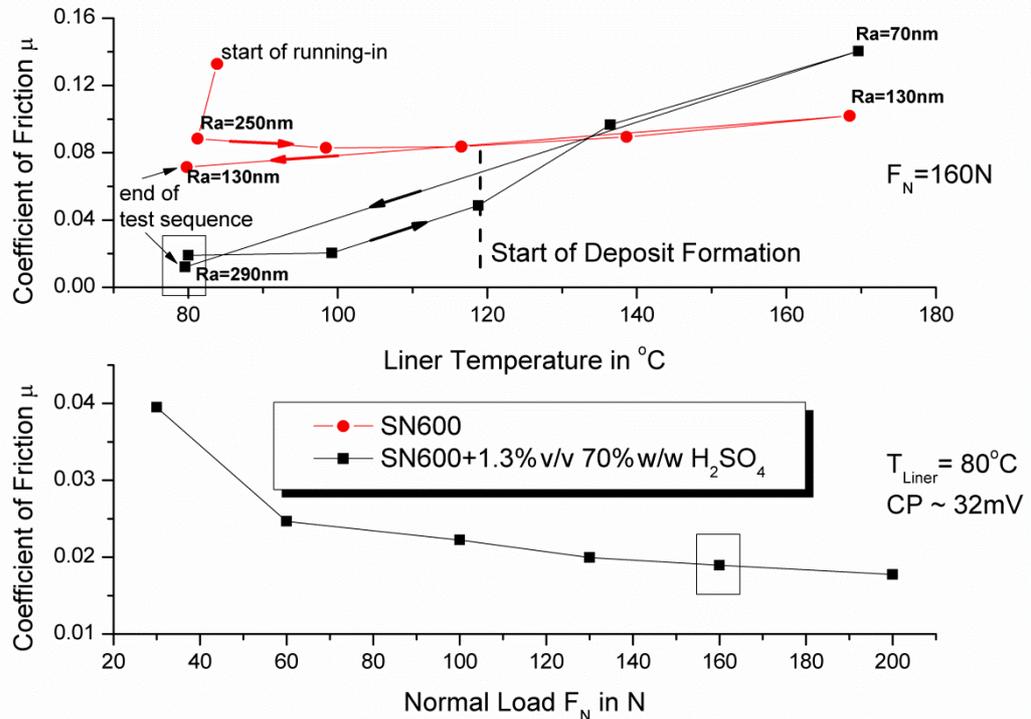
Figure 7.7: Influence of temperature and load on the coefficient of friction for pure and acid contaminated base oil SN600.

7.1.3 Result and Discussion: Tests with SN600 + H₂SO₄ and Fully Formulated Lubricant at 170 °C

Two fully formulated lubricants were tested to compare their performance against pure base oil. Their coefficient of friction was found to be comparably high with $\mu_{Lub.A}$ = 0.17 and $\mu_{Lub.B}$ = 0.15 when running them pure at 170 °C. To find how they react to diluting with SN600, which reduces the viscosity and the concentration of additive, and to see the influence of sulphuric acid, shuttle tests were performed with various combinations of lubricants. The fully formulated lubricants were always fed at the BDC side of the piston ring, while pure SN600 and acid containing SN600 was always fed at the TDC side of the piston ring – a situation typical for the engine. The results for one shuttle test are shown in Figure 7.8. Running-in was undertaken with SN600 and lubricant A. During the first 2500 seconds, the running-in shows no difference to running-in with pure SN600 and the coefficient of friction

drops steadily due to smoothing of the surfaces. Suddenly, the coefficient of friction rises and the contact potential measurement signals a complete separation of the parts. The separation is too perfect to be a plain hydrodynamic separation and the friction values are rising instead of dropping as expected for the lubrication regime, see 7.1.1. Therefore it must be assumed, that a $CaCO_3$ boundary film (Giasson, et al., 1994) has formed which electrically isolates the parts and has high friction properties. After 6540 seconds it was decided to switch to pure SN600. During the subsequent 1000 seconds, the coefficient of friction steadily drops, while the parts remain perfectly separated. Instantly after adding Lubricant A again, the coefficient of friction rises again. One explanation for this behaviour is that the boundary film was not completely worn down by the SN600 but a layer of surface active substances, physically adsorbed onto a chemically attached boundary layer was washed away. The physical layer of surfactants quickly reformed when lubricant A was added again. When running lubricant A on its own, the coefficient of friction stays at the same level, supporting the hypothesis that viscosity has no or neglectable influence on the coefficient of friction.
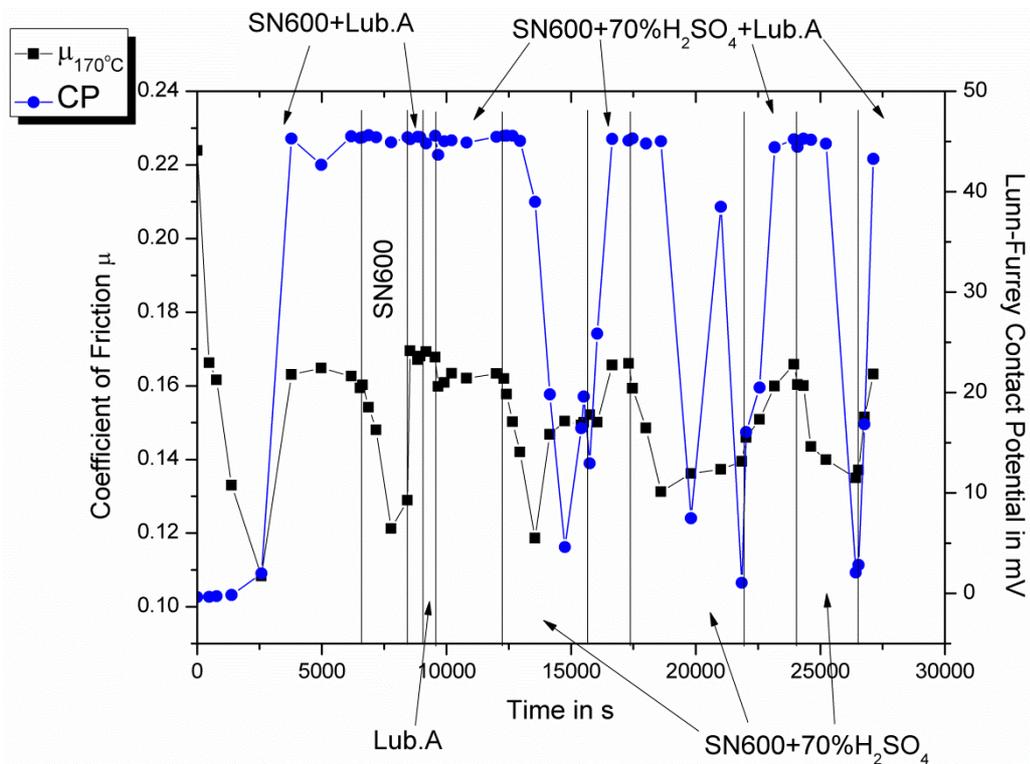
Figure 7.8: Shuttle test between SN600, lubricant A and 70 %w/w H_2SO_4 dispersed in SN600 at 170 °C revealing the influence of lubricant additive on friction.

After running on pure lubricant A, acid containing SN600 was added to the running test. A tiny dip in the contact potential measurement is observed which recovers instantly while a small but constant reduction in friction is observed. A probable explanation is the neutralisation of the acid by the additives in the oil which slightly depresses the constant re-formation of the boundary layer or some of the surfactants are used up by the acid droplets.

After a test duration of 12000 seconds, the feeding of lubricant A is switched of and the test ran on acid containing SN600. With the same rate as seen before, the coefficient of friction drops, possibly due to the mechanical removal of a physical bound surfactant layer. With a time delay of 950 seconds, the contact potential also drops, indicating metallic contact. After a considerable drop in contact potential, suddenly the friction increases again and visually the formation of black deposit can be observed on the wear scar. This causes the contact potential to rise again, just as shown in section 7.1.2. During 950 seconds, the boundary layer is removed by the acid. When the acid is not neutralised anymore, the acid acts more heavily on the oil to form deposit.

When adding lubricant A again, the contact potential drops due to some removal of loosely bound deposit or viscous bituminous matter as formed between oil and acid, chapter 4. During the subsequent 900 seconds, the boundary film is completely formed again and the friction returns back to its former high value.

The observations were repeatable until the end of the test and also hold for lubricant B. Both lubricants are capable of suppressing the formation of black deposit but cannot remove deposit already formed from the wear scar.

7.2 Results and Discussion: Piston Ring Surface Condition After the Tests

The severity of the test conditions is illustrated by Figure 7.9 and Figure 7.10. Both surfaces ran for 6.5 hours lubricated with SN600 at 80 and 170 °C and show clear signs of severe adhesion to the cylinder liner. The surface was not analysed for its chemical composition but dark marks on the wear scar of chrome coated piston rings ran against grey cast iron liners were analysed in the past and found to mainly consist of iron (Zima, 2005).
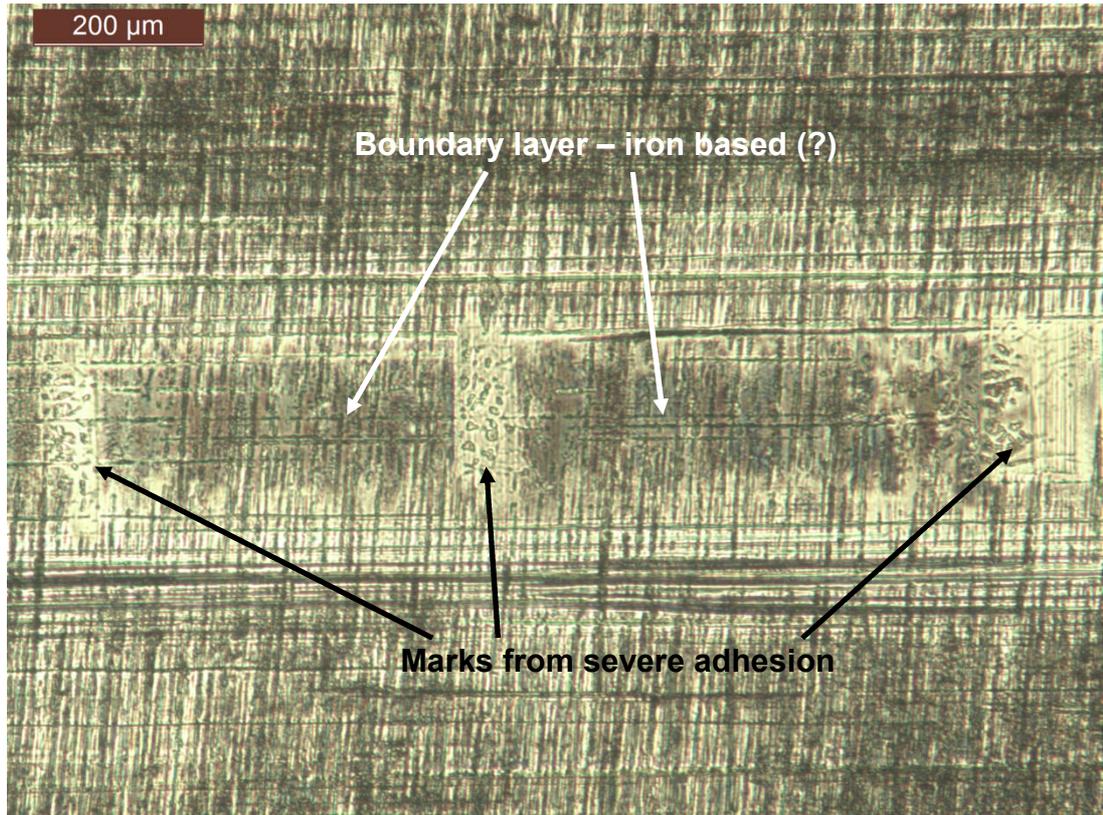
Figure 7.9: Piston ring wear scar, test 8, lubricated with SN600 at 80 °C
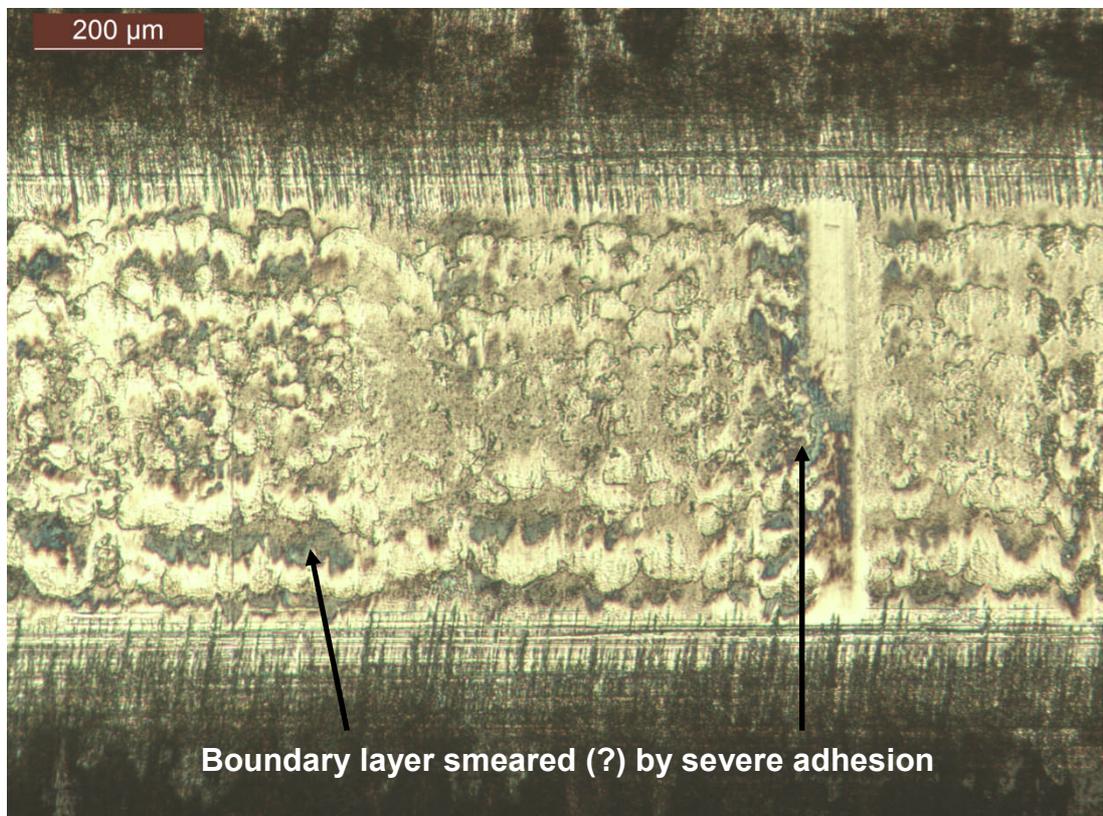
Figure 7.10: Piston ring wear scar, test 13, lubricated with SN600 at 170 °C

Figure 7.11 shows a piston ring which was run-in at 80 °C, followed by a steady temperature increase up to 340 °C. The visual appearance is quite good compared to Figure 7.10. The running-in with moderate temperature seems to have a good influence on the surface development. Outside of the wear scar a loosely bound deposit from degraded lubricant was built up.

Figure 7.12 shows a piston ring after running at 80 °C with a mixture of SN600 and 70 % H_2SO_4. The wear scar shows some localised pitting but is otherwise very smooth and does not show any signs of hard contact with the liner. Outside of the wear scar, the machining marks disappear, most probably due to corrosive attack and the profile measurements show considerable deviation from the original shape.

The piston ring shown in Figure 7.13 ran with the same lubricant acid mixture as the one before but at an increased temperature of 170 °C. The pitting on the wear scare are smaller and seem to be situated mainly in machining grooves. Figure 7.14 shows an enlarged view on the pitting. They are not correlated to the fine crack network, which is also visible in Figure 7.14. The appearance of pitting can be explained by the tendency of more stationary acid droplets on the chrome coating, chapter 5. This is in opposition to self-sustaining 'pitting corrosion' by oxygen depletion in a continuous aqueous phase (Bargel, et al., 1999) and was not observed in this form during the contact angle measurements under static conditions, chapter 5 with sulphuric acid on chrome, but only with water on grey cast iron. To the sides of the wear scar, a dense and well bound deposit from degraded lubricant built up. The shape of the piston ring profile is considerably changed by the deposit, creating a larger radius as shown by profile measurements.

Figure 7.15 and Figure 7.16 show piston ring surfaces after the shuttle tests with fully formulated lubricant B. The main difference is the finish time of 53 and 8 minutes where both piston rings ran with the addition of the fully formulated lubricant after running purely on acid containing lubricant for 50 minutes. While Figure 7.15 shows a piston ring surface which is similar to the harsh conditions created by the reference test with pure base oil, Figure 7.10, Figure 7.16 shows a smooth and healthy looking surface without any traces of hard running. The shuttle test with lubricant A, Figure 7.8, ended just after forming of a boundary film and the surface starts to look similar to Figure 7.15. Round shaped patches on the wear scar of Figure 7.16 are possibly caused by acid droplets resting on the fresh formed calcite

boundary layer, starting to dissolve it. To the sides of the wear track deposit built up when the contact was lubricated with acid containing base oil only.
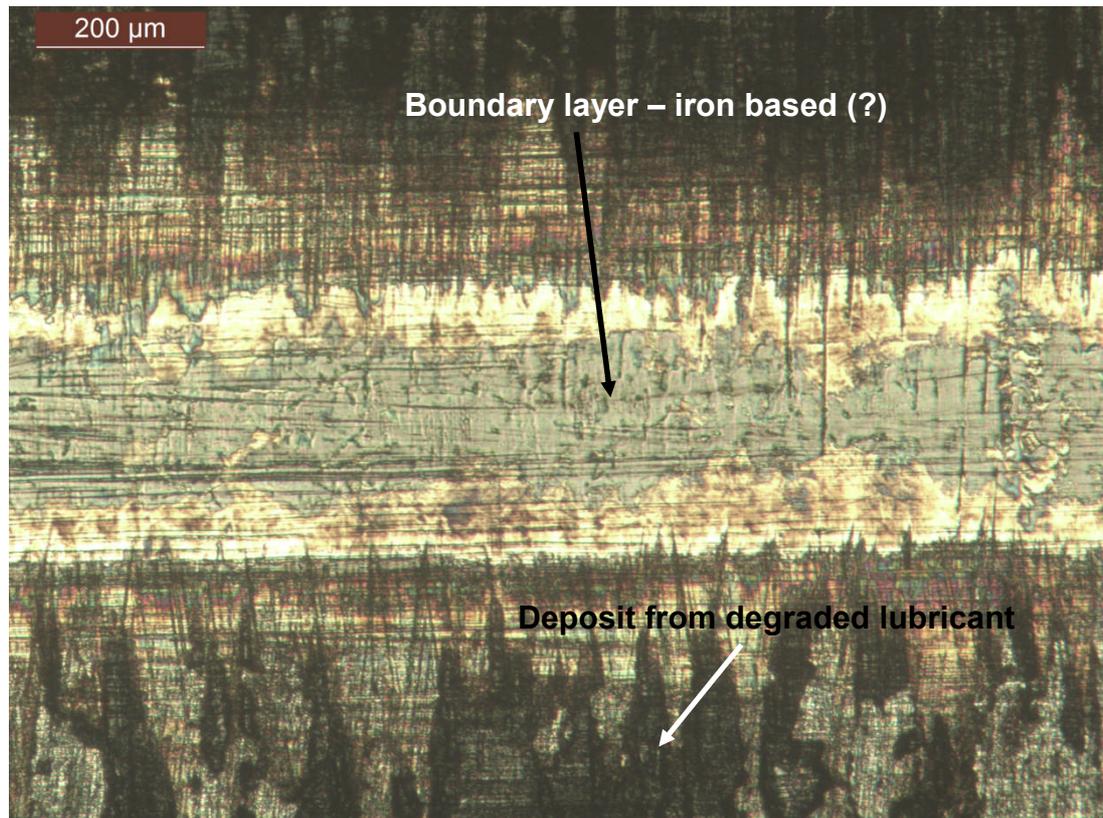
Figure 7.11: Piston ring wear scar, test 21, lubricated with SN600 from 80 to 340 °C
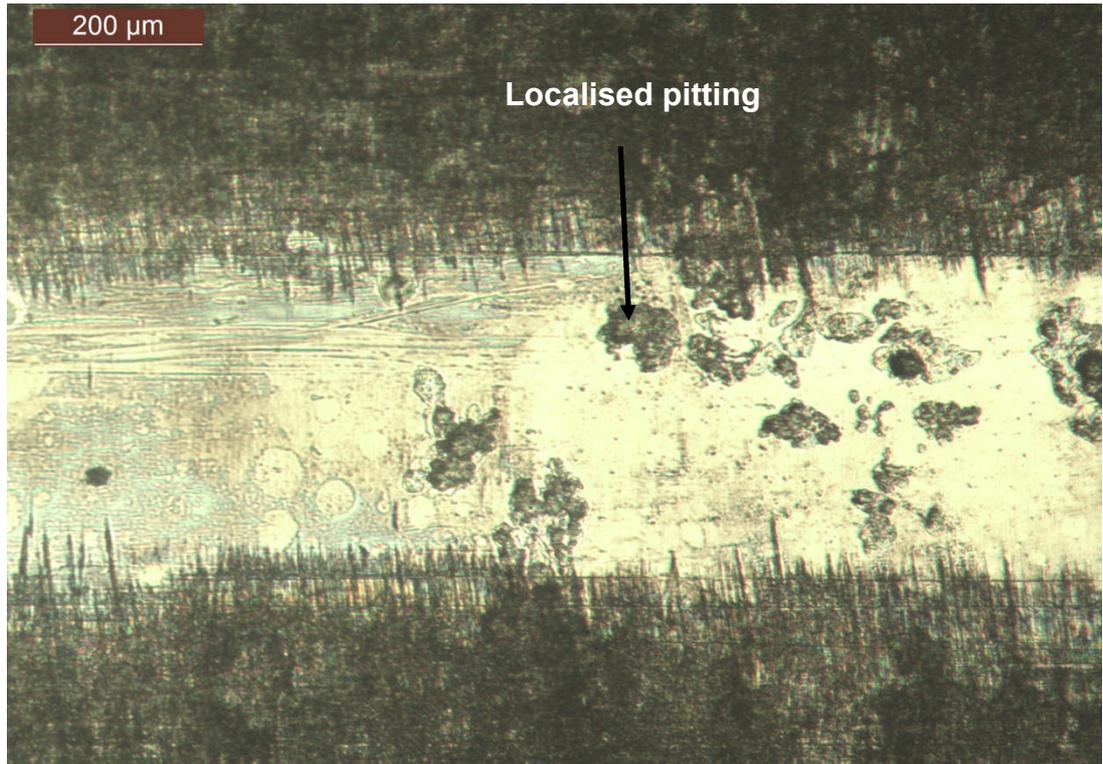
Figure 7.12: Piston ring wear scar, test 10, lubricated with SN600 + 70 %w/w H$_2$SO$_4$ at 80 °C
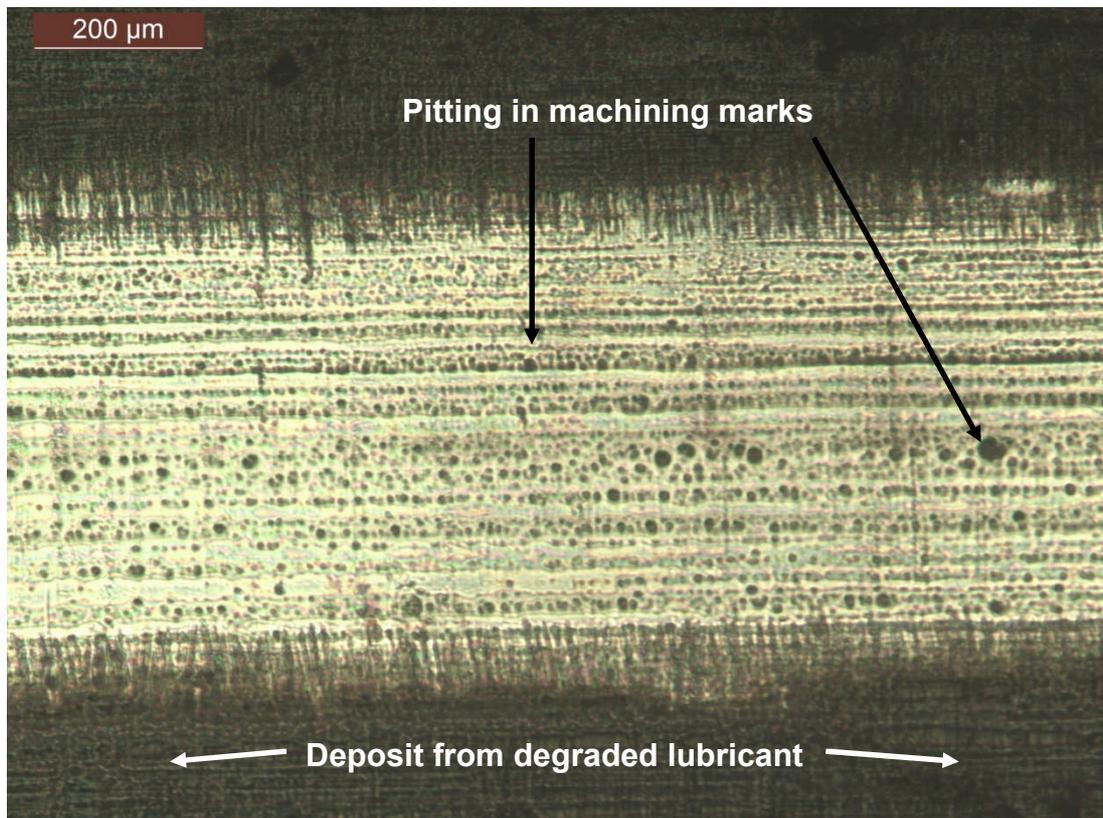
Figure 7.13: Piston ring wear scar, test 12, lubricated with SN600 + 70 %w/w H$_2$SO$_4$ at 170 °C
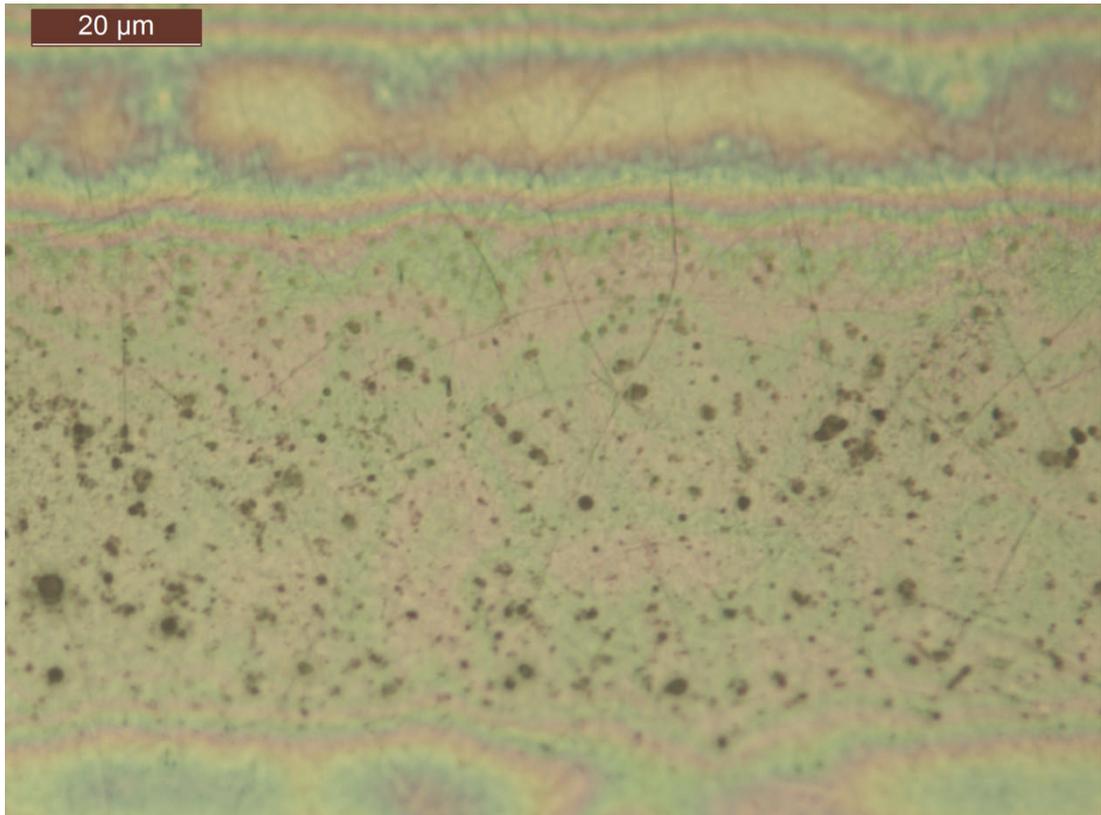
Figure 7.14: Piston ring wear scar, test 12, lubricated with SN600 + 70 %w/w H$_2$SO$_4$ at 170 °C
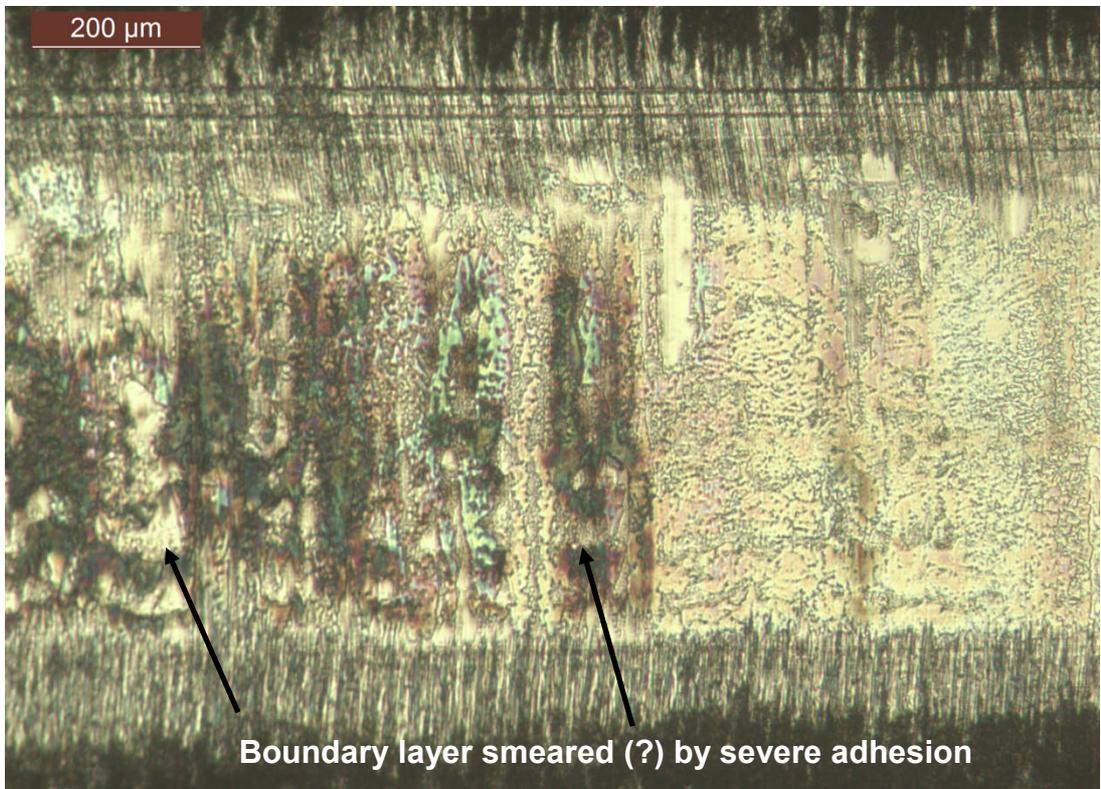
Figure 7.15: Piston ring wear scar, test 18, lubricant B & SN600 + 70 %w/w H$_2$SO$_4$ at 170 °C. Test finished after an 53 minute period of adding lubricant B.
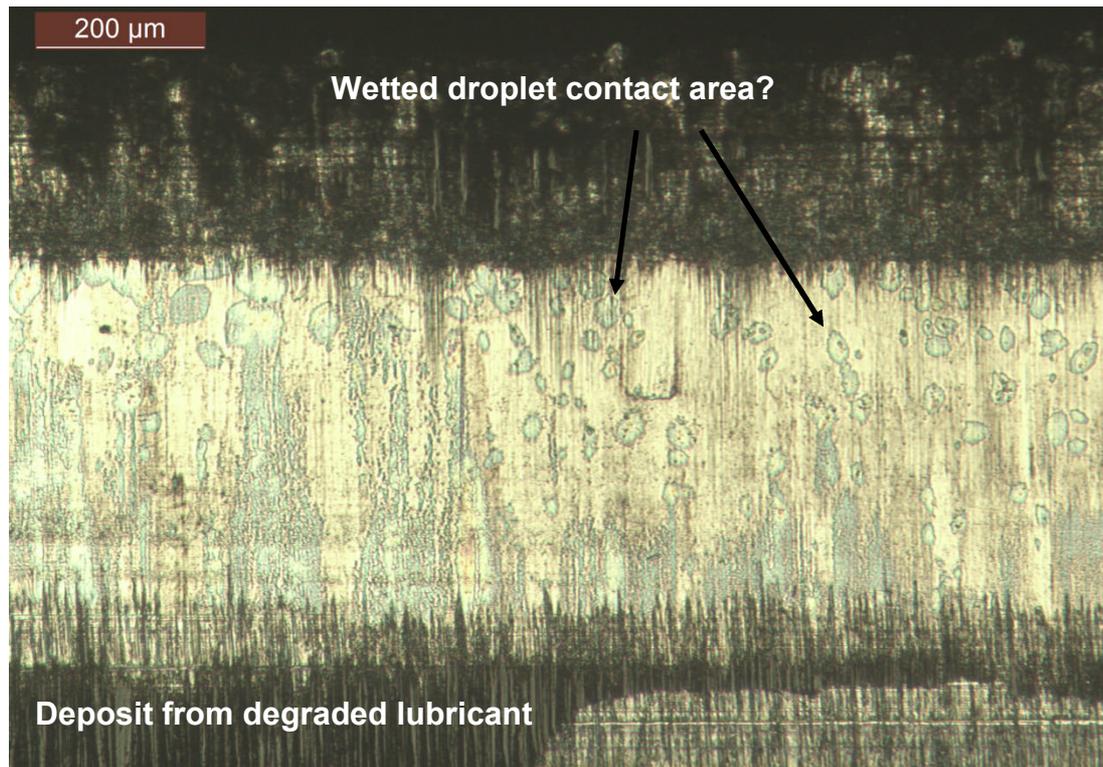
Figure 7.16: Piston ring wear scar, test 19, lubricant B & SN600 + 70 %w/w H$_2$SO$_4$ at 170 °C. Test finished after an 8 minute period of adding lubricant B.

7.3 Results and Discussion: Lubricant Chemistry by FTIR-ATR

Figure 7.17 shows SN600 with a water content of 1.3 %v/v which was used to lubricate the piston ring cylinder liner contact. The peak at 3404 cm^{-1} originates from an O-H stretch and indicates the presence of water. At 80 °C cylinder liner temperature, the water is completely removed from the lubrication oil. Therefore it was decided to lower the temperature but also at 30 °C almost all water is removed from the lubricant. At 30 °C and only 30 N of normal load applied some water is found on the TDC and BDC side. The loss of water is most probably caused by evaporation which is enhanced by local high temperature spots due to friction in combination with low, sub ambient pressures in the lubrication oil film. In Figure 7.18, the hydrodynamic pressure distributions for the test conditions are shown. The results were obtained using the software package Mahle – Summits (V3.2010) & VTL (V3.8) (Tomanik, 2004), (Tomanik, 2008) with SAE40 viscosity grade solving Reynolds equation with Swift-Steiber boundary conditions. Sub ambient pressures were not calculated but drawn for pure illustration purpose by hand after discussion with several experts. The

change in applied load was not found to influence the hydrodynamic pressure distribution, therefore only the results for 30 N are shown. At 80 °C, 0.5 % of the load is carried by asperity contact. The condition for gaseous cavitation is given in both cases because the hydrodynamic pressure drops sharp and is cut off by the set boundary conditions at ambient, which is not a natural behaviour. The program code assumes that gaseous cavitation relaxes sub ambient pressures instantly when reaching ambient atmospheric pressure. For engineering purposes this is a fair assumption as the bearing load is carried by far higher pressures. The growth of the gas bubbles, however, is not arbitrary fast and pressures can fall below ambient for a short time. Cavitation compared to dissolution of air into oil is a very fast process and the hydrodynamic pressures can drop further when the oil film is degassed over time on the reciprocating test rig. It is well possible that the vapour pressure of water is reached. The water dew point is more likely to be reached in case of the higher oil film temperature. The faster drop of the maximum pressure in the case of 80 °C has a higher impact on the increase of the local oil film temperature as the heating power from the drop in pressure is proportional to the pressure relaxation per time unit thus increasing the chance for water evaporation.
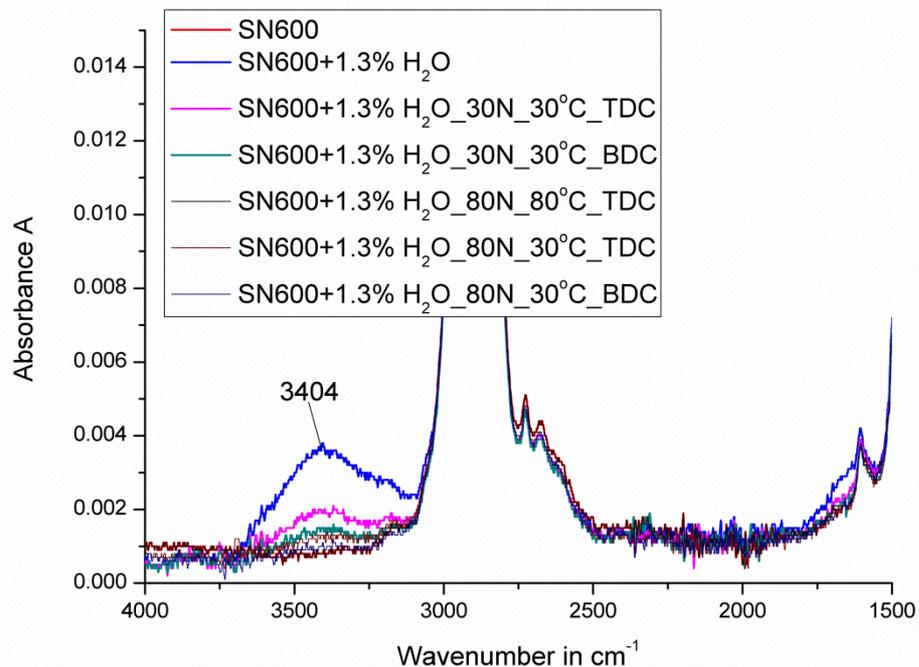
Figure 7.17: FTIR-ATR spectra of SN600+1.3%v/vH$_2$O, fresh and sampled during the friction test at 80 and 30 °C. Test no. 3.
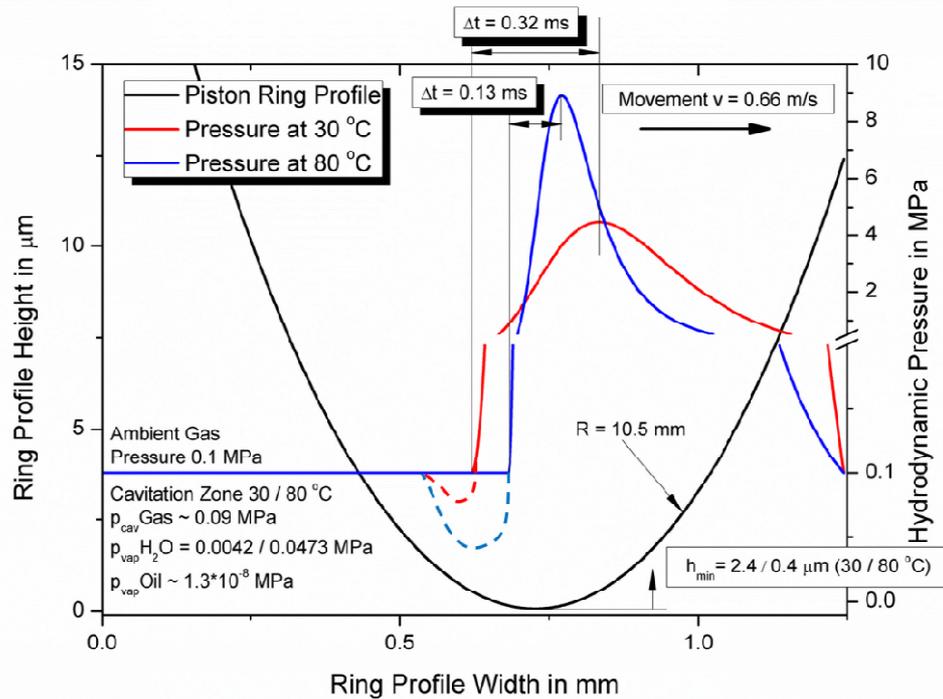
Figure 7.18: Hydrodynamic pressure distribution below a moving piston ring profile at 30 and 80 °C with an applied load of 30 N.

The higher minimum oil film thickness h_{min} in the case of 30 °C eases the passing of water droplets through the lubrication gap. Some of the water might also react with the iron surface of the liner to form Feroxyhyte, FeO(OH), chapter 5, but this reaction is quite slow. More water is lost to the BDC side of the piston ring than to the TDC side, which is the side where new lubricant is continuously fed.

For 10 %w/w H_2SO_4, Figure 7.19, no remaining acid can be found on either side of the piston ring. However, both curves are lifted in absorbance, which might be caused by dispersed fine wear particles in the oil from corrosion. The curve of the oil sampled at TDC shows a slightly higher absorbance.

For 40 %w/w H_2SO_4, Figure 7.20, all peaks caused by H_2SO_4 disappeared and contrary to the previous observation, the lubricant sampled from BDC shows a slightly higher absorbance.

For 70 %w/w H_2SO_4, Figure 7.21, the peaks caused by H_2SO_4 are still recognisable and in the same position but quite surprisingly the absorbance of the oil sampled at BDC exceeds the absorbance for the fresh oil. The test was repeated to exclude sampling mistakes and was found to be repeatable. As shown in chapter 3, the absorption of water from the ambient air can be

excluded, as the peaks would change their position in the case of dilution. Increased oxidation, indicated by the peak at 1709 cm^{-1} could be a plausible cause.

Also for 98 %w/w H$_2$SO$_4$, Figure 7.22, the peaks caused by H$_2$SO$_4$ are still recognisable. A slight shift of the peak at 1032 cm^{-1} to 1045 cm^{-1} and from 1683 cm^{-1} to 1735 cm^{-1} can be observed. An additional peak is created at 1205 cm^{-1} and an O-H stretch at 3399 cm^{-1} is present, which it should not be for concentrated H$_2$SO$_4$. Quite surprisingly, the absorbance of the oil sampled in BDC exceeds the absorbance for the fresh oil. Lubricant oxidation is one explanation for the increased absorbance.

Figure 7.23 shows oil sampled during tests with a fully formulated lubricant. The sample was extracted from the BDC side of the piston ring. Peaks caused by sulphuric acid disappear and peaks present in the fully formulated oil disappear as well which can both be explained by the neutralisation of the sulphuric acid by the additive package in the fully formulated lubricant. However, one would expect the appearance of new peaks caused by the reaction products, namely originating from CaSO$_4$ but this is not the case.
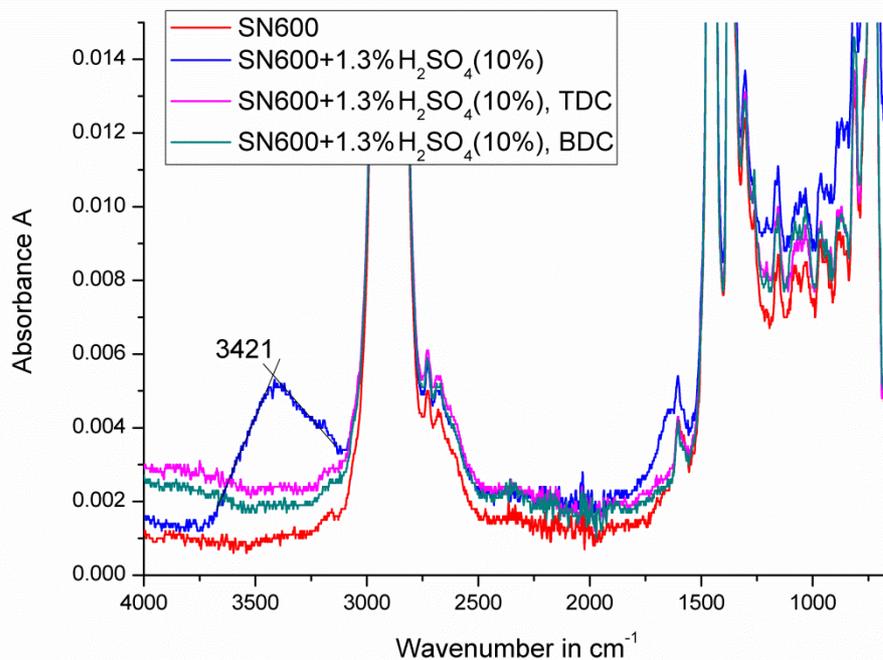
Figure 7.19: FTIR-ATR spectra of SN600+1.3%v/v10%w/wH$_2$SO$_4$, fresh and sampled during the friction test at 80 °C. Test no. 5.
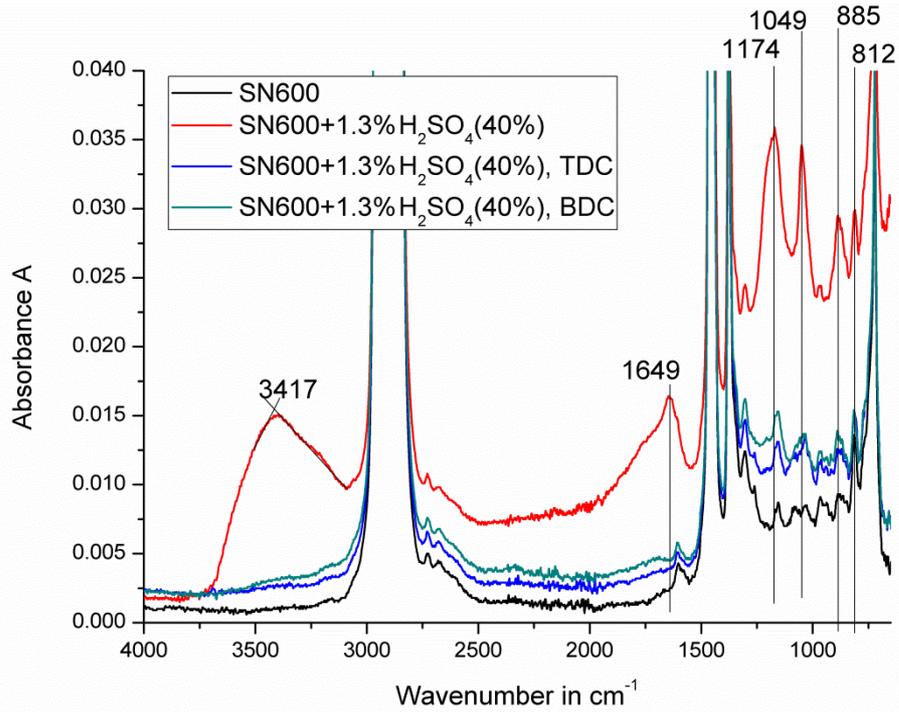
Figure 7.20: FTIR-ATR spectra of SN600+1.3%v/v40%w/wH$_2$SO$_4$, fresh and sampled during the friction test at 80 °C. Test no. 6.
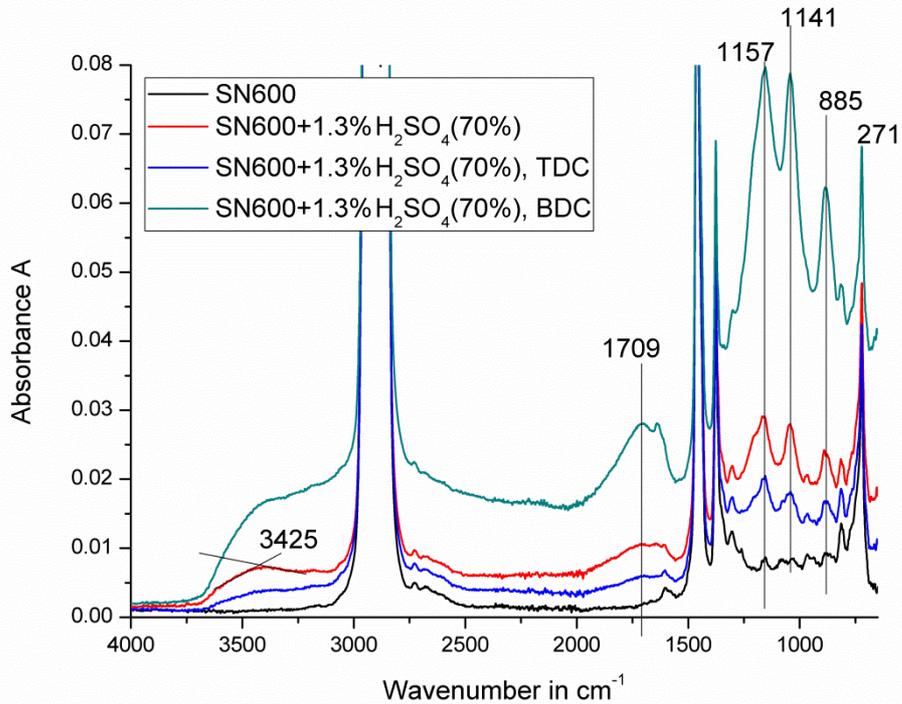
Figure 7.21: FTIR-ATR spectra of SN600+1.3%v/v70%w/wH$_2$SO$_4$, fresh and sampled during the friction test at 80 °C. Test no. 7.
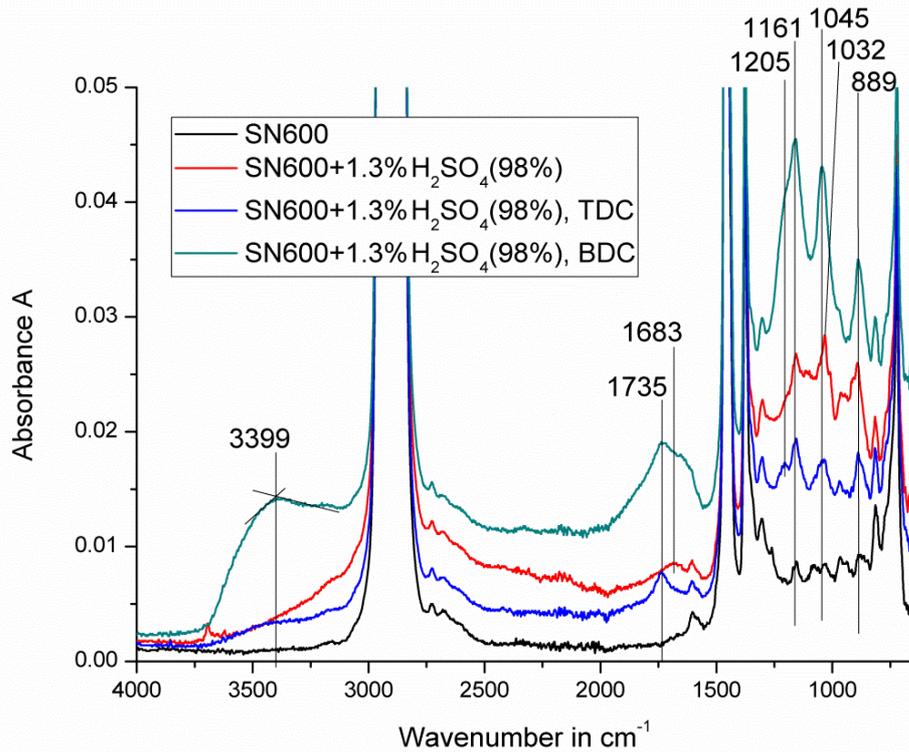
Figure 7.22: FTIR-ATR spectra of SN600+1.3%v/v98%w/wH$_2$SO$_4$, fresh and sampled during the friction test at 80 °C. Test no. 9.
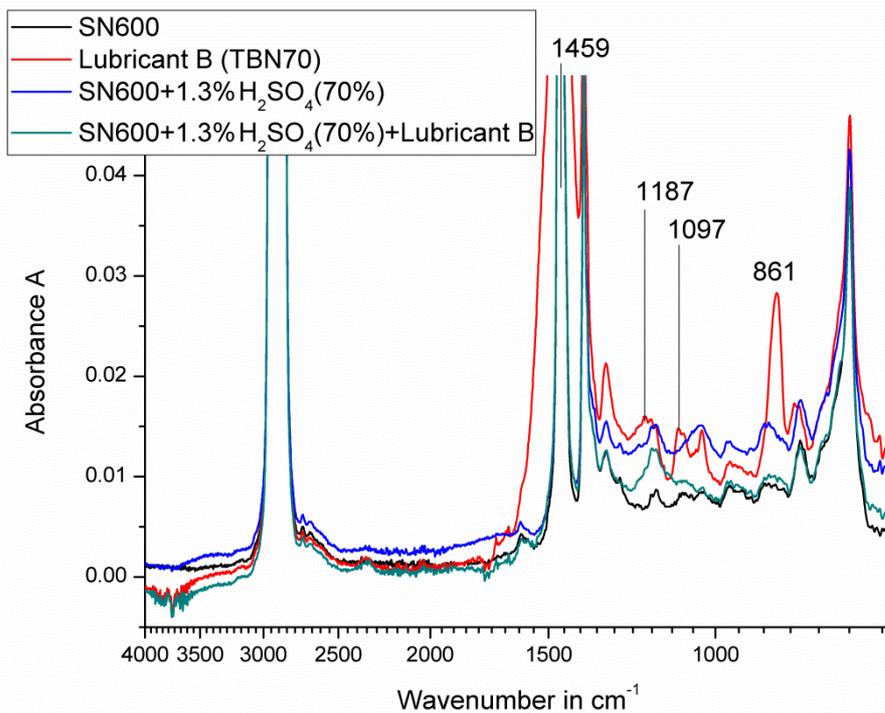
Figure 7.23: FTIR-ATR spectra of SN600+1.3%v/v70%w/wH$_2$SO$_4$ and a fully formulated "lubricant B" with a alkaline reserve of 70 mgKOH/g. Fresh and sampled during the friction test at 170 °C. Test no. 19.

For SN600 with added H_2SO_4 at 70 %w/w concentration, hard deposit formation on the liner was observed to start at about 120 °C. To find the critical value for deposit formation with SN600, the cylinder liner temperature was increased in steps and oil sampled to find the impact of temperature in a sliding metal on metal contact on the chemistry of the base oil. Visually, darkening of the oil started at 250 °C and deposit formation was observed at 300 °C cylinder liner temperature. This observation concurs with the results from the FTIR-ATR spectral analysis, shown in Figure 7.24. At 250 °C, the lubricant starts to oxidise, forming C=O bonds and at 300 °C, the lubricant reacts with nitrogen from the air, to form RNO_2 bonds. With this result, it can be excluded for all other tests that the lubricant would degrade without the action of sulphuric acid. The adding of a nitro group to the hydrocarbon is indicated by the peaks at 1597, 1229 and 890 cm^{-1} but not readily explained as the only nitrogen source during the test was the relative inert gaseous N_2 contained in the air with a very strong triple bond and only traces (~0.3 ppm) of more reactive N_2O, NO_2 and NO (Pischinger, 2000). In the industrial production of ammonia, the triple bond of N_2 is broken in the Haber-Bosch process under high pressure at 500 °C on a iron catalyst to make the nitrogen reactive (Atkins, 2001).
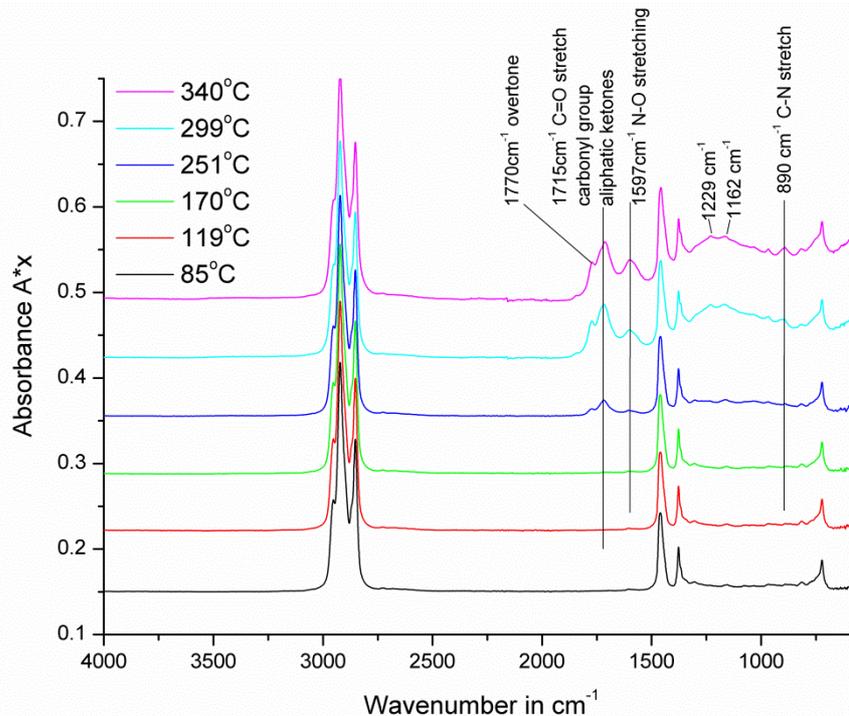
Figure 7.24: FTIR-ATR spectra of SN600 exposed to various cylinder liner temperatures during the friction tests at 85 – 340 °C, revealing the start of lubricant oxidation at 250 °C and nitration at 300 °C combined with the excessive formation of deposit.

It is possible that the formation of NO_2 from N_2 dissolved in the lubricant film was catalysed at a low, non - optimal temperature by the fresh rubbed metal surfaces. At 100 °C in glassware without catalyst, the aeration of lubricant base oil with sulphuric and nitrogen acid carrying air would only yield nitrated hydrocarbons when nitrogen monoxide, a typical by-product from engine combustion, was added to the flow, while oxidation took place with air only. The formation of insoluble sluge and deposit, however, was found to be independent from nitration (Lillywhite, et al., 1990). Also in this study, chapter 3, formation of solids at the acid-oil interface was found to be independent from nitration. For the nitration of the lubricant, according to the reaction shown in chapter 2, it must be assumed that NO_2 from an unspecified source reacted with the hydrocarbon radicals formed by hydrogen atom abstraction by oxygen starting at 250 °C or at 80 °C when catalysed with H_2SO_4 as shown later. Gasses do not homogeneously dissolve in hydrocarbon oils, therefore NO_x content in the lubricant originating from the ambient air could be higher than in air. Unfortunately the Ostwald coefficient for NO_x species was not found in the literature.

7.4   Results and Discussion: FTIR-Microscope

Correlation of peak position with compounds was done using comparison tables found in educational literature (University of Leeds, 2011).

Sample No.0 is the reference sample, which was treated in the same manner as all other samples. Figure 7.25 shows an enlarged view on the cylinder liner sample and a IR-absorbance map.
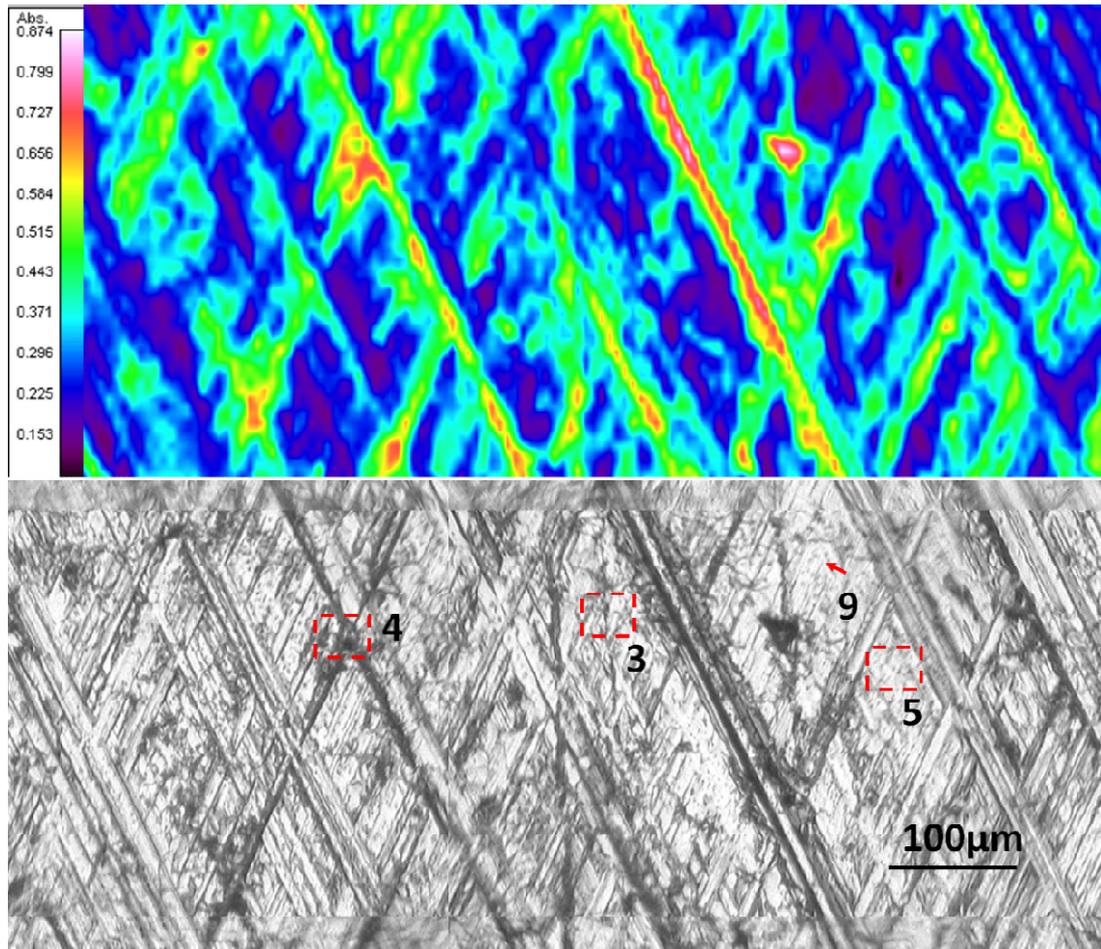
Figure 7.25: FTIR-scan and visual image on "sample 0", the unused liner surface

The position of the extracted spectra are indicated and the spectra shown in Figure 7.26. The spectra of the oiled sample is not indicated. It shows the typical peaks for a hydrocarbon based lubricant. Spectra 9 is a single point of 6.25 µm in diameter. The signal to noise ratio is quite low and it was decided to use only area averaged spectra for the following investigations. The spectra 3 to 9 mainly differ in the amount of absorbance, which seems to be influenced by the topography of the sample. Deep honing marks show higher absorbance than the plateaus between the honing marks. An explanation for the higher absorbance due to geometry of the honing marks can be found in the following chapter 8. Between 2375 and 2313 cm^{-1} all spectra show a peak originating most probably from CO_2.
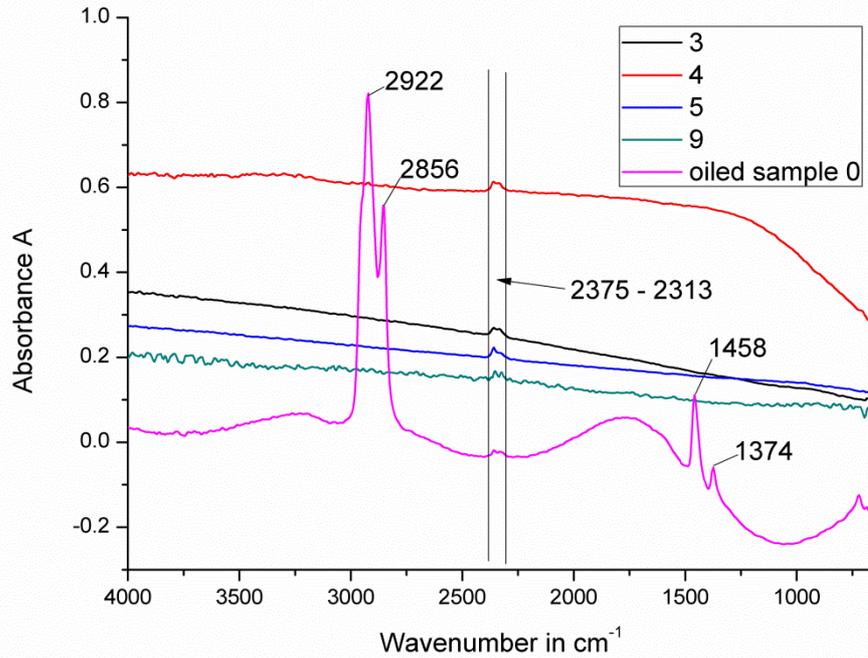
Figure 7.26: FTIR-spectra of the areas indicated in Figure 7.25

Figure 7.27 shows the background scan and a measurement on the gold coated mirror, which was used for the background scan. The instrument is not capable of completely removing this peak and it has to be ignored in the following samples.
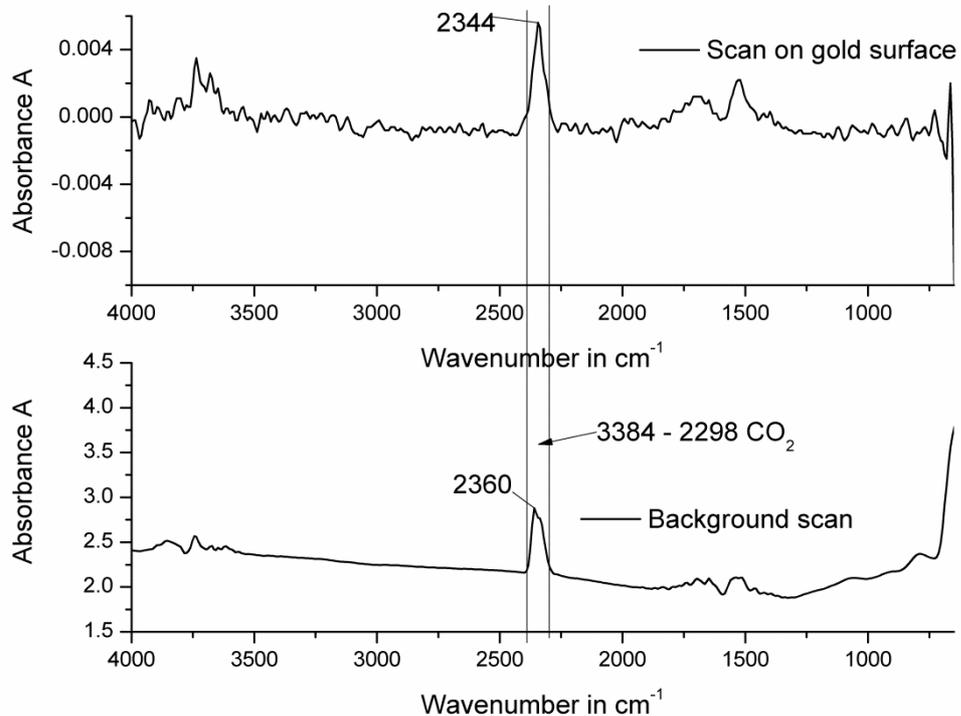
Figure 7.27: FTIR background and measurement scan on a plain gold surface

Sample No.8 was run at 80 °C with SN600 only. Figure 7.28 shows an enlarged view on the cylinder liner sample and a IR-absorbance map. The scan was taken near the "TDC" turning point which can be clearly seen in the enlarged view. The position of the extracted spectra are indicated and the spectra shown in Figure 7.29. The spectrum from a deep honing mark, not indicated in Figure 7.28, shows the typical first peaks for a hydrocarbon based lubricant at 2922 and 2856 cm^{-1} the second peaks are missing, probably covered by the strong response of absorbance to the topography. The cleaning procedure is proven to remove all liquid oil from the honed surface, therefore a slight built up of hydrocarbon based deposit can be assumed. The spectra 23 to 25 show mainly a purely metallic response similar to points 3 to 9 in sample 0. Only spectrum 25 shows a slight "hydrocarbon" response around a honing mark of medium depth.
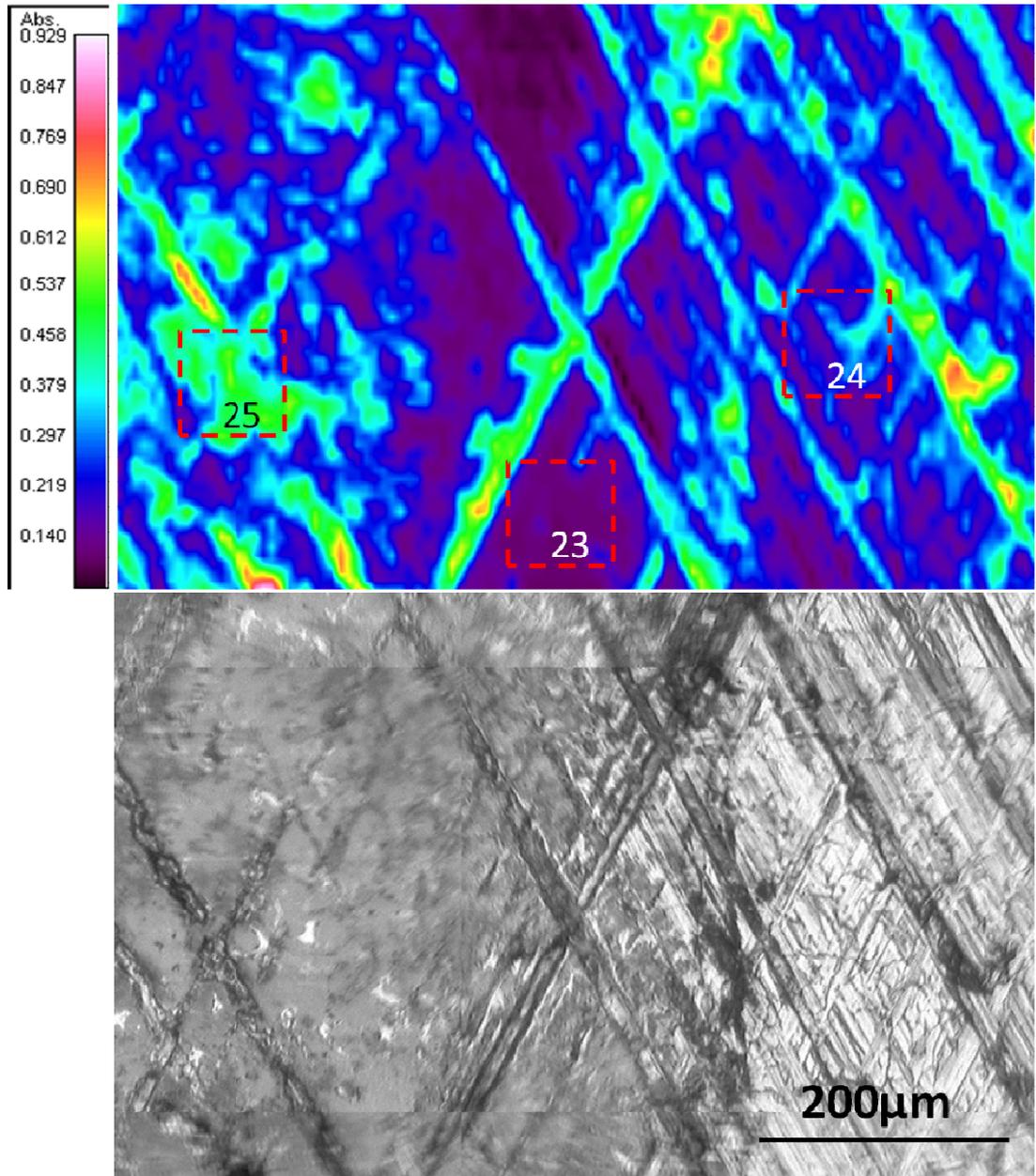
Figure 7.28: FTIR-scan and visual image on sample 8
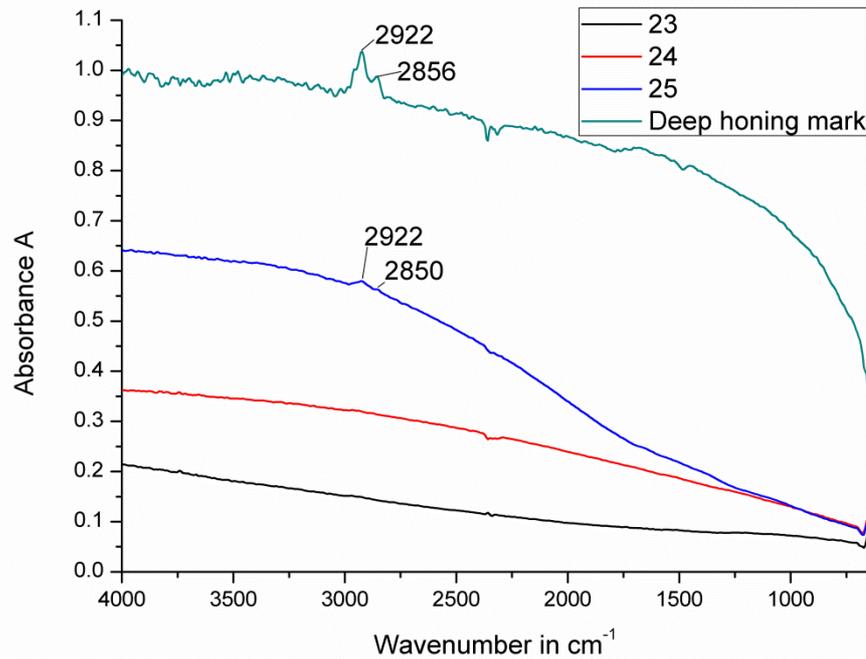
Figure 7.29: FTIR measurement scan on sample 8

Sample No.13 was run at 170 °C with SN600 only. Figure 7.30 shows an enlarged view on the cylinder liner sample and a IR-absorbance map. The scan was taken near the "TDC" turning point. The position of the extracted spectra are indicated and the spectra shown in Figure 7.31. The visual picture shows the honing marks to be filled, which is shown even more by the IR-absorbance map. Spectrum 33, taken on a honing mark, shows the typical hydrocarbon peak at 2922 and 2856 cm^{-1} and at 1458 and 1374 cm^{-1}. The C=O peak at 1716 cm^{-1} indicates the temperature induced oxidation of the oil, which is accelerated by the contact to the metal surfaces of piston ring and cylinder liner, which act as catalysts. The broad peak at around 3300 cm^{-1} and the shoulder after the 1716 cm^{-1} originates from an O-H stretch (Nuevo, et al., 2006). The peak at 1188 and 1116 cm^{-1} is typical for sulphoxides.
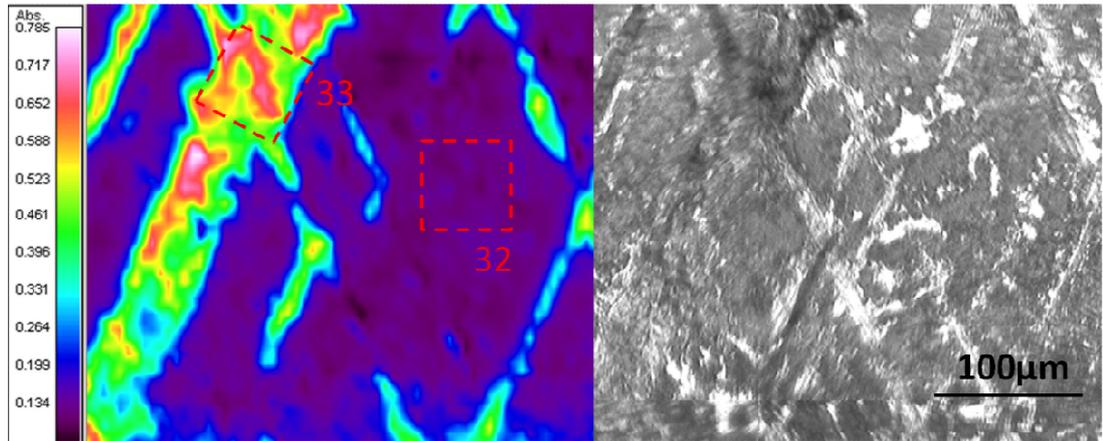
Figure 7.30: FTIR-scan and visual image on sample 13
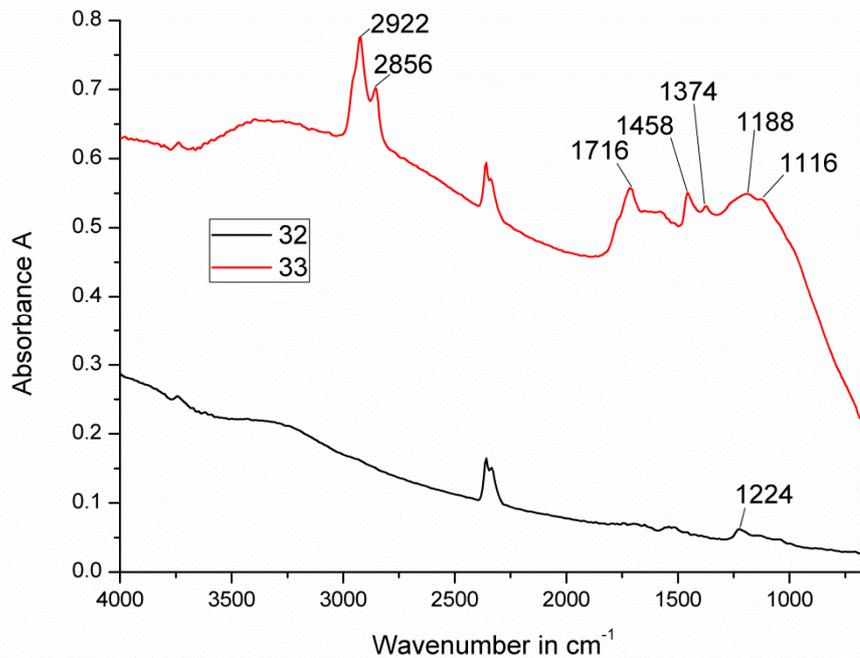
Figure 7.31: FTIR measurement scan on sample 13

Sample No.7 was run at 80 °C with 1.3 %v/v 70 %w/w H_2SO_4 dispersed in SN600. Figure 7.32 shows an enlarged view on the cylinder liner sample and a IR-absorbance map. The scan was taken near the "TDC" turning point. Area i and ii are slightly below the turning point of the piston ring profile centre in area iii while area iv is just outside the running mark on formed deposit. The spectrum, Figure 7.33, iv_15 on the deposit shows a broad peak around 3333 cm^{-1} in the area of O-H stretches. This broad peak almost covers the hydrocarbon peaks at 2934 and 2856 cm^{-1}. At 1650 cm^{-1} a C=O peak can be found. The peak at 1404 cm^{-1} together with the peaks

between 1206 – 1050 cm^{-1} originate from sulphonates. The peaks at 876 and 810 cm^{-1} are typical for aromatics.

Spectra i_6, iii_13 and iii_14 show very similar spectra. All show the characteristic broad O-H peak at around 3300 cm^{-1} and similar peaks between 1200 and 1000 cm^{-1}, typical sulfoxide / sulphonate peaks, and 820 cm^{-1} the aromatic peak. The missing or very weak hydrocarbon peaks indicate that those sulfoxides / sulphonates are mainly bound to a metal, most likely iron in this case. Spectrum ii_11 shows increased absorbance but no clear peaks.
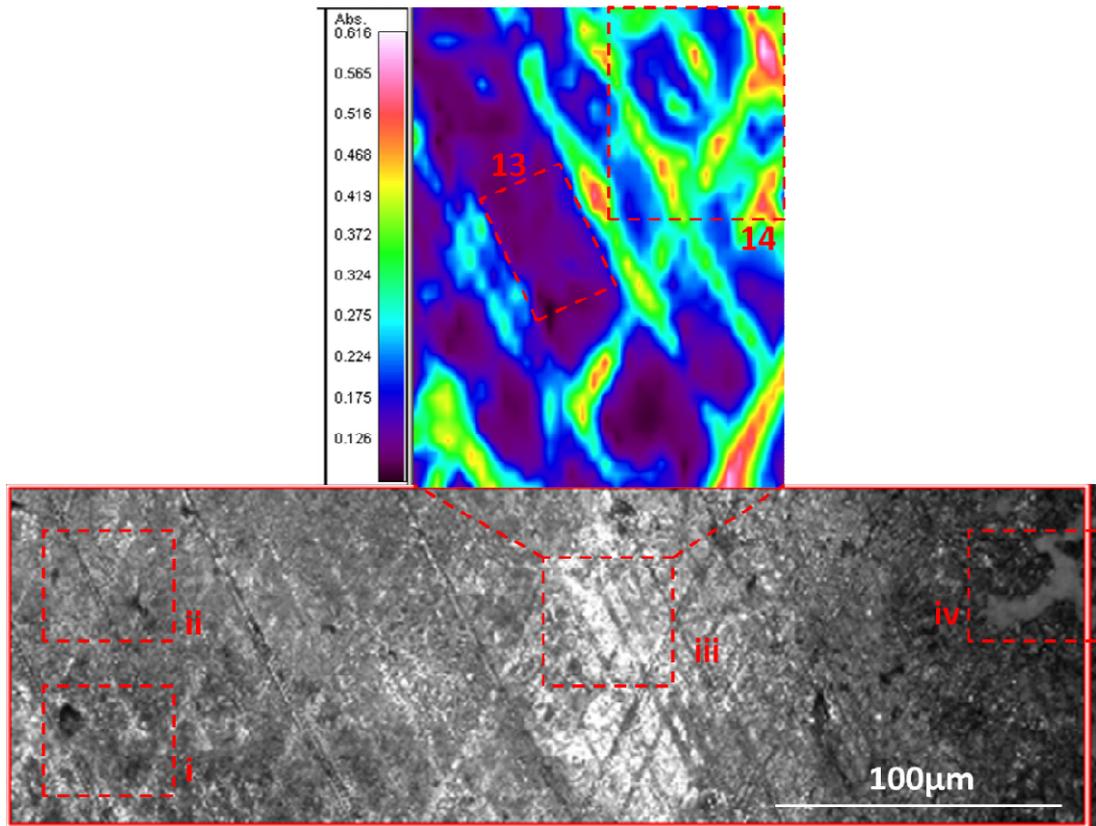
Figure 7.32: FTIR-scan and visual image on "sample 7, TDC"
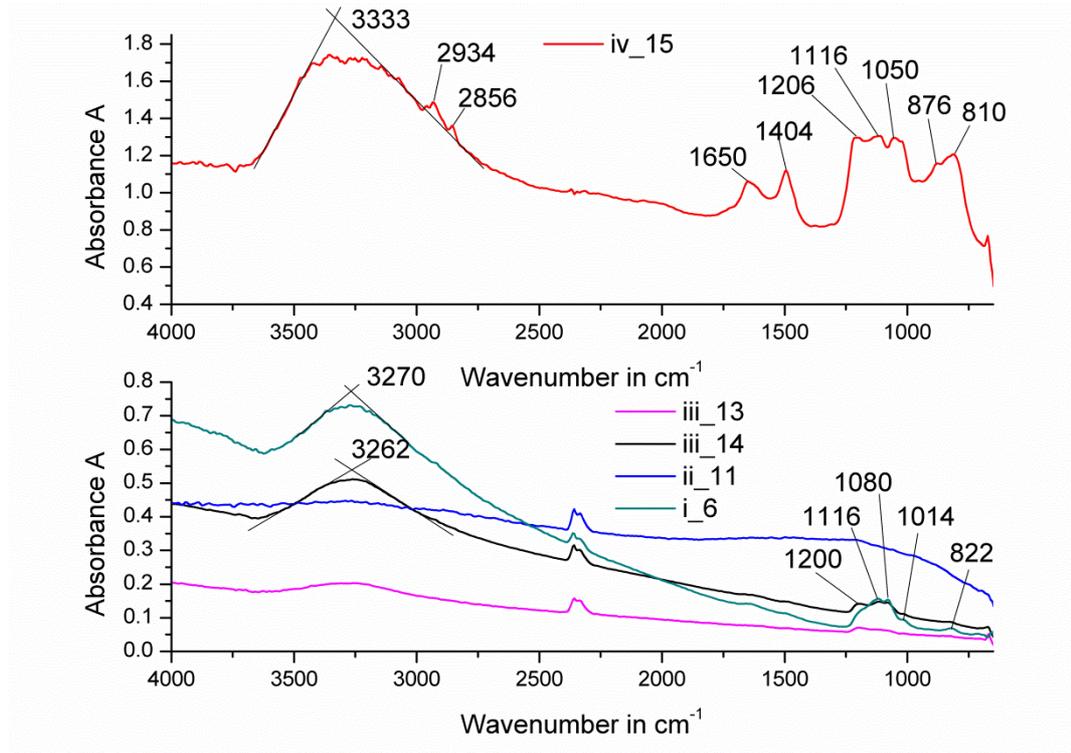
Figure 7.33: FTIR measurement scan on sample 7

Sample No.14 was run at 170 °C with 1.3 %v/v 70 %w/w H_2SO_4 dispersed in SN600. Figure 7.34 shows an enlarged view on the cylinder liner sample and a IR-absorbance map. The scan was taken near the "TDC" turning point. Remarkable is the indication of honing structure below the deposit which shows the depth of penetration of the IR beam. All spectra in Figure 7.35 show the typical broad O-H peak at around 3300 cm^{-1} and the hydrocarbon peaks at 2920, 2856, 1456 an 1376 cm^{-1} or at least a response in these areas. The peaks at 1704 and 1176 cm^{-1} originate from carbonyls, oxidised hydrocarbons. The peak at 1616 and 824 cm^{-1} are typical for nitrides and the peak at 1048 cm^{-1} for sulphoxides.
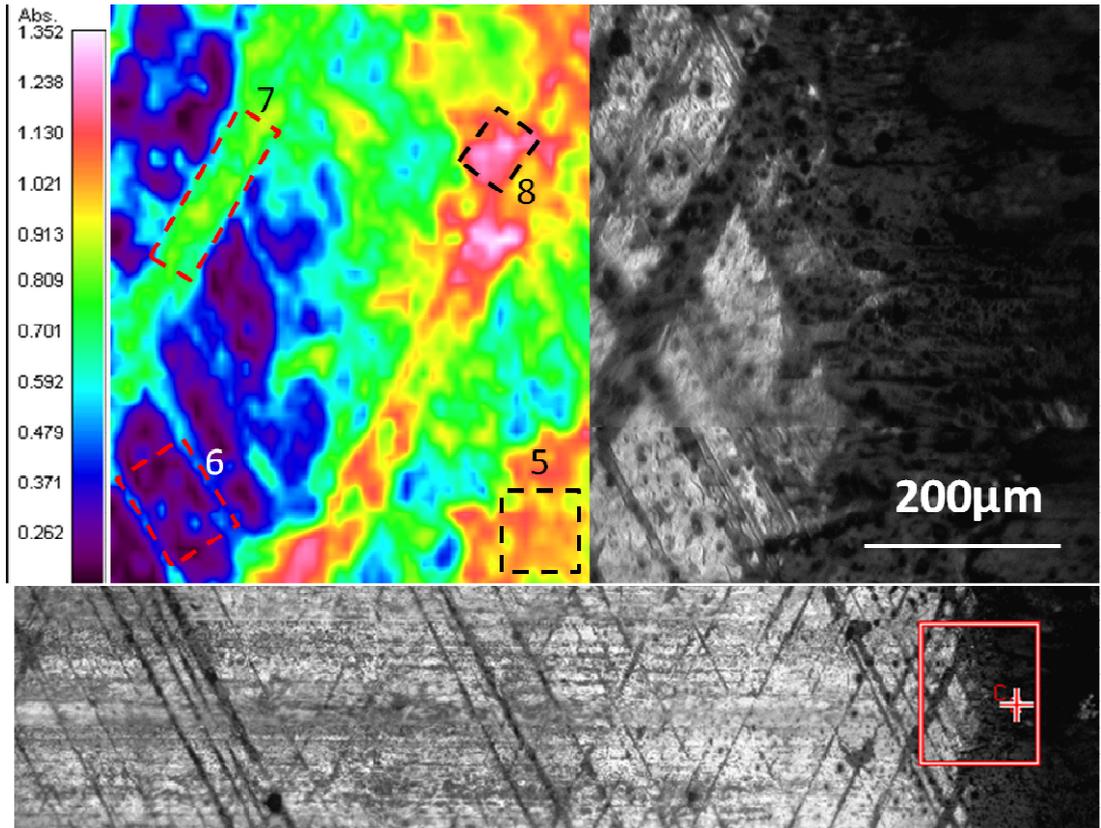
Figure 7.34: FTIR-scan and visual image on sample 14
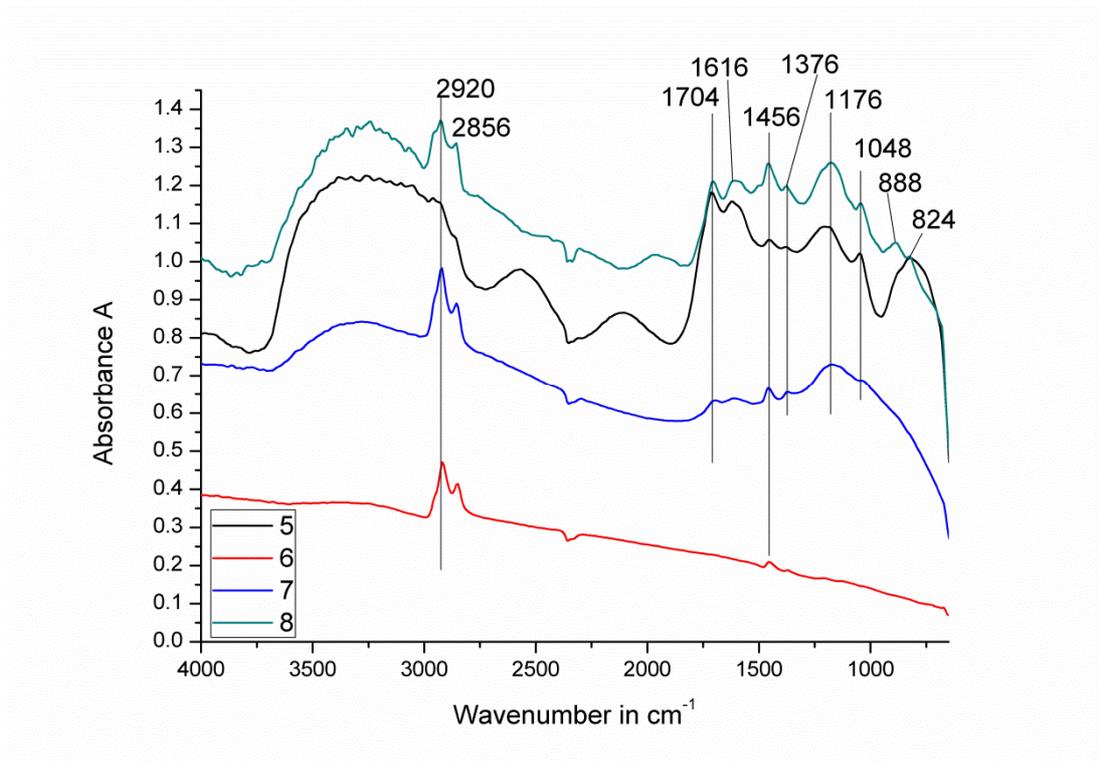
Figure 7.35: FTIR measurement scan on sample 14

Sample No.21 was run at up to 340 °C with SN600 only. Figure 7.36 shows an enlarged view on the cylinder liner sample and a IR-absorbance map. The scans where taken in midstroke near a patch of deposit. The resulting FTIR-spectra in Figure 7.37 reveal a metallic response for the plateaus 29 and 33 between the honing marks with some small peaks at 3732, 2922, 1770 – 1620 and 1536 cm^{-1}. The honing marks are filled with deposit and show very similar spectra, 30 – 32. The deposit shows the typical hydrocarbon peak at 2922 cm^{-1} and a slight indication for the typical second hydrocarbon peaks at 1458 and 1374 cm^{-1}. The strong C=O peak at 1722 cm^{-1} shows the severe oxidation of the lubricant deposit. The peaks at 3732, 1614 and 1536 cm^{-1} are typical for amine salts, a result of the high temperatures the lubricant was exposed to. The C-O peak at 1242 cm^{-1} is another oxidation indicator.
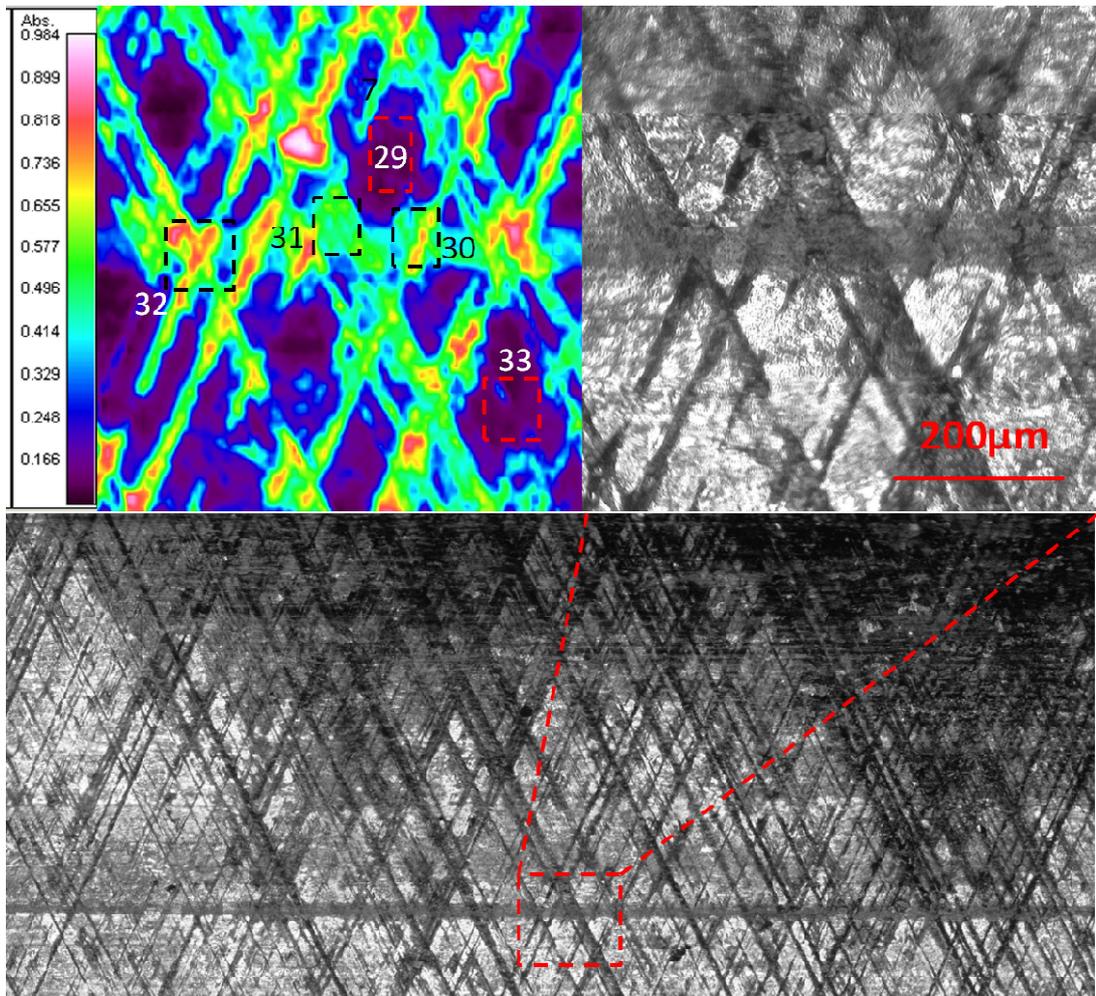
Figure 7.36: FTIR-scan and visual image on sample 21 in midstroke
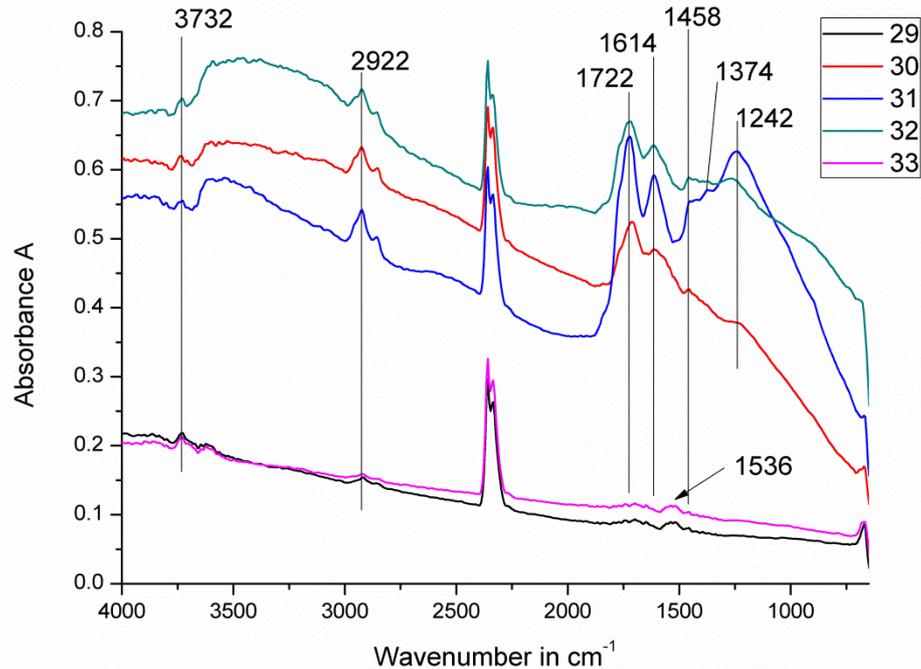
Figure 7.37: FTIR measurement scan on sample 21 in midstroke

7.5 Results and Discussion: Surface Chemistry by XPS

The peak positions for each sample are given in Table 7.1. and the spectra presented in Figure 7.38 - Figure 7.44. As mentioned before, the measured peaks were correlated to an online database (Benoit, et al.).

Sample No.0 is the reference sample. The Cs1 peak at 284.3 eV originates from the graphite lamellas in the grey cast iron, chapter 6. No possible C-H configuration was found like in the other samples, neither by XPS nor by FTIR-microscopy. Together with the missing sulphur peak this indicates, that no organic film was built up due to the storing of the sample in SN600 and all oil was removed by the washing process, because SN600 contains sulphur which would show up if present. The Fe2p3/2 peak at 709.2 eV together with the stronger O1s peak at 528.7 eV correlates well to iron oxides. The weaker O1s peak at 531.2 eV corresponds to oxygen from adventitious hydrocarbons, a possible result of exposing the oiled surface to the atmosphere. However no C=O bonds were found by the FTIR study. The N1s peak is very weak and the source is not obvious. The surface of sample No. 0 mainly consists of iron oxide and graphite.

Sample No.8 was run at 80 °C with SN600 only. The sulphur originates from the oil and is bound to a surface film as shown by the results from sample No.0, where all sulphur was removed by the cleaning. The bigger S2p3/2

peak at 168.3 eV can be correlated to $FeSO_4$ which is supported by the Fe2p3/2 peak at 710.5 eV, which is quite weak, and the O1s peak at 531.6 eV which both can be correlated to FeS_2-oxyde. The smaller S2p3/2 peak at 168.5 eV can be correlated to hydrocarbon sulphates which is supported by the O1s peak at 531.6 eV and the two C1s peaks at 286.3 eV, C-O bonds, and 284.5 eV, C-H bonds and graphite. The FTIR study only supports hydrocarbon bonds in deep honing marks. The surface of sample No.8 mainly consists of a organic carbon based film, which is built up from hydrocarbon sulphates and probably graphite. A small amount of iron sulphates are also present. The substances are mainly present in deep honing marks.

Sample No.13 was run at 170 °C with SN600 only. The sulphur originates from the oil and is bound to a surface film likewise to sample No.8. The Fe2p3/2 peak at 711 eV together with the O1s peak at 531.6 eV and the S2p3/2 peak can be correlated to both iron-sulphate and hydrocarbon-sulphate. The C1s peak at 284.5 eV can be correlated to graphite and C-H bonds and the peak at 288.6 eV to R-COOH carboxyl and CS_3^{2-}. The medium sized N1s peak at 399.4 eV gives the possibility of nitrogen adsorption to the surface but also a C-N bond. C-N bonds are usually created at higher temperatures after the creation of C=O bonds which then supports the presence of C=O bonds. The FTIR study supports C-H, C=O and the presence of sulphoxides deposited in honing marks, without distinguishing between hydrocarbon or iron sulphoxides bonds. C-N bonds are not supported by the FTIR study, therefore plain N adsorption to the surface is more likely. The deposit in the honing structure mainly consists of a oxidised hydrocarbon containing sulphoxides most probably bound to hydrocarbons, given the origin of the sulphur from the SN600. Some nitrogen is adsorbed to the surface.

Sample No.10 was run at 80 °C with 1.3 %v/v 70 %w/w H_2SO_4 dispersed in SN600. The S2p3/2 peak is correlated to iron sulphate species $FeSO_4$ and $Fe_2(SO_4)_3$. The found ratio S : Fe is 4.5 which is far too high for either species. The O1s peak at 532.1 eV supports the $FeSO_4$ and the Fe2p3/2 peak at 710.6 eV both compounds. Both compounds are known (Wu, et al., 2009) to lower friction considerably, which was also observed in this study. The Cr2p3/2 peak at 577.9 eV is clearly due to CrO_3. The N1s peak is an nitrogen adsorption peak. The C1s peak at 284.5 eV supports both graphite and C-H bonds. The second could be part of hydrocarbon sulphates, however no evidence was found for those other than the excess in sulphur.

The peaks might be covered by other peaks. No FTIR study was done on this sample but on sample No.7, which ran under the same conditions. In the deposit of sample No.7, sulphonates and C=O bonds were found by FTIR while on the wear scar the presence of $FeSO_4$ is supported. The surface of sample No.10 consists of iron sulphate with chrome oxide particles embedded. Carbon is most likely to be present in the graphite form but also hydrocarbons can be present in the honing marks in the form of embedded deposit. Nitrogen is adsorbed at the surface.

Sample No.11 was run at 170 °C with 1.3 %v/v 70 %w/w H_2SO_4 dispersed in SN600. The S2p3/2 peak at 168.8 eV is correlated to iron sulphate species $FeSO_4$ and $Fe_2(SO_4)_3$. The found ratio S : Fe is 29.3 which is far too high for either species. The O1s peak at 532.4 eV supports only the $Fe_2(SO_4)_3$ and the Fe2p3/2 peak at 711.5 eV both compounds. In this study friction increased when increasing the temperature. For additives forming a $Fe_2(SO_4)_3$ - $FeSO_4$ surface film, a decay temperature of 160 – 193 °C (Wu, et al., 2009) was reported, unfortunately without reporting upon friction values at this temperature. Weak peaks for S2p3/2 at 164 eV and N1s at 401.5 eV support the presence of amino-sulphates which also contain C-H bonds represented by the C1s peak at 284.5 eV, which can also represent graphite. The FTIR study of sample 14, which was run under the same conditions, supports the presence of the nitrogen bonds in the amino-sulphates, C-H bonds and iron sulphate. The surface of sample No.11 consists of iron sulphate and amino-sulphates, which includes also hydrocarbon bonds.

Sample No.14 was run at 170 °C with 1.3 %v/v 70 %w/w H_2SO_4 dispersed in SN600. The S2p3/2 peak at 168.3eV correlates to iron sulphate $FeSO_4$. The found ratio S : Fe is 6 and too high for this compound. Its presence, however, is supported by the Fe2p3/2 peak at 711.1 eV. The Cr2p3/2 peak at 577.2 eV indicates the presence of chromium oxide. The weak S2p3/2 peak at 164 eV combined with the O1s peak at 531.8 eV and the C1s peak at 284.5 eV indicate the presence of hydrocarbon sulphates. Nitrogen is adsorbed to the surface as indicated by the N1s peak at 399.7 eV. Graphite lamellas are represented by the C1s peak at 284.5 eV. The FTIR study of sample 14 supports the C-H bonds and iron sulphate. Contradictory to Sample No.11, the main nitrogen peak indicates no N-bonds but a small shoulder is supporting them. The surface of sample No.14 is built up of iron sulphate, hydrocarbon sulphates with chromium oxide particles embedded,

nitrogen is adsorbed to the surface but also chemical bond nitrogen is likely to be present.

Table 7.1: Binding energies in eV of elements on the cylinder liner wear scars

Sample No.	Fe	Cr	O	O_{minor}	N	C	C_{minor}	S	S_{minor}
0	709.2	-	528.7	531.7	399.7	284.3	-	-	-
10	710.6	577.9	532.1	-	400	284.5	-	168.8	-
11	711.5	-	532.4	-	401.5	284.5	-	168.8	164
13	711	-	531.6	-	399.4	284.5	288.6	168.2	-
14	711.1	577.2	531.8	-	399.7	284.5	-	168.3	163.9
8	710.5	-	531.6	-	-	284.5	286.3	168.3	168.5
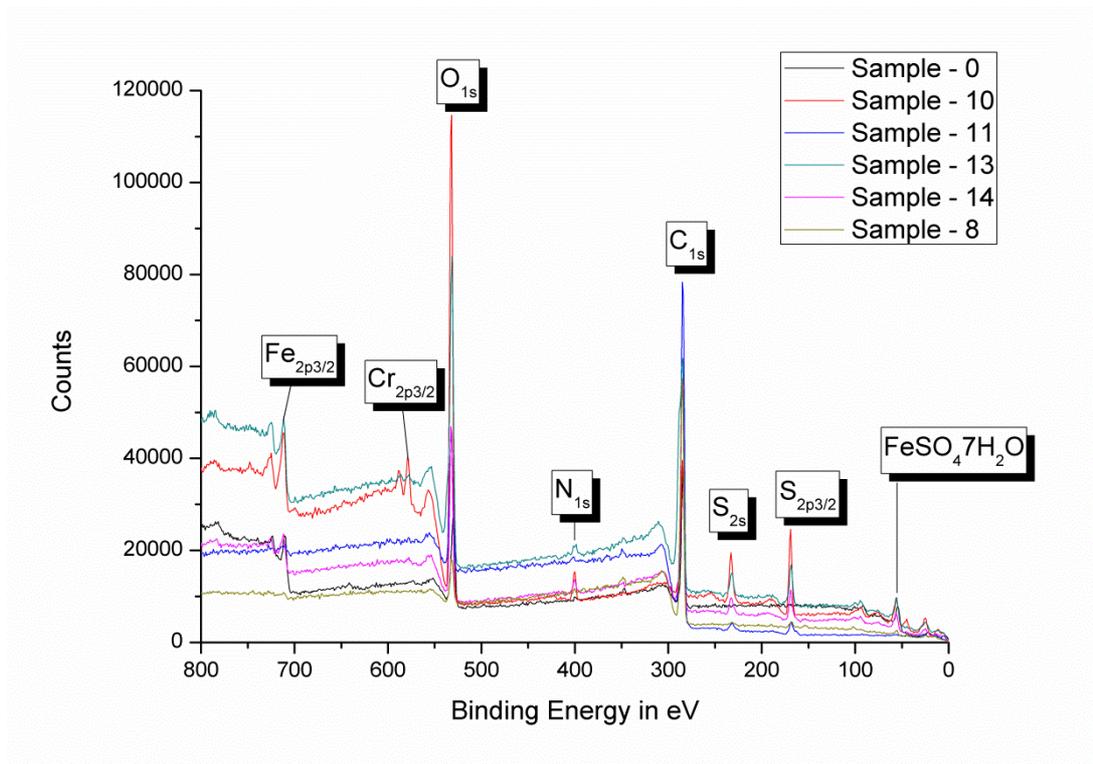
Figure 7.38: Overall XPS spectra for all cylinder liner wear scars
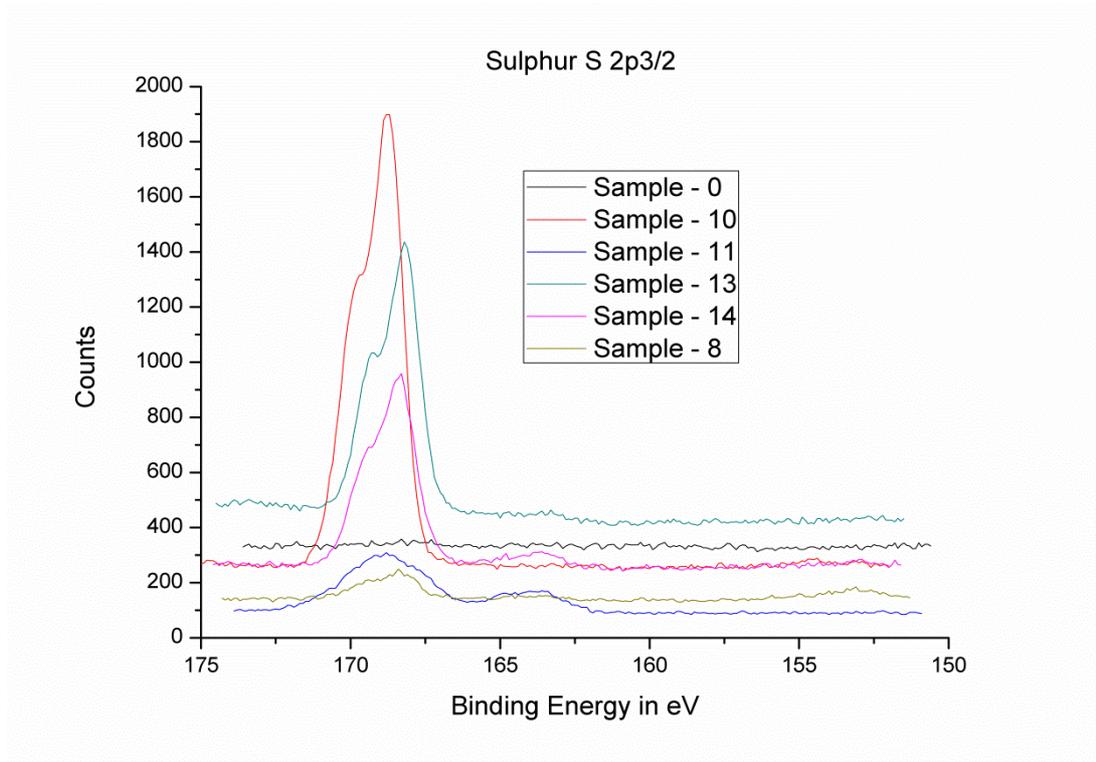
Figure 7.39: S2p3/2 XPS spectra for all cylinder liner wear scars
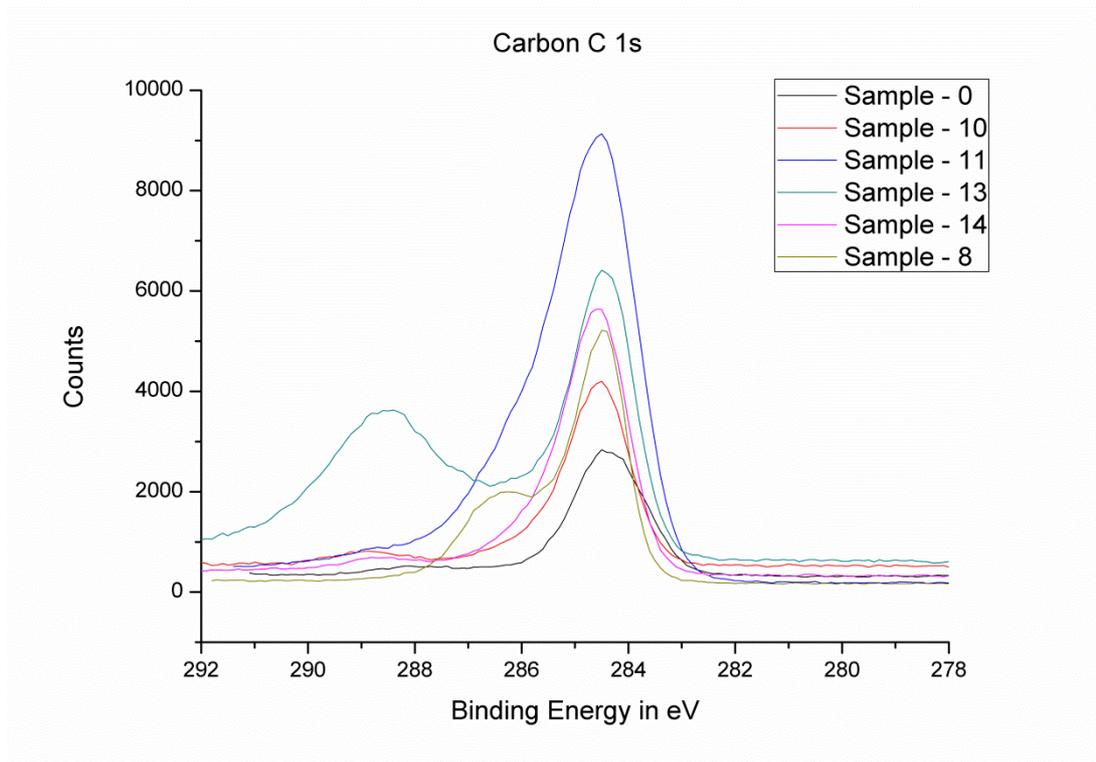
Figure 7.40: C1s XPS spectra for all cylinder liner wear scars
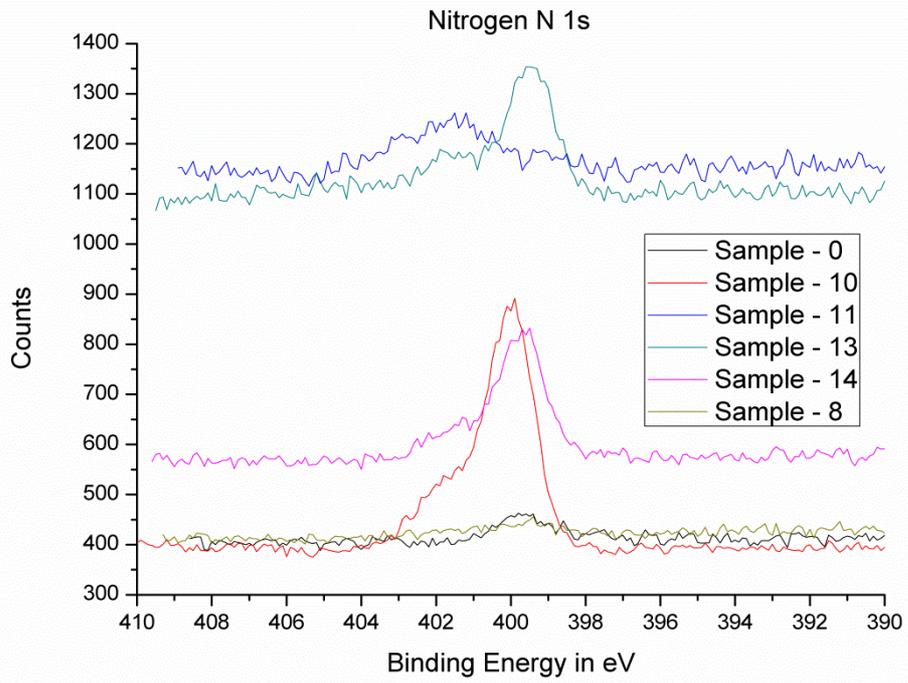
Figure 7.41: N1s XPS spectra for all cylinder liner wear scars
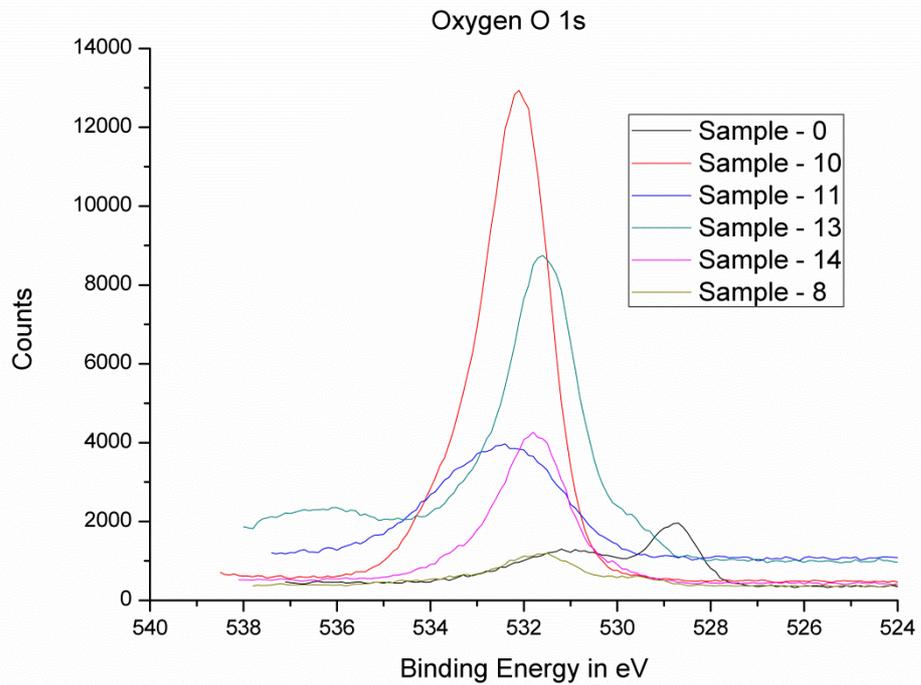
Figure 7.42: O1s XPS spectra for all cylinder liner wear scars
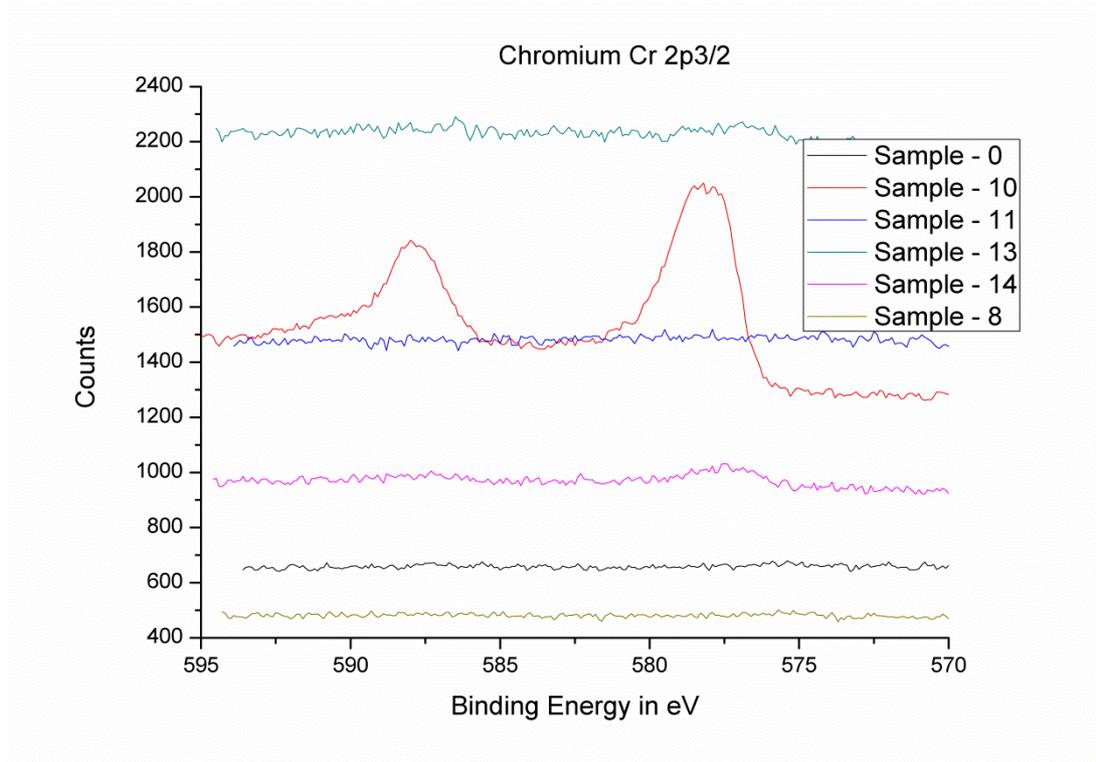
Figure 7.43: Cr2p3/2 XPS spectra for all cylinder liner wear scars
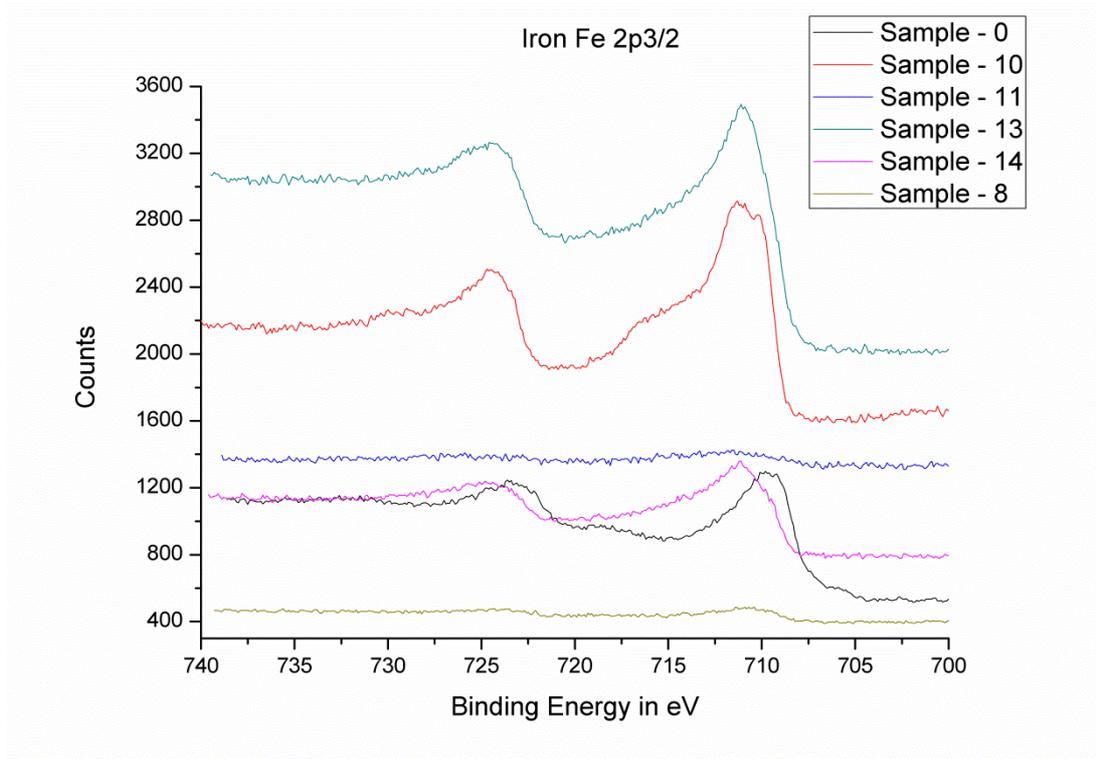
Figure 7.44: Fe2p3/2 XPS spectra for all cylinder liner wear scars

7.6 Results and Discussion: Wear and Surface Topography by WYKO White Light Interferometer

The shuttle tests described in section 7.1.2 make a statistically proven wear evaluation difficult, as the conditions changed constantly. Some tests however ran under constant conditions and made an wear analysis worthwhile. The results of the wear analysis are shown in Figure 7.45. The wear volume is normalised to the applied normal force and the sliding distance resulting in the wear factor k, also used by other researchers and appears in a comparable range (Priest, 2000). The closest test condition to engine reality is the test with 70 %w/w sulphuric acid at 170 °C at relatively low speed and high contact pressure. These conditions can be found in TDC of the engine. Therefore, this condition was run more often under static conditions and the wear results are more statistically proven, as indicated by the error bars.
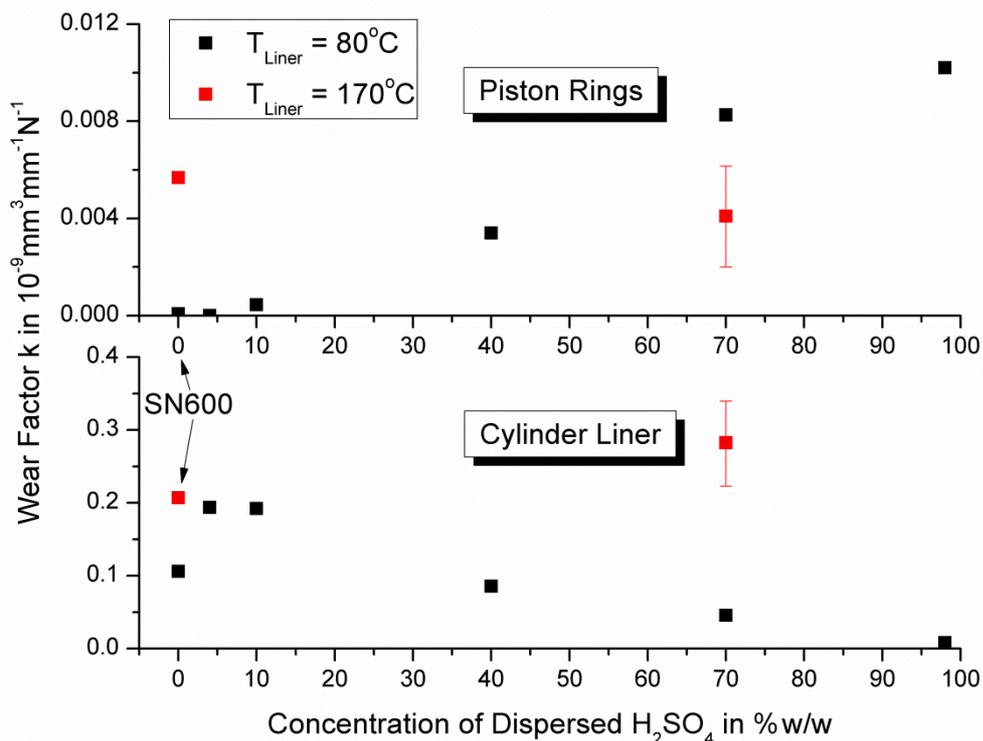
Figure 7.45: Wear factor k of piston ring and cylinder liner over various concentrations of H_2SO_4 at 80 and 170 °C

Acid concentration as well as temperature seem to have a major influence on both cylinder liner and piston ring wear. The point zero on the horizontal acid concentration axis represents the reference condition with pure SN600

as lubricant. Both cylinder liner and piston ring show higher wear when exposed to higher temperatures. This can be explained to some extent by the reduced viscosity. The tensile strength of cast iron EN-GS-400, for example, reduces from 510 MPa at 80 °C to 450 MPa at 170 °C (Memhard, et al., 2011) and this reduction must also be taken in to account as both temperature conditions run close to the mixed lubrication regime, where surface asperities are in contact. The contact potential shows very similar values, meaning the surface contact area is very similar, assuming similar surface chemistry.

At 80 °C cylinder liner temperature, increasing the concentration of the dispersed acid phase, increases the wear of the piston ring while the wear of the cylinder liner decreases even below the values of the reference conditions. For 170 °C cylinder liner temperature, the exact opposite is the case. Increased concentrations reduces the wear on the piston ring while the wear on the cylinder liner increases. This despite the formation of deposits on the cylinder liner surface. For both temperatures the contact potential measurement indicates almost perfect separation. Galvanic-electric effects can be excluded as the potential between chromium and iron lays between 400 and 910 mV (Atkins, 2001) which would be picked up by the Lunn-Furey contact potential circuit and the potential of 45 mV across the contact is not enough to suppress the corrosion. The abrasive action of a mixture of oxides, which are easily removed from the surface, with a bituminous hydrocarbon which also forms deposits on the running surface, seems a more plausible explanation.

In section 7.1, the influence of surface topography on friction and the contact potential measurements are shown. Figure 7.46 shows the combined values of Rp for piston ring and cylinder liner. It is a measure for the minimum oil film thickness needed to completely separate the parts by hydrodynamic action. It is quite remarkable to note that the peak height increases with increased acid concentration while, for a liner temperature of 80 °C, the friction actually decreases. This is another indication of the formation of a surface boundary film with superior friction properties. The extreme value for 4 %w/w H_2SO_4 is not reflected by higher friction measurements, Figure 7.4.
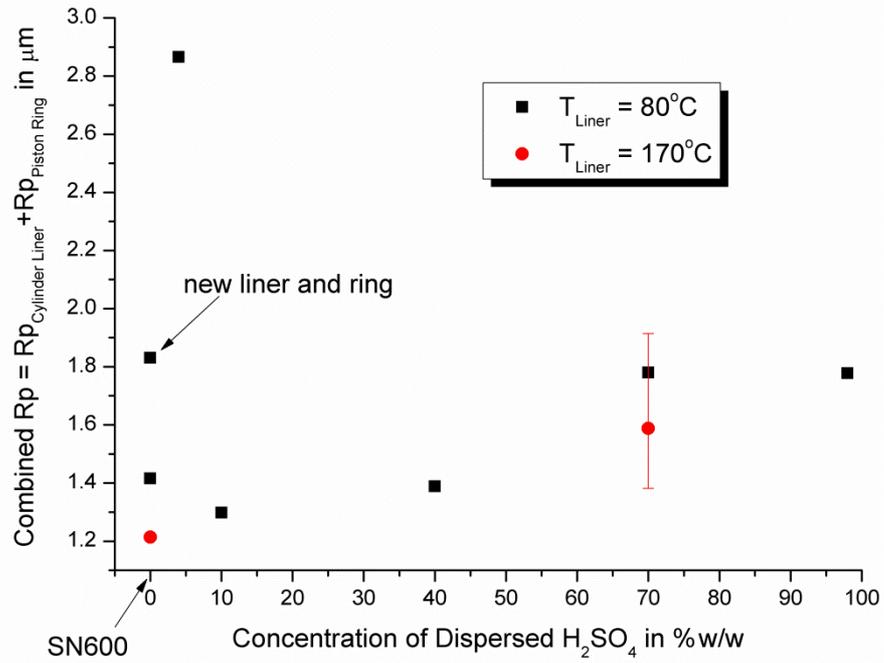
Figure 7.46: Combined roughness peak height form the mean line, Rp, for piston ring and cylinder liner
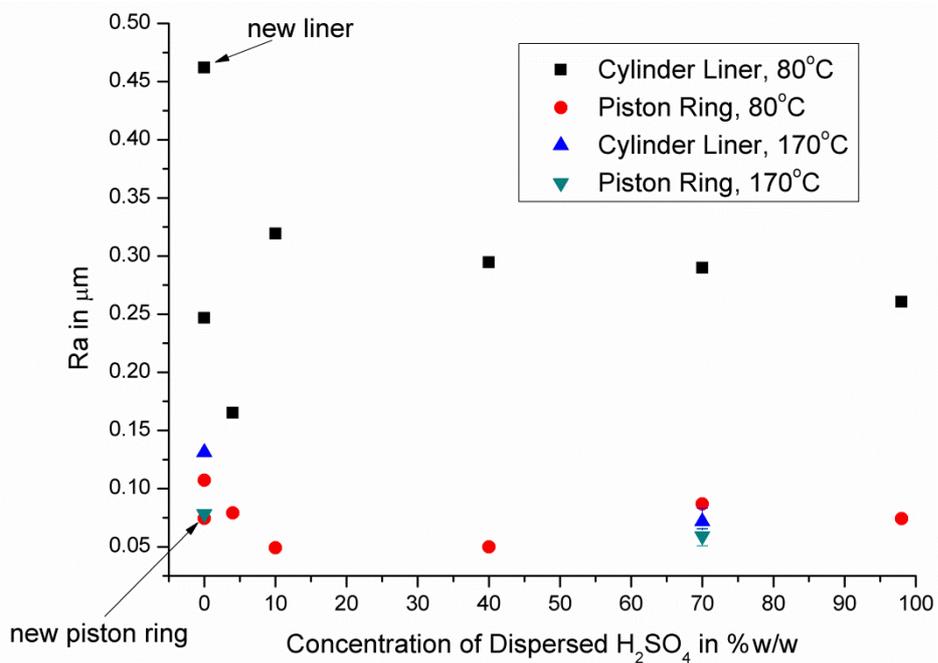
Figure 7.47: Arithmetic average deviation from the mean line, Ra, for piston ring and cylinder liner

The results for the roughness average, Ra, are shown in Figure 7.47. The roughness of the honed new liner decreases, while the roughness of the

lapped piston ring surface increases during running with plain SN600 at both temperatures. At 80 °C liner temperature, the surface roughness of the cylinder liner increases by adding sulphuric acid to the SN600, declining towards higher concentrations. Only 4 % H_2SO_4 shows contrary behaviour. The piston rings become smoother until 40% H_2SO_4 and become rougher towards higher acid concentrations. At 170 °C, surface roughness for both piston ring and cylinder liner decreases and becomes very similar.

At high temperatures and concentrations, the roughness valleys become filled with deposit, which changes the position of the mean line and influences the statistical roughness values.

7.7   Conclusions of the TE77 Bench Test

The tribological properties of API Group I base oil, SN600, alone and in combination with sulphuric acid, was tested on a reciprocating friction testing machine with a piston ring – cylinder liner contact. The main variables were temperature and acid concentration. The influence of fully formulated lubricants was also tested.

The loading conditions were quite severe and passed the criterion for plastic deformation under Hertzian contact. The tests ran in the mixed- / elastohydrodynamic-lubrication regime. Surface analysis by XPS and FTIR-microscope suggests the formation of an organic hydrocarbon sulphate film when running at 80 and 170 °C with the sulphur containing SN600. Deposit formation starts at 300 °C including the formation of nitrogen bonds in the organic surface film. The higher the temperature, the higher the wear and friction, while surface roughness decreases with increased temperature.

For the low temperature of 80 °C up to about 120 °C, the base oil mixed with higher concentrations of sulphuric acid showed superior friction behaviour. The lowest tested acid concentration showing this behaviour was 40 %w/w. Surface analysis by XPS and FTIR-microscope suggests the formation of iron sulphate and oxidised hydrocarbons. The lubricant chemistry tested by FTIR suggests the formation of oil soluble substances, which invites one to speculate on the formation of 'iron-hydrocarbon-sulphate' based soaps or iron sulphonates. The cylinder liner wear under this condition decreased with increased acid concentration, while piston ring wear increased. The combined roughness peak Rp increased for increased acid concentration.

For higher temperature of 120 – 170 °C, the base oil mixed with higher concentrations of sulphuric acid showed the formation of visually

recognisable black deposit on the wear scar and worsening friction behaviour. The breakeven point with pure SN600 was found at 140 °C. Surface analysis by XPS and FTIR-microscope suggests the formation of iron sulphate and nitrided hydrocarbon sulphates. The wear of the liner increases, while the wear of the piston ring decreases by adding acid and increasing the temperature. Surface roughness decreases by adding acid and increasing the temperature. The crystal structure of $FeSO_4$ formed at 80 °C might vary from the structure formed at 170 °C, which would influence the friction.

The addition of small amounts of 70 %w/w sulphuric acid lowered the lubricant oxidation temperature from 250 °C to 80 °C, nitration temperature from 300 °C to 170 °C and solid deposit formation from 300 °C to 120 °C. The nitration under atmospheric conditions is not completely understood as only traces of reactive N_yO_x (~0.3ppm) are available in the atmosphere and the main nitrogen source is present in the inert gaseous form N_2.

A general and probably surprising result of this study is the positive impact of sulphuric acid on the tribological parameters. The marine Diesel engines do not suffer from extremely high wear rates but 'sudden severe wear' or unpredictable scuffing, which starts in line with fresh lubricant supply. Test parts run on fully formulated lubricants show worse conditions than parts run on sulphuric acid dispersed in API Group I base oil.

At the common operation temperature of 170 °C, the fully formulated lubricants disappoint also by their high coefficient of friction which is ~30 % higher than running on plain base oil and most probably originates from an additive film built up on the cylinder liner wall and a layer of surfactants on top of this film. The bad appearance of the piston rings might originate from increased surface traction. The plain base oil mixed with sulphuric acid on the other hand shows deposit build up and high wear paired also with an increased friction.

This study stands at the end of a consequent row of studies to increase the understanding of lubricant interaction with sulphuric acid in a friction contact. It is the closest this research project progressed towards the practical application. Findings on the thermal properties of marine Diesel engine materials, which logically would not fit in the previous flow of argument are presented in the following chapter.

Chapter 8
Thermal Properties of Piston Running Materials

In the previous chapters, temperature was seen to be a major contributor to chemical and physical changes in the tests. In large bore 2-stroke marine Diesel engines with strokes over 3 m, the average cylinder liner surface temperatures can range between 80 °C in the lower to around 300 °C in the upper piston turning point or on the piston respectively. The huge gas volume in the combustion chamber has significant radiation properties. Not only do the dimensions of the engine appear to be enormous but also the micro-structure of the cylinder liner is large compared to the minimum oil film thicknesses. Little however is known about the thermal properties of the cylinder liner material and oil degradation due to thermal radiation.

The base materials of a marine Diesel engine cylinder liner and piston ring coating were tested for their thermal properties. The cylinder liner is a sand-cast grey cast iron with a very coarse structure and inhomogeneous material distribution. For the variety in material chemistry, crystalline structure and physical properties it was expected to also show a microscopic variety in thermal properties such as thermal elongation, absorption of infra-red radiation and conductivity. The piston ring coating is a galvanic coated chrome coating with aluminium oxide particles loosely embedded in the crack network. For the chrome coating only the conductivity was thought to be relevant. A introduction to the material properties can be found in chapter 6.

Differences in thermal elongation within the grey cast iron on a microscopic scale were found by measuring surface roughness on a polished sample by white light interferometry at temperatures up to 300 °C. The polishing was selective and resulted in embossed hard carbides. Increasing temperatures preferentially affected the pearlitic matrix, resulting in a overall smoother surface but stable oil retention ability. Other than differences in thermal elongation and abrasive wear, corrosion was also found to selectively change the surface topography, chapter 5. All these parameters have to be kept in mind when changes in surface topography become an issue for the safe running of piston rings and liners.

For large bore diameters of almost 1 m, gas radiation from the hot combustion gases becomes significant. Glowing soot will act as a Planck radiator over a wide spectrum and although the amount in Diesel engines is low when compared to more typically studied coal burning furnaces, it will play a dominating role at low loads and during load changes. Gas radiation is characteristic of the gas composition and only certain wavelengths will be present during a relatively clean and smokeless combustion. IR absorption by a lubricant film is also very selective and the temperature increase due to gas radiation will be limited to certain small wavelength ranges. Lubricant degradation and deposit formation will widen this range as shown in chapter 7. Plain metals homogeneously reflect and absorb IR radiation over a wide range but show differences in absolute absorption between them; a gold standard is used as a perfect reflector. Graphite is a good IR absorber. In the previous chapter 7, the topography of the honing structure, with a roughness in the range of the IR wavelength, was also found to have an influence on absorption. The FTIR technique is used to show the differences and to compare them with possible gas radiation found in the literature.

Surface conduction in friction contacts is important to transport flash temperatures by asperity contact away from the contact zone to avoid melting or micro welding of the metallic surfaces. The materials used in engines are inhomogeneous while conductivity measurements reported in literature are usually done with homogeneous materials. An atomic force microscope, AFM, with a thermal tip was used to find the existence of conductive contrasts on the surface of grey cast iron and chrome coating in relation to feature size and chemical composition. The required heating power for a constant tip temperature is measured to find differences in conductivity.

8.1 Materials and Methods: Influence of Temperature on Surface Roughness Parameters

A cylinder liner sample was polished by hand to an optically acceptable state.

The sample was placed on a temperature controlled hot plate and the sample temperature measured by a K-type thermocouple.

Surface roughness was measured using a white light vertical scanning interferometer (Veeco – WYKO NT3300S). An introduction to the technique can be found in chapter 6. The movable stage was kept still during the

measurements as the changes in roughness were expected to be miniscule and the tolerances in the movable parts might have influenced the results. The evaluated area was 2.3 x 3 mm. Evaluation of the area roughness was undertaken in x and y directions and then averaged for presentation.

Measurements were taken at 20, 100, 200 and 300 °C. The data at 200 °C is not useful as technique artefact light fringes appeared as surface features and the cause was not found during repeated measurements. The defects may have been caused by the temperature dependent thermal expansion coefficient of Fe_3C which shows a large step at 200 °C, which is close to the Curie-temperature of Fe_3C, (Hartmann, et al., 1995) probably causing the surface to "vibrate" during the measurements for very small changes in temperature. At high temperatures, the build up of a purple oxide layer was observed. Therefore the measurements were repeated after cooling down to 20 °C to find any deviations and exclude selective build up of thick oxides.

Due to limited machine access, the measurements could not be repeated and were only taken in one spot of the sample.

8.2   Materials and Methods: Optical Properties of Cylinder Liner Surface in Comparison to Selective Gas Radiation

The FTIR-microscope, chapter 3 and 6, was used to compare the selective thermal gas radiation by hot combustion gases with the absorption properties of the cylinder liner surface on an microscopic scale. The expected spectrum of gas radiation was obtained from exhaust gas composition. A new honed automotive cylinder liner surface was used to show geometric influence. A highly polished (Buehler Mastermet II, 0.02 µm Si_2O-suspension) marine cylinder liner material was used to show differences between pearlite, iron carbide and graphite.

8.3   Materials and Methods: Thermal Conduction of Cylinder Liner and Piston Ring Coating Base Material

A scanning force microscope (Veeco "Explorer") is equipped with a nanoscale thermistor tip. The tip is kept at a constant temperature of 100 °C and the required electric power recorded. The position of the tip in all directions is recorded in parallel to give information about the topography of the measured surface. When the thermal conductivity of the surface is inhomogeneous, the electric power to keep the tip at a constant temperature changes and a map of the thermal surface properties is created.

The electric resistance of the tip as a function of temperature is found by measuring the resistance of the tip at the melting point of polycaprolactone (~60 °C) and Nylon66 (~265 °C). This calibration also includes the heat lost towards the tip holder. For the tip used, the linear relation was found to be R(T in °K) = 2.188 + T * 0.00326, which gives a tip resistance of 3.4 Ω at 100 °C.

The heat flow towards the surface also fluctuates when the contact area between tip and surface changes. Steep flanks due to changes in topography increase the contact area, while fine cracks with sharp edges decrease the surface area.

Ideally, the measurement of materials with known material properties should be taken in parallel with the unknown samples, to correlate the measurement results to known conductivities. The best known material of this study is chrome followed by iron carbide.

The positioning of the tip on the surface is almost impossible with the given optical access and approaching the area of interest is based on pure luck. The access time to the machine was very limited and restricted the extent of measurements and improvements. Therefore improved calibration techniques could not be implemented.

8.4   Results and Discussion: Influence of Temperature on Surface Roughness Parameters

In the literature, the strong anisotropic thermal expansion of iron carbide in comparison to pure iron is reported (Hartmann, et al., 1995), (Kagawa, et al., 1987). Pure iron shows a linear increase in the thermal expansion coefficient between 40 and 300 °C. Cementite, Fe_3C, dependent upon the direction of the crystal structure, shows a constant behaviour between 40 and 100 °C followed by a dip until about 180 °C, which causes the crystal to shrink in one direction, and then a sharp increase until about 220 °C reaching almost the higher values of pure iron, exceeding it in one direction and behaving almost linear like the iron until about 300 °C (Hartmann, et al., 1995). The aim of this study was to find the influence on surface roughness due to the reported differences in thermal elongation between the different phases of the coarse microstructure of the grey cast iron cylinder liner material. The absolute measurable extent of thermal elongation, however, depends upon the total length of the material in the measured direction. Obviously this cannot be predicted and depends upon luck when choosing the

measurement position. Figure 8.1 - Figure 8.4 show measurements across the same features at 20 and 300 °C. The positioning of the measurement line is not easy as the thermal elongation is three dimensional and the coordinates cannot be used as reference. Therefore distinct features must be used. All the red features are embossed hard phases mainly consisting of the eutectic carbide Fe_3C. The blue features are graphite lamellas, forming valleys. The matrix is lamellar pearlite consisting of pure iron and iron carbide layers. The distinct appearance of phases with varying hardness is an artefact of the polishing process. Compared to the pearlitic matrix, the embossed hard phase peak shrank by 379 nm while the graphite lamella valley became 27 nm deeper during heating.

The evaluation for roughness with the profile average statistics of the area is difficult due to the small number of distinct peaks and valleys. Figure 8.5 shows the result for skewness. Negative skewness originates from more pronounced roughness valleys and less pronounced peaks. A tendency towards more pronounced valleys can be seen from the measurements. Due to dominating single surface features, however, the standard deviation from the mean is very large, making an interpretation difficult.

The results point to a tribological positive development of surface topography with increased temperature, showing a decrease in peak height and a constant lubricant retention ability. Due to a lack of statistic evidence the result is, however, not conclusive.
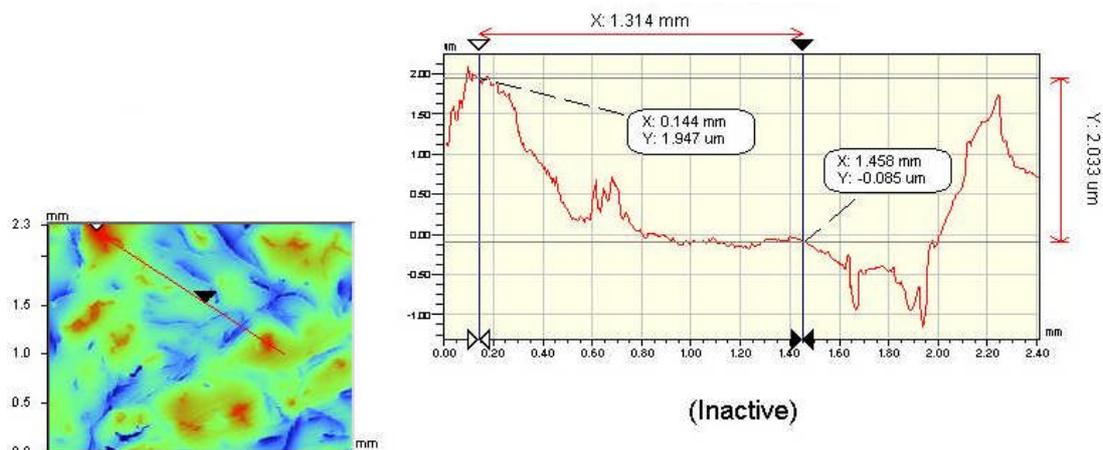
Figure 8.1: Distance between embossed hard phase and pearlitic matrix at 20 °C
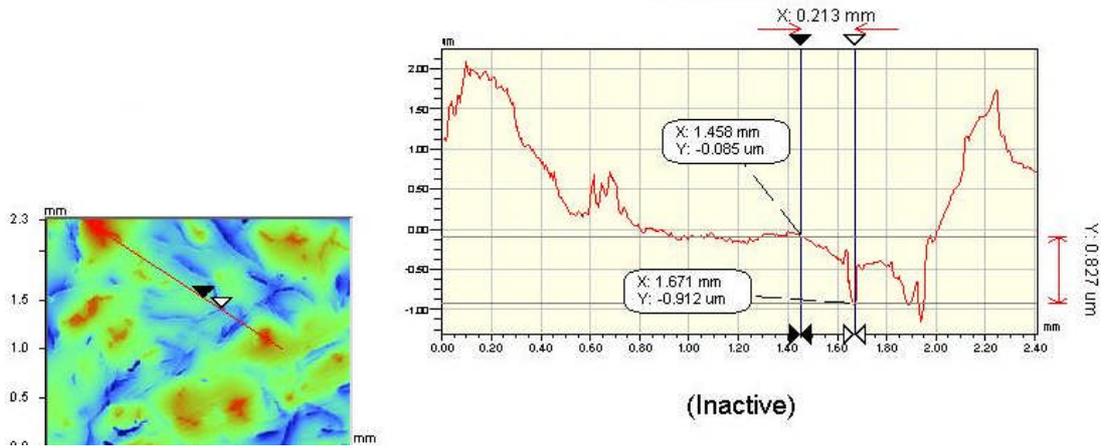
Figure 8.2: Distance between pearlitic matrix and graphite lamella at 20 °C
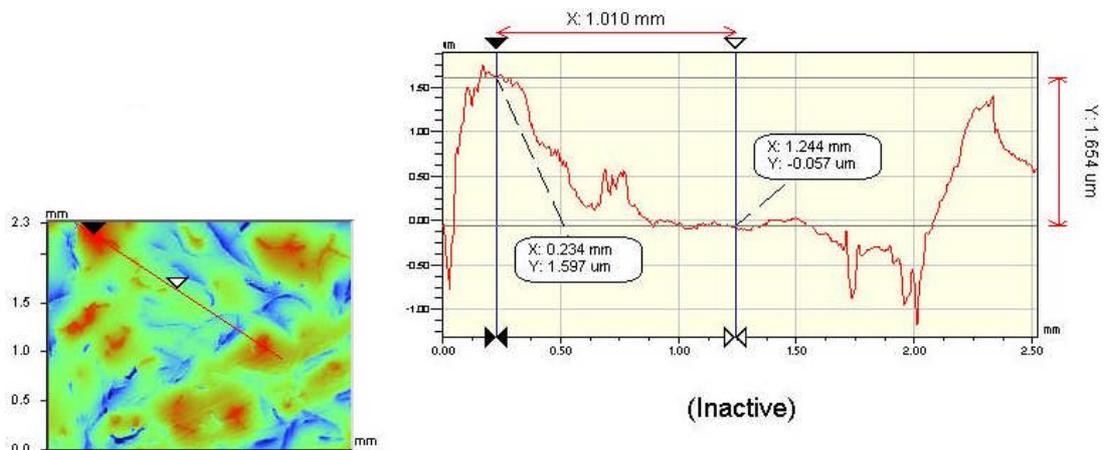
Figure 8.3: Distance between embossed hard phase and pearlitic matrix at 300 °C
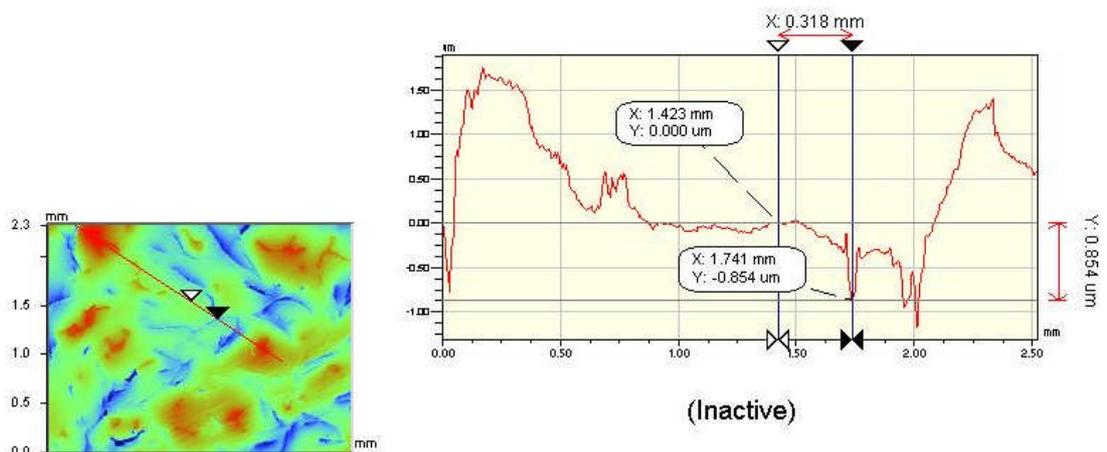
Figure 8.4: Distance between pearlitic matrix and graphite lamella at 300 °C
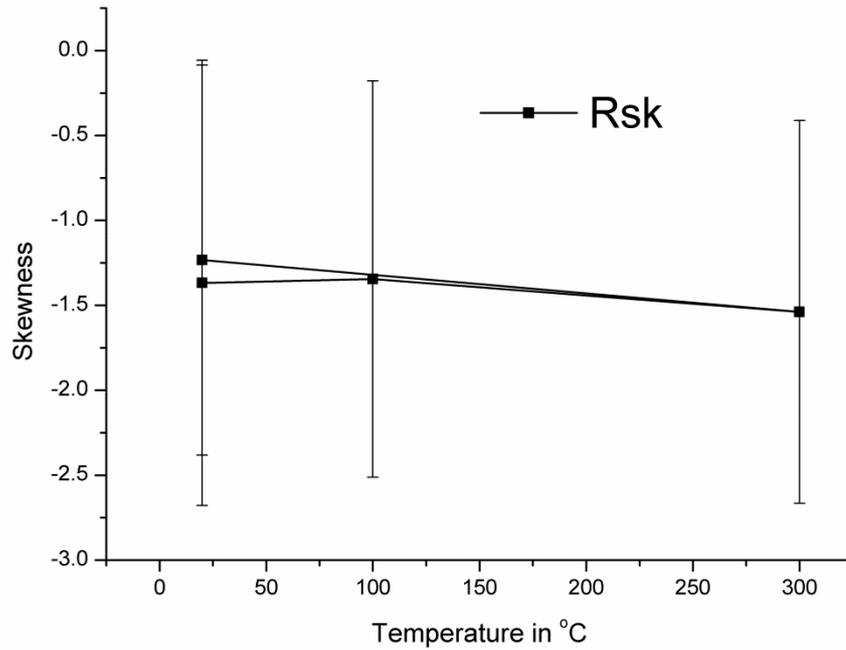
Figure 8.5: Change in surface skewness over temperature. Error bars indicate the standard deviation from the mean

8.5 Results and Discussion: Optical Properties of Cylinder Liner Surface in Comparison to Selective Gas Radiation

Table 8.1 shows the typical exhaust gas composition of a marine Diesel engine and the resulting contribution to IR radiation of each volume fraction. Carbon dioxide and water vapour are the biggest contributors to thermal radiation in the engine as elemental gases do not emit IR radiation.

Table 8.1: Exhaust gas composition (CIMAC Working Group "Exhaust Emission Control", 2008)

Gas	Fraction in %v/v	IR Gas Fraction in %v/v	Gas	Fraction in %v/v	IR Gas Fraction in %v/v
N_2	75	0	Ar	0.8	0
O_2	11.5	0	NO	0.15	1.18
CO_2	6.5	50.96	SO_2	0.09	0.71
H_2O	6	47.04	CO	0.015	0.12

When the idea of grey body radiation is applied, the emissivity of the gas ε_g is dependent upon the type of gas, partial pressure, total pressure, gas temperature and the geometry of the gas body (Vortmeyer, et al., 1993). The main influence, however, originates from the partial pressure of the gas.

Therefore the FTIR spectra of the gases (NIST, 2012) were added according to their volume fraction of all emitting gases. The result is an estimate of the IR spectrum of combustion gas, as shown by the black curve in Figure 8.6. Assuming the temperature of the gas is 1000 K, the absolute maximum energy that could be emitted is that of a black body and is described by Planck's law (Modest, 2003):

$$E_{b\lambda}(T, \lambda) = \frac{2\pi hc_o{}^2}{n^2\lambda^5\left[e^{\frac{h*c_o}{n\lambda kT}} - 1\right]}$$ (8.1)

with

h – Planck's constant – $6.6261*10^{-34}$ Js

c_0 – Speed of light in vacuum – $2.998*10^8$ m/s

n – Refraction index of the medium (vacuum – 1, with increasing pressure and temperature n becomes >1)

λ – Wavelength in m

k – Boltzmann constant – $6.6261*10^{-23}$ J/K

T – Temperature in K

The resulting emissive energy distribution was normalised and also plotted in Figure 8.6, green curve. Multiplied with the IR spectrum of the combustion gas, the maximum IR energy intensity of the combustion gas, red curve Figure 8.6, can be approximated. Two main regions from 3700 – 3000 cm^{-1} (2.7 - 3.33 µm) and 2400 – 2250 cm^{-1} (4.16 - 4.44 µm) for considerable gas radiation can be identified and a third minor region from 1700 – 1600 cm^{-1} (5.87 - 6.24 µm). Absorption by the oil film or the walls in those waveband areas should be avoided to reduce thermal heat flux from the expanding combustion gases. The radiation by soot particles has been neglected; they would radiate like a black body, green curve. It is recommended to conduct measurements on the real emissive spectrum of the combustion gas as soot particle content and gas composition is highly dependent upon engine type, load and fuel.

Integrating and comparing the total area below the green and red curve in Figure 8.6 shows a reduction of 75 % in total radiation maximum intensity from black body to selective gas radiation. A cleaner combustion therefore reduces thermal stress on the oil film.
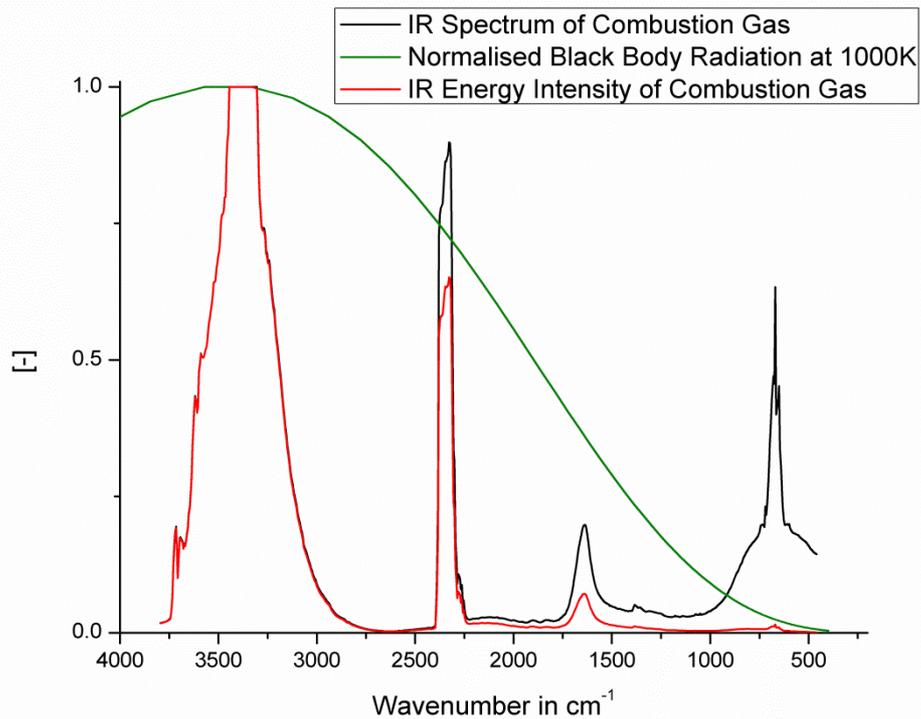
Figure 8.6: Infra red radiation of a black body at 1000 K and estimated chromatographic combustion gas radiation. Combustion gas composition according Table 8.1

In the previous chapter 7 it was already shown how valleys of the plateau honed cylinder liner surface show about five times higher IR absorbance than the surface plateaus, which is caused by the valleys geometry. Depending upon their depth, the steepness of their flanks and the incident angle of the light, which is 0° for the FTIR-microscope, the light gets reflected several times within the valley before it is reflected to the sensor or is scattered and only partially reflected to the sensor (Modest, 2003), (Hollands, 1963). The opening angle of a V-shaped groove starts to play a role in increasing the absorbance for angles smaller than 120° (Hollands, 1963).

Figure 8.7 shows the roughness distribution of a honed automotive cylinder liner measured by white light interferometry. About 16 % of the surface is comprised of deep valleys, blue, in the wavelength range of infra red radiation. Thirty such deep honing marks were evaluated for opening angle β, their depth z and their top width d to find β = 145 ±10°, z = 2.4 ±1 µm and d = 21.8 ±5.7 µm. While the feature size is well within the wavelength range, the opening angle is too wide to play a role and it must be concluded, that the higher absorbance of honing grooves found in chapter 7 is due to

scattering and not due to higher absorbance by internal reflection of the IR light.
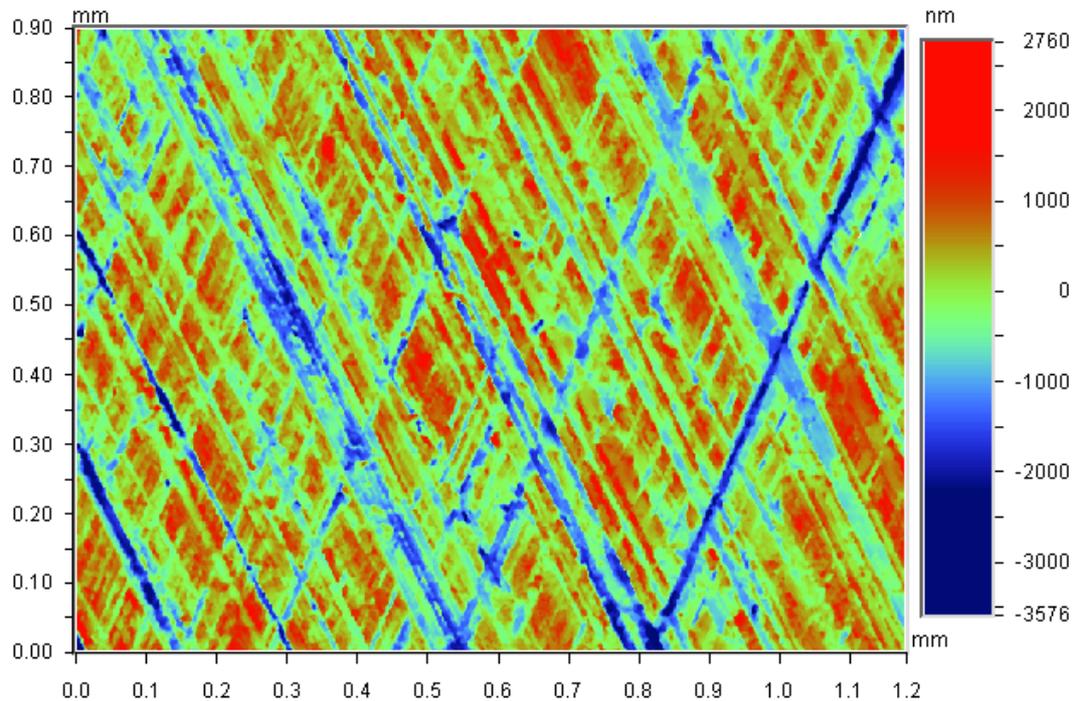
Figure 8.7: Surface topography of a honed automotive cylinder liner.

Other than the geometry of the surface, the base material also has influence on the absorption of thermal radiation. Figure 8.8 and Figure 8.9 show the results for a highly polished grey cast iron as used in 2-stroke marine Diesel engines. The graphite lamella and the iron carbide hard phases are flush with the pearlite matrix, therefore geometric effects can be excluded. The graphite shows about five times higher absorbance than the pearlite and the iron carbides but all phases absorb as grey bodies. There is very little difference between pearlite and iron carbide with the latter showing slightly less absorbance.

On top of the structure and base material, the surface can be covered by an oil film or deposit. In particular, deposits and degraded oils show absorbance near 3300 cm^{-1} and 1650 cm^{-1}, chapter 3, 4 and 7, while fresh lubricant is just slightly within the thermal radiation band near 3000 cm^{-1}. This increased absorbance for the chromatographic gas radiation may cause an increase in degradation rate due to increased thermal heat flux.
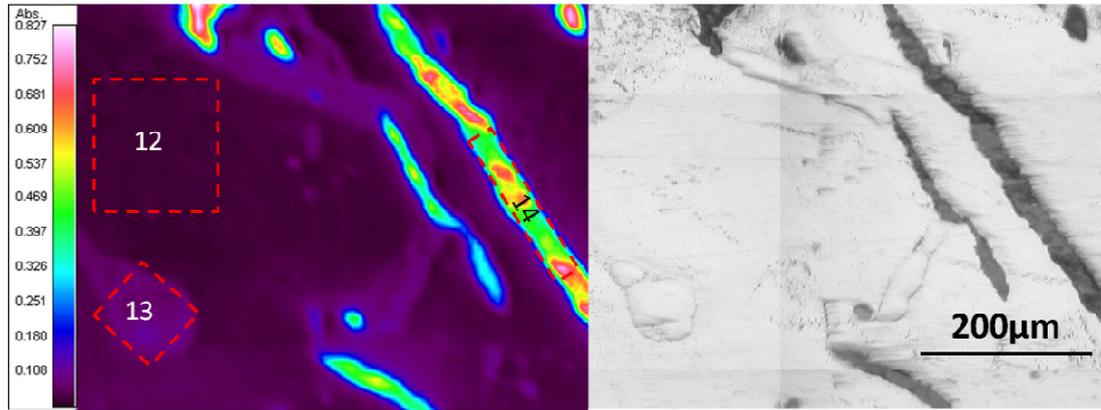
Figure 8.8: FTIR-scan and visual image on highly polished grey cast iron marine Diesel cylinder liner material. Position 12 is the pearlite matrix, 13 a Fe₃C hard phase and 14 a graphite lamella.
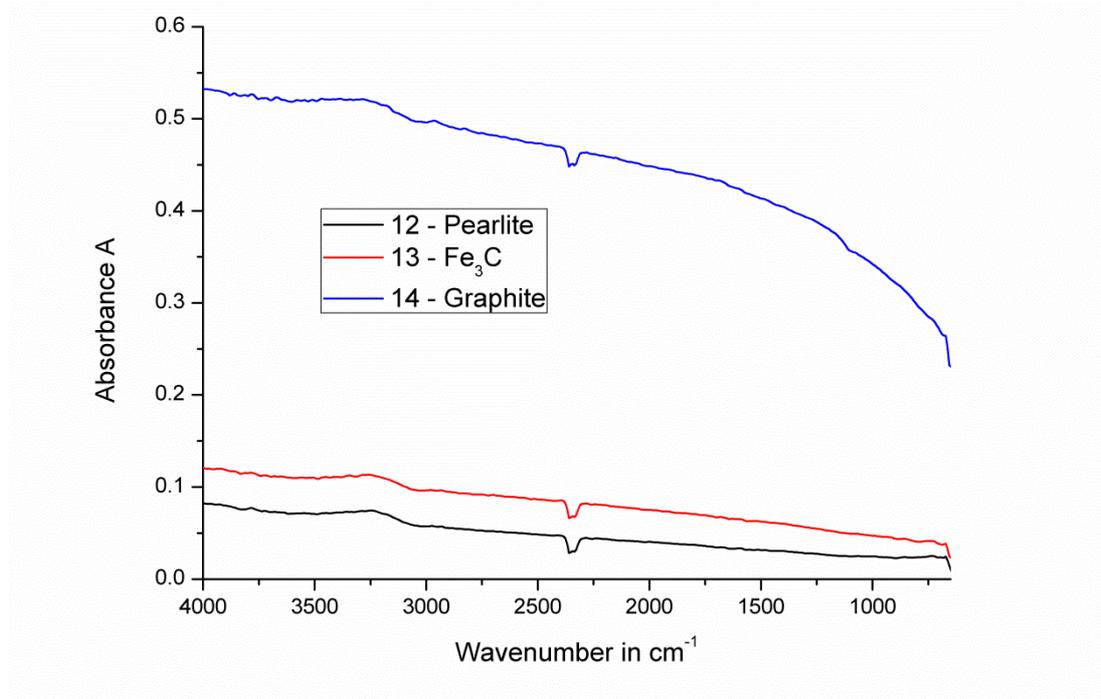
Figure 8.9: FTIR measurement scan on highly polished grey cast iron marine Diesel cylinder liner material. Spectra where taken at the positions indicated in Figure 8.8.

8.6 Results and Discussion: Thermal Conduction of Cylinder Liner and Piston Ring Coating Base Material

Figure 8.10 shows a thermal map of a piston ring surface coated with chrome. The higher the measured power, the higher is the conductivity of the scanned material. Clearly visible is the crack network, which shows lower conductivity than the galvanic coated chrome. The galvanic plated coating is built of many layers. The thickness of the top layer is unknown. Therefore it is speculation if the weaker lines of low conductivity originate

from an underlying chrome layer. The indicated area was averaged to find a required heating power of 3.5 mW. The thermal conductivity of high-purity chromium is reported to be ~92 W/mK at 100 °C (Moore, et al., 1977). This information is later used to approximate the conductivity of a unknown area.
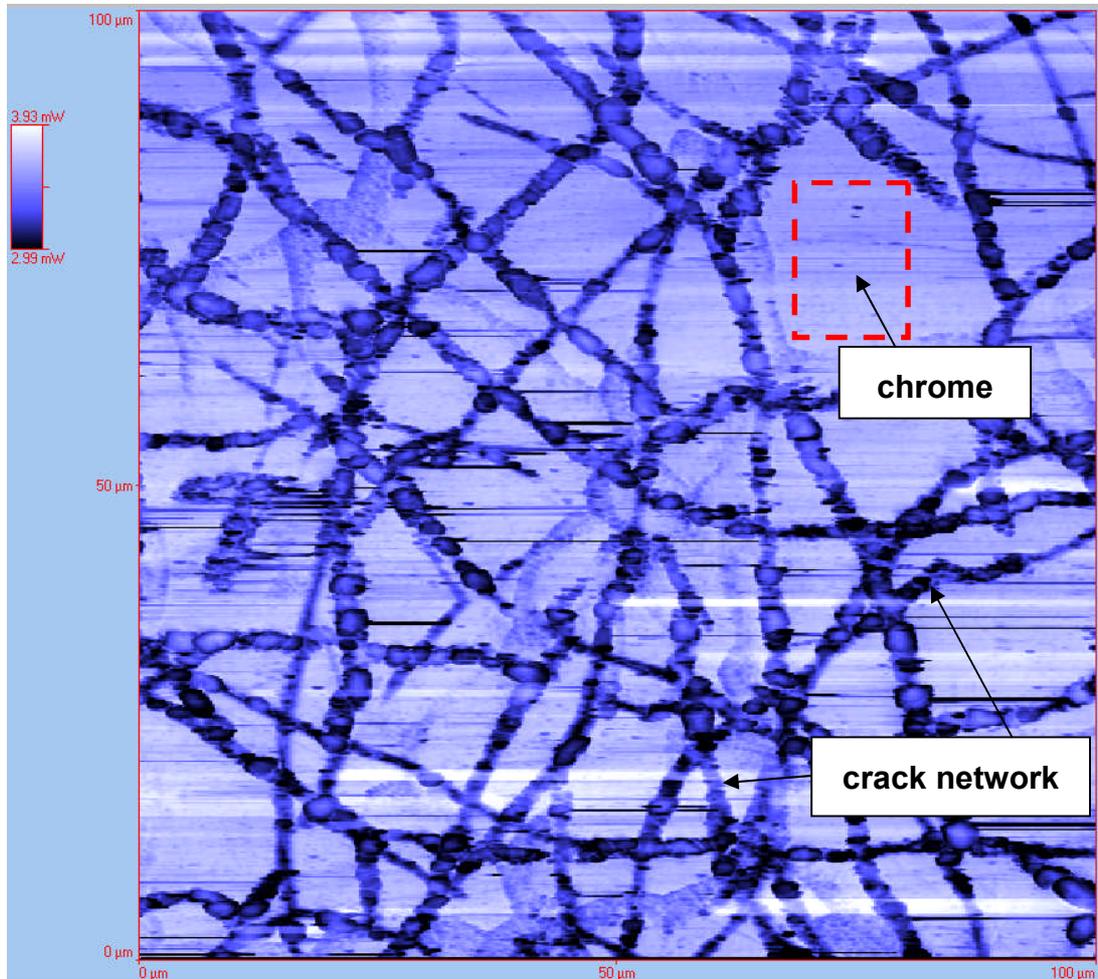
Figure 8.10: Conductivity contrast picture of electro plated piston ring chrome coating by SThM.

Figure 8.11 shows a thermal scan on grey cast iron of a cylinder liner material. The sample was highly polished and etched with NITAL to distinguish the iron carbides. Figure 8.12 shows the effect of NITAL on a polished grey cast iron sample. Iron lamellas in the pearlite and iron phosphide in the hard phase were attacked and recessed by about 100 nm while the iron carbide lamellas and the eutectic iron carbide hard phase remained unaffected. The topography picture was taken by a AFM during a demonstration session at manufacturer Bruker. The white peaks are caused by jumping of the AFM tip over surface features. The pearlitic structure is

also visible in the thermal scan but the low conductivity between the Fe_3C lamellas is caused by the lack of pure iron. The indicated area on the Fe_3C hard phase was averaged to find a required heating power of 2.5 mW. The thermal conductivity of Fe_3C in the form of cementite is reported to be 7 – 8 W/mK (Rukadikar, et al., 1986), (Helsing, et al., 1991) from 0 – 100 °C. This information is used later to approximate the conductivity of an unknown area.
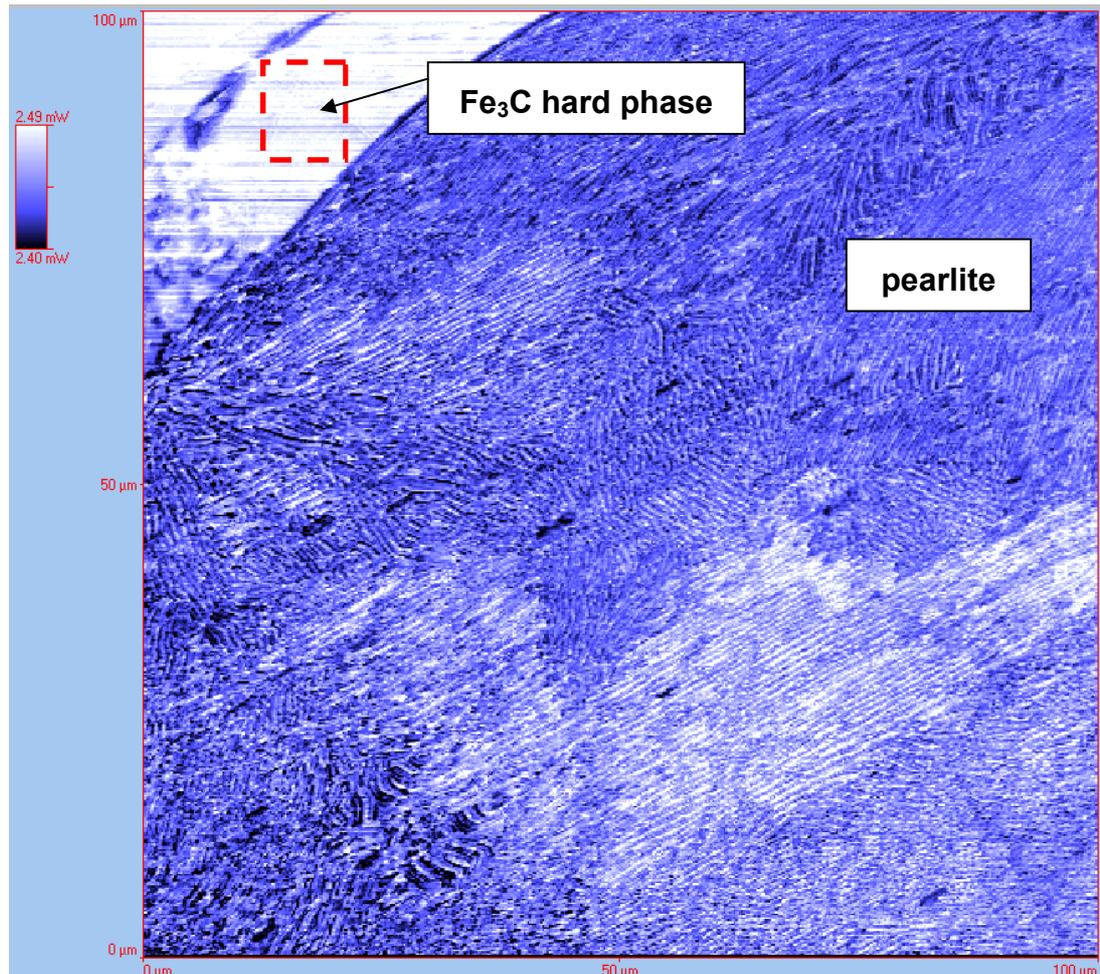
Figure 8.11: Conductivity contrast picture of highly polished and etched grey cast iron cylinder liner material including a hard phase and pearlitic matrix by SThM.

Figure 8.13 shows a thermal scan on grey cast iron of a cylinder liner material, including a graphite lamella which is about 0.45 µm below the matrix surface. Due to the reduced mechanical contact of the tip with the surface, the edges show lower conductivity. Also quite visible are the scratches originating from a poorer polishing process. The indicated areas were averaged to find a required heating power of 3.3 mW for both pearlite

matrix and graphite lamella. Literature reports a strongly anisotropic conductivity behaviour of graphite depending upon the orientation of the crystal structure. Measured values range from ~80 ~ 3000 W/mK at 100 °C depending upon manufacturer source and crystal orientation (Slack, 1962). The thermal conductivity of the pearlitic matrix is reported to be around 40 – 50 W/mK (Holmgren, et al., 2008), (Rukadikar, et al., 1986). No information about the remaining thickness of graphite or even the existence of graphite in the measured surface feature can be given.
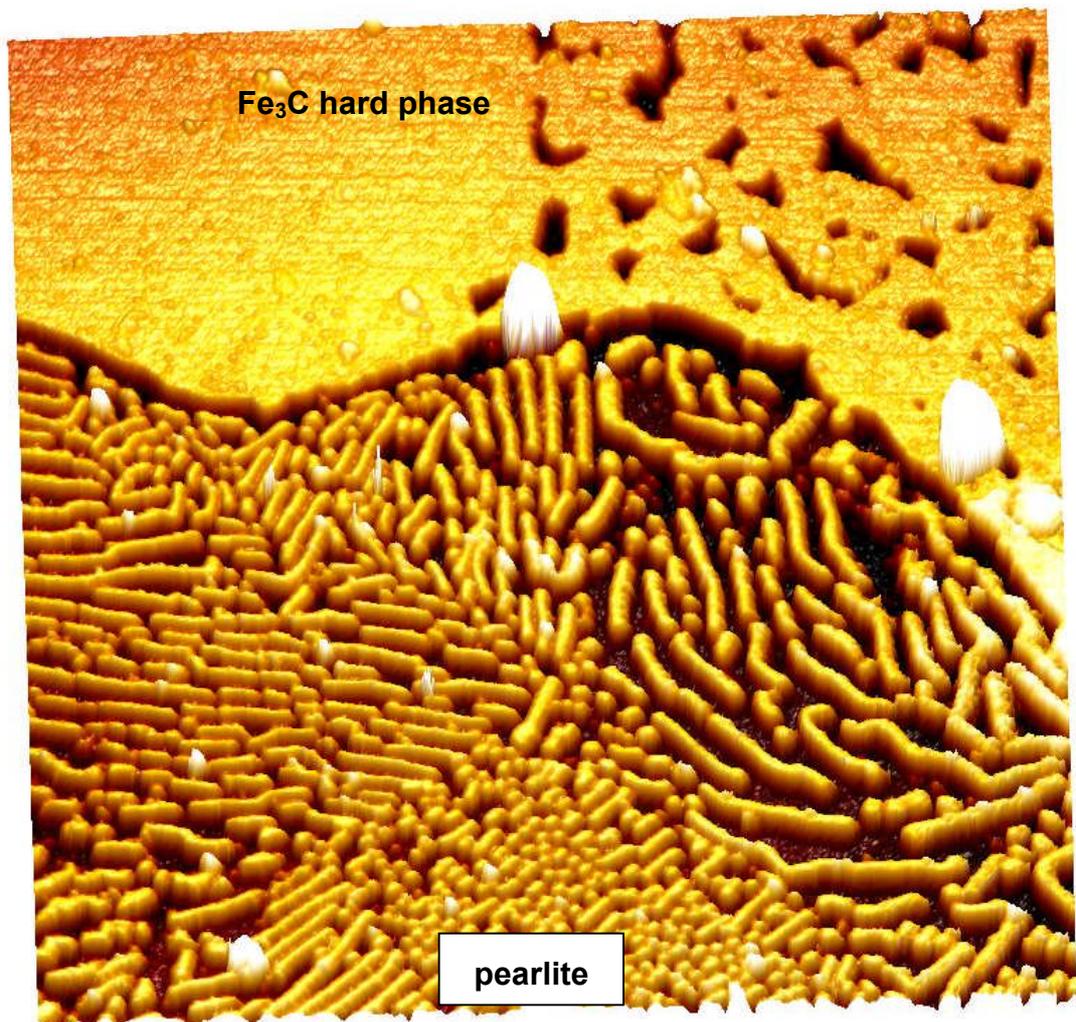
Figure 8.12: 100x100µm AFM scan of grey cast iron polished and etched with NITAL. Iron and iron phosphide removed by ~100 nm

A rough estimation for the thermal conductivity can be given considering the law of electric power $P = U^2 / R$ and the rate of heat flow $Q = \lambda * A * \Delta T / L$. In the experiment the only variables are the voltage U and the thermal conductivity λ. Power P is measured, the temperature T is kept constant

which means the resistance R of the tip is constant and the geometry of the tip, contact area A and distance of heat flow L, is also constant. Therefore $U^2 \sim \lambda$ and with the better characterised measurement results from Figure 8.10 and Figure 8.11 the thermal conductivity found for Figure 8.13 is around 75 W/mK, assuming a linear relationship between U^2 and λ.
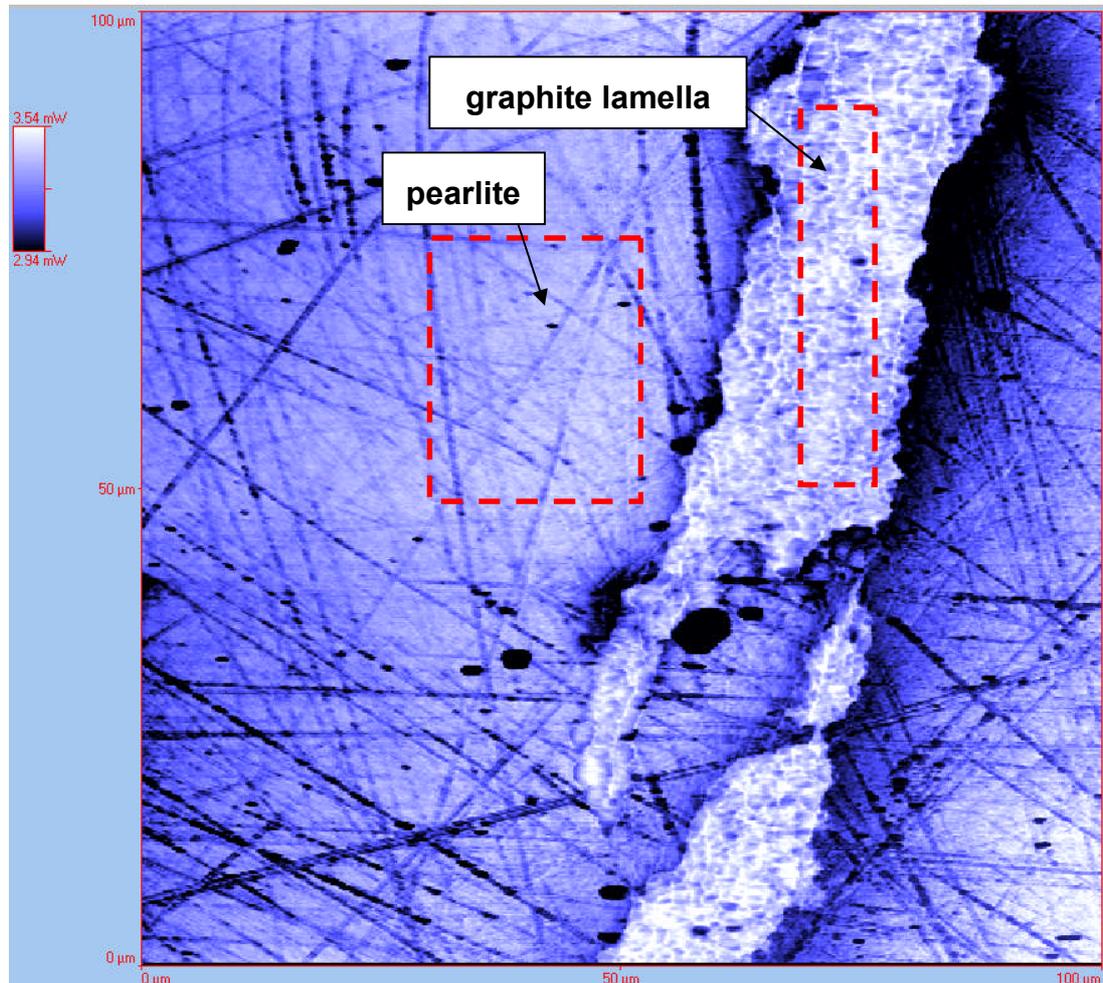
Figure 8.13: Conductivity contrast picture of polished grey cast iron cylinder liner material including a graphite lamella by SThM.

8.7   Conclusions of the Measurements on Thermal Properties of Piston Running Materials

The thermal elongation properties of the various phases in grey cast iron vary greatly. For one position on a polished sample, evidence for changes in surface roughness with changes in temperature was found. The protrusion of iron carbides was lowered by increasing temperature. For roughness measurements under cold conditions this has to be taken into account when

interpreting the results as the cylinder liner surface wears under hot conditions.

Gas radiation for large bore Diesel engines cannot be neglected as a source of thermal heat flux towards the cylinder liner wall. The gas radiation was shown to be selective with gaseous water and carbon dioxide contributing the most. Highest absorption is shown by graphite lamellas. Deep honing marks show a five times increased absorption compared to the base material in FTIR measurements. This was shown to be an effect of scattering and not real absorbance as the opening angle of the honing marks is too big to play a role. The formation of deposit and degradation of the lubricant increases the absorption by the oil film and therefore is likely to increase degradation rate by increased temperature – a self-accelerating process which also influences the concentration of condensing sulphuric acid towards higher concentrations, chapter 1, and therefore again increased deposit formation, chapter 3. The water content in the combustion gas is likely to increase in the future due to techniques like direct water injection for NO_x reduction, thus increasing thermal radiation.

The eutectic iron carbide, Fe_3C has, at 1147 °C, the lowest melting point (Bargel, et al., 1999) and the lowest thermal conductivity of all material phases in the piston ring – cylinder liner contact. Under pure abrasive conditions and certain corrosive conditions, chapter 5, the large iron carbides are protruding from the surface. At operation temperature just below the Curie point, ~200 °C, the carbides can grow suddenly when the Curie temperature is exceeded within a short time interval. This characteristic makes them vulnerable to friction welding on to the piston ring surface when the oil film is not sufficient to separate the parts.

The following chapter 9 finalises this study with conclusive remarks, recommendations for practical applications and suggestions for future research.

Chapter 9
Conclusions and Suggestions for Future Work

During the course of this study the impact of sulphuric acid on piston ring lubrication was investigated by the means of interfacial tension, contact angle and friction measurements. These major techniques were accompanied by various analysis techniques to find the chemical and physical state of resulting products. The results were placed in relation to the typical application by comparison with reactions in fully formulated lubricants. Temperature was found to be a major contributing factor and some investigations were dedicated to thermal surface properties of piston rings and cylinder liners.

The research area is part of the wide field of piston ring lubrication in large 2-stroke marine Diesel engines focusing on the impact of sulphuric acid on the lubrication. The results, however, are valid also for other areas incorporating emulsions of aqueous sulphuric acid in oil and iron or chrome based materials due to the wide breath of the applied physical and chemical range.

The study fills some gaps by transferring chemistry know-how to the engineering application and by using realistic quantities of acid in oil, total lubricant volume and temperatures and by selective isolation and purification of the system. Most test bench studies in the area try to be as close to the application as possible, while others work under purest conditions. In this study, most was learnt working under purified conditions, whilst the validity and limitation of those results was shown under more realistic conditions. Another gap that was filled is the creation of input values to theories found in literature, mainly contact angle, interfacial tension, viscosity of reaction products and friction coefficients. A side effect is the better understanding of the TE77 piston ring on liner contact friction test, which was analysed to a depth not seen before.

9.1   Consolidation of Research Space

The following subsections reflect the objectives set in chapter 1, supporting the aim to find the impact of aqueous sulphuric acid on piston ring lubrication.

9.1.1 The Physical Impact of Droplets on Rheology

Emulsions of aqueous sulphuric acid in API Group I base oil are more distinct, finer dispersed and more stable than emulsions with squalane, which can be explained by polar surface active substances already present in the base oil and a higher reactivity of unsaturated hydrocarbons forming surface active products. It is likely that a higher amount of dispersant must be added to the fully formulated lubricant when moving to higher refined base oils to keep acid droplets finely dispersed.

Following theory, (Taylor, 1932), the viscosity of dilute emulsions below a volume fraction of 0.1 is governed by the viscosity properties of the continuous phase. Heavy reaction products formed at higher acid concentrations have no influence on viscosity in the investigated range. The isolated reaction products, however, show a massive increase in viscosity and shear thinning behaviour, which can be explained by their appearance as concentrated "water" in "oil" emulsions. The viscosity of dispersed bituminous droplets has significance for time dependent droplet displacement, chapter 2. The measurement equipment was not completely corrosion resistant and the temperature and concentration had to be kept under control, limiting the range of investigation. The equipment was also not able to provide the high shear rates and hydrodynamic pressures produced in an engine. The enclosing of about 40 %w/w sulphuric acid in a hard hydrocarbon shell has significance for the neutralising process by the fully formulated lubricant.

Theory, chapter 2 section 2.3.1 and 2.3.3, requires the input of interfacial tension to describe droplet breakup and displacement in a shear flow. The values were measured time, temperature and concentration dependent. A reduction in interfacial tension reduces the shear rate needed for droplet deformation and displacement.

Theory, chapter 2 section 2.3.3, requires the input of contact angles to describe droplet displacement in a shear flow. The contact angle of various concentrations of aqueous sulphuric acid submerged in squalane was measured using the sessile drop technique. The temperature influence was found to be small. For pure water, the contact angles were found to be large while they were found to be small for concentrated sulphuric acid. Contact angles on chrome coating are bigger than on grey cast iron. Advancing contact angles are larger than static and receding contact angles, which is to be expected. The larger contact angle on the chrome coating indicates that the acid droplets are smaller but stationary on the chrome surface, leading to

pitting, chapter 7, while on the grey cast iron corrosion is spread over a larger surface due to droplet creeping. Acid droplet volumes on a surface under shear can become larger for higher refined low viscosity base oils, which is the trend in industry and needs to be addressed by a suitable additive formulation.

9.1.2 The Chemical Interaction Between H_2SO_4 and Base Oils

Reacting hydrocarbon oil with aqueous sulphuric acid results in the formation of bituminous emulsions when exceeding 40 %w/w and formation of solids when exceeding 80 %w/w and high temperatures of around 120 – 165 °C or long storage times. This can be explained by oxidation and sulphonation of the hydrocarbons, forming a surfactant shell around the acid phase which finally solidifies. The findings correspond well with the dissociation of sulphuric acid. Keeping the condensed acid concentration in the engine below 40 %w/w would limit the degradation of the lubricant to levels seen in engines burning low sulphur fuel. The additives in the lubricant, however, must be able to react with this dilute acid, which is very aggressive towards cast iron pearlite at concentrations of around 20 %w/w. The reactivity of API Group I oil was found to be higher than that of squalane and the quantity of deposit in the engine is likely to be reduced when moving to higher refined base oils.

The chemical analysis of the heavy reaction products is only semi-quantitative, confirming oxidation and sulphonation taking place. This is a limitation of the available analysis techniques able to deal with the heavy products and the immense number of possible reaction products. The creation of heavy reaction products, however, is significant as they can either act as very viscous lubricant or as a binder to form hard deposits with wear particles and other reaction products, like gypsum.

Interfacial tension measurements of aqueous sulphuric acid against squalane reveal a close relationship with the dissociation of sulphuric acid. In the literature (Vacha, et al., 2008) the interface between water and oil is explained as a layer of H_3O^+ ions on top of a layer of OH^- ions. Influencing the ion layer by varying the pH (Vellinger, et al., 1933) or by applying a strong electric field (Sato, et al., 1998) reduces the interfacial tension. This could explain the first steep reduction until about 0.5 %w/w acid concentration. The second two reductions can be explained by the creation of surface active substances due to oxidation and sulphonation of the

squalane to various extents. The measurements with squalane were a significant step to find the correlation of the dissociation of sulphuric acid with a turning point at around 40 %w/w, which was found to be the lower limit for bitumen formation, also evident with less refined API Group I base oil.

Analytical grade squalane was used as purchased but for future research it is recommended to further purify it by the treatment described in (Mahe, et al., 1988).

The interfacial tension measurements with API Group I base oil revealed the presence of surface active substances in the base oil as the interfacial tension towards pure water was time dependent. The values are by far smaller than for squalane and the minimum interfacial tension was already reached at 4 %w/w acid concentration. The results were consistent across three different oils of various origins, the responsible components, however, were not identified.

The time dependency of interfacial tension can be observed at higher resolution and for lower values with the pendant drop technique or a electronically controlled ring tension meter.

9.1.3 The Tribological Performance of Fully Formulated Lubricants

At 170 °C the fully formulated lubricants show a 30 % higher friction than base oil, most probably resulting from the formation of a calcite boundary film. Previous research showed reduced friction after the build up of a calcite boundary film (Caixiang, et al., 2008), (Topolovec-Miklozic, et al., 2008), (Vipper, et al., 1998) and it is strongly recommended to improve the formulation of marine lubricants accordingly. The wear rates, however, are very low but the visual appearance of the piston ring surface is worse than in the case of mixing with sulphuric acid. This is important to note, as scuffing in the engine usually starts in-line with fresh lubricant supply.

9.1.4 The Tribological Performance of H_2SO_4 Dispersed in Lubricant Base Oil

The influence of temperature and acid concentration on friction, surface roughness, wear and the chemistry of surface and lubricant was tested using a reciprocating piston ring – liner contact. A hydrocarbon sulphate film was formed when lubricating with plain sulphur containing base oil and excessive deposit formation, visible to the eye, started at 300 °C. The higher the temperature, the higher wear and friction and the lower the resulting surface

roughness. Between 80 and 120 °C, friction decreased for oil containing aqueous sulphuric acid with concentrations between 40 and 98 %w/w. Evaluation of surface and lubricant chemistry suggests the formation of metal soaps, explaining the low friction. The higher the acid concentration, the lower the wear on the grey cast iron liner but the higher the wear of the chrome coated piston ring. Between 140 and 170 °C and 70 %w/w, friction is higher than for plain base oil and the formation of visible black deposit starts at 120 °C. Evaluation of surface chemistry suggests the formation of iron sulphate and nitrided hydrocarbon sulphates. The wear of the piston ring at 170 °C is lower than at 80 °C, while the wear of the liner is higher. The degradation temperature of the base oil was lowered when in contact with H_2SO_4 from 250 to 80 °C for oxidation and from 300 to 170 °C for nitration. One explanation is the catalysing effect of sulphuric acid to promote oxidation. At both temperatures, lubricant oxidation yields hydrocarbon radicals which readily react with NO_2 to form nitrated hydrocarbons. The source of NO_2 is not quite clear. Traces are contained in the air but also the catalysing effect of the freshly rubbed surfaces could yield NO_2. Trace nitrogenated contaminants in the lubricant base oil which become more prominent by evaporation of lighter compounds can be excluded because of the relatively low nitration temperature when catalysed with sulphuric acid. The formation of solids was found to be independent of nitration.

Overall the appearance of the surfaces, made from automotive parts, improved when sulphuric acid was added to both, the API Group I base oil and the fully formulated lubricant. This is in contrast to previous research using specimens machined from marine Diesel engines (Micali, et al., 2010) (Stott, et al., 1988) provoking the converse argument that the current cylinder liner material is not suitable for use under acidic attack. Those studies, however, used unrealistically large quantities of sulphuric acid in the lubricant.

The analysis of the contact yielded the initial Hertzian contact pressure, deformation of the piston ring specimen and the resulting gap between piston ring and cylinder liner. The correlation between liner surface and piston ring temperature was measured. Both evaluations are significant for the understanding of previous and future research studies on this frequently used test bed.

9.1.5 Important Side Findings on Marine Lubricant and Materials

By measuring the gas volume release of fully formulated lubricants in contact with sulphuric acid, the reaction rate was found to differ greatly

between the commercial products. Both products perform best when in contact with concentrated sulphuric acid but lose their neutralising effect when in contact with aqueous solutions and dirty, pre-reacted sulphuric acid. The formation of concentrated and pure sulphuric acid in the engine, however, is rather unlikely and the results of this study show a significant difference between commercial products. The limitation of the presented technique is the inability to detect non-gas releasing metal oxides and the incorporation of a pH-meter is recommended for future work. The 'method of initial rate of reactions' as presented in chapter 3, however, is easily reproducible and can be one tool to underline a purchasing decision. In such a comparative study it is recommended to take more points at various concentrations of sulphuric acid and also at different temperatures to find the temperature dependency of the reaction by using the Arrenius-equation. The present study, however, is not meant to compare performance of different fully formulated lubricants. The resulting differences were unexpected and a by-product of later evaluation. The poor performance of neutralisation efficiency at low concentrations is outside the application specification and an improvement of the additive package in fully formulated lubricants is highly recommended.

The roughness of a relative poorly polished cylinder liner sample was measured stepwise between 20 and 300 °C. In general, the surface became smoother for the highest temperature reflecting the smaller thermal elongation coefficient of Fe_3C. At 200 °C, which is close to the Curie temperature of Fe_3C, it was not possible to take measurements and it is proposed that the surface geometry is changing rapidly for small variations in temperature due to the large step in thermal elongation coefficient of Fe_3C (Hartmann, et al., 1995). Unfortunately the measurements could not be repeated to come to a statistically significant conclusion. Improving the polishing process would result in an easier to establish surface reference line during the evaluation.

The thermal radiation absorption of grey cast cylinder liner material, deposits and oil film was studied in the wavelength range of typical gas radiation in the combustion chamber using the FTIR technique. It was shown that the honing structure with the existing micro-geometry does not increase absorption but scatters light. Graphite lamellas in the grey cast iron show a five times higher absorption than the surrounding metallic phases. The graphite lamellas are very good conductors of heat and often are claimed to transport excessive heat away from the surface. From a thermal radiation

point of view, however, graphite lamellas actually increase surface temperature. This should be kept in mind when a decision on new grades of surface material is made. Fresh lubricant shows an absorption just outside a strong water vapour emission peak while being within the strongest region for black body radiation. A clean combustion with low soot content reduces thermal stress on the oil film. The more degraded the oil becomes and the more deposit is formed, the larger the absorption of thermal radiation; thus increasing the degradation rate.

Differences in thermal conductivity of the various phases in the microstructure of grey cast iron cylinder liner material and piston ring chrome coating were investigated using a scanning thermal microscope SThM. Eutectic iron carbide was shown to have the lowest conductivity and chrome the highest. This is not a new finding but it shows that relatively large areas in the microstructure of the cylinder liner have significantly different properties. Under mild abrasive wear conditions or corrosive attack with dilute sulphuric acid, the hard and inert Fe_3C will protrude and the rough surface will show the thermal properties of Fe_3C instead of the bulk material when metal to metal contact occurs. The readings are not absolute as the calibration of the instrument is quite difficult. The situation could be improved by embedding thin foils of material with known thermal conductivity and measure across these layers into the unknown material sample. The polishing process is crucial and the best results can be expected for the smoothest surface.

9.2 Practical Applications and Recommendations for OEM and Lubricant Supplier

9.2.1 Aqueous H_2SO_4 Droplets in Lubricants

Emulsification of aqueous sulphuric acid in API Group I base oil is more distinct, finer and more stable than in the higher refined squalane. This could mean a higher amount of dispersant is needed for higher refined base oils to keep dispersing properties for acid droplets comparable.

One aspect when considering surface modifications of piston ring and cylinder liner should be the contact angle of aqueous sulphuric acid on the surface. The bigger the contact angle, the smaller is the risk of corrosion under shear flow as the droplets are more easily displaced.

9.2.2 Deposit Formation Catalysed by Aqueous H₂SO₄

The temperature to form hard deposits was reduced by 180 °C in the presence of realistically small amounts of sulphuric acid. The oil industry considers only thermal effects for deposit formation (Lancon, et al., 2010). The argument that the over-based additives would quickly neutralise the acid does not hold for poor lubricant distribution (Spahni, et al., 2010) and long resting times of the lubricant on the cylinder liner surface (Doyen, et al., 2007). Deposits are regularly found on surfaces with operating temperatures substantially below 300 °C and after short running times, thus excluding transport phenomena. This finding calls for an improved laboratory test incorporating sulphuric acid as a catalyst.

9.2.3 Improved Lubricant Additive Formulation

Two commercial fully formulated marine lubricants were tested on a reciprocating piston ring – cylinder liner friction test bed. Both showed an friction increase of 30 % compared to the plain base oil. Differences in viscosity cannot explain this finding. Previous research has clearly shown differences in friction between different formulations while having the same alkaline reserve and similar, low wear (Topolovec-Miklozic, et al., 2008). This deficit of marine lubricants clearly requires addressing by the oil companies.

Care must be taken to formulate additives which are able to neutralise dilute sulphuric acid as concentrated sulphuric acid is a rather unlikely product of combustion and dilute sulphuric acid shows the higher corrosion rate on the pearlitic matrix of grey cast iron.

9.2.4 Considerations for Future Engine Specifications

The coarse microstructure of current large 2-stroke marine Diesel engines is a novel feature of those engines. Several findings in the current study suggest this to be a disadvantage for the piston running behaviour. The development of a commercially feasible coarseness reduction in near surface microstructure should be prioritised by the industry.

Efforts in reducing the soot content during combustion are not only beneficial for the environment but also a factor to reduce irradiative thermal stress on the remaining piston ring lubricant film. A internal reduction of soot content is more beneficial for the engine than a external reduction by exhaust gas after treatment.

9.3 Suggestions for Future Research

9.3.1 Improved Contact Angle Measurements

The contact angle measurements in this study were executed on metal surfaces from piston ring and liner for a single surface roughness. It is sufficient to measure the contact angles with a reduced variety of acid concentrations as the interfacial tension seem to have little influence on the resulting contact angle, which is contradictory to theory (Wang, et al., 2004). An improvement of the measurement setup would be the use of a finer respectively tapered capillary tip which would make the handling of smaller droplets easier, especially in the case of receding contact angles.

It would be interesting to repeat the measurements on pure materials for varying surface roughness between Ra = 0.1 and 1 µm to find Young's contact angle (Wang, et al., 2004). The measurements should be also repeated for run-in surfaces with changed surface chemistry as the influence of the surface material seems to be by far greater than the interfacial tension.

9.3.2 Lubricant Degradation and Deposit Formation

The nitration of lubricant during friction tests in ambient laboratory air with only trace content of NO_2 is not easily explained. In all cases nitration followed oxidation, which yields hydrocarbon radicals as an intermediate reaction product. The targetted exclusion of nitronium ions under controlled atmosphere containing isotopically labelled nitrogen-15 gas would show whether nitration of the lubricant would still take place at maximum temperatures of 300 °C for pure oil or 170 °C when contaminated with H_2SO_4, and if atmospheric nitrogen can be found in the reaction product. It would be quite interesting to note the formation of NO_2 by the rubbing process itself, which would add to the view on lubricant nitration in combustion engines and other machinery without obvious sources of NO_2. Although the formation of solids was found independent from nitration, the product might become tougher, which makes it more likely to form deposit on moving parts under shear.

The engine and load dependent thermal emission spectrum of large 2-stroke marine Diesel engines was not found in literature. The influence of thermal radiation for fuel evaporation is a well established and accepted (Sazhin, et al., 2004) while the impact on the oil film temperature and degradation is an unknown. Gas radiation is strongly dependent on the gas volume and is

expected to be more significant in large engines than in the commonly investigated small bore engines.

9.3.3 Friction Phenomena

Compared to lubrication with plain base oil at 80 °C, the friction coefficient decreases around four times when small amounts of more or less concentrated sulphuric acid are added to base oil. The wear of cast iron decreases as well. This is technically and commercially remarkable and should be followed for other applications or possibly for a "cold running-in oil" for piston ring and cylinder liner under conditions were the use of high sulphur containing fuel is not permitted.

The surface roughness of coarse grey cast iron was shown to be influenced by temperature. The thermal elongation coefficient of Fe_3C shows a sharp increase when exceeding the Curie temperature (Hartmann, et al., 1995). When the surface is run in just below the Curie temperature, the large iron carbides should be more or less flush with the pearlitic matrix. A small increase in temperature, however, should cause the carbides to rapidly grow, thus changing the surface topography and influencing the friction.

9.3.4 Corrosion of Grey Cast Iron with a Coarse Microstructure

The corrosion of grey cast iron during contact angle measurements was found to be concentration and temperature dependent. A study should be made with various concentrations of sulphuric acid over a range of temperatures. The size of carbides acting as potentials should also be taken into account, as the corrosion was seen to start on the edge of the carbides in all cases.

These were the final lines of this study, followed by the listed references, abbreviations and an appendix presenting fluid properties and the publication commenced during this study.

List of References

Abramzon, B., Sazhin, S. (2006): *"Convective vaporization of a fuel droplet with thermal radiation absorption"*, Fuel, Rehovot, Elsevier, 32-46 : Vol. 85.

Adams, J.F., Papangelakis V.G. (2007): *"Optimum reactor configuration for prevention of gypsum scaling during continuous sulphuric acid neutralization"* , Hydrometallurgy, Toronto, Elsevier, 269-278 : Vol. 89.

Agilent Technologies (2001): *"Basics of LC/MS"*, U.S.A., Agilent Technologies

Agnew, W.G., Agnew, J.T., Wark K.Jr. (1955): *"Infrared Emission From Cool Flames Stabilized Cool Flames; Engine Cool Flame Reactions; Gas Temperatures Deduced From Infrared Emission"*, Symposium (International) on Combustion, Elsevier, vol. 5.

Akiyama, E., Yamamoto, T., Yago, Y., Hotta, H., Ihara, T., Kitsuki, T.(2007): *"Thickening properties and emulsification mechanisms of new derivatives of polysaccharide in aqueous solution 2. The effect of the substitution ratio of hydrophobic/hydrophilic moieties"*. J. Colloid Interf. Sci., Tokyo, Elsevier, 438-446, vol. 311

Alwadani, M.S.(2009): *"Characterization and Rheology of Water-in-Oil Emulsion from Deepwater Fields"*, Houston, Rice University

am Ende, D.J., Eckert, R.E., Albright L.F.(1995): *"Interfacial Area of Dispersions of Sulfuric Acid and Hydrocarbons"*, Ind. Eng. Chem. Res., West Lafayette, American Chemical Society , 12, vol. 34.

Ashby, M.F., Abulawi J., Kong H.S.(1991): *"Temperature Maps for Frictional Heating in Dry Sliding"*, Tribol. Trans., Cambridge, STLE, 4, vol. 34.

ASTM, (2011): *"ASTM D1331 - 11 Standard Test Methods for Surface and Interfacial Tension of Solutions of Surface-Active Agents"*, ASTM Volume 06.01 Paint - Tests for Chemical, Physical, and Optical Properties, Appearance, West Conshohocken, ASTM International, Vol. 06.01.

Atkins, P.W.(2001): *"Physikalische Chemie"*, Weinheim, Prof.Dr. A. Hopfner, vol. 3.

Bachman, G.B., Addison, L.M., Hewett, J.V., Kohn, L., Millikan, A. (1952): *„Nitration Studies. I. General Mechanism of Vapor Phase Nitration"*, J. Org. Chem., Purdue, ASC Publication, July., 7, vol. 17.

BAFU & UVEK (2011): *„Entwicklung der schweizerischen Gesetzgebung im Bereich der Abgasemissionen von Motorfahrzeugen und Maschinen"*, Bern, BAFU

Bair, S. (2006): *"Reference liquids for quantitative elastohydrodynamics: selection and rheological characterization"*, Tribol. Lett., Atlanta, Springer, May., 2, vol. 22

Baker, H.R., Bascom, W.D., Sinleterry, C.R. (1961): *"The Adhesion of Ice to Lubricated Surfaces"*, J. Colloid Sci., Washington D.C., 17, 477-491

Bargel, H.J., Schulze, G.(1999): *„Werkstoffkunde"*, Berlin, Springer, vol. 6

Bellamy, M.K. (2010), *"Using FTIR-ATR Spectroscopy to Teach the Internal Standard Method"*, J. Chem. Edu., Vol. 87, 1399-1401.

Benoit, R., Durand, Y., Narjoux, B., Quintana, G., Georges, Y.: *"XPS, AES, UPS and ESCA - lasurface.com"*, CNRS Orléans, accessed: 13-March 2012, http://www.lasurface.com/database/elementxps.php.

Berger, C., Kloos, K.H.(2001): *"2 Materials testing"*, Dubbel Taschenbuch für den Maschinenbau", Beitz, W., Grote, K.H., Berlin, Springer, vol. 20

Bernadin, J.D., Mudawar, I., Walsh, C.B.(1997): *"Contact angle temperature dependence for water droplets on practical aluminum surfaces"*, Int.J.Heat Mass Transfer, West Lafayette, Pergamon, 5, vol. 40

Bethell, D.E., Sheppard, N. (1953), *"The Infrared Spectrum of the H_3O^+ ion in Acid Hydrates"*, J.Chem.Phys., vol. 21, 1421.

Braunovic, M., Konchits, V.V., Myshkin N.K. (2007): *"Part III: Diagnostic and Monitoring Technologies"*, Electrical Contacts: Fundamentals, Applications and Technology (Electrical and Computer Engineering), Taylor & Francis

Buhaug, O.(2003): *"Deposit formation on cylinder liner surfaces in medium-speed engines"*, Trondheim, Norwegian University of Science and Technology

Burstein, G.T., Shreir , L.L., Jarman, R.A. (1994): *"13.8 Chromium coatings"*, Corrosion, vol. 2., Elsevier Butterworth Heinemann, 99–110

Caixiang, G., Qingzhu, L., Zhuoming, G., Guangyao, Z.(2008): *"Study on application of CeO_2 and $CaCO_3$ nanoparticles in lubricating oils"*, J.Rare Earths, Shanghai, Elsevier, April, 2, vol. 26

Cantow, F.G.(2004): *"Paper no. 209 Piston rings for large bore engines"*, Kyoto, CIMAC, 1–14

Carrales, M.Jr., Martin, R.W.(1975): "Sulfur Content of Crude Oils", Dallas, United States Department of the Interior

Chaverot, P., Cagna, A., Glita, S., Rondelez, F.(2008): *"Interfacial Tension of Bitumen-Water Interfaces. Part 1: Influence of Endogenous Surfactants at Acidic pH"*, Energy&Fuels, Solaize, Am.Chem.Soc., 2, vol. 22

Chen, J.K., Chen, S.F.(2011): *"On Thermal Conductivity of an In-Situ Metal Matrix Composite - Cast Iron"*, Cast Iron, Metal, Ceramic and Polymeric Composites for Various Uses, Cuppoletti John, InTech, http://www.intechopen.com/books/metal-ceramic-and-polymeric-composites-for-various-uses/thermal-conductivity-of-an-in-situ-metal-matrix-composite-cast-iron

Chen, S., Chan, T.L., Leung, C.W., Liu, M.A., Pan, K.Y., Zhou, L.B. (2000): *"Multidimensional numerical simulation of heat radiation in direct injection Diesel engines"*, Proc.Instn.Mech.Engrs., Hong Kong, Part D, vol. 214

CIMAC Working Group "Exhaust Emission Control" (2008): *"Guide to Diesel exhaust emission control of NO_x, SO_x, particulates, smoke and CO_2"*

CIMAC Working Group "Heavy Fuel" (2003): *"No. 21 recommendations regarding fuel quality for diesel engines"*, Frankfurt/Main

CIMAC Working Group "Marine Lubricants" (2007): *"No.26 Guidelines for Diesel Engine Lubrication, Impact of Low Sulphur Fuel on Lubrication of Marine Engines"*, Frankfurt/Main

Class NK (2008): *"Guidance for measures to cope with degraded marine heavy fuels"*, version II., Ohnodai, Midori-ku, Chiba: ClassNK, Nippon Kaiji Kyokai

Danov, K.D.(2001): *"On the Viscosity of Dilute Emulsions"*, J.Colloid Interf. Sci., Sofia, Academic Press, 144-149, vol. 235

Davis, F.A., Moore A.J., Pridmore S.(1993): *"The Use of a Laboratory Wear Simulation Technique for the Development of Marine Cylinder Lubricants"*, 20th Int. Congress on Combustion Engines, London, CIMAC, vol. D82.

DECHEMA e.V. DETHERM: *"Thermophysical properties of pure substances & mixtures"*. https://cdsdt.dl.ac.uk/detherm/detherm.php (2005–2008). Accessed 27 May 2010

Demmerle, R., Barrow, S., Terretatz, F., Jaquet, D.(2001): *"New insights into the piston running behaviour of Sulzer large bore diesel engines"*, Frankfurt, CIMAC, 1–14

Demond, A. H., Lindner, A. S.(1993): *"Estimation of interfacial tension between organic liquids and water"*, vol. 27. Ann. Arbor, AmChemSoc

Diaby, M., Sablier, M., Le Negrate, A., El Fassi, M.(2009): *"Kinetic study of the thermo-oxidative degradation of squalane ($C_{30}H_{62}$) modelling the base oil of engine lubricants"*, J. Eng. Gas Turbines Power Trans. ASME 132, 032805.1–032805.9

Ding, H., Gilani M.N.H., Spelt, P.D.M.(2010): *"Sliding, pinch-off and detachment of a droplet on a wall in shear flow"*, J. Fluid Mech., London, Cambridge University Press, 217-244, vol. 644

dos Santos, A.P., Levin, Y.(2012): *"Ions at the Water−oil Interface: Interfacial Tension of Electrolyte Solutions"*, Langmuir, Porto Alegre, Am. Chem.Soc., 1304-1306, vol. 28.

Dowson, D., Taylor C.M.(1979): *"Cavitation in Bearings"*, Leeds, Ann.Rev. Fluid Mech., 11

Doyen, V., Drijfholt, R. K., Delvigne, T.(2007): *"Paper No. 61 Advanced applied research unravelling the fundamentals of 2-stroke engine cylinder lubrication - an innovative on-line measurement method based on the use of radioactive tracers"*, CIMAC

Economou, P.N.(1976): *"A study of the lubrication and dynamics of piston rings"*, Leeds, Department of Mechanical Engineering, The University of Leeds

Elson, J.P., Amin, J.J.(1974): *"Experimental Evaluation of a Scotch-Yoke Compressor Mechanism"*, Int. Compressor Eng. Conference, Paper 146, Lafayette, Purdue University

Elzinga, E.J., Peak, D., Sparks, D.L. (2001), *"Spectroscopic Studies of Pb(II)-sulfate Interactions at the Geothite-Water Interface"*, Elsevier, vol. 65, 2219-2230

Enevoldsen, A. D., Hansen, F. Y., Diama, A., Criswell, L., Taub, H.(2007): *"Comparative study of normal and branched alkane monolayer films adsorbed on a solid surface. I. Structure"*, Lyngby, J.Chem.Phys, vol. 126

Englisch, C.(1958): *"Kolbenringe"*, Wien, Springer

Faguy, P.W., Marinkovic, N.S. (1996): *"An In-Situ Infrared Study on the Effect of pH on Anion Adsorption at Pt(111) Electrodes from Acid Sulfate Solutions"*, Langmuir, vol. 12, 243-247

Feng, X.-d., Ma Y.-f.(2010): *"Studies on Factors Affecting the Interfacial Tension of Oil-Water"*, Advanced Mat.Res., Zibo, Trans.Tech.Pub., vols. 113-114

Finol, C. A., Parker, D. A., Robinson, K. A.(2009): *"Model From First Principles of the Radial Heat Flux in a Cylinder Bore of a Modern Diesel Engine"*, J.Therm.Sci.Eng.Appl., Bath, ASME, vol. 1

Flores-Jardines, E., Schäfer, K., Harig, R., Rusch, P., Grutter, M.(2005): *"Investigation of temperature and gas concentration distributions in hot exhausts (airplanes and burners) by scanning imaging FTIR spectrometry"*, Proc.SPIE., Brugge, Int.Soc.Opt.Eng., 5979, 59791A .

Fogh, J., Weis, A.(1997): *"Piston Top Ring For An Internal Combustion Engine"*, EP 0 742 875 B1, Europe, 28 05 1997

Friesen, T. V., Vrolijk D.J.E.(2001): *"Comparison of Cylinder Oil Detergents for Crosshead Diesel Engines"*, CIMAC Congress, Hamburg, CIMAC

Fu, J., Lu, Y., Campbell, C.B., Papadopoulos, K.D.(2006): *"Acid Neutralization by Marine Cylinder Lubricants Inside a Heating Capillary: Strong/Weak-Stick Collision Mechanisms"*, Ind.Eng.Chem.Res., New Orleans, Am.Chem.Soc., 5619-5627, vol. 45

Fu, J., Papadopoulos, K.D., Lu, Y., Campbell, C.B.(2007): *"Ostwald ripening: a decisive cause of cylinder corrosive wear"*, Tribol.Lett., New Orleans, Springer, July, 1, vol. 27

Furman, A.Y., Shekhter, Y.N., Shkol'nikov, V.M., Shirokova, G.B.(1984): *"Influence of Oil Base Stock on Corrosion-Mechanical Breakdown of Metals"*, Khlmiya i Tekhnologiya Topliv i Masel, Plenum Publishing Corporation, February, 37-39, vol. 2

Garner, T., Voss, L., Marek, K., Aabo, K.(2004): *"Paper No. 129 Development of Marine Diesel Cylinder Oils"*, CIMAC, 1–14

Georg-August Universität Göttingen: *"IBK Instrumentenpraktikum Versuch 3 Feuchte"*, accessed 15-March 2012, http://wwwuser.gwdg.de/~aibrom/ppoek/konzept/IBK_Instrumentenpraktikum_Versuch_3_Feuchte.PDF

Giasson, S.; Palermo, T.; Buffeteau, T.; Desbat, B.; Turlet, J. M.(1994): *"Study of boundary film formation with overbased calcium sulfonate by PM-IRRAS spectroscopy"*, Thin Solid Films, Rueil-Malmaison, Elsevier, Vol. 252

Giasson, S., Espinat D., Palermo T.(1993): *"Study of Microstructural Transformation of Overbased Calcium Sulphonates During Friction"*, Rueil-Malmaison, Lubrication Science, January.

Goldfarb, I., Gol'dshtein, V., Katz, D., Sazhin, S.(2007): *"Radiation effect on thermal explosion in a gas containing evaporating fuel droplets"*, Int.J.Therm. Sci., Beer Sheva, Elsevier, 358 – 370, vol. 46.

Graham, R., Prado, O.S., Collins, M.H., Brandes, E.A., Farmery, H.K. (1960): *"Influence of the Silicon in Cast Iron on Corrosive Wear"*, Proc.Inst.Mech.Eng., Chester, I.Mech.E., June, 19, vol. 174

Grdadolnik, J. (2001), *"ATR-FTIR Spectroscopy: Its Advantages and Limitation"*, Acta Chim. Slov., vol. 49, 631-642

Guohua, C., Wang V.W., Heywood, J.B.(1991): *"A Study on a Multidimensional Instantaneous Heat Transfer Model for the Combustion Chamber of a Diesel Engine"*, 19th CIMAC Conference, Florence, CIMAC

Hadley, A.(2006): *"CombineZ5.3"*; 17-February 2006, http://www.hadleyweb.pwp.blueyonder.co.uk

Harnoy, A.(2005): *"Chapter 3: Bearing Design in Machinery"*, Engineering Tribology and Lubrication, New York, Taylor & Francis e-Library

Hartmann, S., Ruppersberg, H.(1995): *"Thermal expansion of cementite and thermoelastic stresses in white cast iron"*, Mat.Sci.Eng., Saarbrücken, Elsevier, vol. 190

He, L., Ovaert, T.C.(2008): *"Heat Partitioning Coefficient Calculations for Sliding Contacts with Friction"*, Tribol.Trans., Notre Dame, Soc.Tribol.Lubr.Eng., 12-18, vol. 51

Helsing, J., Grimvall, G.(1991): *"Thermal conductivity of cast iron: Models and analysis of experiments"*, J.Appl.Phys., Stockholm, A.I.P., 3, vol. 70

Hollands, K.G.T.(1963): *"Directional Selectivity, Emittance, and Absorptance Properties of Vee Corrugated Specular Surfaces"*, Solar Energy, Victoria, 3, vol. 7

Holmgren, D.:, Dioszegi, A., Svensson, I.L.(2008): *"Effects of Carbon Content and Solidification Rate on the Thermal Conductivity of Grey Cast Iron"*, Tsinghua Sci.Tech., Jonkoping, 2, vol. 13

Hone, D.C., Robinson, B.H., Steytler, D.C.(2000): *"Mechanism of Acid Neutralization by Overbased Colloidal Additives in Hydrocarbon Media"*, Langmuir, Abingdon, ASC, 340-346, vol. 16.

Huijbregts, W.M.M., Leferink, R.(2004): *"Latest advances in the understanding of acid dewpoint corrosion: corrosion and stress corrosion cracking in combustion gas condensates"*, Anti-Corros. Methods Mater, 51, 173–188

Jabbarzadeh, A., Atkinson J.D., Tanner R.I.(2002): *"Effect of branching on the lubricant properties: A molecular dynamics study"*, Boundary and Mixed Lubrication: Science and Applications, D. Dowson et al., Sydney, Elsevier, vol. 1.

Jaeger, J.C.(1942): *"Moving Sources of Heat and the Temperature at sliding Contacts"*, J.Proc.Roy.Soc.N.S.W., August, 203-224

Jakobsen, S.B.(2010): *"Service Experience of MAN B&W Two Stroke Diesel Engines"*, CIMAC Congress Paper NO.17, Bergen, CIMAC

Jansen, K.M.B., Agterof W.G.M., Mellema, J.(2001): *"Droplet breakup in concentrated emulsions"*, J. Rheol., Enschede, Soc.Rheol., Jan./Feb., 1, vol. 45

Joos, P., Vollhardt, D., Vermeulen, M.(1990): *"Interfacial tension of sodium dodecyl sulphate solutions at the hexane–water interface"*, Langmuir, ASC, vol. 6

Kagawa, A., Okamoto, T., Matsumoto, H.(1978): *"Young's Modulus and Thermal Expansion of Pure Iron-Cementite Alloy Castings"*, Acta metall., Osaka, Pergamon Journals, 4, vol. 35

Kang, Q., Zhang, D., Chen, S.(2005): *"Displacement of a three-dimensional immiscible droplet in a duct"*, J.Fluid Mech., Los Alamos, Cambridge University Press, 41-66, vol. 545

Kennedy, T.C., Plengsaard, C., Harder, R.F.(2006): *"Transient heat partition factor for a sliding railcar wheel"*, Wear, Corvallis, Elsevier, 932-936,vol. 261

Kosswig, K.(2000): *"Sulfonic acids, aliphatic"*, Ullmann's Encyclopedia of industrial chemistry, Wiley, Weinheim

Kramer, D.C., Ziemer, J.N., Cheng, M.T., Fry, C.E., Reynolds, R.N., Lok, B.K., Sztenderowicz, M.L., Krug, R.R.(1999): *"Influence of Group II & III Base Oil Composition on VI and Oxidation Stability"*, 66th NLGI Annual Meeting, Tucson, NLGI

Kubo, T., Fujiwara, S., Nanao, H., Minami, I., Mori, S.(2006): *"TOF-SIMS analysis of boundary films derived from calcium sulfonates"*, Tribol.Lett., Morioka, Springer, August, 2, vol. 23

Lackmann, J.(2001): *"Festigkeitslehre"*, Dubbel, Taschenbuch für den Maschinenbau, Beitz, W., Grote, K.H., Berlin, Springer, vol. 20

Lancon, D., Doyen, V.(2010): *"Paper no. 98 The universal concept: The lubrication solution to 2020 and beyond"*, Bergen, CIMAC, 1–11

Land, T.(1977): *"The theory of acid deposition and its application to the dew-point meter"*, J.Inst.Fuel, 50, 68–75

Lillywhite, J.R.F., Sant, P., Saville, S.B.(1990): *"Sludge Formation - Investigation of Sludge Formation in Gasoline Engines"*, Ind.Lubr.Tribol., Chester, MCB University Press, Jan./Feb., 1, vol. 42

Lucassen-Reynders, E. H., Kuijpers, K. A.(1992): *"The role of interfacial properties in emulsification"*, Colloids and Surfaces, Vlaardingen, Elsevier, 175-184, vol. 65

Macdonald, A.G., Stott, F.H.(1987): *"Effect of Temperature on the Corrosive Wear of Cast-Iron in Oil-Sulphuric Acid Environments"*, Reactivity of Solids, Manchester, Elsevier, vol. 4

Mahe, M., Vignes-Adler, M., Rousseau, A., Jacquin, C. G., Adler, P.M.(1988): *"Adhesion of Droplets on a Solid Wall and Detachment by a Shear Flow: I. Pure Systems"*, J.Colloid Interf.Sci., Meudon, Academic Press, Nov. 1, vol. 126

Mahe, M., Vignes-Adler, M., Adler, P.M.(1988): *"Adhesion of Droplets on a Solid Wall and Detachment by a Shear Flow II. Rough Substrates"*, J.Colloid Interf.Sci., Meudon, Academic Press, Nov., 1, vol. 126

Mahe, M., Vignes-Adler, M., Adler, P.M.(1988): *"Adhesion of Droplets on a Solid Wall and Detachment by a Shear Flow: III. Contaminated Systems"*, J. Colloid Interf.Sci., Meudon, Academic Press, Nov., 1, vol. 126.

Malvern Instruments Ltd.(2001): *"Dynamic Light Scattering: An Introduction in 30 Minutes"*, Tech.Note, Worcestershire, MAK656-01

Memhard, D., Andrieux, F., Sun, D.Z., Haecker, R.(2011): *"Development and Verification of a Material Model for Prediction of Containment Safety of Exhaust Turbochargers"*, 8th European LS-DYNA Users Conference, Strasbourg, DYNAmore

Micali, F., Weber, M., Stark, M., Räss, K., Potenza, M.(2010): *"Paper No. 74: Suction air humidity influence on piston running reliability in low-speed two stroke diesel engines"*, CIMAC

Ministry of Transport and Communications Finnland (2009): *"Sulphur content in ships bunker fuel in 2015, A study on the impacts of the new IMO regulations on transportation costs"*, Helsinki, Ministry of Transport and Communications Finnland

Mischler, S., Rosset, E., Stachowiak, G.W., Landolt, D.(1993): *"Effect of sulphuric acid concentration on the rate of tribocorrosion of iron"*, Wear, Lausanne, Elsevier, vol. 167

Mitsui, T., Nakamura, S., Harusawa, F., Machida, Y.(1971): *"Changes in the interfacial tension with temperature and their effects on the particle size and stability of emulsions"*, Kolloid-Zeitschrift & Zeitschrift für Polymere, 227–30.

Miyazaki, M., Takeshima, S., Okuyama, S., Tanaka, M.(1993): *"Evaluation of marine engine lubricating conditions using a cylinder liner surface oil sampling apparatus"*, CIMAC, 1–15

Modest, M.F.(2003): *"Radiative Heat Transfere"*, San Diego, Elsevier

Montgomery, R.S.(1969): *"Run-in and glaze formation on grey cast iron surfaces"*, Wear, Princeton, Elsevier Sequoia, 99-105, vol. 14

Moore, J.P., Williams, R.K., Graves R.S.(1977): *"Thermal conductivity, electrical resistivity, and Seebeck coefficient of high purity chromium from 280 to 1000 K"*, J.Appl.Phys., Oak Ridge, A.I.P., 2, vol. 48

Morra, M., Occiello, E., Garbassi, F.(1989): *"Contact Angle Hysteresis in Oxygen Plasma Treated Poly(tetrafluoroethylene)"*, Langmuir, Novara, ASC, 3, vol. 5

Murphy, S.M., Agrawal, H., Soroshian, A., Padro, L.T., Gates, H., Hershey, S., Welch, W.A., Jung, H., Miller, J.W., Cocker, I., David, R., Nenes, A., Jonsson, H.H., Flagan, R.C., Seinfeld, J.H.(2009): *"Comprehensive Simultaneous Shipboard and Airborne Characterization of Exhaust from a Modern Container Ship at Sea"*, Environ.Sci.Tech., Pasadena, ASC, 13, vol. 43

Nakayama, M., Saeki, S., Ogura, K.T.(1999): *"In Situ Observation of Electrochemical Formation and Degradation Processes of Polyaniline by Fourier-Transform Infrared Spectroscopy"*, JSAC, vol. 15, 259-263

Nash, K.L., Sully, K.J., Horn, A.B.(2001): *"Observation on the Interpretation and Analysis of Sulfuric Acid Hydrate Infrared Spectra"*, J.Phys.Chem, vol. 105, 9422-9426

Nawab, M.A., Mason, S.G.(1958): *"The Viscosity of Dilute Emulsions"*, Trans.Faraday Soc., Montreal, RSC, Jan., 1712-1723, vol. 54

NIST (2011): *"Chemical Formula Search"*, NIST National Institute of Standards and Technology, accessed March 2012, http://webbook.nist.gov/chemistry/form-ser.html

Nuevo, M., Meierhenrich, U.J., Munoz, C.G.M., Dartois, E., d'Hendecourt, L., Deboffle, D., Auger, G., Blanot, D., Bredehoeft, J.H., Nahon, L.(2006): *"The effects of circularly polarized light on amino acid enantiomers produced by the UV irradiation of interstellar ice analogs"*, Orsay, EDPSci.A&A, vol. 457

Ong, E.K.(2011): *"Group III Base Oil Required for Modern Engine Oil Specifications"*, UEIL, Petronas Base Oil (M) Sdn. Bhd., accessed Jul. 2011, http://www.ueil.org/news/documents/8.Ong_000.pdf.

Palmer, K.F., Williams, D. (1975): *"Optical Constants of Sulfuric Acid; Application to the Clouds of Venus?"*, Applied Optics, vol. 14, 208-219

PerkinElmer, Inc. (2005): *"FT-IR Spectroscopy Attenuated Total Reflectance (ATR)"*, Shelton, PerkinElmer, Inc., Product Brochure

Pillon, L.Z.(2003): *"Demulsibility Properties of Hydrocracked Base Stock"*, Petro.Sci.Tech., Sarnia, Marcel Dekker Inc., 9 & 10, vol. 21

Pischinger, S.(2000): *„Verbrennungsmotoren Band II"*, Aachen, RWTH Aachen, vol. 21

Plint, G.(2005): *"Guidance Notes on Lubricated Wear Testing"*, Newbury, Phoenix Tribology Ltd.

Plucinski, P., Nitsch, W.(1994): *"Mechanism of mass transfer between aqueous phase and water-in-oil microemulsion"*, Langmuir, 371–6

Pollock, H.M., Hammiche, A.(2001): *"Micro-thermal analysis: techniques and applications"*, J.Phys.D.Appl.Phys., Lancaster, Inst.Phys.Pub., R23-R53, vol. 34

Priest, M.(2000): *"Factors Influencing Boundary Friction and Wear of Piston Rings"*, Proceedings of the 26th Leeds-Lyon Symposium on Tribology, Thinning Films and Tribological Interfaces, Leeds, Elsevier, vol. 38

Priest, M.(2009): *"Work Unit 1: Introduction to Tribology and Real Surfaces"*, University of Leeds, MECH5570 Introduction to Tribology, Leeds, School of Mechanical Engineering

Priest, M.(2010): *"Work Unit 3: Lubricants and Lubrication"*, University of Leeds, MECH5570 Introduction to Tribology, Leeds, School of Mechanical Engineering

Randolph, J.J.A.(2009): *"Guide to Writing the Dissertation Literature Review"*, Practical Assessment, Research & Evaluation, Walden, 13, vol. 14

Rawle, A.(2012): *"Basic Principles of Particle Size Analysis"*, Worcestershire, Malvern Instruments Ltd.

Reynolds, O.(1886): *"IV. On the Theory of Lubrication and its Application to Mr. Beauchamp Tower's Experiments, including an Experimental Determination of the Viscosity of Olive Oil"*, London, R.Soc., vol. 177

Reynolds, W.C.(1921): *"On interfacial tension. Part II. The relation between interfacial and surface tension in sundry organic solvents in contact with aqueous solutions"*, J.Chem.Soc., Trans., RSC, 466-476, vol. 119

Rhee, K.T.(1995): *"High-Speed Four-Color Infrared Digital Imaging for Studying In-Cylinder Processes in a DI Diesel Engine"*, New Brunswick, Rutgers, The State University of New Jersey

Rode, S.(2010): *"Oberflächenspannung"*, Mainz, Johannes Gutenberg Universität Mainz, 2010

Rudakov, E.S., Volkova, L.K., Tishchenko, N.A.(1988): *"Kinetics and Mechanism of homogeneous reactions of alkanes in sulphuric acid in the presence of carbocations. I. Oxidation, isomerization, fragmentation"*, Kinet.Catal., (Russ. trans.), 29, 1168–1173

Rudakov, E.S., Zamashchinkov, V.V., Lutsyk, A.I.(1976): *"Kinetics of the reaction of saturated hydrocarbons with PdII, PTII–IV, HgII, CrVI, MnIII, MnIII–RuIII–IV, NO_2^+, H_2SO_4, $H_2S_2O_8$, and carbonium ions in sulphuric acid"*, Teoret. Eksp. Khim. (Russ. trans.), 12, 361–368

Ruddy, B.L.(1979): *"The lubrication and dynamics of piston rings and the theoretical prediction of ring pack gas flow"*, Leeds, Department of Mechanical Engineering, The University of Leeds

Rukadikar, M.C., Reddy, G.P.(1986): *"Influence of chemical composition and microstructure on thermal conductivity of alloyed pearlitic flake graphite cast irons"*, J.Mat.Sci., Bombay, Chapman & Hall Ltd., vol. 21

Saito, Y., Yamada, T., Moriyama, K.(2010): *"Paper no. 243 The piston-running behaviour monitoring of large bore low-speed marine diesel engine*

at sea by measurement of piston ring oil film thickness and iron content in cylinder drain oil", Bergen, CIMAC, 1–14

Sato, M., Kudo, N., Saito, M.(1998): *"Surface Tension Reduction of Liquid By Applied Electric Field Using Vibrating Jet Method"*, IEEE, Trans.Ind.Appl., Gunma, Mar./Apr., 2, vol. 34

Saunders, J. A., Thomas, R.C.(1996): *"Origin of 'exotic' minerals in Mississippi salt dome cap rocks: results of reaction-path modelling"*, Appl.Geochem., Auburn, Pergamon, 667-676, vol. 11

Sautermeister, F.A., Priest, M.; Fox, M.F., Lee, P.M.(2012): *"Impact of Sulphuric Acid on Cylinder Lubrication for Large 2-Stroke Marine Diesel Engines: Contact Angle, Interfacial Tension and Chemical Interaction"*, Tribol.Int., DOI: 10.1016/j.triboint.2012.06.002, 38th Leeds-Lyon Symposium on Tribology.

Sautermeister, F.A., Priest, M.(2012): *"Physical and Chemical Impact of Sulphuric Acid on Cylinder Lubrication for Large 2-Stroke Marine Diesel Engines"*, Tribol.Lett., 2, vol. 47, 261-271, Tribology - Industrial and Automotive Lubrication, Esslingen

Sautermeister, F.A., Priest, M., Fox, M.F.(2012): *"FTIR Lubricant Analysis – Concentration of Dispersed Sulphuric Acid"*, Leeds, submitted

Sazhin, S.S., Krutitskii, P.A., Abdelghaffar, W.A., Sazhina, E.M., Mikhalovsky, S.V., Meikle, S.T., Heikal, M.R.(2004): *"Transient heating of diesel fuel droplets"*, Int.J.Heat Mass Trans., Brighton, Elsevier, 3327-3340, vol. 47.

Schlager, D., Wärtsilä (2006): *"EP 1 752 560 B1"*, Europe

Schleizer, A.D., Bonnecaze, R.T.(1999): *"Displacement of a two-dimensional immiscible droplet adhering to a wall in shear and pressure-driven flows"*, J.Fluid Mech., 383, 29–54

Schmitt, G., Stradmann, N.(1998): *"Wettability of Steel Surfaces at CO_2 Corrosion Conditions I. Effect of Surface Active Compounds in Aqueous an Hydrocarbon Media"*, Corrosion98, Paper No.28, Iserlohn, NACE International

Schreiter, W.(2010): *"5.10 Homogene chemische Gleichgewichtsreaktionen"*, Chemische Thermodynamik, Erfurt, Walter de Gruyter GmbH, vol. 1

Shaw, D.J.(2003): *"Introduction to colloid and surface chemistry"*, Oxford, Butterworth-Heinemann

Shchipunov, Y.A., Kolpakov, A.F.(1991): *"Phospholipids at the oil/water interface: Adsorption and interfacial phenomena in an electric field"*, Advances in Colloid and Interface Sci., Vladivostok, Elsevier, 31-138, vol. 35

Sheppard, S.E.(1919): *"Emulsification by Adsorption at an Oil-Water Interface"*, Rochester, Eastman Kodak Company, 82

Sherman Hsu, C.P.(1997): *"Chapter 15: Infrared Spectroscopy"*, Settle, F., Handbook of Instrumental Techniques for Analytical Chemistry, Prentice Hall, Upper Saddle River, NJ, 247-283

Shuttlefield, J.D., Grassian Vicki H.(2008): *"ATR-FTIR Spectroscopy in the Undergraduate Chemistry Laboratry. Part I: Fundamentals and Examples"*, Iowa City, J.Chem.Edu., 2, vol. 85

Shuttlefield, J.D., Larsen, S.C., Grassian, V.H.(2008): *"ATR-FTIR Spectroscopy in the Undergraduate Chemistry Laboratory. Part II: A Physical Chemistry Laboratory Experiment on Surface Adsorption"*, Iowa City, J.Chem.Edu., 2, vol. 85

Sjogren, T., Wigren, P., Vilhelmson, F., Vomacka, P.(2004): *"High Performance Piston Rings for Two-Stroke Marine Engines"*, CIMAC Congress 2004, Kyoto, CIMAC, vol. 79

Slack, G.A.(1962): *"Anisotropic Thermal Conductivity of Pyrolytic Graphite"*, Phys.Rev., New York, 3, vol. 127

Spahni, M., Brunner, H., de Jong, R.(2010): *"Paper no. 86 The new Wärtsilä 820 mm bore engine series - advanced design and first running experience"*, Bergen, CIMAC, 1–15

Stadler, A.F., Kulik, G., Sage, D., Barbieri, L., Hoffman, P.(2006): "A snake-based approach to accurate determination of both contact points and contact angles", Colloids And Surfaces A: Phys.chem.Eng.Aspects, 92–103

State of New South Wales through the Department of Education and Training and Charles Sturt University: *"HSC online. Industrial chemistry:3. Sulphuric acid"*, accessed: 21.4.2011, http://hsc.csu.edu.au/chemistry/options/industrial/2762/Ch953.htm#b3S

Stecher, G.P., Finkel, M.J., Siegmund, O.H., Szafransky, B.M.(1960): *"The Merck index of chemicals and drugs"*, Rahway, Merck & Co.

Stott, F.H., Macdonald A.G.(1988): *"The Influence of Acid Strength on the Corrosive Wear of Grey Cast Irons in Oil-Sulphuric Acid Mixtures"*, Wear, Manchester, Elsevier, vol. 122

Stott, F.H., Breakell, J.E., Newman, R.C.(1990): *"The Corrosive Wear of Cast Iron Under Potentiostatically-Controlled Conditions in Sulphuric Acid Solutions"*, Corrosion Sci., Manchester, Pergamon Press, 8/9, vol. 30.

Strachan, P.J.(1973): *"A study of piston ring lubrication"*, Leeds, Department of Mechanical Engineering, The University of Leeds

Taylor, G.I.(1932): *"The Viscosity of a Fluid Containing Small Drops of Another Fluid"*, Proc.R.Soc.London, London, R.Soc., Oct., 834, vol. 138

Taylor, P.(2002): *"1 Electrophilic addition reactions of alkenes. Alkenes and aromatics"*, Cambridge, RSC

The Petroleum HPV Testing Group (2003): *"Test plan lubricating oil basestocks category"*, API

Thompson, L.(1994): *"The Role of Oil Detachment Mechanism in Determining Optimum Detergency Conditions"*, J.Colloid Interface Sci., Wirral, Academic Press, 61-73, vol. 163

Tian, G., Keyu, P. Fei, C.(2006): *"Investigation on in-cylinder radiation from gases in DI diesel engine"*, J.Xi'an Jiaotong Univ., China, Editorial Board J. of Xi'an Jiaotong Univ, 3, vol. 40

Tipler, P.(1998): *"A. 22.2 Widerstand und Ohmsches Gesetz"*, Physik, Heidelberg, Spektrum Akademischer Verlag, vol. 1

Tomanik, E.(2008): *"Friction and wear bench tests of different engine liner surface finishes"*, Tribol.Int., Sao Paulo, Elsevier,1032 – 1038, vol. 41

Tomanik, E.(2005): *"Modelling of the Asperity Contact Area on Actual 3D Surfaces"*, SAE Int., Sao Paulo, SAE, 1864, vol. 1

Topolovec-Miklozic, K., Forbus, T.R., Spikes, H.(2008): *"Film Forming and Friction Properties of Overbased Calcium Sulphonate Detergents"*, Tribol. Lett., London, Springer, vol. 29

University of Leeds (2011): *"2. Infrared Spectroscopy"*, Applications of Spectroscopy in Organic Chemistry, School of Chemistry, Leeds

Vacha, R., Horinek, D., Berkowitz, M.L., Jungwirth, P.(2008): *"Hydronium and hydroxide at the interface between water and hydrophobic media"*, Phys.Chem.Chem.Phys., Prague, RSC, 32, vol. 10

van Helden, A.K., Valentijn, M.C., van Doorn, H.M.J.(1989): *"Corrosive wear in crosshead diesel engines"*, Tribol.Int., Houston, Butterworth&Co, Jun., 3, vol. 22

Vellinger, E., Radulesco, G.(1933): *"Le Contrôle Du Raffinage Des Huiles Minérales Par Des Mesures De Tension Interfaciale"*, 1st World Petroleum Congress, July 18 - 24, London, World Petroleum Congress, vol. 1

Vipper, A.B., Cook, S.J., Karaulov, A.K., Leahy, R.(1998): *"Antifriction Properties of Calcium Phenate-Type Detergents Used in Marine Cylinder Lubricants"*, Kiev, Lubr.Sci., Feb., vol. 10

Vortmeyer, D., Gnielinski, V., Kast, W.(1993): *"Ka Surface Radiation"; "Kb Gas radiation - radiation from gas mixtures"; "Ga1 Heat transfer in forced single face flow"; "La;Lb;Lc"*, VDI Heat Atlas, Düsseldorf, VDI

Walstra, P.(1993): *"Principles of Emulsion Formation"*, Chem.Eng.Sci., Wageningen, Pergamon Press, 2, vol. 48

Wang, L., Atkinson, D. Small, D.M.(2003): *"Interfacial Properties of an Amphipathic alpha-Helix Consensus Peptide of Exchangeable Apolipoproteins at Air/Water and Oil/Water Interfaces"*, J.Bio.Chem., Boston, ASBMB, Sep., 39, vol. 278

Wang, R., Kido, M.(2007): *"Corrosion Behavior of Pure Iron by Different Droplet Volume of Sulfuric Acid Solution"*, Mat.Trans., Hiroshima, JIM, 6, vol. 48.

Wang, X.D., Peng, X.F., Lu, J.F., Liu, T., Wang, B.X.(2004): *"Contact Angle Hysteresis on Rough Solid Surfaces"*, Heat Transfer - Asian Research, Tsinghua, Wiley Periodicals, 4, vol. 33

Warriner, S., Wright, P.J., Goetz, S.(2011): *"Walk-Up Ion Trap Mass Spectrometer System in a Multi-User Environment Using Compass OpenAccess Software"*, Bremen, Bruker Daltonics

Williams, J.A.: *"3 Contact Between Surfaces"*, Engineering Tribology, Oxford, Oxford University Press, vol. 1

Wirtz, M., Hell, R.(2007): *"Dominant-Negative Modification Reveals the Regulatory Function of the Multimeric Cysteine Synthase Protein Complex in Transgenic Tobacco"*, The Plant Cell, Heidelberg, ASPB, Feb., 625-639, vol. 19

Won, Y.Y., Brannan, A.K., Davis, T.H., Bates, F.S.(2002): *"Cryogenic Transmission Electron Microscopy (Cryo-TEM) of Micelles and Vesicles*

Formed in Water by Poly(ethylene oxide)-Based Block Copolymers", J.Phys.Chem.B., Minneapolis, ACS, 13, vol. 106

Woodyard, D.(2004): *"Pounder's Marine Diesel Engines and Gas Turbines"*, Oxford, Elsevier

Wu, H., Ren, T.(2009): *"Investigation of antiwear additives for diester"*, Ind. Lubr.Tribol., Shanghai, Emerald, 5, vol. 61

Wu, R.C., Papadopoulos, K.D., Campbell, C.B.(2000): *"Acid-neutralising of marine cylinder lubricants: Measurements and effects of dispersants"*, AIChE J., 1471–7

Wu, R.C., Campbell, C.B., Papadopoulos, K.D.(2000): *"Acid-Neutralizing of Marine Cylinder Lubricants: Effects of Nonionic Surfactants"*, Ind.Eng.Chem. Res., New Orleans, ACS, 3926-3931, vol. 39

Young, T.F., Maranville, L.F., Smith, H.M.(1959): *"Raman spectral investigations of ionic equilibria in solutions of strong electrolytes"*, Hamer, W.J. (ed.) The Structure of Electrolytic Solutions, 35–63, Wiley, New York

Zhang, M., Wang, X., Fu, X., Xia, Y.(2009): *"Performance and anti-wear mechanism of $CaCO_3$ nanoparticles as a green additive in poly-alpha-olefin"*, Tribol.Int., Lanzhou, Elsevier, vol. 42

Zima, S.(2005): *"Motorkolben; Bauarten, Betrieb, Schäden"*, Wiesbaden, Vieweg, vol. 1

Zimmermann, B.J.(2010): *"Epitaktisches Wachstum und Charakterisierung ultradünner Eisenoxidschichten auf Magnesiumoxid(001)"*, Osnabrück, Universität Osnabrück

List of Abbreviations

Symbol	Description	Units	Chapter
+	corrosion was observed	-	5
a, b, c	spacing dimension of the crystal structure	nm	2
a	droplet diameter	m	2
a	Langmuir-Von Szyskowski constant	mol/cm^3	4
A	advancing	-	5
A	area	m^2	6, 8
a	acceleration; semi-minor; length	m/s^2; m; m	6
A	parameter to calculate η	-	A
a_c	diameter of a droplet on a wall, forming a spherical cap	m	5
a_i	distance to combined centre of gravity	m	6
a_P	diameter of wetted contact area	m	2, 5
API Group I	1st of 5 base oil standards defined by the American Petroleum Institute	-	3, 4, 5
B	ellipsoid minor axis	m	2
b	width	m	6
b	semi-minor	m	6
B	parameter to calculate η	-	A
BS150	high viscosity grade within API Group I	-	3, 4, A
C	slope of $\gamma_{crit}*a^2$ over a_P	m^2/s*m	2
C	concentration	mol/cm^3	4
c_0	speed of light in vacuum 2.998*10^8	m/s	8
Ca	capillary number	-	2, 5
CA_{rad}	crank angle	rad	6
CKS	manufacturer name for particle reinforced chrome coating	-	5
CMC	critical micelle concentration	-	3, 4
CMC I	1st CMC indicating a 2nd CMC	-	3, 4
CMC II	2nd CMC	-	3, 4
d	top width of honing marks	µm	8
DIN	German institute for standardisation	-	3, 4
e	Euler number 2.71828	-	6
E	Young's modulus	N/m^2	6

Symbol	Description	Units	Chapter
$E_{b\lambda}(T,\lambda)$	emissive power of a black body, temperature and wavelength dependent	W/m^2m	8
EU	European Union	-	1
F	force	N	6
f	frequency	s^{-1}	6
F_A	adhesion force	N	2
G	velocity gradient	1/s	2
g	gravity acceleration	m/s^2	6
h	height	m	6
h	Planck's constant $6.6261*10^{-34}$	Js	8
HFO	Heavy Fuel Oil	-	1
HVI160B	viscosity grade within API Group I	-	3, 4, A
IMO	International Maritime Organization	-	1
I_y	axial moment of area	m^4	6
k	elliptical ratio	-	6
k	Boltzmann constant $1.3807*10^{-23}$	J/K	8
k	wear factor	$mm^3mm^{-1}N^{-1}$	7
L	ellipsoid major axis	m	2
l	length	m	6
L	length	m	6
L	distance of heat flow	m	8
M	molar mass	mol/kg	3, 4
M	momentum	Nm	6
m	mass	kg	6, A
MDO	Marine Diesel Oil	-	1
MGO	Marine Gas Oil	-	1
n	refraction index	-	8
p	pressure	atm, mmHg, Pa(5&6)	1, 5, 6
P	electric power	W	8
p_L	Laplace pressure	N/m^2	2
p_{vap}	vapour pressure	Pa	6
p_{vsat}	saturation vapour pressure	Pa	6
$p_{vsat-wet}$	saturation vapour pressure calculated with T_{wet}	Pa	6
Q	heat flow	W	8
r	droplet radius	m	2, 5
R	characteristic droplet diameter	m	2
R	universal gas constant 8.3145	J/mol K	4, 5
R	receding	-	5
R	resistance; Radius	Ω; m	6

Symbol	Description	Units	Chapter
r	radius	m	6
R	electrical resistance	Ω	8
Re	Reynolds number	-	2
RH	relative humidity	%	6
RT84	engine type, here used to abbreviate the grey cast iron	-	5
s	position of the centre of gravity	m	6
SECA	Sulphur Emission Controlled Area	-	1
SN600	low viscosity grade within API Group I	-	3, 4, A
St	Static	-	5
T	temperature	°C; K	3, 4, 5, 8, A
TBN	total base number	mgKOH/g	2, A
T_c	critical temperature	°C; K	3, 4
t_c	temperature in the contact	°C	6
T_d	dew point temperature	°C	1
T_{dry}	dry bulb temperature	°C	6
T_{wet}	wet bulb temperature	°C	6
U	voltage	V	8
U_{crit}	critical speed on the droplet for displacement	m/s	5
V	Volume	m^3	2
v	velocity	m/s	6
V_m	molar volume	m^3/mol	3, 4, 5
W	normal load = F_N	N	6
$w(x)$	deformation at point x	m	6
We	Weber number	-	2
x	position in x direction	m	6
x, y, z	direction	-	5
XPS 2s	brand name	-	A
y	position in y direction	m	6
z	depth of honing marks	μm	8
α	thermal expansion coefficient	1/K	2
α	Eötvös constant 2.7×10^{-7}	J/K*mol$^{2/3}$	3, 4
α	temperature coefficient; latitude	K^{-1}; °	6
β	opening angle of honing marks	°	8
γ	shear rate	1/s	2
γ	surface tension	N/m	3, 4, A
Γ^∞	saturation adsorption	mol/cm^2	4
γ_{crit}	critical shear rate	1/s	5
γ_{mol}	molar surface tension	J/mol$^{2/3}$	3, 4

Symbol	Description	Units	Chapter
γ_o	surface tension of organic liquid	N/m	3, 4
γ_w	surface tension of water	N/m	3, 4
δ	deformation in the centre of Hertzian contact	m	6
η	dynamic viscosity	Pa*s	5, A
$\eta_{c/d/em}$	viscosity continuous / dispersed / emulsion phase	Pa*s	2
θ	contact angle	°	5
$\theta_{R/A}$	receding / advancing contact angle	°	2
λ	wavelength; thermal conductivity	m; W/mK	8
μ	friction coefficient	-	2, 6, 7
ν	Poisson's ratio	-	6
ξ	complete elliptical integral of the 2nd kind	-	6
ρ	density	kg/m^3	2, 3, 4
ρ	resistivity	Ωm	6
σ	interfacial tension	N/m	2, 3, 4, 5
σ_0	initial interfacial tension	N/m	4
σ_{ow}	interfacial tension between organic liquid and water	N/m	3, 4, 5
σ_y	yield point	Pa	6
τ	surface traction	Pa	6
Φ	volume fraction	-	2
ψ	complete elliptical integral of the 1st kind	-	6

Appendix A
Physical Properties of the Liquids Used

The physical properties of the used liquids are presented in the following. They were either measured or taken from other sources, as indicated.

A.1   Lubricants
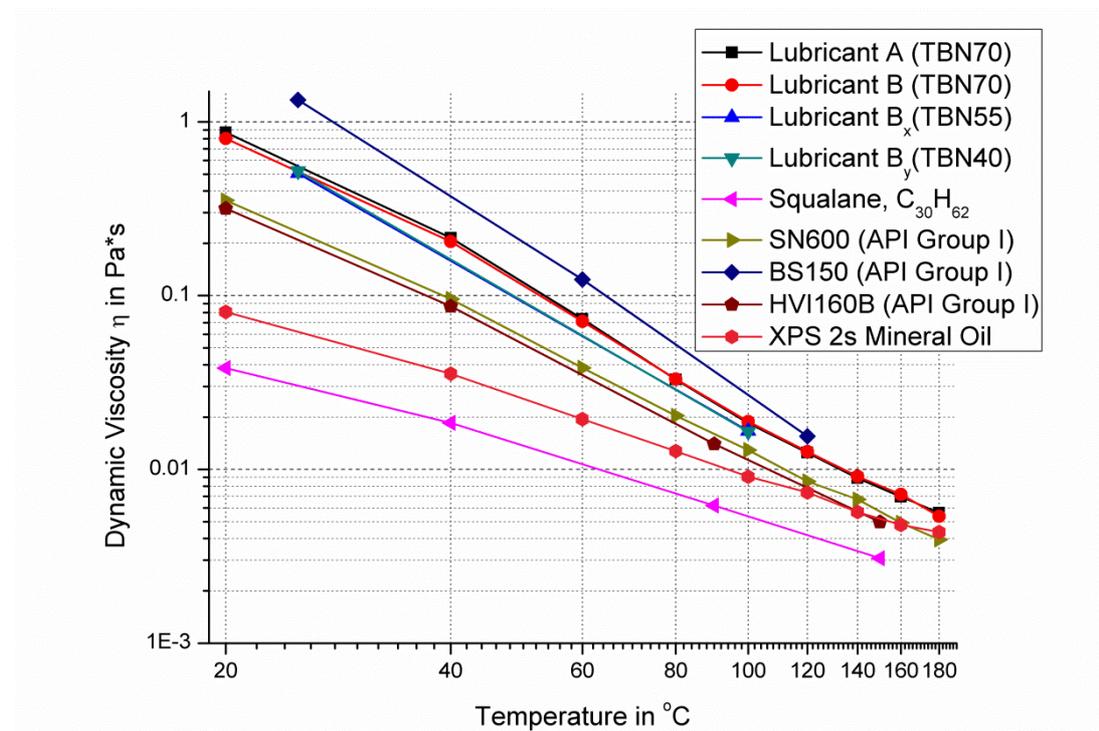
Figure A.1: Temperature dependent dynamic viscosity, η, for all used lubricants. Measured with cone on plate 1/50 at 800 s^{-1} at ambient pressure

Table A.1 gives the parameters A and B to calculate the dynamic viscosity, η [Pa*s], presented in Figure A.1 in the measured temperature range, T [°C], at the 800 s^{-1} shear rate and ambient pressure by:

$$\eta = A \cdot T^B \tag{A.1}$$

Table A.1: Parameters to calculate the dynamic viscosity η by equation (A.1)

Name	A	B	Name	A	B
Lub. A	1151.934	-2.374	SN600	184.412	-2.074
Lub. B	950.078	-2.333	BS150	12682.235	-2.835
Lub. B_X	1397.782	-2.462	HVI160B	172.925	-2.085
Lub. B_Y	1573.619	-2.49	XPS2sM.O.	5.152	-1.37
$C_{30}H_{62}$	1772	-1.26			

Table A.2: Density of used oils at 15°C according to the safety data sheets and (DECHEMA e.V., 2005 - 2008)*

Name	Density kg/m^3, 15°C	Name	Density kg/m^3, 15°C
Lub. A	932	SN600	886
Lub. B	930	BS150	890
Lub. B_X	920	HVI160B	888
Lub. B_Y	-	XPS 2s M.O.	865
$C_{30}H_{62}$	811.51*		

Table A.3: Surface tension, γ, of squalane at various temperatures, T (DECHEMA e.V., 2005 - 2008)

T in °C	20	80	140	200
γ in N/m	0.02815	0.02385	0.01953	0.0152
$\gamma = -7*10^{-5} * T + 0.0296$				

A.2 Aqueous Sulphuric Acid

Table A.4: Density of aqueous sulphuric acid at 25 °C (DECHEMA e.V., 2005 - 2008)

concentration in %w/w	0	10	20	30	40	50
density in kg/l at 25 °C	0.997	1.064	1.136	1.215	1.299	1.395
concentration in %w/w	60	70	80	90	98	
density in kg/l at 25 °C	1.494	1.606	1.722	1.809	1.831	
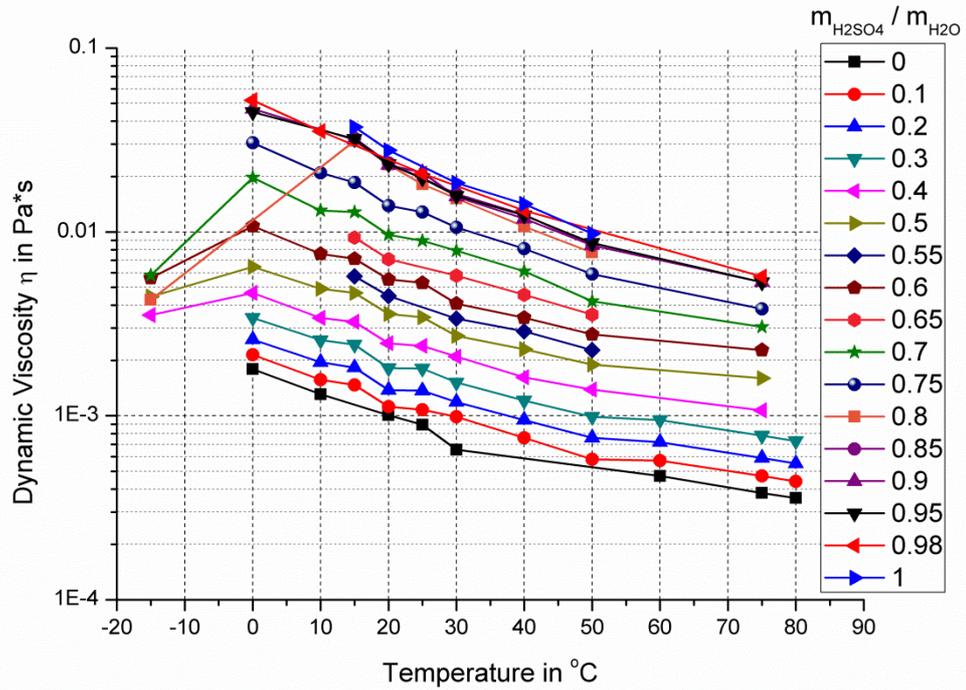
Figure A.2: Temperature dependent dynamic viscosity, η, for various concentrations of aqueous sulphuric acid (DECHEMA e.V., 2005 - 2008)

Table A.5: Surface tension, γ, of aqueous sulphuric acid at various concentrations, for temperatures, T, between 10 – 50 °C (DECHEMA e.V., 2005 - 2008)

Conc. in %w/w	γ in N/m	Conc. in %w/w	γ in N/m
0	$= -2 \cdot 10^{-4} \cdot T + 0.0756$	73.1	$= -3 \cdot 10^{-5} \cdot T + 0.0742$
5.43	$= -1 \cdot 10^{-4} \cdot T + 0.0765$	86	$= -3 \cdot 10^{-5} \cdot T + 0.0683$
10.13	$= -9 \cdot 10^{-5} \cdot T + 0.078$	91.75	$= -3 \cdot 10^{-5} \cdot T + 0.0625$
26.49	$= -3 \cdot 10^{-5} \cdot T + 0.0758$	98.5	$= -4 \cdot 10^{-5} \cdot T + 0.0561$
45.35	$= -8 \cdot 10^{-5} \cdot T + 0.0781$		

Appendix B
Publications commenced during the cause of this study

The below listed publications can be found in the following. The last two articles were not published in this form at the date of printing.

• Sautermeister, F.A., Priest, M. (2012): "Physical and Chemical Impact of Sulphuric Acid on Cylinder Lubrication for Large 2-Stroke Marine Diesel Engines" Tribology Letters, Vol. 47, Issue 2, 261-271, DOI: 10.1007/s11249-012-9979-7, "The final publication is available at www.springerlink.com"

• Sautermeister, F.A., Priest, M., Fox, M.F., Lee, P. M.(2012): "Impact of Sulphuric Acid on Cylinder Lubrication for Large 2-Stroke Marine Diesel Engines: Contact Angle, Interfacial Tension and Chemical Interaction", Tribology International, DOI: 10.1016/j.triboint.2012.06.002

• Sautermeister, F.A., Priest, M., Fox, M.F.(2012): "Impact of Sulphuric Acid on Cylinder Lubrication: Friction and Surface Modification", draft version for publication in Tribology Letters

• Sautermeister, F.A., Priest, M., Fox, M.F.(2012): "FTIR Lubricant Analysis – Concentration of Dispersed Sulphuric Acid", submitted, under review by Industrial Lubrication and Tribology

ORIGINAL PAPER

Physical and Chemical Impact of Sulphuric Acid on Cylinder Lubrication for Large 2-Stroke Marine Diesel Engines

Falko A. Sautermeister · Martin Priest

Abstract The influence of sulphuric acid, H_2SO_4, on the physical and chemical behaviour of marine Diesel engine lubricant base oils was investigated. To understand the basic interaction of H_2SO_4 with the lubricant film, the saturated hydrocarbon squalane, $C_{30}H_{62}$, was chosen as a simple model oil in addition to a fully formulated lubricant and its corresponding API Group I base oil HVI160B. To understand droplet formation in the lubricant, the interfacial tension between aqueous H_2SO_4 (0–98 %w/w) and $C_{30}H_{62}$ measured in a previous study (Sautermeister et al., Tribology International, 38th Leeds-Lyon Symposium on Tribology, 2011) and is compared with three different API Group I base oils. Interfacial tension decreases with increasing acid concentration, but is much lower for the base oil. Both oils were emulsified with a constant volume fraction of aqueous H_2SO_4. The droplet size was smaller and more distinct for the base oil under the same shearing conditions and the emulsions with base oil were are more stable. The concentration of the dispersed phase had no significant influence on the viscosity of the emulsions compared to the viscosity of the bulk oil alone. In addition to the physical measurements, chemical reaction between H_2SO_4 and the API Group I base oil HVI160B was observed yielding bituminous matter which appears to be a complex emulsion. The critical acid concentration for the formation of bitumen was found to be 40 %w/w. Between 50 and 80 %w/w, bitumen was formed spontaneously at 85 °C and above 85 %w/w, bitumen was formed spontaneously at room temperature. The observed concentrations for bitumen formation correlate well with the first and second dissociation steps of H_2SO_4. HSO_4^- ions are likely to be the driving force for bitumen formation. Finally, the viscosity characteristics of two different bitumen were measured. Both were found to exhibit shear thinning and the one formed with highly concentrated H_2SO_4 created a solid deposit on the measurement equipment above 120 °C.

1 Introduction

Current marine Diesel engines burn refined and residual fuels with a legislated sulphur maximum content between 0.005 and 4.5 %w/w sulphur. The aim is to reduce SO_x exhaust gas emissions for environmental reasons. The fuel sulphur reacts completely in the combustion chamber to form 100 % sulphur dioxide, SO_2. Further oxidation yields 0.3–7 % sulphur trioxide, SO_3, which rapidly reacts with water forming sulphuric acid, H_2SO_4, at various concentrations [1].

$$2SO_2(g) + O_2(g) \rightarrow 2SO_3(g) + heat$$

$$SO_3(g) + H_2O(l) \rightarrow H_2SO_4(aq) + heat$$
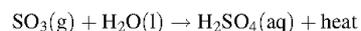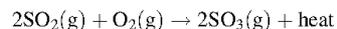
The sulphuric acid condenses on the cylinder wall of the engine. The dew point equation of SO_3 according to Verhoff [2] shows a massive increase in dew point for small amounts of SO_3. The higher the dew point, the more readily condensation occurs on the hot engine surfaces.

F. A. Sautermeister (✉) · M. Priest
iETSI, School of Mechanical Engineering, University of Leeds, Leeds LS2 9JT, UK
e-mail: mnfasa@leeds.ac.uk

From exhaust gas composition [3] and the phase diagram for vapour of sulphuric acid and water [4], concentrations of sulphuric acid between 5 and 80 %w/w can be expected during condensation on the cylinder wall. Therefore, this study covers the range of concentrations from 0 to 98 %w/w.

Dependent on concentration and temperature, H_2SO_4 dissociates in water into HSO_4^-, SO_4^{2-} and pure H_2SO_4 molecules with changing concentration and temperature as two steps [5].

$$H_2SO_4 + H_2O \rightleftarrows HSO_4^- + H_3O^+$$

$$HSO_4^- + H_2O \rightleftarrows SO_4^{2-} + H_3O^+$$
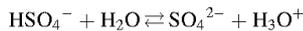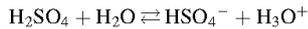
The engine components can be subject to corrosion-induced wear. To neutralise the sulphuric acid formed by combustion, the lubricants have an alkaline reserve with total base number, TBN, levels of 40–70 mg KOH/g. The alkaline reserve is usually formulated into the lubricant by dispersing calcium carbonate, $CaCO_3$, particles as reversed micelles. Distribution of fresh lubricant, however, is inhomogeneous and lubricant was found to stay in the engine for up to 30 min [6].

Other than corrosion, marine Diesel engines also suffer from deposit formation. Two-stroke marine Diesel engines are typically lubricated with API Group I base mineral oils [1]. These are the least refined lubricants and contain <90 %w/w saturated hydrocarbons (alkanes). The other hydrocarbons are unsaturated compounds such as alkenes and alkynes. The chain length of these oils lies between C15 and C50 [7]. For this study three different API Group I base oils, a fully formulated cylinder oil and, for comparison, the alkane $C_{30}H_{62}$ were used.

Unsaturated hydrocarbons react very exothermically with SO_3 and H_2SO_4, yielding hydrocarbon sulphonates and water. Used oil has been found to be degraded by water droplets and solid carbon. Also the rather inert alkanes can react with sulphuric acid. Isomerisation can take place where the methyl group, $-CH_3$, moves in the molecule chain from the second carbon to, for example, the third carbon, to form a hydrocarbon with the same molecular weight but different properties, a process used in refineries. The induction time for reactions to take place at room temperature can be explained by the increasing amount of carbocations, which are oxidation product of hydrocarbons, RH, by H_2SO_4. Reaction products differ depending on acid concentration and process temperature [8]. In this study, induction times for the reaction to take place at low acid concentrations were suppressed by heating the samples to 85 °C. Possible isomerisation products depend on the carbon chain length. Even the relatively simple $C_{30}H_{62}$ used in this study has more than 4 billion possible isomers, which makes an analysis or prediction unfeasible, and the base oil is more complex still.

Other than isomerisation, alkane oxidation with sulphuric acid can also take place. The oxidation rate increases with increasing sulphuric acid concentration and is particularly steep for pure sulphuric acid [9]. In air, alkanes such as the squalane used in this work are rather inert to oxidation. After 3 h at 150 °C a measurable mass loss due to evaporation of light products was observed and after 48 h at 180 °C there was a considerable increase in heavy products [10]. In this study the lubricants in contact with sulphuric acid formed bituminous mater within 2 min at 85 °C and the formation of carbonyl, C=O bonds, was revealed by Fourier transform infrared spectroscopy in attenuated total reflectance mode, FTIR-ATR.

Instead of isomerisation or oxidation, sulphonation can also take place where a tertiary H-atom is replaced by a $-SO_3H$ group to form a sulphonic acid, which associate in aqueous solution to form micelles [11] and influence interfacial tension.

$$C_nH_{n+2} + HOSO_2OH \rightarrow C_nH_{n+1}SO_3H + H_2O$$
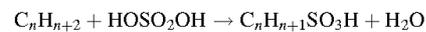
In industrial processes concentrated or even fuming sulphuric acid is used in order to obtain a high yield of products. The increased formation of water slows the process down or even stops it completely and it is therefore removed. In this work, however, formation of reaction products was observed for acid concentrations as low as 40 %w/w. In the Diesel engine heavy products accumulate over time in the form of deposits and the yield rate is of secondary interest. Oxidation in marine lubricants is seen as a plain thermal effect and the corresponding lubricant tests introduce heating of the oil for extended periods to temperatures well above 300 °C and evaluating deposit formation and viscosity increase [11, 12]. This is surprising because where low sulphur fuel is used for comparative engine tests a significantly lower deposit formation is observed in the piston ring pack [11, 13–15].

Surfactants are surface active substances which arrange themselves at the interface between immiscible substances, usually to lower the interfacial energy thus influencing emulsification and droplet displacement from walls [16]. For a water/oil interface, a surfactant needs a hydrophilic and a oleophilic side. Hydrocarbon sulphonates are a typical group of surfactants acting at the oil–water interface and lower the interfacial tension between the two liquids. They consist of a polar head group which attaches to the water and a long hydrocarbon tail which remains in the oil phase. When they reach a certain concentration at the interface, the interfacial tension reaches a plateau and is not reduced further and micelles are formed; this is the 'critical micelle concentration' or CMC. Micelles are droplets of one liquid in the other stabilised by the surfactants. Given the yellow colour and the results for interfacial tension, it is

likely that hydrocarbon sulphonates are already present in the API Group I base oil.

Viscosity of emulsions in general depend upon the viscosity of the bulk phase, the volume fraction and the particle size distribution of the dispersed phase, temperature, shear stress and the concentration and type of the surfactant [17, 18]. In this study all prepared emulsions followed the temperature–shear stress–viscosity behaviour of the bulk oil in the temperature and shear stress range of interest. The main differences were found in the isolated bituminous reaction products for which the exact chemical composition is unknown.

The aim of this study was to find the influence of acid concentration on viscosity, interfacial tension, emulsification and formation of reaction products of API Group I base oils in comparison with higher refined oil, represented by the model oil squalane, and to shed light on the physical and chemical state of the reaction products.

2 Materials and Methods

2.1 Fluids and Preparation

For the study, the following substances were used: Squalane (99 % Sigma Aldrich), API Group I base oils HVI160B, BS150 and SN600, fully formulated lubricant TBN 70 mg KOH/g and sulphuric acid (>95 % Fisher Scientific UK Ltd. analytical reagent grade). Lower concentrations of sulphuric acid were made with deionised water by weighing. Emulsions were prepared prior each measurement by placing the samples for 30 min in an ultrasonic bath at 40 °C. Bitumen was formed between API Group I base oil HVI160B and H_2SO_4 by mixing the two liquids at 90 °C. Bitumen was formed with acid concentrations of 80 and 98 %w/w H_2SO_4. The yield with 80 %w/w H_2SO_4 was very small and the bitumen was captured from the very distinct interface. With 98 %w/w H_2SO_4 the yield was very high but no distinct interface was visible, Fig. 13. Bitumen and oil were separated by pouring the sample in water and separation was instantaneous. The remaining oil settled on top of clear water and the bitumen settled in the bottom of the beaker. The water and oil were poured away and the residual bitumen heated to evaporate any remaining water. After cooling, the bitumen separated into an extremely viscous phase and a black far more fluid phase which exhibited a boiling point beyond 160 °C and a strong SO_2 smell.

2.2 Interfacial Tension

A standard Du-Noüy ring surface tension balance (White Torsion Balance) was used and the correct working of the arrangement was verified by surface tension measurements on distilled water. After adding oil to the top surface of the more dense acid, a series of time-dependent measurements were taken. To reach equilibrium the sample was heated to 90 °C and then allowed to cool to room temperature to facilitate measurements under stabilised conditions.

The platinum ring circumference was 40 mm and the inner diameter of the beaker was 41 mm which is the reaction area between oil and acid. The ring was cleaned after each measurement, following the order of solubility, in deionised water, isopropanol and heptanes. Between each step the Pt ring was dried on laboratory tissue. Finally the ring was heated until it glowed light red in a blue gas flame.

2.3 Droplet Size

The size of the droplets produced in the ultrasonic bath was measured in a Malvern "Mastersizer 2000" which uses laser diffraction by the droplets as a measurement principle. The samples were diluted with mineral oil. The refractive index of the corresponding acid concentration was used for the internal calculation of the droplet diameter.

2.4 Viscosity

Viscosities were measured using a Malvern "Kinexus" Rheometer with cone on plate arrangement. Cone geometries were 1/50 and 4/40 mm. Temperatures were set at 20, 40, 90, 120 and 150 °C in turn. A Shear rate ramp time of 2 min between 0.1 and 1,000 s^{-1} was chosen.

Measurements under equilibrium were not possible for the emulsions as the time until consecutive results are stable within very narrow limits was too long and phase separation would occur.

2.5 Thermal Stability

The oil was brought into contact with various concentrations of aqueous sulphuric acid and heated on a hot plate. The temperature when the first discolouration on the interface occurred was recorded. The ramp time for heating was 2 min from 20 to 100 °C.

2.6 Analysis of Reaction Products

A PerkinElmer Spectrum100 FTIR-ATR was used to analyse for chemical changes. A Leica DM6000M microscope was used to visualise the physical state of reaction products.

3 Results and Discussion

3.1 Interfacial Tension

After 8–16 min the interfacial tension between sulphuric acid and the API Group I base oils HVI160B, BS150 and SN600 stabilised, Fig. 1. This corresponds well to the behaviour observed with squalane as presented previously. However, the interfacial tension for the API Group I base oils was also time-dependent when in contact with water which was not the case with squalane. This indicates the presence of surfactants in the base oils.

In equilibrium, Fig. 2, the interfacial tension is substantially lower for the base oil HVI160B compared to squalane [19]. At 4 %w/w acid concentration the minimum
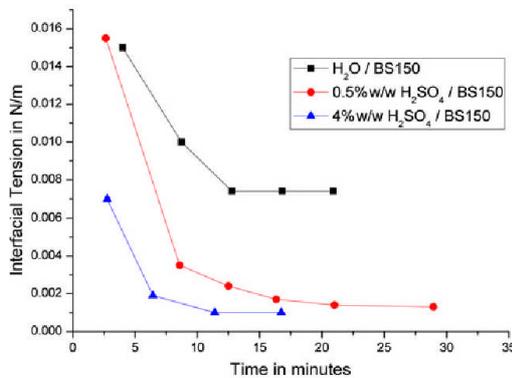
Fig. 1 Time-dependent drop of interfacial tension between API Group I base oil BS150 and water and aqueous H_2SO_4 at 22 °C
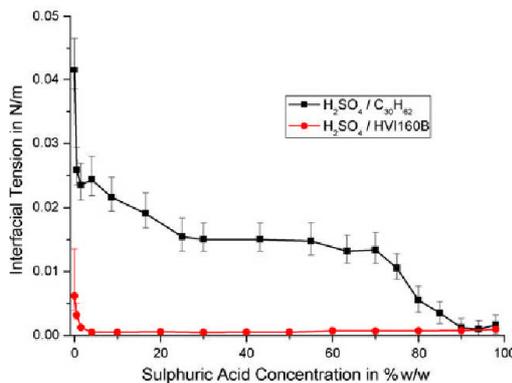
Fig. 2 Interfacial tension of H_2SO_4 to squalane and API Group I base oil HVI160B at 22 °C after heating to 90 °C

is reached and no further reduction can be observed. A comparison with API Group I base oil SN600 & BS150 shows the exact same behaviour.

3.2 Stability of Emulsions

For viscosity measurements, emulsions with various acid concentrations were prepared as described previously and any unused samples were left to settle. The result after 72 h can be seen in Fig. 3. In case of $C_{30}H_{62}$ settling was almost complete after 72 h. Only slight turbidity could be observed, but most of the aqueous phase accumulated as big droplets at the bottom of the bottles. Discolouration of the acid phase was only observed for 80 %w/w concentration and settling was complete. In case of HVI160B settling was neither complete after 72 h nor after 168 h. The uppermost quarter of the sample showed less turbidity than the lower three quarters and started to clear after 288 h. Discolouration was observed for 50 and 80 %w/w acid concentration, which shows the higher reactivity of HVI160B with sulphuric acid.

3.3 Droplet Size of Emulsion

The droplet diameter was evaluated before viscosity measurement and Figs. 4 and 5 show the droplet size distributions for $C_{30}H_{62}$ and HVI160B with various acid concentrations. $C_{30}H_{62}$ shows a much wider variety in droplet diameters and interestingly all acid concentrations below 25 %w/w, which corresponds to CMC I, Fig. 2, show two main droplet sizes. The droplet size distribution in the case of HVI160B is much narrower and there is a tendency for smaller droplets than $C_{30}H_{62}$. For both base oils the results for 80 %w/w acid concentration show a tendency for bigger droplet sizes. This could be a result of a drift in refractive index when the colour of the acid changes due to chemical reactions between acid and hydrocarbon and/or the formation of bigger bituminous droplets.

Figure 6 shows a statistical evaluation of the results in Figs. 4 and 5. The Sauter mean diameter, SMD, rates the surface area of the droplets higher than the volume mean diameter, VMD. For $C_{30}H_{62}$ there is a significant difference between SMD and VMD for acid concentrations below 25 %w/w, showing that a large part of the dispersed phase is present in a few bigger droplets.

For viscosity measurement, however, the active surface area of the droplets is more important. For both oils the dispersed phases shows a very similar and relatively constant behaviour.

Fig. 3 1.3 %v/v aqueous H_2SO_4 dispersed in $C_{30}H_{62}$ (**a**) and HVI160B (**b**) after 72 h of settling. *From left* 0, 0.5, 4, 10, 25, 50 and 80 %w/w
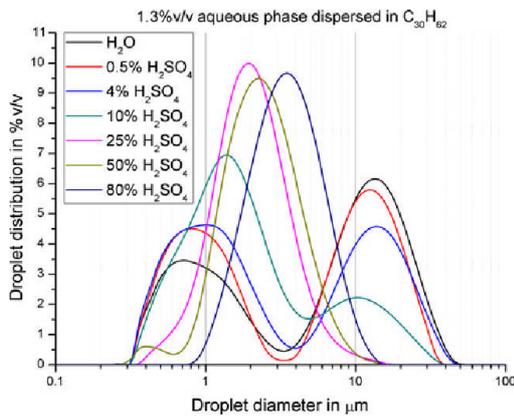
Fig. 4 Droplet size distribution of 1.3 %v/v aqueous H_2SO_4 dispersed in $C_{30}H_{62}$
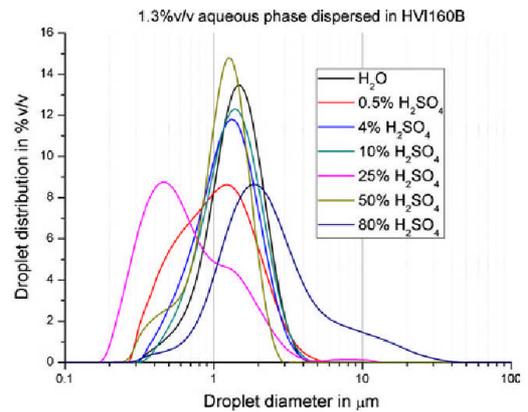
Fig. 5 Droplet size distribution of 1.3 %v/v aqueous H_2SO_4 dispersed in API Group I base oil HVI160B

3.4 Viscosity

The change in viscosity with increasing amount of water dispersed in HVI160B was measured for 1.5 and 7 %w/w water in the lubricant, Fig. 7. 1.5 %w/w is a value found in marine engines under tropical ambient conditions [20] and corresponds to 1.3 %v/v used for the measurements with increasing acid concentration, Figs. 8 and 9, to keep the volume of the dispersed phase constant. Changes in viscosity are minor in the evaluated shear rate range. The emulsions are Newtonian over a shear rate range from 200 to 700 s^{-1}, but below 100 s^{-1} shear thinning was observed.

Above 10 %w/w acid concentration only measurements at 20 °C were performed to prevent corrosive attack of the measurement equipment.

The correct working of the rheometer was verified by measuring $C_{30}H_{62}$ alone. For the given working sequence and cone arrangement, it produced higher results compared with values found in literature [21] especially at low viscosities, Fig. 10. The measured minima, however, meet the literature values which are given with an accuracy of ±3 %. The bitumen formed between HVI160B and 80 %w/w H_2SO_4, Fig. 13, 12th bottle, exhibits high viscosities and does not form deposits between 20 and 150 °C,

🖄 Springer
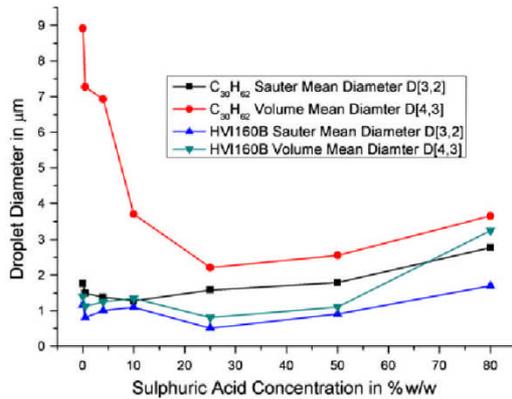
Fig. 6 Statistic evaluation of the droplet size distribution for dispersed H_2SO_4 in $C_{30}H_{62}$ and HVI160B; volume and surface rated

Fig. 7 Viscosity of pure and emulsified API Group I base oil HVI160B with water as dispersed phase. Applied shear rate was 200–700 s^{-1}

Fig. 8 Viscosity of pure and emulsified API Group I base oil HVI160B with 1.3 %v/v aqueous H_2SO_4 as dispersed phase. Applied shear rate was 200–700 s^{-1}
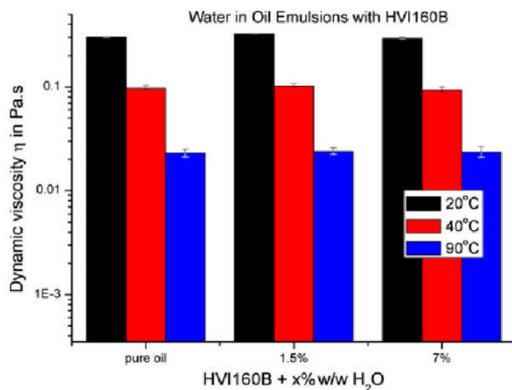
Fig. 9 Viscosity of pure and emulsified $C_{30}H_{62}$ with 1.3 %v/v aqueous H_2SO_4 as dispersed phase. Applied shear rate was 200–700 s^{-1}

Fig. 10. It shows slight shear thinning behaviour between 200 and 700 s^{-1}, explaining the large error bars which represent minimum and maximum values.

The viscosity measurements on the bitumen formed between 98 %w/w H_2SO_4 and HVI160B, Fig. 13, last bottle, proved to be difficult, Fig. 11. At low temperatures, the soft bitumen squeezed out of the gap at high shear rates. At increased temperatures, SO_2 gas release was observed. At high temperatures the sample started to solidify and formed a dry, solid deposit on the measurement equipment, Fig. 12. The deposit was not overly brittle and formed swarfs when scraped off. Despite the gas release, the results at 90 °C seem to be the most realistic. Over all, the bitumen shows a strong shear thinning behaviour which could be explained by poor wall adhesion for low temperatures, but not for higher temperatures. The shear
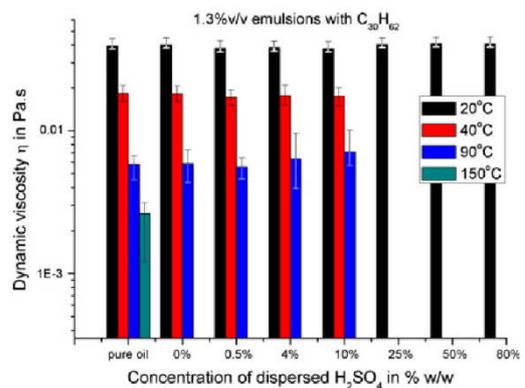
thinning behaviour can be explained by the revealed physical structure of the bitumen, as discussed in Sect. 3.7 and Fig. 18.

3.5 Critical Acid Concentration to Form Bitumen

Figure 13 shows the samples of HVI160B after their use in the interfacial tension measurements and a storage time of 2 weeks. During the measurements the samples were exposed to a maximum temperature of 90 °C after a heating time of 10 min. Above 80 % acid concentration both acid and oil phase show a strong discolouration and emitted a strong SO_2 odour. Between 60 and 80 % acid concentration only the acid phase shows a discolouration. All samples above 30 % acid concentration, Fig. 14, form a bituminous substance which has a high affinity to the
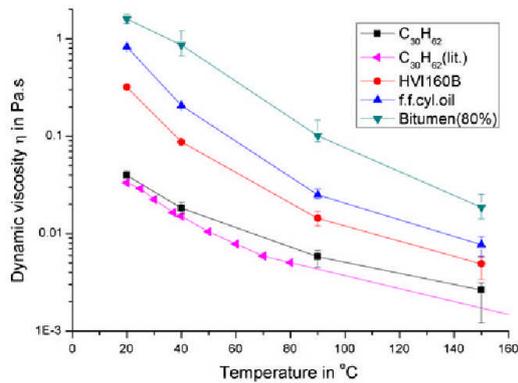
Fig. 10 Measured viscosity of $C_{30}H_{62}$ and values found in literature [21], a fully formulated cylinder lubricant, the corresponding base oil HVI160B and the bitumen formed between HVI160B and 80 %w/w H_2SO_4
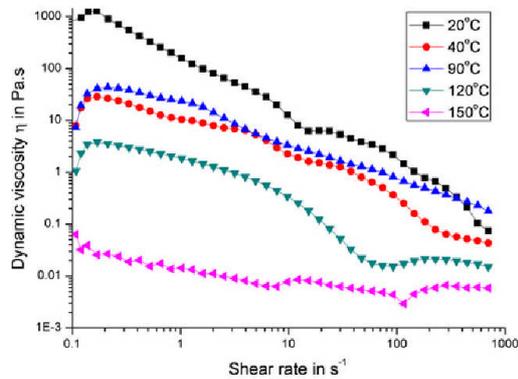
Fig. 11 Viscosity of bitumen formed between HVI160B and 98 %w/w H_2SO_4. See text for encountered difficulties

Fig. 12 Solidification of bitumen formed between HVI160B and 98 %w/w H_2SO_4 during viscosity measurements at 150 °C

glass walls of the sample containers. A comparison with API Group I base oil SN600 and BS150 shows exactly the same behaviour.

3.6 Critical Temperature to Form Bitumen

The HVI160B base oil was brought in contact with various concentrations of sulphuric acid and heated from room temperature to 100 °C within 2 min, Fig. 15. For concentrations below 40 %, discolouration was observed neither up to the limit of the boiling point nor during cooling down. Between 50 and 80 %w/w acid concentration the formation of a bitumen-like substance on the interface was observed at about 85 °C. Between 80 and 90 %w/w acid concentration, this temperature significantly dropped to reach room temperature for concentrations of 90 %w/w and above.

3.7 Analysis of Reaction Products

The bituminous reaction products appear to be quite complex emulsions, Figs. 16, 17 and 18. The bitumen formed with 80 %w/w H_2SO_4, Fig. 16, shows a dark bulk phase containing a light phase which contains irregular-shaped solids; presumably former cell walls. The microscopic investigation was done after the viscosity measurements. The bituminous phase formed with 98 %w/w H_2SO_4, Fig. 17, contains three different coloured phases which form droplets within each other. The bitumen formed after separating the bituminous phase formed with 98 %w/w H_2SO_4 in water, Fig. 18, shows droplets of an emulsion contained in a very dark and viscous phase. Figure 18 shows the bitumen after being squeezed hard between two microscope slides. Some drops burst and connected to form fingers and other drops remained contained in the black substance. Some of the light phase got squeezed out on the borders of the bitumen droplet. This can explain the extreme shear thinning behaviour, Fig. 11. The deposit, which was formed during viscosity measurements, Fig. 12, shows a porous structure which still contains liquid phase (Fig. 20).

The excitation spectra of the reaction products were recorded with the FTIR-ATR technique, Fig. 19. Comparing the position of the peaks for the acid species, the concentration of the acid can be determined. For the bitumen formed with 80 %w/w H_2SO_4, a concentration of 40–50 %w/w was found. The bituminous phase in 98 %w/w H_2SO_4 showed an acid concentration of 91–96 %w/w. For the bitumen formed in 98 %w/w H_2SO_4 and separated in water, a 50–60 %w/w concentration was found. The watery phase which was separated out from the water washed bitumen after heating showed a concentration of 70–75 %w/w which corresponds well with the observed boiling point of

Fig. 13 API Group I base oil HVI160B in contact with various concentrations of aqueous H$_2$SO$_4$, rising from 0 to 98 %w/w. *From left*: 0, 0.5, 1.5, 4, 10, 20, 30, 40, 50, 60, 70, 80, 90 and 98 %w/w
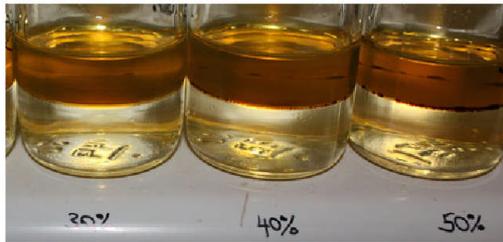
Fig. 14 Close-up of Fig. 13 on 30, 40 and 50 %w/w H$_2$SO$_4$
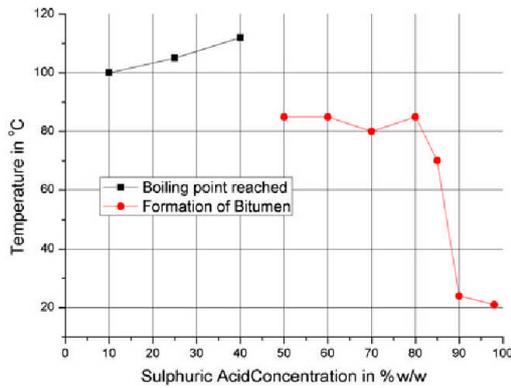
Fig. 15 Fast heating of API Group I base oil HVI160B in contact with various concentrations of aqueous H$_2$SO$_4$ until bitumen is formed

Fig. 16 Microscopic view on bituminous matter formed between 80 %w/w H$_2$SO$_4$ and HVI160B. Magnification: ×200
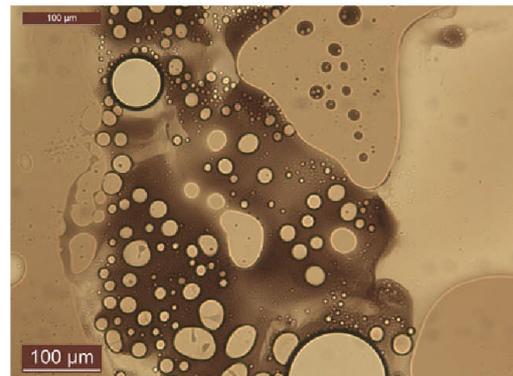
Fig. 17 Microscopic view on bituminous matter formed between 98 %w/w H$_2$SO$_4$ and HVI160B before separating from oil phase. Magnification: ×100

160 °C. The deposit formed on the viscometer contained ∼50 %w/w acid concentration. In all black very viscous bitumen and deposits, there seemed to be acid trapped within the hydrocarbon having a concentration of ∼50 %w/w; this is the critical concentration for a reaction to take place as shown in Sect. 2.5. All bitumen and deposits also contained residual HVI160B. However, in the bituminous phase created with 98 %w/w H$_2$SO$_4$ no HVI160B can be detected prior the washing because the strong and broad peaks from the acid cover the hydrocarbon peaks (Fig. 19).

To investigate the more viscous phase in the bitumen, the bitumen was heated to 300 °C to evaporate the less viscous sulphuric acid. Figure 22 shows scratched deposit under the microscope. It appears to be brittle and contains very small droplets. The FTIR-ATR analysis Fig. 21 reveals the presence of the base oil HVI160B and surprisingly species of the sulphuric acid, which were already found in the non-heated bitumen. In addition C=O double bonds were found which could be formed with the surrounding atmosphere, although the sample was trapped
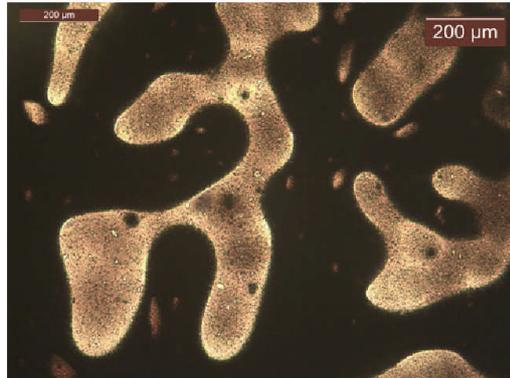
Fig. 18 Microscopic view on bituminous matter formed between 98 %w/w H_2SO_4 and HVI160B after separating from oil phase in water. Squeezed between glass slides. Magnification: $\times 50$

Fig. 19 FTIR-ATR analysis of reaction products and starting material

Fig. 20 Deposit formed during viscosity measurements at 150 °C with the water washed bitumen created with 98 %w/w H_2SO_4. Magnification: $\times 100$

Fig. 21 FTIR-ATR analysis of deposit formed at 300 °C with bitumen created with 98 %w/w H_2SO_4

Fig. 22 Deposit formed at 300 °C with bitumen created with 98 %w/w H_2SO_4. Magnification: $\times 200$

between two microscope slides. In the so-called fingerprint area (400–1,500 cm^{-1}) a small C–H peak at 965 cm^{-1} and a peak at 814 cm^{-1} were found. The latter peak was also found in the deposit formed at 150 °C but could not be related to any specific bond.

4 Conclusions

The absolute volume and the relative concentration of aqueous sulphuric acid in $C_{30}H_{62}$ and HVI160B have very little influence on viscosity in the shear rate range of 200–700 s^{-1}. No correlation of viscosity to interfacial tension or droplet size was found.

The interfacial tension between API Group I base oils and H_2SO_4 is also time-dependent but significantly lower than between $C_{30}H_{62}$ and H_2SO_4. Also the interfacial

tension between base oils and water is time-dependent, indicating the presence of polar substances in the base oil, most probably formed during the refinery process.

Emulsions of aqueous H_2SO_4 in HVI160B are more stable than in $C_{30}H_{62}$. Droplet sizes vary a lot for emulsions in $C_{30}H_{62}$ below CMC 1 (25 %w/w H_2SO_4). Droplet sizes are smaller and more distinct for emulsions in HVI160B compared to $C_{30}H_{62}$. In the fully formulated lubricant dispersants are added to emulsify the condensate. Moving to higher refined base oils might require an increase in dispersant volume. The homogeneous and stable emulsions of H_2SO_4 in oil were produced safely in an ultrasonic bath in a closed container.

Two different kinds of bitumen were formed in the study. One was formed at 80 %w/w H_2SO_4 concentration and most probably forms down to 40 %. The yield is very small. Its viscosity and temperature behaviour might be acceptable or even improve piston ring lubrication. The other was formed at 98 % and is most probably formed down to 85 %. The yield is very high but its viscosity properties and its tendency to form deposit influence piston ring lubrication negatively. These properties, however, may have been badly influenced by the chosen separation process in water. The deposit contains very small droplets of oil and probably acid to temperatures up to 300 °C. Under dry or boundary running conditions it might therefore have a positive influence on piston ring tribology when deposited on the sliding surfaces and is not blocking free movement of the parts.

The trapping of acid in a hydrocarbon shell is likely to reduce neutralisation efficiency with the alkaline reserve in the fully formulated lubricant. A test, which is not presented in this paper, with two commercial lubricants of TBN 70 mg KOH/g showed a reduction in neutralisation rate of 35 and 61 %, respectively, when the acid was in contact with the base oil before the test.

The critical acid concentration to form bitumen is about 40 %w/w H_2SO_4. This is important information for engine design and lubricant formulation. When the acid concentration is kept below 40 %, the hydrocarbon will not be attacked nor yield deposit forming bitumen.

Under thermally dynamic conditions, the critical concentration to form bitumen is about 50 %w/w and 85 °C for concentrations between 50 and 80 %w/w. Above 85 %w/w, bitumen is formed at room temperature. The concentration range 50–80 %w/w corresponds well with the second dissociation step of sulphuric acid, which has its peak at 50 %w/w and is gradually suppressed until 85 %w/w. At 85 %w/w all free water molecules are used up and the first dissociation step gets suppressed while free H_2SO_4 molecules start to appear. Below 50 %w/w the first and second dissociation steps are in a balance and the reaction of HSO_4^- ions with H_2O molecules is favourable [5].

HSO_4^- ions are likely to be the driving force for bitumen formation.

References

1. CIMAC Working Group "Marine Lubricants": No. 26 Guidelines for Diesel engines lubrication impact of low sulphur fuel on lubrication of marine engines. In: CIMAC, 2007
2. Huijbregts, W.M.M., Leferink, R.: Latest advances in the understanding of acid dewpoint corrosion: corrosion and stress corrosion cracking in combustion gas condensates. Anti-Corros. Methods Mater. **51**, 173–188 (2004)
3. CIMAC Working Group "Exhaust Emission Control": Guide to Diesel exhaust emission control of NO_x, SO_x, particulates, smoke and CO_2. In: CIMAC, 2008
4. Land, T.: The theory of acid deposition and its application to the dew-point meter. J Inst Fuel **50**, 68–75 (1977)
5. Young, T.F., Maranville, L.F., Smith, H.M.: Raman spectral investigations of ionic equilibria in solutions of strong electrolytes. In: Hamer, W.J. (ed.) The Structure of Electrolytic Solutions, pp. 35–63. Wiley, New York (1959)
6. Doyen, V., Drijfholt, R. K., Delvigne, T.: Paper No. 61 Advanced applied research unravelling the fundamentals of 2-stroke engine cylinder lubrication—an innovative on-line measurement method based on the use of radioactive tracers. In: CIMAC, 2007
7. The Petroleum HPV Testing Group: Test plan lubricating oil basestocks category. In: API, 2003
8. Rudakov, E. S., Volkova, L. K., Tishchenko, N. A.: Kinetics and Mechanism of homogeneous reactions of alkanes in sulphuric acid in the presence of carbocations. I. Oxidation, isomerization, fragmentation. Kinet. Catal. (Russ. trans.), **29**, 1168–1173 (1988)
9. Rudakov, E. S., Zamashchinkov, V. V., Lutsyk, A. I.: Kinetics of the reaction of saturated hydrocarbons with PdII, PTII–IV, HgII, CrVI, MnIII, MnIII–RuIII–IV, NO_2^+, H_2SO_4, $H_2S_2O_8$, and carbonium ions in sulphuric acid. Teoret. Eksp. Khim. (Trans.) **12**, 361–368 (1976)
10. Diaby, M., Sablier, M., Le Negrate, A., El Fassi, M.: Kinetic study of the thermo-oxidative degradation of squalane ($C_{30}H_{62}$) modelling the base oil of engine lubricants. J. Eng. Gas Turbines Power Trans. ASME **132**, 032805.1–032805.9 (2009)
11. Kosswig, K.: Sulfonic acids, aliphatic. Ullmann's Encyclopedia of industrial chemistry. Wiley, Weinheim (2000)
12. Garner, T., Voss, L., Marek, K., Aabo, K.: Paper No. 129 Development of marine Diesel cylinder oils. In: CIMAC, pp. 1–14, 2004
13. Miyazaki, M., Takeshima, S., Okuyama, S., Tanaka, M.: Evaluation of marine engine lubricating conditions using a cylinder liner surface oil sampling apparatus. In: CIMAC, pp. 1–15, 1993
14. Freund, M., Pallay, I., Cenkrari, I.: Einfluss des Schwefelgehalts von Dieselkraftstoff im Betrieb bei Verwendung von Schmieroelen verschiedenen Legierungsgrades. Erdoel und Kohle - Erdgas – Petrochem. vereiningt mit Brennstoff-Chem.,. Stuttgart: 21. Jahrestagung der Deutschen Gesellschaft fuer Mineraloelwissenschaft und Kohlechem, vol. 4 (1970)
15. Dunlap, H. L.: Effect of sulphur in liquid fuels. Chem. Metall. Eng. 298 (1927)
16. Schleizer, A.D., Bonnecaze, R.T.: Displacement of a two-dimensional immiscible droplet adhering to a wall in shear and pressure-driven flows. J. Fluid Mech. **383**, 29–54 (1999)

17. Djakovic, Lj.M., Dokic, P.P.: Changes of viscous characteristics of oil in water emulsions during homogenization. Colloid Polym. Sci. **256**, 1177–1181 (1978)
18. Farah, M.A., Oliveira, R.C., Caldas, J.N., Rajagopal, K.: Viscosity of water-in-oil emulsions: variation with temperature and water volume fraction. J. Petroleum Sci. Eng. **48**, 169–184 (2005)
19. Sautermeister, F. A., Priest, M., Fox, M., Lee, P. M.: Impact of sulphuric acid on cylinder lubrication for large 2-stroke marine diesel engines: contact angle, interfacial tension and chemical interaction. In: Tribology International, 38th Leeds-Lyon Symposium on Tribology, 2011
20. Micali, F., Weber, M., Stark, M., Raess, K., Potenza, M.: Paper No. 74 Suction air humidity influence on piston running reliability in low-speed two stroke diesel engines. In: CIMAC, 2010
21. DECHEMA e.V. DETHERM: Thermophysical properties of pure substances & mixtures. https://cdsdt.dl.ac.uk/detherm/detherm.php (2005–2008). Accessed 27 May 2010

Impact of sulphuric acid on cylinder lubrication for large 2-stroke marine diesel engines: Contact angle, interfacial tension and chemical interaction

F.A. Sautermeister*, M. Priest, P.M. Lee, M.F. Fox

iETSI, School of Mechanical Engineering, University of Leeds, Leeds LS2 9JT, UK

ABSTRACT

The effect of sulphuric acid on the chemical and physical behaviour of the piston ring lubricant in a marine engine cylinder was investigated. To reveal the basic influence of H_2SO_4 on the lubricant film, the saturated hydrocarbon Squalane ($C_{30}H_{62}$) was chosen as a simple model oil. The interfacial tension between aqueous H_2SO_4 (0–98% w/w) and $C_{30}H_{62}$ was measured between -3 and 165 °C to understand droplet formation in the lubricant. Interfacial tension decreases with increasing acid concentration and is temperature dependent.

The wettability of engine parts with corrosive sulphuric acid was characterised by the contact angle. The contact angle of H_2SO_4 (0–98% w/w) on a grey cast iron cylinder liner material (Wärtsilä, RT84) and a piston ring chrome-ceramic coating (Federal Mogul Goetze, CKS, ø960 mm) immersed in $C_{30}H_{62}$ was measured over a temperature range from 20 to 165 °C. In general, larger contact angles were measured under higher temperature conditions and on chrome surfaces.

In addition to the physical measurements, chemical reaction between H_2SO_4 and $C_{30}H_{62}$ was observed which influenced the interfacial tension, visual appearance, phase separation and formation of solid matter. The reaction time was found to be faster than the neutralisation times of commercially formulated lubricants. The reaction products were analysed using FTIR spectroscopy and EDX to find oxidation and sulphonation.

1. Introduction

At present, marine diesel engines burn refined but mostly residual fuels with a legislated maximum sulphur content between 0.005% and 4.5% w/w sulphur. The intention is to reduce SO_x exhaust gas emissions for environmental reasons. The fuel sulphur converts completely during combustion to form 100% sulphur dioxide, SO_2. Further oxidation yields 0.3–7% sulphur trioxide, SO_3, which rapidly reacts with water to form sulphuric acid, H_2SO_4, at various concentrations [1]. Catalysis by vanadium pentoxide, V_2O_5, at 450–600 °C increases the yield of SO_3 [2]. V_2O_5 arises in marine diesel engines from the combustion of heavy fuel oil (HFO) with restricted maximum vanadium levels of 600 mg/kg [3,4]. These reactions are specified below.

$$2SO_2(g) + O_2(g) \xrightarrow{V_2O_5 \, 450-600\ °C} 2SO_3(g) + heat$$

$$SO_3(g) + H_2O(l) \rightarrow H_2SO_4(aq) + heat$$
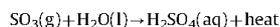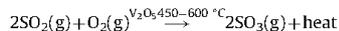
The resulting sulphuric acid condenses on the cylinder wall and the higher the dew point, the more readily the condensation occurs. The dew point equation of SO_3 with H_2O according Verhoff

[5] results in a large increase in dew point for small amounts of SO_3. The equation uses the partial pressures p in the gas phase. The resulting condensate is H_2SO_4.

$$T_d = \frac{1000}{[2.276 - 0.0294 \times \ln(p_{H_2O}) - 0.0858 \times \ln(p_{SO_3}) + 0.0062 \times \ln(p_{H_2O} \times p_{SO_3})]}$$
(1)

Applying typical values for an engine to Eq. (1), dew point temperatures T_d are found to be substantially below the gas temperature in the cylinder; therefore no condensation occurs in the gas volume. But the dew point temperatures are well above cylinder wall temperatures; therefore condensation will take place at the wall. High concentrations of sulphuric acid can be predicted from the vapour–liquid equilibrium diagram for sulphuric acid [6]. Therefore this study covers the range of concentrations from 0% to 98% w/w.

Depending upon concentration and temperature, H_2SO_4 dissociates in water to form HSO_4^-, H_3O^+, SO_4^{2-} and pure H_2SO_4 molecules as two steps [7]

$$H_2SO_4 + H_2O \rightleftharpoons HSO_4^- + H_3O^+$$

$$HSO_4^- + H_2O \rightleftharpoons SO_4^{2-} + H_3O^+$$
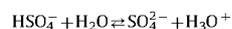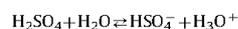
The engine components can experience corrosive wear; however, corrosion can only take place when droplets adhere to the

* Corresponding author.
  E-mail address: mnfasa@leeds.ac.uk (F.A. Sautermeister).

wall and are not removed by shear in the surrounding liquid. Adherence of a droplet to a wall under shear is quantified by the capillary number, $Ca = \mu \times U/\gamma$. When a critical value of Ca is reached, the droplets deform so extensively that they split or become completely detached from the wall. Above the critical capillary number, droplets with contact angles between 60° and 90° will split leaving smaller droplets on the wall, while droplets of 120° are likely to detach from the wall completely [8]. The contact angles found in this study cover the whole range, depending on the surface material and acid concentration. Whilst the dynamic viscosity, μ, of the bulk liquid is known, the viscosity of the droplet has no influence on droplet displacement [9]. The velocity experienced by the droplet is given by the variation in piston speed and droplet size.

Typical droplet diameters found in used engine lubricant are between 5 and 30 μm in stable emulsions [10]. Under 'dry' ambient conditions water content can reach 0.5–0.65% w/w and under tropical conditions a higher 0.75–1.3% w/w [10]. Water-in-oil emulsions of up to 45% w/w in marine cylinder lubricants are stable mainly due to the sulphonates contributed by the detergents which significantly lower the interfacial tension [11]. It is very difficult to prove the influence of droplets on lubrication in a laboratory environment using conventional tribometers as the droplets are unlikely to enter the lubricated interface [12].

The cylinder liner material for large 2-stroke marine diesel engines is a sand-cast grey cast iron and this study used a typical cylinder liner sample from a Wärtsilä RT84 engine. A description of corrosive attack of this material by sulphuric acid is given in [13]. The wear rates observed at Top Dead Centre for the latest large bore engines are around 0.01 mm/1000 h after 6000 h [14].

The coating materials used for the piston rings are more diverse but this study concentrates on the aluminium oxide filled galvanic chrome coating "CKS" from FM-Goetze [15], as predominantly used in Wärtsilä 2-stroke engines. In the plating process, hot dilute sulphuric acid is used to etch porosities to give improved oil retention of the surface [16]. It therefore seems strange to find chrome-plated parts in an environment attacked by sulphuric acid. However, service experience with chrome plated piston rings and piston ring grooves in marine diesel engines is good although wear rates are high compared to other heavy duty engines burning low sulphur fuels. The top ring wear rates for the latest large bore engines are approximately 0.02 mm/1000 h after 6000 h [14].

The neutralisation of the sulphuric acid, formed by combustion, is taken care of by an alkaline reserve in the lubricants with total base number, TBN, levels of 40–70 mg KOH/g. The alkaline reserve is usually added into the lubricant by dispersing calcium carbonate, $CaCO_3$, particles as reversed micelles. An excess of surfactant disperses solid particles and acid droplets and "form(s) a surfactant monolayer on the oil–acid interface" [17]. 'Docking' an additive-containing inverse micelle on to the monolayer at the oil–acid interface forms a channel through which acid can enter the micelle and react with the neutralising agent. When a critical amount of surfactant is reached on the oil–acid interface, the inverse micelles now containing the neutralisation products can leave the oil–acid interface. The adsorption of fresh unreacted micelles was found to be rate limiting and increasing the micelle concentration or TBN decreased the neutralisation time [17]. Adding dispersants dramatically reduced the neutralisation efficiency of nitric acid due to blocking of the interface by the dispersing additives. For sulphuric acid, the dispersing additives can transport the hydrated calcium sulphate crystals away from the interface into the lubricant. This is a reaction product which blocks the interface and is removed by the dispersant, increasing the neutralisation efficiency again to some extent [17]. Neutralisation times of sulphuric acid in fully formulated cylinder oils at 200 °C are between 10 and 15 min [18].

1.1. Deposit formation

Other than corrosion, marine diesel engine cylinder systems also suffer from deposit formation arising from deposition of unused additives and lubricant degradation by fuel impingement [19].

Two stroke marine diesel engines are typically lubricated with API Group I base mineral oils [1], the least refined lubricants containing < 90% w/w saturated hydrocarbons (alkanes) with the remainder formed from unsaturated hydrocarbons such as alkenes and alkynes. The chain length of these oils lies between C15 and C50 [20] and for this study a C30 alkane was chosen as typical of this range.

The exothermic reaction of unsaturated hydrocarbons with SO_3 and H_2SO_4, yields hydrocarbon sulphonates and water [21]. Lubricant sampled from the engine, has been found to be degraded by water droplets [10] and solid carbon [18]. The rather inert alkanes can also undergo various reactions with sulphuric acid. When the methyl group, $-CH_3$, moves in the molecular chain during isomerisation, a process used in refineries, a hydrocarbon with the same molecular weight but different properties is formed. Induction times for the reaction to take place of several hours were observed for low temperatures but the time decreased for temperatures between 60 and 70 °C. The induction time was explained by the increasing amount of carbocations, which are an oxidation product of hydrocarbons, RH, by H_2SO_4. The induction time was eliminated by adding RH's which oxidise easily in H_2SO_4 or by adding strong oxidising agents like chromium trioxide, CrO_3. The surrounding atmosphere has no influence on the reaction products but the reaction products differ depending on acid concentration and process temperature [22]. Possible isomerisation products depend on the carbon chain length and the $C_{30}H_{62}$ used in this study has more than 4 billion possible isomers, which makes an analysis or prediction unfeasible.

In addition to isomerisation, alkane oxidation can also take place. Metal ions can act as catalysts of hydrocarbon oxidation; for example Cr^{VI} shows a higher oxidation potential than Pt^{II-IV} which is more oxidising than pure H_2SO_4. With increasing sulphuric acid concentration the oxidation rate increases and is highest for pure sulphuric acid [23]. In air, alkanes such as the squalane used in this work are rather inert to oxidation. After 3 h at 150 °C a measurable mass loss due to evaporation of light products occurs and a considerable increase in heavy products is observed after 48 h at 180 °C [24].

Instead of an isomerisation reaction or oxidation, where C–H bonds are broken, sulphonation can also take place where a tertiary H-atom is replaced by a $-SO_3H$ group to form a sulphonic acid, which associate in aqueous solution to form micelles [25].

$$C_nH_{n+2} + HOSO_2OH \rightarrow C_nH_{n+2}SO_3H + H_2O$$
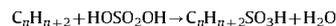
In industrial processes, concentrated and even fuming sulphuric acid are used in order to obtain a high yield of products. The increased formation of water slows the process down or even stops it completely and it must be removed.

Oxidation in marine lubricants is seen as a plain thermal effect. Test methods introduce heating of the oil for extended time to temperatures well above 300 °C and evaluation of deposit formation and viscosity increase [18,25]. This is surprising because where low sulphur fuel is used for comparative engine tests a significantly smaller deposit formation in the piston ring pack is observed [37,26].

Surface active agents or 'surfactants' usually lower the interfacial energy between immiscible substances by arranging themselves at the interface. A surfactant needs a hydrophilic and a oleophilic side to affect a water/oil interface. Hydrocarbon sulphonates are a typical group of surfactants acting at the oil–water interface, consisting of a polar head group which

attaches to the water and a long hydrocarbon tail which remains in the oil phase. When the surfactant molecules reach a certain concentration at the interface, the interfacial tension is not lowered further, reaching a plateau, and thereafter micelles are formed; the 'critical micelle concentration' or CMC. Micelles are droplets of one liquid in another, stabilised by a surplus of surfactant. Depending on their concentration, micelles can arrange in many formations, in some cases double layers of surfactants are formed on the interface and the interfacial tension drops for a second time, a point called CMC II [27]. When this second drop in interfacial tension is found, the first CMC is named CMC I.

2. Materials

For interfacial tension measurements squalane (99% Sigma Aldrich) and sulphuric acid (> 95% Fisher Scientific UK Ltd. analytical reagent grade) were used. Lower concentrations of sulphuric acid were made with deionised water by weight.

Surface samples were prepared from a galvanic chrome-coated piston ring (∅960 mm, CKS, FM-Goetze) and a grey cast iron cylinder liner segment (RT84, Wärtsilä Switzerland Ltd.). The samples were hand-ground and polished with a 15 μm Buehler Diamond suspension and then cleaned in an ultrasonic bath with a Decon90 solution and then deionised water for 10 min each. After cleaning the samples were dried on a hot plate at 150 °C for 5 min and oiled with squalane after a short cooling down period to protect the surface.

3. Methods

3.1. Interfacial tension measurements

A standard Du-Noüy ring surface tension balance (White Torsion Balance) [28] was modified to incorporate a temperature controlled hot plate under the beaker containing the liquid. The correct working of the arrangement was verified by surface tension measurements on distilled water.

Measurements under three different conditions were taken. First the oil was added to the top surface of the (more dense) acid at room temperature and directly measured to see the time dependent development of interfacial tension. Secondly the same samples were heated to 90 °C and then cooled down to measure at room temperature when all reactions between oil and acid were finalised. Thirdly a new batch of samples was prepared by adding oil and acid at room temperature and stored for at least 12 h. The samples were then cooled in a refrigerator and measured until room temperature was reached. The temperature was then increased in steps of 15 °C and each step was held for 30 min to allow for stabilisation before measurements were taken. A K-type thermocouple (NiCr–Ni) was directly placed in the oil phase to avoid corrosion.

The platinum ring circumference was 40 mm. The inner diameter of the sample beaker was 41 mm which defined the reaction area between squalane and sulphuric acid. The platinum ring was cleaned after each measurement, following the order of solubility in deionised water, isopropanol and heptanes. Between each step the ring was dried on laboratory tissue and finally it was heated until it glowed light red in a blue gas flame.

3.2. Contact angle measurements

The contact angle of various acid concentrations on surfaces submerged in squalane was measured by the 'pendant' or 'sessile' drop method [29]. To avoid corrosive attack the steel needle of a glass syringe containing the aqueous acid was replaced by a 1 mm glass capillary with one tapered end to create a tight fit in the small hole of the syringe. A custom-built oil bath with parallel glass windows was placed on a temperature controlled hot plate mounted on a 3-axis movable stage and the surface samples were placed in the oil bath. The evaluation was done by ImageJ software plug-in [29]. The correct operation and accuracy of the whole arrangement was shown by measuring 1 mm diameter steel balls located in various smaller holes in a calibration plate.

3.3. Analysis of reaction products

Mixtures with acid concentrations of 0%, 0.5%, 10%, 25%, 40%, 65%, 80% and 90% w/w were stored for several days between 80 and 110 °C, 15 °C below their boiling point. The mixtures were freshly prepared and out of contact with any metal that could act as a catalyst.

Solid reaction products were separated and neutralised in water, washed with isopropanol and heptanes and dried at 60 °C prior to analysis by Fourier transform infrared spectroscopy (PerkinElmer Spotlight 400-Spectrum100 FTIR microscope) and with attenuated total reflectance (ATR) accessories.

Visual examination of the solids was achieved with a reflected light microscope (PolyvarMET) and an SEM (Philips XL30 with tungsten source operating at 20 kV, working distance of 10 mm). The SEM included EDX analysis capability for elemental identification in the near-surface layer (Oxford Instruments INCA System with X-sight SiLi detector). To gain greater depth of field from the light microscope, stacking of several pictures with incremental focal lengths was achieved using image analysis software [30]. For measuring droplet sizes in liquid samples a Zeiss Axiovert135TV transmission microscope was used.

For FTIR analysis, acidic or aqueous liquid samples were placed in a CaF$_2$ transmission cell, which were found to be resistant to concentrated sulphuric acid and for the discoloured oil, KBr cells with a 0.05 mm path length were used. The droplets observed in the oil phase were small and stable and no chemical reaction with the KBr was observed. The background scan was done with the empty cells in place. The FTIR ATR with diamond covered ZnSe optics was used for acidic samples.

4. Results and discussion

4.1. Interfacial tension and chemical interaction

For the time variation measurements as described in Section 3.1 it was found that the interfacial tension for all aqueous acid concentrations against squalane at 20 °C decreases over time and stabilises after approximately 16 min. This behaviour was not observed for pure water against squalane and the value found is in good agreement with Antonov's rule [31]. The higher the acid concentration, the sharper the decrease and the lower the resulting values, Fig. 1.

The most plausible explanation for the decrease in interfacial tension with time is the reaction of squalane with the acid to form surfactants which form a monolayer, micelles and consequently multiple layers. Applying the general rule that chemical reaction rates at least double for every 10 °C increment, the reaction between oil and acid at 200 °C would be complete after 0.22 s. A couple of minutes seem to be more realistic but it is still faster than the neutralisation time for commercial oils with concentrated sulphuric acid at 200 °C with stirring, which is 10–15 min [18].

The results obtained for equilibrium measurements as described in Section 3.1 are shown in Fig. 2 (σ H$_2$SO$_4$/C$_{30}$H$_{62}$).

At this temperature and time-range, discolouration was observed for the acid phase for highly concentrated sulphuric acid of ~98% w/w. The discolouration commenced at approximately 70 °C, a value confirmed in the literature [32].

All mixtures below 40% concentration remained clear, the 40% w/w mixture did not exhibit discolouration but instead some solid formation and slight clouding and all mixtures above 40% w/w showed discolouration.

The results for the interfacial tension measurements in Fig. 2 (σ $H_2SO_4/C_{30}H_{62}$) show a sharp decrease in interfacial tension for a very low concentration (0.5% w/w) of sulphuric acid. From 0.5% w/w to 25% w/w a more shallow drop is observed, followed by a constant level of interfacial tension between 25% and approximately 65% w/w. A further decrease occurs until 90% w/w, where the lowest values are reached. The error bars include all possible sources of error and do not reflect the repeatability of the measurements which showed a standard deviation of $\pm$ 0.0002 N/m. The decrease in interfacial tension with increasing concentration is a well established observation in interfacial science. Usually the Langmuir–Szyskowski equation [33] is used to describe interfacial tension on the oil–water interface for

known surfactants. At higher concentrations, more but unknown surface active molecules can be formed, leading to the drop in interfacial tension.

Also shown in Fig. 2 are the chemical species formed as acid concentration is increased [7]. Point A in Fig. 2 marks the sharp decrease in interfacial tension, which is explained by the large difference in molecular concentration ratio between squalane, at 1.92 mol/L, and sulphuric acid, 18.64 mol/L. This is illustrated further at point B where the HSO_4^- ion reaches a concentration of 1.98 mol/L which means that for every molecule of $C_{30}H_{62}$ at the interface, there is a molecule of HSO_4^- available. At point B, the interface becomes saturated and the interfacial tension remains constant as the concentration of HSO_4^- increases further. In colloid science, this point is called 'CMC I'. At point C the second dissociation step reaches a maximum and from this point onwards as the concentration of sulphuric acid increases, the second step of dissociation into SO_4^{2-} becomes increasingly suppressed. This effect increases the rate of HSO_4^- ion release and the interfacial tension begins to decrease slowly. At point D the number of acid species is greater than the number of free H_2O molecules and a second sharp decrease in interfacial tension is observed. At point E the available HSO_4^- ions are in equilibrium with free H_2SO_4 molecules and interfacial tension reaches its minimum. Finally, a slight increase in interfacial tension is observed when squalane is exposed to the most concentrated sulphuric acid.

Figs. 3 and 4 show the results for the temperature dependent interfacial tension measurements as described in Section 3.1.

Discolouration and formation of solid particles was observed in solutions down to 40% w/w acid concentration when stored for several days at 90 °C. During the temperature dependent interfacial tension measurements, discolouration of the samples containing higher acid concentrations was also observed. The moment of discolouration was captured during the interfacial tension measurements for 80% w/w and 65% w/w acid concentration, Fig. 3. During the measurements and before discolouration occurred, the interfacial tension was directly correlated to the temperature of the system and followed the upper values. When a certain high temperature was reached, or a lower temperature was held for several days, the sample started to change colour and the interfacial tension decreased significantly. After the decrease,
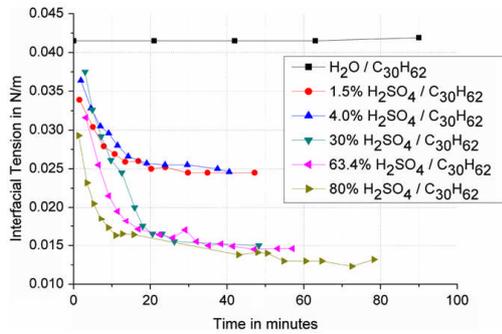
Fig. 1. Time dependent development of interfacial tension between aqueous concentrations (% w/w) of H_2SO_4 and $C_{30}H_{62}$.
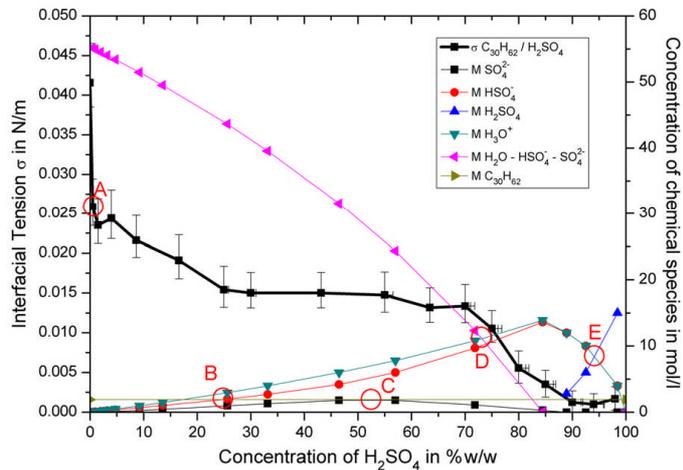
Fig. 2. Results of interfacial tension measurements between squalane and sulphuric acid (σ $C_{30}H_{62}/H_2SO_4$) at 21 °C in comparison to molecular concentration of species in the acid phase, according to [7].
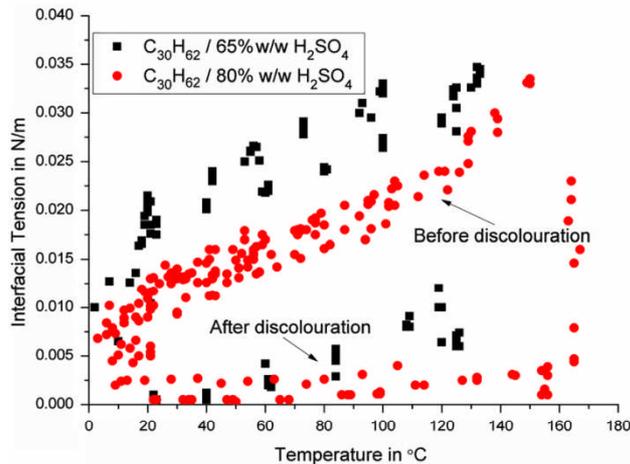
Fig. 3. Temperature dependent interfacial tension of 65% and 80% H_2SO_4 towards $C_{30}H_{62}$.
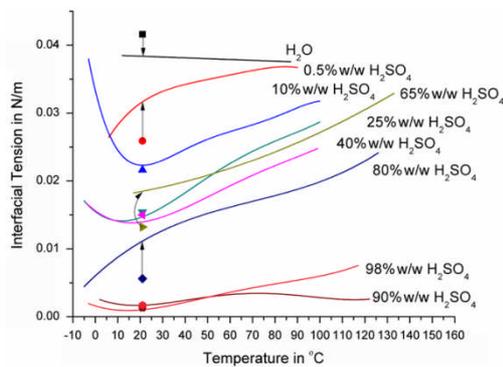
Fig. 4. Concentration and temperature dependency of the interfacial tension between sulphuric acid, H_2SO_4, and squalane, $C_{30}H_{62}$. The values from Fig. 2 are added for comparison.

the correlation between interfacial tension and temperature was changed irreversibly, as shown by the lower values in Fig. 3.

The upper values, without discolouration, were measured for nine acid concentrations and for each a closest fit function was found, which can be found in appendix A and are illustrated in Fig. 4. For comparison and orientation the 21 °C values from the stirred and heated trial are added in the plot as single points. Measurements of the two different treated sample batches show good agreement at most concentrations but are higher for 0.5%, 65% and 80% in the case of the samples that were only stored for extended time at room temperature.

The interfacial tension between squalane and deionised water decreases linearly with increasing temperature but also is more shallow than the linear surface tension of pure water and pure squalane for which the linearity is described by the Eötvös rule [28]. For all solutions containing sulphuric acid, the interfacial tension rises with temperature increase above approximately 20 °C. For 0.5% w/w and 80% w/w solutions, the interfacial tension decreases disproportionately at temperatures below 20 °C. All

other solutions show a contrary disproportionate increase in interfacial tension at temperatures below 20 °C.

The temperature–interfacial tension correlation for all concentrations of sulphuric acid was non-linear. A similar fishhook or J-shape behaviour was observed at the interface between water and liquid paraffin [34] when POE (polyoxyethylene) stearyl ether was dissolved in the water phase. This behaviour was also concentration dependent. The authors explained the temperature dependence in terms of the pulling forces on the polar head groups of the surfactant. The hydrophilic head group and the oleophilic tail find a concentration dependent energetic ideal position at a certain temperature, where the interfacial tension therefore is at a minimum. When the temperature rises or falls, the head group changes its position to the oil or water side and thereby increases the interfacial tension.

No correlation was found between the temperature dependent extent of dissociation of H_2SO_4 in water [7] to the temperature dependency of interfacial tension. This can be explained by a chemical reaction which binds the HSO_4^- ion strongly to the oil phase and excludes it from the dissociation process.

The change in colour and creation of solid particles at high temperature or extended time of exposure and irreversible shift in interfacial tension indicate a chemical reaction within the system which produces surface active substances. EDX analysis, Section 4.4, revealed both sulphur and oxygen in a dry reaction product. This indicates that either HSO_4^-, SO_4^{2-} or both reacted with the squalane. The solid sample was formed at 80% w/w (14 mol/L) sulphuric acid concentration and 165 °C, where HSO_4^- is the predominant species in the acid and therefore the only available sulphur donator. The sulphur to oxygen ratio should therefore be 1:4 based on the species but the EDX analysis showed a ratio of 1:8. Although the EDX technique is more precise for heavier elements like the sulphur, with an error of about ± 2–5%, and less accurate for lighter elements like carbon or oxygen, with an error of about ± 10%, this possible error cannot explain the surplus of oxygen. Therefore either 50% of the sulphur left the reaction in liquid or gaseous (H_2S, SO_2) form or 50% of the oxygen originates from dissolved gaseous oxygen in the liquid or was added from other liquid species, which are H_3O^+ or molecular H_2O which is available in excess of 5.07 mol/L at 80% w/w, see Fig. 2. Experiments in the oven at lower

temperature over a longer time revealed that the formation of solids is concentration dependent and not due to dissolved oxygen. Furthermore, no reaction between water and squalane was observed. Formation of H_2S would give a typical odour of foul eggs which was not observed but after storing the samples for several months a typical SO_2 odour was evident. The oxidation peak found in the FTIR spectrum reveals an extra sulphur independent C—O bond, Sections 4.3.1 and 4.3.2, and therefore it is likely that the squalane reacted with both HSO_4^- and H_3O^+.

The surface tension of squalane to air was unaffected by chemical contact with sulphuric acid and was in good agreement with values found in literature [35]. This indicates that any surface active substances formed act only upon interfaces to polar fluids and not with the non-polar air.

4.2. Contact angle

Contact angle measurements were made for a piston ring chrome coating (CKS) and for a cylinder liner grey cast iron (RT84). Advancing angle, receding angle and static angle were measured. Advancing and receding angle were not averaged, as is normal practice, because the parts in the engine do move and to understand transport phenomena it is important to know the difference. The full results are given in appendix B.

In general it can be said that observed contact angles for the CKS piston ring coating were larger than for the RT84 cylinder liner material. Receding angles θ_R are less than static angles θ_{st}, which in turn are less than advancing angles θ_A. In most cases, the contact angle is larger at higher temperatures, but not for all cases:

- θ_{CKS_A}: stays high between 0% and 80% w/w (H_2SO_4) with a sharp drop at 98% w/w acid concentration.
- θ_{CKS_R}: unstable between 0.5% and 40% w/w but higher than between 65% and 98% w/w where it is stable.
- θ_{CKS_st}: higher between 0% and 40% w/w than 65–98% w/w.
- θ_{RT84_A}: high for 0% w/w, rising from low 0.5% and 80%, lower than 0% w/w for 90% and 98% w/w.
- θ_{RT84_R}: stable low between 0.5% and 98% w/w, lower than for pure water.
- θ_{RT84_st}: high for 0% w/w, stable low for 0.5–98% w/w.

For low interfacial tension one would expect a low contact angle but for the chrome surface the contact angles stayed stable at a high level for most of the acid concentrations.

With the critical capillary numbers Ca for droplet displacement given by [8], the measured contact angles θ and interfacial tension γ, it is possible to predict where droplets will remain stable on the cylinder wall. The velocities acting on the acid droplets are given by the piston speed, oil film thickness and droplet diameter. Assuming planar parallel plates, the velocity profile in the oil film is linear and therefore the absolute shear stress is equal near both walls.

Latest measurements [38] and theoretical studies [15] show good agreement in the range of minimum oil film thickness between piston ring and liner. Minimum film thicknesses at TDC are between 2 and 5 μm and at higher piston speed reach 10–12 μm. Typical droplet diameters found in engines are reported [10] to be between 5 and 30 μm. In this paper droplets in the oil phase were found to be 1–8 μm diameter (Table 1).

The critical speed for droplet displacement from a wall [8] calculates to

$$U_{crit} = \frac{Ca_{crit} \times \gamma}{\mu} \qquad (2)$$

At 100 °C for 40% w/w H_2SO_4 concentration the following values apply.

Table 1
Critical speeds for droplet displacement, after [8].

Interfacial tension	$Ca_{crit\ CKS}$	$Ca_{crit\ RT84}$	Dynamic viscosity
$\gamma_{C_{30}H_{62}/40\%\ H_2SO_4\ at\ 100\ °C}$ 0.0248 N/m	For $\theta_{CKS}{\sim}90°$ 0.37	For $\theta_{RT84}{\sim}15°$ $>0.52{\sim}0.7$ (linear interpolated)	$\mu_{C_{30}H_{62}}$ ${\sim}0.004$ Pa s
Result U_{crit}	**2.29 m/s**	**4.34 m/s**	

The maximum piston speed in the engine is 16 m/s resulting in the before mentioned 10 μm oil film. Assuming a 'moving plate on stationary plate laminar couette flow' for the piston ring-liner contact, the velocity distribution in the oil film is linear. For this case, the critical speed for droplet displacement is reached at 1.4 μm from the chrome coated piston ring and at 2.7 μm from the grey cast iron cylinder liner wall. The volume of the droplets depends upon their shape and the contact angle. The volume on the cylinder liner can be much greater than on the piston ring. At the piston reversal points, the droplet size can become bigger. This approximation illustrates that small acid droplets can be picked up and transported by the piston ring. In non-wetted, unsheared areas of the piston ring profile, the droplets may be bigger. For piston rings with asymmetric barrel shaped profiles, typically of axial piston ring heights of 20–24 mm in marine engines, one would expect to find acidic attack on the upper half of the ring profile.

Gas velocities in the piston ring gap are much higher than the piston speed. However, the gas temperatures are well above the boiling point of sulphuric acid for the top ring and in addition the influenced surface area is very small compared to the main circumference of the piston ring. Therefore the piston ring gap is not included in this consideration.

4.3. FTIR analysis

4.3.1. FTIR analysis of liquids

Reacted, brown squalane which had been exposed to 80% w/w H_2SO_4 at 165 °C for 15 min was analysed by transmission FTIR. Comparison with a fresh unreacted sample of squalane showed peaks at 1723 cm^{-1} and 1739 cm^{-1} in the reacted sample, typical indicators of oxidation to carbonyl C—O bonds.

The ATR has a working range down to 500 cm^{-1} which allows analysis of sulphur containing compounds. The squalane samples which had been in contact with 65–98% w/w sulphuric acid showed an underlying H_2SO_4 spectra and a strong SO_2 smell was revealed when opening the sample bottles after a storage time of two months. The acidity in the oil phase most probably originates from dispersed droplets as the acid phase of the samples revealed no change in dissociation when compared with spectra from freshly prepared acid. This means that no water was produced during the reaction with squalane or the levels were too small to be detected. Only the 65 and 80% w/w acid samples that were heated to 165 °C, Fig. 3, showed traces of squalane in the acid phase. This, however, may be due to the broad IR response of acid and water which may mask the hydrocarbon peaks. Dark liquid, taken from the interface of the same samples, revealed a strong carbonyl peak and strong acidity that correspond well to the underlying bulk acid. The squalane peaks were weak but present.

4.3.2. FTIR analysis of solids

A solid particle formed during the experiments with 80% w/w H_2SO_4 at 165 °C for 15 min was analysed by an FTIR microscope. To reveal the peaks corresponding to minor components, the bulk

7

components $C_{30}H_{62}$ and H_2SO_4 were subtracted from the resulting spectrum. Four significant peaks were found at $3350\,cm^{-1}$(O–H; carboxylic acids), $1750\,cm^{-1}$(C O bond; oxidation of alkane), $1595\,cm^{-1}$(C–C or C C or C O carboxylates) and $1340\,cm^{-1}$ (C–H methyl; residual amount of squalane).

The same particle was also analysed with the ATR to observe lower wave numbers. The spectrum pattern for sulphuric acid was revealed but the peaks shifted from the expected 80% to 30% w/w acid concentrations but with weakened water peaks.

4.4. SEM/EDX

At high temperatures, solids were formed on the interface between squalane and sulphuric acid. The example shown in Fig. 5 was formed within 3 min at 165 °C and a acid concentration of 80% w/w. During rinsing with heptane, two edges of the sample rolled up, revealing the bottom side of the flake. Fig. 5 shows the difference between the top and bottom of the sample. While the top side is smooth, the bottom side reveals an open or shrunk, foam like structure with feature diameters between 10 and 50 μm. It seems likely that the bottom surface pointed towards the acid side.

EDX elemental analysis revealed $70.31 \pm \sim 7\%$ carbon, $26.34 \pm \sim 2.6\%$ oxygen and $3.3 \pm \sim 0.07$–0.17% sulphur. All results are given in at%.

4.5. Light microscopy

4.5.1. Light microscopy—liquids

The used liquid samples were investigated under a transmission light microscope. For all acid containing samples, droplets were found in the acid phase. When the acid phase changed colour, more droplets of 5–70 μm diameter were found. When the oil phase stayed clear, no droplets were found in the oil phase. When the oil phase did change colour, tiny droplets of 1–8 μm diameter were found in the oil phase. It was also observed that dark particles, the structure of which was too small to be revealed, would stay on the outside of the droplets in the oil phase and were more likely to be found on the inside of the droplet in the acid phase.

Fig. 6 shows an example of $C_{30}H_{62}$ on top of 80% w/w H_2SO_4 exposed to a temperature of 165 °C over 15 min; both phases changed colour. The samples were stored for several weeks at room temperature before the phases were extracted for microscopic examination.

The difference in droplet size, with smaller droplets in the oil phase and larger droplets in the acid phase, suggests the formation of surfactants with hydrophilic head groups and oleophilic tails yielding micelles or inverse micelles. The density of head groups per surface area should be the same for all droplets but in the acid bulk phase, the oleophilic tails require space within the micelle droplet, therefore enlarging the volume of the droplets. In the oil phase, the tails point outwards from the inverse micelle droplets and thereby allow them to be smaller in volume.

4.5.2. Light microscopy—solids

Fig. 7 shows a solid particle formed within 3 min at 165 °C and an acid concentration of 80% w/w. Under the light microscope (200×, stacked) a foam like structure was revealed with feature sizes comparable to the droplets found in the acid phase. It was observed that some bubbles shrank after rinsing with solvent, suggesting that the cells were filled with oil and the reaction
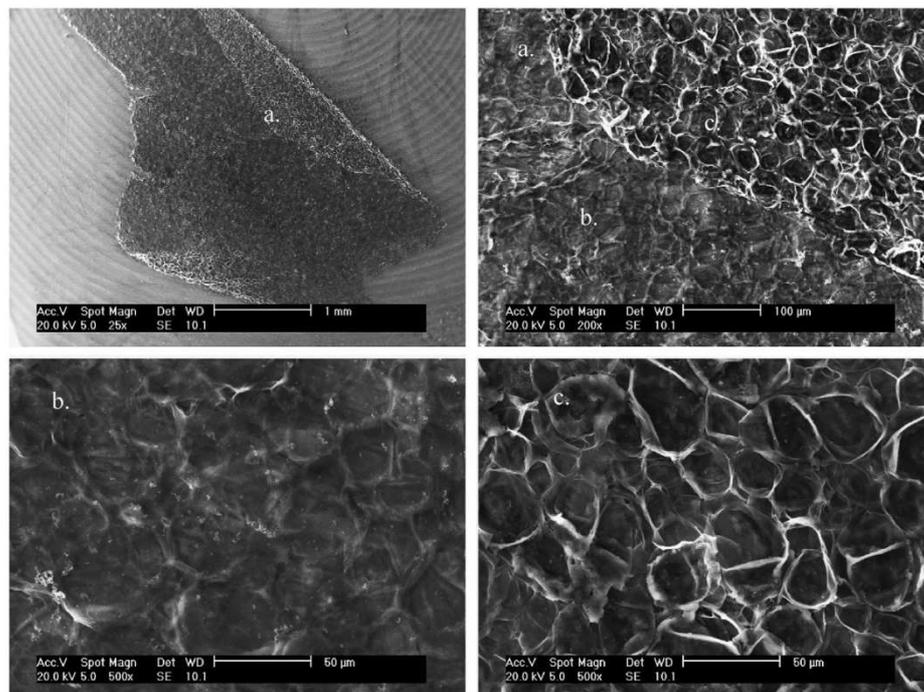
Fig. 5. SEM pictures of solid reaction product created between 80% w/w H_2SO_4 and $C_{30}H_{62}$ at 165 °C; (a) overview; (b) top side; (c) bottom side.

Oil phase with acid droplets 400x   Acid phase with oil droplets 400x
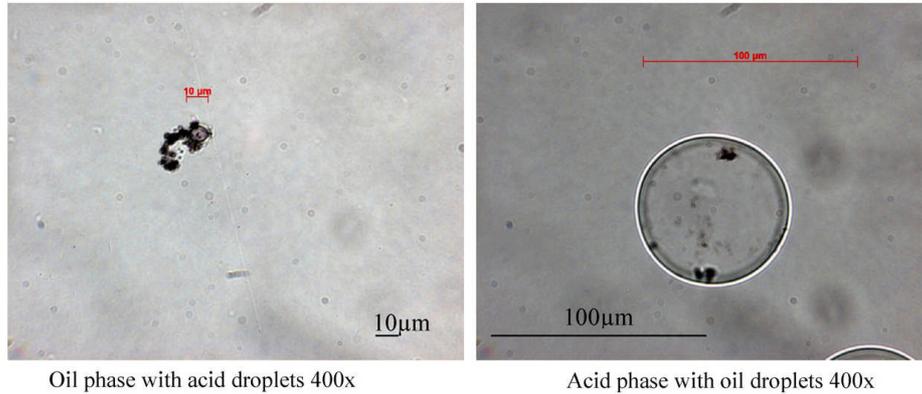
Fig. 6. Transmission microscopic image of the oil and acid phase of the mixture 80% w/w H_2SO_4 and $C_{30}H_{62}$ after exposure to 165 °C.
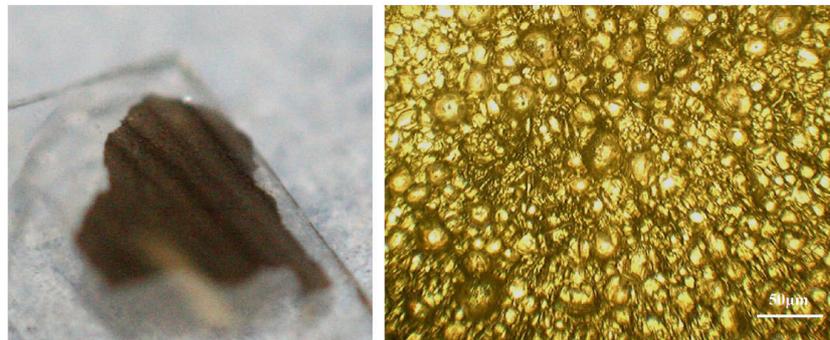
Fig. 7. Solid reaction product after separation, left an overview of the approximately 2 mm × 3 mm flake, right a 200 × microscopic image of the same flake.

leading to solidification is taking place at droplet interfaces, meaning on the head groups of surfactants to form micelles.

5. Conclusions

5.1. Thermal stability of the lubricant

The thermal stability of squalane was significantly reduced in the presence of sulphuric acid. Oxidation and sulphonation occurs, Sections 4.3 and 4.4, resulting in deposit, Sections 4.4 and 4.5.2, and surfactant, Section 4.1, formation which can lead in the engine to ring sticking and can reduce the neutralisation efficiency of lubricant additives [36].

The chemical reaction was time dependent, Section 4.1, but significantly faster than neutralisation in commercial lubricants [18] which means that the acid neutralising additives cannot prevent the lubricant to be degraded by the sulphuric acid.

The reactivity of API Group I base oils is expected to be higher due to the higher content of unsaturated and reactive hydrocarbons [1].

5.2. Emulsifying

The study has shown that squalane when brought into contact with sulphuric acid will form stable emulsions due to reduction in interfacial tension by forming surface active substances. This is not significant for the engine, as fully formulated lubricants contain dispersants which readily emulsify water droplets.

5.3. Corrosion

The contact angle measurements indicate that droplets adhering to the moving chrome coated piston ring will be more easily displaced and will be smaller than droplets on the stationary grey cast iron cylinder liner.

ARTICLE IN PRESS

Table A1
Best fit equations as shown in Fig. 4.

Acid conc. in % w/w	Closest fit of interfacial tension measurements in N/m, T in °C	Valid temperature range in °C
0	$= -1.2236E\text{-}5 \times T + 0.03864$	12–87
0.5	$= -8.43983E\text{-}10 \times T^4 + 1.92715E\text{-}07 \times T^3 - 1.64371E\text{-}5 \times T^2 + 6.87675E\text{-}4 \times T + 0.02285$	6–90
10	$= -2.86798E\text{-}11 \times T^5 + 8.95547E\text{-}09 \times T^4 - 1.06049E\text{-}06 \times T^3 + 5.86861E\text{-}5 \times T^2 - 1.3666E\text{-}3 \times T + 0.03332$	−3–100
25	$= 5.79812E\text{-}10 \times T^4 - 1.5079E\text{-}07 \times T^3 + 1.31115E\text{-}5 \times T^2 - 2.50671E\text{-}4 \times T + 0.01547$	−5–100
40	$= 3.50765E\text{-}10 \times T^4 - 9.849E\text{-}08 \times T^3 + 9.68993E\text{-}06 \times T^2 - 2.41447E\text{-}4 \times T + 0.0156$	−4–99
65	$= 5.78778E\text{-}07 \times T^2 + 3.98494E\text{-}5 \times T + 0.01738$	17–133
80	$= 1.46677E\text{-}08 \times T^3 - 3.10118E\text{-}06 \times T^2 + 3.01794E\text{-}4 \times T + 6.03057E\text{-}3$	−5–126
90	$= 2.34344E\text{-}10 \times T^4 - 6.43761E\text{-}08 \times T^3 + 5.51694E\text{-}06 \times T^2 - 1.41965E\text{-}4 \times T + 2.78768E\text{-}3$	2–122
98	$= 1.94661E\text{-}10 \times T^4 - 5.1293E\text{-}08 \times T^3 + 4.65421E\text{-}06 \times T^2 - 1.0321E\text{-}4 \times T + 1.58747E\text{-}3$	−3–117

Table B1

Contact angle of aqueous H_2SO_4 on engineering material submerged in squalane ($C_{30}H_{62}$) in degrees

H_2SO_4 conc. in % w/w	CKS (galvanic piston ring chrome coating)							RT84 (grey cast iron cylinder liner)							T in °C
	Advancing angle		Receding angle		Static angle		Corrosion	Advancing angle		Receding angle		Static angle		Corrosion	
	Rec. range	Aver.	Rec. range	Aver.	Rec. range	Aver.	+= Yes	Rec. range	Aver.	Rec. range	Aver.	Rec. range	Aver.	+= Yes	
0	100–140	130	50–90	104		88			138	15–35	33	80–120	121	+(slow)	20
		132		72		115			110		20		94	+(slow)	50
		117		47		25			98		29		88	+(slow)	100
0.5		127	90–110	88		106		30–60	56	10–25	14	25–45	29	+	20
		105		66		97			41		22		39	+	50
		115		59		96			47		16		31	+	100
10		128	10–40			116			56	5–20	17	20–55	47	+	20
		101		29		69			36				33	+	50
		116		20		59	+		36				21	+	100
25		134		91		119			51		15	25–35	32	+	20
		139		101		89			27		21		33	+	50
		103		34		78	+							+	100
40		110	35–65	41	80–100	88		30–70	67		15	30–50	39	+	20
		119		50		95			40					+	50
		122		57		85	+		33					+	100
65		116	10–25	19		46	+		102		19	25–45	43	+	20
		122		19		67	+		115					+	50
		61		18		37			49					+	100
		24				19	+						22	+	145
80		132	5–20			75		100–120	119			20–60	55	+	20
		119		12		50			107					+	50
				8		27							29	+	100
		110					+		109				25	+	165
90	60–100	127		8	20–60	43	+	50–90	68	5–20			29	+	20
		79		10		52			75		3		57	+	50
		44		12		27	+		71				27	+	100
		91				31	+		59				17	+	155
98	25–65	27		8	15–50	25		60–90	72		8		41	+	20
		22		13		24			79		2		56	+	50
		68		9		39			80		10		40	+	100
									62				0	+	165

Appendix A

See Table A1.

Appendix B. Results of contact angle measurements. "rec. range"=recommended range. "aver."=averaged results.

See Table B1.

References

[1] CIMAC Working Group "Marine Lubricants". No. 26 guidelines for diesel engines lubrication impact of low sulphur fuel on lubrication of marine engines. Frankfurt/Main: CIMAC; 2007.

[2] © State of New South Wales through the Department of Education and Training and Charles Sturt University. HSC online. Industrial chemistry: 3. Sulphuric acid. Online: ⟨http://hsc.csu.edu.au/chemistry/options/industrial/2762/Ch953.htm#b3⟩.

[3] Schlager D. Wartsila. EP 1 752 560 B1 Europe; 2006.

[4] CIMAC Working Group "Heavy Fuel". No. 21 recommendations regarding fuel quality for diesel engines. Frankfurt/Main: CIMAC; 2003.

[5] Huijbregts WMM, Leferink R. Latest advances in the understanding of acid dewpoint corrosion: corrosion and stress corrosion cracking in combustion gas condensates. Anti-Corrosion Methods and Materials 2004;51(3):173–88.

[6] Land T. The theory of acid deposition and its application to the dew-point meter. Journal of the Institute of Fuel 1977:68–75.

[7] Young TF, Maranville LF, Smith HM. Raman spectral investigations of ionic equilibria in solutions of strong electrolytes. In: Hamer WJ, editor. The structure of electrolytic solutions. New York: John Wiley and Sons; 1959. p. 35–63 [book auth.].

[8] Schleizer AD, Bonnecaze RT. Displacement of a two-dimensional immiscible droplet adhering to a wall in shear and pressure-driven flows. Journal of Fluid Mechanics 1999:29–54.

[9] Dussan VEB. On the ability of drops to stick to surfaces of solids. Part 3. The influences of the motion of the surrounding fluid on dislodging drops. Journal of Fluid Mechanics 1987:381–97.

[10] Micali F, et al. Paper no. 74 suction air humidity influence on piston running reliability in low-speed two stroke diesel engines. Bergen: CIMAC; 2010 [CIMAC Congress].

[11] Lu Ya, Chen Xiaoxu. The effects of a demulsifier on the interface of marine engine oil and water. Lubrication Science 2011.

[12] Benner JJ, et al. Lubricating Properties of Water in Oil Emulsions. Transactions of ASME, Journal of Tribology 2006;128(2):296–311.

[13] Demmerle R, et al. New insights into the piston running behaviour of sulzer large bore diesel engines. Frankfurt: CIMAC Central Secretariat c/o VDMA e.V.; 2001 [International Council on Combustion Engines. p. 1–14].

[14] Spahni, Marc, Brunner H, de Jong R. Paper no. 86 the new wartsila 820 mm-bore engine series advanced design and first running experience. Bergen: CIMAC; 2010 [International Council on Combustion Engines. p. 1–15].

[15] Cantow FG. Paper no. 209 piston rings for large bore engines. 2004 [International Council on Combustion Engines. p. 1–14].

[16] Burstein GT, Shreir LL, Jarman RA. 13.8 Chromium coatings. Corrosion, vol. 2. s.l.: Elsevier Butterworth Heinemann; 1994 [p. 99–110].

[17] Plucinski P, Nitsch W. Mechanism of mass transfer between aqueous phase and water-in-oil microemulsion. Langmuir 1994:371–6.

[18] Garner T, et al. Paper no. 129 development of marine diesel cylinder oils. Kyoto: CIMAC; 2004 [International Council on Combustion Engines. p. 1–14].

[19] Class NK. Guidance for measures to cope with degraded marine heavy fuels, version II. Ohnodai, Midori-ku, Chiba: ClassNK, Nippon Kaiji Kyokai; 2008.

[20] The Petroleum HPV Testing Group. Test plan lubricating oil basestocks category. API; 2003 [s.l.].

[21] Taylor, Peter. 1 Electrophilic addition reactions of alkenes. Alkenes and aromatics. Cambridge: Royal Society of Chemistry; 2002.

[22] Rudakov ES, Volkova LK, Tishchenko NA. Kinetics and mechanism of homogeneous reactions of alkanes in sulphuric acid in the presence of carbocations. I. Oxidation, isomerization, fragmentation. Kinetics and catalysis 1988:1168–73 [элмл, Russian translation].

[23] Rudakov ES, Zamashchinkov VV, Lutsyk AI. Kinetics of the reaction of saturated hydrocarbons with PdII, PTII–IV, HgII, CrVI, MnIII, MnIII–RuIII–IV, NO^{2+}, H_2SO_4, $H_2S_2O_8$, and carbonium ions in sulphuric acid. Teoretcheskaya i Eksperimental'naya Khimiya 1976(July–August):361–8 [Translation].

[24] Diaby M, et al. Kinetic study of the thermo-oxidative degradation of squalane ($C_{30}H_{62}$) modelling the base oil of engine lubricants. Journal of Engineering for Gas Turbines and Power 2009.

[25] Kosswig K. Sulphonic acids, aliphatic. Ullmann's encyclopedia of industrial chemistry. Weinheim: Wiley-VCH Verlag GmbH & Co. KGaA; 2000.

[26] Miyazaki M, et al. Evaluation of marine engine lubricating conditions using a cylinder liner surface oil sampling apparatus. London: CIMAC; 1993 [CIMAC 20th International Congress on Combustion Engines. p. 1–15].

[27] Shaw DJ. Introduction to colloid and surface chemistry. Oxford: Butterworth-Heinemann; 2003.

[28] Rode Sebastian. Oberflaechenspannung. Mainz: Johannes Gutenberg Universitaet Mainz; 2010.

[29] Stadler AF, et al. A snake-based approach to accurate determination of both contact points and contact angles. Colloids And Surfaces A: Physicochemical and Engineering Aspects 2006:92–103.

[30] Hadley A. CombineZ5.3; 17-February 2006.

[31] Demond Avery H, Lindner Angela S. Estimation of interfacial tension between organic liquids and water, vol. 27. Ann Arbor: American Chemical Society; 1993.

[32] Stecher GP, et al. The Merck index of chemicals and drugs. Rahway: Merck & Co., Inc.; 1960.

[33] Joos P, Vollhardt D, Vermeulen M. Interfacial tension of sodium dodecyl sulphate solutions at the hexane–water interface, vol. 6. Langmuir, American Chemical Society; 1990 [s.l.].

[34] Mitsui T, et al. Changes in the interfacial tension with temperature and their effects on the particle size and stability of emulsions. Kolloid-Zeitschrift und Zeitschrift fuer Polymere 1971:227–30.

[35] DECHEMA e.V. DETHERM thermophysical properties of pure substances & mixtures. ⟨https://cdsdt.dl.ac.uk/detherm/detherm.php⟩; 2005–2008 [Online, Cited: 27-May 2010].

[36] Wu RC, Papadopoulos KD, Campbell CB. Acid-neutralising of marine cylinder lubricants: measurements and effects of dispersants. AIChE Journal 2000:1471–7.

[37] Lancon D, Doyen V. Paper no. 98 the universal concept: the lubrication solution to 2020 and beyond. Bergen: CIMAC; 2010 [International Council on Combustion Engines. p. 1–11].

[38] Saito Y, Yamada T, Moriyama K. Paper no. 243 the piston-running behaviour monitoring of large bore low-speed marine diesel engine at sea by measurement of piston ring oil film thickness and iron content in cylinder drain oil. Bergen: CIMAC; 2010 [International Council on Combustion Engines. p. 1–14].

Impact of Sulphuric Acid on Cylinder Lubrication: Friction and Surface Modification

Falko A. Sautermeister, mnfasa@leeds.ac.uk; Martin Priest; Malcolm Fox

iETSI, School of Mechanical Engineering, University of Leeds, Leeds LS2 9JT, UK

Abstract The influence of temperature and sulphuric acid, H_2SO_4, on friction and chemistry of a lubricated contact was investigated. The H_2SO_4 was dispersed in marine Diesel engine lubricant API Group I base oil SN600 and compared with pure SN600 and fully formulated lubricants. The contact was a reciprocating chrome plated piston ring on a grey cast iron cylinder liner with an initial Hertzian contact pressure of 0.35 GPa.

Results for the basic interaction between the acid and the lubricant base oil and towards the metal surfaces were published previously (Sautermeister, et al., 2012) (Sautermeister, et al., 2012).

For reference, the contact was initially lubricated with pure SN600 at various temperatures and contact pressures. Measurable lubricant oxidation was found to start at 250 °C followed by deposit formation and nitration at 300 °C. The lubrication regime was found to be elastohydrodynamic towards mixed lubrication in the Stribeck diagram. Friction increased linearly between 80 – 170 °C from μ = 0.07 - 0.1 for a liner surface roughness of Ra = 130 nm. At 80 °C, hydrocarbon- and iron-sulphates and at 170 °C hydrocarbon-oxides and -sulphoxides were accumulated in deep honing marks. Some nitrogen adsorbed on the surface at 170 °C. Lower running-in temperatures were found to be beneficial for later piston ring appearance.

When 70 %w/w H_2SO_4 was dispersed in SN600, the friction was significantly reduced for temperatures up to 140 °C, the breakeven point with pure SN600. At 120 °C excessive formation of deposit occurred and friction rose significantly. At 80 °C, piston ring wear was higher than at 170 °C, while liner wear was higher at the higher temperature. At 80 °C, the cylinder liner surface mainly consists of iron sulphate and some adsorbed nitrogen, while at 170 °C amino- and iron-sulphates were formed. The piston ring surface showed corrosive pit holes, which can be explained by shear induced droplet detachment theory.

Fully formulated lubricants show with μ~0.16 comparably high friction, attributed to the formation of a calcite boundary film. The boundary film acted protective when H_2SO_4 was added. The wear was found to be very low, but the surface appearance of the piston rings was found to be comparable with the harsh conditions when lubricated with plain base oil and only improved when H_2SO_4 was added.

The adding of H_2SO_4 of any concentration was never found to initiate scuffing.

Keywords: Mineral Base Stocks, Marine Diesel Engine, Lubricant Degradation, Piston Rings, Friction Mechanisms, Surface Modification

Introduction

1.1. Fuel

A key factor for a commercial competitive marine Diesel engine design is the ability to function on the cheapest available fuel. The current standard fuel for this engines is colloquial called 'Heavy Fuel Oil', HFO, residual fuel with high sulphur content. The high sulphur fuel content traces back to the sulphur crude oil content, ranging from 0.01 - 5.54 %w/w within geological small areas. Venezuela's sulphur crude oil content for example ranges between 0.09 – 5.54 %w/w (Carrales, et al., 1975). Biological organisms, the source of crude oil, contain sulphur in their cells. Dry tobacco leaves, for example, contain 0.5 – 0.8 %w/w sulphur (Wirtz, et al., 2007), not sufficient to explain the high sulphur crude oil content, which is more readily explained by the dissolution of minerals like anhydrite gypsum following the reaction:

$$CH_4 + CaSO_4 \rightarrow CaCO_3 + H_2S(aq. \, or \, gas) + H_2O \qquad (1)$$
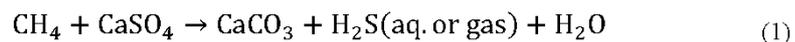
Anhydrite gypsum forms on top of salt domes regularly found locally within the area of oil reservoirs (Saunders, et al., 1996) originating from prehistoric fertile shallow sea water areas under cycles of evaporation and flooding, consequently buried in the earth crust by tectonic action. The salt is lighter than the surrounding rock and rises, creating cracks, allowing the oil to rise from deeper zones to depths accessible by mining equipment.

The International Maritime Organisation, IMO, reduced maximum sulphur fuel content for ocean going ships from 4.5 to 3.5 %w/w in 2012 and in Sulphur Emission Controlled Areas, SECA, from 1.5 to 1 %w/w in 2010. The intention was to reduce SO_x exhaust gas emissions for environmental reasons. Both IMO legislations, however, foresee the use of exhaust gas after treatment plants to reduce SO_x emissions instead of reduced fuel sulphur content. Apart from the legislation, the available average sulphur fuel content in 2005 was 2.8 %w/w (CIMAC Working Group "Marine Lubricants", 2007). SO_x after treatment plants are economically only feasible for either large ships or ships primarily operating in SEC areas with supply of cheap high sulphur fuels. While the demand for low sulphur fuels will rise, the sulphur fuel content for vessels with after treatment plants might actually rise.

2

The minimum sulphur fuel content for test bed engines or ships entering strictly legislated territorial waters is 0.005 %w/w (BAFU & UVEK, 2011). Irrespective of the general trend for fuel sulphur reduction, the engines have to function for both highest and lowest sulphur fuel content.

1.2. Acid Concentration and Neutralization on the Piston Running Parts

The formation and condensation of H_2SO_4 in the engine and its dissociation in water was explained in previous publications (Sautermeister, et al., 2012), (Sautermeister, et al., 2012). This study covers the range of concentrations from 0 – 98 %w/w H_2SO_4. Based on exhaust gas composition (CIMAC Working Group "Exhaust Emission Control", 2008), realistic condensate concentrations, however, range between ~5 – 80 %w/w, also confirmed in literature (Graham, et al., 1960). The neutralisation of the H_2SO_4 formed by combustion, is taken care of by an alkaline reserve in the lubricants with Total Base Number, TBN, levels of 40 – 70 mg KOH/g. The alkaline reserve is usually added into the lubricant by dispersing group-II metal (Ca or Mg) carbonate particles and 5 – 15 % hydroxylic base (Wu, et al., 2000) as reversed micelles. Neutralization follows the reaction (Adams, et al., 2007):

$$H_2SO_4 + CaCO_{3(s)} + H_2O \rightarrow CaSO_4 \cdot 2H_2O_{(s)} + CO_{2(g)} \uparrow \qquad (2)$$
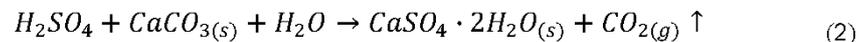
In practise, higher TBN or a increased feed rate reduce the wear of piston ring and cylinder liner (van Helden, et al., 1989) up to a point were problems with deposit built up from unused additive or bore polishing occur (Jakobsen, 2010).

For a remaining lubricant film thickness in top dead centre of 0.01 μm and TBN70, the depletion time of the alkaline reserve was calculated to be 0.08 – 0.4 s for a sulphur fuel of 5 – 2 %w/w (van Helden, et al., 1989).

The surfactant stabilising the core of the reversed micelles is a metal salt of a surfactant acid (Fu, et al., 2006) namely sulphonates, phenates, carboxylates or salycilates (Hone, et al., 2000). A surplus of these detergents is used to disperse acid droplets and solid soot or wear particles (Wu, et al., 2000) and as anti-oxidants. Adding of phenates to sulphonates containing lubricant significantly reduced hard deposit built up on piston crowns, attributed to the anti-oxidant properties of the phenates (Friesen, et al., 2001).

Dispersed $CaCO_3$ under friction can also be deposited on the surfaces to form a calcite boundary layer (Giasson, et al., 1994). In an engine such a highly

3

protective boundary layer can lead to uneven wear, so called 'clover leafing' in case the lubricant is not homogeneously distributed.

1.3. Piston Ring Lubrication

Large 2-stroke marine Diesel engines feature a forced and one through piston ring lubrication independent from the crank case lubricant. The cylinder lubricant has to withstand higher temperatures, dirt and condensate input as well as higher mechanical stress.

Many researchers and engineers theoretically worked out minimum oil film thickness between piston ring and cylinder liner by the equation derived by Prof. Osborne Reynolds in 1885 (Reynolds, 1886). The integration terms for radial velocity of the lubricant by radial pressure gradient and entraining action (Priest, 2010) is usually neglected to safe numerical calculation recourses, arguing the neglect able influence. The argument is practical, shown by the difficulty of circumferential oil distribution by the movement of the piston rings alone. Design measures to improve oil distribution incorporate increased oil misting or radial high pressure injection of the lubricant.

1.4. Corrosive Attack

The engine components can experience corrosive wear by the formation of H_2SO_4. Corrosion, however, only takes place when condensate droplets adhere to the wall against the shear of the surrounding liquid with viscosity, η, and velocity, U. Adherence of a droplet to a wall under shear is quantified by the capillary number , $Ca=\eta*U/\sigma$. Exceeding a critical value of Ca causes the droplets to deform until they split or completely detach from the wall (Schleizer, et al., 1999). The critical capillary number decreases with increasing contact angle (Kang, et al., 2005). For higher interfacial tension, σ, droplets detach more complete. Viscous droplets are more easily detached (Ding, et al., 2010), a time effect on the droplet shape, equalising for long times (Schleizer, et al., 1999) and reduced for higher capillary numbers (Kang, et al., 2005).

When shear forces exceed the adhesion forces, the droplets start creeping on the wall. The critical shear rate, γ_{crit}, for droplet movement can be approximated (Mahe, et al., 1988):

$$\gamma_{crit} \sim \frac{\sigma \cdot a_P \cdot (\cos\theta_R - \cos\theta_A)}{\eta \cdot a^2} \tag{3}$$

A free floating droplet with diameter 'a' is wetting an area with the width 'a_p'

For dilute emulsions of Newtonian fluids containing spherical droplets, the viscosity of the emulsion, η_{em}, can be predicted by the extended Einstein equation according to Taylor (Taylor, 1932):

$$\eta_{em} = \eta_c \cdot \left[1 + 2.5\phi \left(\frac{\eta_d + \frac{2}{5}\eta_c}{\eta_d + \eta_c}\right)\right] \tag{4}$$

The volume fraction Φ is the ratio of the dispersed phase with viscosity η_d in the continuous phase with viscosity η_c. Taylor assumed deformable droplets to break up until they stay spherical. From the relations above, it can be seen that the continuous phase governs the viscosity of a dilute emulsion.

Advancing, receding and static contact angles $\theta_{A/R/St}$, interfacial tension σ and dynamic viscosity η were published previously (Sautermeister, et al., 2012) (Sautermeister, et al., 2012).

The cylinder liner material is a non-homogeneous and coarse sand-cast grey cast iron. There are various kinds of surface machining methods specified, one is plateau honing, similar to automotive applications. Depending on acid concentration the corrosion can be very selective. Concentrated H_2SO_4 dissolves the hard iron phosphides leading to increased abrasive wear by foreign particles. Corrosion of the perlitic matrix by dilute H_2SO_4 results in protruding hard phases, likely to brake and fall out (Demmerle, et al., 2001), causing deep gouges with protruding edges on piston ring and liner, which can lead to further damage.

The piston rings are made of grey cast iron with a great variety of surface and material configurations. One type is coated with a particle reinforced electro plated pre-profiled chrome coating (Cantow, 2004) also similar to automotive applications. In the electro chrome plating process for the piston rings, hot dilute H_2SO_4 is used to etch porosities to give improved oil retention of the surface (Burstein, et al., 1994).

1.5. Deposit Formation

Other than corrosion, marine Diesel engine cylinder systems also suffer from deposit formation (ClassNK, 2008). Oxidation in marine lubricants is seen as a plain thermal effect. Test methods introduce heating of the oil for extended time to temperatures well above 300 °C and evaluation of deposit formation and

viscosity increase (Garner, et al., 2004), (Lancon, et al., 2010), (Friesen, et al., 2001). For comparative engine tests, however, deposit formation was significantly reduced for low sulphur fuels (Lancon, et al., 2010), (Miyazaki, et al., 1993). The critical acid concentration and temperatures for oil degradation together with the nature of reaction products was shown in previous publications where also pathways for the degradation are shown (Sautermeister, et al., 2012) (Sautermeister, et al., 2012). The thermal formation of deposit and catalysed by H_2SO_4 in a piston ring - cylinder liner friction contact is presented in the following.

1.6. Friction Measurements

Montgomery studied the running-in of grey cast iron against steel in white mineral oil at 82 °C at an average speed of 0.04 m/s and an initial surface load of 0.17 GPa. He found the friction coefficient to decrease from initial 0.21 to a final 0.12. On top of the wear track he found a hard ~25 µm thick glazing layer consisting of Fe_3O_4 and carbon assumed to be graphitic (Montgomery, 1969).

For dry sliding of grey cast iron as pin on a rotating disc, a friction coefficient of µ = 0.275 at 3 m/s and loads between 0.001 - 0.0031 GPa was found (Sjogren, et al., 2004).

The wear mechanism of grey cast iron in emulsions of aqueous H_2SO_4 in base oil was studied incorporating a reciprocating pin on disc machine, without giving information on friction. The average reciprocating speed was kept at 0.09 m/s and the maximum initial Hertzian contact pressure at ~0.7 GPa. A 17 %m/m H_2SO_4 was mixed into oil by a quantum of 10 %v/v and tested at temperatures of 20, 40 and 60 °C. At 60 °C, degradation of the oil, increasing for higher acid concentrations, and dark material deposited on the wear scar was found and the temperature therefore kept at 20 °C. In general a higher wear rate at higher temperatures and the formation of $FeSO_4\cdot4H_2O$ on the wear scar was found (Macdonald, et al., 1987). For concentrations of 31.5 – 55 %m/m H_2SO_4, lower wear rates than for pure water in oil were found. Highest wear rates were found with 17 %m/m H_2SO_4 dispersed in quantities of 5 – 10 %v/v in oil (Stott, et al., 1988). The overall conclusion for the series of trials is corrosion induced abrasive wear to be the wear mechanism in the given environment (Stott, et al., 1990).

Draft-version for submission to Tribology Letters

Sliding a pure aluminium pin on pure iron in various concentrations of H_2SO_4 at a nominal contact pressure of 0.025 GPa and a mean sliding speed of 0.05 m/s at room temperature for 60 minutes resulted in the friction coefficient and plate roughness given in Table 1. The higher the acid concentration, the lower the friction coefficient but no correlation to surface roughness nor acid viscosity was found. The non-conclusive surface analysis by Auger electron spectroscopy revealed oxygen content on the iron plate and, for concentrated H_2SO_4, sulphur on the transition between oxygen layer and iron bulk material. No wear on the aluminium pin was found (Mischler, et al., 1993) probably by a inert aluminium oxide layer.

Table 1: Friction coefficient μ of Al-pin on Fe-plate at various concentrations of H_2SO_4 (Mischler, et al., 1993)

%w/w	0	18	45	56	66	82	96
μ	0.21	0.175	0.175	0.18	0.125	0.125	0.105
Ra[μm]	0.06	0.13	0.44	0.25	0.06	0.03	0.04

A TE77 reciprocating pin on plate test was lubricated with fully formulated lubricants mixed with concentrated H_2SO_4. The pin was loaded to a resulting surface pressure of 0.025 GPa at 250°C for 5.5 hours. The lubricant had a alkaline reserve of 50 mgKOH/g and was premixed with 3.5 %w/w concentrated H_2SO_4 resulting in a theoretical reduction to 10.3 mgKOH/g. The coefficient of friction, COF, was found at a constant 0.08 but the wear increased for the acid premixed oil and the contact potential, CP, measurement showed almost perfect separation for the fully formulated oil and metallic contact for the premixed oil (Davis, et al., 1993).

One candidate for ZDTP replacement in automotive applications (Kubo, et al., 2006) is over based calcium sulphonates, used for a long time in marine Diesel engines mainly to neutralize H_2SO_4 (Vipper, et al., 1998). Common for all studies is the formation of boundary films on the surfaces. The thickness of these films range from 10 nm (Topolovec-Miklozic, et al., 2008) to 2 μm (Vipper, et al., 1998) but mainly in the range of 100 ±50 nm depending on the lubrication conditions. The boundary layers were reported to be CaO and $CaCO_3$ (Caixiang, et al., 2008) or calcite, the crystalline compact form of $CaCO_3$, with adsorbed $CaCO_3$ on top (Giasson, et al., 1994), (Topolovec-Miklozic, et al., 2008). Under friction a film thickness of 80 nm was reached after only 5 minutes (Topolovec-

Miklozic, et al., 2008). The formation of a boundary film only occurred under friction or when submerged at 150 °C but not at room temperature and the compacting of the $CaCO_3$ was shown to be independent from pure pressure (Giasson, et al., 1993). It is proposed that the calcium sulphonate surfactants have to be stripped mechanically or decomposed at high local temperatures from the $CaCO_3$ core to enable deposition on the surfaces (Zhang, et al., 2009). The displacement of the surfactants from the core is favoured when water penetrates the micelle (Giasson, et al., 1993) but water also delays the calcite formation (Giasson, et al., 1994) and distilled water dissolves the formed boundary layer (Topolovec-Miklozic, et al., 2008). For adsorbed films calcium sulphonate chains were found to stand perpendicular to the metallic surface (Giasson, et al., 1994). For a $CaCO_3$ content of TBN 2.2 - 11.2 the friction coefficient was found to be lower, $\mu = 0.087 - 0.113$, than with pure oil, $\mu = 0.12$ on a four-ball tester. The minimum was reached with TBN7, unfortunately without reporting on test speed and temperature (Caixiang, et al., 2008).

The influence of speed on the friction coefficient was shown in the range of 0.004 – 2 m/s at 100 °C and 0.95 GPa initial Hertzian contact pressure. For low speeds, the friction coefficient varied the most within $\mu = 0.06 - 0.12$ for different additives. The biggest influence of the boundary film thickness was found at 0.1 m/s were a increased COF was measured for all additives. The values range between $\mu = 0.08 - 0.1$ after 2 hours compared to initial $\mu = 0.05$. At the highest speed of 2 m/s all lubricants show the same friction of $\mu = 0.04$. The differences are concluded to originate from hydrodynamic influence of varying topography pattern by the additives (Topolovec-Miklozic, et al., 2008). Differences in frictional behaviour, film formation and temperature respond was also observed by Vipper and was attributed to differences in the micellar structure (Vipper, et al., 1998) which is given by the property of the detergent.

2. Materials and Methods

2.1. Materials and Preparation

A piston ring – cylinder liner contact was chosen for the study to force dispersed acid droplets into the contact zone. The piston rings were 25 mm long near gap

segments of chrome coated automotive piston rings for a 86 mm cylinder liner

bore diameter (FM Goetze) with a radius of 43.34 mm.

The cylinder liner were segments of a Ø 90 mm SJ4213 Jaguar/Daimler

automotive cylinder liner (AE, FM Goetze) with a radius of 45.47 mm.

Automotive parts were used for their ease of acquisition and the readily available

holders for the bench test machine. One could argue that the study is not relevant

for materials used in marine Diesel engines. The surface machining and finishing,

however, is very similar to marine Diesel engines and all potential tribological

anomalies of the grey cast iron, like free ferrite and large eutectic carbides, were

removed from the study. This puts greater emphasis on the properties of the

lubricant.

Before each test, the piston ring and cylinder liner were aligned using proper

symmetrical removal of black ink pen paint (Staedtler Lumocolor 317 permanent

M) by the piston ring as an indicator. Residual colour was removed from piston

ring and cylinder liner by isopropanol.

For the lubrication of the piston ring – cylinder contact, the following substances

were used: API Group I base oil SN600 (Chevron) and H_2SO_4 (>95 % Fisher

Scientific UK Ltd. analytical reagent grade). Lower concentrations of H_2SO_4 were

made with deionised water by weighing. Two fully formulated marine lubricants,

A & B, with a alkaline reserve of 70 mgKOH/g were used (Shell and Chevron).

For tests with H_2SO_4, 1.3 %v/v of the acid, a typical quantity found in the engine

(Micali, et al., 2010), was dispersed in SN600 in a ultra sonic bath. The physical

properties of the liquids are given in Table 2.

Table 2: Physical properties of the liquids used

Name	Viscosity in Pa*s at 40 and 100 °C		Density in kg/m^3
SN600	0.1	0.0103	886 (15 °C)
Lubricant A + B	0.11	0.011	930 (15 °C)
70 %w/w H_2SO_4	0.0015	-	1606 (25 °C)

2.2. The Reciprocating Friction Testing Machine

A TE77 Reciprocating Friction Testing Machine (Phoenix Tribology Ltd.) was

used for the tests. A normal force of 160 N, a typical value within the range of

previous research, was applied to the reciprocating piston ring holder by a spring

loaded balance. The normal force was transmitted through two pins to the back of

Draft-version for submission to Tribology Letters

the piston ring segment. The cylinder liner sample was fitted on a temperature controlled holder. The piston ring specimen had a smaller circumferential radius than the cylinder liner to avoid edge loading. The deformation of the piston ring was established by methods found in (Lackmann, 2001) and the resulting Hertzian contact pressure was calculated according (Priest, 2009) and is shown for one half of the contact in Figure 1. The piston ring lifts in the middle of the contact to create two peaks of Hertzian contact. Taking also surface traction into account, the initial Hertzian contact pressure rises to 0.35 GPa. Following the Tresca maximum shear stress criterion, the material undergoes plastic deformation. Non-uniform wear of the engine cylinder by non-homogeneous lubricant distribution can also lead to uneven loaded piston rings.
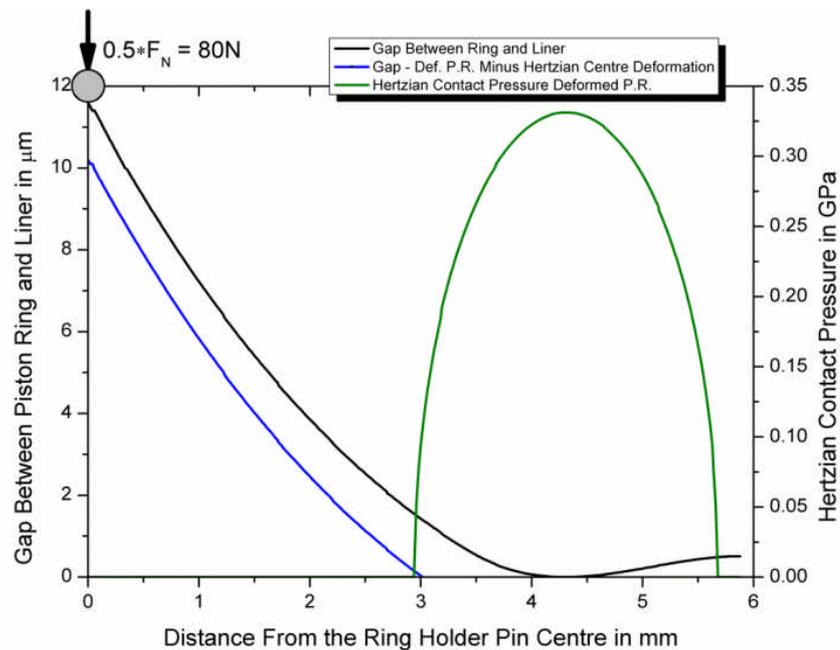
Figure 1: Influence of piston ring deformation on the Hertzian contact pressure and conformity of the parts in unworn condition on the TE77 test bed.

Wear causes an increase in the ring profile radius and greater conformity of the parts, considerably reducing Hertzian contact pressure. The influence of geometry, hydrodynamics and Hertzian contact pressure on friction was found and consequently excluded by shuttle-tests were test conditions were switched in intervals back to the reference conditions.

The lubricant was supplied to the front (TDC) or back (BDC) of the piston ring from two syringe pumps (Aladdin, World Precision Instruments, Inc.) through

10

flexible PTFE tubes at a combined feed rate of 0.5 ml/h, which is very close to running-in feed rates of ~2 g/kwh in marine Diesel engines, comparing the lubricated area. Top dead centre, TDC, and bottom dead centre, BDC, corresponds to the orientation of the piston ring side faces in the engine.

The temperature of piston ring and cylinder liner sample was measured through K-type thermocouples, spot welded to the running surface of the cylinder liner and the flank of the piston ring. In a oven, correlation with traditionally welded K-type thermocouples was found to be within 1 °C up to 230 °C.

The resistance of the contact zone between the otherwise electrical insulated cylinder liner and piston ring was measured by a Lunn-Furey CP Circuit (Braunovic, et al., 2007), (Plint, 2005). Reduced metallic contact increases the measured CP difference with a maximum of 45 mV. A thick oil film, deposits, boundary surface films or oxide layers act as electric isolators.

The friction force F_R is measured by a piezo force transducer calibrated by known mass. For increased temperatures a slight unspecified deviation from linearity was found. Mechanical noise was transmitted through the piston ring holder and the force signal showed peaks at 30 and 60 °CA, identified as back-lash from the Scotch-Yoke mechanism (Elson, et al., 1974). The natural frequency of the measurement arrangement was found to be 1250 Hz, appearing as overlaying wave pattern.

The stroke length, x, was set to 15 mm and the frequency to f = 14 Hz.

The relative air humidity was recorded and found to be fairly stable throughout the study, thus not influencing the measured differences.

The samples were run-in for 2.5 hours on SN600 with a normal force of 160 N, sufficient to stabilise the friction, applied at a cylinder liner temperature of 80 or 170 °C respectively. The temperatures are typical for a cylinder liner with the upper test temperature also governed by the dew point temperature of the dispersed aqueous phase at ambient pressure.

2.3. Method: Lubricant Chemistry by FTIR-ATR

Excess lubricant, thrown off in the turning points of the piston ring, was sampled with a syringe needle for analysis by Fourier Transformation Infra Red Spectroscopy with Attenuated Total Reflectance accessory, FTIR-ATR. The samples were kept separated to distinguish between oil feeding and trailing side of

the piston ring. Most of the oil was thrown off at the BDC side of the piston ring. The idea was to reveal the passing of dispersed droplets through the lubrication gap.

2.4. Method: Surface Analysis

A white light vertical scanning interferometer (Veeco – WYKO NT3300S) was used to analyse the samples for their roughness and profile.

The sum of roughness peak Rp, the highest peak distance from the mean line per cut off length, equals the minimum oil film thickness, h_{min}, required to hydrodynamically separate two surfaces in contact, thus important for the interpretation of CP measurements. The roughness average, Ra, is the arithmetic average deviation from a surface centreline. Ra is a traditional value often found in tribology literature, for example in the specific film thickness λ which is h_{min} over the sum of Ra and sometimes used as the abscissa for the Stribeck diagram.

The liner samples were analysed using a FTIR-Microscope (PerkinElmer Spotlight 400) in reflectance mode. Calibration and background scan was taken by a gold mirror. Peak positions were identified by comparison tables found in educational literature (University of Leeds, 2011).

Chemical compounds in the boundary layer of the cylinder liner wear scar were also identified by X-ray photoelectron spectroscopy, XPS. The samples were cut out from the cylinder liner near the turning points by hand to avoid high temperature impact and contamination. The samples were cleaned by rinsing with heptanes for five seconds. The cleaning procedure was proven by FTIR-Microscope and XPS on a reference sample to remove all liquid oil from a rough, honed surface. The results were evaluated by a online XPS-database (Benoit, et al.).

Piston ring samples were examined by a Leica DM6000M light microscope.

3. Results and Discussion

3.1. Result and Discussion: Reference Tests with SN600

Figure 2 shows the resulting average COF before and after running-in and the corresponding average CP after running-in. In the beginning of the running in phase the CP shows 0 mV, indicating high metallic contact. After running-in,

there is almost no metallic contact between the parts. Interesting to note is that the decrease in CP at higher temperature is due to a dip in midstroke, not in the turning points. During running-in the separation starts in midstroke, indicating the influence of oil viscosity on part separation and a reduction in surface roughness. The CP measurement, after running-in, is very close for both temperatures. The influence of lower viscosity is also shown by the slightly increased COF, $\Delta\mu = 0.014$, and lower surface roughness at higher temperatures after running-in. The film thickness is reduced by the lower viscosity which increases the surface contact resulting in lower roughness values. In the beginning of running-in, at the same surface roughness and high metallic contact, the influence of temperature dependent material properties can be found by subtracting the before described influence of viscosity ($\Delta\mu = 0.014$) from the resulting total difference, to find $\Delta\mu_{T-Mat} = 0.069 - 0.014 = 0.055$. The Young's modulus reduces with increased temperature, resulting in a larger piston ring deformation, Figure 1, and Hertzian contact area, thus bringing more asperities in contact.
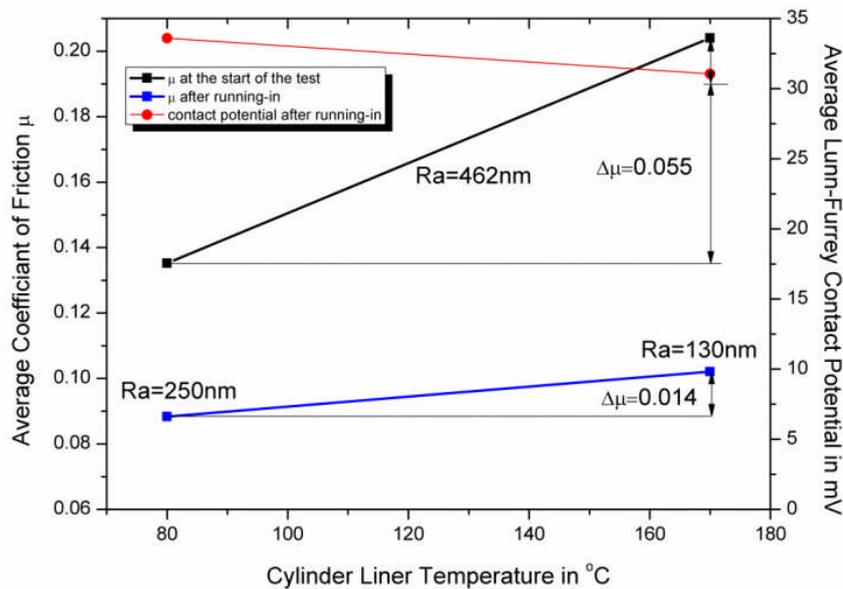
Figure 2: COF before (upper square markers) and after (lower square markers) running-in with SN600 and the corresponding CP measurement after running-in (round markers)

A sharp drop in temperature, due to a malfunctioning temperature control unit, caused an increase of viscosity at a stable surface roughness. Figure 3 shows the

influence of increasing viscosity on the COF. The drop from 80 to 40 °C occurred just on the end of a running-in phase and the starting COF ($\mu_{80\,°C} = 0.097$) is higher than the value shown in Figure 2 ($\mu_{80\,°C} = 0.088$). The drop from 170 to 80 °C ends at a lower value (0.072) than the other starting value, which can be explained by the influence of surface topography, which is $\Delta\mu_{Ra} = 0.025$. If both surfaces would be fully run-in, the difference would be $\Delta\mu_{Ra\_theoretic} = 0.088 - 0.072 = 0.016$. The drop in COF with increasing viscosity, indicates the lubrication regime to be elasto-hydrodynamic towards the mixed lubrication regime, despite the good separation of the parts found by the CP measurement. The viscosity was established using an average temperature formed from piston ring and liner temperature. The temperature dependent viscosity was measured using a Malvern "Kinexus" Rheometer with cone on plate arrangement at a shear rate of 1000 s^{-1}. The Lunn-Furey CP indicates a slight touching of roughness peaks. The sum of the measured peak heights from the mean, Rp, for piston ring and liner surface is 1.3 µm for 80 °C and 1.1 µm for 170 °C. In the area of the mixed to elastohydrodynamic lubrication regime, this is a reasonable value for oil film thickness (Priest, 2010). The average speed of the test bed is 0.43 m/s, resulting in a shear rate of 3.3 - 3.9*10^5 s^{-1}. Squalane, a typical model lubricant, was predicted to exhibit shear thinning behaviour when exceeding a shear rate of ~11*10^{10} s^{-1} (Jabbarzadeh, et al., 2002) while showing a linear increase of viscosity at low shear rate by ~5 Pa*s at 65 °C when pressures increased from ambient to 1.25 GPa (Jansen, et al., 2001). A simulation using the software package Mahle – Summits (V3.2010) & VTL (V3.8) (Tomanik, 2004),(Tomanik, 2008) with SAE40 oil at 80 and 170 °C predicts maximum hydrodynamic pressures of 61 and 33 MPa resulting in maximum viscosity pressure corrections of 123 and 24 %. The viscosity corrections for shear thinning are within ±2 % for resulting maximum shear rates of 7.2*10^6 and 19.3*10^6 s^{-1}. The significant influence of hydrodynamic pressure on the viscosity must be noted but was not incorporated as the non homogeneous lubrication gap, as shown above, can not be reflected by the two dimensional simulation. The information gained from the drop in temperature can later be used to distinguish between influence of viscosity and surface active substances when more viscous fully formulated lubricants are used. The reduction of friction due to the increased Young's module at lower temperatures is not taken into account for this assumption as the contact potential

14

indicates very little surface contact, which on the other hand could also result from isolating oxide layers.
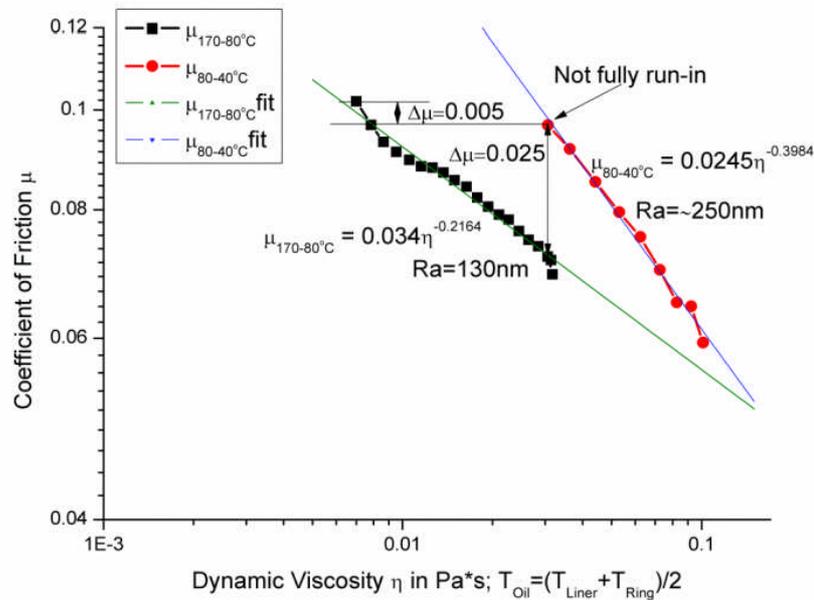
Figure 3: Influence of viscosity on the COF, measured by dropping the temperature on a run-in surface.

Figure 4 shows the average COF plotted over the bearing number for varying loads. The bearing number combines viscosity η with mean slider speed v and load F_N applied over the wetted piston ring circumference l_b. Compared with the Stribeck diagram the lubrication regime for the reference test at an applied load of 160N is elasto-hydrodynamic towards the mixed lubrication regime. For both temperatures, the COF decreases with decreasing load which increases the film thickness and decreases the surface contact area. For 80 °C a minimum is found at 60 N and the COF increases due to hydrodynamic friction for lower loads. The tests were both commenced from 160 N towards lower loads, keeping the surface topography stable. Therefore a difference between the curves of $\Delta\mu_{Ra160N} = 0.017$ can be seen in good agreement with the findings above on the influence of surface roughness on friction. At 170 °C a point at 200 N was added and recorded after the COF was stabilised.
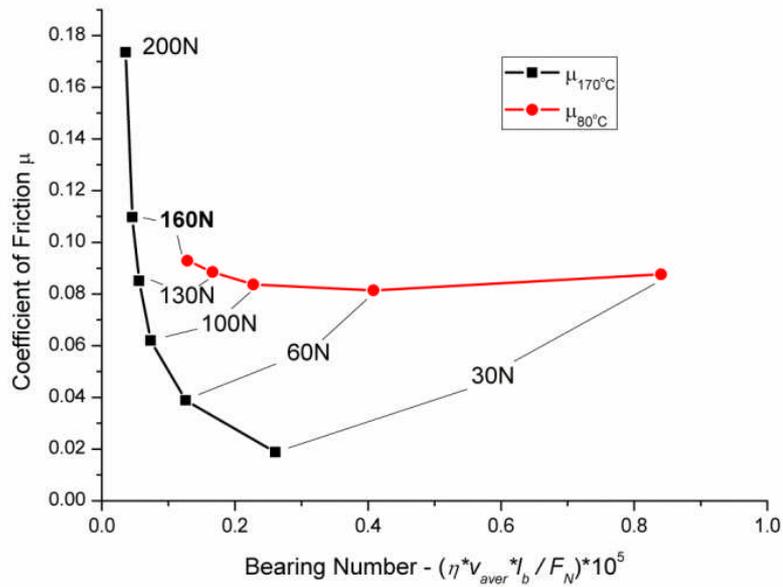
Figure 4: Partial Stribeck diagram for piston ring cylinder liner contact lubricated with SN600 at 80 and 170 °C.

3.2. Result and Discussion: Tests with SN600 + H_2SO_4

For the impact on lubricant chemistry and to find most interesting acid concentrations, a screening test was undertaken over the whole range of concentrations. Figure 5 shows the effect of acid concentration on the COF, mainly at 80 °C. It is pointless to perform tests with low acid concentrations at increased temperatures and ambient pressure, as the aqueous phase would boil, increase the acid concentration but loose volume. Previous tests showed an impact on the oil starting at 40 %w/w H_2SO_4 (Sautermeister, et al., 2012). The main tests were performed with 70 %w/w H_2SO_4, which is a condensate concentration that can be expected in the engine, and to be sure. The screening tests, however, showed a clear impact on the COF at 40 %w/w.

16
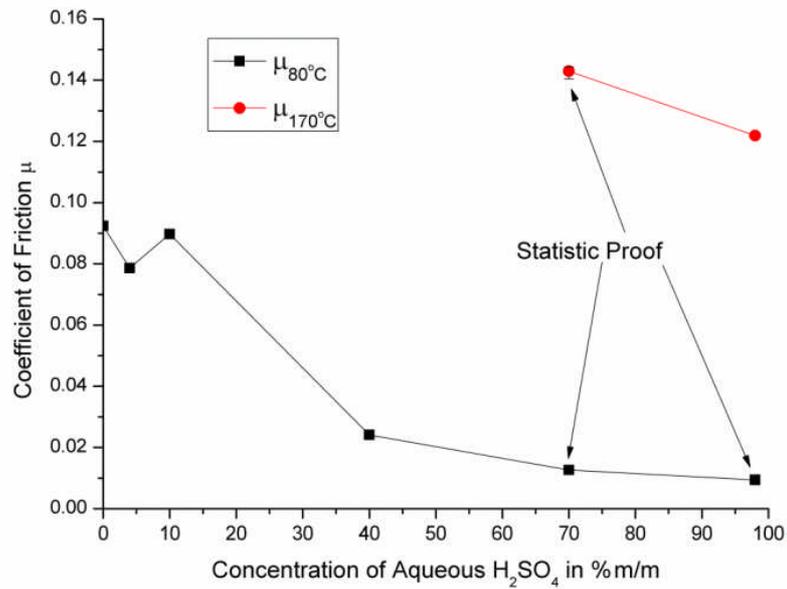
Figure 5: COF for various concentrations of aqueous H₂SO₄ at 80 and 170 °C

As mentioned earlier, the geometry of the contact changes during testing due to wear, increasing the contact area. Therefore, "shuttle tests" were done and the lubricant switched during running. Figure 6 shows the outcome of one shuttle test between SN600 and SN600 + 70 %w/w H_2SO_4 at 80 °C. The COF drops almost instantly after switching to a acid containing lubricant, most probably excluding a reduction of friction by a changed contact geometry. The CP drops quite sharply but recovers after a short period of time possibly indicating the initial release of ions followed by the formation of a non-conducting boundary layer with superior low friction properties. The impact of wear and modification of the boundary film chemistry on friction is indicated in Figure 6.
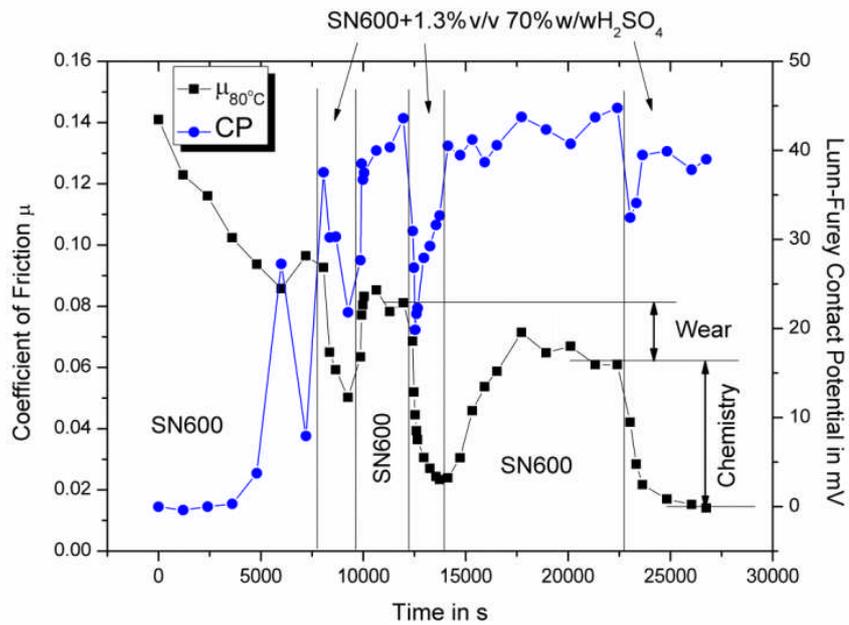
Figure 6: Shuttle test between pure SN600 and SN600+70%H₂SO₄ at 80 °C

Shuttle tests with the same lubricant were also undertaken at 170 °C and the outcome of one is shown in Figure 7. Instantly after switching to acid containing lubricant, the CP droped, probably from the release of ions and the friction increased significantly. The formation of black deposit was observed on the cylinder liner wear scar. After switching back to pure SN600, the friction slowly decreases while the CP stays on a high level. The repeated switch to acid containing lubricant created a drop in CP, suggesting that the deposit has worn flush with the metallic roughness peaks.
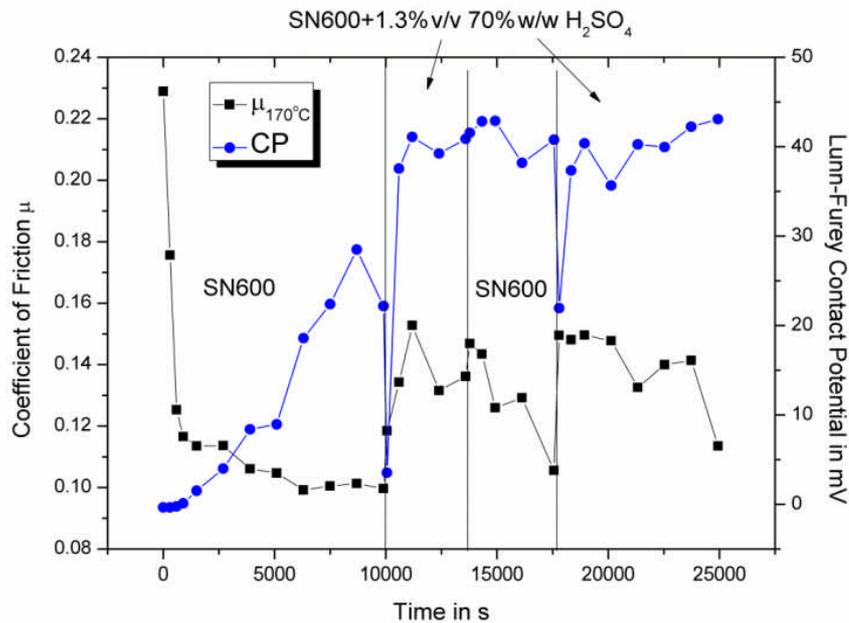
Figure 7: Shuttle test between pure SN600 and SN600+70%H$_2$SO$_4$ at 170 °C

Figure 8 compares the temperature dependency of the COF when lubricated with pure SN600 and with 70 %w/w H$_2$SO$_4$ dispersed in the oil. The surfaces exposed to acid show a higher roughness at low temperatures while being smoother at high temperatures. This is counterintuitive to the measured COF, which stayed constant low until 120 °C where visually the formation of deposit on the cylinder liner wear scar was observed. At about 140 °C, the friction exceeded the values found for pure SN600. The CP shows a good electrical separation for all conditions other than running-in. When deposit formation set in, the CP was approaching its maximum value.

An attempt was made to understand the nature of the low friction contact at 80 °C by varying the load. Decreasing the load, increased the COF, potentially indicating a still elastohydrodynamic lubrication regime but towards the hydrodynamic side.

19
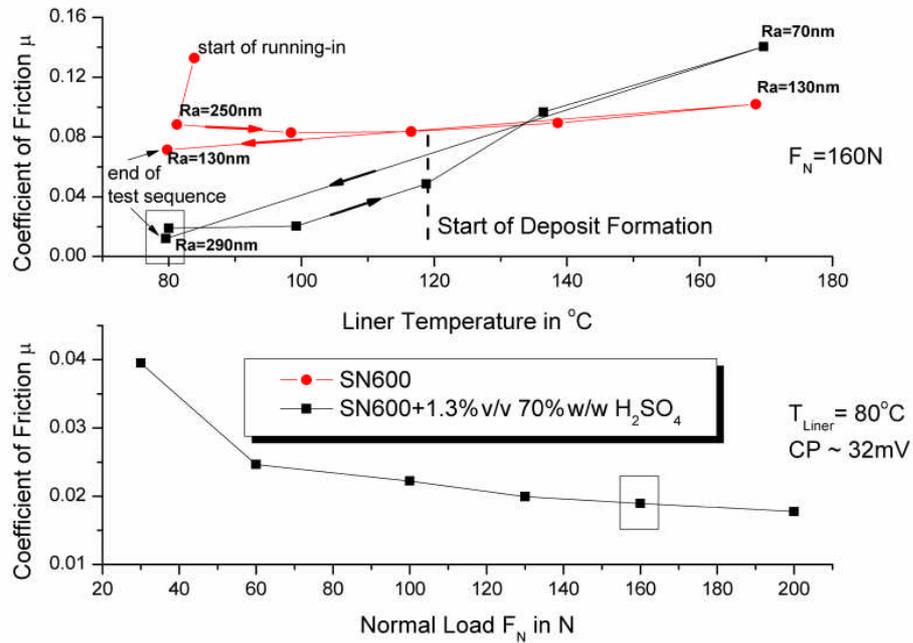
Figure 8: Influence of temperature and load on the COF

3.3. Result and Discussion: Tests with SN600 + H₂SO₄ and Fully Formulated Lubricant at 170 °C

Two fully formulated lubricants were tested. In undiluted condition, their COF was found to be comparably high with $\mu_{Lub.A} = 0.17$ and $\mu_{Lub.B} = 0.15$ at 170 °C. Shuttle tests with various combinations of lubricants were used to find the influence of dilution with SN600 and the influence of H₂SO₄.

The fully formulated lubricants were always fed at the BDC side of the piston ring, while pure SN600 and acid containing SN600 was always fed at the TDC side of the piston ring – a situation typical for the engine. The results for one shuttle test are shown in Figure 9. Running-in was done with SN600 and Lubricant A. During the first 2'500 seconds, the running-in showed no difference to running-in with pure SN600 and the COF dropped steadily due to smoothening of the surfaces. Suddenly, the COF rose and the CP measurement indicated a complete separation of the parts. The separation was too perfect to be a plain hydrodynamic separation and the friction values rose instead of declining as expected for the lubrication regime. Therefore, the formation of an electrically isolating CaCO₃ boundary film, exhibiting high friction, must be assumed (Giasson, et al., 1994). After 6540 seconds lubrication was switched to pure

20

SN600. During the subsequent 1'000 seconds, the COF steadily dropped, while the parts remained perfectly separated. The COF rose instantly after adding Lubricant A again. One explanation for this behaviour is that the boundary film was probably not completely worn down during lubrication with SN600 but a layer of surface active substances, physically adsorbed on to a chemical attached boundary layer was washed away. The physical layer of surfactants quickly reformed when Lubricant A was added again. When Lubricant A was used undiluted, the COF remained at the same level, supporting the hypothesis that viscosity has no or neglectable influence on the COF.

After running on pure Lubricant A, acid containing SN600 was added to the running test. A instantly recovered tiny dip in the CP measurement was observed, while a small but constant reduction in friction was observed. Some of the acid got neutralised by the additives in the oil, depressing the constant re-formation of the boundary layer and some of the surfactants are used up by the acid droplets. After a test duration of 12'000 seconds, Lubricant A was replaced by acid containing SN600. With the same rate as seen before, the COF drops, possibly by the mechanical removal of a physical bound surfactant layer. With a time delay of 950 seconds, the CP also drops, indicating metallic contact. After a considerable drop in CP, suddenly the friction increased again and visually the formation of black deposit was observed on the wear scar. This caused the CP to rise again. During 950 seconds, the boundary layer was removed by the acid. When the acid was not neutralised anymore, the acid acted more heavily on the oil to form a deposit.

When Lubricant A was used again, the CP dropped due to removal of loosely bound deposit or viscous bituminous matter formed between oil and acid (Sautermeister, et al., 2012). Within the subsequent 900 seconds the boundary film was completely reformed and the friction returned back to its former high value.

The observations were repeatable until the end of the test and also hold for Lubricant B. Both lubricants were capable of suppressing the formation of black deposit but could not remove deposit already formed from the wear scar.
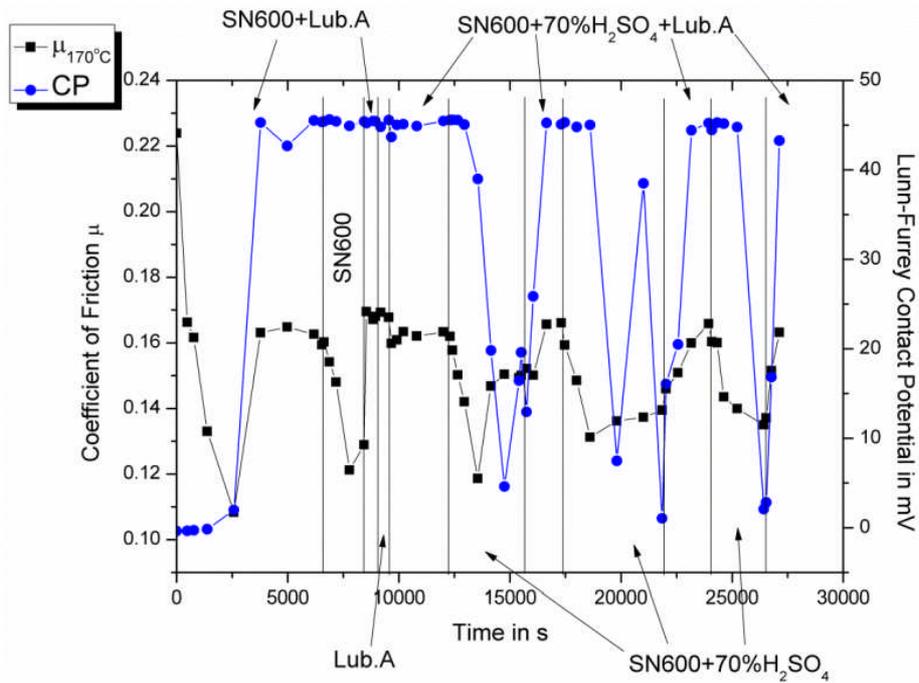
Figure 9: Shuttle test between SN600, lubricant A and 70 %w/w H₂SO₄ dispersed in SN600

3.4. Results and Discussion: Piston Ring Surface Condition After the Tests

The severity of the test conditions is illustrated by Figure 10 and Figure 11. Both surfaces ran for 6.5 hours lubricated with SN600 at 80 and 170 °C respectively. Both show clear signs of severe adhesion to the cylinder liner.

22
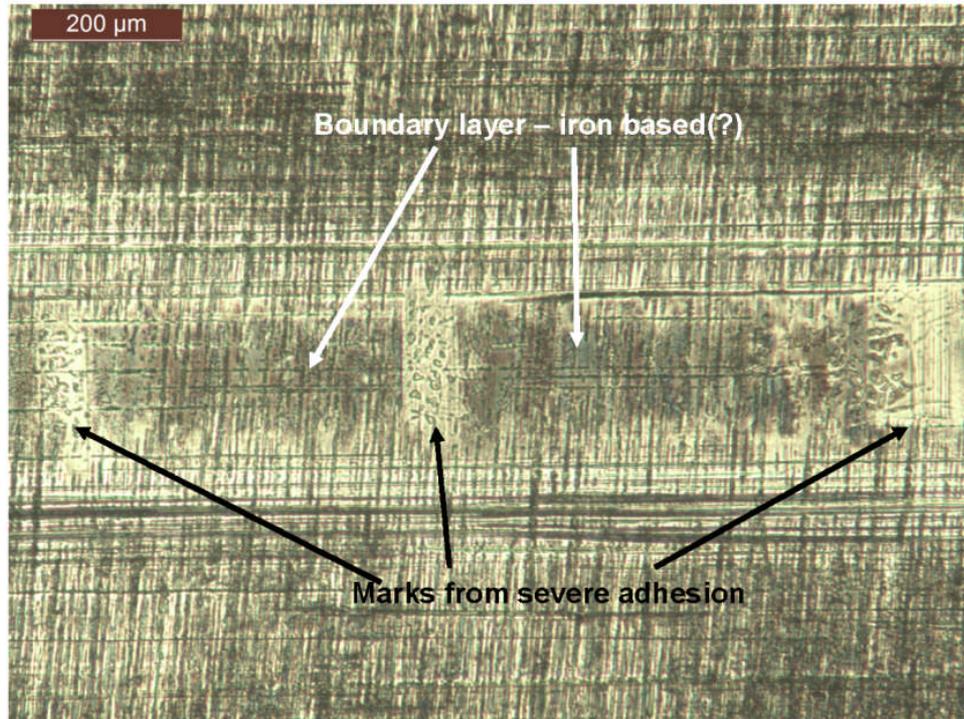
Figure 10: Piston ring wear scar, lubricated with SN600 at 80 °C for 6.5 hours
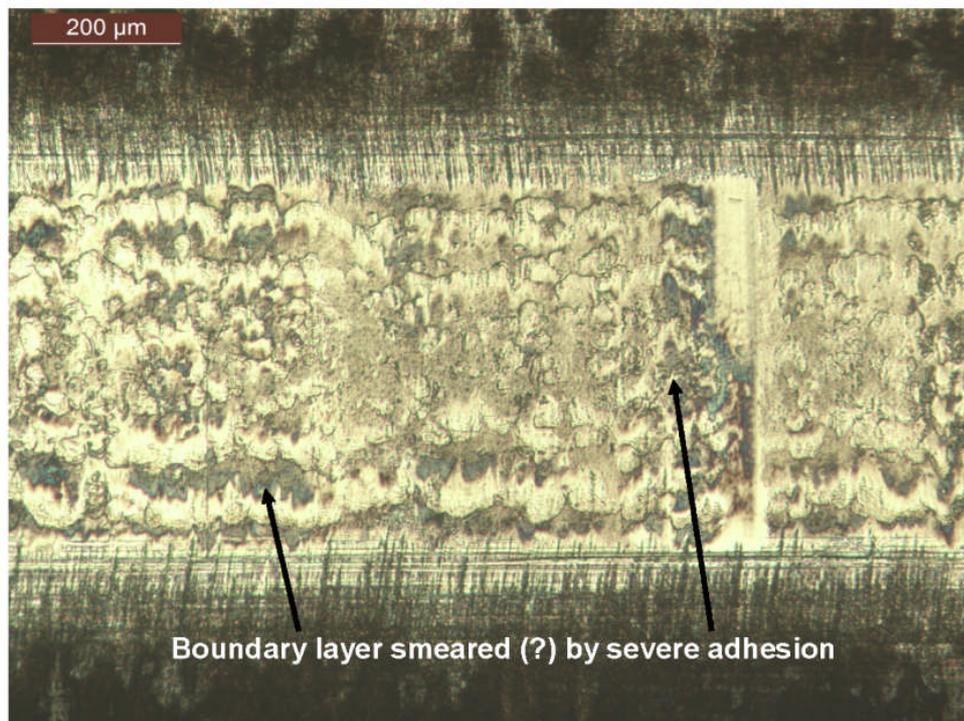
Figure 11: Piston ring wear scar, lubricated with SN600 at 170 °C for 6.5 hours

A piston ring, which was run-in at 80 °C, followed by a steady temperature increase up to 340 °C showed a better visual appearance than the one in Figure 11

23

always running on 170 °C. The width of the worn area was comparable to the test run with 80 °C, Figure 10. The running-in with moderate temperature seems to have a good influence on the surface development and wear.

Figure 12 shows a piston ring lubricated with 70 % H_2SO_4 dispersed in SN600 at 80 °C. The surface shows some corrosive pit holes but is otherwise very smooth and does not show any signs of severe adhesion with the liner.

The same applies to the piston ring surface shown in Figure 13. The piston ring was lubricated as the one before but at an increased temperature of 170 °C. The corrosive pit holes are smaller and seem to be situated mainly in machining grooves. An enlarged view on the corrosive pit holes revealed no correlation to the fine crack network of the chrome coating. The appearance of pit wholes by corrosion can be explained by the tendency of more stationary acid droplets on the chrome coating found by an evaluation for droplet displacement (Schleizer, et al., 1999) (Mahe, et al., 1988). This is in opposition to self-sustaining 'pit whole corrosion' by oxygen depletion in a continuous acid phase (Bargel, et al., 1999) and was not observed in this form during contact angle measurements under static conditions (Sautermeister, et al., 2012).
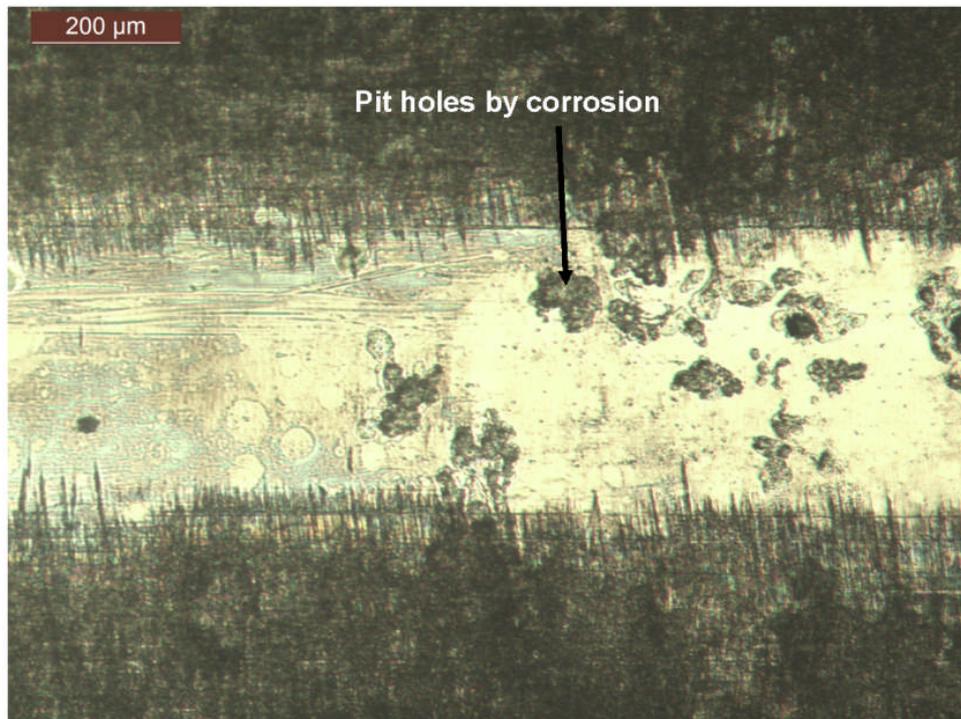
Figure 12: Piston ring wear scar, lubricated with SN600+70%w/w H_2SO_4 at 80 °C for 6.5 hours
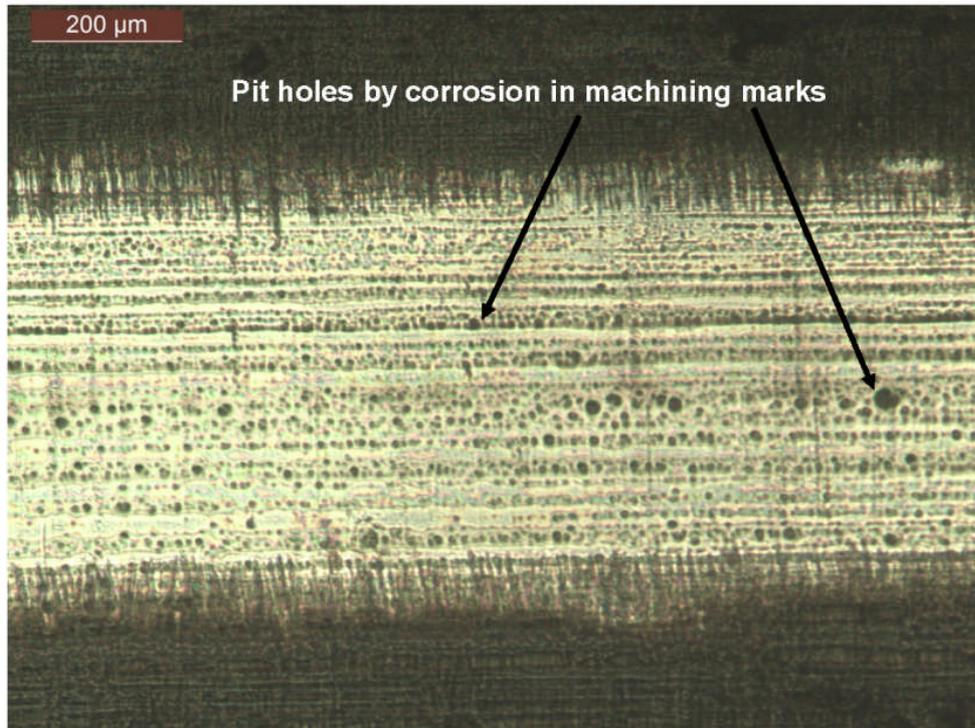
Figure 13: Piston ring wear scar, lubricated with SN600+70%w/w H₂SO₄ at 170 °C for 6.5 hours

Figure 14 and Figure 15 show piston ring surfaces after the shuttle tests with fully formulated lubricant B. The main difference is the finish time, 53 and 8 minutes, where both piston rings were lubricated with the addition of the fully formulated lubricant after running on acid containing lubricant for 50 minutes. While Figure 14 shows a similar appearance to the harsh conditions created by the reference test with pure base oil, Figure 11, Figure 15 shows a smooth and healthy looking surface without any traces of hard contact. The same appearance was found for lubricant A.
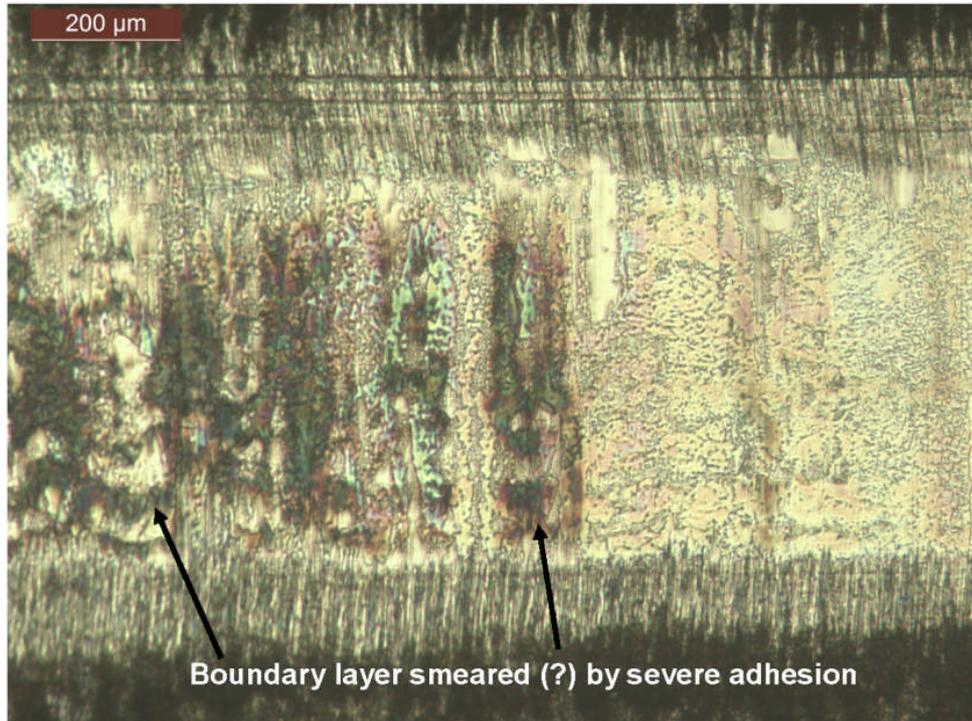
Figure 14: Piston ring wear scar, lubricated with lubricant B & SN600 + 70 %w/w H_2SO_4 at 170 °C. The test finished after an 53 minute period of adding lubricant B.
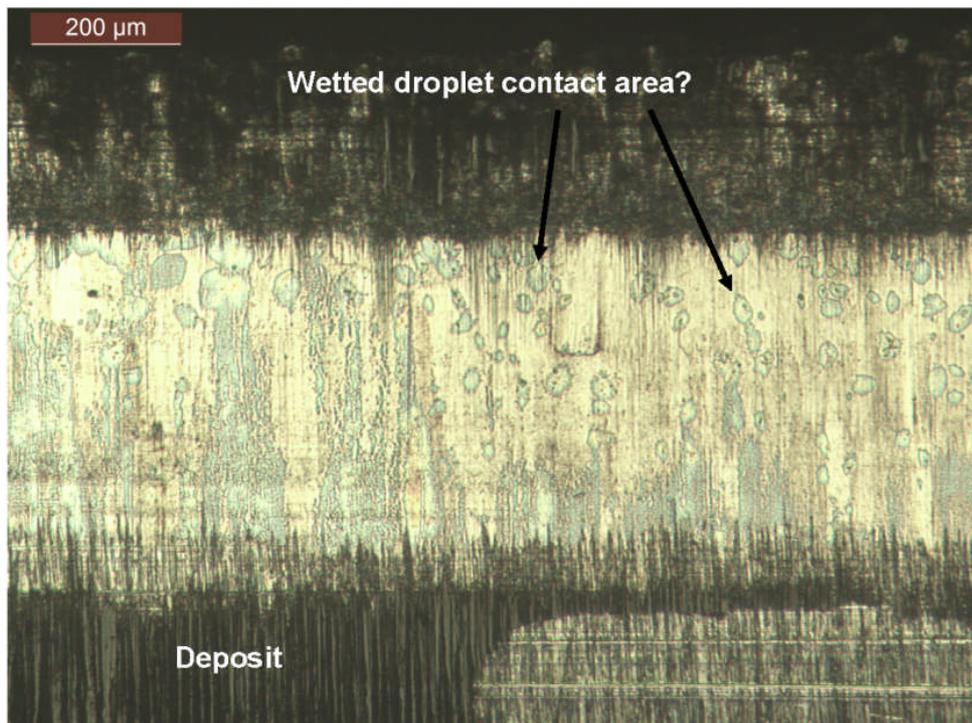
Figure 15: Piston ring wear scar, lubricated with lubricant B & SN600 + 70 %w/w H_2SO_4 at 170 °C. The test finished after an 8 minute period of adding lubricant B.

26

3.5. Results and Discussion: Lubricant Chemistry by FTIR-ATR

SN600 with a water content of 1.3 %v/v was used to lubricate the piston ring cylinder liner contact. A peak at 3404 cm^{-1} in the fresh lubricant originating from an O-H stretch indicated the presence of water. At 80 °C cylinder liner temperature, the water was completely removed from the lubricant. The temperature was lowered but also at 30 °C almost all water was removed from the lubricant. At 30 °C and a applied normal load of only 30 N, some water was found on the TDC and BDC side of the piston ring. The lost water was most probably evaporated by frictional induced high temperature and low, sub ambient pressures in the lubricant film (Dowson, et al., 1979). The condition for cavitation below the vapour pressure of water is given in both cases which was found using the software package Mahle – Summits (V3.2010) & VTL (V3.8) (Tomanik, 2004), (Tomanik, 2008). Some of the water might also react with the iron surface of the liner to form iron oxide and hydrogen gas. This reaction, however, is quite slow. More water was lost on the BDC side of the piston ring than on the TDC side, the side where new lubricant is continuously fed.

For SN600 contaminated with 10 %w/w H_2SO_4, no remaining acid can be found on either side of the piston ring. However, both absorbance spectra are lifted, probably the effect of dispersed fine wear particles in the oil from corrosion. The spectra of the oil sampled at TDC showed a higher absorbance.

For SN600 contaminated with 40 %w/w H_2SO_4, all peaks caused by H_2SO_4 disappeared and contrary to the previous observation, the lubricant sampled from BDC showed a slightly higher absorbance.

For SN600 contaminated with 70 %w/w H_2SO_4, Figure 16, the peaks caused by H_2SO_4 are still recognisable and in the same position but quite surprisingly the absorbance of the oil sampled at BDC exceeds the absorbance for the fresh oil. The test was found to be repeatable. The absorption of water from ambient air can be excluded, as the peaks would change their position in the case of dilution (Sautermeister, et al., 2012).
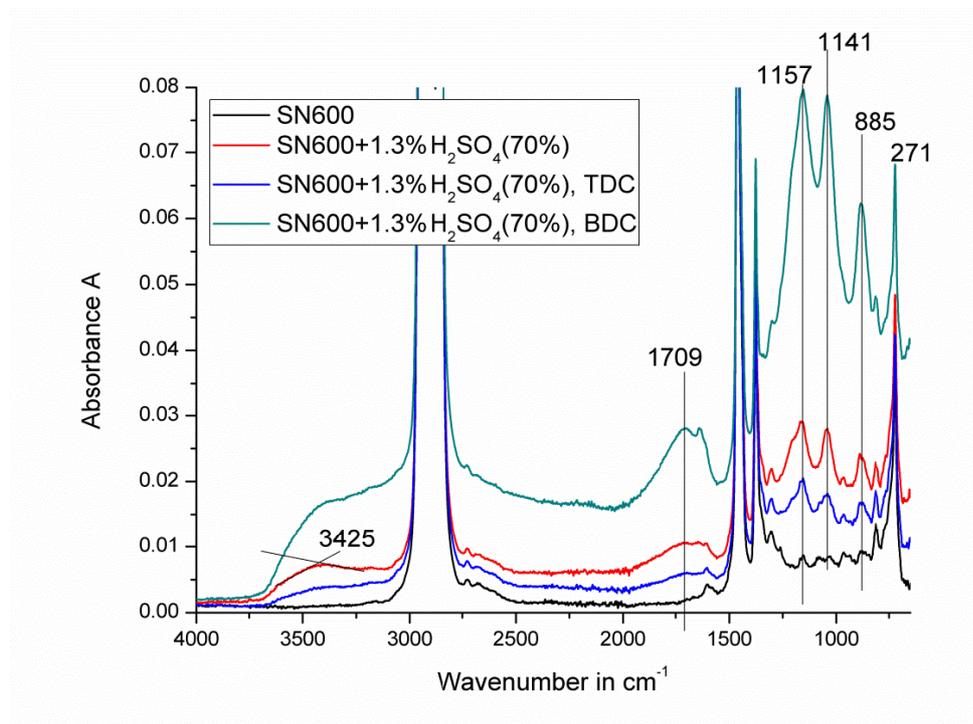
Figure 16: FTIR-ATR spectra of SN600+1.3 %v/v 70 %w/w H₂SO₄, fresh and sampled during the friction test at 80 °C

Also for SN600 contaminated with 98 %w/w H_2SO_4 the peaks caused by H_2SO_4 are still recognisable. A slight shift of the peak at 1032 cm^{-1} to 1045 cm^{-1} and from 1683 cm^{-1} to 1735 cm^{-1} can be observed. An additional peak is created at 1205 cm^{-1} and an O-H stretch at 3399 cm^{-1}, which should not be present for concentrated H_2SO_4. As for the example with 70 %w/w H_2SO_4 the absorbance of the oil sampled in BDC exceeds the absorbance of the unused contaminated lubricant. For concentrated H_2SO_4 atmospheric water absorption is a plausible explanation.

Peaks caused by H_2SO_4 disappeared in lubricant extracted from the BDC side during tests with a fully formulated lubricant. Also peaks present in the fully formulated oil disappear, which both can be explained by the neutralization of the H_2SO_4. However, one would expect the appearance of new peaks caused by the reaction products, namely originating from $CaSO_4$ but this is not the case.

For SN600 with added H_2SO_4 at 70 %w/w concentration, hard deposit formation on the liner was observed to start at about 120 °C. The cylinder liner temperature was increased in steps to find the critical value for deposit formation with pure SN600 in a sliding metal on metal contact and influence on the oil film chemistry.

Visually, darkening of the oil started at 250 °C and deposit formation was observed at 300 °C cylinder liner temperature. FTIR-ATR spectral analysis, shown in Figure 17, correlate well with this observation. At 250 °C, the lubricant started to oxidise, forming C=O bonds, and at 300 °C, the lubricant reacted with atmospheric nitrogen adding a nitro group to the hydrocarbon to form RNO_2. It must be assumed that traces of NO_2 ions in the laboratory air or catalysed by the rubbing process, were sufficient to react with hydrocarbon radicals formed during the oxidation as gaseous nitrogen is not reactive at this low temperatures. Excessive thermal degradation of the lubricant for tests with a maximum temperature of 170 °C can be excluded.
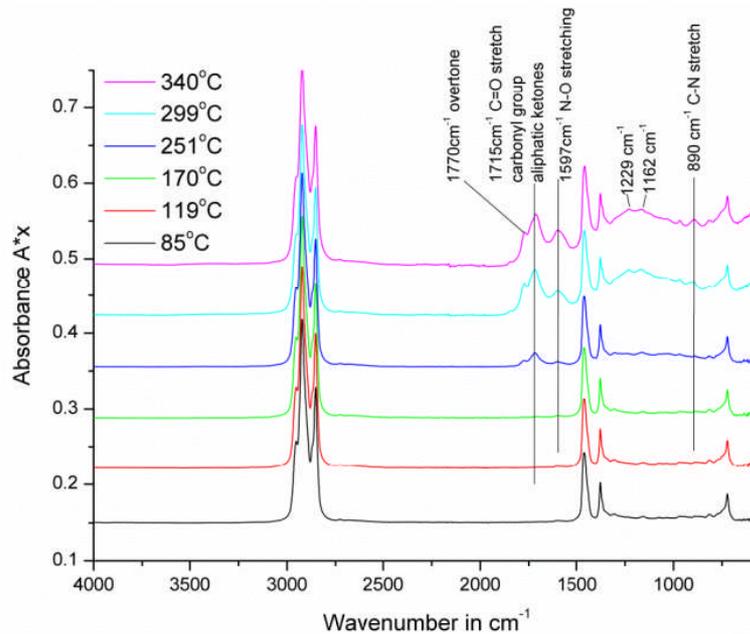
Figure 17: FTIR-ATR spectra of SN600 exposed to various cylinder liner temperatures during the friction tests at 85 - 340 °C

3.6. Results and Discussion: Surface Analysis by FTIR-Microscope and XPS

The FTIR analysis on a cylinder liner sample lubricated with SN600 at 80 °C, revealed typical hydrocarbon peaks at 2922 and 2856 cm^{-1} in deep honing marks and a otherwise metallic grey reflecting response. A slight built up of hydrocarbon based deposit in honing marks can be assumed as the cleaning procedure was found to remove all liquid oil. XPS on the same surface reveals sulphur bound to a surface film originating from the base oil. A strong S2p3/2 peak at 168.3 eV and a

weak Fe2p3/2 peak at 710.5 eV can be correlated to $FeSO_4$. A weaker S2p3/2 peak at 168.5 eV can be correlated to hydrocarbon sulphates and two C1s peaks at 286.3 eV to C-O bonds and at 284.5 eV to C-H bonds and graphite. The FTIR study only supports hydrocarbon bonds in deep honing marks. The cylinder liner surface mainly consist of a organic carbon based film, built up from hydrocarbon sulphates, probably graphite and a small amount of iron sulphates. The substances accumulated in deep honing marks.

The visual examination of the cylinder liner surface lubricated with SN600 at 170 °C showed the honing marks to be filled with deposit, which was even more pronounced in the IR-absorbance scan. The honing marks showed the typical hydrocarbon peaks at 2922 and 2856 cm^{-1} and at 1458 and 1374 cm^{-1}. A C=O peak at 1716 cm^{-1} indicated the temperature induced lubricant oxidation catalysed by the metal surfaces of piston ring and cylinder liner. A broad peak at around 3300 cm^{-1} and a shoulder after a peak at 1716 cm^{-1} originats from an O-H stretch (Nuevo, et al., 2006). A peak at 1188 and 1116 cm^{-1} is typical for sulphoxides. Outside the honing marks, the surface shows a plain metallic grey reflectance. XPS on the same surface revealed a Fe2p3/2 peak at 711 eV and a S2p3/2 peak correlated to either iron-sulphate or hydrocarbon-sulphate. A C1s at 284.5 eV correlates to graphite or C-H bonds and a peak at 288.6 eV to R-COOH carboxyl and CS_3^{2-}. A medium sized N1s peak at 399.4 eV correlates to both nitrogen adsorption on the surface or a C-N bond. C-N bonds are usually created at higher temperatures and was not supported by the FTIR study, therefore plain N adsorption to the surface is more likely. The deposit in the honing structure mainly consists of a oxidised hydrocarbon containing sulphoxides most probably bound to hydrocarbons, given the origin of the sulphur from the SN600. Some nitrogen was adsorbed to the surface.

The resulting FTIR-spectra near a patch of deposit on a cylinder liner sample lubricated with SN600 up to 340 °C showed a metallic reflection on plateaus between the honing marks including minor peaks at 3732, 2922, 1770 – 1620 and 1536 cm^{-1}. The honing marks were filled with deposit and showed very similar but more pronounced spectra for the typical hydrocarbon peak at 2922 cm^{-1} and a slight indication for the typical second hydrocarbon peaks at 1458 and 1374 cm^{-1}.

A strong C=O peak at 1722 cm^{-1} originated from severe oxidation of the lubricant deposit. Peaks at 3732, 1614 and 1536 cm^{-1} are typical for amine salts, a result of the high temperatures the lubricant was exposed to. A C-O peak at 1242 cm^{-1} is another indicator for hydrocarbon oxidation. No XPS scan was taken on this sample.

The FTIR scan on a cylinder liner lubricated with 1.3 %v/v 70 %m/m H_2SO_4 dispersed in SN600 at 80 °C showed a characteristic broad O-H peak at around 3300 cm^{-1}, typical sulfoxide / sulphonate peaks between 1200 – 1000 cm^{-1} and a aromate peak at 820 cm^{-1}. The missing or very weak hydrocarbon peaks indicated the binding of the sulfoxides / sulphonates to metal, most likely iron in this case. Deposit outside the wear track showed a broad peak around 3333 cm^{-1} in the area of O-H stretches. This broad peak almost covered the hydrocarbon peaks at 2934 and 2856 cm^{-1}. At 1650 cm^{-1} a C=O peak was found. A peak at 1404 cm^{-1} together with peaks between 1206 – 1050 cm^{-1} originate from sulphonates. Peaks at 876 and 810 cm^{-1} are typical for aromatics.

An XPS scan on the wear track revealed a S2p3/2 peak at 168.8 eV correlated to either iron sulphate species $FeSO_4$ or $Fe_2(SO_4)_3$. The S : Fe ratio was 4.5, far too high for either specie. A Fe2p3/2 peak at 710.6 eV supported both compounds. Both compounds are known to lower friction considerably (Wu, et al., 2009), also observed of this study. A Cr2p3/2 peak at 577.9 eV originated from CrO_3. A N1s peak at 400 eV originated from nitrogen adsorption. A C1s peak at 284.5 eV supported both graphite and C-H bonds. The C-H bonds could be part of hydrocarbon sulphates, however, no evidence was found for those other than the excess in sulphur. The surface consisted of iron sulphate with chrome oxide particles embedded. Carbon was most likely to be present in the graphite form but also hydrocarbons could have been present in the honing marks in the form of embedded deposit. Nitrogen is adsorbed at the surface.

The FTIR scan on a cylinder liner lubricated with 1.3 %v/v 70 %m/m H_2SO_4 dispersed in SN600 at 170 °C revealed a typical broad O-H peak at around 3300 cm^{-1} and hydrocarbon peaks at 2920, 2856, 1456 and 1376 cm^{-1} or at least a response at this wavelengths. Peaks at 1704 and 1176 cm^{-1} originated from

carbonyls, oxidised hydrocarbons. Peaks at 1616 and 824 cm^{-1} are typical for nitrides and a peak at 1048 cm^{-1} for sulphoxides.

The XPS scan on this surface revealed a S2p3/2 peak at 168.8 eV correlated to either iron sulphate specie $FeSO_4$ or $Fe_2(SO_4)_3$. The S : Fe ratio was 29.3, far too high for either specie. A Fe2p3/2 peak at 711.5 eV supported both compounds. A rise in friction was found for increased temperatures. For additives forming a $Fe_2(SO_4)_3$ - $FeSO_4$ surface film, a decay temperature of 160 – 193 °C was reported (Wu, et al., 2009) unfortunately without reporting upon friction values at this temperature. Weak peaks for S2p3/2 at 164 eV and N1s at 401.5 eV supported the presence of amino-sulphates containing C-H bonds represented by a C1s peak at 284.5 eV which correlates also to graphite. The FTIR study supported the presence of nitrogen bonds in the amino-sulphates, C-H bonds and iron sulphate. The surface consisted of iron sulphate, amino-sulphates, including hydrocarbon bonds.

3.7. Results and Discussion: Wear and Surface Topography by WYKO White Light Interferometer

The changing conditions of the shuttle tests undermine a statistically sound wear evaluation. Some tests under constant conditions, however, made a wear analysis worthwhile. The results are shown in Figure 18. The wear volume is normalised to the applied normal force and the sliding distance resulting in the wear factor k, also used by other researchers and appears in a comparable range (Priest, 2000). Lubrication with 70 %w/w H_2SO_4 at 170 °C at relatively low speed and high contact pressure is the closest test condition to engine reality and typical for the piston TDC. Therefore, this condition was run more often under static conditions, indicated by the error bars.

Acid concentration and temperature have a major influence on both cylinder liner and piston ring wear. The origin of the acid concentration abscissa represents the reference condition, lubricated with pure SN600. While lubricated with plain base oil, both cylinder liner and piston ring showed increased wear at higher temperatures explained by the reduced viscosity, resulting in a thinner oil film. At both temperatures, however, the test operated in the mixed lubrication regime, where surface asperities are in contact and the CP showed very similar values for

similar surface chemistry, meaning the surface contact area is very similar. The tensile strength of cast iron EN-GS-400, for example, reduces from 510 MPa at 80 °C to 450 MPa at 170 °C (Memhard, et al., 2011). Therefore, reduced tensile strength of the material must also be taken in to account leading to higher wear at increased temperatures.

Increasing the concentration of the dispersed acid phase at 80 °C cylinder liner temperature, increased the wear of the piston ring while the wear of the cylinder liner decreased even below the values of the reference condition. At 170 °C, the opposite was observed. Increased concentrations reduced the wear on the piston ring, while the wear on the cylinder liner increased despite the formation of deposits on the surface. For both temperatures the CP measurement indicated almost perfect separation. Galvanic-electric effects can be excluded as the potential between chromium and iron lays between 400 and 910 mV (Atkins, 2001) which would be picked up by the Lunn-Furey CP circuit and the potential of 45 mV across the contact is not high enough to suppress corrosion. The abrasive action of entrained metal oxides in bituminous hydrocarbon, forming deposits on the running surface, seems a more plausible explanation for the increased wear at 170 °C.
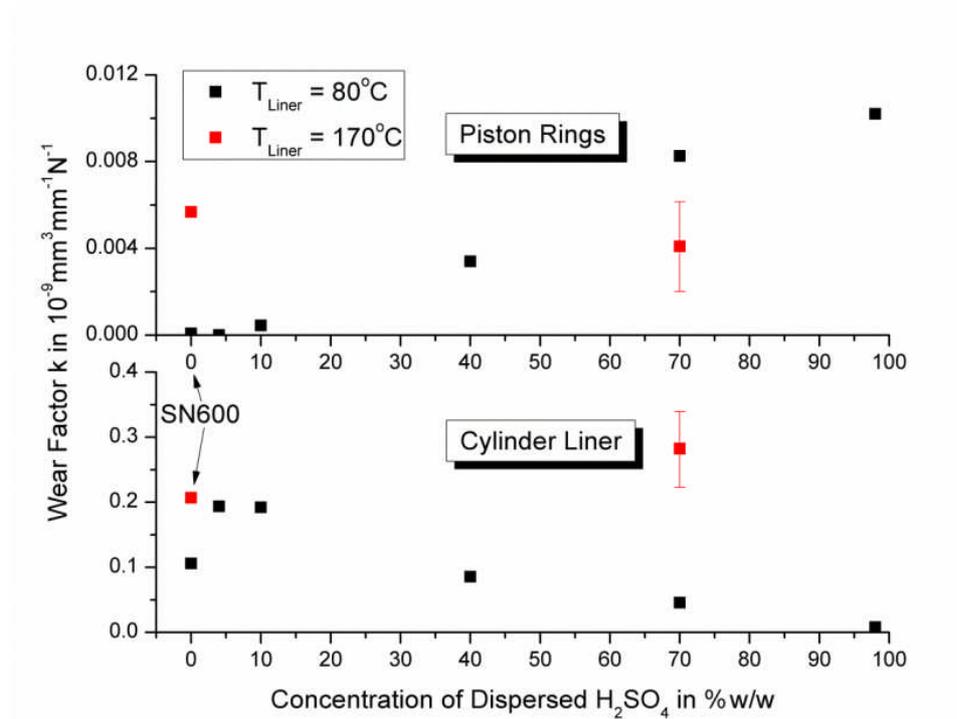
Figure 18: Wear factor k of piston ring and cylinder liner over various concentrations of H$_2$SO$_4$ at 80 and 170 °C

The combined peak height, $\sum$Rp, for both 80 and 170 °C increased with increased acid concentration from ~1.3 to ~1.8 μm, while the friction decreased at a liner temperature of 80 °C, indicating the formation of a surface boundary film with superior friction properties. The roughness Ra of the honed liner decreased, Figure 2, while the roughness of the lapped piston ring surface increased from 0.08 to 0.11 μm during running with plain SN600 at both temperatures. At 80 °C liner temperature, the surface roughness of the cylinder liner increased to 0.3 μm by dispersing H$_2$SO$_4$ in SN600, declining towards higher concentrations. The piston rings became slightly smoother until 40 % H$_2$SO$_4$ and became slightly rougher towards higher acid concentrations.

At 170 °C, surface roughness of both piston ring and cylinder liner decreased and became very similar with Ra ~0.07 μm.

At high temperatures and concentrations, the roughness valleys became filled with deposit, changing the position of the mean line, resulting in lower statistical roughness values.

4. Conclusions

The tribological properties of API Group I base oil, SN600, alone and in combination with H_2SO_4, was tested on a reciprocating friction testing machine with a piston ring – cylinder liner contact. The main variables were temperature and acid concentration. The influence of fully formulated lubricants was also tested.

The loading conditions were quite severe and passed the criterion for plastic deformation under Hertzian contact. The tests ran in the mixed- / elastohydrodynamic-lubrication regime. Surface analysis by XPS and FTIR-microscope suggested the formation of an organic hydrocarbon sulphate film when running at 80 and 170 °C with the sulphur containing SN600. Deposit formation starts at 300 °C including the formation of nitrogen bonds in the organic surface film. Increasing the temperature increased wear and friction, while surface roughness decreased.

The contact showed very low friction when lubricated with 1.3 %v/v 40 – 98 %m/m H_2SO_4 dispersed in SN600 at 80 to 120 °C. Surface analysis by XPS and FTIR-microscope suggested the formation of iron sulphate and oxidised hydrocarbons. The lubricant chemistry tested by FTIR suggested the formation oil soluble substances, inviting one to speculate on the formation of 'iron-hydrocarbon-sulphate' based soaps or iron sulphonates. The cylinder liner wear under this condition decreased with increased acid concentration, while piston ring wear increased. The combined roughness peak, $\sum Rp$, increased for increased acid concentration.

Between 120 and 170 °C, the same lubricant showed the formation of visually recognisable black deposit on the wear scar and increasing friction. The breakeven point with pure SN600 was found at 140 °C. Surface analysis by XPS and FTIR-microscope suggested the formation of iron sulphate and nitrided hydrocarbon sulphates. The wear of the liner increased, while the wear of the piston ring decreases and surface roughness decreases. The formation of nitrogen bonds was observed when excessive deposit was formed.

A general and probably surprising result of this study is the positive impact of H_2SO_4 on the tribological parameters. The marine Diesel engines do not suffer from extremely high wear rates but 'sudden severe wear' or unpredictable scuffing, starting in line with fresh lubricant supply. Piston ring surfaces run on

35

Draft-version for submission to Tribology Letters

fully formulated lubricants show visually worse conditions compared to lubrication with H_2SO_4 dispersed in API Group I base oil.

At 170 °C, the fully formulated lubricants disappoint also by their high COF which is ~30 % higher than running on pure base oil. A likely explanation is the formation of a chemically bound calcite boundary film and a physical bound layer of surfactants on top of this film. The bad appearance of the piston rings might originate from increased surface traction by increased friction.

Acknowledgements

References

Adams, J.F., Papangelakis V.G. (2007): *"Optimum reactor configuration for prevention of gypsum scaling during continuous sulphuric acid neutralization"*, Hydrometallurgy, Toronto, Elsevier, 269-278 : Vol. 89.

BAFU & UVEK (2011): *„Entwicklung der schweizerischen Gesetzgebung im Bereich der Abgasemissionen von Motorfahrzeugen und Maschinen"*, Bern, BAFU

Bargel, H.J., Schulze, G.(1999): *„Werkstoffkunde"*, Berlin, Springer, vol. 6

Benoit, R., Durand, Y., Narjoux, B., Quintana, G., Georges, Y.: *"XPS, AES, UPS and ESCA - lasurface.com"*, CNRS Orléans, accessed: 13-March 2012, http://www.lasurface.com/database/elementxps.php.

Braunovic, M., Konchits, V.V., Myshkin N.K. (2007): *"Part III: Diagnostic and Monitoring Technologies"*, Electrical Contacts: Fundamentals, Applications and Technology (Electrical and Computer Engineering), Taylor & Francis

Burstein, G.T., Shreir, L.L., Jarman, R.A. (1994): *"13.8 Chromium coatings"*, Corrosion, vol. 2., Elsevier Butterworth Heinemann, 99–110

Caixiang, G., Qingzhu, L., Zhuoming, G., Guangyao, Z.(2008): *"Study on application of CeO_2 and CaCO_3 nanoparticles in lubricating oils"*, J.Rare Earths, Shanghai, Elsevier, April, 2, vol. 26

Cantow, F.G.(2004): *"Paper no. 209 Piston rings for large bore engines"*, Kyoto, CIMAC, 1–14

Carrales, M.Jr., Martin, R.W.(1975): "Sulfur Content of Crude Oils", Dallas, United States Department of the Interior

CIMAC Working Group "Exhaust Emission Control" (2008): *"Guide to Diesel exhaust emission control of NO_x, SO_x, particulates, smoke and CO_2"*

CIMAC Working Group "Marine Lubricants" (2007): *"No.26 Guidelines for Diesel Engine Lubrication, Impact of Low Sulphur Fuel on Lubrication of Marine Engines"*, Frankfurt/Main

Class NK (2008): *"Guidance for measures to cope with degraded marine heavy fuels"*, version II., Ohnodai, Midori-ku, Chiba: ClassNK, Nippon Kaiji Kyokai

Davis, F.A., Moore A.J., Pridmore S.(1993): *"The Use of a Laboratory Wear Simulation Technique for the Development of Marine Cylinder Lubricants"*, 20th Int. Congress on Combustion Engines, London, CIMAC, vol. D82.

Demmerle, R., Barrow, S., Terretatz, F., Jaquet, D.(2001): *"New insights into the piston running behaviour of Sulzer large bore diesel engines"*, Frankfurt, CIMAC, 1–14

Ding, H., Gilani M.N.H., Spelt, P.D.M.(2010): *"Sliding, pinch-off and detachment of a droplet on a wall in shear flow"*, J. Fluid Mech., London, Cambridge University Press, 217-244, vol. 644

Dowson, D., Taylor C.M.(1979): *"Cavitation in Bearings"*, Leeds, Ann.Rev. Fluid Mech., 11

Elson, J.P., Amin, J.J.(1974): *"Experimental Evaluation of a Scotch-Yoke Compressor Mechanism"*, Int. Compressor Eng. Conference, Paper 146, Lafayette, Purdue University

Friesen, T. V., Vrolijk D.J.E.(2001): *"Comparison of Cylinder Oil Detergents for Crosshead Diesel Engines"*, CIMAC Congress, Hamburg, CIMAC

Fu, J., Lu, Y., Campbell, C.B., Papadopoulos, K.D.(2006): *"Acid Neutralization by Marine Cylinder Lubricants Inside a Heating Capillary: Strong/Weak-Stick Collision Mechanisms"*, Ind.Eng.Chem.Res., New Orleans, Am.Chem.Soc., 5619-5627, vol. 45

Garner, T., Voss, L., Marek, K., Aabo, K.(2004): *"Paper No. 129 Development of Marine Diesel Cylinder Oils"*, CIMAC, 1–14

Giasson, S.; Palermo, T.; Buffeteau, T.; Desbat, B.; Turlet, J. M.(1994): *"Study of boundary film formation with overbased calcium sulfonate by PM-IRRAS spectroscopy"*, Thin Solid Films, Rueil-Malmaison, Elsevier, Vol. 252

Giasson, S., Espinat D., Palermo T.(1993): *"Study of Microstructural Transformation of Overbased Calcium Sulphonates During Friction"*, Rueil-Malmaison, Lubrication Science, January.

Graham, R., Prado, O.S., Collins, M.H., Brandes, E.A., Farmery, H.K. (1960): *"Influence of the Silicon in Cast Iron on Corrosive Wear"*, Proc.Inst.Mech.Eng., Chester, I.Mech.E., June, 19, vol. 174

Hone, D.C., Robinson, B.H., Steytler, D.C.(2000): *"Mechanism of Acid Neutralization by Overbased Colloidal Additives in Hydrocarbon Media"*, Langmuir, Abingdon, ASC, 340-346, vol. 16.

Jabbarzadeh, A., Atkinson J.D., Tanner R.I.(2002): *"Effect of branching on the lubricant properties: A molecular dynamics study"*, Boundary and Mixed Lubrication: Science and Applications, D. Dowson et al., Sydney, Elsevier, vol. 1.

Jakobsen, S.B.(2010): *"Service Experience of MAN B&W Two Stroke Diesel Engines"*, CIMAC Congress Paper NO.17, Bergen, CIMAC

Jansen, K.M.B., Agterof W.G.M., Mellema, J.(2001): *"Droplet breakup in concentrated emulsions"*, J. Rheol., Enschede, Soc.Rheol., Jan./Feb., 1, vol. 45

Kang, Q., Zhang, D., Chen, S.(2005): *"Displacement of a three-dimensional immiscible droplet in a duct"*, J.Fluid Mech., Los Alamos, Cambridge University Press, 41-66, vol. 545

Kubo, T., Fujiwara, S., Nanao, H., Minami, I., Mori, S.(2006): *"TOF-SIMS analysis of boundary films derived from calcium sulfonates"*, Tribol.Lett., Morioka, Springer, August, 2, vol. 23

Lackmann, J.(2001): *"Festigkeitslehre"*, Dubbel, Taschenbuch für den Maschinenbau, Beitz, W., Grote, K.H., Berlin, Springer, vol. 20

Lancon, D., Doyen, V.(2010): *"Paper no. 98 The universal concept: The lubrication solution to 2020 and beyond"*, Bergen, CIMAC, 1–11

Macdonald, A.G., Stott, F.H.(1987): *"Effect of Temperature on the Corrosive Wear of Cast-Iron in Oil-Sulphuric Acid Environments"*, Reactivity of Solids, Manchester, Elsevier, vol. 4

Mahe, M., Vignes-Adler, M., Adler, P.M.(1988): *"Adhesion of Droplets on a Solid Wall and Detachment by a Shear Flow II. Rough Substrates"*, J.Colloid Interf.Sci., Meudon, Academic Press, Nov., 1, vol. 126

Memhard, D., Andrieux, F., Sun, D.Z., Haecker, R.(2011): *"Development and Verification of a Material Model for Prediction of Containment Safety of Exhaust Turbochargers"*, 8th European LS-DYNA Users Conference, Strasbourg, DYNAmore

Micali, F., Weber, M., Stark, M., Räss, K., Potenza, M.(2010): *"Paper No. 74: Suction air humidity influence on piston running reliability in low-speed two stroke diesel engines"*, CIMAC

Mischler, S., Rosset, E., Stachowiak, G.W., Landolt, D.(1993): *"Effect of sulphuric acid concentration on the rate of tribocorrosion of iron"*, Wear, Lausanne, Elsevier, vol. 167

Miyazaki, M., Takeshima, S., Okuyama, S., Tanaka, M.(1993): *"Evaluation of marine engine lubricating conditions using a cylinder liner surface oil sampling apparatus"*, CIMAC, 1–15

Montgomery, R.S.(1969): *"Run-in and glaze formation on grey cast iron surfaces"*, Wear, Princeton, Elsevier Sequoia, 99-105, vol. 14

Plint, G.(2005): *"Guidance Notes on Lubricated Wear Testing"*, Newbury, Phoenix Tribology Ltd.

Priest, M.(2000): *"Factors Influencing Boundary Friction and Wear of Piston Rings"*, Proceedings of the 26th Leeds-Lyon Symposium on Tribology, Thinning Films and Tribological Interfaces, Leeds, Elsevier, vol. 38

Priest, M.(2009): *"Work Unit 1: Introduction to Tribology and Real Surfaces"*, University of Leeds, MECH5570 Introduction to Tribology, Leeds, School of Mechanical Engineering

Draft-version for submission to Tribology Letters

Priest, M.(2010): *"Work Unit 3: Lubricants and Lubrication"*, University of Leeds, MECH5570 Introduction to Tribology, Leeds, School of Mechanical Engineering

Reynolds, O.(1886): *"IV. On the Theory of Lubrication and its Application to Mr. Beauchamp Tower's Experiments, including an Experimental Determination of the Viscosity of Olive Oil"*, London, R.Soc., vol. 177

Saunders, J. A., Thomas, R.C.(1996): *"Origin of 'exotic' minerals in Mississippi salt dome cap rocks: results of reaction-path modelling"*, Appl.Geochem., Auburn, Pergamon, 667-676, vol. 11

Sautermeister, F.A., Priest, M.; Fox, M.F., Lee, P.M.(2012): *"Impact of Sulphuric Acid on Cylinder Lubrication for Large 2-Stroke Marine Diesel Engines: Contact Angle, Interfacial Tension and Chemical Interaction"*, Tribol.Int., DOI: 10.1016/j.triboint.2012.06.002, 38th Leeds-Lyon Symposium on Tribology.

Sautermeister, F.A., Priest, M.(2012): *"Physical and Chemical Impact of Sulphuric Acid on Cylinder Lubrication for Large 2-Stroke Marine Diesel Engines"*, Tribol.Lett., 2, vol. 47, 261-271, Tribology - Industrial and Automotive Lubrication, Esslingen

Sautermeister, F.A., Priest, M., Fox, M.F.(2012): *"FTIR Lubricant Analysis – Concentration of Dispersed Sulphuric Acid"*, Leeds, submitted

Schleizer, A.D., Bonnecaze, R.T.(1999): *"Displacement of a two-dimensional immiscible droplet adhering to a wall in shear and pressure-driven flows"*, J.Fluid Mech., 383, 29–54

Sjogren, T., Wigren, P., Vilhelmson, F., Vomacka, P.(2004): *"High Performance Piston Rings for Two-Stroke Marine Engines"*, CIMAC Congress 2004, Kyoto, CIMAC, vol. 79

Stott, F.H., Macdonald A.G.(1988): *"The Influence of Acid Strength on the Corrosive Wear of Grey Cast Irons in Oil-Sulphuric Acid Mixtures"*, Wear, Manchester, Elsevier, vol. 122

Stott, F.H., Breakell, J.E., Newman, R.C.(1990): *"The Corrosive Wear of Cast Iron Under Potentiostatically-Controlled Conditions in Sulphuric Acid Solutions"*, Corrosion Sci., Manchester, Pergamon Press, 8/9, vol. 30.

Taylor, G.I.(1932): *"The Viscosity of a Fluid Containing Small Drops of Another Fluid"*, Proc.R.Soc.London, London, R.Soc., Oct., 834, vol. 138

Tomanik, E.(2008): *"Friction and wear bench tests of different engine liner surface finishes"*, Tribol.Int., Sao Paulo, Elsevier,1032 – 1038, vol. 41

Tomanik, E.(2005): *"Modelling of the Asperity Contact Area on Actual 3D Surfaces"*, SAE Int., Sao Paulo, SAE, 1864, vol. 1

Topolovec-Miklozic, K., Forbus, T.R., Spikes, H.(2008): *"Film Forming and Friction Properties of Overbased Calcium Sulphonate Detergents"*, Tribol. Lett., London, Springer, vol. 29

van Helden, A.K., Valentijn, M.C., van Doorn, H.M.J.(1989): *"Corrosive wear in crosshead diesel engines"*, Tribol.Int., Houston, Butterworth&Co, Jun., 3, vol. 22

Vipper, A.B., Cook, S.J., Karaulov, A.K., Leahy, R.(1998): *"Antifriction Properties of Calcium Phenate-Type Detergents Used in Marine Cylinder Lubricants"*, Kiev, Lubr.Sci., Feb., vol. 10

Wirtz, M., Hell, R.(2007): *"Dominant-Negative Modification Reveals the Regulatory Function of the Multimeric Cysteine Synthase Protein Complex in Transgenic Tobacco"*, The Plant Cell, Heidelberg, ASPB, Feb., 625-639, vol. 19

Wu, H., Ren, T.(2009): *"Investigation of antiwear additives for diester"*, Ind. Lubr.Tribol., Shanghai, Emerald, 5, vol. 61

Wu, R.C., Papadopoulos, K.D., Campbell, C.B.(2000): *"Acid-neutralising of marine cylinder lubricants: Measurements and effects of dispersants"*, AIChE J., 1471–7

Wu, R.C., Campbell, C.B., Papadopoulos, K.D.(2000): *"Acid-Neutralizing of Marine Cylinder Lubricants: Effects of Nonionic Surfactants"*, Ind.Eng.Chem. Res., New Orleans, ACS, 3926-3931, vol. 39

Zhang, M., Wang, X., Fu, X., Xia, Y.(2009): *"Performance and anti-wear mechanism of $CaCO_3$ nanoparticles as a green additive in poly-alpha-olefin"*, Tribol.Int., Lanzhou, Elsevier, vol. 42

FTIR Lubricant Analysis – Concentration of Dispersed Sulphuric Acid

Falko A. SAUTERMEISTER,*[†] Martin Priest* and Malcolm F. Fox*

* iETSI, School of Mechanical Engineering, University of Leeds, Leeds LS2 9JT, UK

[†] To whom correspondence should be addressed, E-mail: mnfasa@leeds.ac.uk

Abstract

Purpose – Small quantities of aqueous sulphuric acid, H_2SO_4, where found to be trapped within hydrocarbon shells, making them inaccessible for concentration evaluation by titration.

Approach – Fourier Transform Infrared spectroscopy used in the Attenuated Total Reflection mode (FTIR-ATR) was applied to study the reaction products of squalane, $C_{30}H_{62}$, and an API Group I base oil with various concentrations of aqueous sulphuric acid, H_2SO_4 (Sautermeister et al., 2012), (Sautermeister et al., 2012).

Findings – The absorbance comparison usually used for estimating acid concentrations was found to fail when small quantities of acid are trapped in the reaction product. It was found that the peak shift and changes in absorbance found for various pure aqueous acid concentrations were useful to establish the remaining concentration of the trapped sulphuric acid.

Originality – This paper fulfils the indentified need to study acid dissociation dependent peak shifts of H_2SO_4 to find the acid concentration of finely dispersed droplets in hydrocarbon oils.

Keywords: FTIR; lubricant degradation; emulsion; sulphuric acid; marine diesel engine

Introduction

The FTIR-ATR technique can determine the concentration of substances in mixtures. Bellamy (Bellamy, 2010) has presented the 'Internal Standard Method' the ratio of absorbance peaks from two different substances to establish their mixing ratio, based on the Beer-Lambert law which relates absorption band intensity linearly to the substance concentration in a homogeneous mixture (Sherman Hsu, 1997). Deviation from the Beer-Lambert law for the sample arise from chemical reactions and molecular interactions.

1

A peak shift due to ionic interaction of ClO_4^- with the H-O bond of water was observed by Raman spectroscopy (Walrafen, 1970). A comparative study of Raman and IR spectroscopy found good agreement and influence on the peak positions of the H-O bond in water in the presence of ions (Walrafen, 1971). The FTIR-ATR technique was also used to find peak shifts in the spectra of water with increasing NaCl content (Masuda, 2003). The spectroscopic shift in the frequencies of water infrared absorption bands is explained by changes in molecular structure through bond angles and lengths caused by interactions with dissolved substances, temperature or pressure. The distances and stiffness of the bond changes and therefore the vibration frequencies of the molecular bonds (Walrafen, 1970), (Walrafen, 1971), (Masuda et al., 2003).

Experimental Method

Reagents and chemicals: the substances used in this study were: API Group I base oil HVI160B (Shell) and sulphuric acid, H_2SO_4 (> 95 % Fisher Scientific UK Ltd., analytical reagent grade). Lower concentrations of sulphuric acid were made with deionised water by weighing. Reaction products were formed under conditions described previously (Sautermeister et al., 2012), (Sautermeister et al., 2012). Solvents were iso-propanol, heptanes and hexanes (Fisher Scientific UK Ltd., analytical reagent grade).

Apparatus: The PerkinElmer Spectrum100 FTIR-ATR spectrophotometer was used for the analyses. The ATR accessory had a Zink-Selenide (ZnSe) optic with a diamond cover plate; the optic is embedded into stainless steel (PerkinElmer, Inc., 2005). To prevent the stainless steel from corrosion by acid, the plate was covered by a Kapton[©DuPont] polyimide tape with an oil-resistant silicon-based adhesive. The optic was freed by cutting a hole in the film. The tape was replaced when signs of deterioration appeared, which only occurred for the highest acid concentration. No influence of the polyimide on the measurements were found. The results were obtained at 22°C ambient and used without further processing or correction.

Bituminous reaction product was extracted by pipette. Some quantity was washed with water to

2

neutralize surrounding H_2SO_4, washed with isopropanol to remove water and washed with heptanes to remove excess oil. The remaining matter is microscopic non-homogenious. A second quantity was washed with water followed by dissolving in hexane which liberates encapsulated H_2SO_4. Hexane extracted from the top and dried off at 40°C. The remaining mater was microscopic homogeneous.

Results and Discussion

The bottom plot of Figure 1 shows the FTIR-ATR spectra of aqueous H_2SO_4 at thirteen concentrations between 0.5 and 98 %; the dependence of absorbance on concentration is very strong and is also shown in Figure 2. The HSO_4^- asymmetric stretch in Figure 2 is very similar to measurements presented earlier for dissociation of H_2SO_4 in H_2O (Young et al., 1959). The conventional method (Bellamy, 2010), (Sherman Hsu, 1997) establishes a sample's acid concentration from its FTIR absorbance. The absorbance spectra presented in Figure 1 are very similar to spectra of refractive index presented earlier (Palmer et al., 1975). The analyses of the absorption band maxima and their associated absorbances show a complex behaviour in the upper plots of Figure 1 and quantified in Table 1.

However Figure 3 andFigure 4 illustrate the problem when sulphuric acid is mixed with a hydrocarbon. Figure 3 first compares the FTIR-ATR spectrum of 80 %w/w aqueous sulphuric acid used in the reaction with API Goup I base oil HVI160B, and the FTIR-ATR spectrum of pure 80 %w/w aqueous H_2SO_4. The two spectra overlay each other although the used H_2SO_4 is decolourised. The hydrocarbon content is too small to be detected and the acid peaks are broad and strong and mask any hydrocarbon absorbance peaks. Second, Figure 3 compares the 80 %w/w H_2SO_4 with a bituminous reaction product formed at the interface of 80 %w/w H_2SO_4 and API Group I base oil HVI160B. The reaction product was mechanically extracted by a pipette and its FTIR-ATR spectrum obtained without further treatment. Very small indications of hydrocarbons can be seen but more apparent is the significant decrease in absorbance

between 500 – 1500 cm^{-1}. This is contrasted by the same absorbances in the region of 3300 –

4000 cm^{-1} and ~1400 cm^{-1} for the three spectra. The concentration of the used H_2SO_4 is stable,

therefore it can be stated that no or only minute amounts of water were created during the

reaction. However, the absorbance of the sulphuric acid in the reaction product is lowered while

the peak position is stable.

When the bituminous reaction product produced at the oil-acid interface is extracted from

that interface contamination of the sample is unavoidable with surrounding H_2SO_4 and oil. To

analyse the real H_2SO_4 content of the black bituminous matter the sample was washed with

water, to neutralise the surrounding H_2SO_4, followed by washing with isopropanol, to remove

excess water and finally by treatment with heptane to remove excess oil and isopropanol. The

washing procedure was followed by drying to evaporate the heptane. Figure 4 compares the

spectrum of a reaction product subjected to the washing process described with the spectrum of

the unwashed reaction product. For comparison of the peak positions, the spectrum of 40 %w/w

H_2SO_4 is included in Figure 4. The massive change in absorbance is apparent but there is also

the very distinct presence of hydrocarbons and H_2SO_4 species. The comparison of change in

absorbance would lead to an underestimation of H_2SO_4 concentration. The close correlation

shown with the peak position of a 40 %w/w solution H_2SO_4 is a more appropriate comparison.

To analyse only the black mater which encapsulates sulphuric acid, the extracted bitumen was

washed with water to neutralize surrounding H_2SO_4 and dissolved in Hexane. The more dense

sulphuric acid settles and the dissolved bitumen can be extracted and analysed after evaporating

the Hexane. The results are also shown in Figure 4. The analysis reveals a sulphonated

hydrocarbon. The sulphur containing species correlate well with a acid concentration of

40 %w/w which is the critical acid concentration for bitumen formation found in a previous

study (Sautermeister et al., 2012).

From the results of Figure 3 and Figure 4, attention is drawn to the upper four graphs of Figure

1 corresponding to the peak positions as a function of acid concentration, the values are also

given in Table 1. This information can be used to estimate acid concentrations when the acid is

contaminated or trapped within a hydrocarbon. The assignment of peak position to species was

used as given in the literature (Nakayama et al., 1999), (Nash et al., 2001), (Bethell et al., 1953),

(Elzinga et al., 2001), (Grdadolnik, 2001), (Faguy et al., 1996).
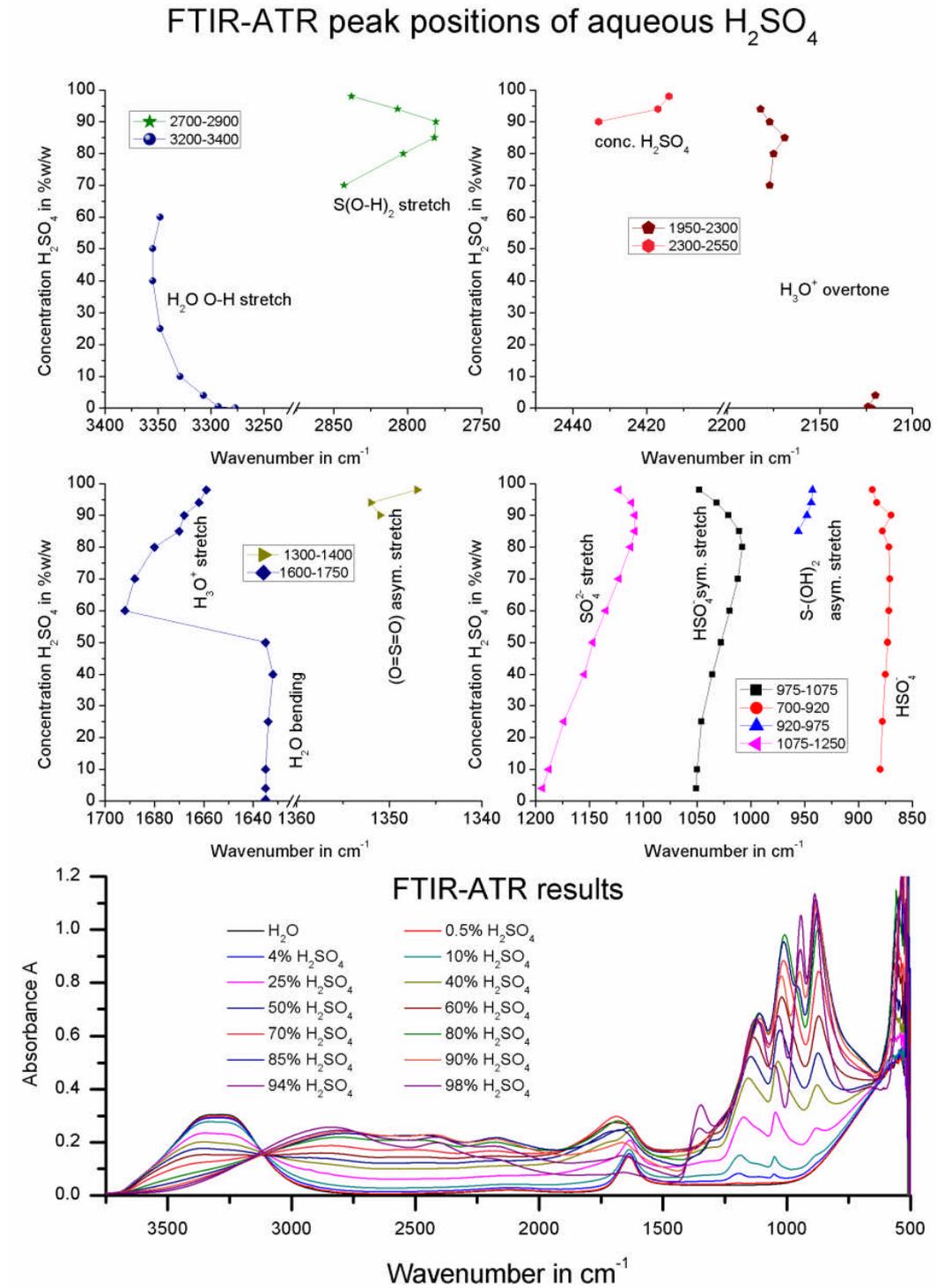
Figure 1: FTIR-ATR peak position of aqueous H₂SO₄ of various concentrations.

Under review by "Industrial Lubrication and Tribology"

Table 1: FTIR-ATR peak position and absorbance of aqueous H$_2$SO$_4$ of various concentrations.

H$_2$SO$_4$ conc.	%w/w	0	0.5	4	10	25	40	50	60	70	80	85	90	94	98
HSO$_4^-$	cm^{-1}				880	878	875	873	842	871	872	878	870	883	887
	A				0.153	0.235	0.4164	0.5374	0.6738	0.843	1.0006	1.0535	1.0956	1.1168	1.1356
S-(OH)$_2$	cm^{-1}											956	948	944	943
asymetric stretch	A											0.7852	0.843	0.9247	1.0546
HSO$_4^-$	cm^{-1}			1051	1050	1046	1036	1028	1020	1012	1008	1011	1021	1032	1048
symetric stretch	A			0.0802	0.1459	0.3141	0.5056	0.6228	0.746	0.8833	0.9813	0.9544	0.8248	0.6741	0.4888
SO$_4^{2-}$ stretch	cm^{-1}			1194	1188	1174	1155	1147	1135	1123	1112	1108	1108	1111	1123
	A			0.0825	0.1517	0.2946	0.4427	0.5237	0.5956	0.6575	0.6851	0.683	0.665	0.6525	0.6641
(O=S=O)	cm^{-1}												1351	1352	1347
asymetric strech	A												0.1918	0.2531	0.3408
H$_2$O bending	cm^{-1}	1635	1635	1635	1635	1634	1632	1635	1692	1688	1680	1670	1668	1662	1659
& H$_3$O$^+$ stretch	A	0.1458	0.1477	0.1573	0.1729	0.2078	0.2433	0.2571	0.2755	0.2975	0.2808	0.2468	0.1992	0.15	0.087
H$_3$O$^+$ overtone	cm^{-1}	2122	2124	2120						2177	2175	2169	2177	2182	
	A	0.0204	0.0221	0.0288						0.1682	0.2007	0.2181	0.2119	0.1865	
H$_2$SO$_4$	cm^{-1}												2433	2417	2414
	A												0.2292	0.2198	0.1986
S(O-H)$_2$ stretch	cm^{-1}								2880	2843	2803	2782	2781	2807	2838
	A								0.16	0.1878	0.2194	0.2338	0.2408	0.2453	0.2575
H$_2$O O-H stretch	cm^{-1}	3277	3293	3307	3329	3348	3355	3355	3348						
	A	0.3049	0.2979	0.2925	0.2775	0.2353	0.2017	0.1774	0.1537						
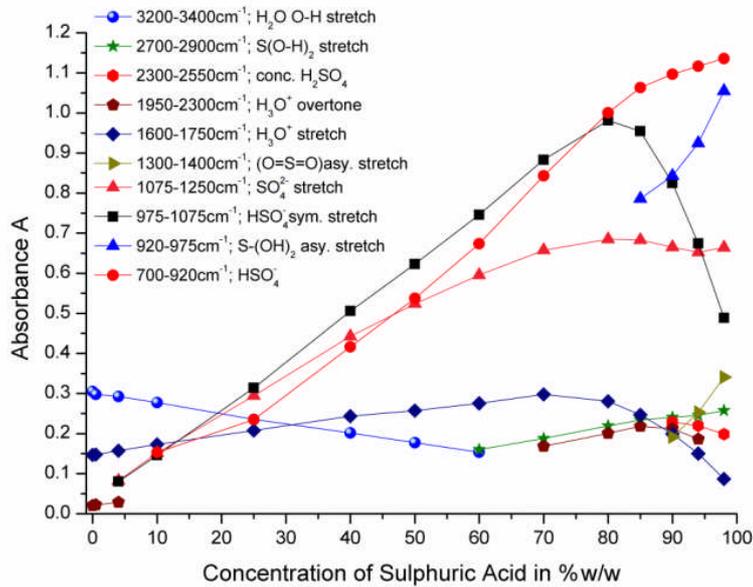
Figure 2: FTIR-ATR absorbance in correlation to the concentration of H$_2$SO$_4$
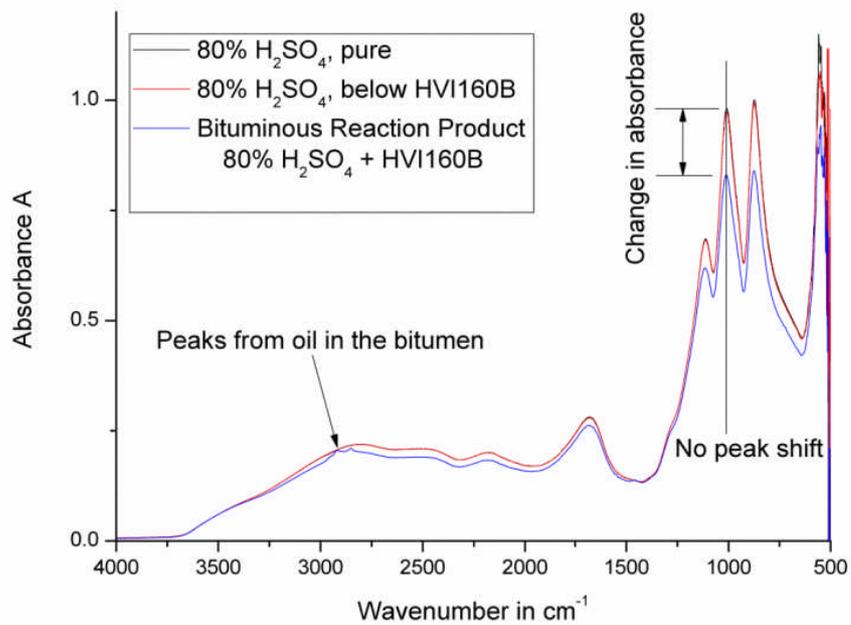
Figure 3: FTIR-ATR absorbance spectra of pure 80% H$_2$SO$_4$, remaining acid used in the reaction and the reaction product
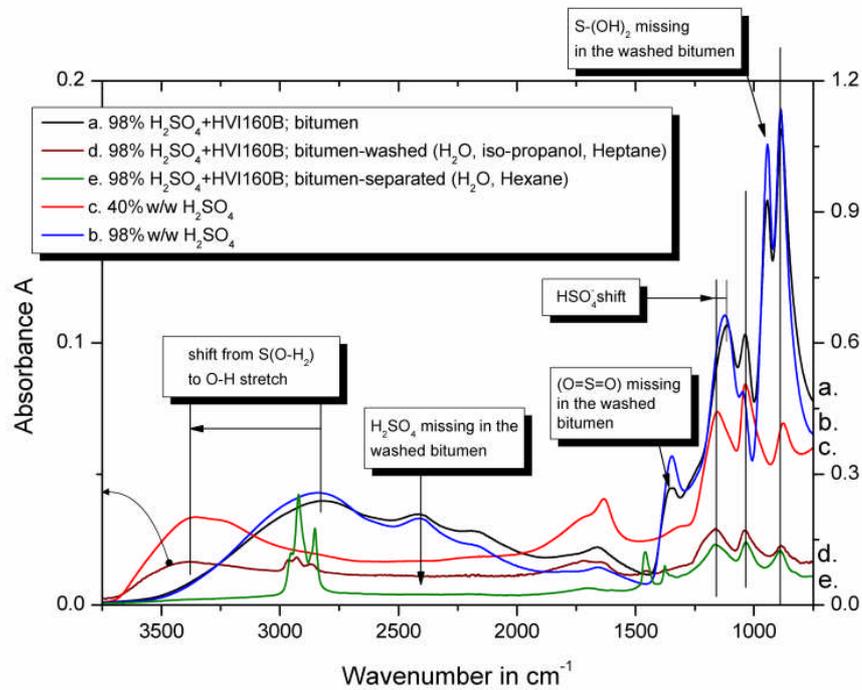
Figure 4: FTIR-ATR absorbance spectra of bituminous reaction product (a.), solvent washed bituminous reaction product (d.), solvent separated bituminous reaction product (e.) and pure 40 %w/w and 98 %w/w H$_2$SO$_4$ (c. and b.).

Conclusions

Mixing hydrocarbons with H$_2$SO$_4$ causes a chemical interaction yielding bituminous mater in the form of emulsions. An unproportional change in absorbance is observed in the infrared spectra of the acidic components compared to pure H$_2$SO$_4$. The concentration-dependent peak positions of H$_2$SO$_4$ species, however, remains unaltered when the reaction product is not freed from surrounding acid contaminant. When the surrounding acid is neutralized, the acid related peaks shift to values of enclosed remaining acid. Therefore the peak positions of the H$_2$SO$_4$ species can be used to evaluate the concentration of H$_2$SO$_4$ in the mixture.

This work is part of piston ring lubrication study for large 2-stoke marine diesel engines using high sulphur fuel levels. At present the FTIR-ATR technique has only been used in the

9

laboratory but it is possible to consider an in-situ test where the acid peak positions would give in-situ and correct measurement of the condensed H_2SO_4 concentration in the oil film. A scan of only a small infrared bandwidth would be sufficient, greatly decreasing processing time compared to a full screen.

Acknowledgements

References

Bellamy, M.K. (2010), "Using FTIR-ATR Spectroscopy To Teach the Internal Standard Method", *Journal of Chemical Education*, Vol. 87, pp. 1399-1401.

Bethell, D.E., Sheppard, N. (1953), "The Infrared Spectrum of the H_3O^+ ion in Acid Hydrates", *The Journal of Chemical Physics*, Vol. 21, p. 1421.

Elzinga, E.J., Peak, D., Sparks, D.L. (2001), "Spectroscopic Studies of Pb(II)-sulfate Interactions at the Geothite-Water Interface", *Elsevier Science Ltd.*, Vol. 65, pp. 2219-2230

Faguy, P.W., Marinkovic, N.S. (1996), "An In-Situ Infrared Study on the Effect of pH on Anion Adsorption at Pt(111) Electrodes from Acid Sulfate Solutions", *Langmuir*, Vol. 12, pp. 243-247.

Grdadolnik, J. (2001), "ATR-FTIR Spectroscopy: Its Advantages and Limitation", *Acta Chim. Slov.*, Vol. 49, pp. 631-642.

Masuda, K., Haramaki, T., Nakashima, S., Habert, B., Martinez, I., Kashiwabara, S. (2003), "Structural Change of Water with Solutes and Temperature up to 100°C in Aqueous Solutions as Revealed by Attenuated Total Reflectance Infrared Spectroscopy", *Applied Spectroscopy*, Vol. 57, pp. 274-281.

Nakayama, M., Saeki, S., Ogura, K. T. (1999), "In Situ Observation of Electrochemical Formation and Degradation Processes of Polyaniline by Fourier-Transform Infrared Spectroscopy", *The Japan Society for Analytical Chemistry*, Vol. 15, pp. 259-263.

Nash, K.L., Sully, K.J., Horn, A.B. (2001), "Observation on the Interpretation and Analysis of

Under review by "Industrial Lubrication and Tribology"

Sulfuric Acid Hydrate Infrared Spectra", *Journal of Physical Chemistry*, Vol. 105, pp. 9422-9426.

Palmer, K.F. and Williams, D. (1975), "Optical Constants of Sulfuric Acid; Application to the Clouds of Venus?", *Applied Optics*, Vol. 14, pp. 208-219.

PerkinElmer, Inc. (2005), "FT-IR Spectroscopy Attenuated Total Reflectance (ATR)". Shelton : PerkinElmer, Inc., Product Brochure.

Sautermeister, F.A., Priest, M.; Fox, M.F., Lee, P. M. (2012), "Impact of Sulphuric Acid on Cylinder Lubrication for Large 2-Stroke Marine Diesel Engines: Contact Angle, Interfacial Tension and Chemical Interaction", *Tribology International*, online DOI: 10.1016/j.triboint.2012.06.002. *38th Leeds-Lyon Symposium on Tribology.*

Sautermeister, F.A., Priest, M. (2012), "Physical and Chemical Impact of Sulphuric Acid on Cylinder Lubrication for Large 2-Stroke Marine Diesel Engines", *Tribology Letters*, Vol. 47, Issue 2, pp. 261-271. *Tribology - Industrial and Automotive Lubrication, Esslingen, 2012*

Sherman Hsu, C. P. (1997) "Chapter 15: Infrared Spectroscopy", Settle, F., *Handbook of Instrumental Techniques for Analytical Chemistry*, Prentice Hall, Upper Saddle River, NJ, pp. 247-283.

Walrafen, G. E. (1970), 'Raman Spectral Studies of the Effects of Perchlorate Ion on Water Structure'. *The Journal of Chemical Physics*, Vol. 52, pp. 4176-4198.

Walrafen, G. E. (1971), 'Raman Spectral Studies of the Effects of Solutes and Pressure on Water Structure', *The Journal of Chemical Physics*, Vol. 55, pp. 768-792.

Young, T. F., Maranville, L. F. and Smith, H. M. (1959), "Raman Spectral Investigations of Ionic Equilibria in Solutions of Strong Electrolytes." Hamer, W. J., *The Structure of Electrolytic Solutions*, John Wiley and Sons, pp. 35-63.